University of Rochester
Laboratory for Laser Energetics

DOE/SF/19460-583
January 2005

# LLE 2004 Annual Report

## October 2003 — September 2004

UR LLE

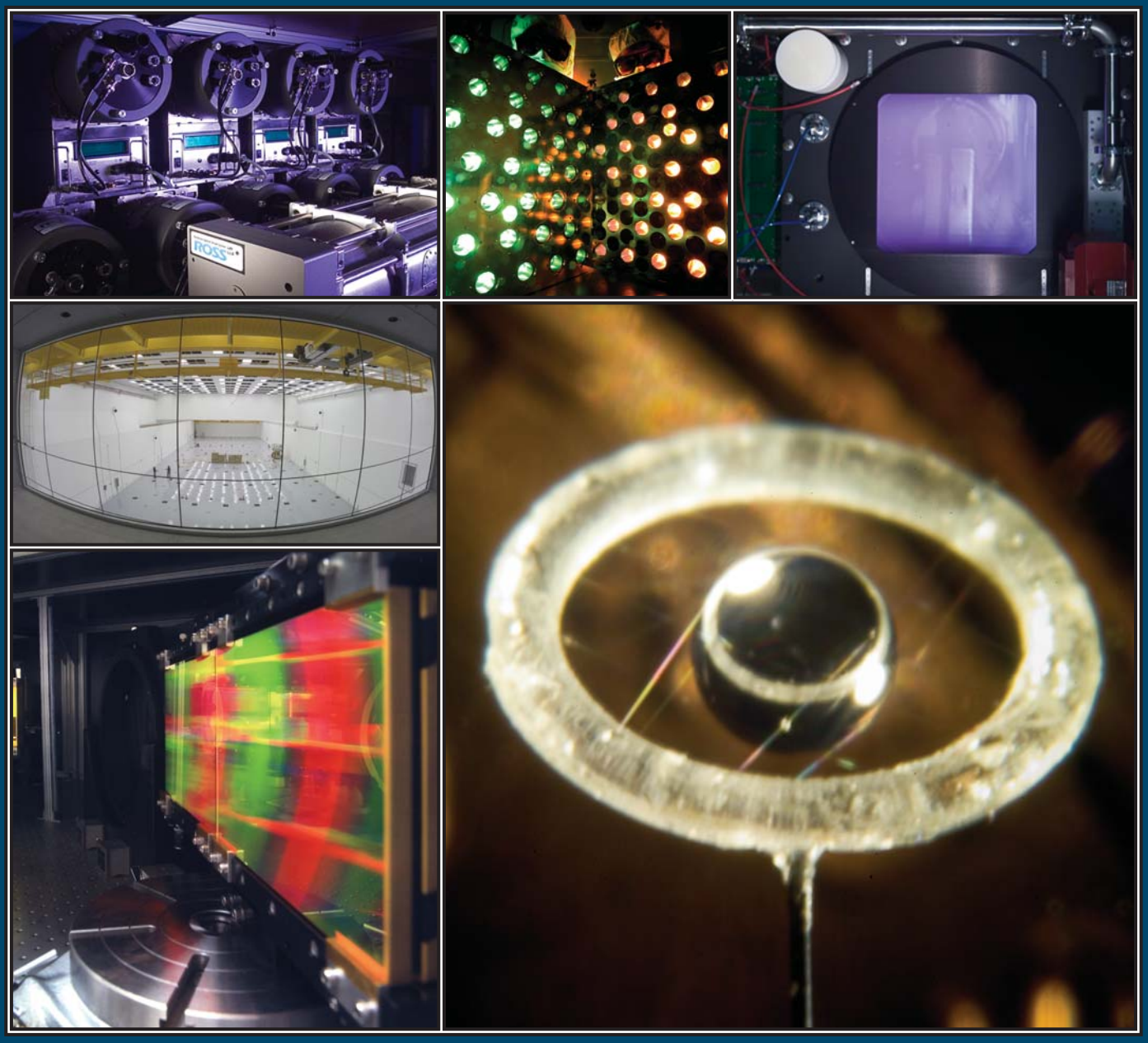

## Cover Photos

Upper Left: Rochester optical streak systems (ROSS's). The ROSS camera is a comprehensive diagnostic system with autofocus and self-calibrating capabilities.

Middle Left: View of the OMEGA EP laser bay from the visitor's gallery of the new OMEGA EP building. The OMEGA EP building construction was completed in December 2004. Completion of the laser facility is scheduled to occur in 2007.

Lower Left: Tiled-grating assembly of three gratings being developed for use on OMEGA EP. The diffracted fields from the three gratings are coherently added so that they behave as one larger monolithic grating.

Upper Center: Two NIF deformable mirror (DM) assemblies undergoing fabrication and testing at LLE. The NIF DM's are all being coated and assembled at LLE.

Upper Right: A single-aperture plasma-electrode Pockels cell (PEPC) under test. The 40-cm-aperture PEPC is similar in requirements to the NIF PEPC. Four of these units will be used on OMEGA EP.

Lower Right: Photograph of the "Saturn" target, one of the polar-direct-drive (PDD) options being investigated as a potential direct-drive-ignition configuration for the NIF.

Prepared for
U.S. Department of Energy
San Francisco Operations Office
DOE/SF/19460-583

Distribution Category UC712
October 2003–September 2004

Printed in the United States of America
Available from
National Technical Information Services
U.S. Department of Commerce
5285 Port Royal Road
Springfield, VA 22161

Price codes: Printed Copy A11
Microfiche A01



The work described in this volume includes current research at the Laboratory for Laser Energetics, which is supported by New York State Energy Research and Development Authority, the University of Rochester, the U.S. Department of Energy Office of Inertial Confinement Fusion under Cooperative Agreement No. DE-FC03-92SF19460, and other agencies.

For questions or comments, contact Laboratory for Laser Energetics, 250 East River Road, Rochester, NY 14623-1299, (585) 275-5286.
Worldwide-Web Home Page: http://www.lle.rochester.edu/

University of Rochester
Laboratory for Laser Energetics

DOE/SF/19460-583
January 2005

# LLE 2004 Annual Report


## October 2003 – September 2004

## Inertial Fusion Program and National Laser Users' Facility Program

# Contents

# Executive Summary

The fiscal year ending September 2004 concluded the second year of the second five-year renewal of the cooperative agreement DE-FC03-92SF19460 with the U.S. Department of Energy (DOE). This report summarizes research at the Laboratory for Laser Energetics (LLE) conducted during the year, operation of the National Laser Users' Facility (NLUF), a status report of the new OMEGA Extended Performance (EP) laser project, and programs concerning the education of high school, undergraduate, and graduate students during the year.

**Progress in Laser Fusion Research**

1. OMEGA Direct-Drive Experiments

Layered and characterized cryogenic $D_2$ capsules have been imploded using high-contrast pulse shapes on the 60-beam OMEGA laser at the Laboratory for Laser Energetics. These experiments (p. 1) measure the sensitivity of the direct-drive implosion performance to parameters such as the inner-ice-surface roughness, the adiabat of the fuel during the implosion, and the laser power balance. The goal is to demonstrate a high neutron-averaged fuel $\rho R$ with low angular variance using a scaled $\alpha \sim 3$ ignition pulse shape driving a scaled all-DT ignition capsule. Results are reported with improvements over previous experiments in target layering and characterization and in laser pointing and target positioning on the OMEGA laser. These capsules have been imploded using up to 23 kJ of 351-nm laser light with an on-target energy imbalance of less than 2% rms, full beam smoothing (1-THz bandwidth, 2-D SSD, and polarization smoothing), and new, optimized, distributed phase plates. Pulse shapes include high-adiabat ($\alpha \sim 25$) square pulses and low-adiabat ($\alpha < 5$) shaped pulses. The data from neutron and charged-particle diagnostics, as well as static and time-resolved x-ray images of the imploding core, are compared with 1-D and 2-D numerical simulations. Scaling of target performance to a weighted quadrature of inner ice roughness at the end of the acceleration phase is investigated.

We have characterized the compressed-core, temperature-density profiles of a cryogenic deuterium ($D_2$) target using measured primary deuterium–deuterium (DD) and secondary deuterium–tritium (DT) yields, neutron-averaged ion temperature, and x-ray images at peak neutron production, and to infer the electron pressure and the areal density of the neutron production region to be 2.7±0.4 Gbar and ~10 mg/cm$^2$, respectively.

"Performance of 1-THz-Bandwidth, 2-D Smoothing by Spectral Dispersion and Polarization Smoothing of High-Power, Solid-State Laser Beams" (p. 49) discusses the laser-beam smoothing achieved with 1-THz-bandwidth, two-dimensional smoothing by spectral dispersion and polarization smoothing on the 60-beam, 30-kJ, 351-nm OMEGA laser system. These beam-smoothing techniques are directly applicable to direct-drive ignition target designs for the 192-beam, 1.8-MJ, 351-nm National Ignition Facility. Equivalent-target-plane images for constant-intensity laser pulses of varying duration were used to determine the smoothing. The properties of the phase plates, frequency modulators, and birefringent wedges were simulated and found to be in good agreement with the measurements.

The target areal-density ($\rho R$) asymmetries in OMEGA direct-drive spherical implosions can be inferred experimentally. The rms variation for a low-mode-number structure is approximately proportional to the rms variation of on-target laser intensity with an amplification factor of $\sim 1/2(C_r - 1)$, where $C_r$ is the capsule convergence ratio. This result has critical implications for future work on the National Ignition Facility (NIF) as well as on OMEGA (see p. 67). In related work (p. 122) we investigate models for determining the areal density of hot fuel ($\rho R_{\text{hot}}$) in compressed, $D_2$-filled capsules. Measurements from three classes of direct-drive implosions on OMEGA were combined with Monte Carlo simulations to assess the impact of mix and other factors on the determination of $\rho R_{\text{hot}}$. The results of the Monte Carlo calculations were compared to predictions of simple commonly used models that use ratios of either secondary D$^3$He proton yields or secondary DT neutron yields to primary DD neutron yields to provide estimates of $\rho R_{\text{hot},p}$ or $\rho R_{\text{hot},n}$, respectively, for $\rho R_{\text{hot}}$.

Measurements of the imprint efficiency in 20-$\mu$m-thick plastic foils driven by 351-nm laser light at an intensity ~$2 \times 10^{14}$ W/cm$^2$ are described beginning on p. 90. The measured target spatial modulations were imprinted from spatial laser nonuniformities during laser-ablated plasma formation at the beginning of the drive. The laser modulations consisted of broadband nonuniformities from six beams incident at 23° to the target normal and single-mode perturbations from one beam incident at 48° to the target normal. The measurements were performed at a spatial wavelength of 60 $\mu$m with and without smoothing by spectral dispersion (SSD). The measured imprint efficiencies at 60-$\mu$m spatial wavelength were 2.5±0.2 $\mu$m for the beam with 48° angle of incidence and 3.0±0.3 $\mu$m for the beams with 23° angle of incidence. The SSD reduced modulations by a factor of ~2.5 at the same spatial wavelength.

The article "Multidimensional Simulations of Plastic-Shell Implosions on the OMEGA Laser" (p. 139) describes the application of the multidimensional hydrodynamic code *DRACO* to study shell stability during the acceleration phase in the presence of nonuniform illumination and target roughness. Simulations show that for thick shells remaining integral during the acceleration, the target yield is reduced by a combination of long-wavelength modes due to surface roughness and beam-to-beam imbalance and intermediate modes due to single-beam nonuniformities. Compared to 1-D predictions, the neutron-production rate for these shells truncates. Diminished yield for thin shells is mainly due to shell breakup at short-wavelength scales of the order of the in-flight shell thickness. *DRACO* simulation results are consistent with experimental observations.

2. Diagnostic Techniques

We report on shielding strategies to optimize the signal-to-background ratio and to obtain high-quality x-ray spectra (p. 103). The use of a single-photon–counting x-ray CCD camera as an x-ray spectrometer is a well-established technique in ultra-short-pulse laser experiments. In the single-photon–counting mode, the pixel value of each readout pixel is proportional to the energy deposited from the incident x-ray photon. For photons below 100 keV, a significant fraction of the events deposits all energy in a single pixel. A histogram of the pixel readout values gives a good approximation of the x-ray spectrum. This technique requires almost no alignment, but it is very sensitive to signal-to-background issues, especially in a high-energy petawatt environment.

A comprehensive overview of the methodology and issues involved in the preparation of deuterium-ice layers in OMEGA targets is given beginning on p. 160. The process of first forming and then smoothing the ice layer is governed by multiple parameters that, when optimally controlled, yield ice layers approaching a 1-$\mu$m-rms roughness in low-spatial-frequency modes.

During the year, we have developed and fielded a new, modular x-ray streaked imager that combines a four-mirror Kirkpatrick–Baez microscope with a high-current PJX streak tube (p. 183). The streak tube has been designed for optimum performance at 1.5 keV with better-than-5 $\mu$m spatial resolution over its central 200-$\mu$m field of view.

LLE scientists discuss several prototypes of NIF neutron-time-of-flight detectors developed and tested on OMEGA (p. 202). Based on OMEGA results, these detectors will be able to measure ion temperatures of, and neutron yields from, NIF targets generating between $10^9$ and $10^{19}$ neutrons.

A new method for accurately measuring beam position, shape, and relative intensity of the OMEGA system's 60 beams from CID-recorded, focal-spot x-ray images from 4-mm, Au-coated pointing targets is discussed beginning on p. 252. This method provides pivotal input into efforts to improve target-illumination uniformity by improving beam pointing and reducing variations in beam intensities from average.

3. Theory and Simulation

A brief study was completed on the contribution of the gradients in the laser-induced electric field to the current flow, heat flux, and electric stress tensor in laser-produced plasmas (p. 54). The transport coefficients, previously derived in the limit $Z >> 1$, are obtained for an arbitrary ion charge $Z$. It is shown that the ponderomotive terms significantly modify the thermal transport near the laser turning points and the critical surface.

The ion-fluid and Poisson (IFP) equations with phenomenological damping terms and the light-wave equation are used to describe stimulated Brillouin scattering (SBS) in one- and two-ion plasmas (p. 73). Comparing numerical and analytical results in the linear limit tested the computer code. The code is used to compare effects of Landau damping, pump depletion, and ion-acoustic nonlinearities on the saturation of SBS in one- and two-ion plasmas. In the latter, SBS from fast and slow ion-acoustic waves is considered separately. SBS is

simulated for hydrocarbon (CH) plasmas with parameters typical for experiments on OMEGA.

LLE scientists collaborating with scientists from the Massachusetts Institute of Technology developed an analytical model of the interaction of directed energetic electrons with a high-temperature hydrogenic plasma (p. 97). The randomizing effect of scattering off both plasma ions and electrons is treated from a unified point of view. For electron energies of less than 3 MeV, electron scattering is equally important. The net effect of multiple scattering is to reduce the penetration from 0.54 to 0.41 g/cm$^2$ for 1-MeV electrons in a 300-g/cm$^3$ plasma at 5 keV. These considerations are relevant to "fast ignition" and to fuel preheat for inertial confinement fusion.

The theory of the adiabat profile induced by a strong shock propagating through a relaxed density profile in inertial confinement fusion (ICF) capsules is described in the article beginning on p. 106. The relaxed profile is produced through a laser prepulse, while the foot of the main laser pulse drives the adiabat-shaping shock. The adiabat shape is calculated for the cases of intense, short prepulses and weak, long prepulses. The theoretical adiabat profiles accurately reproduce the simulation results to within a few-percent error. ICF capsules with a shaped adiabat are expected to benefit from improved hydrodynamic stability while maintaining the same one-dimensional performances as constant-adiabat shells.

Wetted foams are of great interest in improving the gain by increasing the absorption in ignition-scale targets. Aspects of the hydrodynamic behavior of foams are discussed in the article "Shock Propagation in Deuterium–Tritium–Saturated Foam" (p. 227). Testing the assumption of homogeneous mixing in fibrous foams saturated with cryogenic deuterium and tritium, shock passage in wetted-foam mixtures was simulated by the adaptive-mesh, two-dimensional hydrodynamic code *AstroBEAR*. For foam fibers of ~1/10-$\mu$m diameter and relevant foam densities, the mixing length behind the shock is found to be of the order of microns. Transverse motion dampens out sufficiently that, at the mixing region's edge farthest from the shock, Rankine–Hugoniot jump conditions are obeyed to within a few percent and shock speeds are also within a few percent of their homogeneous values. In addition, questions of feedthrough and feedout are addressed, showing that the stability of the shock front, once it leaves the wetted-foam layer, minimizes the effect of feedthrough. As a result, simulations of whole-foam-pellet implosions may model the wetted foam as a homogeneous mixture.

4. High-Energy-Density Physics

Scientists at LLE and a number of institutions have collaborated on an experiment that uses a laser-source–based, extended x-ray absorption fine structure (EXAFS) measurement to study the properties of laser-shocked metals on a nanosecond time scale (p. 16). The ability to measure shock-induced temperatures of the order of 0.1 eV is essentially unique to EXAFS. EXAFS measurements of vanadium shocked to ~0.5 Mbar with a 3-ns laser pulse yield a compression and temperature in good agreement with hydrodynamic simulations and shock-speed measurements. In laser-shocked titanium at the same pressure, the EXAFS modulation damping is much higher than warranted by the increase in temperature. This is explained by the $\alpha$-Ti to $\omega$-Ti phase transformation known to occur around ~0.1 Mbar in the longer ($\mu$s) shocks obtained in gas-gun experiments. In the $\omega$-Ti phase, the disparate neighbor distances cause a beating of the modulation frequencies and thus an increased damping. These results demonstrate that EXAFS measurements can be used for the study of nanosecond-scale shocks and phase transformations in metals.

**Lasers, Optical Materials, and Advanced Technology**

An ytterbium fiber laser mode-locked at its 280th harmonic, which corresponds to a repetition rate greater than 10 GHz, has been demonstrated (p. 36). The laser produces linearly polarized, 2.6-ps chirped pulses with up to 38 mW of average output power. The mode-locked pulses are tunable over a 55-nm window centered on 1053 nm.

We have conducted a series of microgrinding and polishing experiments on glass-ceramics (p. 40). Microgrinding includes deterministic microgrinding (fixed infeed rate) and loose-abrasive lapping (fixed pressure). Material mechanical properties (Young's modulus, hardness, fracture toughness) and chemical properties (chemical susceptibility, or mass loss under chemical attack) are correlated with the quality of the resulting surface (surface microroughness and surface grinding–induced residual stresses). Deterministic microgrinding (at fixed infeed) and loose-abrasive microgrinding (at fixed pressure) are compared in terms of material removal rates and resulting surface quality.

We have demonstrated a technique to improve laser power-amplifier performance through compensating laser-rod bulk inhomogeneities by magnetorheological single-surface wavefront correction (p. 194). Large-aperture rods corrected in this manner render nearly diffraction limited output-beam performance.

The chemical durability of water-sensitive phosphate laser glass to different polishing and cleaning conditions has been examined (p. 257). We find the absence of an unambiguous correlation between initial finished surface quality of any glass type tested and quantifiable magnitude of humidity-driven degradation, whereas subsequent aqueous cleaning does increase haze: more so for pitch and pad–finished surfaces than for MRF-processed ones.

We provide an update on the OMEGA EP tiled-grating-compressor technology (p. 242). For the first time, real-time, computer-controlled phasing of a grating triplet, using interferometric feedback via nanopositioners, has been demonstrated and a transform-limited far-field spot achieved.

We have tested metal–semiconductor–metal ultraviolet photodiodes fabricated on GaN in the picosecond regime with an electro-optic sampling system (p. 25). The best performance of a device with a feature size of 1 $\mu$m showed a 1.4-ps rise time and 3.5-ps full width at half maximum, which represents the fastest ultraviolet GaN photodiode reported to date. The derived electron velocity in GaN was in good agreement with an independent photoexcitation measurement. A comparison with Monte Carlo simulation was made, and slower impulse response observed in a device with a smaller feature size of 0.5 $\mu$m was discussed. In related work we introduce a submicron-scale ultraviolet photodiode based on a metal–semiconductor–metal structure on GaN (p. 212). The authors built, tested, and then simulated the circuit by a distributed-circuit approach that yielded close agreement between theory and observation of the impulse-response, space-charge-screening broadening found in the device.

Photonic crystals offer great promise in a variety of applications in optoelectronics, from lasers to the creation of all-optical circuits for computing (p. 25). The research project focused on the creation of novel photonic crystals through the self-assembly of core-shell structured colloidal particles. Layer-by-layer electrostatic self-assembly was used to deposit polyelectrolyte shells around spherical colloidal particles. By exploiting electrostatic attraction, shells of controllable thickness were formed by alternating the deposition of positive- and negative-charged polyelectrolytes. The coated colloidal particles were deposited as thin films of hexagonally close-packed crystals onto glass slides. The crystalline films display a partial photonic band gap and preferentially reflect light of a wavelength dependent on the size of the particles making up the crystal. The chemical functional groups in the shell surrounding the colloidal particles offer a potential route to immobilize optically active species in the shell to enhance the photonic band gap of the crystal.

Ultrafast current sensing has reached a new level of sensitivity and speed by taking advantage of the magneto-optic Faraday effect in CdMnTe single crystals (p. 208). To date, response times of a few hundred femtoseconds can be realized at a current sensitivity of ~0.1 mA at 10 K.

A new method for patterning nanoparticles and self-assembled monolayers through the use of elastomeric stamps and their controlled deformation by overpressure has been developed (p. 218). The method enables pattern formation on a scale length up to an order of magnitude smaller than the original stamps as well as patterns that do not exist in the original masters. As one example, magnetic ring and anti-ring structures are being fabricated for memory-device applications.

Single-walled carbon nanotubes have been analyzed at a spatial resolution of 10 to 20 nm by employing near-field Raman imaging and spectroscopy (p. 269). For individual, isolated carbon nanotubes, they find a nonuniform distribution of Raman bands along the tube axis.

An ac-stabilizing field has been used to control the orientation and motion of polymer cholesteric-liquid-crystal flakes suspended in a host fluid (p. 274). With a display application in mind, the authors show that the field acts on an induced dipole moment on the flake surface due to interfacial Maxwell–Wagner polarization.

**Status and Progress on OMEGA EP**

The OMEGA EP (Extended Performance) project completed the majority of the preliminary design phase and moved into the project execution phase during FY04. Starting in FY03 with $13 million in funding, the project continued with $20 million in FY04 funding. Concomitantly, NNSA project authorizations in FY04 included the approval of the Performance Baseline (Critical Decision 2) and approval to Start Construction (Critical Decision 3). Many acquisitions were started in FY04, and some of the materials will be stored until the building is completed in the second quarter of FY05.

The OMEGA EP laser will be housed in a new facility adjacent to the OMEGA facility. The building, under construction throughout FY04, was funded entirely by the University of Rochester. When completed, it will provide the required stable optical platform, 262 feet long by 82 feet wide, within a clean-room envelope. The 82,000-sq-ft facility will also house

ancillary laboratories for construction and operation of the laser. The building construction exterior masonry, windows, loading docks, curbing, and grading were all completed in FY04. Interior work highlights for FY04 include the single-pour, 2000-cu-yd (~8 million lbs) concrete slab to support the laser, installation of the clean-room equipment, installation and certification of the two overhead 10-ton cranes for the laser and target areas, and installation of the laser system infrastructure such as the electrical subsystems, cooling water, and vacuum piping.

The goals of the project did not change in FY04. Principal to the mission is to provide OMEGA with a short-pulse, high-energy backlighting capability for new high-energy-density physics experiments under conditions that also allow the development of backlighting techniques for the NIF. Additionally, the EP laser will provide the capability to carry out integrated fast-ignition experiments on OMEGA using OMEGA's unique cryogenic target implosion capability. Two short-pulse (1- to 100-ps), high-power, high-energy beams will be provided to meet the mission-need requirements. These two beamlines will be completed and coupled to the OMEGA laser by the end of FY07. The OMEGA EP system will have a separate auxiliary target chamber funded through a grant from New York State that will be used during laser start-up and ultimately for independent experiments. The two short-pulse beams will use chirped-pulse amplification (CPA) and NIF multipass architecture to provide irradiation to targets in either the OMEGA or OMEGA EP target chambers. Throughout the design and construction phases, an option of building two additional beamlines and an ultraviolet capability has been preserved. At modest incremental cost, the project's two additional beamlines provide the capability to operate all four beams in long-pulse mode (1 to 10 ns).

Six key optical technologies were identified early in the project as critical to the success of the project. These elements and highlights of FY04 progress mirror the overall progress of the project. These six elements range from leveraging and expanding existing LLE capabilities to adaptation of NIF technology for OMEGA EP requirements:

1. A CPA laser source capable of seeding a NIF-like beamline and greater than 250 mJ at 5 Hz for pre-shot setup. In FY04 the energy, repetition rate, and temporal and spectral characteristics required were demonstrated on a full-scale prototype laser developed at LLE (p. 194). Amplification by optical parametric chirped-pulse amplification (OPCPA) was optimized for the OMEGA EP requirements by tuning the laser pump system. A technique for magnetorheological finishing (MRF) of large-aperture, 1-in.-diam Nd:YLF crystal amplifier rods was developed for the pump laser and transferred to the manufacturer for production.

2. A single-aperture plasma electrode Pockels cell (PEPC), with requirements similar to the NIF PEPC. An LLE-engineered PEPC was manufactured, assembled, and coupled to NIF-like, high-voltage pulsers. Integrated plasma testing started in FY04 in a purpose-built laboratory that will be used to characterize spatially and temporally resolved contrast.

3. An LLE-style amplifier that utilizes a 40-cm-square-aperture laser disk. A prototype amplifier designed, manufactured, and assembled in FY03 was tested in FY04 with over 1000 shots in a spatially and temporally resolved wavefront and small-signal-gain instrument. The performance requirements were met, and production of 36 amplifiers was initiated.

4. Adaptation of the NIF-design deformable mirror (DM) to the OMEGA EP system including wavefront sensing and LLE-developed feedback controls. In FY04 LLE implemented wavefront sensing and mirror control hardware and software that enabled setting the DM to the required wavefront for compensating expected errors from the beamline and compressor systems.

5. High-damage-threshold, large-area, multiplayer dielectric diffraction gratings. LLE played a strong role using unique damage-testing capabilities at 10 ps to aid suppliers in identifying and mitigating processing issues that cause damage to fall below intrinsically possible thresholds. In FY04 the damage thresholds required for greater-than-2-kJ-per-beam operation were demonstrated on sub-aperture samples, and orders were placed with two suppliers for a total of 16 grating tiles.

6. Grating tiling to coherently add the diffracted fields from three gratings so that they behave as one larger monolithic grating (p. 242). A reduced-scale tiled grating compressor and closed-loop control system was demonstrated at LLE. The closed-loop tiling system used interferometric feedback to position grating tiles. Full-scale tiled grating assemblies were designed in FY04 along with a test stand that will validate the production design performance in FY05.

**National Laser Users' Facility and External Users' Programs**

FY04 was a record year for external user experiments on OMEGA. As reported in the FY04 Laser Facility Report beginning on p. 286, a total of 802 target shots were taken on OMEGA for external users' experiments, accounting for 51.5% of the total OMEGA shots produced this year. External users in FY04 included eight collaborative teams under the National Laser Users' Facility (NLUF) program as well as collaborations led by scientists from the Lawrence Livermore National Laboratory (LLNL), Los Alamos National Laboratory (LANL), Sandia National Laboratory (SNL), Naval Research Laboratory (NRL), and the Commissariat à l'Énergie Atomique (CEA) of France. The number of shots for these external users is shown in the graph below.

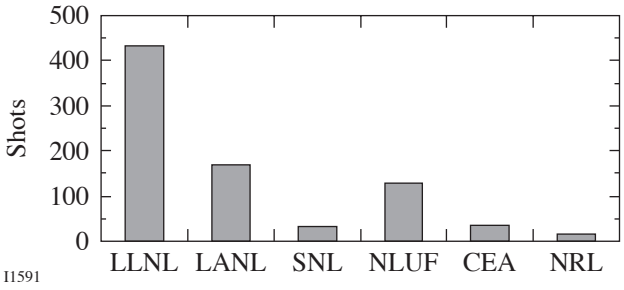


1. NLUF Programs

The fiscal year was the second of a two-year period of performance for the nine NLUF projects approved for FY03–FY04 funding and OMEGA shot time. Eight of the nine NLUF campaigns received a total of 127 shots on OMEGA in FY04.

The Department of Energy (DOE) issued solicitations in FY04 for NLUF proposals for work to be carried out in FY05–FY06. DOE raised the available NLUF funding to $1,000,000 for FY04 proposals to accommodate the high level of interest in using OMEGA to carry out experiments of relevance to the National Nuclear Security Agency (NNSA) Stockpile Stewardship Program (SSP).

A total of 16 NLUF proposals were submitted to DOE for consideration for FY05–FY06 support and OMEGA shot allocation. An independent DOE Technical Evaluation Panel reviewed the proposals on 15 June 2004 and recommended that up to 8 of the 16 proposals receive DOE funding and 7 of the 8 teams be approved for shot time on OMEGA in FY05–FY06. The following projects were carried out in FY04:

- *Optical Mixing Controlled Simulated Scattering Instabilities (OMC SSI): Generating Electron Plasma Waves and Ion-Acoustic Waves to Suppress Backscattering Instabilities*
- *Studies of Ion-Acoustic Waves (IAW's) Under Direct-Drive NIF Conditions*
- *Experimental Astrophysics on the OMEGA Laser*
- *Recreating Planetary Core Conditions on OMEGA*
- *Experimental and Modeling Studies of 2-D Core Gradients in OMEGA Implosions*
- *OMEGA Laser Studies of the Interaction of Supernova Blast Waves with Interstellar Clouds*
- *Time Evolution of Capsule* ρR *and Proton Emission Imaging of Core Structure*

2. FY04 LLNL OMEGA Experimental Program

Lawrence Livermore National Laboratory (LLNL) conducted 431 target shots on OMEGA in FY04. Approximately half of the shots were for the High-Energy-Density Science (HEDS) Program, and the other half were for inertial confinement fusion (ICF) experiments. The ICF experiments included gas-filled, cocktail, lined, or foam-filled hohlraums; long-scale-length plasma physics; high-resolution imaging of cores; roughened capsules; and ablator materials studies.

Studies of laser–plasma interaction were done on large-scale-length plasmas created by preheating large gas-filled targets with the main laser. Various experiments, some using a $2\omega$ or $4\omega$ probe beam, were conducted to obtain data on stimulated Raman scattering (SRS), stimulated Brillouin scattering (SBS), and beam propagation as functions of beam-smoothing level. The results show reduced beam spray and backscatter by using increased smoothing on a $2\omega$ probe beam. More crossing-beam power transfer experiments (a form of Brillouin scattering of special interest to the NIF) were performed as a function of polarization state. Thomson scattering was used frequently to measure the electron temperature of these plasmas, while backscattered light (FABS) diagnostics monitored the amount of SBS or SRS. Still other experiments demonstrated the ability to measure the time-resolved spectrum of H- and He-like Ti (5-keV) x rays scattered by free electrons in a hot plasma; careful fits to the data yield temperature and density data. Finally, a hohlraum experiment was

conducted to quantify the amount of laser light that, at early times, is refracted from the hohlraum wall directly onto the implosion capsule.

Continued systematic improvements were made in using target-mounted pinholes to image implosion cores at moderately high (>7-keV) energies. Asymmetric core images were obtained at 87× magnification, demonstrating a method for measuring higher-order (up to 6, possibly 8) mode structure in the hohlraum drive.

A first experiment was conducted to look at the effect of DT-fill tubes on an imploded capsule, using a deposited bump on the capsule as a surrogate for the fill tube.

Building on the work on hot hohlraums (see HEDS below), several implosion experiments were conducted using smaller-than-standard (3/4-size) hohlraums. These represented the highest radiation-driven temperature implosions shot on laser facilities, reaching 275 to 285 eV, and producing symmetric cores. In some experiments, $DHe^3$ supplied by LLE was used as the fuel; $DHe^3$ fusion proton yields and spectra were recorded and analyzed by MIT.

In collaboration with the University of Nevada, Reno (NLUF), multiple pinhole-imaged and spectrally dispersed data were obtained from indirectly driven, Ar-doped fuel implosions.

Finally, several days of experiments were done in collaboration with LANL and LLE, using direct-drive, DT-filled targets, for the purpose of developing neutron diagnostics. These relatively high-yield shots have indicated that significant background will be present for any diagnostics or electronics that are neutron sensitive.

The other half of the LLNL shots was devoted to high-energy-density-science (HEDS)–relevant experiments. These are summarized as follows:

- Hot hohlraum experiments used hohlraums that were as small as possible to create as-high-as-possible radiation environments. Measurements were made on effective radiation temperature, high-energy ("suprathermal") x rays, and laser–target coupling.

- Equation-of-state (EOS) experiments continued on OMEGA in FY04. These involved VISAR measurements of shock propagation times in various materials. Other experiments focused on creating and using an adiabatic (shockless) drive to smoothly ramp up the pressure for EOS measurements of solid (not melted) materials. Finally, experiments done in collaboration with an NLUF investigator used gases that were precompressed in a diamond anvil cell to explore equations of state relevant to the giant planets.

- OMEGA shots were also used to explore various options for obtaining x-ray point backlighters. It is expected this knowledge will be used on future OMEGA and NIF shots.

- A number of shots were devoted to studying alternative approaches to the standard indirect-drive concept of a simple hohlraum with a single-shell capsule. These included "dynamic hohlraums," where a high-*Z* gas is directly driven and compressed and its resulting x rays are used to drive a second, concentric implosion capsule; and "double shells," where the first driven shell collides with an inner shell, resulting in implosion velocity multiplication.

- The radiation flow campaign continued in FY04, focusing on x-ray propagation through low-density foams.

- A series of experiments were conducted to develop appropriate backlighter sources and detectors to measure the opacity of warm materials. The results of this campaign are expected to be used on experiments in FY05.

- LLNL continued a collaboration with LANL and AWE (United Kingdom) on the "Jets" experiments, looking at large-scale hydrodynamic features.

- Finally, shots onto gas-bag targets were conducted with various mid- to high-*Z* gases, in connection with developing x-ray sources.

3. FY04 LANL OMEGA Experimental Programs

Los Alamos National Laboratory (LANL) fielded a wide range of direct-drive-implosion experiments in both spherical and cylindrical geometries during FY04. The primary emphasis of these experiments was to measure mixing in convergent geometries to understand basic hydrodynamic behavior that will help validate our inertial confinement fusion (ICF) codes. Direct measurements of the stability of grainy Be were performed as part of the national effort to characterize ignition-capsule ablator materials. Collaborations with LLNL, LLE, and AWE are an important part of LANL's program on the OMEGA laser at LLE. The Astrophysical Jets experiment and the development of the burn-history diagnostic were continued

with these collaborating institutions. LANL also fielded its first experiments designed specifically as staging experiments for future execution on the NIF. LANL conducted a total of 168 target shots on OMEGA in FY04.

4. FY04 SNL OMEGA PROGRAMS

SNL carried out 31 target shots on the OMEGA laser in FY04 and also participated in several of the campaigns led by other laboratories. The SNL-led campaigns included the following:

- *Modification of a Laser Hohlraum Spectrum via a Mid-Z Wall Liner*
- *The Effectiveness of Mid-Z Dopants in Reducing Preheat in Indirect-Drive ICF Ablator Materials*
- *Long-Pulse Au Hohlraum Wall Albedo Measurements*
- *Tests of a VISAR Time-Resolved Hohlraum Temperature Measurement Technique*

5. FY04 NRL Program

As part of a collaborative effort with NRL, a series of 13 OMEGA target shots were taken to investigate the control of laser imprinting.

The objectives of this experiment were to evaluate the impact of laser imprint under conditions similar to ICF-like reactor implosions and to test the effectiveness of controlling imprint from a high-power glass laser with the use of thin, high-*Z*-layer targets.

6. FY04 CEA Program

A total of 32 target shots led by CEA (Commissariat à l'Énergie Atomique, France) were carried out on OMEGA in FY04. The corresponding four experimental campaigns studied (a) laser–plasma interaction (LPI) in long-scale-length plasmas relevant to NIF/LMJ indirect-drive conditions; (b) irradiation symmetry and x-ray conversion efficiency in empty gold hohlraums; (c) production and optimization of multi-keV x-ray sources (performed on LLNL-owned shots); and (d) hydrodynamic instabilities in planar geometry.

**Education at LLE**

As the only major university participant in the National ICF Program, education continues to be an important mission for the Laboratory. Graduate students are using the world's most powerful ultraviolet laser for fusion research on OMEGA, making significant contributions to LLE's research activities. Twenty faculty from five departments collaborate with LLE's scientists and engineers. Presently 63 graduate students are pursuing graduate degrees at the Laboratory, and LLE is directly funding 45 University of Rochester Ph.D. students through the Horton Fellowship program. The research includes theoretical and experimental plasma physics, high-energy-density physics, x-rays and atomic physics, nuclear fusion, ultrafast optoelectronics, high-power-laser development and applications, nonlinear optics, optical materials and optical fabrications technology, and target fabrication. Technological developments from ongoing Ph.D. research will continue to play an important role on OMEGA.

One hundred sixty-eight students have earned Ph.D. degrees at LLE since its founding. An additional 14 graduate students, 6 undergraduate students, and 2 postdoctoral and 7 faculty positions from other universities were funded by NLUF grants. The most recent University of Rochester Ph.D. graduates and their thesis titles include the following:

| | |
|---|---|
| Bentley, Sean J. | "*Use of Coherently Prepared Media for Efficient, High-Fidelity Frequency Conversion of Electromagnatic Radiation*" |
| Chen, Deqing | "*Multi-Level Shared State and Application-Specific Coherence Models*" |
| Rencuzogullari, Umit | "*Dynamic Resource Management for Parallel Applications in an Autonomous Cluster of Workstations*" |
| Xu, Ying | "*Optical Studies of Ultrafast Carrier Dynamics in High Temperature Superconductors*" |
| Zhang, Jim | "*Ultrafast Nbn Superconducting Single-Photon Detectors for Non-Invasive CMOS Circuit Testing*" |
| Zheng, Xuemei | "*Ultrafast Characterization of Optoelectronic Devices and Systems*" |
| Bhattacharya, Mishkatul | "*Forbidden Transitions in a Magneto-Optical Trap*" |

Approximately 66 University of Rochester undergraduate students participated in work or research projects at LLE this past year. Student projects include operational maintenance of the OMEGA laser system; work in laser development, materials, and optical-thin-film coating laboratories; and programming, image processing, and diagnostic development. This is a unique opportunity for students, many of whom will go on to pursue a higher degree in the area in which they gained experience at the Laboratory.

In addition, LLE directly funds research programs within the MIT Plasma Science and Fusion Center, the State University of New York (SUNY) at Geneseo, and the University of Wisconsin. These programs involve a total of approximately 5 graduate students, 13 undergraduate students, and 3 faculty from other universities.

For the past 16 years LLE has run a Summer High School Student Research Program (p. 282). This year 16 high school juniors spent eight weeks performing individual research projects. A staff scientist or an engineer individually supervises each student. At the conclusion of the program, the students make final oral and written presentations on their work. The reports are published as an LLE report.

In 2004, LLE presented its seventh William D. Ryan Inspirational Teacher Award to Mr. Claude Meyers, a former Physics Teacher at Greece Arcadia High School. Alumni of our Summer High School Student Research Program were asked to nominate teachers who had a major role in sparking their interest in science, mathematics, and/or technology. This award, which includes a $1000 cash prize, was presented at the High School Student Summer Research Symposium. David Bowen, a participant in the 2001 Summer Program, nominated Mr. Meyers.

**Robert L. McCrory**
*Director and CEO*

# Direct-Drive Cryogenic Target Implosion Performance on OMEGA

## Introduction

Direct-drive, cryogenic inertial confinement fusion (ICF) capsule implosion experiments under investigation using the 30-kJ OMEGA laser system[1] at LLE will validate the scaled-ignition performance of low-adiabat, cryogenic DT capsules. This validation is pivotal in the development of direct-drive ignition target designs for the 1.6-MJ National Ignition Facility[2] (NIF), currently under construction at the Lawrence Livermore National Laboratory. The physical limitations of the target fabrication and laser subsystems on the NIF, however, place restrictions on the robustness of ICF ignition designs. Demonstrating the viability of the ignition designs driven under a variety of perturbation scenarios is critical to the success of direct-drive ICF.

Target designers have, in the past, had to trade target performance (thermonuclear gain) for increased target stability.[3] Many studies have been undertaken to examine the minimum laser energy required to achieve ignition.[4–7] All of these studies have concluded that the minimum energy required for ignition scales as $\sim\alpha^2$, where $\alpha$ is the shell adiabat, defined as the ratio of the local pressure to the Fermi-degenerate pressure. As the compressibility of the fuel is increased ($\alpha$ decreased), less laser energy is required to achieve ignition; however, more-compressible fuel develops thinner fuel layers during the implosion, resulting in reduced stability and, potentially, layer failure. As the nonuniformity levels are reduced, it becomes possible to field targets with lower fuel adiabat, examining regions of higher target gain for fixed laser energy. Eventually, targets with a fuel adiabat approaching $\alpha = 1$ will be used in direct-drive ignition.

The cryogenic implosion campaign at LLE is a staged program comprised of several concurrent efforts including experimental validation of target performance for progressively lower fuel adiabat target designs employing cryogenic $D_2$ fuel; physical minimization of the interfacial cryogenic surface roughness; and ultimately the implosion of cryogenic DT targets on the OMEGA laser system. Recent advances in all three of these efforts have LLE poised to demonstrate scaled-ignition performance with DT on OMEGA by the end of FY05. Significant progress has been made in cryogenic implosion experiments evaluating target performance with high-adiabat solid-$D_2$ and wetted-foam targets and low-adiabat solid-$D_2$ targets. It has been shown that there is good agreement between the experimental observables and the results of two-dimensional *DRACO*[8] simulations for targets imploded near target chamber center (TCC). The use of adiabat shaping[9] has been shown theoretically to lead to increased stability for both the "all-DT" and wetted-foam direct-drive NIF point designs and the corresponding ignition-scaled experiments for OMEGA. Dramatic advances in cryogenic layer characterization and layering over the last year have resulted in the production of sub-2-$\mu$m inner surface ice layers in targets for implosion on OMEGA. The cryogenic DT fill and transfer station (FTS) is currently being qualified and will be DT-charged by the end of this fiscal year. With this system in place, full-scale layering studies of cryogenic DT targets will be undertaken, resulting in the fielding of ignition-scale cryogenic DT experiments on OMEGA.

This article reviews the performance characteristics of recent OMEGA cryogenic implosion experiments and outlines the theoretical basis for new cryogenic experiments that will examine low, $\alpha = 2$ implosions for OMEGA. In the following sections, (1) the experimental setup is presented; (2) results of the implosion experiments are compared with results from one- and two-dimensional (1-D, 2-D) radiation-hydrodynamics simulations; (3) the direct-drive ignition design is optimized for better hydrodynamic stability using a picket prepulse; and (4) the scaling of this design to OMEGA operating conditions is examined. Conclusions are presented in the last section.

## Experimental Setup

1. Laser-System Configuration

Cryogenic capsules were imploded using two pulse shapes: a high-adiabat ($\alpha \sim 25$), 23-kJ, 1-ns square pulse and a low-adiabat ($\alpha \sim 4$), 17-kJ, 2.5-ns shaped pulse. The $\alpha \sim 4$ pulse shape has been scaled from the standard all-DT as shown in

Fig. 97.1. Full beam smoothing techniques were applied to each pulse using distributed phase plates (DPP's),[10] polarization smoothing with distributed polarization rotators (DPR's),[11] and 2-D, single-color-cycle, 1-THz smoothing by spectral dispersion (SSD).[12] Laser power balance was optimized using techniques employing x-ray fluence measurements of standard OMEGA pointing targets.[13] With these techniques the variance of incident energy imbalance among all 60 OMEGA beams is ~2% rms, with a 4- to 5-ps rms mistiming when taken to target.

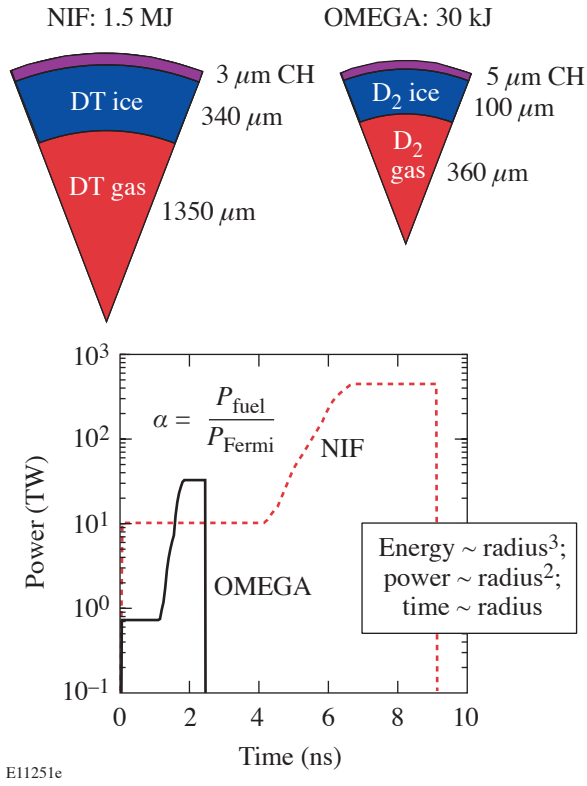


Figure 97.1
The direct-drive NIF point design target is shown with the corresponding OMEGA $\alpha = 4$, energy-scaled capsule. The scaled pulse shapes are given in the inset.

## 2. Capsule Metrology and Layering

Capsules used in these experiments fell into one of two categories: utilizing fuel layers comprised of either solid $D_2$ (SD) or a $D_2$ wetted-foam (WF) layer over a solid $D_2$ layer. The SD target employs a thin, plastic outer shell composed of a "strong GDP" (glow discharge polymer) (a high-strength plastic, $CH_{1.1}$ $\rho \sim 1.20$ g/cc) approximately 4 $\mu$m thick. This shell, nominally 850 $\mu$m in diameter, is permeation filled with $D_2$ to pressures at room temperature in excess of 1000 atm, which, when properly cooled, forms an ice layer of approximately 100 $\mu$m. Layering this surface requires the proper selection of the triple-point isotherm in the capsule, cooling gas pressure, and IR heating laser energy input. Currently a quality layer (<2 $\mu$m rms) requires several days of technician time. Optimization of this effort is being studied. Layer roughness for this study spanned a range of values from 2 to 7 $\mu$m rms.

The WF shell used in these experiments was not optimized for implosion on OMEGA but was part of initial foam–ice layering studies in collaboration with General Atomics. The shell consisted of a 4-$\mu$m CH layer overcoating a 62-$\mu$m foam shell. The foam had a dry density of 120 mg/cc, with fibers consisting of the same GDP mentioned above and an average cell size of less than 1 $\mu$m. This shell underwent the same permeation fueling as the standard SD cryogenic target, which resulted in an inner ice layer estimated to be 65 $\mu$m in depth. Accurate knowledge of the wetted-foam density and the resultant ice-layer thickness depends on the modeling of the freezing of the liquid $D_2$ fuel within the foam matrix. For this experiment it was assumed that the foam, as it was cooled, became impermeable to the liquid $D_2$, preventing any diffusion of liquid $D_2$ in or out of the foam matrix. Conserving mass, the wetted-foam density remains constant (~240 mg/cc) as densification proceeds.

While characterization of WF targets remains an issue due to significant diffraction of the incident probe light, the SD targets are characterized with white-light shadowgraphy similar to that first proposed and implemented by Koch.[14] The shadowgraphy technique produces a wealth of experimental signal represented by a series of rings in the target image plane. Recent analysis[15] has identified the source of the faint trace rings and confirmed the validity of the "bright ring" as the primary carrier of information about the interfacial ice roughness. After processing the information for a particular target orientation, the target is rotated about its polar axis and another sample is taken and processed. Such information can then be interpolated and processed to give a full, 3-D representation of the inner ice surface. The number of experimentally obtained traces, as was pointed out by Stephens,[16] limits the spatial scale of this representation. OMEGA capsules undergo a minimum of 20 roughness scans, which describe the amplitude and nature of the first ten spherical harmonics. Complete spectral decomposition of the ice surface would require more than a hundred angular samples.

3. Target Positioning

Sangster[17] reported the early problems with positioning cryogenic targets in the center of the OMEGA target chamber. At the heart of this problem was static mis-positioning due to image distortion through the shroud windows and dynamic mis-positioning due to target vibration. The static mis-positioning was corrected with careful and detailed procedures comparing and documenting the position of surrogate targets as viewed through the shroud windows and their true position after the shroud was retracted. Each of the four moving cryogenic transfer carts (MCTC's) was examined and given a unique set of positioning reticules for use with target experiments.

The target vibration was caused by two problems: (1) the vibration induced to the target stalk as the cryogenic shroud, used to maintain the correct environment for the ice layer, was pulled away from the target before laser irradiation, and (2) an occasional, weak collision between the articulated target stalk and the cryogenic shroud during this retraction. Many engineering improvements were applied to the target shroud and the MCTC. The most effective of these included the modification to the shroud control software allowing a slower retraction of the shroud and the replacement of the articulated target stalks with a simple, narrower staple design. The slower retraction speed allows transmitted vibrations to self-damp, while the narrower stalk reduces the possibility of a collision between the target and the retracting shroud.

With these modifications in place, the static mis-pointing has now been reduced to less than 40 $\mu$m for all of the MCTC's, while target vibration has been virtually eliminated. All target implosions discussed in this article were located within 40 $\mu$m of TCC, with many achieving 20 $\mu$m at shot time.

4. Diagnostics

Cryogenic implosions on the OMEGA laser system are diagnosed with a large number of instruments, including laser scattering and absorption diagnostics; time-dependent and time-integrated x-ray imaging; time-dependent and time-integrated x-ray spectroscopy; time-dependent and time-integrated fusion yield measurement; and fusion product spectroscopy. The fusion product diagnostics include measurements of both neutrons and charged particles. Data presented here include measurements from the time-integrated x-ray imaging, primary[18] and secondary fusion yield,[19] neutron[20] and proton spectroscopy,[21] and time-dependent neutron and proton emission.[22]

Time-integrated x-ray imaging is used to determine the position of the target at the time of the shot. These measurements are made with both x-ray pinhole cameras and x-ray microscopes. Three x-ray microscopes and five x-ray pinhole cameras located in fixed positions around the target chamber allow several views of the target emission to be recorded. Subsequent analysis of the images locates the position of the target to within ±10 $\mu$m.

The primary and secondary fusion product yields are measured with a combination of activation, scintillation, and track detectors. These provide a direct measure of the implosion performance. The ratio of secondary to primary product yields is a measure of the final core conditions. Neutron spectroscopy is used to determine the ion temperature, and the proton spectroscopy determines the total areal density of the implosion from the energy loss measured by wedged range filters.[23]

Time-dependent neutron emission is measured with a scintillator coupled to an optical streak camera. The time evolution of the fusion emission is sensitive to the overall coupling of the laser energy to the target, and the emission from both the shock wave and compression can be observed. These data and those taken from laser absorption measurements are used to determine the accuracy of the hydrodynamic simulation of the implosion.

**Implosion Results**

1. High-Adiabat Pulses

The cryogenic implosion campaign is divided into several phases dealing with the validation of stable implosions with progressively lower fuel adiabat. The first phase of these implosions used a high-adiabat (1-ns square, $\alpha$ = 25) laser pulse to minimize the effects of laser imprint on target performance. This allows experimental investigation of the effect of ice roughness on target performance. Implosions were carried out using several SD targets and one WF target. For brevity we will examine one SD shot in detail and then speak briefly about the wetted-foam shot.

The SD capsule used was ~875 $\mu$m in diameter and contained a 92-$\mu$m $D_2$-ice layer surrounded by a 3.8-$\mu$m GDP wall. The inner ice roughness was measured to be ~4 $\mu$m rms when averaged over 23 views. The power spectrum, shown in Fig. 97.2(a), is heavily weighted toward the lowest end of the spectrum with ~90% of the power contained in the first few modes ($\ell$ = 1 to 3). The capsule was determined experimentally[13] to be offset 22 $\mu$m from target chamber center at the

(a)

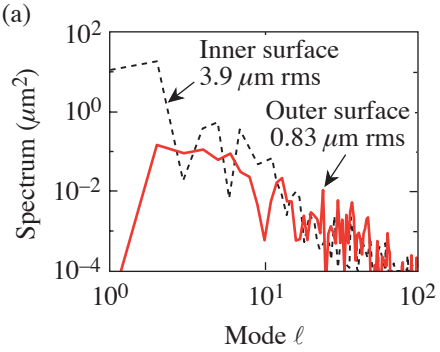


(b)

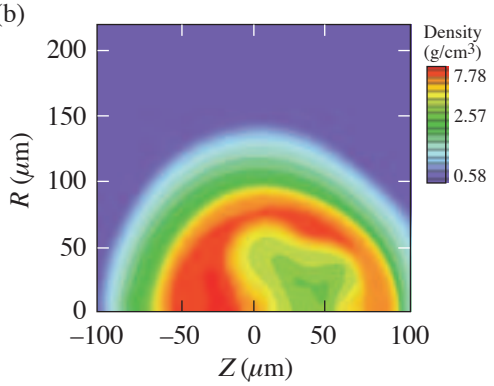


(c)

| | Expt. | 1-D | 2-D |
|---|---|---|---|
| $Y_{1n}$ | $6.49 \times 10^{10}$ | $1.84 \times 10^{11}$ | $6.86 \times 10^{10}$ |
| $Y_{2n}$ | $6.86 \times 10^{8}$ | $1.90 \times 10^{9}$ | $6.92 \times 10^{8}$ |
| $\langle \rho R \rangle$ | 49 | 38 | 52 |
| $T_{ion}$ | 2.9 | 2.6 | 2.0 |

(d)

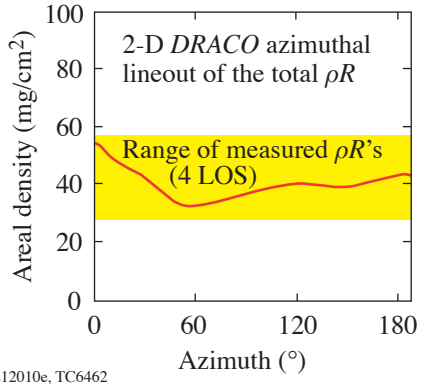


E12010e, TC6462

Figure 97.2
Two-dimensional *DRACO* input and results for shot 33599. (a) Input ice roughness spectrum, (b) isodensity contours drawn near the time of peak burn, (c) tabular comparison of secondary-neutron yields and neutron-averaged areal density and ion temperature, and (d) angular variation of the total areal density calculated from the isodensity contours. Yellow region represents the range of experimentally obtained areal-density measurements.

beginning of the implosion. This capsule produced a neutron yield of $6.5 \times 10^{10}$ neutrons—roughly 36% of the simulated 1-D *LILAC*[24] yield. A *DRACO* simulation was run with the roughness spectra from Fig. 97.2(a) and an initial 4.4% rms $\ell = 1$ illumination nonuniformity corresponding to the 22-$\mu$m offset.[13] The simulated neutron yield of $6.9 \times 10^{10}$ falls very close to the experimental result. As can be seen from the isodensity contours given in Fig. 97.2(b) (taken near the time of peak neutron production), the core has developed under the strong influence of the low modes with the effect of the $\ell = 1$ and 2 most prominent. The secondary-proton yields and average-areal-density results, shown in Fig. 97.2(c), are also in good agreement between the experiment and the *DRACO* simulation. One of the more-interesting results from this implosion is the agreement between the range of experimentally observed areal-density measurements with those predicted by *DRACO* as shown in Fig. 97.2(d).

Additional results obtained for the other shots are compiled in Fig. 97.3. In Fig. 97.3 the experimental yield-over-clean [(YOC), the experimentally obtained yield divided by the 1-D simulated yield] for all shots in this series is compared with the trends of several series of perturbed *DRACO* simulations run with increasing initial ice roughness for a specific fixed target offset. The *DRACO* trend lines merge with increasing ice

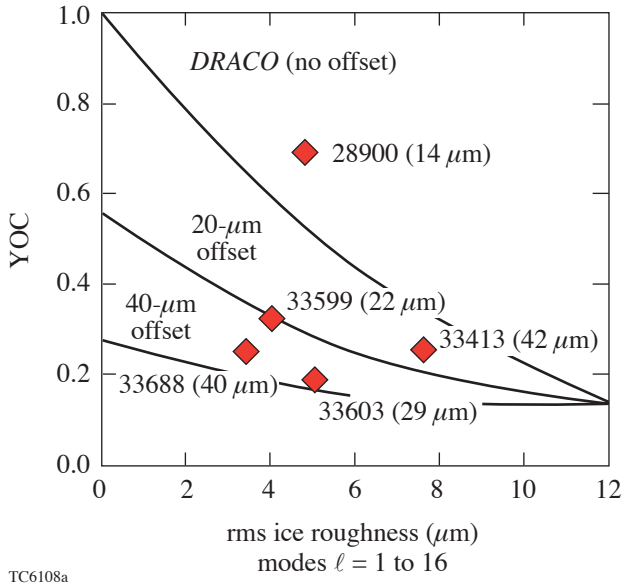


TC6108a

Figure 97.3
Analysis of experimental neutron YOC drawn as a function of the target's initial ice roughness. Curves are drawn for several series of *DRACO* runs analyzing the degradation of YOC with increasing ice roughness. Each of these series was computed with a different initial target offset.

roughness due to the dominance of the ice perturbation at these high levels. The experimental results are in good agreement with the *DRACO* predictions.

The other part of the high-adiabat cryogenic implosion series was the use of a WF target to measure the absorption fraction and shock speed in this material. Such experiments, carried out in spherical geometry, help to develop a predictive capability for target performance. The need for examining shock propagation within a wetted-foam matrix was pointed out earlier[25,26] in theoretical studies analyzing shock propagation in foam. Studies at LLE use the 2-D astrophysical code AMRCLAW[27] that employs the adaptive-mesh-refinement (AMR) scheme to highly resolve the shock flow around and through the fiber elements. The results of such simulations are shown in Fig. 97.4 and indicate that shocks travel faster in wetted foam when compared to traditional Lagrangian hydrodynamics simulations that model the foam as a homogeneous mixture. Of particular interest to target designers, in addition to ascertaining the proper value of the shock velocity, are the perturbed nature of the shock front and mechanisms for the CH-DT homogeneous annealing in the wake of the shock. Both of these processes will be examined in more detail when a new three-dimensional (3-D) AMR code, ASTROBEAR,[27] becomes available.

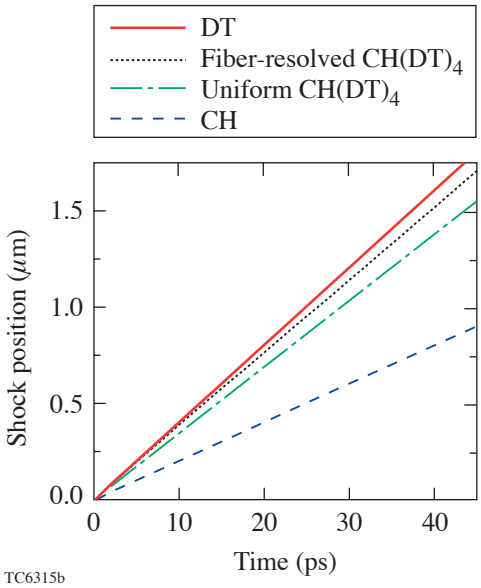


Figure 97.4
Numerical results detailing the difference in shock velocity for a variety of materials including CH, $CH(DT)_4$ mixture, fiber-resolved foam, and pure DT.

The first cryogenic wetted-foam implosion on OMEGA produced the highest-ever cryogenic neutron yield: $1.8 \times 10^{11}$. The target was imploded with the high-adiabat, 1-ns square pulse. The neutron burn history was obtained and is shown as the solid curve in Fig. 97.5. Several 1-D *LILAC* simulations were run with varying the wetted-foam density, and an example of the numerical burn history ($\rho_{WF} \sim 240$ mg/cc) is drawn as the dotted line in Fig. 97.5. Discrepancies between the simulated and experimental bang times may be attributed to lower shock velocities in low-density foams when modeled as a homogeneous mixture (as predicted in Refs. 25 and 26). The numerically obtained 1-D yield underestimates the experimental yield by roughly 15%.

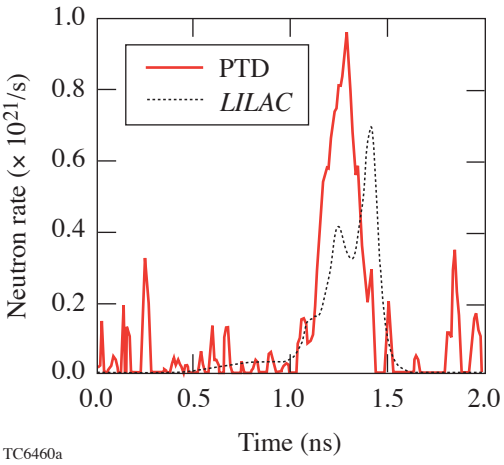


Figure 97.5
Comparison of neutron burn histories between the results of the particle temporal diagnostic (PTD) and *LILAC*.

Clearly, more work needs to be done in addressing the use of WF targets in ICF ignition experiments. Over the coming year we will repeat the spherical experiments for various density dry foams and couple this information with ongoing planar foam experiments studying shock transit with picket pulses in warm foams and standard shock development in cryogenic wetted foams. Additionally, techniques must be developed to characterize the ice layer within the foam shell.

2. Low-Adiabat Pulses

The next phase of the OMEGA cryogenic implosion program involves the validation of low-adiabat, ignition-scaled implosions on OMEGA. The first set of experiments in this phase employs the $\alpha = 4$ pulse shape, shown earlier in Fig. 97.1. Several implosions were undertaken using the

OMEGA laser, but, again, only a single SD shot will be described in detail.

The SD target was 865 $\mu$m in diameter with a 3.8-mm GDP overcoat, an ice layer of ~92-$\mu$m depth, and an interior ice surface roughness of ~4.5 $\mu$m. The power spectrum for this surface, as shown in Fig. 97.6(a), is again heavily weighted toward low-order modes. The capsule was determined to be 28 $\mu$m from target chamber center at the beginning of the implosion. The neutron yield for this implosion was $4.3 \times 10^9$, which represents the highest-ever experimental yield obtained from a cryogenic $\alpha \sim 4$ implosion (YOC ~ 16%). The spectra from Fig. 97.6(a) and an initial 5.6% $\ell = 1$ illumination nonuniformity, again due to the target offset, were used in a *DRACO* simulation (laser imprint was excluded from this calculation because the growth of these two perturbations, at these levels, overwhelms the effect of the imprint as was demonstrated in Ref. 3). The simulated yield was $5.9 \times 10^9$. The secondary-yield comparison also showed the *DRACO* simulation slightly overpredicting the experimental result; however, the simulated average $\langle \rho R \rangle$ was again in good agreement as shown in Fig. 97.6(c) and the azimuthal variation in Fig. 97.6(d).

Previously,[3] low-adiabat target performance has been presented as a compilation of all perturbation sources using a sum-in-quadrature representation of each source's contribution to the roughness of the inner ice layer at the end of the acceleration phase of the implosion. The scaling parameter $\bar{\sigma}$ is defined as

$$\bar{\sigma}^2 = 0.06 \times \sigma_\ell^2 (\ell < 10) + \sigma_\ell^2 (\ell \geq 10),$$

where $\sigma_\ell$ is the rms roughness computed over the mode range indicated. At this time during the implosion, this surface decouples from the ablation region of the target. As such, the effects of all major sources of perturbation leading to the initial seed of the deceleration-phase Rayleigh–Taylor (RT) instability have been set. An example of the $\bar{\sigma}$ scaling is shown in Fig. 97.7, where a comparison is made between the NIF $\alpha = 3$ and OMEGA $\alpha = 4$ designs.

Using the $\bar{\sigma}$ scaling with yield allows the experimental validation of the numerical modeling of current OMEGA experiments, which, in turn, lends credibility to the ability of these numerical models to predict ignition for direct-drive target designs on the NIF. The $\bar{\sigma}$ parameter and yield performance were extracted from the *DRACO* simulations of the

(a)

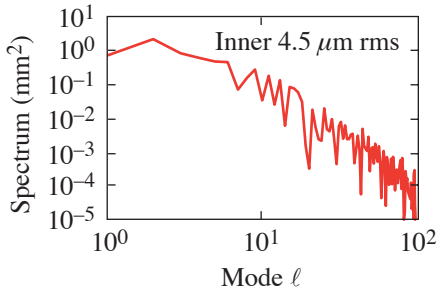


(b)

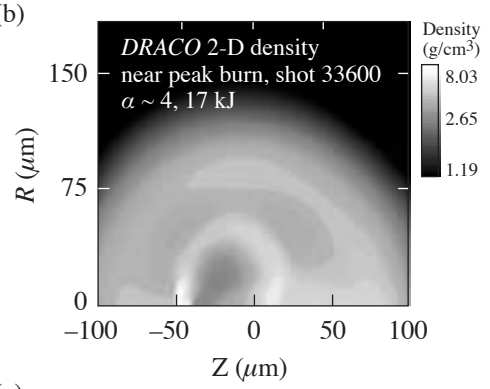


(c)

| | Expt. | 1-D | 2-D |
|---|---|---|---|
| $Y_{1n}$ | $4.30 \times 10^9$ | $2.68 \times 10^{10}$ | $5.85 \times 10^9$ |
| $Y_{2n}$ | $4.43 \times 10^7$ | $1.40 \times 10^9$ | $5.97 \times 10^7$ |
| $\langle \rho R \rangle$ | 52 | 63 | 55 |
| $T_{ion}$ | 2.7 | 1.6 | 1.4 |

(d)

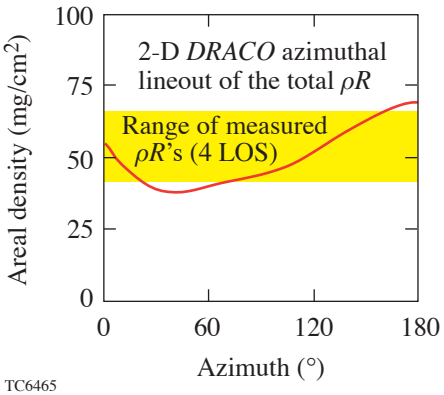


TC6465

Figure 97.6
Two-dimensional *DRACO* input and results for shot 33600. (a) Input ice roughness spectrum, (b) isodensity contours drawn near the time of peak burn, (c) tabular comparison of secondary-neutron yields and neutron-averaged areal density and ion temperature, and (d) angular variation of the total areal density calculated from the isodensity contours. Yellow region represents the range of experimentally obtained areal-density measurements.

$\alpha$ = 4 implosion experiments and placed on the graph in Fig. 97.7. It can be seen that the points are in reasonable agreement with the $\bar{\sigma}$ scaling. When nonuniformities on OMEGA are improved, implosion experiments will approach the ~40% YOC goal for these implosions as denoted by the dashed lines in Fig. 97.7.

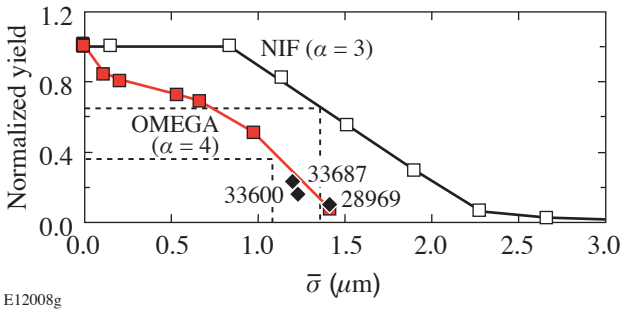


Figure 97.7
Comparison of the $\bar{\sigma}$ stability analysis for the NIF $\alpha$ = 3 and the OMEGA $\alpha$ = 4 designs. The dashed lines indicate the predicted value of $\bar{\sigma}$ and the corresponding target performance for each of the two designs when all NIF specifications for levels of nonuniformity are applied. The solid diamonds represent results from 2-D *DRACO* simulations of the noted OMEGA experiments.

**Re-baseline of the Direct-Drive Point Design**

The baseline direct-drive point design has not experienced any significant changes since its introduction by Verdon[28] in the early 1990s. The design, consisting of a levitated 340-$\mu$m-thick cryogenic DT layer coated with 3 $\mu$m of CH and irradiated with 1.8 MJ of 351-nm light, has undergone several design studies[3,29,30] and has consistently been shown to be robust to moderate levels of perturbation. The design's only weakness, which can be attributed to low ablation velocities, is its strong susceptibility to laser imprint during the acceleration phase of the implosion. The limited ablation velocities cannot effectively stabilize the RT growth of the fast-growing, short-wavelength-laser nonuniformities present in the laser-beam profile. While several schemes have been adopted to smooth these nonuniformities,[10–12] the maximum ratio of the perturbation amplitude to the in-flight shell thickness has been shown to approach 70% during the acceleration phase of the implosion.[31]

Recently, an old idea of modifying the seeds of RT growth within the ablation region using picket pulses[32] has been examined for the point design.[33] Goncharov[9] modified this process by employing a very narrow Gaussian picket added to the foot of the drive pulse to launch an early, unsupported shock wave into the target. Because the shock wave is unsupported, it begins to decay after the rarefaction wave from the front surface (created at the end of the picket) catches up to it. As the shock decays, it creates a shaped adiabat within the fuel layer—low near the shock front and high near the ablation region. The high adiabat in the ablation region results in much higher ablation velocities, which, in turn, provide for increased stabilization of the RT growth present there.

The decaying shock technique has recently been applied to several direct-drive, high-gain target designs,[34–36] including the Verdon point design. In all cases the scheme has been shown to dramatically reduce the deleterious effects of laser imprint. As such, the direct-drive-ignition design has been modified to include a 200-ps laser picket, and an energy-scaled design has been set for implosion experiments on OMEGA. The energy-scaled design serves as the basis of all following calculations.

The $\bar{\sigma}$ stability analysis mentioned previously becomes doubtful in cases of targets with very poor stability characteristics. This is because the analysis assumes a continuous inner ice layer to evaluate. For seriously perturbed implosions, however, the target shell can break apart, failing to provide the continuous interface. Such is the case for the $\alpha$ = 2 design without the benefit of a stabilizing picket. The effective $\bar{\sigma}$ value for this design with the current levels of nonuniformities present on OMEGA is greater than 10 $\mu$m. As was shown in Ref. 9, the main fuel layer for this implosion was seriously perturbed and on the verge of breakup. Dramatic improvement in layer integrity was achieved, however, when a stabilizing picket was employed. The calculated $\bar{\sigma}$ for the $\alpha$ = 2 with picket ($\alpha 2p$) falls close to 1 $\mu$m. With the addition of the picket it now becomes possible to evaluate $\alpha 2p$ target performance using the $\bar{\sigma}$ analysis.

Many 2-D *DRACO* simulations were run to evaluate the performance of the $\alpha 2p$ design under the influence of various levels of laser imprint, laser power imbalance, and cryogenic ice roughness. For example, we show two isodensity contours of the $\alpha 2p$ target imploded with a 1-$\mu$m inner ice roughness in Fig. 97.8(a). The image shows split contours taken at $t$ = 2.3 ns (end of acceleration) and at $t$ = 2.7 ns (peak neutron production). Analyzing the inner-ice-roughness spectrum at the first time yields the $\bar{\sigma}$ parameter for this run ($\bar{\sigma}$ = 0.52), while the final neutron performance is determined by the core conditions at the second time (YOC = 77%). A scan of target performance for the $\alpha 2p$ design as a function of ice roughness is shown in Fig. 97.8(b).

Such simulations provide the necessary information to develop the $\bar{\sigma}$ scaling for this design as shown in Fig. 97.9. From this graph it can be seen that the OMEGA $\alpha 2p$ design is almost as stable as the $\alpha = 4$ design. Such results allow for the confident fielding of low-adiabat direct-drive target designs on both OMEGA and the NIF. The design and testing of the laser picket required for the OMEGA $\alpha 2p$ target is already underway at LLE, and experiments should commence in mid-FY04.

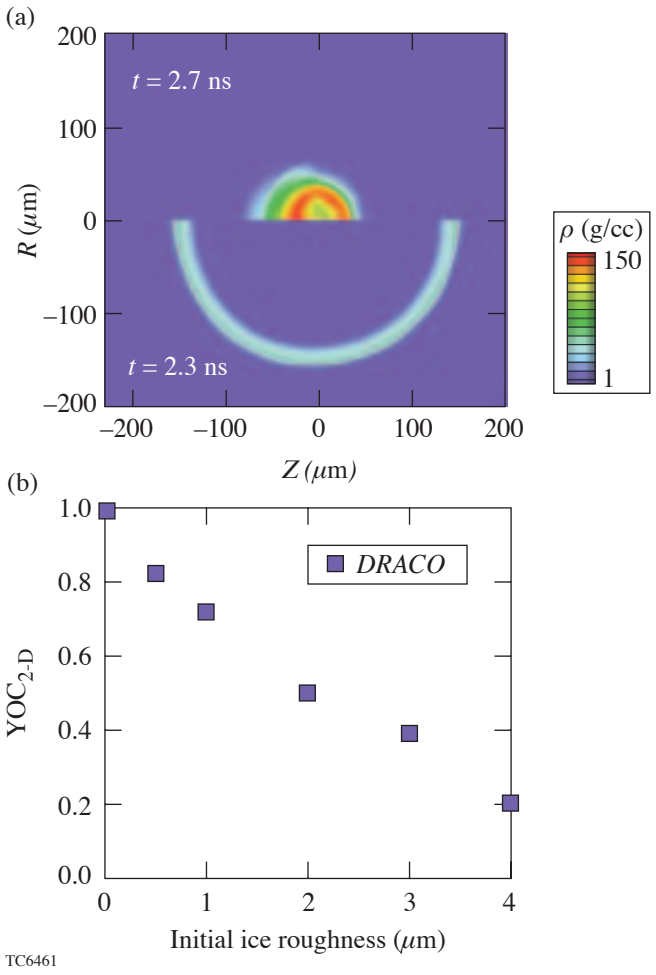


Figure 97.8
Results of a series of *DRACO* simulations evaluating YOC degradation due to increasing inner ice roughness. (a) Split isodensity contours drawn at $t$ = 2.3 ns (end of acceleration phase) and at $t$ = 2.7 ns (stagnation); (b) decay of YOC with increasing ice roughness.

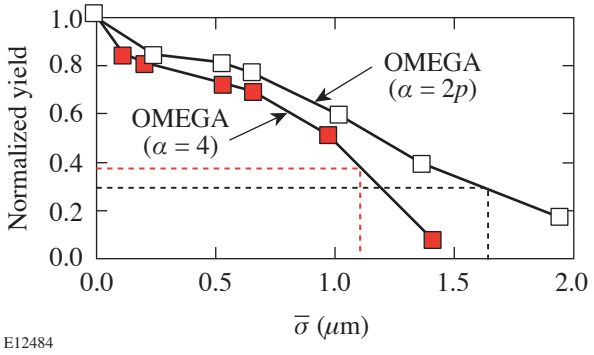


Figure 97.9
Comparison of the $\bar{\sigma}$ stability analysis for the OMEGA $\alpha = 4$ and the OMEGA $\alpha = 2p$ designs. The dashed lines indicate the predicted value of $\bar{\sigma}$ and the corresponding target performance for each of the two designs when all NIF specifications for levels of nonuniformity are applied.

## Conclusion

The cryogenic implosion campaign at LLE is a staged program comprised of several concurrent efforts including the experimental validation of target performance for progressively lower fuel-adiabat target designs; the physical minimization of the interfacial cryogenic surface roughness; and ultimately the fielding and imploding of cryogenic DT targets on the OMEGA laser system. Recent advances in all three of these efforts have LLE poised to demonstrate scaled-ignition performance with DT on OMEGA by the end of FY05. In the area of target implosions, significant progress has been made with several series of cryogenic implosion experiments evaluating target performance with high-adiabat solid-$D_2$ and WF targets and low-adiabat solid-$D_2$ targets. It has been shown that there is good agreement between the experimental observables and the results of 2-D *DRACO* simulations for targets imploded near target chamber center. The use of adiabat shaping has led to increased stability for both the "all-DT" and wetted-foam direct-drive NIF point designs and the corresponding ignition-scaled experiments for OMEGA. Dramatic advances in cryogenic layer characterization and layering over the last year have resulted in LLE producing sub-2-$\mu$m ice layers in targets for implosion on OMEGA. The cryogenic DT fill and transfer station (FTS) is currently being qualified and will be DT-charged by the end of this fiscal year. With this system in place, full-scale layering studies of cryogenic DT ice will be undertaken, resulting in the fielding of ignition-scale cryogenic DT targets on OMEGA.

## ACKNOWLEDGMENT

The authors are extremely grateful to the staff of the Laboratory for Laser Energetics for their tireless dedication to the cryogenic implosion program and the operation of the OMEGA laser system. In particular, the authors would like to acknowledge the efforts of the Cryogenic Target Fabrication Group for the production of layered and characterized capsules on a regular schedule. This work was supported by the U. S. Department of Energy Office of Inertial Confinement Fusion under Cooperative Agreement No. DE-FC03-92SF19460, the University of Rochester, and the New York State Energy Research and Development Authority. The support of the DOE does not constitute an endorsement by the DOE of the views expressed in this article.

## REFERENCES

1. T. R. Boehly, D. L. Brown, R. S. Craxton, R. L. Keck, J. P. Knauer, J. H. Kelly, T. J. Kessler, S. A. Kumpan, S. J. Loucks, S. A. Letzring, F. J. Marshall, R. L. McCrory, S. F. B. Morse, W. Seka, J. M. Soures, and C. P. Verdon, Opt. Commun. **133**, 495 (1997).
2. W. J. Hogan, E. I. Moses, B. E. Warner, M. S. Sorem, and J. M. Soures, Nucl. Fusion **41**, 567 (2001).
3. P. W. McKenty, V. N. Goncharov, R. P. J. Town, S. Skupsky, R. Betti, and R. L. McCrory, Phys. Plasmas **8**, 2315 (2001).
4. R. Betti, K. Anderson, V. N. Goncharov, R. L. McCrory, D. D. Meyerhofer, S. Skupsky, and R. P. J. Town, Phys. Plasmas **9**, 2277 (2002).
5. W. K. Levedahl and J. D. Lindl, Nucl. Fusion **37**, 165 (1997).
6. M. C. Herrmann, M. Tabak, and J. D. Lindl, Phys. Plasmas **8**, 2296 (2001).
7. A. Kemp, J. Meyer-ter-Vehn, and S. Atzeni, Phys. Rev. Lett. **86**, 3336 (2001).
8. D. Keller, T. J. B. Collins, J. A. Delettrez, P. W. McKenty, P. B. Radha, B. Whitney, and G. A. Moses, Bull. Am. Phys. Soc. **44**, 37 (1999).
9. V. N. Goncharov, J. P. Knauer, P. W. McKenty, P. B. Radha, T. C. Sangster, S. Skupsky, R. Betti, R. L. McCrory, and D. D. Meyerhofer, Phys. Plasmas **10**, 1906 (2003).
10. T. J. Kessler, Y. Lin, J. J. Armstrong, and B. Velazquez, in *Laser Coherence Control: Technology and Applications*, edited by H. T. Powell and T. J. Kessler (SPIE, Bellingham, WA, 1993), Vol. 1870, pp. 95–104.
11. T. R. Boehly, V. A. Smalyuk, D. D. Meyerhofer, J. P. Knauer, D. K. Bradley, R. S. Craxton, M. J. Guardalben, S. Skupsky, and T. J. Kessler, J. Appl. Phys. **85**, 3444 (1999).
12. S. Skupsky, R. W. Short, T. Kessler, R. S. Craxton, S. Letzring, and J. M. Soures, J. Appl. Phys. **66**, 3456 (1989).
13. F. J. Marshall, J. A. Delettrez, R. Epstein, R. Forties, R. L. Keck, J. H. Kelly, P. W. McKenty, S. P. Regan, and L. J. Waxer, Phys. Plasmas **11**, 251 (2004).
14. J. Koch, Lawrence Livermore National Laboratory, private communication (2000).
15. S. Jin, *2002 Summer Research Program for High School Juniors at the University of Rochester's Laboratory for Laser Energetics*, Laboratory for Laser Energetics Report No. 329, NTIS document No. DOE/SF/19460-479 (2003). Copies may be obtained from the National Technical Information Service, Springfield, VA 22161.
16. R. Stephens, General Atomics, private communication (2003).
17. T. C. Sangster, J. A. Delettrez, R. Epstein, V. Yu. Glebov, V. N. Goncharov, D. R. Harding, J. P. Knauer, R. L. Keck, J. D. Kilkenny, S. J. Loucks, L. D. Lund, R. L. McCrory, P. W. McKenty, F. J. Marshall, D. D. Meyerhofer, S. F. B. Morse, S. P. Regan, P. B. Radha, S. Roberts, W. Seka, S. Skupsky, V. A. Smalyuk, C. Sorce, J. M. Soures, C. Stoeckl, K. Thorp, J. A. Frenje, C. K. Li, R. D. Petrasso, F. H. Séguin, K. A. Fletcher, S. Padalino, C. Freeman, N. Izumi, J. A. Koch, R. A. Lerche, M. J. Moran, T. W. Phillips, and G. J. Schmid, Phys. Plasmas **10**, 1937 (2003).
18. V. Yu. Glebov, D. D. Meyerhofer, C. Stoeckl, and J. D. Zuegel, Rev. Sci. Instrum. **72**, 824 (2001).
19. F. H. Séguin, C. K. Li, D. G. Hicks, J. A. Frenje, K. M. Green, R. D. Petrasso, J. M. Soures, D. D. Meyerhofer, V. Yu. Glebov, C. Stoeckl, P. B. Radha, S. Roberts, C. Sorce, T. C. Sangster, M. D. Cable, S. Padalino, and K. Fletcher, Phys. Plasmas **9**, 2725 (2002).
20. T. J. Murphy, R. E. Chrien, and K. A. Klare, Rev. Sci. Instrum. **68**, 610 (1997).
21. C. K. Li, F. H. Séguin, D. G. Hicks, J. A. Frenje, K. M. Green, S. Kurebayashi, R. D. Petrasso, D. D. Meyerhofer, J. M. Soures, V. Yu. Glebov, R. L. Keck, P. B. Radha, S. Roberts, W. Seka, S. Skupsky, C. Stoeckl, and T. C. Sangster, Phys. Plasmas **8**, 4902 (2001).
22. C. Stoeckl, V. Yu. Glebov, S. Roberts, T. C. Sangster, R. A. Lerche, R. L. Griffith, and C. Sorce, Rev. Sci. Instrum. **74**, 1713 (2003).
23. R. D. Petrasso, J. A. Frenje, C. K. Li, F. H. Séguin, J. R. Rygg, B. E. Schwartz, S. Kurebayashi, P. B. Radha, C. Stoeckl, J. M. Soures, J. Delettrez, V. Yu. Glebov, D. D. Meyerhofer, and T. C. Sangster, Phys. Rev. Lett. **90**, 095002 (2003).
24. M. C. Richardson, P. W. McKenty, F. J. Marshall, C. P. Verdon, J. M. Soures, R. L. McCrory, O. Barnouin, R. S. Craxton, J. Delettrez, R. L. Hutchison, P. A. Jaanimagi, R. Keck, T. Kessler, H. Kim, S. A. Letzring, D. M. Roback, W. Seka, S. Skupsky, B. Yaakobi, S. M. Lane, and S. Prussin, in *Laser Interaction and Related Plasma Phenomena*, edited by H. Hora and G. H. Miley (Plenum Publishing, New York, 1986), Vol. 7, pp. 421–448.
25. G. Hazak *et al*., Phys. Plasmas **5**, 4357 (1998).
26. A. D. Kotelnikov and D. C. Montgomery, Phys. Fluids **10**, 2037 (1998).
27. A. Frank, Department of Physics and Astronomy, University of Rochester, private communication (2003).

28. C. P. Verdon, Bull. Am. Phys. Soc. **38**, 2010 (1993).

29. S. V. Weber *et al.*, *ICF Quarterly Report* **7**, 43, Lawrence Livermore National Laboratory, Livermore, CA, UCRL-LR-105821-97-2 (1997).

30. Laboratory for Laser Energetics LLE Review **79**, 121, NTIS document No. DOE/SF/19460-317 (1999). Copies may be obtained from the National Technical Information Service, Springfield, VA 22161.

31. V. N. Goncharov, P. McKenty, S. Skupsky, R. Betti, R. L. McCrory, and C. Cherfils-Clérouin, Phys. Plasmas **7**, 5118 (2000).

32. M. Tabak, *ICF Program Annual Report 1989 (U)*, Lawrence Livermore National Laboratory, Livermore, CA, UCRL-LR-116901-88/80, 141 (1989) (unpublished).

33. T. J. B. Collins and S. Skupsky, Phys. Plasmas **9**, 275 (2002).

34. T. J. B. Collins, Laboratory for Laser Energetics, private communication (2003).

35. J. Perkins, Lawrence Livermore National Laboratory, private communication (2003).

36. A. J. Schmitt *et al.*, "Large-Scale, High-Resolution Simulations of High-Gain, Direct-Drive ICF Targets," to be published in Physics of Plasmas.

# Hot-Core Characterization of a Cryogenic $D_2$ Target at Peak Neutron Production in a Direct-Drive Spherical Implosion

In inertial confinement fusion[1] (ICF), a spherical shell is irradiated either directly by a large number of overlapping laser beams (direct drive) or by x rays produced in a high-$Z$ "hohlraum" (indirect drive).[2] During the laser-driven acceleration phase of an implosion, the target compresses while it converges to the center, then decelerates to peak compression as the core of the target is heated to high temperatures, causing a thermonuclear burn within its fuel. The current goal of ICF research is to achieve ignition and a positive gain, where the amount of energy released through thermonuclear fusion is equal to or higher than the amount of laser energy used to drive the target. The combination of high temperature and areal density ($\rho R$) in the compressed fuel is necessary to ignite the target.[2] This goal is expected to be achieved on the National Ignition Facility (NIF),[2] currently under construction at Lawrence Livermore National Laboratory. In the direct-drive ignition target design[3] for the NIF, a 3.4-mm-diam, 350-$\mu$m-thick cryogenic deuterium–tritium (DT) shell is imploded by 192 overlapped laser beams with a total energy of 1.5 MJ. The fusion energy will be released through the nuclear reaction D + T$\rightarrow{}^4$He (3.5 MeV) + $n$(14.1 MeV). An expected neutron yield of $2.5 \times 10^{19}$ (corresponding to a gain of ~45) will be achieved at a fuel temperature of ~30 keV and an areal density of ~1200 mg/cm$^2$ at peak compression.

While cryogenic DT targets[4,5] will be used for fusion energy production, the current implosion program on the 60-beam, 351-nm OMEGA laser system[6] uses cryogenic $D_2$ targets to study the relevant implosion physics. The $D_2$ targets are hydrodynamically equivalent to DT targets, but much simpler to produce and more useful for diagnosing target conditions near peak compression. The primary fusion reaction in $D_2$ fuel has two branches: (a) D + D$\rightarrow{}^3$He (0.82 MeV) + $n$(2.45 MeV), and (b) D + D$\rightarrow$T(1.01 MeV) + $p$(3.02 MeV). The primary reaction product T reacts with D through the secondary reaction D + T(0 to 1.01 MeV)$\rightarrow{}^4$He + $n$(11.9 to 17.2 MeV). Experiments with plastic targets estimated target compression by using the size of the core emission and the ratio of secondary DT to primary DD neutron yields. This technique was first used by Azechi *et al.*[7] and by Cable and Hatchett.[8] In their calculations, the core $\rho R$ was inferred from the ratios of secondary to primary yields, assuming the core had uniform temperature and density. For ICF to succeed, it is necessary to infer core temperature–density profiles and directly compare them with hydrocode simulations. Because the target ignition designs are based on hydrocode predictions, they should be benchmarked by the most-comprehensive set of measurements.

Recently Radha *et al.* modeled[9] core temperature–density profiles at peak neutron production in plastic-shell targets. About ten different experimental observations with several different types of targets (having various dopants in a gas fuel and plastic shell) were necessary for a comprehensive characterization of the core conditions.[9] Kurebayashi *et al.*[10] studied the usefulness of secondary particles (neutrons and protons) for hot-core modeling of plastic and cryogenic capsules. The cryogenic $D_2$ targets cannot have dopants, but because they are much simpler (there is no complication of mixing of different materials in the core), it is possible to characterize them (with the same level of detail as plastic shells) with fewer experimental observables. This article describes experiments where measured primary DD and secondary DT neutron yields, neutron-averaged ion temperatures, and x-ray images at peak neutron production are used to infer the electron-pressure and temperature–density profiles in cryogenic $D_2$ implosions for the first time. The areal densities of neutron production and "triton-stopping" regions are introduced here to characterize target compression. These quantities are the compression measurements that are extended from the $\rho R$ inferred from the ratios of secondary to primary yields. Because they are derived from the temperature–density profiles consistent with experimental measurements, they provide more-accurate measurements of compression.

The experiments were direct-drive implosions of ~920-$\mu$m-initial-diam targets with shells that consisted of ~100-$\mu$m-thick inner $D_2$-ice layers and outer 5-$\mu$m-thick plastic CD layers.[11] The targets were imploded with a 1-ns square pulse shape with a total on-target energy of ~23 kJ on OMEGA.[6]

The laser beams were smoothed with distributed phase plates,[12] 1-THz two-dimensional smoothing by spectral dispersion,[13] and polarization smoothing[14] using birefringent wedges. The measured experimental yield ratios relative to the predicted yields using 1-D simulations were typically ~30% in a large number of similar implosions. In one implosion, the experimental yield was closer to the predicted yield (59%); therefore, this implosion was used for the analysis presented here. The measured primary DD and secondary DT neutron yields for this implosion were $Y_1 = 1.24 \times 10^{11} \pm 8 \times 10^8$ and $Y_2 = 1.17 \times 10^9 \pm 3 \times 10^7$, respectively.[10] The measured neutron-averaged ion temperature was $T_i = 3.6 \pm 0.5$ keV and the neutron burn width was $\tau = 170 \pm 25$ ps.[11] The core images[11] were measured with an x-ray framing camera with a spatial resolution of ~10 $\mu$m, a temporal resolution of ~40 ps, and a 200-$\mu$m-thick beryllium filter (which transmitted x rays with energies of more than ~2 keV).

The target core at peak neutron production was characterized by choosing temperature [$T(\mathbf{r})$] and density [$n(\mathbf{r})$] profiles that produced the same primary and secondary neutron yields, the neutron-averaged ion temperature, and the size of x-ray images as measured within experimental uncertainties.[9] In the first stage of modeling, only those temperature–density profiles that were consistent with the primary DD neutron yield and neutron-averaged ion temperature were selected from all possible combinations at a particular electron pressure (the hot core was assumed to be isobaric). In the second stage, profiles consistent with the secondary DT neutron yield were chosen from those selected in the first stage. Similarly, the temperature–density profiles consistent with all neutron measurements were chosen at each electron pressure in the range of 1 to 10 Gbar. Finally, only those temperature–density profiles that were consistent with the size of the x-ray core images were chosen to characterize the hot core at peak neutron production. The following assumptions were used in the core modeling: (1) the core plasma was a fully ionized ideal gas; (2) the core was isobaric $\left[P_e(\mathbf{r}) = \text{const}\right]$ at stagnation; (3) the temperature–density profiles were spherically symmetric; (4) the electron and ion temperatures as well as the densities were equal;[9] (5) the core was static during the time of neutron production $\tau$ (therefore, the inferred pressure and temperature–density profiles were considered to be neutron averaged); and (6) the temperature decreased monotonically from the center. These secondary DT neutron yields used Li and Petrasso's plasma stopping powers[15] to calculate the triton's energy loss as it propagated through a 3-D core. The x-ray images were constructed using radiation-transport calculations in a fully ionized deuterium plasma with free-free emission and absorption.[16]

Figure 97.10(a) shows one of the grids used to construct temperature profiles. The temperature step was 250 eV, and the distance step was 20 $\mu$m (distance steps of 15, 10, and 5 $\mu$m were used in additional, more-detailed grids). The curves show examples of two (out of nearly ~$10^{10}$) temperature profiles $T(\mathbf{r})$ used in the modeling. The corresponding density profiles $n(\mathbf{r})$ were calculated using $P_e(\mathbf{r}) = n(\mathbf{r}) \times T(\mathbf{r})$. The range of temperatures that satisfy the measured DD neutron yield and neutron-averaged ion temperature (calculated in the first stage of modeling) is shown by the lightly shaded region in Fig. 97.10(b) at an electron pressure of 2.6 Gbar. The results of the second stage of modeling—the temperature profiles consistent with secondary DT neutron yield (in addition to primary DD yield and neutron-averaged ion temperature)—are shown by the darkly shaded region. Similar calculations were conducted for electron pressures in the range from 1 to 10 Gbar. As an example, the ranges of temperature profiles consistent with all neutron measurements for three different electron pressures (1.3, 2.6, and 5.2 Gbar) are shown in Fig. 97.11(a). It was found that for any electron pressure above 1.3 Gbar, temperature–density profiles consistent with all neutron measurements exist; therefore, neutron measurements by themselves are not sufficient to accurately characterize the target core at peak neutron production. The profiles at different pressures, however, would make different sizes of x-ray emission, as can be seen from the profiles shown in Fig. 97.11(b). Therefore, for various temperature–density profiles, the x-ray images were constructed and compared with the one measured at peak neutron production. In these calculations, the transmis-

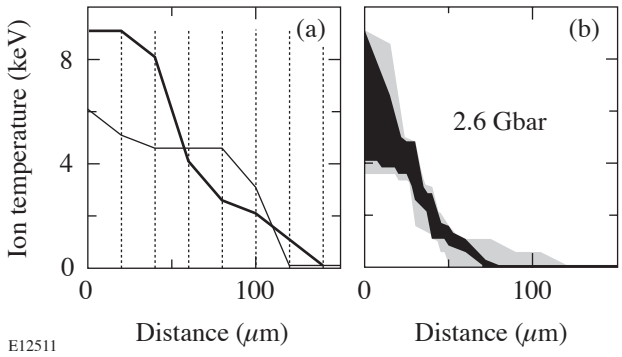


Figure 97.10
(a) The temperature–radius grid. The temperature step is 250 eV, and the distance step is 20 $\mu$m, as shown by the vertical dotted lines. The thick and thin solid lines show examples of monotonically decreasing temperature profiles as a function of distance used in core modeling. (b) The range of ion-temperature profiles consistent with the measured primary DD yield and neutron-averaged ion temperature (lightly shaded area), and in addition, the secondary DT yield (darkly shaded area), at electron pressure of 2.6 Gbar.

sion of the Be filter and the x-ray spectral response of the framing camera's gold photocathode were taken into account. The size of the x-ray image is very sensitive to the core pressure [see Fig. 97.11(b)]. The measured core image at peak neutron production is shown in Fig. 97.12(a). Figure 97.12(a) also shows two central lineouts of the measured image in horizontal and vertical directions by thick and thin solid lines. The image is slightly elliptical with FWHM's (full width at half maximum) ranging from about 94 to 100 $\mu$m in two perpendicular directions. The measured image is consistent with calculated images in the electron-pressure range from 2.3 to 3.1 Gbar. The shaded area in Fig. 97.12(a) is between the 2.3- and 3.1-Gbar lineouts, and the measured lineouts lie within this area. The ranges of inferred core temperature and density profiles, corresponding to this range of electron pressures, are shown in Figs. 97.12(b) and 97.12(c), respectively. As a result, only a relatively narrow range of temperature–density profiles is consistent with all neutron and x-ray measurements, simultaneously. The dashed curves correspond to simulations using the 1-D hydrocode *LILAC*,[11] which are discussed below.

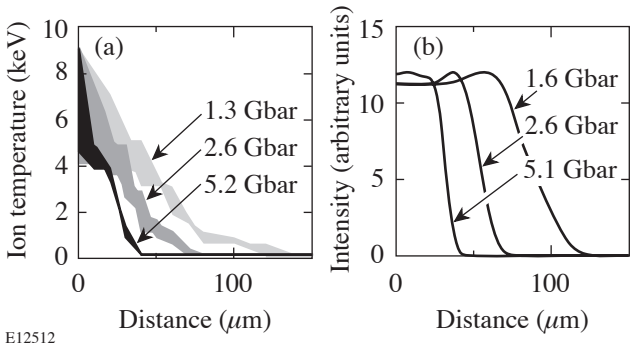


Figure 97.11
(a) The range of temperature profiles that satisfy measured primary DD, secondary DT yields, and neutron-averaged ion temperature, calculated for electron pressures of 1.6 (light), 2.6 (medium), and 5.1 Gbar (darkly shaded area). (b) Examples of x-ray radial lineouts (normalized to their highest values) calculated for the same pressures of 1.6, 2.6, and 5.1 Gbar.

Even though temperature–density profiles contain all information about the core condition, the core $\rho R$ has always been a simple and useful measurement[7,8] of target performance in ICF. Modeling based on flat temperature–density profiles[7,8] allows only approximate estimates of the areal density. Detailed temperature–density profiles consistent with all neutron and x-ray measurements are required for accurate determination of the core $\rho R$. The solid line in Fig. 97.13(a) shows a cumulative DD neutron yield as a function of the core areal density, calculated using temperature–density profiles at an electron pressure of 2.6 Gbar. The $\rho R$ of the "burn" region of ~10 mg/cm$^2$ was defined at 95% of the maximum value of the cumulative yield. The burn region $\rho R$ inferred from the temperature–density profiles at 1.3 Gbar [see Fig. 97.11(a)] is a factor of 2 smaller. Even though the 1.3-Gbar profiles are consistent with all neutron measurements, they were rejected because they did not predict the measured x-ray images. This means that the core $\rho R$ inferred solely from the yield ratio of primary to secondary neutrons (especially using flat profiles that are not consistent with all measurements) could be very

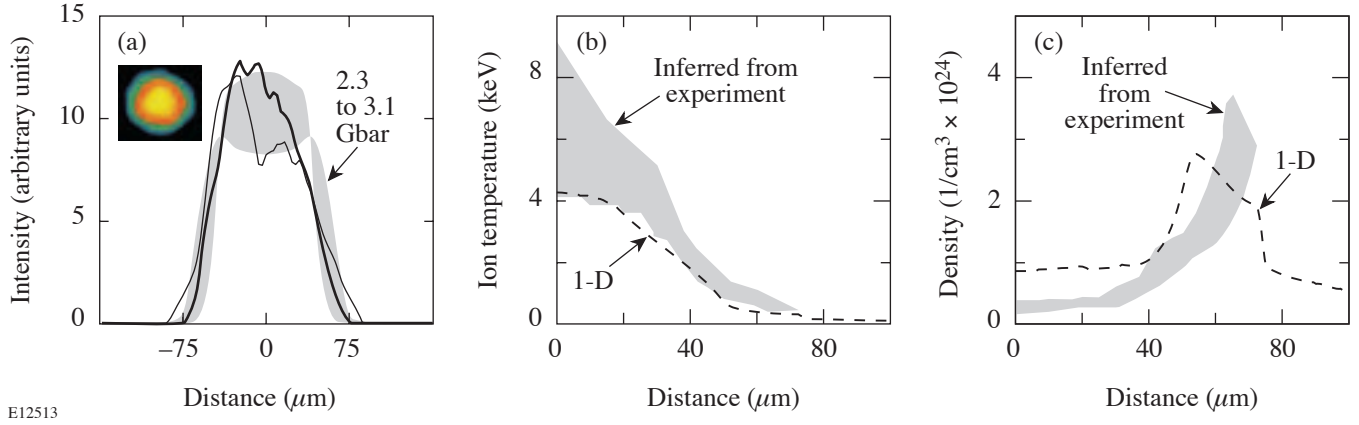


Figure 97.12
(a) X-ray framing camera image of the core at peak neutron production (upper left side); the horizontal and vertical lineouts of this image (thick and thin lines). The shaded area lies in between the lineouts of calculated images at electron pressures of 2.3 and 3.1 Gbar. All lineouts are normalized to the integrated intensities under the curves. The range of (b) core temperature and (c) density profiles corresponding to electron pressures in the range from 2.3 to 3.1 Gbar, which produce sizes of x-ray emission consistent with that of the measured x-ray image (shown by gray areas). The 1-D *LILAC* predictions are shown by dashed lines.

inaccurate. The total target $\rho R$ was measured to be ~61 mg/cm$^2$ at peak neutron production using a downshift in the secondary proton spectra.[10]

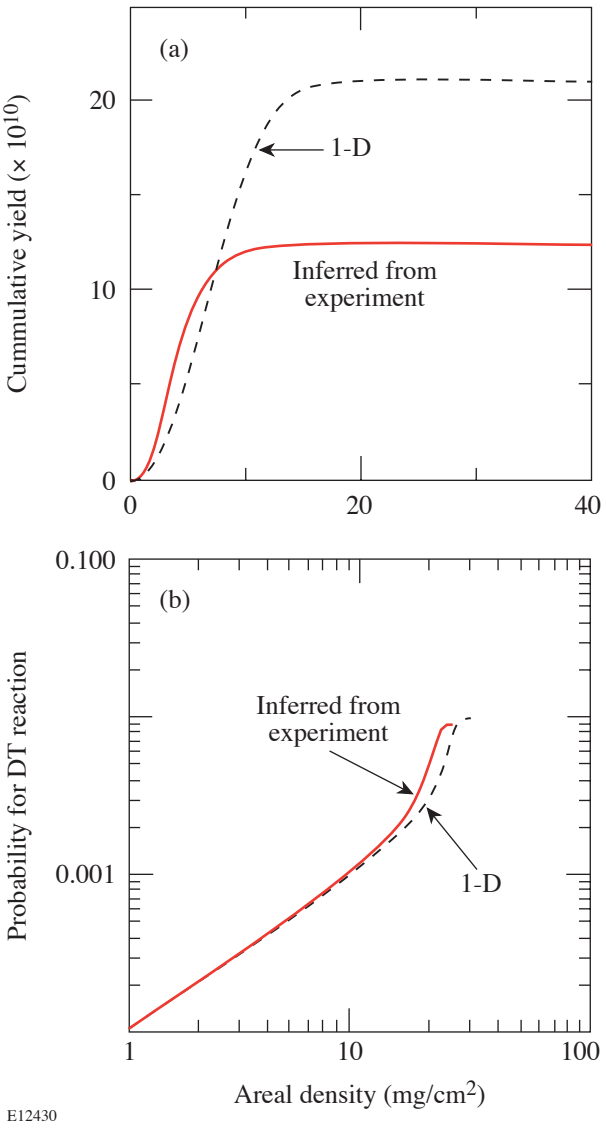


Figure 97.13
(a) Cumulative yields as a function of core $\rho R$, inferred from the experiment, for an electron pressure of 2.6 Gbar (solid curve), and from a 1-D simulation (dashed curve). The $\rho R$'s of the "burn" regions (~10 and ~15 mg/cm$^2$, respectively) were defined at 95% of the maximum value of the cumulative yield. (b) Probability for a secondary DT reaction (equal to a ratio of DT to DD yields) as a function of core $\rho R$, calculated for an electron pressure of 2.6 Gbar (solid curve). The triton probes a core $\rho R$ of ~23 mg/cm$^2$ before being stopped in the core. The dashed curve corresponds to a 1-D simulation with a "triton-stopping" $\rho R$ of ~27 mg/cm$^2$.

The $\rho R$ of a "triton-stopping" region is another useful parameter describing the extent of the hot core that is probed by the neutron measurements. The tritons are born in the neutron-production region through the DD fusion reaction. They are slowed down while they move through the core[15] until they are stopped in the target. The triton-slowing rate depends strongly on plasma temperature and density: it is higher in colder, less-dense plasmas;[7,8] therefore the $\rho R$ of a triton-stopping region (or the $\rho R$ necessary to stop the triton) is higher in hotter, denser cores. As the triton propagates in the core, it can react with deuterium through a secondary DT reaction, producing a secondary DT neutron.[7,8] Figure 97.13(b) shows (by a solid line) the probability for the DT reaction as a function of the core areal density, calculated for the same conditions as in Fig. 97.13(a) at an electron pressure of 2.6 Gbar. In this calculation, the triton is born at the core center and propagates toward the outer surface until it is stopped after probing ~23 mg/cm$^2$ of the core plasma. The probability for the DT reaction dramatically increases right before the triton is stopped because the DT-reaction cross section increases as the triton slows down in the plasma. Therefore, the secondary DT neutron yield is very sensitive to the temperature–density conditions in the outer part of the hot core, while the primary DD yield is more sensitive to conditions in the central part of the core.

The modeling results were compared with the predictions[11] of a 1-D *LILAC* simulation (dashed lines in Figs. 97.12 and 97.13). The predicted DD neutron yield of $2.1 \times 10^{11}$ was close to the measured yield of $1.24 \times 10^{11}$, while the simulated neutron-averaged ion temperature of 3.1 keV was a little lower than that measured 3.6 keV. As a result, the simulated temperature profile [see Fig. 97.12(b)] was a little lower than the temperature range inferred from the experiment, while the density profile was a little higher [see Fig. 97.12(c)]. In the 1-D simulation, the burn and triton-stopping region $\rho R$'s were very close to those inferred from the experiment. In the simulation, the burn $\rho R$ was ~15 mg/cm$^2$ (~10 mg/cm$^2$ in the experiment) and the triton-stopping region $\rho R$ was ~27 mg/cm$^2$ (~23 mg/cm$^2$ in the experiment), as shown in Fig. 97.13. Measurements based on monochromatic differential imaging[17,18] of core x rays are planned to infer the time-resolved evolution of $D_2$-core profiles in the near future, using techniques similar to those described elsewhere.[19]

In conclusion, the compressed-core, electron temperature–density profiles of a cryogenic deuterium ($D_2$) target have been characterized using measured primary DD and secondary DT yields, neutron-averaged ion temperature, and core x-ray im-

ages at peak neutron production. The inferred temperature–density profiles are in good agreement with predictions of the 1-D hydrocode *LILAC*. The electron pressure, burn, and triton-stopping region $\rho R$'s were inferred to be 2.7±0.4 Gbar, ~10 mg/cm$^2$, and ~23 mg/cm$^2$, respectively.

## ACKNOWLEDGMENT

One of the authors (V.A.S.) would like to thank D. C. Wilson for helpful discussions. This work was supported by the U.S. Department of Energy Office of Inertial Confinement Fusion under Cooperative Agreement No. DE-FC03-92SF19460, the University of Rochester, and the New York State Energy Research and Development Authority. The support of DOE does not constitute an endorsement by DOE of the views expressed in this article.

## REFERENCES

1. J. Nuckolls *et al*., Nature **239**, 139 (1972).
2. J. D. Lindl, Phys. Plasmas **2**, 3933 (1995).
3. P. W. McKenty, V. N. Goncharov, R. P. J. Town, S. Skupsky, R. Betti, and R. L. McCrory, Phys. Plasmas **8**, 2315 (2001).
4. R. L. McCrory, J. M. Soures, C. P. Verdon, F. J. Marshall, S. A. Letzring, S. Skupsky, T. J. Kessler, R. L. Kremens, J. P. Knauer, H. Kim, J. Delettrez, R. L. Keck, and D. K. Bradley, Nature **335**, 225 (1988).
5. Y. Kitagawa *et al*., Phys. Rev. Lett. **75**, 3130 (1995).
6. T. R. Boehly, D. L. Brown, R. S. Craxton, R. L. Keck, J. P. Knauer, J. H. Kelly, T. J. Kessler, S. A. Kumpan, S. J. Loucks, S. A. Letzring, F. J. Marshall, R. L. McCrory, S. F. B. Morse, W. Seka, J. M. Soures, and C. P. Verdon, Opt. Commun. **133**, 495 (1997).
7. H. Azechi *et al*., Appl. Phys. Lett. **49**, 555 (1986).
8. M. D. Cable and S. P. Hatchett, J. Appl. Phys. **62**, 2233 (1987).
9. P. B. Radha, J. Delettrez, R. Epstein, V. Yu. Glebov, R. Keck, R. L. McCrory, P. McKenty, D. D. Meyerhofer, F. Marshall, S. P. Regan, S. Roberts, T. C. Sangster, W. Seka, S. Skupsky, V. Smalyuk, C. Sorce, C. Stoeckl, J. Soures, R. P. J. Town, B. Yaakobi, J. Frenje, C. K. Li, R. Petrasso, F. Séguin, K. Fletcher, S. Padalino, C. Freeman, N. Izumi, R. Lerche, and T. W. Phillips, Phys. Plasmas **9**, 2208 (2002).
10. S. Kurebayashi, J. A. Frenje, F. H. Séguin, J. R. Rygg, C. K. Li, R. D. Petrasso, V. Yu. Glebov, J. A. Delettrez, T. C. Sangster, D. D. Meyerhofer, C. Stoeckl, J. M. Soures, P. A. Amendt, S. P. Hatchett, and R. E. Turner, "Use of Secondary Nuclear Particles for Studying the Areal Density of $D_2$-Filled Inertial Confinement Fusion Capsules," to be published in Physics of Plasmas.
11. T. C. Sangster, J. A. Delettrez, R. Epstein, V. Yu. Glebov, V. N. Goncharov, D. R. Harding, J. P. Knauer, R. L. Keck, J. D. Kilkenny, S. J. Loucks, L. D. Lund, R. L. McCrory, P. W. McKenty, F. J. Marshall, D. D. Meyerhofer, S. F. B. Morse, S. P. Regan, P. B. Radha, S. Roberts, W. Seka, S. Skupsky, V. A. Smalyuk, C. Sorce, J. M. Soures, C. Stoeckl, K. Thorp, J. A. Frenje, C. K. Li, R. D. Petrasso, F. H. Séguin, K. A. Fletcher, S. Padalino, C. Freeman, N. Izumi, J. A. Koch, R. A. Lerche, M. J. Moran, T. W. Phillips, and G. J. Schmid, Phys. Plasmas **10**, 1937 (2003).
12. Y. Lin, T. J. Kessler, and G. N. Lawrence, Opt. Lett. **20**, 764 (1995).
13. S. P. Regan, J. A. Marozas, J. H. Kelly, T. R. Boehly, W. R. Donaldson, P. A. Jaanimagi, R. L. Keck, T. J. Kessler, D. D. Meyerhofer, W. Seka, S. Skupsky, and V. A. Smalyuk, J. Opt. Soc. Am. B **17**, 1483 (2000).
14. T. R. Boehly, V. A. Smalyuk, D. D. Meyerhofer, J. P. Knauer, D. K. Bradley, R. S. Craxton, M. J. Guardalben, S. Skupsky, and T. J. Kessler, J. Appl. Phys. **85**, 3444 (1999).
15. C. Li and R. D. Petrasso, Phys. Plasmas **2**, 2460 (1995).
16. W. J. Karzas and R. Latter, Astrophys. J. Suppl. Ser. **6**, 167 (1961).
17. J. A. Koch, S. W. Haan, and R. C. Mancini, "Multispectral Imaging of Continuum Emission for Determination of Temperature and Density Profiles Inside Implosion Plasmas," to be published in the Journal of Quantitative Spectroscopy and Radiative Transfer.
18. V. A. Smalyuk, V. N. Goncharov, J. A. Delettrez, F. J. Marshall, D. D. Meyerhofer, S. P. Regan, and B. Yaakobi, Phys. Rev. Lett. **87**, 155002 (2001).
19. I. Golovkin, R. Mancini, S. Louis, Y. Ochi, K. Fujita, H. Nishimura, H. Shirga, N. Miyanaga, H. Azechi, R. Butzbach, I. Uschmann, E. Förster, J. Delettrez, J. Koch, R. W. Lee, and L. Klein, Phys. Rev. Lett. **88**, 045002 (2002).

# Extended X-Ray Absorption Fine Structure Measurements of Laser Shocks in Ti and V and Phase Transformation in Ti

## Introduction

Recently, x-ray diffraction has been used to study dynamic material response to shocks of high pressure (~0.1 to 1 Mbar) and high strain rate (~$10^7$ to $10^8$ $s^{-1}$).[1–3] The goal of this work is to demonstrate the use of extended x-ray absorption fine structure (EXAFS)[4] as a complementary characterization of such laser-shocked metals. EXAFS is the modulation in the x-ray absorption above the *K* edge (or *L* edge) due to the interference of the photoelectron wave packet with the waves reflected from neighboring atoms. Unlike synchrotron experiments where the imposed temperature is known independently and the main emphasis is on the study of the chemical structure, in this experiment the emphasis is on the measurement of the compression and temperature of the shocked material through the EXAFS spectrum itself. The frequency of EXAFS modulations is related to the interparticle distance, hence to the compression. The damping rate of the modulation can yield the lattice temperature, *which is not available by other methods*. The assumption of three-dimensional compression, required to relate the EXAFS-determined inter-atomic distance to the density, was verified by comparison with measurements of the shock speed, which yield the compression (through the known Hugoniot equation of state).

EXAFS measurements were performed on vanadium and titanium shocked to ~0.5 Mbar with a 3-ns laser pulse. The radiation source for the EXAFS measurement was obtained by imploding a spherical target using the 60-beam OMEGA laser.[5] For vanadium (where no phase transformation exists below ~1 Mbar) the measurements demonstrate that EXAFS is a useful method for measuring the compression and temperature of sub-Mbar shocks. For Ti, where an $\alpha$-Ti to $\omega$-Ti crystal phase transformation is known to occur around ~0.1 Mbar, over longer time scales ($\mu$s) behind a steady shock,[6,7] the measurements show that EXAFS can be used to study such transformations over subnanosecond time scales.

In a previous paper[8] we showed that a CH shell imploded by a multibeam laser system constitutes a ~120-ps source of intense and relatively smooth spectrum of x-ray radiation, suitable for EXAFS measurements. Using the 60-beam OMEGA laser, the measured room-temperature Ti EXAFS spectrum agreed with synchrotron results under similar conditions.

The subject of laser-shocked metals can be viewed from two complementary points of view: as a problem in solid-state physics and/or as a problem in plasma physics. The EXAFS measurements in this experiment, and particularly the diffraction measurements[1–3] of similar laser shocks, indicate that laser-shocked metals for pressures under ~1 Mbar largely retain their crystal-order properties. This is why the crystal phase transformation in Ti could be demonstrated with laser-driven shock waves. The shock dynamics have been simulated with a plasma-physics hydrodynamic code (see **Hydrodynamic Simulations**). The laser-deposition region where the shock is generated is certainly a plasma region and can be simulated only with a plasma-physics code. However, the same code is used to simulate both shock generation and propagation through the sample, thus relating the incident laser intensity to the resulting shock strength. The hydrodynamic code can well simulate the compressed solid because the semi-empirical equation of state[9] is normalized to known experimental properties of the metal (such as specific heat, Grüneisen parameter, and bulk modulus). The comparison of the code and experimental results forms the basis for the study of the compressed solid, which apart from its crystalline order is also a high-density or strongly coupled plasma. Such plasmas are of great interest in understanding the interior of planets and the behavior of matter under extreme conditions.

## Experimental

Figure 97.14 shows a schematic view of the target used to measure EXAFS spectra in laser-shocked targets. Of the 60 OMEGA laser beams, 57 beams of ~21-kJ total energy are focused on an empty CH shell whose implosion generates the radiation source for measuring the absorption spectrum in V or Ti. In previous laser-based EXAFS experiments[10,11] a planar high-*Z* target was used where the spectrum was dominated by spectral-line emission and was thus not smooth. The low-*Z* imploding target used here produces a very intense and smooth

continuum spectrum,[8] appropriate for absorption measurements. The three remaining OMEGA beams are stacked and used to launch a planar shock wave in the metal target. The laser pulse shape was 1 ns square (each of energy ~50 J); thus the three-stacked beams formed a 3-ns-long square pulse. These beams were focused onto the planar target in a 3.8-mm-diam focal spot, giving an irradiance of 0.4 to 0.5 TW/cm$^2$. The delay time of the three-stacked beams with respect to the remainder of the beams was adjusted so that peak implosion (and emission) of the spherical target occurred when the shock wave had just exited the metal layer. The spherical target had a diameter ~950 $\mu$m and a CH wall thickness ~20 $\mu$m. The planar target consisted of 10-$\mu$m-thick polycrystalline V or Ti, coated on both sides with a 17-$\mu$m-thick CH layer. The purpose of the front CH layer was to prevent laser heating and ablation of the metal. The purpose of the back CH layer was to prevent shock unloading at the back metal surface. The heat shield (0.5-mm-thick CH foil) minimizes the heating of the metal layer due to soft radiation from the imploding spherical target.

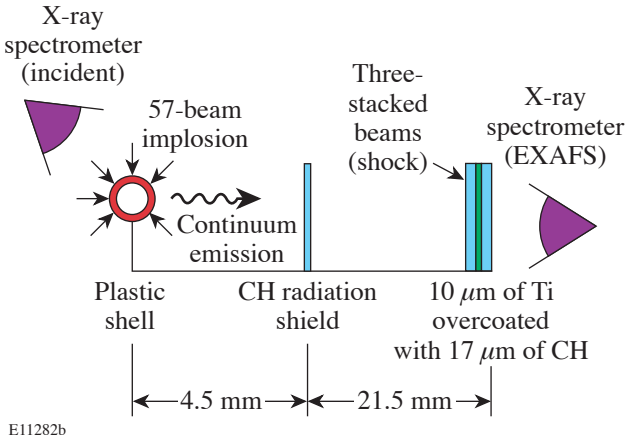


Figure 97.14
Schematic view of the experimental configuration. The imploding spherical target serves as a radiation source for EXAFS measurements. The three-stacked beams launch a shock through the Ti (or V) layer.

Two cross-calibrated x-ray spectrometers measured the spectrum on calibrated film. One spectrometer measured the EXAFS spectrum, the other the incident spectrum. The spectra were measured simultaneously on a single target shot. A typical record of the transmitted spectrum showing EXAFS modulation is shown in Fig. 97.15. As explained in Ref. 8, the high incident intensity enabled us to choose a relatively thick sample (giving an optical depth of 3.5 just above the Ti *K* edge), which yields high relative modulation amplitude in the measured spectrum. However, the spectrum below the *K* edge is then saturated; to accurately determine the *K*-edge position and below-the-edge signal intensity, we used an Al attenuator on part of the entrance slit, as seen in Fig. 97.15. A typical incident spectrum is shown in Fig. 2(a) of Ref. 8. The spectral resolution of the spectrometer, limited by the source size, was ~5 eV, much smaller than a typical EXAFS modulation period (~60 eV).

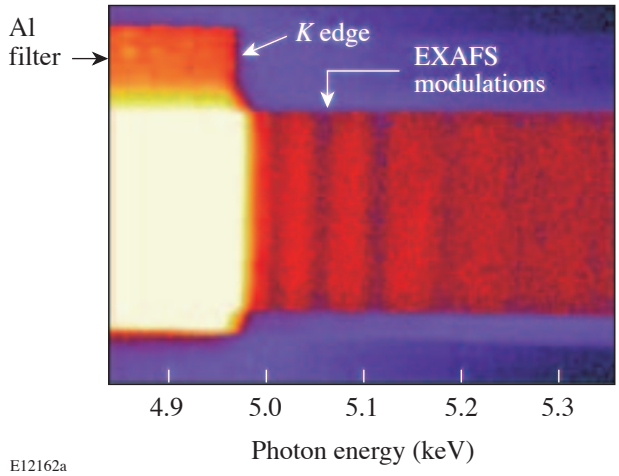


Figure 97.15
Typical record of the transmitted spectrum (from unshocked Ti) showing EXAFS modulations above the *K* edge.

Although the EXAFS measurement is time integrated, a meaningful shock diagnosis can be obtained without streaking the spectrum in time because the x-ray pulse width is ~120 ps,[8] much shorter than the shock transit time through the metal (~2 ns). The timing of the shock relative to the implosion-induced backlighter pulse was measured by the method of active shock breakout (ASBO),[12] a method that uses a frequency-doubled YAG laser probe, reflected from the backside of the target. Figure 97.16 shows a schematic of the setup and a typical streak result; $\tau$(Ti) and $\tau$(CH) are the times when the shock has traversed the metal layer and the back CH layer, respectively. This measurement determines the correct timing between the implosion beams and shock-producing beams. It also yields the shock speed in the metal (~5 $\mu$m/ns), from which, using the known Hugoniot equation of state, the shock compression and pressure can be obtained. Finally, images such as in Fig. 97.16 indicate a lateral nonuniformity (due to the laser's focal-spot distribution) of ±10% in the shock speed, thus also in the shock compression.

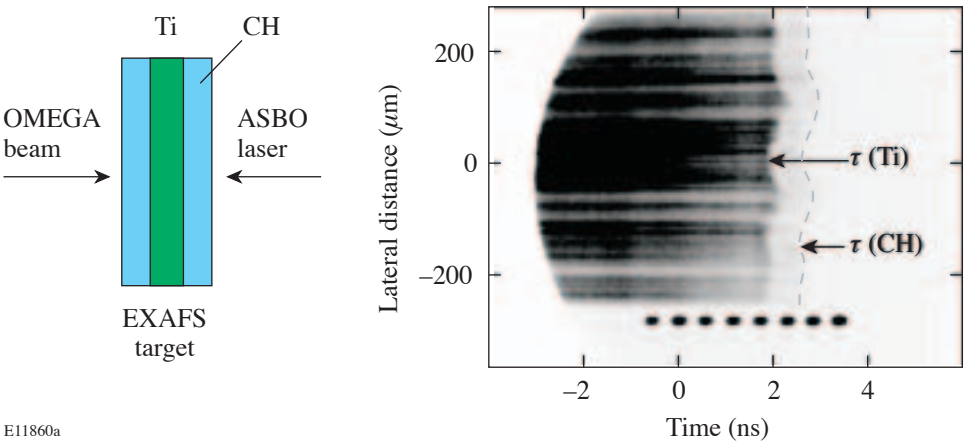


Figure 97.16
Schematic and a typical streak of the ASBO probe beam reflected from the backside of the target. $\tau$(Ti) and $\tau$(CH) are the times when the shock exits the metal layer and the back CH layer, respectively. This measurement provides (a) the correct timing between the capsule-implosion beams and shock-producing beams, (b) the shock speed in the metal, and (c) the lateral shock uniformity.

**Hydrodynamic Simulations**

The expected shock strength and the properties of the shocked vanadium and titanium were determined using one-dimensional simulations with the hydrodynamic code *LASNEX*.[13] The profiles of pressure, density, and temperature versus position are shown for V in Fig. 97.17 and for Ti in Fig. 97.18, at the time of arrival of the shock at the rear surface of the metal layer for an incident laser intensity of ~0.5 TW/cm$^2$. The range (around the volume average) of parameter values within the V layer is (1) pressure: 0.43±0.03 Mbar; (2) temperature: 980±160 K; and (3) volume compression: 1.19±0.05. These variations in the axial direction are larger than the lateral variations due to laser nonuniformity; for this reason a one-dimensional simulation of the shocked metals is adequate. For Ti the comparable ranges are (1) pressure: 0.33±0.05 Mbar; (2) temperature: 900±130 K; and (3) volume compression: 1.2±0.06. The EXAFS measurements (in the case where the metals were shocked) are averaged over the shocked volume; thus, the volume averages are the appropriate theoretical quantities to compare with the experiment.

**Theory**

The measured spectra were analyzed with the FEFF8 *ab initio* EXAFS software package.[14] The basic theory of EXAFS[4] yields an expression for the relative absorption $\chi(k) = \mu(k)/\mu_0(k) - 1$, where $\mu(k)$ is the absorption coefficient and $\mu_0(k)$ is the absorption of the isolated atom. The wave number $k$ of the ejected photoelectron is given by the de Broglie relation $\hbar^2k^2/2m = E - E_K$, where $m$ is the electron rest mass, $E$ is the absorbed photon energy and $E_K$ is the energy of the $K$ edge. The basic EXAFS formula for a single reflection in the plane-wave approximation is given by[4]

$$\chi(k) = \sum_j N_j S_0^2 F_j(k) \exp\left[-2\sigma^2 k^2 - 2R_J/\lambda(k)\right] \times \sin\left[2kR_j + \phi_j(k)\right]/kR_j^2, \quad (1)$$

where $N_j$ is the number of atoms in the the $j$-th shell, that is, the number of atoms surrounding the absorbing atom at a distance $R_j$, and $\lambda(k)$ is the electron mean free path for collisions. FEFF8 uses the scattering potential to calculate the amplitude and phase shift of the photoelectron waves scattered from several shells of neighboring atoms including multiple-scattering paths. The total $\chi(k)$ is constructed in the curved-wave approximation (i.e., the assumption of plane wave is removed) and iteratively fitted to the experimental $\chi(k)$. The main fitting parameters are the nearest-neighbor distance $R$ and the vibration parameter $\sigma^2$ appearing in the Debye–Waller term. $R$ yields the density or compression if we assume three-dimensional compression. The agreement of the resulting compression with the value derived from the shock-speed measurement justifies this assumption. The vibration

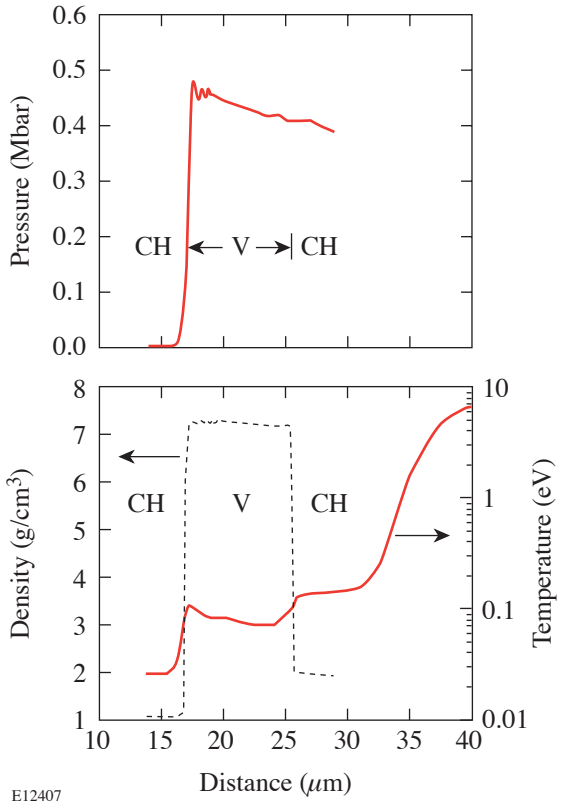


Figure 97.17
One-dimensional shock profiles versus position calculated by the hydrodynamic code *LASNEX* for the instant when the shock has just traversed the V layer, assuming an incident laser intensity of ~0.5 TW/cm$^2$ in a 3-ns square pulse.

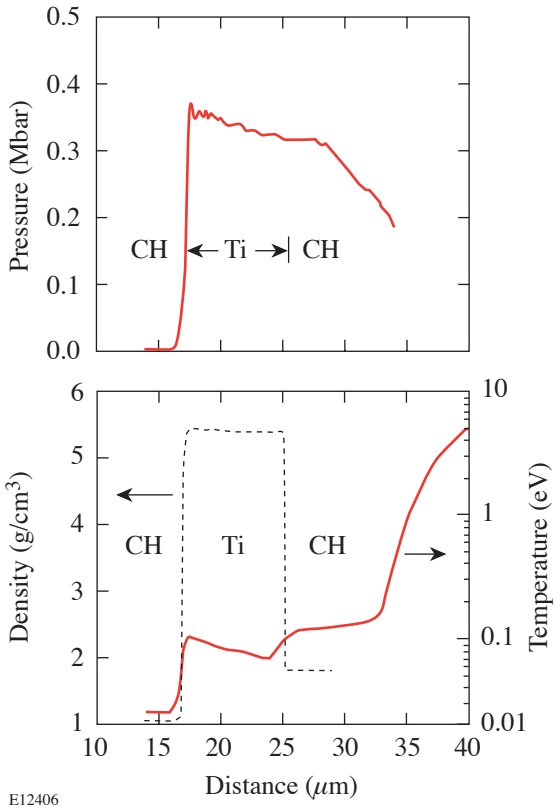


Figure 97.18
One-dimensional shock profiles versus position calculated by the hydrodynamic code *LASNEX* for the instant when the shock has just traversed the Ti layer, assuming an incident laser intensity of ~0.5 TW/cm$^2$ in a 3-ns square pulse.

amplitude $\sigma^2$ depends mainly on the temperature but also on the compression. $\sigma^2$ is calculated as a function of temperature, using the Debye model[15] for the phonon density of states, including correlation between the motions of the absorbing and neighboring atoms; $\sigma^2$ depends on the density through the Debye temperature. The density dependence of the Debye temperature was calculated using an empirical model.[9] Figure 97.19 the shows the resulting $\sigma^2$ for V as a function of temperature and compression. As seen, compression increases the amplitude of the EXAFS signal because of the decrease in $\sigma^2$. Similar curves have been calculated for titanium. Thus, knowing the compression and $\sigma^2$, the temperature can be derived.

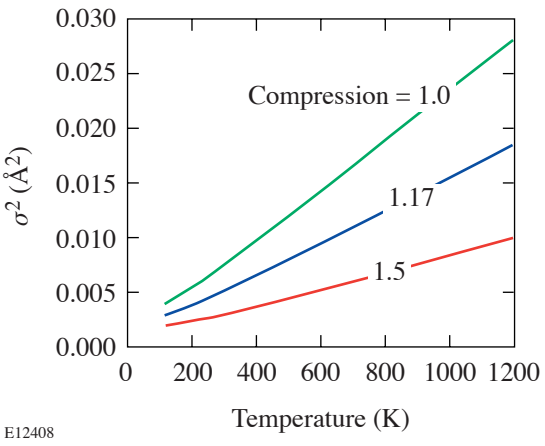


Figure 97.19
Calculated $\sigma^2$ due to thermal vibrations for V from a correlated Debye model.

**Results and Analysis**

1. Vanadium

The measured absorption spectra from V are shown in Figs. 97.20 and 97.21. Figure 97.20 shows the total absorption curve in V, with and without shocking. The frequency of the

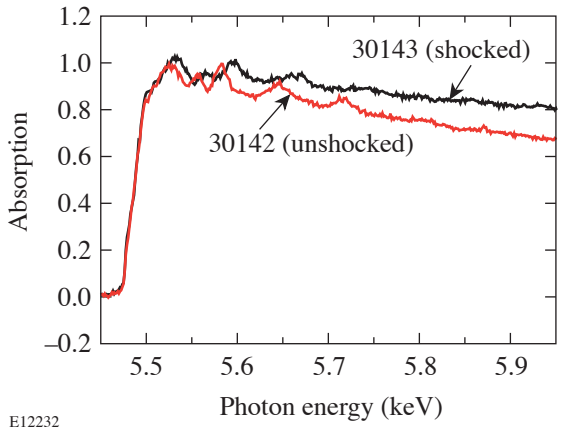


Figure 97.20
Measured absorption in V (normalized to 1), with and without shocking. The lengthening of the period of EXAFS modulation in the shocked case is evidence for compression. The shock pressure was 0.45 Mbar.

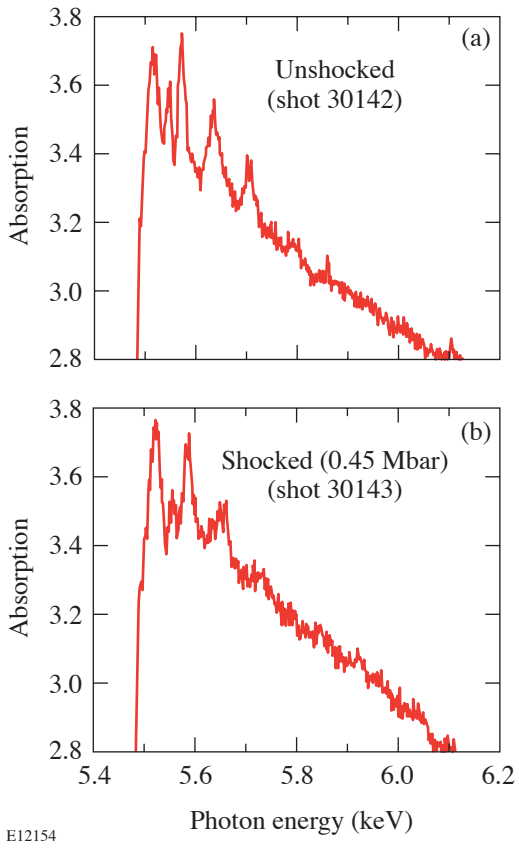


Figure 97.21
Expanded view of the EXAFS modulations in V shown in Fig. 97.20 for the unshocked case (a) and the shocked case (b). The modulations are clearly seen to decay faster when the V is shocked, due to the increased temperature. This comparison demonstrates the usefulness of EXAFS spectra in measuring the temperature of shocked metals.

EXAFS oscillations is seen to become smaller when the shock is applied. Since that frequency (in $k$ space) is proportional to the distance $R$ to the nearest neighbors [see Eq. (1)], the lowering of the frequency indicates a smaller $R$, thus a shock compression. Figure 97.21 shows a magnified view of the EXAFS modulations for the unshocked case (a) and the shocked case (b). The modulations are clearly seen to decay faster when the vanadium is shocked, due to the increased temperature. *This comparison demonstrates the usefulness of EXAFS spectra in measuring the temperature of shocked metals in the range of* T ~ *10 to 100 meV.*

The results of fitting the V EXAFS spectra with the FEFF8 code[14] for the unshocked and shocked cases are shown in Fig. 97.22. For the unshocked case, the fitting parameters were (for the first shell) $R$ = (2.585±0.008) Å and $\sigma^2$ = (0.0111±0.0006) Å2. In the vanadium crystal (body-centered

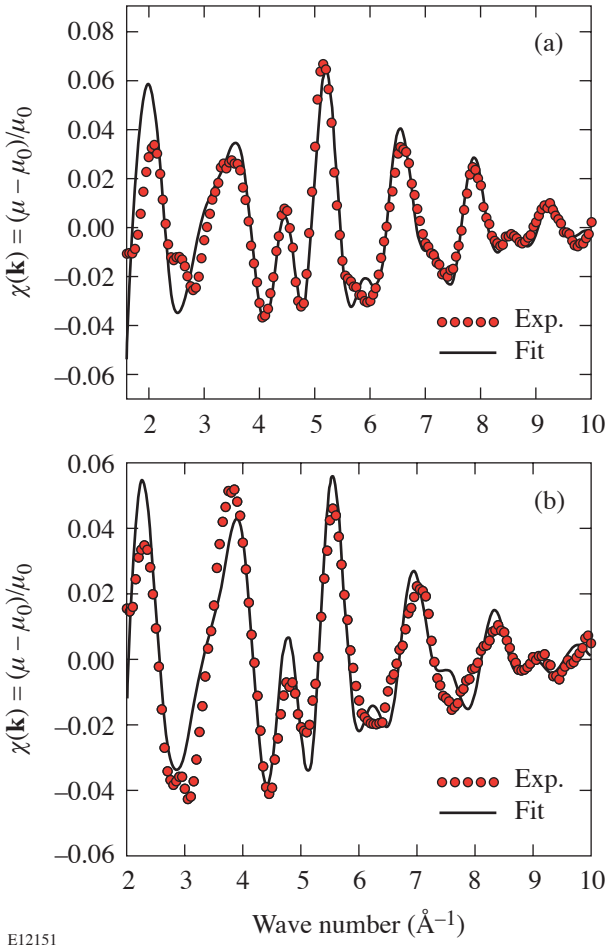


Figure 97.22
Fitting the measured V EXAFS spectra for the unshocked case (a) and the shocked case (b) with the FEFF8 code.

cubic), the first shell has eight atoms at a distance of $(3/5)^{1/2}a$, where the crystallographic parameter $a$ is 3.02 Å, yielding for the nearest neighbors a distance of 2.615 Å. Thus, the $R$ found here is smaller than the expected value by ~0.03 Å; interestingly, the value found for $R$ (vanadium) in V EXAFS synchrotron experiment[16] was also 2.58 Å, in agreement with our value. From the measured value of $\sigma^2$, we derive (using Fig. 97.19) the temperature 530±25 K. The increase of ~130 K over room temperature is due to the radiation heating caused by the imploding target.

For the shocked case, the fitting parameters (for the first shell) were $R = (2.570\pm0.013)$ Å and $\sigma^2 = (0.0157\pm0.0011)$ Å$^2$. Comparing $R$ for the unshocked and shocked cases, we derive a volume compression of $(2.585/2.570)^3 \sim 1.15$. The value of $\sigma^2$ results in a temperature of 900±70 K. This increase in temperature includes the effect of radiation heating; the net temperature due to the shock alone is 770±70 K.

Table 97.I summarizes the measured and computed parameters for the shocked-V experiment. EXAFS results indicate a weaker shock than predicted by *LASNEX*, but they are in agreement with the shock-speed measurement (as seen by the compression values). The measured values are accompanied by their uncertainties, whereas the *LASNEX* values are accompanied by their ranges in the axial direction. The uncertainty in the EXAFS measurement is determined by the fitting procedure and is smaller than the axial or the lateral nonuniformities described above. The EXAFS-derived values relate to the average over the shock volume. Likewise, the compression in the last column of Table 97.I is derived from the shock speed averaged (laterally) over the streak record, and its uncertainty is smaller than the range of variation in the speed.

2. Titanium

Phase transformations in shocked metals can be measured by a discontinuity in the Hugoniot curves or directly by x-ray diffraction. EXAFS can indicate a phase transformation if the Debye–Waller factor $\sigma^2$ undergoes an abrupt increase.[17] This can occur if the transformation is to a disordered state or if the nearest-neighbor distances in the new crystal are disparate and the beating of the frequencies corresponding to the various distances causes a stronger modulation damping. Shocked titanium (at much longer duration than here) is known to undergo an $\alpha$-Ti to $\omega$-Ti phase transformation at a pressure in the range of 0.029 to 0.09 Mbar, depending on sample purity.[6,7] The pressure in this experiment is well above this range. It is not known, however, whether the transformation can occur on the nanosecond time scale. Figure 97.23 shows the EXAFS spectra from Ti, before (a) and after (b) being compressed with an ~0.5 Mbar shock. The experimental conditions were the same as in the vanadium experiment except

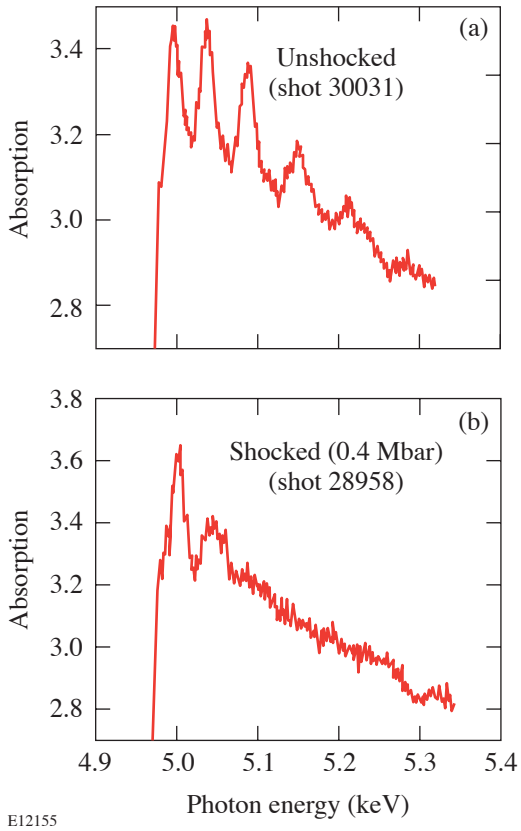


Figure 97.23
EXAFS spectra from Ti, before (a) and after (b) being compressed by a ~0.5 Mbar shock. The modulation with shocking is seen to be strongly damped. This is shown to reflect an $\alpha$-Ti to $\omega$-Ti phase transformation.

Table 97.I: *LASNEX*-calculated and measured parameters for shocked vanadium.

| *LASNEX* Parameter Ranges | | EXAFS Measurement | | Shock-Speed Measurement |
|---|---|---|---|---|
| Compression | Temperature | Compression | Temperature | Compression |
| 1.19±0.05 | 980±160 K | 1.15±0.01 | 770±70 K | 1.15±0.06 |

that the laser intensity was 0.5 TW/cm$^2$. As in the case of vanadium (Fig. 97.20), the EXAFS modulations in the shocked case have a lower frequency than in the unshocked case, indicating shock compression. However, the modulations in the shocked case are seen to be much more strongly damped than in the case of vanadium. This is shown below to reflect an $\alpha$-Ti to $\omega$-Ti phase transformation.

Figure 97.24 shows the fitting of the FEFF8 EXAFS code to the measured Ti EXAFS spectra taken before (a) and after (b) the shock, assuming $\alpha$-Ti for both. The first-shell fitting parameters result in a volume compression of 1.2±0.03. This compares well with the *LASNEX* value of 1.2±0.06, but the error is much larger than for vanadium. The $\sigma^2$ value of the unshocked case is 0.0088 Å$^2$, which corresponds to a temperature of 380 K. For the shocked case, $\sigma^2$ = 0.029±0.008 Å$^2$, which corresponds to a temperature of $T$ = 2100±570 K. The obtained temperature is in sharp disagreement with the *LASNEX*-predicted value (~900 K). This strongly suggests that the large $\sigma^2$ value is not due to a high temperature but due to a structural rearrangement such as a phase transformation. The large fitting errors also suggest that the assumed crystal structure (*hcp*) is not the correct structure for the shocked titanium. These conclusions are supported by the good agreement between measurements and simulation for comparable shocks in vanadium (Fig. 97.22), where no phase transformation is expected. In fact, whereas each $\alpha$-Ti atom has six equidistant neighbors, $\omega$-Ti atoms have two possible atomic environments:[6] at site A there are 15 neighbors at two different distances, and at site B there are 11 neighbors at three different distances. Different distances translate to different EXAFS frequencies that, through beating, cause enhanced damping. Figure 97.25 shows this to be the case. Here FEFF calculations assuming the $\omega$-Ti crystal structure, averaging over sites A and B, were carried out for the *LASNEX*-predicted temperature of 900 K. Only the compression was adjusted to fit the experiment, and the resulting value of 1.23 is close to the predicted value of 1.2. It should be noted that the $\alpha$-Ti to $\omega$-Ti phase transformation entails an ~2% volume compression.[7] Also shown is the FEFF calculation for the $\alpha$-Ti phase, using the *LASNEX*-predicted temperature and adjusting the compression to agree with the data. Figure 97.25 clearly shows that assuming the $\omega$-Ti phase agrees with the experiment much better than assuming the $\alpha$-Ti phase. Thus, the damping is dominated by the crystal structure of $\omega$-Ti rather than by the temperature.

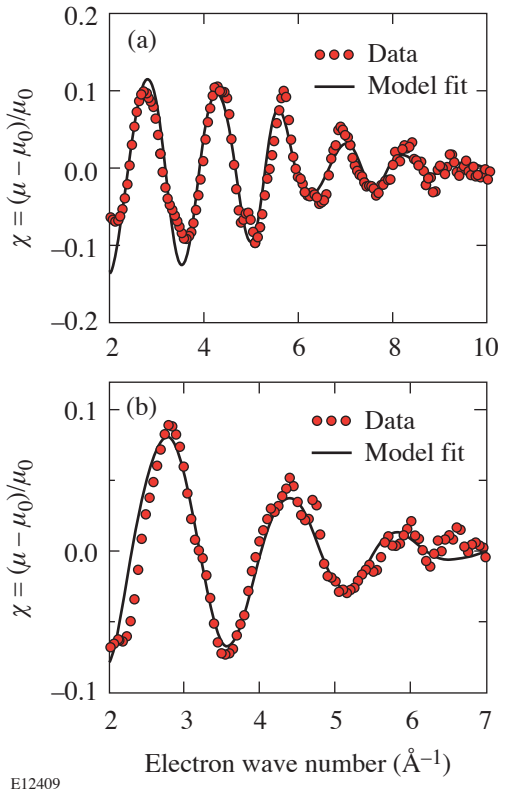


Figure 97.24
Fitting the FEFF8 EXAFS code to the measured Ti EXAFS spectra taken before (a) and after (b) being compressed by a ~0.5 Mbar shock, assuming $\alpha$-Ti phase.

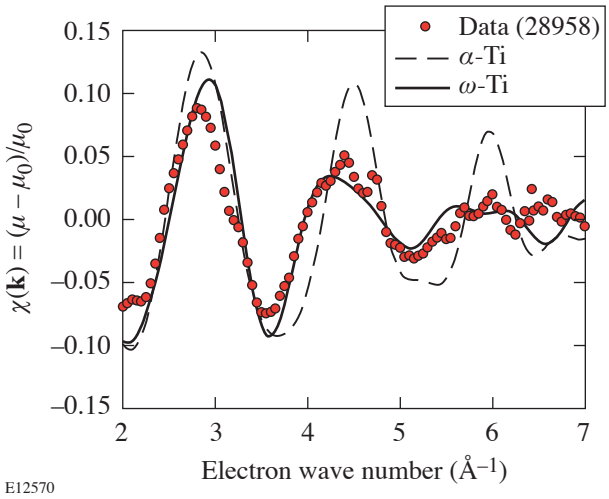


Figure 97.25
Fitting the FEFF8 EXAFS code to the measured Ti EXAFS spectrum, assuming the $\alpha$-Ti phase (the *hcp* phase at normal conditions) and the $\omega$-Ti phase. Only the compression was adjusted (to fit the frequency of modulation) and the *LASNEX*-predicted temperature $T$ = 900 K was assumed.

A critical test of the assumption of phase transformation can be obtained by repeating the measurement for successively weaker shocks. Figure 97.26 shows the transmitted spectrum from a Ti sample for four different values of laser intensity (volume-averaged pressures from *LASNEX* are indicated). The reduction of the intensity by a factor ~2 to 0.23 TW/cm$^2$ shows no significant change in the spectrum. This clearly proves that the high damping rate is not due to a high temperature. At an intensity of ~0.12 TW/cm$^2$ (corresponding to a pressure of ~0.12 Mbar) the damping rate is intermediate between the unshocked and shocked cases. Thus, the results are consistent with a phase transformation occurring, very roughly, around 0.12 Mbar.

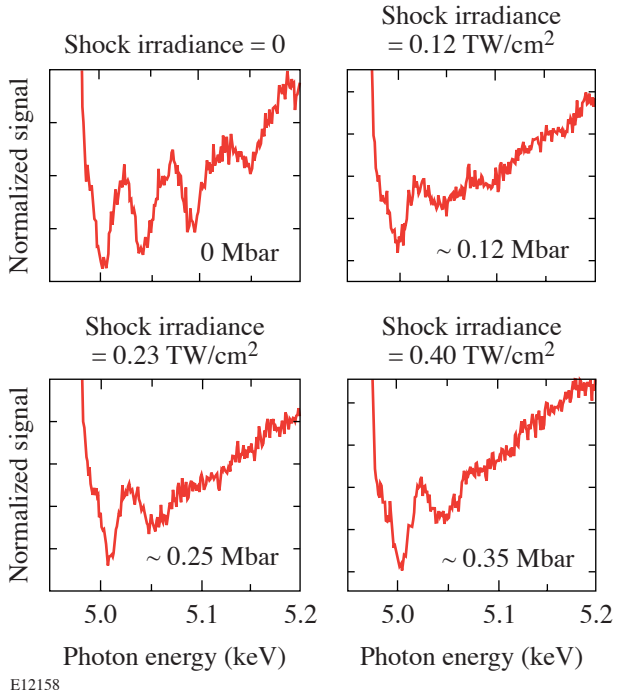


Figure 97.26
Transmitted intensity from the Ti sample for four different values of laser intensity (average pressure values from *LASNEX* are also shown). The comparison indicates that a phase transformation occurs for laser intensity of ~0.12 TW/cm$^2$, which corresponds to a pressure of ~0.12 Mbar.

Laser-shocked monocrystalline silicon was found[1–3] to compress uniaxially, at least during the ~5-ns time scale of the diffraction measurement. The question arises as to whether the fast damping of the Ti EXAFS spectrum could be the result of such elastic (1-D) compression, where the varied neighbor distances would lead to beating of the corresponding EXAFS frequencies. To address this question we calculated the first-shell Ti EXAFS spectrum under the assumption of 1-D compression for $\alpha$-Ti. The result is compared in Fig. 97.27 with a calculated first-shell EXAFS curve for a 3-D compression as well as with the experimental result (in Ti the contribution of more-distant shells is relatively small). The assumed 1-D and 3-D compressions (both for $T = 900$ K) were adjusted to yield agreement between the measured and calculated EXAFS modulation frequency. In each case the coordinates of a cluster of atoms around the absorbing atom were adjusted to reflect the assumed compression. The ratio $R_0/R$ is the reduction in distances in the direction of shock propagation (in the 1-D case). In the case of 1-D compression, the results depend on the direction of compression with respect to the atomic planes, whose orientation is different for each crystallite of the poly-

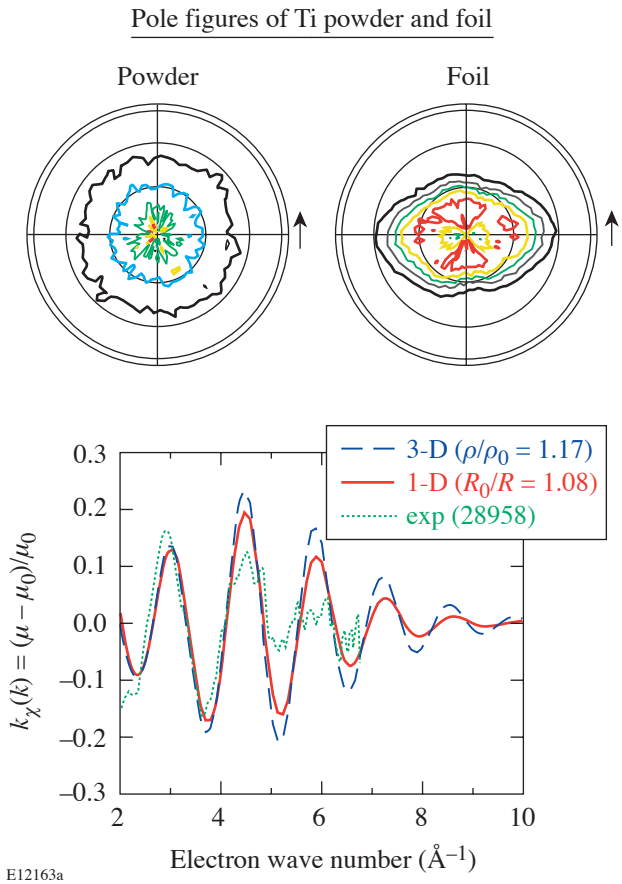


Figure 97.27
Demonstration that the fast damping of EXAFS from shocked Ti is not due to a 1-D compression. The calculated 1-D compression in $\alpha$-Ti (in the polycrystalline sample) was averaged over all directions of (0002) poles in space, weighted by the measured pole figure of the Ti sample. The latter was normalized to the pole figure of an equivalent powdered-Ti sample.

crystalline sample. To account for this, we measured the pole figure of a Ti sample (Fig. 97.27, labeled "foil"), i.e., the statistical distribution map of the normals (or poles) to the (0002) basal planes. Since the pole-figure measurement of this distribution has an instrumental component, we corrected the result by deconvolving the measured pole figure of a powdered, i.e., an isotropically distributed, Ti sample (see Fig. 97.27). The 1-D curve in Fig. 97.27 was obtained by averaging the EXAFS spectrum of the compressed cluster over all pole directions in space, weighted by the pole figure (normalized as explained above). Figure 97.27 shows that 1-D compression does increase the EXAFS damping rate but not nearly enough to explain the measurements. We therefore conclude that the observed high damping rate in shocked Ti is very likely due to the $\alpha$-Ti to $\omega$-Ti phase transformation. Furthermore, the agreement of compression in Ti and V deduced from shock-speed and EXAFS measurements indicates 3-D compression, since the latter has been assumed in order to arrive at a compression value from the EXAFS results.

## ACKNOWLEDGMENT

The pole figures obtained by Prof. S. Burns are gratefully acknowledged. This work was supported by the U.S. Department of Energy Office of Inertial Confinement Fusion under Cooperative Agreement No. DE-FC03-92SF19460, the University of Rochester, and the New York State Energy Research and Development Authority. The support of DOE does not constitute an endorsement by DOE of the views expressed in this article.

## REFERENCES

1. D. H. Kalantar *et al.*, Phys. Plasmas **7**, 1999 (2000); D. H. Kalantar *et al.*, Phys. Plasmas **10**, 1569 (2003).
2. L. Loveridge-Smith, A. Allen, J. Belak, T. Boehly, A. Hauer, B. Holian, D. Kalantar, G. Kyrala, R. W. Lee, P. Lomdahl, M. A. Meyers, D. Paisley, S. Pollaine, B. Remington, D. C. Swift, S. Weber, and J. S. Wark, Phys. Rev. Lett. **86**, 2349 (2001).
3. P. A. Rigg and Y. M. Gupta, Phys. Rev. B, Condens. Matter **63**, 094112 (2001).
4. P. A. Lee *et al.*, Rev. Mod. Phys. **53**, 769 (1981).
5. T. R. Boehly, R. S. Craxton, T. H. Hinterman, J. H. Kelly, T. J. Kessler, S. A. Kumpan, S. A. Letzring, R. L. McCrory, S. F. B. Morse, W. Seka, S. Skupsky, J. M. Soures, and C. P. Verdon, Rev. Sci. Instrum. **66**, 508 (1995).
6. S. K. Sikka, Y. K. Vohra, and R. Chidambaram, Prog. Mater. Sci. **27**, 245 (1982).
7. C. W. Greeff, D. R. Trinkle, and R. C. Albers, J. Appl. Phys. **90**, 2221 (2001).
8. B. Yaakobi, F. J. Marshall, T. R. Boehly, R. P. J. Town, and D. D. Meyerhofer, J. Opt. Soc. Am. B **20**, 238 (2003).
9. R. M. More *et al.*, Phys. Fluids **31**, 3059 (1988).
10. R. W. Eason *et al.*, J. Phys. C, Solid State Phys. **17**, 5067 (1984).
11. B. A. Shiwai *et al.*, Laser Part. Beams **10**, 41 (1992).
12. P. M. Celliers *et al.*, Appl. Phys. Lett. **73**, 1320 (1998).
13. G. B. Zimmerman and W. L. Kruer, Comments Plasma Phys. Control. Fusion **2**, 51 (1975).
14. J. J. Rehr, R. C. Albers, and S. I. Zabinsky, Phys. Rev. Lett. **69**, 3397 (1992).
15. E. Sevillano, H. Meuth, and J. J. Rehr, Phys. Rev. B, Condens. Matter **20**, 4908 (1979).
16. G. Hug *et al.*, Ultramicroscopy **59**, 121 (1995).
17. A. Yoshiasa *et al.*, J. Synchrotron Radiat. **6**, 43 (1999).

# Picosecond Response of Ultraviolet Photodiodes on GaN

Experimental results on the fabrication, packaging, and testing of very fast metal-semiconductor-metal photodiodes (MSM-PD's) made on gallium nitride (GaN) have been previously reported.[1] The devices—with feature sizes ranging from 0.3 $\mu$m to 5 $\mu$m—were packaged in a circuit that was designed to easily couple the electrical transients out of the device, thus making them suitable for practical applications. A temporal response of 55±5-ps full width at half maximum (FWHM) was measured in all devices, independent of feature size. External bias was changed from 1 V to 10 V, and the device area was decreased by a factor of 4 to reduce the total capacitance, neither of which had a significant effect on the measured speed. Only high illumination levels produced a change in the device response. This change was attributed to space-charge screening effect. These results led to the conclusion that the device response was dominated by the packaging and measurement system. Theoretical calculations[2–5] have predicted, however, that the steady-state peak electron velocity in GaN is around $3 \times 10^7$ cm/s, which is higher than that in GaAs. This implies that the inherent speed in GaN detectors should be substantially faster than in GaAs devices. Joshi *et al.*,[6] in particular, using Monte Carlo simulations, studied the dynamic response of GaN MSM-PD and predicted a FWHM of 3.5 ps for a device with 0.25-$\mu$m feature size under low-bias and low-level illumination.

To explore the inherent device response, a double-pulse measurement was performed[1] by splitting the optical beam into two parts with an adjustable delay and then recombining them to excite the device under test. Separable pulses from a typical device were observed at delays of less than 26 ps, confirming a much-faster inherent response.

In this article results measured with electro-optic (EO) sampling are reported.[7,8] This technique is connector-free and has a bandwidth of more than 1 THz, corresponding to a temporal resolution of 360 fs, providing a much-faster measurement system. To minimize the capacitance effect inherent to the MSM structure, small devices with active area of 25 × 25 $\mu m^2$ were selected. The sampling point, defined by the laser spot, was close to the active device area. A sufficient time window existed (about 15 ps) before the transient reflections from the circuit terminals set in, ensuring that the measurement of the intrinsic response could be separated from the packaging circuit.

The devices were made on GaN wafers (2-$\mu$m thickness) grown on c-plane sapphire and purchased from a commercial source. The residual impurities produced an electron concentration below $1 \times 10^{16}$ $cm^{-3}$. Fabrication was carried out at the Cornell Nanofabrication Facilities (CNF) using electron-beam lithography. Metallization used to form Schottky contacts was either Ni/Au or Ti/Pt. Details of the device fabrication can be found in Ref. 1.

The device was excited by beams from a femtosecond, frequency-doubled, Ti:sapphire, mode-locked laser tuned at $\lambda$ = 720 nm, with a 76-MHz repetition rate and an average power of 1 mW. The fundamental beam was used to probe the photogenerated electrical signal via a movable $LiTaO_3$ electro-optic crystal positioned close to the active area (Fig. 97.28), which served as a detector of the electrical transient. The excitation beam was focused down to the active area without passing through the electro-optic (EO) crystal. To maximize the EO coupling, the sampling beam was precisely focused on the edge of the metal pad, where the strongest electric field is located. The distance between the ends of the metal pads (1.3 mm in Fig. 97.28) defines the onset of the first reflection of the electric pulse and was seen in the evanescent portion of the transient. The dc bias needed to generate the dark electric field between the fingers was applied via wire bonds.

It should be noted that even though the optical wavelength of 360 nm was only 5 nm above the energy gap of the GaN film, the penetration depth was around 370 nm, as determined by transmission measurement at this wavelength. This is significantly shorter than the 2-$\mu$m thickness of GaN film and the 1-$\mu$m distance of the finger spacing. Therefore, the deep-carrier effect as observed in a silicon MSM diode[9] is negligible here.

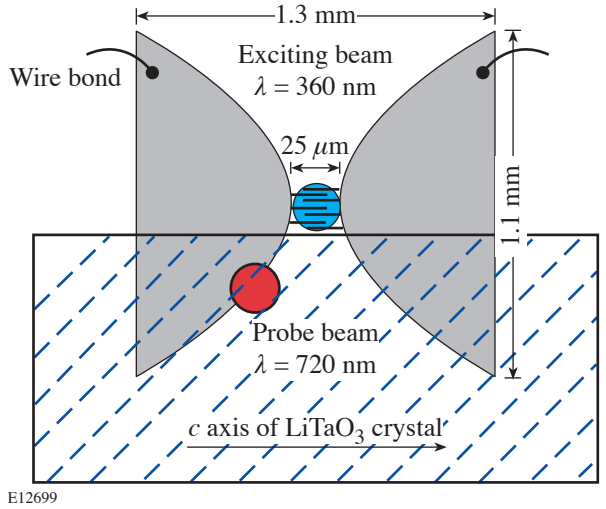


Figure 97.28
A schematic view of the sample configuration for measuring the electrical response of the MSM GaN photodiodes.

Figure 97.29 shows the fastest temporal response of the photodiode with 1-$\mu$m finger width and spacing and 25 × 25-$\mu$m$^2$ active area, under 12-V bias. The pulse shape in Fig. 97.29 is strongly asymmetrical: the 1.4-ps rise time is limited by the optical pulse width and by the RC time constant in the MSM structure and pads. The slower trailing transient, determined by the carrier transit across the finger gap, can be fitted with a bi-exponential function with time constants of 2.1 ps and 22 ps. They are attributed to the electron and the hole components, respectively. It should be pointed out that while the faster electron part is closely fitted with an exponential, the slower hole component is masked with reflections from the ends of the metal pads.

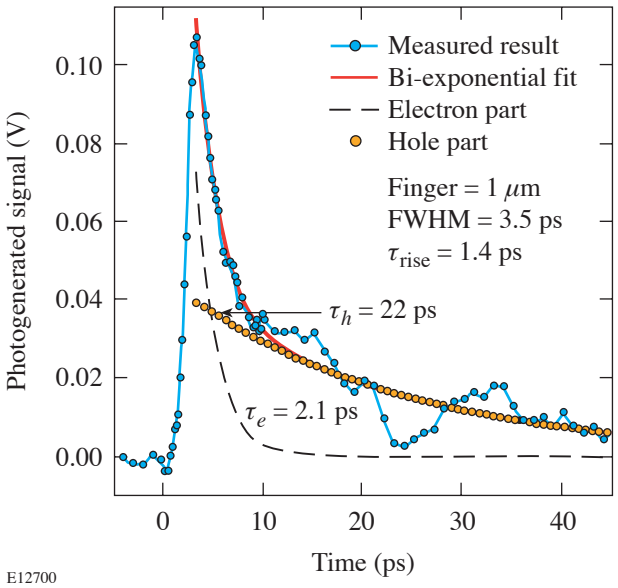


Figure 97.29
Electrical pulses generated by illumination of 360-nm photons and the bi-exponential fitting. The finger spacing and width of the diode are both 1 $\mu$m.

The electron velocity from the ratio of the half-distance between the electrodes (0.5 $\mu$m) to the measured FWHM (3.5 ps) is estimated to be 1.43±0.1 × 10$^7$ cm/s. This result compares favorably with the value of 1.5 × 10$^7$ cm/s measured[10,11] under an electric field of 120 kV/cm in a femtosecond optical time-of-flight experiment that monitors the change in the electro-absorption associated with the transport of photogenerated carriers in a GaN *p-i-n* diode.

The dependence of pulse duration and electron velocity on the electric field was extracted by changing the bias voltage from 5 V to 14 V. The inset in Fig. 97.30 shows the measured FWHM as a function of average electric field, which is calcu-

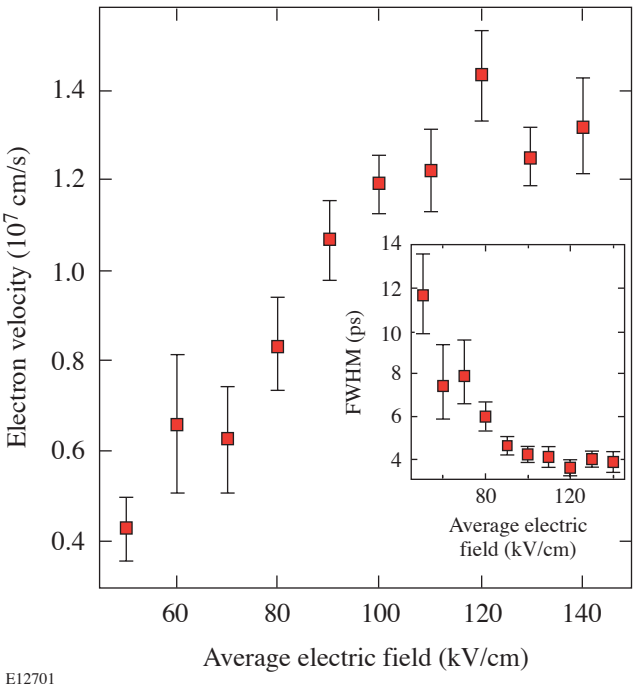


Figure 97.30
The experimentally determined electron velocity and measured FWHM (inset) as a function of average electric field.

lated by dividing the bias voltage by 1-$\mu$m finger spacing. In the low-field region, the experimentally determined electron velocity, shown in Fig. 97.30, increases with bias. Above 100 kV/cm, the electron velocity begins to flatten, reaching a plateau at 120 kV/cm. If the average of the plateau region is used, rather than the peak, then the estimated electron velocity becomes $1.3\pm0.1 \times 10^7$ cm/s. The fact that the peak velocity measured in our experiment is lower than the calculated steady-state peak electron velocity for GaN[2] may be attributed to the high defect density in the device and/or the capacitance effect of MSM structure that are not accounted for by theory.

The high-field results of Fig. 97.30 can be compared with Monte Carlo simulations.[6] For a device with 0.25-$\mu$m finger spacing, the corresponding FWHM is expected to be around 1 ps, based on our measured electron speed. This is substantially faster than the simulated results of 3.5 ps.[6] To check further, a device with 0.5-$\mu$m finger spacing was tested. A typical transient, shown in Fig. 97.31, shows two features distinct from the 1-$\mu$m device: a slower rise time of 3.2 ps and a broader FWHM of 6.2 ps. This result is at first surprising; however, it is consistent with an increased capacitance that dominated the measured response from the smaller device. In the MSM structure, the device capacitance increases with smaller finger spacing. For our samples, the capacitances are calculated[12] to be 0.0126 pF and 0.0263 pF for the 1-$\mu$m and 0.5-$\mu$m devices, respectively. With a measured package-circuit impedance of 63 Ω,[1] the corresponding RC time constant would increase with increased capacitance and gives a 10%–90% rise time of 3.7 ps for the 0.5-$\mu$m device, essentially accounting for the slower response observed in Fig. 97.31. Further comparison with theory will then require devices fabricated with much smaller detection areas.

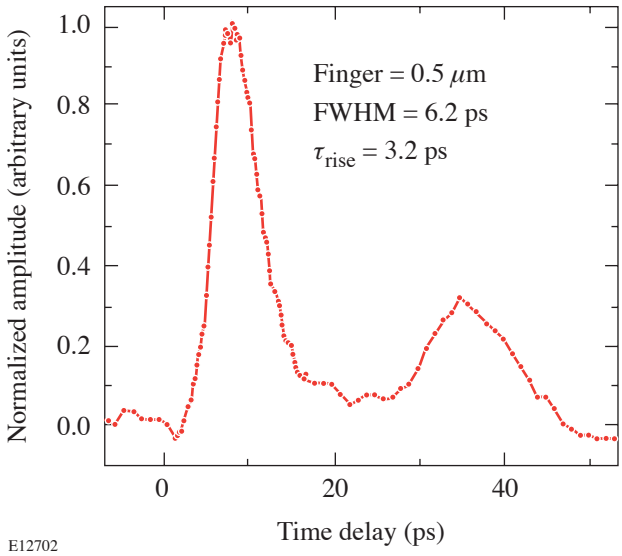


Figure 97.31
Impulse response measured from a device with 0.5-$\mu$m finger width and spacing. Both rise time and FWHM are longer than those from a device with 1-$\mu$m finger width and spacing as discussed in text.

In summary, EO sampling has been used to test the intrinsic response of GaN MSM photodiodes. The best performance measured from devices with 1-$\mu$m feature size showed a fast 10%–90% rise time of 1.4 ps and FWHM of 3.5 ps. This result represents the fastest ultraviolet GaN photodiode reported to date. The peak velocity of electrons in GaN was determined to be $1.43 \times 10^7$ cm/s, which compares favorably with independent photoexcitation experiments.

## ACKNOWLEDGMENT

This work was supported by the U.S. Department of Energy Office of Inertial Confinement Fusion under Cooperative Agreement No. DE-FC03-92SF19460, the University of Rochester, and the New York State Energy Research and Development Authority. The support of DOE does not constitute an endorsement by DOE of the views expressed in this article.

## REFERENCES

1. J. Li, W. R. Donaldson, and T. Y. Hsiang, IEEE Photonics Technol. Lett. **15**, 1141 (2003).
2. U. V. Bhapkar and M. S. Shur, J. Appl. Phys. **82**, 1649 (1997).
3. J. D. Albrecht *et al.*, J. Appl. Phys. **83**, 4777 (1998).
4. J. Kolnik *et al.*, J. Appl. Phys. **78**, 1033 (1995).
5. B. Gelmont, K. H. Kim, and M. Shur, J. Appl. Phys. **74**, 1818 (1993).
6. R. P. Joshi, A. N. Dharamsi, and J. McAdoo, Appl. Phys. Lett. **64**, 3611 (1994).
7. S. Alexandrou, R. Sobolewski, and T. Y. Hsiang, IEEE J. Quantum Electron. **28**, 2325 (1992).
8. U. D. Keil and D. R. Dykaar, Appl. Phys. Lett. **61**, 1504 (1992).
9. C.-C. Wang, S. Alexandrou, D. Jacobs-Perkins, and T. Y. Hsiang, Appl. Phys. Lett. **64**, 3578 (1994).
10. M. Wraback *et al.*, Appl. Phys. Lett. **76**, 1155 (2000).
11. M. Wraback *et al.*, Appl. Phys. Lett. **79**, 1303 (2001).
12. Y. C. Lim and R. A. Moore, IEEE Trans. Electron Devices **ED-15**, 173 (1968).

# Self-Assembly of Coated Colloidal Particles for Optical Applications

**Introduction**

Nearly two decades ago, theoretical predictions indicated the possibility of creating omnidirectional photonic-band-gap materials that would prevent the propagation of certain wavelengths of light in all directions, while allowing transmission of other light wavelengths.[1,2] Since that time, there has been a growing interest in creating these materials experimentally due to the wide variety of potential applications afforded by the control of light propagation, including use in optical computing and telecommunications.[3] Researchers have taken two approaches to construction of photonic-band-gap materials: (1) lithographic technologies similar to that used in microelectronics manufacture and (2) colloidal self-assembly of spherical particles. The self-assembly approach is promising due to its simplicity and low cost.

Under appropriate conditions, spherical colloidal particles will self-assemble to form a hexagonal close-packed structure called a "colloidal crystal." There are regularly spaced air voids in the interstitial regions between colloidal particles making up the crystal. Since air has a much lower refractive index than the particles, the refractive index of the crystal varies periodically on a length related to the diameter of the particles making up the crystal. The periodic variation of refractive index within the colloidal crystal leads to preferential reflection of certain wavelengths of light. The maximum reflectance occurs at a wavelength equal to roughly twice the diameter of the particles making up the crystal. Therefore, the position of the band gap and thus the color of the crystal may be adjusted by adjusting the size of the particles making up the crystal. Colloidal crystals are often referred to as "photonic crystals" due to the photonic-band-gap properties. They are also referred to as "artificial opals" due to the similarity with gemstone opal. Naturally occurring opal is a colloidal crystal of spherical silica particles. The "opalescence" observed in gemstone opal is caused by preferential reflection of light within the photonic band gap.

Colloidal crystals exhibit a "pseudo" photonic band gap; that is, only a portion of the light in the photonic band gap is reflected while some fraction propagates into the crystal. The rejected fraction of light can be enhanced by increasing the refractive index contrast between the particles and air voids in the structure. The photonic band gap is also very sensitive to the quality of the crystal. A few faults or dislocations in the crystal structure will greatly diminish the intensity of the reflected light. It is desirable to have a complete photonic band gap with 100% of the light in the band gap reflected. Theoretical predictions have indicated, however, that even with a perfect colloidal crystal, a full band gap may not be attained, no matter how high the refractive index contrast.[4] Since a simple colloidal crystal is unable to form a complete band gap, researchers have focused on creating more complex structures to attempt to create a complete photonic band gap. One approach is to form binary colloidal crystals made up of two different-sized particles.[5] Another approach is to use the colloidal crystal as a template for creating an "inverse opal" structure in which the air voids within a colloidal crystal are filled and then the colloidal particles are removed, leaving spherical hexagonally close packed holes in a solid matrix.[6] The inverse opal structure has been shown to yield a complete photonic band gap.[3] Yet another approach is to form colloidal crystals from core-shell structured particles.[7] Theoretical predictions indicate that colloidal crystals of some types of core-shell particles should exhibit a full photonic band gap.[8]

In the present study, core-shell structured particles were formed using electrostatic layer-by-layer self-assembly as depicted in Fig. 97.32. In the layer-by-layer technique, coatings of polyelectrolytes with alternating charges are deposited onto colloidal particles through electrostatic attraction.[9] In addition to polyelectrolytes, other charged species may be deposited during the coating process, including proteins and luminescent nanoparticles.[10] The thickness of the polyelectrolyte shell surrounding the particle may be adjusted by the number of layers deposited. Each layer deposited is typically of the order of 1 nm thick. Layer-by-layer self-assembly is a simple, versatile technique for controlling size and composition of colloidal particles with nanometer-scale precision. Typically, only a small fraction of the ionic groups in the

polyelectrolytes are neutralized during deposition. After coating, therefore, ionic species such as organic dyes or fluorophores may be immobilized in the shell via ion exchange with the polyelectrolyte counterions. By introducing luminescent or high-refractive-index species in the shell surrounding the particles, the technique offers potential as a simple route for creating optically modified particles that may be used to create photonic crystals with enhanced properties.

A variety of techniques may be employed to crystallize electrostatically charged colloidal particles. The simplest technique is simple evaporation of a few drops of an aqueous colloid on a clean, flat surface. If the surface has the same electrostatic charge as the suspended particles, opalescent colloidal crystals will form as the water evaporates. At room temperature, complete drying occurs in a few hours. Crystals are generally deposited on the outer fringes of where the droplets were placed on the surface, similar to "coffee ring" formation. While simple evaporation provides a relatively rapid route to crystallization, crystal quality is usually poor with small domain sizes. Also, it is not possible to control crystal area and thickness to obtain a uniform crystalline film over a large area of the surface.

If the liquid interface is moved across the surface at a constant velocity while evaporating, a colloidal crystal can be deposited as a uniform thin film. Colvin *et al.*[11] demonstrated that a uniform crystalline film can be deposited as a liquid interface moves down a solid surface, referred to as "vertical deposition." The technique involves placing a clean glass slide oriented perpendicular to the liquid surface of the colloidal suspension so that the glass is partially submerged. As the solvent evaporates, a crystalline deposit forms where the meniscus meets the slide surface. A thin crystal film forms over a large area of the slide surface as the meniscus slowly moves downward due to solvent evaporation. Vertical deposition was first reported for colloidal silica suspended in ethanol and is effective because of the relatively rapid rate of evaporation of ethanol. For aqueous colloids, vertical deposition is also effective, but the lower rate of evaporation makes the time required prohibitively long. Fujishima *et al.*[12] recently modified the vertical deposition technique by slowly lifting the glass slide from the colloidal suspension, as shown in Fig. 97.33. By lifting, aqueous colloids can be crystallized more rapidly than in the case where the meniscus moves

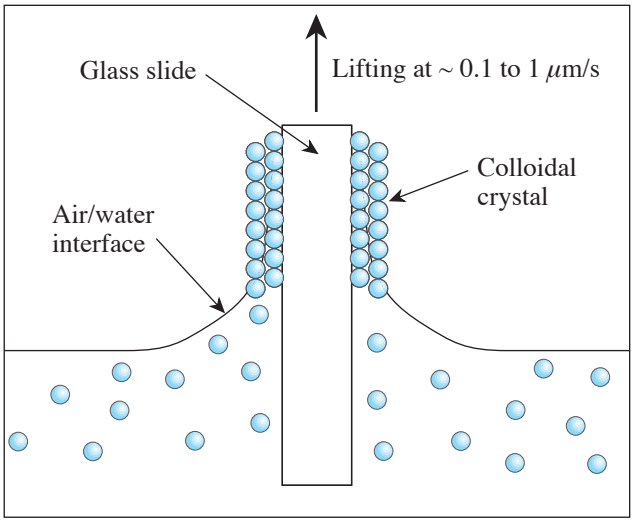


Figure 97.33
Vertical deposition technique for colloidal crystallization.

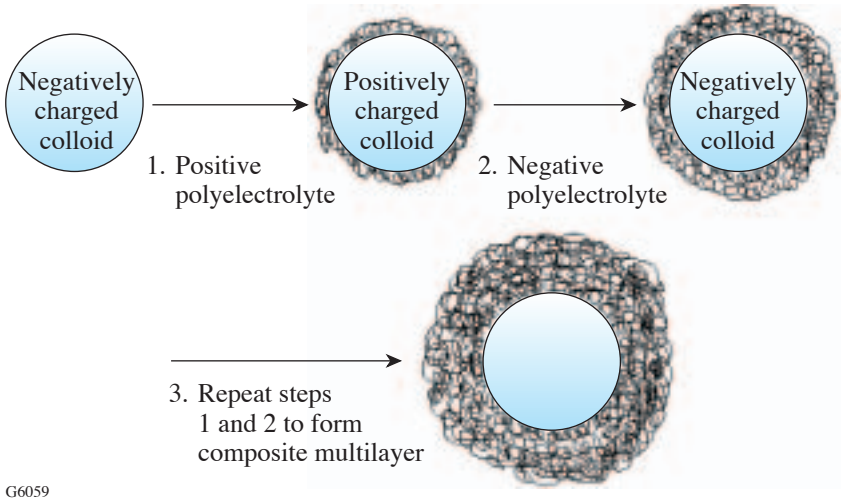


Figure 97.32
Layer-by-layer electrostatic self-assembly technique for coating colloidal particles with polyelectrolytes. The technique may also be employed to coat particles with a variety of electrostatically charged species including nanoparticles and proteins. After shell formation, charged species may be immobilized through ion exchange with the polyelectrolyte counterions.

downward by solvent evaporation. In addition, the thickness of the crystal may be adjusted by varying the lifting velocity, with thinner crystals forming with higher lifting velocity. Fujishima's technique was used in the present study to crystallize core-shell structured particles.

**Experimental**

Monodisperse-sized polystyrene particles (640 and 270 nm in diameter) were purchased from Microparticles GmbH Berlin, Germany. Poly(sodium 4-styrene sulfonate) (PSS, MW = 70,000 g/mol), poly(allylamine hydrochloride) (PAH, MW = 15,000 g/mol), sodium chloride (NaCl, 99%), hydrogen peroxide (30% aqueous solution), and ammonium hydroxide (28% aqueous solution) were purchased from Sigma-Aldrich and used as received. Glass microscope slides (Fisher Scientific) were cleaned prior to use by heating at 70°C for 15 min in a solution of hydrogen peroxide, ammonium hydroxide, and deionized water in a ratio of 1:1:5, respectively, by volume. After cleaning, microscope slides were stored under deionized water until used. Particles were crystallized through vertical deposition from an ~1-wt% colloidal suspension by lifting a clean glass slide at a velocity of 0.15 $\mu$m/s.

**Findings**

1. Crystallization of Uncoated Colloidal Particles

Vertical deposition of 270-nm-diam polystyrene particles produced the crystals shown in Fig. 97.34. Figure 97.34(a) is a high-magnification image (1-$\mu$m bar) showing hexagonal packing and long-range order of the crystal on the surface. The crystal quality is very good, although there are some faults and dislocations in the structure. In addition, there are periodically cracks in the crystal due to contraction of the crystal upon drying. Figure 97.34(b) is a low-magnification image (10-$\mu$m bar) of the same sample showing drying cracks in the crystalline film. It was not possible to eliminate drying cracks in the sample. Overall, however, vertical deposition produces the highest-quality crystals of the techniques investigated. A crystalline film covering a 1-cm$^2$ area can be formed rapidly (in approximately 12 h), and several crystals can be formed in parallel. In addition, the optical properties of the crystals can be studied using standard reflectance or transmission spectroscopy since the crystals form in a thin film on a microscope slide. Vertical deposition with controlled lifting was used exclusively for crystallization of coated colloidal particles because of the numerous advantages of the technique over the others that were studied.

2. Crystallization of Coated Colloidal Particles

Initial coating experiments were conducted using 640-nm-diam polystyrene colloids that had sulfate groups on their surface. These negatively charged particles were coated with alternating PAH/PSS layers using an established procedure from the literature.[7] The coating procedure has been optimized for particles near 640 nm in diameter. Briefly, each polyelectrolyte layer was deposited from an aqueous solution containing 1 mg/mL of polyelectrolyte and 0.25 M of NaCl. The high salt concentration has been shown to produce thicker polyelectrolyte layers by screening electrostatic repulsion in the polyelectrolyte chain to allow a more-coiled polymer conformation. After each coating step, the particles were washed three times

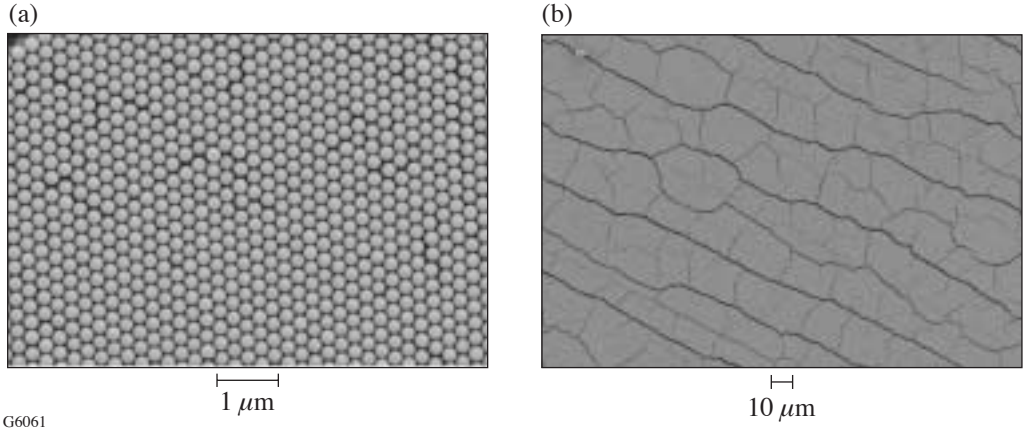


Figure 97.34
Crystals of uncoated polystyrene colloids (270-nm diam) formed through vertical deposition. (a) A high-magnification image (1-$\mu$m bar) shows the hexagonal packing and long-range order of the crystal. (b) A low-magnification view (10-$\mu$m bar) of the same sample shows drying cracks in the crystalline film.

with pure deionized water using repeated centrifugation/redispersion steps prior to coating the next layer. Particles coated in this manner had minimal aggregation and could be crystallized rapidly by placing a few drops of an ~1-wt% suspension onto a clean glass slide and allowing it to evaporate as reported by Liang.[7] While crystal formation is rapid, the crystal area is small and difficult to control, as discussed above. We focused on vertical deposition to create high-quality crystals from coated colloids over a large surface area.

The position of the photonic band gap is at a wavelength equal to roughly twice the diameter of the particles making up the crystal, which, for 640-nm-diam particles, places the band gap in the near-infrared region. Our interest is in creating photonic crystals with band gaps in the visible-light wavelength range (~400 to 700 nm). Therefore, we began investigating methods to coat and crystallize smaller 270-nm-diam particles. An initial attempt at coating these smaller particles was made using the same coating procedure that had been effective for 640-nm-diam particles. It was found, however, that gross aggregation of the particles occurred after the first layer was deposited. The particles were very difficult to redisperse after centrifugation. Aggregation could be minimized by placing the particles into an ultrasonic cleaning bath to disperse. Once dispersed, the particles were centrifuged slowly for several minutes to sediment aggregated particles. The aggregated particles were redispersed by the ultrasonic cleaning bath. This sedimentation/redispersion process was repeated several times to minimize aggregation of particles; however, aggregation could not be completely eliminated.

In the first attempts to crystallize the coated 270-nm particles via vertical deposition, nothing was deposited onto the glass surface because of slow flocculation of the particles. It was postulated that some rearrangement of the polyelectrolyte multilayers was occurring and leading to flocculation. If the polyelectrolytes rearrange so that portions of the oppositely charged layer beneath the outermost layer are exposed, this will lead to patches of both positive and negative electrostatic charge on the particle surface. Flocculation will then occur via electrostatic attraction between particles. To maintain electrostatic repulsion, the coated particles were kept in a dilute solution (0.1 mg/mL) of polyelectrolyte with the same charge as the outermost layer on the particle surface. If any oppositely charged patch is exposed, the free polyelectrolyte in solution around the particles can adsorb to cover it more rapidly than a charged particle will attach via flocculation. The stability of the particles was greatly enhanced by the small excess polyelectrolyte. In pure water, the 270-nm-diam polyelectrolyte-coated polystyrene particles flocculated and sedimented in less than one day. In 0.1-mg/mL polelectrolyte solution, there was no visible flocculation of the particles even after two weeks.

The PAH/PSS-coated, 270-nm polystyrene particles were crystallized via vertical deposition from an ~1-wt% aqueous suspension (containing 0.1 mg/mL of PSS for maintaining colloidal stability). Figure 97.35 shows scanning-electron-microscopy images of the crystalline deposit. Figure 97.35(a) is the deposit formed by particles coated with two polyelectrolyte layers. By comparison with crystals of uncoated particles (Fig. 97.34), it can be seen that the coated particles produce a much-lower-quality crystal. Hexagonal packing is present, but there are many areas where the crystal structure is disrupted. Figure 97.35(b) shows the deposit formed from particles

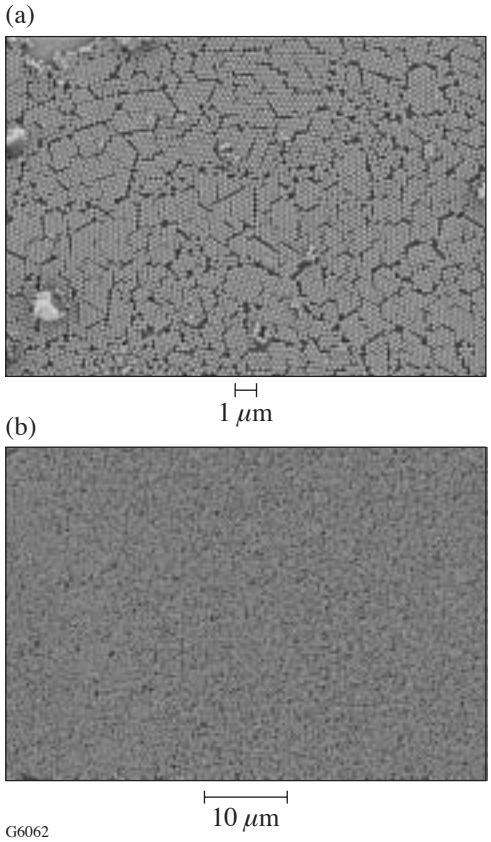


Figure 97.35
Crystals of 270-nm-diam polystyrene particles coated using the "standard" coating procedure with 0.25-M NaCl concentration. (a) Particles coated with two polyelectrolyte layers (1-$\mu$m bar). Some hexagonal packing is observed, but crystal quality is poor. (b) Particles coated with four alternating polyelectrolyte layers (10-$\mu$m bar). Crystallization is completely disrupted due to aggregation of the particles during the coating process.

coated with four alternating PAH/PSS layers. After four coating layers, the crystal structure is completely disrupted. The coating process introduces aggregation of the particles, and aggregation increases after each layer is coated. The procedure developed for coating 640-nm particles is clearly not as effective for coating the smaller 270-nm particles.

A greatly improved coating procedure was developed following modifications suggested recently by Gittins.[13] In Gittins' study, gold nanoparticles as small as 11-nm diameter were coated with polyelectrolyte layers without inducing particle aggregation. It was reported that much-lower salt concentration (1 mM) was required to prevent aggregation of the particles. It is well known that salt reduces electrical double-layer repulsion between particles. By lowering the salt concentration, electrostatic repulsion could be maintained while coating the particles. The same approach was applied for coating 270-nm polystyrene colloids. The particles were coated with alternating layers of PAH and PSS using solutions containing 1 mg/mL of polyelectrolyte and 1 mM of NaCl (instead of 0.25 M of NaCl). With the lower salt concentration, the aggregation of particles was greatly reduced. Upon centrifugation of the coated particles, the sediment appeared opalescent, indicating crystal formation. The crystal formation in the sediment also suggested there was very little particle aggregation and strong electrostatic repulsion was being maintained throughout the coating process.

To test if the new procedure was coating the particles as expected, the zeta potential was measured after each layer was deposited. Figure 97.36 shows the zeta potential results. The zeta potential is related to the surface charge of the particles. The sign of the zeta potential alternates from positive to negative as expected when the alternating polyelectrolyte layers are deposited. The high magnitude of the zeta potential (>40 mV for every layer) indicates that good colloidal stability is maintained. Unfortunately, we could not measure the growth of the polyelectrolyte layers using single-particle light scattering because the particles are too small for accurate measurement. We can infer, however, that the polyelectrolytes are being deposited from the zeta potential measurements.

The particles coated using the improved procedure were crystallized through vertical deposition from an ~1-wt% aqueous colloidal suspension (containing 0.1 mg/mL of PSS). Figure 97.37 shows the crystalline deposit formed by particles coated with two polyelectrolyte layers. The image shown in Fig. 97.37(a) depicts a broken section of the crystalline film, showing that it is approximately ten particle layers thick. The image shown in Fig. 97.37(b) depicts the hexagonal packing and long-range order of the crystal. There are numerous drying cracks present, but overall crystal quality is very good. The quality of the crystals formed from the two-layer–coated, 270-nm particles is very nearly the same as that for the uncoated particles (shown in Fig. 97.34).

Figures 97.38(a) and 97.38(b) show crystals of particles coated with four and six alternating polyelectrolyte layers, respectively. The particles coated with four polyelectrolyte layers produce very good crystals. There are drying cracks where the crystal has contracted, but the overall packing of the crystal is good. There are some areas where the crystal structure is disrupted. Particles coated with six polyelectrolyte layers produce noticeably poorer-quality crystals [Fig. 97.38(b)].

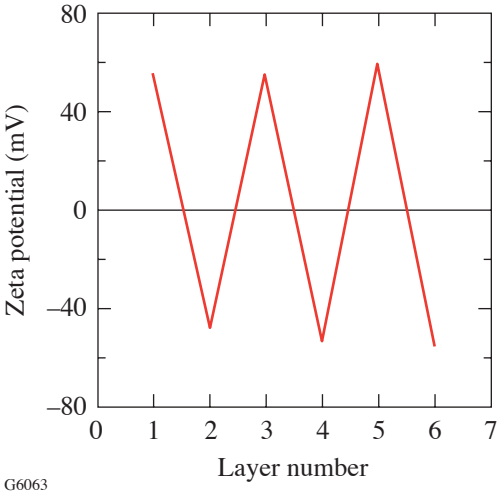


Figure 97.36
Zeta potential of 270-nm-diam polystyrene particles as a function of layer number during layer-by-layer deposition of PAH/PSS with improved coating procedure. The polyelectrolytes were deposited from a 1-mg/mL solution containing 1 mM of NaCl. Layer 1 is PAH (positive), layer 2 is PSS (negative), and additional layers are deposited with an alternating polyelectrolyte charge. The alternating sign of the zeta potential implies that the polyelectrolytes are adsorbing onto the particles via electrostatic attraction.

There are regions where the particles are randomly oriented, probably due to aggregation during the coating process. Since the crystal quality degrades as a function of number of layers coated, it can be inferred that some small amount of particle aggregation occurs during the coating process. Each layer applied leads to additional aggregation and further reduction in crystal quality.

The photonic band gap of the crystals was probed with reflectance spectroscopy as shown in Fig. 97.39. The peak reflectance located near 575 nm is due to the photonic band gap. The band gap causes the crystals to appear green in color. The most-prominent feature of the reflectance spectra of the samples is the decrease in band-gap intensity with an increasing number of polyelectrolyte layers coating the particles. The

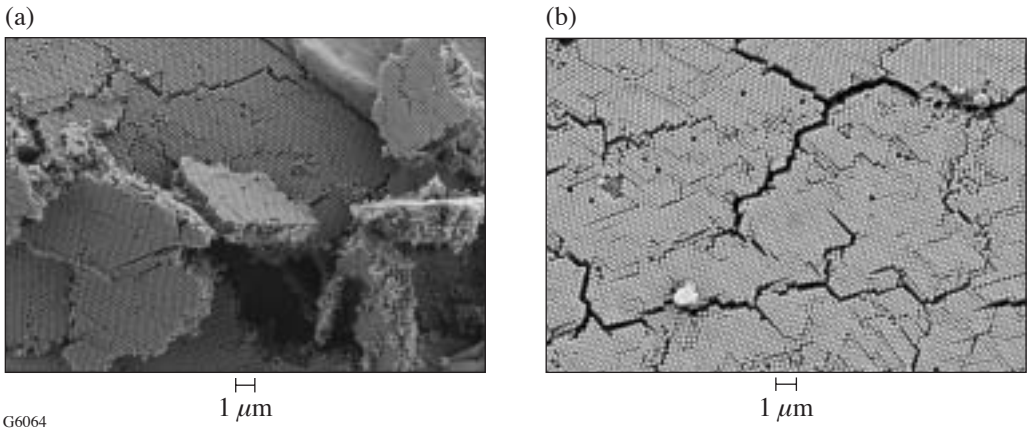


Figure 97.37
Crystals of 270-nm-diam polystyrene particles coated with two polyelectrolyte layers using the improved coating procedure. (a) Image of a broken section of the film showing the crystal thickness (1-$\mu$m bar). (b) Surface of the crystal showing the long-range-hexagonal, close-packed structure with drying cracks visible (1-$\mu$m bar).

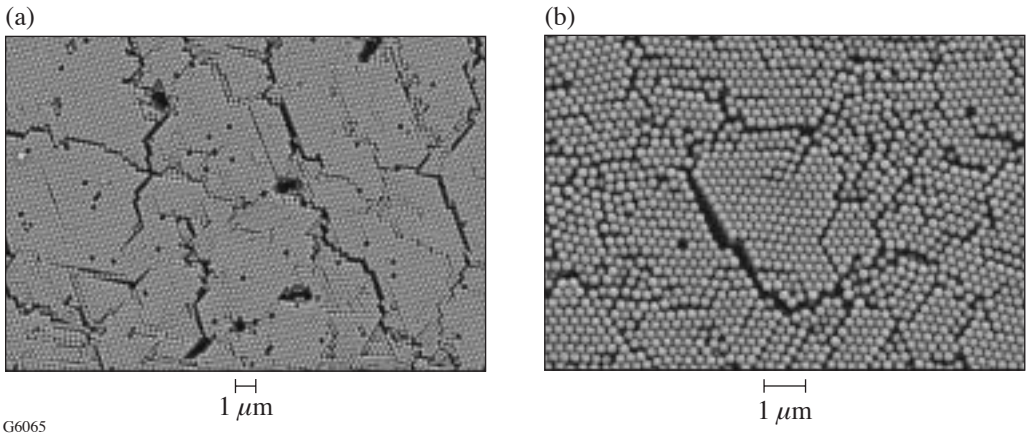


Figure 97.38
Crystals of 270-nm-diam polystyrene particles coated with (a) four alternating PAH/PSS layers (1-$\mu$m bar) and (b) six alternating PAH/PSS layers (1-$\mu$m bar). As the number of polyelectrolyte layers increases, the crystal quality decreases. In image (b), regions of randomly aggregated particles are visible.

intensity decreases and the width of the band gap increases due to poorer crystal quality. The optical data in Fig. 97.39 confirm the observation in Figs. 97.37 and 97.38 that crystal quality decreases with an increasing number of polyelectrolyte layers. Even with the improved coating technique, a small amount of particle aggregation occurs during each coating. Particles coated with two polyelectrolyte layers produce crystals nearly as high in quality as the uncoated particles. High-quality crystals are obtainable with up to four polyelectrolyte coatings, but poorer quality is produced with six-layer–coated particles.

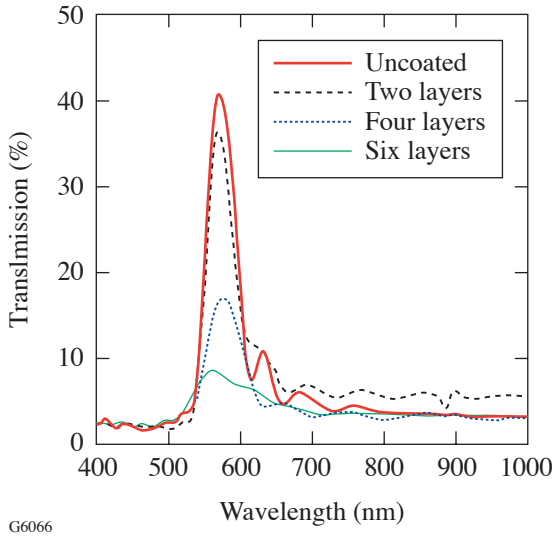


Figure 97.39
Reflectance spectra of colloidal crystals in Figs. 97.34, 97.37, and 97.38 taken at a 6° angle. The crystals have a pseudophotonic band-gap reflectance peak located at ~575 nm, which visually gives them a green appearance. The peak height and sharpness decrease with an increasing number of polyelectrolyte layers coating the particles because of poorer crystal quality. The decrease in crystal quality is most likely due to a small amount of particle aggregation in each coating step.

It is notable that the band gap does not significantly shift position when coated. Since the position of the band gap is related to the particle diameter, one would expect a shift to longer wavelengths as the particle diameter becomes larger due to deposition of polyelectrolytes. The band gap of the sample coated with two layers is actually slightly shifted to shorter wavelengths. It is unclear at this point why the blue shift occurs. The band gap is slightly shifted to longer wavelengths for the crystals formed with particles coated with four layers. Further coating broadens and weakens the peak so that the shift is not discernible. It is known that salt increases the thickness of the polyelectrolyte layers during deposition. Since our improved coating process uses less salt, we expect the thickness to be small; unfortunately, we were unable to actually measure the layer thickness. The small layer thickness would cause the band gap to shift only slightly. Coupled with a blue shift, the net effect is that the band gap stays in nearly the same position. Further work is needed to fully understand the optical properties.

## Conclusions and Future Directions

We have demonstrated that high-quality crystals of polyelectrolyte-coated particles may be formed by vertical deposition. The colloidal crystals display preferential reflection of light due to the pseudo band gap of the crystal. The crystal quality degrades with the number of polyelectrolyte layers coated on the particles. It is postulated that there is slight particle aggregation during the coating process that disrupts crystallization. The crystal degradation is apparent from the reduction in the maximum intensity of reflected light. Particles coated with two polyelectrolyte layers have a maximum intensity of reflectance nearly the same as the uncoated particles. The reflectance intensity decreases for particles coated with four layers, and there is almost no reflectance for particles coated with six layers. Further work is needed to completely eliminate particle aggregation during the particle-coating process.

The polyelectrolyte-coated particles offer intriguing possibilities for controlling and enhancing the optical properties of the colloidal crystals. The polyelectrolyte shells surrounding the particles have a high number of free ionic groups. A variety of optically active species may be immobilized in the shell through ion exchange. For example, ionic fluorophores may be immobilized in the polyelectrolyte shell by simply dispersing the particles in an aqueous solution of the dye.[14] In addition, optically active species, including fluorescent quantum dots, may be introduced into the shells during the coating process.[15,16] It should be possible to enhance the band gap by choosing a dye that adsorbs near the band-gap maxima. In addition, it should be possible to choose luminescent compounds that emit light at a wavelength near the photonic-band-gap maxima. It has been shown recently that lasing from colloidal crystals is possible when a dye that emits in the band-gap wavelength is incorporated into the structure.[17]

ACKNOWLEDGMENT

We acknowledge support from the NSF International Research Fellowship Program and the Laboratory for Laser Energetics.

## REFERENCES


1. S. John, Phys. Rev. Lett. **58**, 2486 (1987).
2. E. Yablonovitch, Phys. Rev. Lett. **58**, 2059 (1987).
3. A. Blanco *et al*., Nature **405**, 437 (2000).
4. K. M. Ho, C. T. Chan, and C. M. Soukoulis, Phys. Rev. Lett. **65**, 3152 (1990).
5. K. P. Velikov *et al*., Science **296**, 106 (2002).
6. D. J. Norris and Y. A. Vlasov, Adv. Mater. **13**, 371 (2001).
7. Z. Liang, A. S. Susha, and F. Caruso, Adv. Mater. **14**, 1160 (2002).
8. A. Moroz, Phys. Rev. Lett. **83**, 5274 (1999).
9. F. Caruso, Adv. Mater. **13**, 11 (2001).
10. D. Wang, A. L. Rogach, and F. Caruso, Nano Lett. **2**, 857 (2002).
11. P. Jiang *et al*., Chem. Mater. **11**, 2132 (1999).
12. Z. Z. Gu, A. Gujishima, and O. Sato, Chem. Mater. **14**, 760 (2002).
13. D. I. Gittins and F. Caruso, J. Phys. Chem. B **105**, 6846 (2001).
14. F. Caruso *et al*., Macromolecules **32**, 2317 (1999).
15. W. Yang *et al*., J. Colloid Interface Sci. **234**, 356 (2001).
16. A. S. Susha *et al*., Colloid Surf. A, Physiochem. Eng. Aspect **163**, 39 (2000).
17. M. N. Shkunov *et al*., Adv. Funct. Mater. **12**, 21 (2002).

# A Tunable, High-Repetition-Rate, Harmonically Mode-Locked, Ytterbium Fiber Laser

Fiber laser and amplifier development in the wavelength region near 1 $\mu$m has experienced significant progress owing to the exceptional efficiency and gain bandwidth of ytterbium-doped fibers.[1–5] In fact, both ytterbium fiber lasers and amplifiers are becoming more attractive than their bulk counterparts due to their confined spatial mode, impressive bandwidth, good pump absorption, ease of alignment, and inherent compatibility with optical fiber. To date, however, experimental efforts regarding ytterbium fiber lasers have been directed only toward fundamental mode-locking, which typically limits pulse repetition rates below 100 MHz.[1–5]

This article focuses on another important parameter of mode-locked lasers that has thus far attracted little attention in this wavelength regime—high repetition rate. High-repetition-rate ytterbium fiber lasers would be a useful source of ultrafast picket-fence pulse trains that have been proposed to improve the performance of fusion laser systems.[6] In this scheme, shaped nanosecond pulses are replaced by a train of ultrafast "picket" pulses that deliver the same average power while increasing the third-harmonic conversion efficiency. A high-repetition-rate and broadly tunable source would also be useful for synchronously pumping multi-GHz optical parametric oscillators.[7]

The laser considered in this research uses a 976-nm pumped linear cavity, shown in Fig. 97.40, similar to that reported by Lefort *et al.* in 2002.[2] A bulk phase modulator[8] actively FM mode-locks the laser, enabling synchronization to an external reference frequency. Velocity matching between the optical and microwave fields in the modulator's $LiNbO_3$ crystal, in conjunction with a resonant design, offers efficient phase modulation at the device's resonance frequency ≈10.3 GHz. A synthesized microwave signal generator (HP model 83732B) amplified by a traveling-wave tube amplifier (Hughes model 8010H) provides up to 10 W of microwave power to the modulator. To reduce intracavity loss, the crystal facets were antireflection coated, resulting in an insertion loss of <1% at 1053 nm.

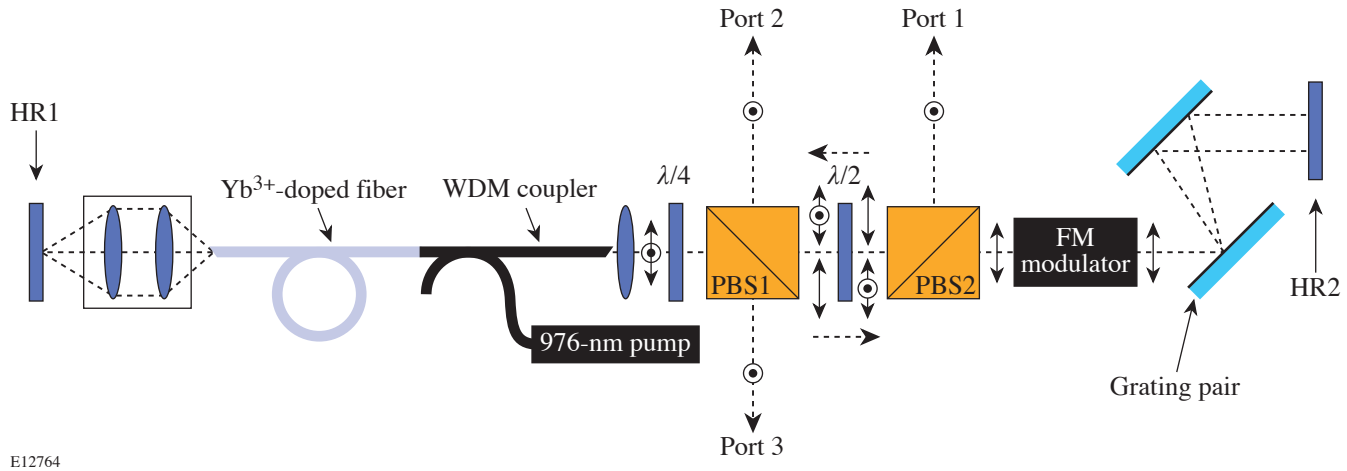


Figure 97.40
Laser cavity configuration: HR, high-reflectivity mirrors; PBS, polarizing beam splitters; WDM, 976/1050-nm wavelength division multiplexer. The double-sided arrows and the dots surrounded by circles represent the horizontal and vertical polarizations, respectively.

The laser delivers output to three different ports, as shown in Fig. 97.40. The combination of a half-wave plate ($\lambda/2$) and a polarizing beam splitter not only provides variable output coupling, yielding up to 38 mW from port 1 and up to 6.5 mW from port 2, but also selects the optimum polarization for the FM modulator and grating pair. Depolarization in the fiber section of the cavity results in 2.5 mW of leakage from port 3.

The mode-locking threshold was measured to be as low as 30 mW, but the pump laser was operated at a power of 150 mW in an effort to maximize the output power and facilitate autocorrelation measurements. All of the results presented in this article were obtained using this pump power and the output from port 1, where the laser had a slope efficiency of 32% (if we consider all three ports the slope efficiency is 40%). The cavity also incorporates a grating pair, which compensates the normal dispersion introduced by 1 m of ytterbium-doped fiber and 1.2 m of fiber associated with the 976/1050 WDM coupler.

A typical mode-locked pulse spectrum, measured with an optical spectrum analyzer (Ando model AQ6315A), reveals a bandwidth of 0.9 nm, as seen in Fig. 97.41. This spectrum is best fit by a sech$^2$ function shown by the dashed curve. Considering this to be the spectral shape, a 0.9-nm bandwidth (FWHM) implies a 1.3-ps (FWHM) transform-limited sech pulse. According to the simple FM mode-locking theory, an FM modulator in a purely linear dispersionless cavity should produce chirped Gaussian output pulses with Gaussian spectra.[9] In light of this, our spectral measurements suggest that cavity dispersion and fiber nonlinearity play a role in shaping the laser pulses.

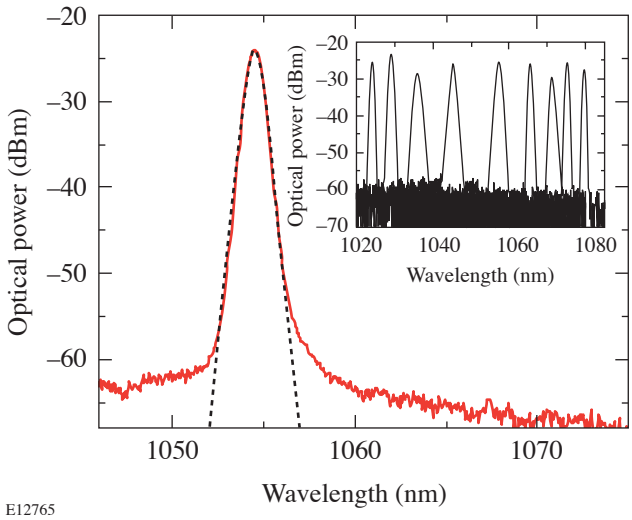


Figure 97.41
Mode-locked optical pulse spectrum and its associated sech$^2$ fit. The inset contains superimposed mode-locked spectra illustrating the 1025- to 1080-nm tuning range.

An interferometric autocorrelator employing two-photon absorption (TPA) in the photocathode of a photomultiplier tube was used to perform autocorrelation measurements (Fig. 97.42).[10] This sensitive diagnostic was required to measure the ≲4-pJ pulses resulting from the extremely high repetition rate. The autocorrelation trace was also best fit by the TPA response to a sech pulse, indicating a pulse width of 2 ps (FWHM).[11] Comparing the fit with the 1.3-ps pulse expected for a transform-limited field, the output pulses are found to be broadened by a factor of ≈1.5 due to chirp and resulting in a time-bandwidth product of 0.49.

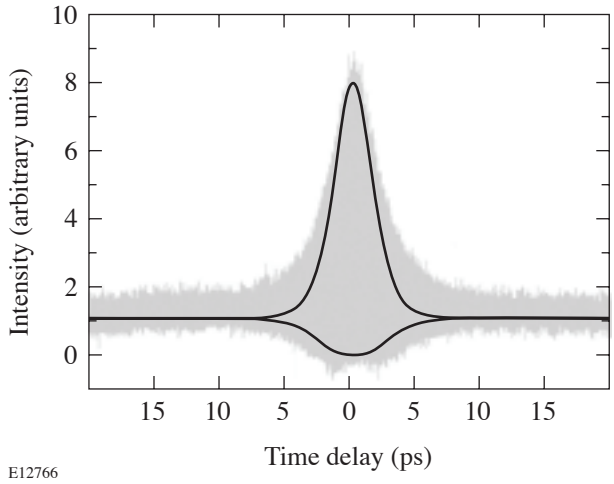


Figure 97.42
Autocorrelation results. The fit shown in this figure was obtained by using the two-photon absorption response to a 2-ps hyperbolic-secant pulse.

Mode-locked operation was achieved with central wavelengths ranging from 1022 nm to 1080 nm by inserting a razor blade in front of HR2 (not depicted in Fig. 97.40) and adjusting its position. The central wavelength also depended on the driving modulation frequency, the cavity length, and the angular position of mirror HR2. The effect of tuning on the pulse spectrum is shown in the inset of Fig. 97.41, where several different spectra in the tuning range of 1022 to 1080 nm have been superimposed on one another. The spectral shape varies little over the tuning range, although the spectral width increases as the center wavelength is decreased.

Side-mode suppression and timing jitter are two common figures of merit used to evaluate the quality of a mode-locked pulse train. These quantities are derived from the pulse-train power spectrum shown in Fig. 97.43 and obtained using a 25-GHz photodetector with a nominally flat frequency response (New Focus model 1414) and a 26.5-GHz microwave spectrum analyzer (Agilent model E4407B). As expected, the microwave spectrum shown in the inset of Fig. 97.43 is composed of peaks at the 10.31455-GHz driving frequency, its harmonics, and much weaker structures spaced by the 36.8-MHz fundamental repetition rate of the laser cavity (not visible in the figure), which are due to supermode noise.[12] A side-mode suppression of greater than 72 dB was measured with respect to the largest of these side modes. Dividing the laser's mode-locked repetition rate by its fundamental repetition rate reveals that there are 280 pulses simultaneously circulating in this cavity.

Since Fig. 97.43 shows that each peak is $\delta$-function-like, having a FWHM narrower than the minimum resolution (1 Hz) of the spectrum analyzer, the timing jitter and pulse energy fluctuations of the output pulse train were characterized. An upper bound on rms timing jitter is related to the integrated spectral power over the offset frequency range $f_l$–$f_h$ according to[13]

$$\sigma = \frac{1}{2\pi f_m}\left[2\int_{f_l}^{f_h} L(f)\,df\right]^{1/2},$$

where $\sigma$ is the rms timing jitter, $f_m$ is the repetition frequency of the $m^{\text{th}}$ harmonic around which this measurement is made, and $L(f)$ is the single-sided phase-noise spectral density detuned from $f_m$. Integration of the ~20-GHz peak over an offset range from 10 Hz to 12 kHz yields an upper bound on rms timing jitter of 370 fs, which is only slightly larger than the 283-fs jitter measured for the microwave signal generator using the same range. Above 12 kHz, $L(f)$ was dominated by the ≈ –81-dBc electronic noise floor (seen in Fig. 97.43 at the 20-kHz detuning) of the detector/spectrum analyzer combination, prohibiting an accurate jitter quantization over the typically quoted range (10 Hz to 10 MHz). The rms-energy fluctuations were quantified[13] over the 10-Hz to 10-MHz range, indicating an rms fluctuation of 16.9 fJ, which corresponds to an energy fluctuation of 0.85% for the 2-pJ pulses.

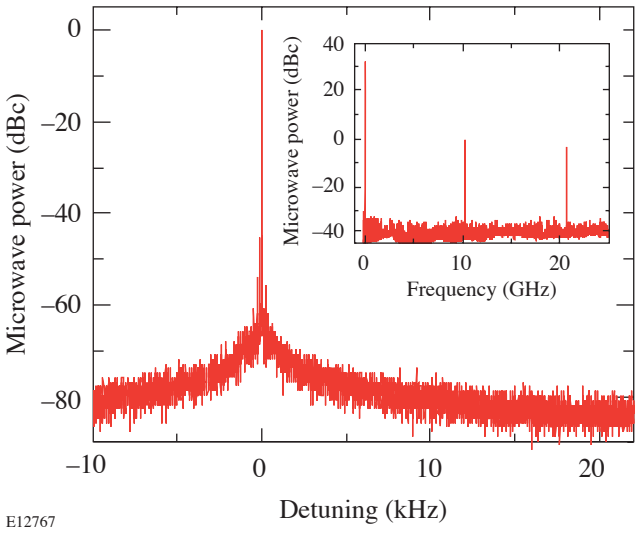


Figure 97.43
The microwave spectrum of the laser versus detuning from the 10.31455-GHz modulation frequency. The figure reveals that the signal at the modulation frequency is located 80 dBs above the noise floor. The inset shows the signal at 0 Hz, the ≈ 10.3-GHz repetition rate, and the first harmonic located at ≈ 20.6 GHz. Note that the strength of the noise floor has increased (in the inset) due to the reduced resolution of the spectrum analyzer over the broad frequency range used.

In conclusion, a tunable, high-repetition-rate, mode-locked, ytterbium fiber laser has been demonstrated. The hyperbolic-secant pulse spectrum indicates that the chirp introduced by the FM modulator is interacting with the cavity dispersion and fiber nonlinearity to play a role in shaping the laser pulses. The pulse-train timing jitter was found to be primarily due to the electronics and could be reduced by using a cleaner signal generator for jitter-sensitive applications. Finally, this laser's output pulse train consisting of linearly polarized, 2-ps chirped pulses could produce up to 38 mW of average power, making it suitable for many future applications.

## ACKNOWLEDGMENT

The authors thank Y. Deng for his assistance with the autocorrelation measurements, W. Bittle for his advice on electronics issues, and W. Knox for his support of this work. This work was supported by the U.S. Department of Energy Office of Inertial Confinement Fusion under Cooperative Agreement No. DE-FC03-92SF19460, the University of Rochester, and the New York State Energy Research and Development Authority. The support of DOE does not constitute an endorsement by DOE of the views expressed in this article.

## REFERENCES


1. V. Cautaerts *et al*., Opt. Lett. **22**, 316 (1997).
2. L. Lefort *et al*., Opt. Lett. **27**, 291 (2002).
3. H. Lim, F. Ö. Ilday, and F. W. Wise, Opt. Lett. **28**, 660 (2003).
4. O. G. Okhotnikov *et al*., Opt. Lett. **28**, 1522 (2003).
5. A. Liem *et al*., Appl. Phys. B **71**, 889 (2000).
6. J. E. Rothenberg, Appl. Opt. **39**, 6931 (2000).
7. S. Lecomte *et al*., Opt. Lett. **27**, 1714 (2002).
8. J. D. Zuegel and D. W. Jacobs-Perkins, "An Efficient, High-Frequency Bulk Phase Modulator," to be published in Applied Optics.
9. D. Kuizenga and A. Siegman, IEEE J. Quantum Electron. **6**, 694 (1970).
10. J. M. Roth, T. E. Murphy, and C. Xu, Opt. Lett. **27**, 2076 (2002).
11. K. Mogi, K. Naganuma, and H. Yamada, Jpn. J. Appl. Phys. 1, Regul. Pap. Short Notes Rev. Pap. **27**, 2078 (1988).
12. F. Rana *et al*., J. Opt. Soc. Am. B **19**, 2609 (2002).
13. D. von der Linde, Appl. Phys. B **39**, 201 (1986).

# Deterministic Microgrinding, Lapping, and Polishing of Glass-Ceramics

## Introduction

Glass-ceramics are attractive structural materials due to their good mechanical properties, chemical stability at higher temperatures, and tailored microstructures via appropriate heat treatments. In the cold working of glass-ceramics, several options are available: loose-abrasive grinding (lapping, at fixed nominal pressure) or deterministic microgrinding (at fixed nominal infeed, with bound-abrasive tools), both of which primarily remove material by microcracking. These manufacturing operations are usually followed by polishing to remove the residual stresses or damage left from the grinding operations.

The goal of the work described in this article is twofold: to determine which properties of glass-ceramics are responsible for material removal and the quality of the resulting surface (roughness, residual stresses induced by grinding), and to compare loose-abrasive grinding with deterministic microgrinding.

## Measurements

Five novel glass-ceramic materials (labeled GC1-GC5) were provided by Corning, Inc. The surface roughness of the as-received samples was in the range of 4 to 8 $\mu$m (peak-to-valley).

1. Elastic Properties and Microindentation Measurements

Longitudinal and shear wave speeds were first measured and then converted to Young's and shear moduli. Young's modulus was also independently measured from the load-displacement curve in 4-pt bending tests. Modulus of rupture was measured in 4-pt bend tests for as-received samples, as well as for samples in which controlled flaws were introduced on the tension side by Vickers indentation. Knoop hardness was measured at loads of 50 to 200 gf. Vickers hardness was measured at loads from 10 to 1000 gf. Between five to ten indents at each load were performed (15-s dwell time). All materials were measured in air.

For the fracture toughness measurements, the length $c$ of the cracks emanating from the Vickers indentation corners was measured optically. We used indentation[1]—the approach of Evans[2]—to extract the fracture toughness $K_c$ from the measured indentation crack size. In our glass-ceramics tests, the range of indentation crack size to indent diagonal $c/(D/2)$ was from 2 to 3 and thus covered by the Evans approach. Ponton and Rawlings[3,4] published an exhaustive analysis comparing the prediction of the fracture toughness by many different indentation models to the fracture toughness measured by bulk methods. They examined many ceramics (zirconias and aluminas), as well as many glass-ceramics, concluding that several models gave good agreement between the bulk and indentation fracture toughness measurements. The Evans model[2] was one such model. Our work on the fracture toughness of optical glasses[5] also has shown that the Evans model provides a good prediction of fracture toughness.

2. Chemical Susceptibility Measurements

The alkali resistance of the glass-ceramics was tested by immersing two test pieces in a boiling aqueous solution of equal parts $Na_2CO_3$ and NaOH for 3 h. The resulting mass loss, measured in an analytical balance, indicates the material's chemical susceptibility or alkali resistance. Table 97.II summarizes the measured micromechanical and chemical properties of the glass-ceramic materials.

3. Deterministic Microgrinding Measurements

Deterministic microgrinding is a fixed-infeed-rate material removal process utilizing computer-numerically-controlled (CNC) machining platforms. We sequentially used three thin-walled diamond-bound-abrasive (metal bond 75N, medium hardness) cup wheel tools on the Opticam SX CNC machining platform.[6] The tools were dressed before grinding each new type of material. To examine the effect of abrasive size in deterministic microgrinding, we used the three tools on glass-ceramics samples in the form of thin disks (aspect ratio about 30/1): first, a rough tool (average abrasive size of 70 $\mu$m) at an infeed rate of 100 $\mu$m/min, then a medium tool (abrasive size 10 to 20 $\mu$m) at an infeed rate of 50 $\mu$m/min, and finally a fine tool (abrasive size 2 to 4 $\mu$m) at an infeed rate of 10 $\mu$m/min. The tool rotation rate was 5000 rpm, and the work rotation rate

was 150 rpm. The tool rotation rate and diameter correspond to a surface speed of about 14.1 m/s. Three to five samples were tested at each setting. Following grinding with each tool, the surface roughness was measured with a white-light interferometer (Model NewView 1000, Zygo Corp., Middlefield, CT) and so was the power (sag), induced by the grinding process.

4. Loose-Abrasive Lapping and Polishing Removal Rate Measurements

Lapping and polishing experiments used thin glass-ceramic disks of approximately 2.2-mm thickness and 62-mm diameter. The as-received saw-cut specimens were first lapped on a Strasbaugh platform with 22-$\mu$m alumina abrasives (cast-iron plate and aqueous slurry), then with 7-$\mu$m alumina abrasives (same slurry composition), and finally polished with 1-$\mu$m alumina abrasives (aqueous slurry, new polyurethane lap used for each material). The initial condition for each process was the final surface from the previous step. In the lapping and polishing experiments, the pressure was maintained at 10 to 14 kPa and the relative speed at 1.22 m/s. Surface roughness was measured at the center and near the edge of the circular surfaces.

5. Grinding-Induced Surface Residual Stress Measurements

Surface residual stresses induced by the lapping process (see the previous section), i.e., the Twyman effect for glass-ceramics, were measured on flat disks of samples (aspect ratio of about 30/1) whose two sides (S1 and S2) were first polished to approximately one-wave flatness. Subsequently, one surface (surface S1) was lapped by 22-$\mu$m $Al_2O_3$ abrasives for about 2 to 3 min, then by 7-$\mu$m $Al_2O_3$ abrasives for about 30 min, and finally polished by 1-$\mu$m $Al_2O_3$ abrasives for about 20 to 45 min. The slurry and processing conditions were as described in the previous section. During this process, the other surface (S2) remained polished, and its power (sag) was measured with the white-light interferometer.

Table 97.II: Summary of the measurements of the mechanical and chemical properties of glass-ceramics.

| | GC1 | GC2 | GC3 | GC4 | GC5 |
|---|---|---|---|---|---|
| **Thermoelastic properties** | | | | | |
| Density $\rho$ (kg m$^{-3}$) | 3.18 | 2.93 | 2.98 | 2.99 | 2.98 |
| Thermal expansion coefficient $\alpha$ ($10^{-6}$ °C$^{-1}$) | 8.6 | 6.02 | – | – | 4.21 |
| Young's modulus $E$ (GPa), ±5% | 130 | 130 | 123 | 138 | 113 |
| Shear modulus $G$ (GPa), ±5% | 52.2 | 53.4 | 48.9 | 56.8 | 46.0 |
| Poisson ratio $\nu$ | 0.242 | 0.219 | 0.255 | 0.217 | 0.229 |
| **Modulus of rupture (MPa), ±10%** | | | | | |
| As-received | 178 | 162 | 145 | 159 | 124 |
| With Vickers flaw @ $P$ = 1 kgf | 138 | 120 | 80 | 118 | 76 |
| **Microindentation hardness** | | | | | |
| Knoop hardness @ 0.2 kgf (GPa), ±5% | 9.3 | 10.0 | 9.4 | 9.9 | 8.7 |
| Vickers hardness @1 kgf (GPa), ±10% | 9.5 | 9.4 | 9.3 | 10.0 | 8.2 |
| **Microindentation cracking** | | | | | |
| Crack size 2$c$ ($\mu$m) @ 500 gf | 83.6 | 70.6 | 81.7 | 73.0 | 80.8 |
| Indent. fracture toughness $K_c$ $\left(\text{MPa}\sqrt{m}\right)$, ±10% | 1.41 | 1.75 | 1.53 | 1.63 | 1.55 |
| **Chemical susceptibility (alkali attack)** | | | | | |
| Mass loss per unit area (mg/cm$^2$) | 162±20 | 43±12 | 41.3±3.3 | 33±2.3 | 114±0.3 |

**Results**

For the deterministic microgrinding experiments (fixed infeed rate), Fig. 97.44 shows the correlation of surface roughness and chemical susceptibility (alkali resistance). The results generally indicate that materials with higher chemical susceptibility also lead to higher surface roughness. Figure 97.45 shows the correlation of surface microroughness with abrasive size, indicating that, for a given material, finer abrasives lead to lower surface roughness. Figure 97.46 shows the dependence of the grinding-induced surface residual force per unit length on the Vickers indentation crack size.

For the loose-abrasive lapping experiments, Fig. 97.47 shows the dependence of the material removal rate on the material figure of merit $E^{5/4}/[K_c\,\mathrm{Hv}]$, Fig. 97.48 the dependence of surface microroughness on hardness, and Fig. 97.49 the dependence of surface roughness on chemical susceptibility.

For the polishing experiments, Fig. 97.50 shows the dependence of the polishing rate on Vickers hardness and Fig. 97.51 the polishing rate versus the material figure of merit $E^{5/4}/[K_c\,\mathrm{Hv}]$. Figure 97.52 shows the dependence of the lapping-induced surface-grinding force on microindentation crack size.

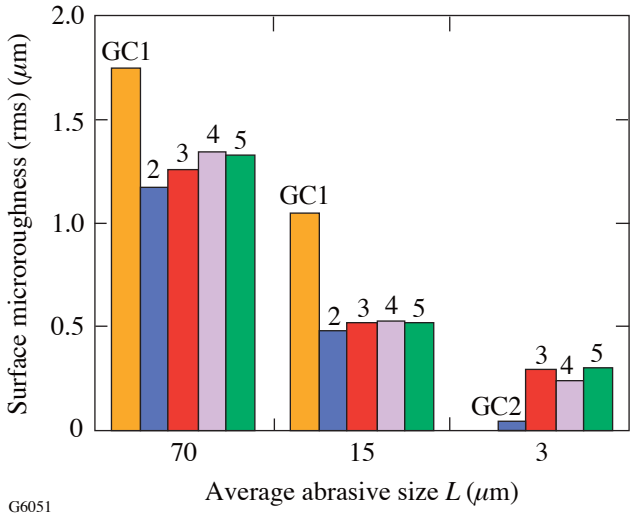


Figure 97.45
Dependence of surface microroughness on abrasive size in deterministic microgrinding.

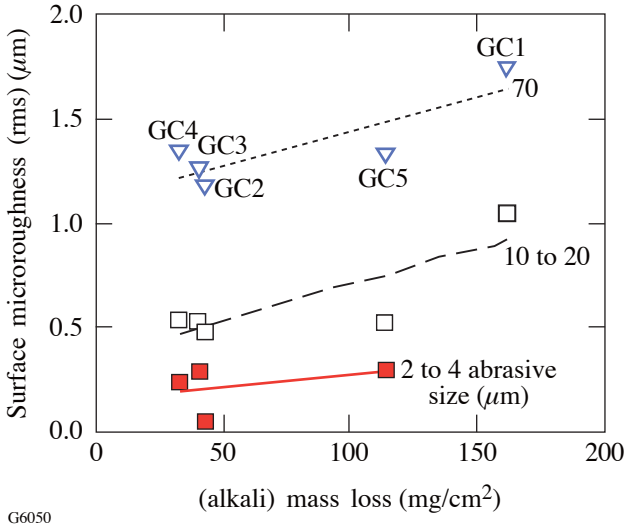


Figure 97.44
Dependence of surface roughness induced by deterministic microgrinding on chemical susceptibility, as measured by the mass loss under alkali attack.

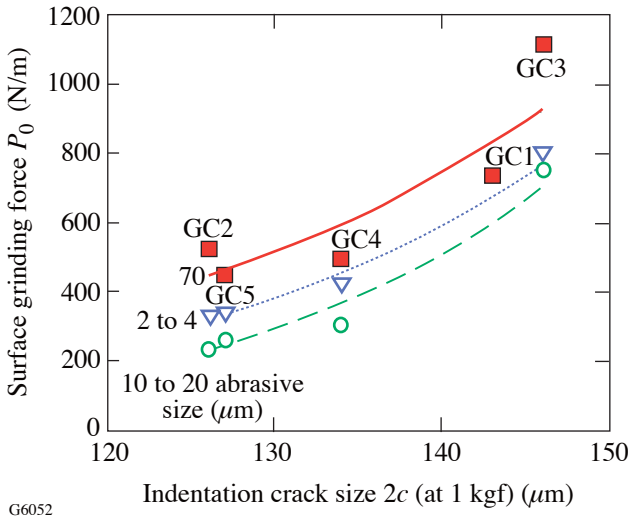


Figure 97.46
Dependence of grinding-induced force $P_0$ on indentation crack size (at 1 kgf).

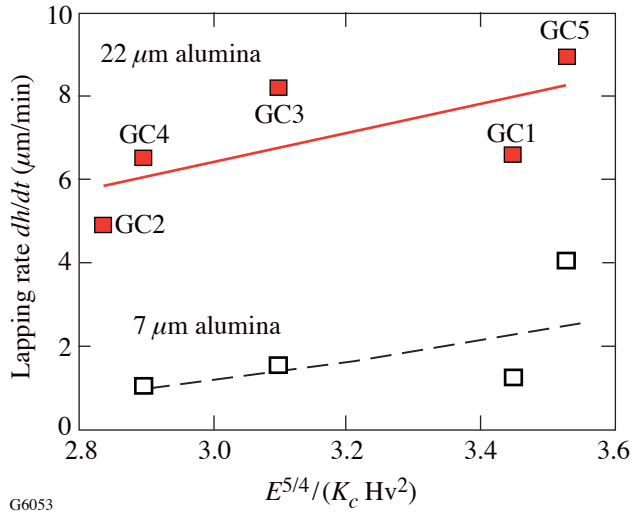


Figure 97.47
Dependence of lapping rate on mechanical properties. Fracture toughness $K_c$ (MPa m$^{1/2}$) and Vickers hardness Hv (GPa, at 1 kgf).

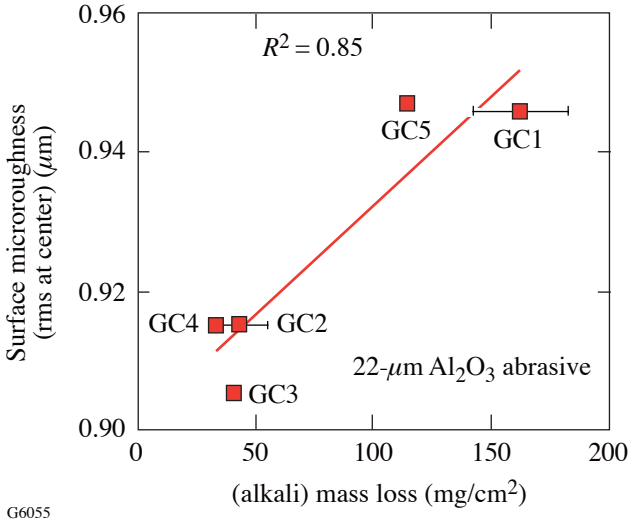


Figure 97.49
Dependence on chemical susceptibility of surface roughness (measured in center of the plate) induced by lapping with 22-$\mu$m $Al_2O_3$ abrasives.

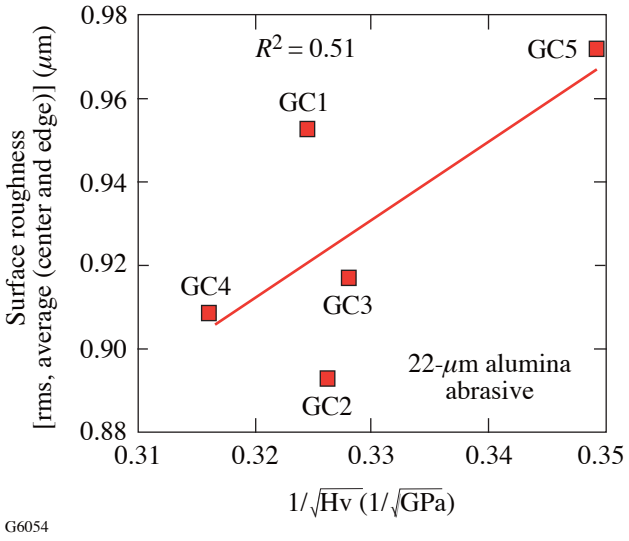


Figure 97.48
Dependence of surface roughness induced by lapping with 22 $\mu$m $Al_2O_3$ on material hardness.

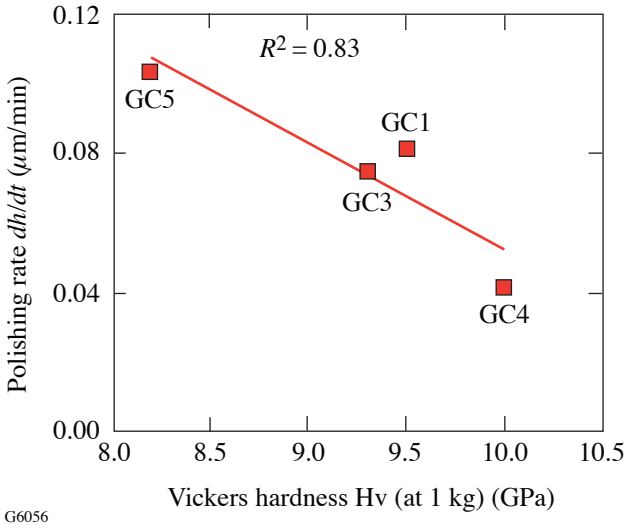


Figure 97.50
Dependence of polishing rate on Vickers hardness (at 1 kgf).

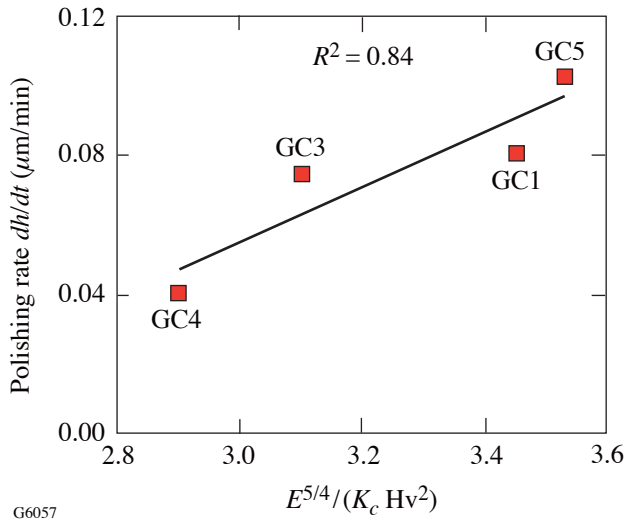


Figure 97.51
Dependence of polishing rate on mechanical properties: fracture toughness $K_c$ (MPa m$^{1/2}$) and Vickers hardness Hv (GPa, at 1 kgf) from microindentation.

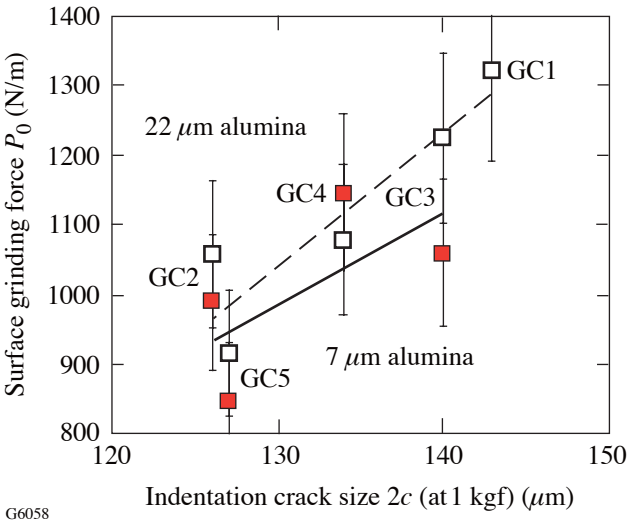


Figure 97.52
Dependence on microindentation crack size (at 1 kgf) of lapping-induced surface grinding force $P_0$ for lapping with 22-μm and 7-μm $Al_2O_3$ abrasives. The lapped surface is S1 (originally polished). $P_0$ is proportional to the change in power, measured on the polished surface S2, from the initial power (S1 polished) to the value after S1 is lapped.

**Discussion**

Some of our results are as intuitively expected. For example, Figs. 97.44 and 97.49 indicate that higher chemical susceptibility leads to higher surface roughness, both under deterministic microgrinding and under loose-abrasive lapping. Similarly, Fig. 97.45 indicates that larger abrasives lead to higher surface roughness. However, the dependence of grinding-induced surface residual force on abrasive size is not entirely obvious.

It is well known that grinding of brittle surfaces with loose or bound abrasives induces a state of residual compression on the ground surface. This phenomenon is often referred to as the Twyman effect.[7] The measured power (sag) of the surface is an indication of the extent of the residual force per unit of length along the edge of the ground surface. In the Twyman effect, a thin brittle disk is ground on one side, without altering the other side. As a result of grinding, the ground side is in a state of compressive stress and becomes convex, whereas the other side (on which the power is measured) is concave. The measured power $\Delta h$ (sag of the thin plate) was converted to an equivalent force $P_0$ per unit length along the circumference of the ground edge, as described in Ref. 7:

$$P_0 = \frac{4E}{3(1-\nu)}\Delta h\left(\frac{t}{D}\right)^2, \qquad (1)$$

where $E$ is the Young's modulus, $\nu$ the Poisson ratio, $t$ the plate thickness, and $D$ the plate diameter. The computed force $P_0$ is shown in Fig. 97.46 for deterministic microgrinding and in Fig. 97.52 for the loose-abrasive lapping experiments.

The results in Fig. 97.46 show that the surface grinding force does not necessarily diminish as the size of the abrasive gets smaller. Rather, for deterministic microgrinding, the intermediate abrasive (10 to 20 μm) gives the lowest surface grinding force. This result may be a consequence of the onset of ductile grinding, i.e., suppression of lateral cracking as the dominant material-removal mechanism in favor of plastic scratching. Ductile grinding is known to lead to high surface grinding forces.[8]

The correlation, reported in Fig. 97.46, between grinding-induced surface force $P_0$ and indentation crack size 2$c$ was first reported for optical glasses by Lambropoulos *et al.*,[7] whose results show that the same correlation holds also for glass-ceramics.

Figure 97.47 shows the lapping material removal rate versus the combination of mechanical properties, which was used previously by Lambropoulos *et al.*[9] in optical glasses, extending the work by Buijs and Korpel-Van Houten.[10,11] Thus, it is concluded that, in lapping of glass-ceramics,

$$\frac{dh}{dt} \sim \frac{E^{5/4}}{K_c H^2}, \tag{2}$$

where $E$ is Young's modulus, $K_c$ is fracture toughness, and $H$ is the hardness. This correlation results from using a lateral crack model as the basis for the material removal mechanism.

Figure 97.48 shows the dependence of the surface roughness of the 22-$\mu$m alumina-lapped surface on the glass-ceramic hardness. As in optical glasses,[8]

$$\text{surface roughness} \sim \frac{1}{\sqrt{H}}. \tag{3}$$

The results for polishing material removal rate show that increasing hardness generally leads to a diminishing removal rate, an expected result (see Fig. 97.50). Figure 97.51 shows a new result, however, instances of which have been reported by Lambropoulos *et al.*[12,13] for polishing of optical glasses: The polishing rate has the same dependence on material properties combination $E^{5/4}/K_c$ Hv as the lapping rate (Fig. 97.47). This result is not unexpected from a fundamental point of view: since in any material removal process atomic bonds must be broken among surface atoms, a property characterizing such bond strength (for example, fracture toughness) is expected to influence the polishing removal rate.

Our measurements on the deterministic microgrinding and lapping of glass-ceramics also allow us to compare these two processes in terms of the material removal rate and quality (surface roughness, residual stresses) of the resulting surface. Table 97.III summarizes the data for the samples studied in this report. Deterministic microgrinding maintains a faster removal rate than lapping (over the range of lapping pressures and relative speeds used), while for comparable abrasive sizes the surface roughness is lower than that for lapping, and the grinding-induced surface residual forces are significantly reduced as compared to lapping.

Table 97.III: Comparison of deterministic microgrinding and loose-abrasive grinding (lapping) for the cold working of glass-ceramic materials ($L$ is the nominal abrasive size used). For deterministic microgrinding the abrasives are diamonds embedded in a metal bond. For lapping and polishing the abrasives are alumina.

| | Surface Removal Rate ($\mu$m/min) | rms Surface Roughness ($\mu$m) | Surface Residual Force (N/m) |
|---|---|---|---|
| Determinisitic microgrinding (fixed infeed) | | | |
| $L$ = 70 $\mu$m | 100 | 1.2–1.7 | 400–1100 |
| $L$ = 15 $\mu$m | 50 | 0.5–1 | 200–700 |
| $L$ = 2 to 4 $\mu$m | 10 | 0.05–0.3 | 300–800 |
| Lapping (fixed pressure) | | | |
| $L$ = 22 $\mu$m | 5–9 | 0.9–1 | 900–1300 |
| $L$ = 7 $\mu$m | 1–4 | 0.7–0.8 | 800–1200 |
| Polishing (fixed pressure) | | | |
| $L$ = 1 $\mu$m | 0.04–0.1 | 0.01–0.1 | — |

In this article mechanical and chemical properties of glass-ceramics and their response under deterministic or loose abrasive grinding conditions have been correlated. The quality of the resulting surface in terms of the material removal rate, the surface microroughness, and the surface residual stresses induced by microgrinding have been characterized. Neither the effects of material grain size and abrasive grain size nor the correlation of "feeds and speeds" have been examined since these alter the rate at which the tool penetrates into the work surface. In addition, the issue of subsurface damage and that of the deepest flaw induced by microgrinding have not been addressed. These issues should be studied in the context of the mechanical strength of the glass-ceramic components, especially in relation to applied thermal or mechanical forces acting on these components after grinding.

**Conclusions**

The microgrinding and polishing behavior of five novel glass-ceramics have been studied. The mechanical properties of the glass-ceramics, as well as their material removal rate and quality of the resulting surface, have been measured for deterministic microgrinding (fixed infeed rate; metal bond diamond cup wheel on a CNC machining platform; embedded diamond abrasives of 70 mm, 15 $\mu$m, and 3 $\mu$m in size), loose-abrasive lapping (fixed nominal pressure, 22 $\mu$m and 7 $\mu$m $Al_2O_3$ loose abrasives), and polishing (fixed nominal pressure, 1 $\mu$m $Al_2O_3$ abrasives). The quality of the worked surface was characterized in terms of the grinding-induced surface microroughness and the grinding-induced surface residual force.

Findings on deterministic microgrinding of glass-ceramics under fixed infeed rate include the following:

1. Workpiece surface microroughness scales linearly with chemical susceptibility of the glass-ceramics under alkali attack conditions. Higher mass loss under alkali attack generally leads to higher surface roughness in deterministic microgrinding and higher tool-wear rate.
2. Smaller bound abrasives lead to lower surface microroughness.
3. Intermediate bound abrasives (10 to 20 $\mu$m) lead to the lowest grinding-induced surface residual compressive force. Very large or very small bound abrasives lead to higher surface residual forces.
4. The grinding-induced surface residual compressive force increases with indentation-produced surface cracks; thus, microindentation may be used to predict surface-grinding force.

Findings on the loose-abrasive grinding and polishing of glass-ceramics under fixed nominal pressure include the following:

1. The lapping removal rate increases with $E^{5/4}/K_c$ Hv, as in optical glasses.
2. The surface roughness for 22-$\mu$m abrasives increases with $1/\sqrt{H}$, as in optical glasses.
3. The surface roughness for 22-$\mu$m abrasives increases with chemical susceptibility to alkali attack, as it did for deterministic microgrinding.
4. The polishing removal rate decreases with increasing hardness $H$, and increases with increasing $E^{5/4}/K_c$ Hv. This result identifies fundamental similarities between the lapping and polishing material removal mechanisms.
5. The grinding-induced surface residual compressive force is an increasing function of indentation-produced surface cracks; thus, microindentation may be used to predict surface-grinding force.

In comparing deterministic microgrinding with loose-abrasive microgrinding, it was found that deterministic microgrinding maintains a faster removal rate than lapping, while for comparable abrasive sizes, the surface roughness induced by deterministic microgrinding is lower than that for lapping, while the grinding-induced surface residual forces are significantly reduced.

ACKNOWLEDGMENT

The authors acknowledge technical assistance in property measurements (Prof. S. Gracewski for the NDE measurements; Prof. S. Burns and Dr. F. Dahmani for MOR; and Mr. D. Pomonti and Dr. Fang for the indentation measurements) and the grinding experiments (Dr. Y.-Y. Zhou), and also acknowledge insights on microstructural observations provided by Prof. Paul Funkenbusch.

REFERENCES

1. A. R. Boccaccini, J. Mater. Sci. Lett. **15**, 1119 (1996).
2. A. G. Evans, in *Fracture Mechanics Applied to Brittle Materials*, edited by S. W. Freiman (American Society for Testing and Materials, Philadelphia, 1979), Vol. ASTM STP 678, Part 2, pp. 112–135.
3. C. B. Ponton and R. D. Rawlings, Mater. Sci. Technol. **5**, 865 (1989).
4. *ibid.*, Mater. Sci. Technol. **5**, 961 (1989).
5. J. C. Lambropoulos, T. Fang, P. D. Funkenbusch, S. D. Jacobs, M. J. Cumbo, and D. Golini, Appl. Opt. **35**, 4448 (1996).

6. H. M. Pollicove and D. T. Moore, in *Optical Fabrication and Testing Workshop*, Vol. 24, 1992 Technical Digest Series (Optical Society of America, Washington, DC, 1992), pp. 44–47.

7. J. C. Lambropoulos, S. Xu, T. Fang, and D. Golini, Appl. Opt. **35**, 5704 (1996).

8. D. Golini and S. D. Jacobs, Appl. Opt. **30**, 2761 (1991).

9. J. C. Lambropoulos, S. Xu, and T. Fang, Appl. Opt. **36**, 1501 (1997).

10. M. Buijs and K. Korpel-van Houten, J. Mater. Sci. **28**, 3014 (1993).

11. *ibid*., Wear **166**, 237 (1993).

12. J. C. Lambropoulos, in *Optical Fabrication and Testing Workshop*, Vol. 7, 1996 OSA Technical Digest Series (Optical Society of America, Washington, DC, 1996), pp. 88–91.

13. J. C. Lambropoulos, S. D. Jacobs, and J. Ruckman, in *Finishing of Advanced Ceramics and Glasses*, edited by R. Sabia, V. A. Greenhut, and C. G. Pantano, Ceramic Transactions, Vol. 102 (The American Ceramic Society, Westerville, OH, 1999), pp. 113–128.

# Performance of 1-THz-Bandwidth, 2-D Smoothing by Spectral Dispersion and Polarization Smoothing of High-Power, Solid-State Laser Beams

## Introduction

A direct-drive inertial confinement fusion (ICF) implosion of a spherical capsule containing thermonuclear fuel is initiated by the ablation of material from the outer shell surface with overlapped, intense laser beams.[1] The ablated shell mass forms a coronal plasma that surrounds the target and accelerates the shell inward via the rocket effect.[1,2] Perturbations at the ablation surface resulting from target imperfections and laser irradiation nonuniformities (known as laser imprint) are amplified by the ablative Rayleigh–Taylor (RT) instability as the shell accelerates inward and are further amplified during the deceleration phase.[3–9] The RT instability can reduce the thermonuclear yield of the implosion.[1,2] The direct-drive ICF program strives to reduce laser imprint levels by uniform laser irradiation of the target. High-compression direct-drive experiments require a 1% rms level of the on-target laser irradiation nonuniformity averaged over a few hundred picoseconds.[10] This is accomplished on the 60-beam, 30-kJ, 351-nm OMEGA laser system[11] using two-dimensional smoothing by spectral dispersion (2-D SSD),[10,12–14] distributed phase plates (DPP's),[15,16] polarization smoothing (PS) utilizing birefringent wedges,[17–19] and multiple-beam overlap.[20] These techniques are directly applicable to direct-drive ignition target designs[21] planned for the 1.8-MJ, 351-nm, 192-beam National Ignition Facility (NIF) at the Lawrence Livermore National Laboratory.[22]

The 2-D SSD UV bandwidth ($\Delta\nu_{UV}$) on OMEGA was recently increased to 1 THz, and polarization smoothing was added through the installation of a birefringent wedge in each of the 60 beams. The amount of smoothing achieved with 1-THz, 2-D SSD and PS is reported. The experimental techniques outlined in Ref. 14 are used to determine the single-beam irradiation nonuniformity from the measured ultraviolet equivalent-target-plane (UVETP) images of laser pulses having constant intensity and varying duration. Simulations of the experimental data using the properties of the phase plates, frequency modulators, and birefringent wedges are shown to be in good agreement with the measured results.

## 2-D SSD and PS

Laser-beam nonuniformities can be significantly reduced for high-power/energy glass lasers using 1-THz, 2-D SSD and PS. Two-dimensional SSD reduces the single-beam irradiation nonuniformity as a function of time, while the PS provides an additional, instantaneous reduction by a factor of $\sqrt{2}$ in the on-target nonuniformity.[10] The temporal dynamics of the laser-beam smoothing with 2-D SSD and PS are illustrated in Fig. 98.1. The curves plotted in Fig. 98.1 for 0.2-THz, 2-D SSD (dashed line); 1-THz, 2-D SSD (dotted line); and 1-THz,

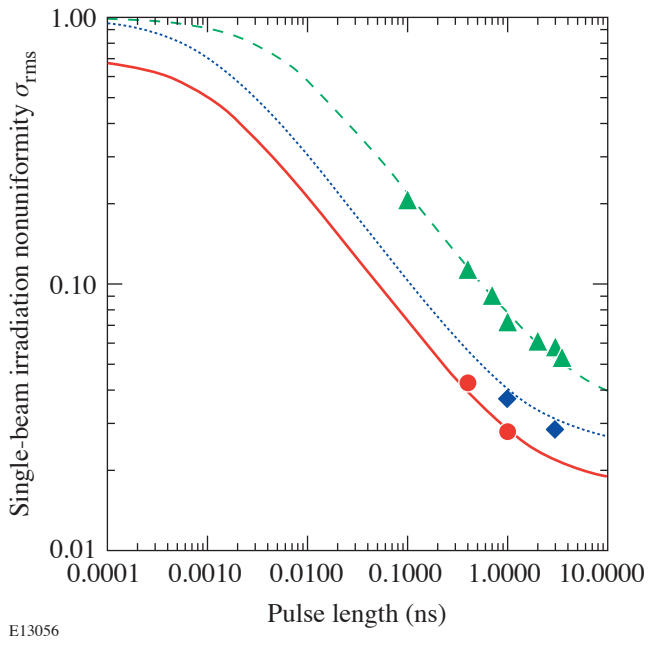


Figure 98.1
The single-beam irradiation nonuniformity $\sigma_{rms}$ is plotted as a function of time for three laser-beam-smoothing conditions under consideration. Smoothing curves of the predicted $\sigma_{rms}$ [see Eq. (1)] are plotted for 0.2-THz, 2-D SSD (dashed line); 1-THz, 2-D SSD (dotted line); and 1-THz, 2-D SSD with PS (solid line). The experimental results are plotted for 0.2-THz, 2-D SSD (triangles); 1-THz, 2-D SSD (diamonds); and 1-THz, 2-D SSD with PS (circles). The model shows excellent agreement with the experimental results that are a compilation of data from more than 200 laser shots. The error bars are smaller than the symbols.

2-D SSD with PS (solid line) represent the model predictions[14] for the single-beam irradiation nonuniformity $\sigma_{\text{rms}}$:

$$\sigma_{\text{rms}} = \sqrt{\sigma_0^2\left(\frac{t_c}{t+t_c}\right) + \sigma_{\text{asymp}}^2}\ , \tag{1}$$

where $t_c = 1/\Delta\nu_{\text{UV}}$ is the coherence time, $t$ is the averaging time (i.e., pulse length), $\sigma_0$ is the initial laser nonuniformity, and $\sigma_{\text{asymp}}$ is the asymptotic level of smoothing with 2-D SSD and PS taken from Eq. (8) of Ref. 23. The $\sigma_{\text{rms}}$ predicted with Eq. (1) has been shown to be nearly indistinguishable from the $\sigma_{\text{rms}}$ predicted with the time-integrated simulation described below.[14] The model shows excellent agreement with the experimental results as discussed in the next section. The laser-beam smoothing parameters are listed in Table 98.I. As seen in Fig. 98.1, prior to reaching asymptotic levels, increasing $\Delta\nu_{\text{UV}}$ of the 2-D SSD from 0.2 THz (dashed line) to 1 THz (dotted line) reduces the amount of time needed to smooth to a given level of nonuniformity by a factor of 5. Also, for time $t >> t_c$, it reduces the level of nonuniformity at any given time by a factor of $\sqrt{5}$. A comparison of the smoothing curve for the 1-THz, 2-D SSD (dotted line) with the curve for 1-THz, 2-D SSD with PS (solid line) shows that PS provides an instantaneous reduction in $\sigma_{\text{rms}}$ by $\sqrt{2}$.

Table 98:I: Specifications for laser-beam smoothing.

| 2-D SSD $\Delta\nu_{\text{UV}}$ (THz) | PS | $t_c = 1/\Delta\nu_{\text{UV}}$ (ps) | $\sigma_0$ | $\sigma_{\text{asymp}}$ |
|---|---|---|---|---|
| 0.2 | off | 5 | 1.00 | $3.30 \times 10^{-2}$ |
| 1.0 | off | 1 | 1.00 | $2.52 \times 10^{-2}$ |
| 1.0 | on | 1 | 0.707 | $1.77 \times 10^{-2}$ |

Laser-beam smoothing with PS is instantaneous, while 2-D SSD produces uniform far-field spots on target in a time-averaged sense. One-dimensional SSD is achieved on OMEGA by frequency modulating the phase of the laser beam, wavelength dispersing the beam using a diffraction grating, and passing the beam through a phase plate placed just before the focusing lens.[10,12] Two-dimensional SSD is achieved by applying the 1-D SSD operations in two orthogonal directions.[10] Highly reproducible spatial intensity envelopes and speckle distributions are produced in the far field. The implementation of PS on OMEGA is described elsewhere.[10] Each UV beam, polarized at 45° to the ordinary and extraordinary axes of a birefringent wedge placed before the phase plate, is split into two beams of equal intensities that refract through the wedged surface at slightly different angles and focus on target with a separation of ~85 $\mu$m, about 37 times the beam's diffraction limited width ($f$ number times the laser wavelength = 2.3 $\mu$m). The two beams each produce essentially the same speckle pattern on target, determined by the phase plate, but since these patterns are spatially uncorrelated with opposite polarization states, they combine through the addition of intensities rather than electric fields. This leads to the instantaneous reduction in the nonuniformity by a factor of $\sqrt{2}$.

The time-integrated far field is calculated by temporally integrating the modulus squared of a 2-D spatial Fourier transform of the UV near field. The complex-valued electric field that describes the UV near field can be written as

$$\begin{aligned}\vec{E}(x,y,t) \equiv\ & E_0(x,y,t)\exp\left[i\phi_{\text{2-D SSD}}(x,y,t)\right] \\ & \cdot \exp\left[i\phi_B(x,y,t)\right]\cdot\exp\left[i\phi_{\text{DPP}}(x,y)\right] \\ & \cdot \left\{\hat{x} + \exp\left[i\phi_{\text{PS}}(y)\right]\hat{y}\right\},\end{aligned} \tag{2}$$

where $E_0(x,y,t)$ defines the temporal and spatial beam envelope, $\phi_{\text{2-D SSD}}(x,y,t)$ is the 2-D SSD phase contribution, $\phi_B(x,y,t)$ is the intensity-dependent phase contribution of the $B$-integral,[24] $\phi_{\text{DPP}}(x,y)$ is the static phase-plate contribution that depends on the particular phase-plate design, and $\phi_{\text{PS}}(y)$ is a linear phase term due to the birefringent wedge. The ideal spatially and temporally varying phase due to 2-D SSD can be expressed as

$$\begin{aligned}\phi_{\text{2-D SSD}}(x,y,t) \equiv\ & 3\delta_{M_x}\sin\left[\omega_{M_x}\left(t+\xi_x x\right)\right] \\ & + 3\delta_{M_y}\sin\left[\omega_{M_y}\left(t+\xi_y y\right)\right],\end{aligned} \tag{3}$$

where the $x$ and $y$ subscripts denote the two smoothing dimensions, $\delta_{M_{x,y}}$ is the modulation depth, $\nu_{M_{x,y}} \equiv \omega_{M_{x,y}}/2\pi$ is the RF modulation frequency, and $\xi_{x,y}$ describes the variation in phase across the beam due to the angular grating dispersion. The factor of 3 in Eq. (3) indicates that the electric field has undergone frequency tripling from the IR to UV. The 2-D SSD system parameters on OMEGA for the UVETP measurements are $\delta_{M_x} = 14.3$, $\nu_{M_x} \equiv 10.4$ GHz, $\xi_x = 0.300$ ns/m, $\delta_{M_y} = 6.15$, $\nu_{M_y} \equiv 3.30$ GHz, and $\xi_y = 1.13$ ns/m, assuming a nominal beam diameter of 27.5 cm. The modulation depths

are given for the IR. The IR bandwidths, defined as $\Delta\nu_x = 2\delta_{M_x}\nu_{M_x}$ and $\Delta\nu_y = 2\delta_{M_y}\nu_{M_y}$, correspond to $\Delta\lambda_x$ = 11.0 Å and $\Delta\lambda_y$ = 1.50 Å. The maximum angular spread $\Delta\theta$ is given by $\Delta\theta = \xi(c/\lambda)\Delta\lambda$, where $c$ is the speed of light and $\lambda$ = 1053 nm. $B$-integral effects are negligible for all cases except when the frequency modulation is turned off.[14] The linear phase term due to the birefringent wedge is

$$\phi_{\mathrm{PS}}(y) = k_0 \sin(\Delta\theta_{\mathrm{PS}})y,$$

where $k_0 = 2\pi/\lambda_{\mathrm{UV}}$ is the UV laser wave number with $\lambda_{\mathrm{UV}}$ = 351 nm and $\Delta\theta_{\mathrm{PS}}$ = 47 $\mu$rad is the angular separation due to the birefringent wedge.

**Experimental Results and Analysis**

A description of the UVETP diagnostic used in this study can be found in Ref. 14. This diagnostic uses a full-aperture optical wedge in one of the 60 beams to direct a small fraction of the laser light to a phase plate and an OMEGA focusing lens, and it records the UVETP image on a CCD camera (see Fig. 1 of Ref. 14). The capability of the UVETP diagnostic to resolve fully individual speckles has been demonstrated.[14] Shots with PS have the birefringent wedge placed in the beam before the full-aperture optical wedge. A far-field image recorded with the UVETP diagnostic of a 1-ns square laser pulse with 1-THz, 2-D SSD and PS is presented in Fig. 98.2. The UVETP diagnostic was configured with a phase plate that produced a far-field spot with a super-Gaussian spatial-intensity envelope $\left[I \sim \exp(r/r_0)^{2.3}\right]$. The image, which has been flat fielded, shows a smooth spatial-intensity envelope [see the single-pixel lineout overplotted on the image in Fig. 98.2]. The spatial resolution and overall detector size of the CCD restrict the UVETP measurement to slightly more than one-half of the laser-beam diameter. As seen in Fig. 98.2, the laser beam is centered on the photodetector, and 560 $\mu$m of the 1010-$\mu$m (defined as the 95% enclosed energy contour) laser spot is sampled. Alignment constraints for the compilation of laser shots under consideration restrict the analysis to the central ~410 $\mu$m of the laser spot.

The amount of smoothing achieved with 1-THz, 2-D SSD and PS is quantified from the power spectrum of the measured UVETP image of Fig. 98.2. The UVETP images are Fourier transformed with a 2-D Hamming filter applied to the data, in order to obtain the power spectrum defined as the azimuthal sum at each spatial frequency of the square of the Fourier amplitudes. Good agreement is observed between the measured power spectrum for the 1-THz, 2-D SSD, and PS presented in Fig. 98.3(a) and the modeled spectrum determined from simulated time-integrated far field. The wave number is defined as $k = 2\pi/\lambda_{\mathrm{SN}}$, where $\lambda_{\mathrm{SN}}$ is the spatial nonuniformity wavelength, and the $\ell$ mode is defined as $\ell = kR$, where $R$ = 500 $\mu$m is the spherical target radius. The $\sigma_{\mathrm{rms}}$ reaches 2.7% averaged over 1 ns, in agreement with the predicted 2.8%. The $\sigma_{\mathrm{rms}}$ is defined here as the square root of the ratio of the integral of power in the high frequencies (i.e., $k \geq 0.04\ \mu\mathrm{m}^{-1}$ in the OMEGA target plane) to the integral of power in the low frequencies (i.e., $k < 0.04\ \mu\mathrm{m}^{-1}$). The envelope and speckle were separated at wave number 0.04 $\mu\mathrm{m}^{-1}$ in the calculation of $\sigma_{\mathrm{rms}}$ for two reasons. First, virtually all of the envelope power is contained in the first three terms of the Fourier transform, which have wave numbers $k < 0.04\ \mu\mathrm{m}^{-1}$; therefore, inclusion of additional terms in this sum increases the envelope power by insignificant amounts. Second, the smallest wave number of nonuniformity that can be smoothed on OMEGA with 1-THz, 2-D SSD falls between the third and fourth terms of the Fourier transform with wave numbers 0.031 and 0.046 $\mu\mathrm{m}^{-1}$. Therefore, all the wave numbers that 2-D SSD can smooth are in the range $0.04\ \mu\mathrm{m}^{-1} \leq k < k_c$, where $k_c$ = 2.7 $\mu\mathrm{m}^{-1}$ is the cutoff wave number. The birefringent wedge was removed from the beamline, and another UVETP image was recorded to quantify the amount of smoothing

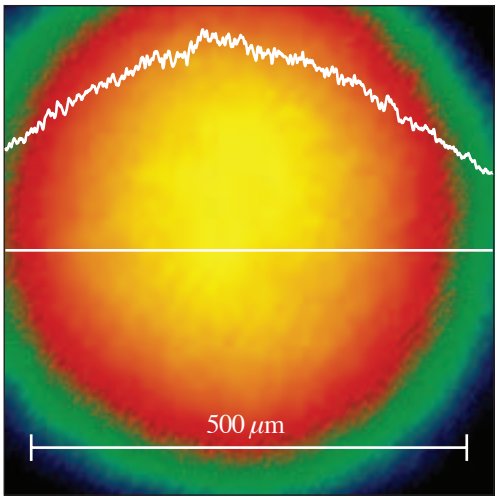


E13057

Figure 98.2
Measured UVETP image of a 1-ns square laser pulse with 1-THz, 2-D SSD and PS (shot 22835). As demonstrated with the single-pixel lineout through the center of the beam, the laser beam has a smooth spatial-intensity envelope. The spatial resolution and overall detector size of the CCD restrict the UVETP measurement to slightly more than one-half of the laser-beam profile. The laser beam is centered nominally on the photodetector, and 560 $\mu$m of the 1010-$\mu$m laser spot (defined as the 95% enclosed energy contour) is sampled.

achieved with 1-THz, 2-D SSD alone (i.e., no PS). Again, good agreement is shown in Fig. 98.3(b) between the measured power spectrum and the simulation with the expected $\sqrt{2}$ increase in $\sigma_{rms}$ observed.

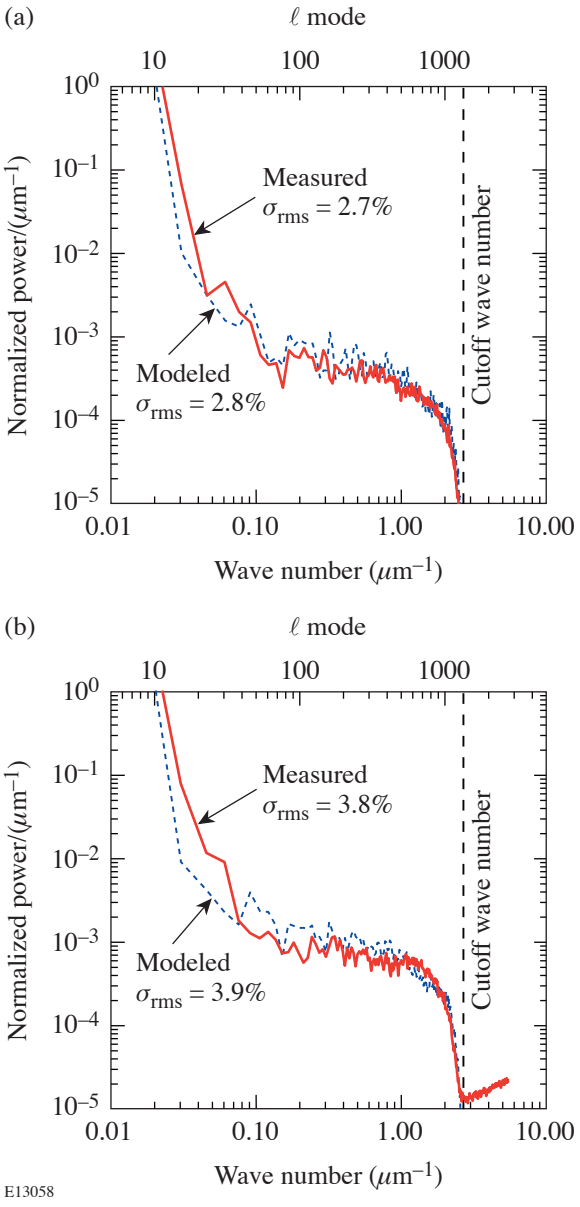


Figure 98.3
Power spectra calculated from UVETP images of (a) 1-ns square laser pulse with 1-THz, 2-D SSD and PS (shot 22835) and (b) 1-ns square laser pulse with 1-THz, 2-D SSD and no PS (shot 18249). The wave number is defined as $k = 2\pi/\lambda_{SN}$, where $\lambda_{SN}$ is the spatial nonuniformity wavelength, and the $\ell$ mode is defined as $\ell = kR$, where $R = 500$ μm is the spherical target radius. The solid lines represent the measured power spectra; the dashed lines represent the simulations, which are in agreement with the measured results.

The measured $\sigma_{rms}$ with 1-THz, 2-D SSD was also examined using 0.4-, 1.0-, and 3.0-ns square laser pulses. As shown in Fig. 98.1, the 1-THz, 2-D SSD model [Eq. (1)] is in agreement with the measured results. A more-extensive study of the smoothing rates for 0.2-THz, 2-D SSD was reported in Ref. 14, where it was shown with laser pulses having constant peak power and pulse lengths ranging from 100 ps to 3.5 ns, that the reduction in laser-irradiation nonuniformity is dependent on the spatial nonuniformity wavelength. The measured $\sigma_{rms}$ for 0.2-THz, 2-D SSD is also plotted in Fig. 98.1 for comparison with the 1-THz, 2-D SSD results. As can be seen in Fig. 98.1 for the time $t >> t_c$, but prior to reaching asymptotic levels, the measured $\sigma_{rms}$ is reduced by $\sqrt{5}$ when $\Delta\nu_{UV}$ is increased from 0.2 THz to 1 THz, and it is further reduced by $\sqrt{2}$ with PS. On OMEGA, beam overlap provides an additional $\sqrt{10}$ reduction in the nonuniformity on target; therefore, with perfect energy balance and timing of the laser beams, a $\sigma_{rms}$ ~1% can be achieved on target with 1-THz, 2-D SSD and PS in a few hundred picoseconds.

## Conclusion

Direct-drive ICF experiments require a laser system with excellent irradiation uniformity. Laser-beam nonuniformities can be significantly reduced for high-power/energy glass lasers using 1-THz, 2-D SSD and PS. UVETP images of a single OMEGA laser beam were recorded to quantify the single-beam irradiation nonuniformity. The amount of smoothing achieved with 1-THZ, 2-D SSD and PS was determined by analyzing the power spectra of measured UVETP images of square laser pulses of varying duration. Simulated power spectra are in excellent agreement with the experimental data and permit confident extrapolation to MJ-class laser systems.

## ACKNOWLEDGMENT

The authors appreciate the support of the entire OMEGA engineering staff, especially C. Kellogg, S. Stagnitto, R. Huff, and M. Kamm. This work was supported by the U.S. Department of Energy Office of Inertial Confinement Fusion under Cooperative Agreement No. DE-FC03-92SF19460, the University of Rochester, and the New York State Energy Research and Development Authority. The support of DOE does not constitute an endorsement by DOE of the views expressed in this article.

## REFERENCES

1. S. E. Bodner, D. G. Colombant, J. H. Gardner, R. H. Lehmberg, S. P. Obenschain, L. Phillips, A. J. Schmitt, J. D. Sethian, R. L. McCrory, W. Seka, C. P. Verdon, J. P. Knauer, B. B. Afeyan, and H. T. Powell, Phys. Plasmas **5**, 1901 (1998).

2. J. D. Lindl, *Inertial Confinement Fusion: The Quest for Ignition and Energy Gain Using Indirect Drive* (Springer-Verlag, New York, 1998).

3. D. K. Bradley, J. A. Delettrez, and C. P. Verdon, Phys. Rev. Lett. **68**, 2774 (1992).

4. J. Delettrez, D. K. Bradley, and C. P. Verdon, Phys. Plasmas **1**, 2342 (1994).

5. J. D. Kilkenny, S. G. Glendinning, S. W. Haan, B. A. Hammel, J. D. Lindl, D. Munro, B. A. Remington, S. V. Weber, J. P. Knauer, and C. P. Verdon, Phys. Plasmas **1**, 1379 (1994).

6. R. Epstein, J. Appl. Phys. **82**, 2123 (1997).

7. V. A. Smalyuk, T. R. Boehly, D. K. Bradley, V. N. Goncharov, J. A. Delettrez, J. P. Knauer, D. D. Meyerhofer, D. Oron, and D. Shvarts, Phys. Rev. Lett. **81**, 5342 (1998).

8. V. N. Goncharov, J. P. Knauer, P. W. McKenty, P. B. Radha, T. C. Sangster, S. Skupsky, R. Betti, R. L. McCrory, and D. D. Meyerhofer, Phys. Plasmas **10**, 1906 (2003).

9. S. P. Regan, J. A. Delettrez, V. N. Goncharov, F. J. Marshall, J. M. Soures, V. A. Smalyuk, P. B. Radha, B. Yaakobi, R. Epstein, V. Yu. Glebov, P. A. Jaanimagi, D. D. Meyerhofer, T. C. Sangster, W. Seka, S. Skupsky, C. Stoeckl, D. A. Haynes, Jr., J. A. Frenje, C. K. Li, R. D. Petrasso, and F. H. Séguin, "Dependence of Shell Mix on Feedthrough in Direct-Drive Inertial Confinement Fusion," to be published in Physical Review Letters.

10. S. Skupsky and R. S. Craxton, Phys. Plasmas **6**, 2157 (1999).

11. T. R. Boehly, D. L. Brown, R. S. Craxton, R. L. Keck, J. P. Knauer, J. H. Kelly, T. J. Kessler, S. A. Kumpan, S. J. Loucks, S. A. Letzring, F. J. Marshall, R. L. McCrory, S. F. B. Morse, W. Seka, J. M. Soures, and C. P. Verdon, Opt. Commun. **133**, 495 (1997).

12. S. Skupsky, R. W. Short, T. Kessler, R. S. Craxton, S. Letzring, and J. M. Soures, J. Appl. Phys. **66**, 3456 (1989).

13. J. E. Rothenberg, J. Opt. Soc. Am. B **14**, 1664 (1997).

14. S. P. Regan, J. A. Marozas, J. H. Kelly, T. R. Boehly, W. R. Donaldson, P. A. Jaanimagi, R. L. Keck, T. J. Kessler, D. D. Meyerhofer, W. Seka, S. Skupsky, and V. A. Smalyuk, J. Opt. Soc. Am. B **17**, 1483 (2000).

15. T. J. Kessler, Y. Lin, J. J. Armstrong, and B. Velazquez, in *Laser Coherence Control: Technology and Applications*, edited by H. T. Powell and T. J. Kessler (SPIE, Bellingham, WA, 1993), Vol. 1870, pp. 95–104.

16. Y. Lin, T. J. Kessler, and G. N. Lawrence, Opt. Lett. **21**, 1703 (1996).

17. Y. Kato, unpublished notes from work at LLE, 1984; K. Tsubakimoto *et al*., Opt. Commun. **91**, 9 (1992); K. Tsubakimoto *et al*., Opt. Commun. **103**, 185 (1993).

18. Laboratory for Laser Energetics LLE Review **45**, 1, NTIS document No. DOE/DP40200-149 (1990). Copies may be obtained from the National Technical Information Service, Springfield, VA 22161; T. E. Gunderman, J.-C. Lee, T. J. Kessler, S. D. Jacobs, D. J. Smith, and S. Skupsky, in *Conference on Lasers and Electro-Optics*, Vol. 7, 1990 OSA Technical Digest Series (Optical Society of America, Washington, DC, 1990), p. 354.

19. T. R. Boehly, V. A. Smalyuk, D. D. Meyerhofer, J. P. Knauer, D. K. Bradley, R. S. Craxton, M. J. Guardalben, S. Skupsky, and T. J. Kessler, J. Appl. Phys. **85**, 3444 (1999).

20. F. J. Marshall, J. A. Delettrez, R. Epstein, R. Forties, R. L. Keck, J. H. Kelly, P. W. McKenty, S. P. Regan, and L. J. Waxer, Phys. Plasmas **11**, 251 (2004).

21. P. W. McKenty, T. C. Sangster, M. Alexander, R. Betti, R. S. Craxton, J. A. Delettrez, L. Elasky, R. Epstein, A. Frank, V. Yu. Glebov, V. N. Goncharov, D. R. Harding, S. Jin, J. P. Knauer, R. L. Keck, S. J. Loucks, L. D. Lund, R. L. McCrory, F. J. Marshall, D. D. Meyerhofer, S. P. Regan, P. B. Radha, S. Roberts, W. Seka, S. Skupsky, V. A. Smalyuk, J. M. Soures, K. A. Thorp, M. Wozniak, J. A. Frenje, C. K. Li, R. D. Petrasso, F. H. Séguin, K. A. Fletcher, S. Padalino, C. Freeman, N. Izumi, J. A. Koch, R. A. Lerche, M. J. Moran, T. W. Phillips, G. J. Schmid, and C. Sorce, "Direct-Drive Cryogenic Target Implosion Performance on OMEGA," to be published in Physics of Plasmas.

22. J. Paisner *et al*., Laser Focus World **30**, 75 (1994).

23. J. E. Rothenberg, in *Solid State Lasers for Application to Inertial Confinement Fusion*, edited by W. F. Krupke (SPIE, Bellingham, WA, 1995), Vol. 2633, pp. 634–644.

24. J. A. Marozas, S. P. Regan, J. H. Kelly, D. D. Meyerhofer, W. Seka, and S. Skupsky, J. Opt. Soc. Am. B **19**, 7 (2002).

# Effect of Electric Fields on Electron Thermal Transport in Laser-Produced Plasmas

## Introduction

Thermal transport plays an important role in direct-drive inertial confinement fusion. The Spitzer–Härm heat flux[1] $\mathbf{q}_{SH} = -\kappa_{SH}\nabla T$ has been conventionally used in the direct-drive inertial confinement fusion (ICF) hydrocodes. Here, $\kappa_{SH}$ is the Spitzer heat conductivity and $T$ is the electron temperature. In the regions of the steep temperature gradients where $\mathbf{q}_{SH}$ exceeds a fraction $f$ of the free-stream limit $q_{FS} = nTv_T$, the Spitzer flux is replaced[2] by $fq_{FS}$, where $n$ is the electron density, $v_T = \sqrt{T/m}$ is the electron thermal velocity, and $f = 0.05 - 0.1$ is the flux limiter. It has been known for more than two decades[3–5] that, in addition to the terms proportional to the temperature gradients (thermal terms), the heat flux in laser-produced plasmas contains ponderomotive terms that are due to the gradients in the laser electric field. To our best knowledge, no systematic analysis has been performed to address the effect of such terms on the hydrodynamic flow in ICF plasmas. As shown later, the ratio of the ponderomotive terms to the thermal terms is proportional to $R = \alpha\left(v_E/v_T\right)^2\left(L_T/L_E\right)$, where $v_E = eE/m\omega_L$ is the electron quiver velocity, $e$ is the electric charge, $E$ is the amplitude of the electric field, $m$ is the electron mass, $\omega_L$ is the laser frequency, $L_T$ and $L_E$ are the temperature and the electric field scale length, and $\alpha$ is a constant. The ratio of the electron quiver velocity to the thermal velocity is small for typical plasma parameters. Indeed, $\left(v_E/v_T\right)^2 \simeq 0.4\ I_{15}\lambda_{\mu m}^2/T_{keV}$, where $I_{15}$ is the laser intensity in $10^{15}$ W/cm$^2$, $\lambda_{\mu m}$ is the laser wavelength in microns, and $T_{keV}$ is the electron temperature in keV. Using $I_{15} \sim 1$ and $T \sim 2$ keV, we obtain $\left(v_E/v_T\right)^2 \sim 0.02$ for $\lambda_{\mu m} = 0.353$ $\mu$m. The ratio $R$, however, can be of the order of unity due to a large ratio $L_T/L_E$. Indeed, as the laser reaches the turning point where the electron density equals $n_c \cos^2\theta$, the electric field decays toward the overdense portion of the shell as[6] $E \sim E_{max}\exp\left(-2/3\zeta^{3/2}\right)$, where $n_c = m_e\omega_L^2/4\pi e^2$ is the critical density, $\theta$ is the laser incidence angle, $\zeta = \left(\omega_L L_n/c\right)^{2/3} z/L_n$, $L_n \sim L_T$ is the electron-density scale length, and $z$ is the coordinate along the density gradient. Therefore, the electric-field scale length near the turning point becomes $L_E \sim L_T/\left(\omega_L L_T/c\right)^{2/3}$. Substituting this estimate to the ratio $R$ and using $L_T \sim 10$ $\mu$m and $\left(v_E/v_T\right)^2 \sim 0.02$ gives $R \sim \alpha\left(v_E/v_T\right)^2\left(\omega_L L_T/c\right)^{2/3} \sim 0.6\ \alpha$. As will be shown later, the coefficient $\alpha$ is numerically large and proportional to the ion charge $Z$; this makes $R$ larger than 1. This simple estimate shows that the ponderomotive terms become comparable to the thermal terms in the electron thermal flux near the turning point. In addition, the $p$-polarization of the electric field (polarization that has a field component directed along the density gradient) tunnels through the overdense portion of the shell and gives a resonance electric field at the critical surface.[6] The gradient of such a field is proportional to the ratio $\omega_L/\nu_{ei}$, where $\nu_{ei}$ is the electron–ion collision frequency at the critical surface. Substituting typical direct-drive experiment parameters into an expression for the electron–ion collision frequency at the critical surface, $\nu_{ei}/\omega_L \simeq 1.5 \times 10^{-3}\ Z/T_{keV}^{3/2}$, shows a significant contribution of the ponderomotive terms to the heat flux near the critical surface.

In this article, the ponderomotive transport coefficients are derived. Such coefficients have been considered previously.[3–5,7–9] Reference 7 developed a method of solving the kinetic equation by separation of the electron distribution function on the high-frequency component due to the laser field and the low-frequency component of the time-averaged plasma response. Using such a method, the laser fields' contribution to the electron stress tensor was obtained. A similar method was used in Ref. 3, where the importance of the ponderomotive effects on the electron thermal conduction was emphasized. P. Mora and R. Pellat[4] and I. P. Shkarofsky[5] have evaluated the contributions of the laser fields into the heat and momentum fluxes. As was pointed out in Ref. 8, by not, however, consistently taking into account the contribution of the electron–electron collisions—the transport coefficients in their results contain wrong numerical factors. A consistent analysis was performed in Ref. 8, where results were obtained in the limit of large ion charge. Such a limit was relaxed in Ref. 9. The latter reference, however, contains numerous typographical errors, so the results will therefore be rederived in this article. The effect of ponderomotive terms on the hydrodynamic flow in direct-drive ICF experiments will be discussed in detail in a forthcoming publication.

**Model**

We consider a fully ionized plasma in a high-frequency electromagnetic field:

$$\varepsilon = \frac{1}{2}\left[\mathbf{E}(r,t)e^{-i\omega_L t} + \mathbf{E}(r,t)^* e^{i\omega_L t}\right], \tag{1}$$

$$\beta = \frac{1}{2}\left[\mathbf{B}(r,t)e^{-i\omega_L t} + \mathbf{B}(r,t)^* e^{i\omega_L t}\right], \tag{2}$$

where $\mathbf{E}$ and $\mathbf{B}$ are slowly varying (with respect to $e^{i\omega_L t}$) electric and magnetic fields and $\mathbf{E}^*$ and $\mathbf{B}^*$ are the complex conjugate (c.c.) of $\mathbf{E}$ and $\mathbf{B}$. The electron distribution function $f$ obeys the Boltzmann equation

$$\partial_t f + \mathbf{v}\partial_{\mathbf{r}} f + e\left(\mathbf{E}_0 + \varepsilon + \frac{\mathbf{v}\times\beta}{c}\right)\partial_{\mathbf{p}} f$$

$$= J_{ee}[f,f] + J_{ei}[f], \tag{3}$$

where $\mathbf{E}_0$ is the low-frequency electric field. Here,

$$J_{ei}[f] = 3\sqrt{\frac{\pi}{8}}\left(\frac{v_T}{v}\right)^3 \nu_{ei}\frac{\partial}{\partial v_k}\left[\left(v^2\delta_{kj} - v_k v_j\right)\frac{\partial f}{\partial v_j}\right] \tag{4}$$

is the ion–electron collision operator,

$$\nu_{ei} = \frac{4\sqrt{2\pi}e^4 n\bar{Z}\Lambda}{3m^2 v_T^3} \tag{5}$$

is the electron–ion collision frequency,

$$\bar{Z} = \sum_i e_i^2 n_i \Big/ \sum_i e_i n_i \tag{6}$$

is the average ion charge, $n_i$ is the ion number density, $n$ is the electron density, $e_i$ is the ion charge, $m$ is the electron mass, $\Lambda$ is the Coulomb logarithm, $v_T = \sqrt{T/m}$, and $T$ is the electron temperature. The sum in $\bar{Z}$ is taken over all ion species in the plasma. The electron–electron collision integral is taken in Landau form

$$J_{ee}[f,f] = \frac{2\pi e^4\Lambda}{m^2}$$

$$\times \frac{\partial}{\partial v_k}\int d\mathbf{v}' \frac{\left(\mathbf{v}-\mathbf{v}'\right)^2\delta_{kj} - \left(v-v'\right)_k\left(v-v'\right)_j}{\left|\mathbf{v}-\mathbf{v}'\right|^3}$$

$$\times \left(\frac{\partial}{\partial v_j} - \frac{\partial}{\partial v_j'}\right) f(\mathbf{v}) f(\mathbf{v}'). \tag{7}$$

Next, following Ref. 7, we separate the electron distribution function on the slowly varying part $f_0$ and the high-frequency component $f_1$:

$$f = f_0 + \frac{1}{2}\left(f_1 e^{-i\omega_L t} + f_1^* e^{i\omega_L t}\right). \tag{8}$$

Substituting Eqs. (1), (2), and (8) into Eq. (3) and collecting the terms with equal powers of $e^{i\omega_L t}$, we obtain

$$\partial_t f_1 - i\omega_L f_1 + \mathbf{v}\partial_{\mathbf{r}} f_1 + e\mathbf{E}_0\partial_{\mathbf{p}} f_1$$

$$+ e\mathbf{E}\partial_{\mathbf{p}} f_0 - \frac{ie}{\omega_L}\left[\mathbf{v}\times\left(\nabla\times\mathbf{E}\right)\right]\partial_{\mathbf{p}} f_0$$

$$= J_{ee}[f_0, f_1] + J_{ee}[f_1, f_0] + J_{ei}[f_1], \tag{9}$$

$$\partial_t f_0 + \mathbf{v}\partial_{\mathbf{r}} f_0 + e\mathbf{E}_0\partial_{\mathbf{p}} f_0 - J_{ei}[f_0] - J_{ee}[f_0, f_0]$$

$$= \left\{-\frac{e}{4}\mathbf{E}\partial_{\mathbf{p}} f_1^* + \frac{ie}{4\omega_L}\left[\mathbf{v}\times\left(\nabla\times\mathbf{E}\right)\right]\partial_{\mathbf{p}} f_1^*\right.$$

$$\left. + \frac{1}{4}J_{ee}\left[f_1, f_1^*\right] + \text{c.c.}\right\}. \tag{10}$$

Then, to relate $f_1$ with $f_0$, we assume that the laser frequency is high enough so $f_1$ can be expanded in series of

$\omega_L^{-1}$: $f_1 = f_1^{(1)} + f_1^{(2)} + \cdots$, where $f_1^{(2)}/f_1^{(1)} \sim \nu_{ei}/\omega_L << 1$. Substituting the latter expansion into Eq. (9) gives

$$f_1^{(1)} = -\frac{ie}{\omega_L}\mathbf{E}\partial_{\mathbf{p}} f_0, \tag{11}$$

$$f_1^{(2)} = -\frac{e}{\omega_L^2}\left\{\left(\partial_t + \mathbf{v}\partial_{\mathbf{r}}\right)\mathbf{E}\partial_{\mathbf{p}} f_0 - J_{ei}\left[\mathbf{E}\partial_{\mathbf{p}} f_0\right]\right\}. \tag{12}$$

To eliminate $f_1$ from Eq. (10) for the low-frequency component of the distribution function, we substitute Eqs. (11) and (12) into Eq. (10). The result takes the form[8]

$$\partial_t f_0 + \mathbf{v}\partial_{\mathbf{r}} f_0 + e\mathbf{E}_0\partial_{\mathbf{p}} f_0 - J_{ei}\left[f_0\right] - J_{ee}\left[f_0, f_0\right]$$

$$= \frac{e^2}{4\omega_L^2}\left\{\frac{\nabla|\mathbf{E}|^2}{m}\partial_{\mathbf{p}} f_0 + \frac{1}{2}\frac{\partial^2 f_0}{\partial p_i\,\partial p_j}\left(\partial_t + \mathbf{v}\partial_{\mathbf{r}}\right)\left(E_i E_j^* + \text{c.c.}\right)\right.$$

$$+ \left(E_i E_j^* + \text{c.c.}\right)\left[\frac{1}{m}\frac{\partial^2 f_0}{\partial r_i\,\partial p_j} + \left(\partial_t + \mathbf{v}\partial_{\mathbf{r}}\right)\frac{\partial^2 f_0}{\partial p_i\,\partial p_j}\right.$$

$$\left.\left. - \partial_{p_i} J_{ei}\left(\partial_{p_j} f_0\right) + J_{ee}\left(\partial_{p_i} f_0, \partial_{p_j} f_0\right)\right]\right\}. \tag{13}$$

Equation (13) is solved assuming a small deviation of the electron distribution function $f_0$ from Maxwellian $f_M$:

$$f_0 = f_M\left[1 + \psi\left(\mathbf{v}, \mathbf{p}, t\right)\right], \tag{14}$$

where $|\psi| << 1$. The kinetic equation for $\psi$ is obtained by substituting the expansion (14) into Eq. (13) and replacing the time derivatives $\partial_t f_M$ using the transport conservation equations. These equations, according to the standard procedure,[10] are obtained by multiplying the kinetic equations by $(\mathbf{v} - \mathbf{v}_0)^k$ with $k$ = 0, 1, 2,... and integrating the latter in the velocity space. Here,

$$\mathbf{v}_0 = \frac{1}{\rho}\left(\int d\mathbf{v} m\mathbf{v} f_0 + \int d\mathbf{v}_i m_i \mathbf{v}_i f_i\right) \tag{15}$$

is the mass velocity, $\rho = nm + n_i m_i \simeq n_i m_i$ is the mass density, $m_i$ is the ion mass, $\mathbf{v}_i$ is the ion velocity, and $f_i$ is the ion distribution function. When $k$ = 0, the described procedure yields the mass conservation equation; $k$ = 1 and $k$ = 2 give the momentum and energy conservation equations, respectively. Omitting lengthy algebraic manipulations we report the final result:[8]

$$\partial_t n + \nabla\left(n\mathbf{v}_0\right) + \nabla\left(n\mathbf{V}\right) = 0, \tag{16}$$

$$\rho\partial_t v_{0k} + \rho\left(\mathbf{v}_0\partial_{\mathbf{r}}\right)v_{0k} = -\partial_{r_k}\left(p_e + p_i\right) - \partial_{r_j}\sigma_{kj} + \rho_e E_{0k}$$

$$- \frac{e^2}{4m\omega_L^2}\left\{n_e\partial_{r_k}|E|^2 - \partial_{r_j}\left[n\left(E_k E_j^* + \text{c.c.}\right)\right]\right\}, \tag{17}$$

$$\left(\partial_t + \mathbf{v}_0\partial_{\mathbf{r}}\right)\left(T + \frac{e^2|E|^2}{6m\omega_L^2}\right) - \frac{T}{n}\nabla\left(n\mathbf{V}\right) + \frac{2}{3n_e}\nabla\mathbf{q} + \frac{2p_e}{3n}\nabla\mathbf{v}_0$$

$$= \frac{mv_E^2\nu_{ei}}{3} + \frac{2e}{3}\mathbf{E}_0\mathbf{V} - \frac{2m}{m_i}\nu_{ei}\left(T - T_i\right). \tag{18}$$

Here we use the standard definitions

$$n = \int d\mathbf{v} f_0, \quad n\mathbf{V} = \int d\mathbf{v}\left(\mathbf{v} - \mathbf{v}_0\right)f_0 = \mathbf{j}/e, \tag{19}$$

$$\mathbf{q} = \frac{m}{2}\int d\mathbf{v}\left(\mathbf{v} - \mathbf{v}_0\right)\left(\mathbf{v} - \mathbf{v}_0\right)^2 f_0, \tag{20}$$

$$\sigma_{kj} = m\int d\mathbf{v}\left(v - v_0\right)_k\left(v - v_0\right)_j f_0 - p_e\delta_{kj}, \tag{21}$$

where $T_i$ is the ion temperature, $n$ is the electron density, $\mathbf{j}$ is the current density, $\mathbf{q}$ is the heat flux, $\sigma_{kj}$ is the stress tensor, $p_e$ and $p_i$ are the electron and ion pressures, $v_E = eE/m\omega_L$, and $\rho_e = en + e_i n_i$ is the charge density. To simplify the derivation of the transport coefficients, we assume $\mathbf{v}_0 = 0$ and neglect terms of the order of $m/m_i$. Next, the equation for the correction $\psi$ to the Maxwellian distribution function is derived by substituting Eq. (14) into Eq. (13) and using the conservation equations (16)–(18). The resulting equation takes the form[8]

$$\partial_t \psi + \mathbf{v}\partial_{\mathbf{r}}\psi - \delta J_{\mathrm{ei}}[\psi] - \delta J_{\mathrm{ee}}[\psi]$$

$$= \left(\frac{3}{2} - x + \frac{3}{4}\sqrt{\frac{\pi}{x}}\right)\frac{\nu_{\mathrm{ei}}}{3}\frac{v_E^2}{v_T^2} + \left(x - \frac{3}{2}\right)\frac{2\nabla \mathbf{q}}{3nT} + \left(\frac{5}{2} - x\right)\frac{\nabla(n\mathbf{V})}{n}$$

$$+\mathbf{v}\left[\left(\frac{5}{2} - x\right)\nabla \ln T - \nabla \ln nT + \frac{e\mathbf{E}_0}{T} + \left(\frac{x}{3} - 1\right)\frac{\nabla v_E^2}{2v_T^2}\right]$$

$$+\frac{x}{10}v_k\frac{\partial_{r_j}\left(\mathbf{v}_E^2\right)_{jk}}{v_T^2} + \frac{3\nu_{\mathrm{ei}}}{8x^{3/2}}\frac{\left(\mathbf{v}^2\right)_{jk}\left(\mathbf{v}_E^2\right)_{jk}}{v_T^4}$$

$$\times\left[\frac{\sqrt{\pi}}{2}\left(1 + \frac{3}{2x}\right) + \frac{3}{\bar{Z}}\int_0^x dx' e^{-x'}\sqrt{x'}\left(1 - \frac{x'}{x}\right)\right]$$

$$+\frac{\left(\mathbf{v}^3\right)_{jkl}}{8v_T^4}\partial_{r_l}\left(\mathbf{v}_E^2\right)_{jk}, \tag{22}$$

where $x = v^2/\left(2v_T^2\right)$,

$$\delta J_{\mathrm{ei}}[\psi] = \frac{3\sqrt{\pi}}{8x^{3/2}}\nu_{\mathrm{ei}}\partial_{v_k}\left[\left(v^2\delta_{kj} - v_k v_j\right)\partial_{v_j}\psi\right], \tag{23}$$

$$\delta J_{\mathrm{ee}}[\psi] = \frac{3\sqrt{2\pi}\nu_{\mathrm{ei}}v_T^3}{4\bar{Z}n_e f_{\mathrm{M}}}\partial_{v_k}\left\{f_{\mathrm{M}}\int d\mathbf{v}' f_{\mathrm{M}}(v')\right.$$

$$\times\frac{\left(\mathbf{v} - \mathbf{v}'\right)^2\delta_{kj} - \left(v - v'\right)_k\left(v - v'\right)_j}{\left|\mathbf{v} - \mathbf{v}'\right|^3}$$

$$\left.\times\left[\partial_{v_j}\psi(\mathbf{v}) - \partial_{v_j'}\psi(\mathbf{v}')\right]\right\}, \tag{24}$$

$$\left(\mathbf{v}^2\right)_{jk} \equiv v_j v_k - \frac{v^2}{3}\delta_{jk},$$

$$\left(\mathbf{v}^3\right)_{jkl} \equiv v_j v_k v_l - \frac{v^2}{5}\left(v_j\delta_{kl} + v_k\delta_{jl} + v_l\delta_{jk}\right), \tag{25}$$

and

$$\left(\mathbf{v}_E^2\right)_{jk} \equiv \frac{e^2}{\omega_L^2 m^2}\left(E_j E_k^* + E_j^* E_k - \frac{2}{3}\delta_{jk}|E|^2\right). \tag{26}$$

Next, we solve Eq. (22) assuming that the electron quiver velocity is much smaller than the electron thermal velocity, $v_E/v_T << 1$, and ordering $\nabla T/T \sim \nu_{\mathrm{ei}}v_E^2/v_T^3$. The function $\psi$ is expanded as $\psi = \psi_1 + \psi_2 + \ldots$, where $\psi_2 << \psi_1$. The first approximation $\psi_1$ is obtained by keeping only the terms of the order of $v_T\nabla T/\left(T\nu_{\mathrm{ei}}\right)$. The second-order correction $\psi_2$ is derived by retaining the first derivative of the electric field and the second derivative of the electron temperature and density.

**First-Order Approximation**

Retaining the first spatial derivatives in temperature and density and also terms proportional to $v_E^2/v_T^2$, Eq. (22) yields

$$\delta J_{\mathrm{ei}}[\psi_1] + \delta J_{\mathrm{ee}}[\psi_1] = \left(x - \frac{3}{2} - \frac{3}{4}\sqrt{\frac{\pi}{x}}\right)\frac{\nu_{\mathrm{ei}}}{3}\frac{v_E^2}{v_T^2}$$

$$-\mathbf{v}\left[\left(\frac{5}{2} - x\right)\nabla \ln T - \nabla \ln nT + \frac{e\mathbf{E}_0}{T}\right] - \frac{3\nu_{\mathrm{ei}}}{8x^{3/2}}\frac{\left(\mathbf{v}^2\right)_{ij}\left(\mathbf{v}_E^2\right)_{ij}}{v_T^4}$$

$$\times\left[\frac{\sqrt{\pi}}{2}\left(1 + \frac{3}{2x}\right) + \frac{3}{\bar{Z}}\int_0^x dx' e^{-x'}\sqrt{x'}\left(1 - \frac{x'}{x}\right)\right]. \tag{27}$$

We look for a solution of Eq. (27) in the form

$$\psi_1 = \Phi_{11}(x)\frac{\left(\mathbf{v}^2\right)_{ij}\left(\mathbf{v}_E^2\right)_{ij}}{v_T^4} + \Phi_{12}\frac{v_E^2}{v_T^2}$$

$$+\Phi_{13}\frac{\mathbf{v}}{\nu_{\mathrm{ei}}}\nabla \ln T + \Phi_{14}\frac{\mathbf{v}}{\nu_{\mathrm{ei}}}\left[\nabla \ln nT - \frac{e\mathbf{E}_0}{T}\right]. \tag{28}$$

Using definitions (19)–(21), the current density, heat flux, and stress tensor in the first approximation become

$$\mathbf{j}^{(1)} = env_T\lambda_e\left[\alpha_{j1}^T\nabla\ln T + \alpha_{j2}^T\left(\nabla\ln nT - \frac{e\mathbf{E}_0}{T}\right)\right], \quad (29)$$

$$\mathbf{q}^{(1)} = nTv_T\lambda_e\left[\alpha_{q1}^T\nabla\ln T + \alpha_{q2}^T\left(\nabla\ln nT - \frac{e\mathbf{E}_0}{T}\right)\right], \quad (30)$$

$$\sigma_{kj}^{(1)} = \frac{4}{15}\alpha_\sigma^E mn\left(\mathbf{v}_E^2\right)_{kj}, \quad (31)$$

where $\lambda_e = v_T/\nu_{ei}$ is the electron mean-free path. The numerical coefficients in Eqs. (29)–(31) have the forms

$$\alpha_{j1(j2)}^T = \frac{4}{3\sqrt{\pi}}\int_0^\infty dx x^{3/2}e^{-x}\Phi_{13(14)}(x), \quad (32)$$

$$\alpha_{q1(q2)}^T = \frac{4}{3\sqrt{\pi}}\int_0^\infty dx x^{5/2}e^{-x}\Phi_{13(14)}(x), \quad (33)$$

$$\alpha_\sigma^E = \frac{4}{\sqrt{\pi}}\int_0^\infty dx x^{5/2}e^{-x}\Phi_{11}(x). \quad (34)$$

Equations (29)–(31) show that the electric current and the heat flux in the first approximation are proportional to the gradients in temperature and pressure.[1,10,11] The stress tensor, on the other hand, depends on the laser electric field.[3,7] Even though the functions $\Phi_{11}$ and $\Phi_{22}$ do not enter into the first-order heat flux, they contribute to the heat flux in the second approximation. Thus, we need to find all four functions $\Phi_{11-14}$. The general form of the solution $\psi_1$ [Eq. (28)] can be separated on the following three types of functions: type I depends only on the velocity modulus $\psi_1^{(\mathrm{I})} = \Phi(x)$; type II is proportional to the velocity vector and velocity modulus $\psi_1^{(\mathrm{II})} = A_j v_j\Phi(x)$; and type III depends on the velocity tensor and velocity modulus $\psi_1^{(\mathrm{III})} = \left(\mathbf{v}^2\right)_{ij}\left(\mathbf{v}_E^2\right)_{ij}\Phi(x)$, where $A_i$ is the vector proportional to the temperature, pressure gradients, or the electric field $\mathbf{E}_0$. According to such a classification, the governing equations for the functions of each type become

$$\text{Type I: } \delta J_{ee}\left[\Phi(x)\right] = \phi(x), \quad (35)$$

$$\text{Type II: } A_j\left\{\Phi(x)\delta J_{ei}\left[v_j\right] + \delta J_{ee}\left[v_j\Phi(x)\right]\right\} = \phi(x)\mathbf{vA}, \quad (36)$$

$$\text{Type III: } \left(\mathbf{v}_E^2\right)_{ij}\left\{\Phi(x)\delta J_{ei}\left[\left(\mathbf{v}^2\right)_{ij}\right] + \delta J_{ee}\left[\left(\mathbf{v}^2\right)_{ij}\Phi(x)\right]\right\} = \phi(x)\left(\mathbf{v}^2\right)_{ij}\left(\mathbf{v}_E^2\right)_{ij}, \quad (37)$$

where $\phi(x)$ is defined by the right-hand side of Eq. (27). Since the ion–electron collision operator has a very simple form, it is straightforward to calculate $J_{ei}\left[v_j\right]$ and $J_{ei}\left[\left(\mathbf{v}^2\right)_{ij}\right]$ using Eq. (23):

$$\delta J_{ei}\left[v_j\right] = -\frac{3\sqrt{\pi}}{4x^{3/2}}\nu_{ei}v_j, \quad (38)$$

$$\delta J_{ei}\left[\left(v^2\right)_{ij}\right] = -\frac{9\sqrt{\pi}}{4x^{3/2}}\nu_{ei}\left(\mathbf{v}^2\right)_{ij}. \quad (39)$$

The electron–electron operator is more complicated, and the evaluation of $\delta J_{ee}\left[\Phi(x)\right]$, $\delta J_{ee}\left[v_j\Phi(x)\right]$, and $\delta J_{ee}\left[\left(\mathbf{v}^2\right)_{ij}\Phi\right]$ requires lengthy algebra. Below is a detailed calculation of $\delta J_{ee}\left[\Phi(x)\right]$. The integral part in the electron–electron collision operator can be rewritten as

$$\int d\mathbf{v}' f_M(v')\frac{(\mathbf{v}-\mathbf{v}')^2\delta_{kj} - (v-v')_k(v-v')_j}{|\mathbf{v}-\mathbf{v}'|^3}$$

$$\times\left[\frac{v_j}{v_T^2}\Phi'(x) - \frac{v_j'}{v_T^2}\Phi'(x')\right] = \sum(x)v_k, \quad (40)$$

where function $\Sigma(v)$ is found by multiplying Eq. (40) by $v_k$. This yields

$$2\pi\int dv'\frac{v'^2}{v_T^2}f_M(v')v^2v'^2\left[\Phi'(x) - \Phi'(x')\right]$$

$$\times\int_{-1}^{1} dy\frac{1-y^2}{\left(v^2+v'^2-2vv'y\right)^{3/2}} = \sum(x)v^2, \quad (41)$$

where $y = \cos\theta$ and $\theta$ is the angle between $\mathbf{v}$ and $\mathbf{v}'$. Integration over the angles gives

$$\int_{-1}^{1} dy \frac{1-y^2}{\left(v^2+v'^2-2vv'y\right)^{3/2}}$$

$$= \frac{2}{3v'^3v^3}\left[v^3+v'^3-\left(v^2+vv'+v'^2\right)\left|v-v'\right|\right]$$

$$= \begin{cases} 4/\left(3v^3\right) & \text{if } v' < v \\ 4/\left(3v'^3\right) & \text{if } v' > v \end{cases}. \tag{42}$$

Substituting Eq. (42) into Eq. (41) yields

$$\sum(x) = \frac{4n}{3v_T^3\sqrt{2\pi}x^{3/2}}\overline{\sum}(x), \tag{43}$$

$$\overline{\sum}(x) = \int_0^x dx x'^{3/2}e^{-x'}\left[\Phi'(x)-\Phi'(x')\right]$$

$$+ x^{3/2}\int_x^\infty dx' e^{-x'}\left[\Phi'(x)-\Phi'(x')\right]. \tag{44}$$

Thus, the electron–electron collision integral reduces to

$$\delta J_{ee}\left[\Phi(x)\right] = \frac{\nu_{ei}}{\overline{Z}f_M}\partial_{v_k}\left[v_k f_M(v)\frac{\overline{\sum}(x)}{x^{3/2}}\right]. \tag{45}$$

The next step is to substitute Eq. (45) into Eq. (35) and solve the latter for $\Phi$. To simplify the integration, the right-hand side of Eq. (35) can be rewritten in the form

$$\phi(x) = \frac{1}{f_M}\partial_{v_k}\left[v_k f_M\frac{\bar{\phi}(x)}{x^{3/2}}\right]. \tag{46}$$

Then, integrating Eq. (35) once, the following integro-differential equation is obtained:

$$\bar{\phi} = \frac{\nu_{ei}}{\overline{Z}}\overline{\sum}(x), \tag{47}$$

where function $\bar{\phi}$ is related to $\phi$ by integrating Eq. (46),

$$\bar{\phi} = \frac{e^x}{2}\int_\infty^x dx'\phi(x')\sqrt{x'}e^{-x'}. \tag{48}$$

To solve Eq. (47) we take the $x$ derivative of both sides of Eq. (47). This gives

$$\frac{2\overline{Z}}{3\nu_{ei}}\bar{\phi}' = \Phi''\gamma\left(\frac{3}{2},x\right) - \sqrt{x}\int_x^\infty dx' e^{-x'}\Phi''(x'), \tag{49}$$

where $\gamma(\alpha,x) = \int_0^x x'^{\alpha-1}e^{-x'}dx'$ is the incomplete gamma function. Introducing a new function $g(x) = \int_x^\infty dx'\Phi''(x)e^{-x'}$, Eq. (49) becomes

$$g(x) = -\frac{2\overline{Z}}{3\nu_{ei}\gamma(3/2,x)}\int_0^x dx'\bar{\phi}'(x')e^{-x'} + \frac{C}{\gamma(3/2,x)}, \tag{50}$$

where $C$ is the integration constant. Thus, the function $\Phi(x)$ can be expressed as a multiple integral of $\bar{\phi}$:

$$\Phi(x) = \overline{C}_1 + \overline{C}_2 x - \int dx'\int dx'' e^{x''}g'(x''). \tag{51}$$

Next, we report the equations corresponding to the function of the second and third types [Eqs. (36) and (37), respectively]. Equation (36) reduces to

$$\frac{x^{3/2}}{3}\phi(x) + \frac{\sqrt{\pi}\nu_{ei}}{4}\Phi(x) = \frac{\nu_{ei}}{\overline{Z}}\left\{\Phi(x)\left[x^{3/2}e^{-x} - \gamma\left(\frac{3}{2},x\right)\right]\right.$$

$$+ \Phi'(x)\left[(1-x)\gamma\left(\frac{3}{2},x\right) + x^{3/2}e^{-x}\right] + \Phi''(x)x\gamma\left(\frac{3}{2},x\right)$$

$$+ \int_0^x dx' e^{-x'}x'^{3/2}\left(\frac{2x'}{5}-\frac{1}{3}\right)\Phi(x')$$

$$\left. + x^{3/2}\left(\frac{2x}{5}-\frac{1}{3}\right)\int_x^\infty dx'\Phi(x')e^{-x'}\right\}. \tag{52}$$

Equation (37) for the function of the third type becomes

$$\frac{2x^{3/2}}{3}\phi(x)+\frac{3\sqrt{\pi}}{2}\nu_{ei}\Phi(x)$$

$$=\frac{\nu_{ei}}{\bar{Z}}\left\{\Phi(x)\left[\gamma\left(\frac{5}{2},x\right)\left(\frac{1}{x}-\frac{10}{3}\right)-\frac{4}{3}x^{3/2}e^{-x}\right]\right.$$

$$+2\Phi'(x)\left[\gamma\left(\frac{3}{2},x\right)(2-x)+x^{3/2}e^{-x}\right]+2x\Phi''(x)\gamma\left(\frac{3}{2},x\right)$$

$$+\frac{2}{x}\int_0^x dx'x'^{5/2}e^{-x'}\Phi(x')\left(\frac{12}{35}x'-\frac{2}{15}x-\frac{1}{5}\right)$$

$$\left.+2x^{3/2}\int_x^\infty dx'e^{-x'}\left(\frac{12}{35}x-\frac{2}{15}x'-\frac{1}{5}\right)\Phi(x')\right\}. \quad (53)$$

The heat transport coefficients in the first approximation depend on functions $\Phi_{13}$ and $\Phi_{14}$, which belong to the function of the second type and can be found by solving Eq. (52) with

$$\phi(x)=\left(x-\frac{5}{2}\right), \quad \text{for} \quad \Phi=\Phi_{13}/\nu_{ei}, \quad (54)$$

$$\phi(x)=1, \quad \text{for} \quad \Phi=\Phi_{14}/\nu_{ei}. \quad (55)$$

To solve the integro-differental equation (52), function $\Phi(x)$ is traditionally expanded[10,11] in Laguerre polynomials[12] $\Phi(x)=\sum_n A(n)L_n^{3/2}$. As proposed in Ref. 9, it is more convenient to use a more-generalized expansion in terms of Laguerre polynomials $L_n^\alpha(x)$. The choice of these polynomials comes from their orthogonal properties

$$\int_0^\infty e^{-x}x^\alpha L_m^\alpha(x)L_n^\alpha(x)dx$$

$$=\begin{cases}0 & \text{if } m\neq n\\ \Gamma(n+\alpha+1)/n! & \text{if } m=n,\ \alpha>-1,\quad n=0,\ 1,\ 2,\ldots\end{cases}. \quad (56)$$

Evaluation of the integrals in Eqs. (32) and (33) becomes particularly simple if

$$\Phi_{13(14)}=x^\beta\sum_n A(n)L_n^{\beta+3/2}. \quad (57)$$

Index $\beta$ is determined by matching the polynomial expansion (57) with the exact solution of $\Phi$ in the limit of $\bar{Z}\to\infty$. Calculations show that such matching speeds up the convergence of the transport coefficients with the number of polynomials in expansion (57). Taking the limit $\bar{Z}\to\infty$ in Eq. (52) yields

$$\Phi\big|_{\bar{Z}\to\infty}=-\frac{4}{3\sqrt{\pi}\nu_{ei}}x^{3/2}\phi. \quad (58)$$

Then, the choice $\beta = 3/2–k$ with $k = 0, 1, 2,\ldots$ will satisfy the requirement of matching Eq. (57) with the exact solution (58). The parameter $k$ is determined by minimizing the number of terms in the polynomial expansion (1) to match the exact solution for $\bar{Z}\to\infty$ and (2) to reach the desired accuracy of the transport coefficients for $\bar{Z}\sim 1$. Calculations show that for the case of functions $\Phi_{13}$ and $\Phi_{14}$, $\beta = 1/2$ satisfies such a minimization criteria [it takes five terms in Eq. (57) to obtain the transport coefficients with 1% accuracy]. Therefore, the expansion becomes

$$\Phi_{13(14)}=\sqrt{x}\sum_n A_{13(14)}(n)L_n^2. \quad (59)$$

Multiplying Eq. (52) by $x^{3/2}e^{-x}L_s^\alpha(x)$ with $s = 0, 1, 2,\ldots, N–1$ [where $N$ is the number of polynomials in the expansion (57)] and integrating the latter in $x$ from 0 until $\infty$, we obtain the system of $N$ algebraic equations. Figure 98.4 shows a dependence of the coefficients $\alpha_{j1}^T$ and $\alpha_{q1}^T$ on the number of polynomials in the expansion (57) with $\beta = –1/2$, $\beta = 1/2$, and $\beta = 3/2$, respectively. Observe that the coefficients converge faster with $\beta = 1/2$.

Next, we derive the numerical coefficient $\alpha_\sigma^E$ of the stress tensor $\sigma_{ij}^{(1)}$. This requires that Eq. (53) be solved with $\Phi(x) = \Phi_{11}$ and

$$\phi=-\frac{3\nu_{ei}}{8x^{3/2}}\left\{\frac{\sqrt{\pi}}{2}\left(1+\frac{3}{2x}\right)+\frac{3}{\bar{Z}}\left[\gamma\left(\frac{3}{2},x\right)-\frac{1}{x}\gamma\left(\frac{5}{2},x\right)\right]\right\}. \quad (60)$$

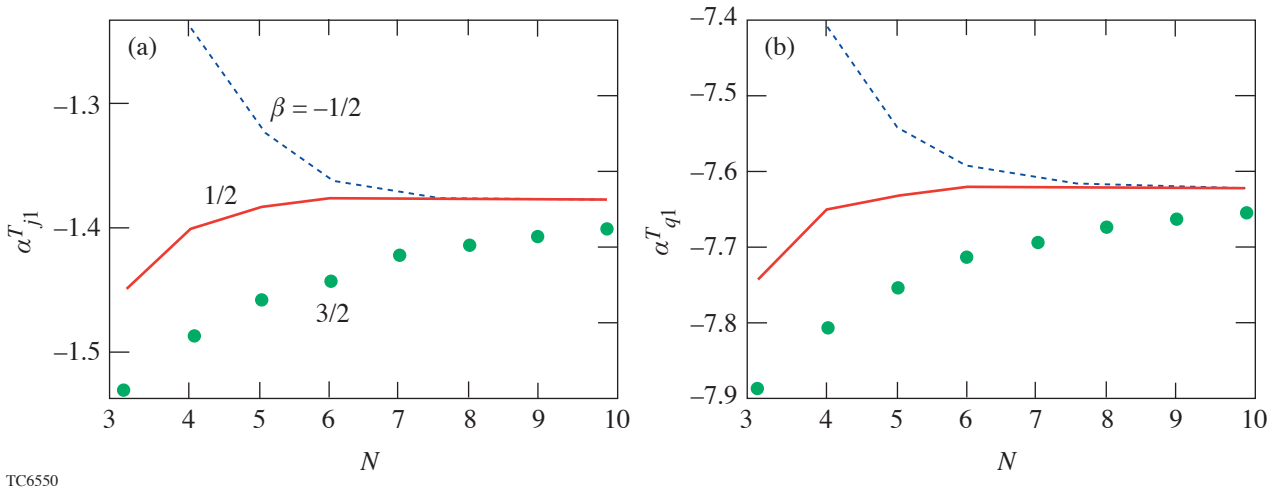


Figure 98.4
Coefficients $\alpha^T_{j1}$ and $\alpha^T_{q1}$ as functions of the number of polynomials in the expansion (57). The results correspond to $\beta = -1/2$ (dashed line), $\beta = 1/2$ (solid line), and $\beta = 3/2$ (dots).

Similar to the previously considered case, we expand function $\Phi_{11}$ in Laguerre polynomials. To express $\alpha^E_\sigma$ through just one coefficient in such an expansion, we take

$$\Phi_{11} = x^{\beta_1} \sum_n B(n) L_n^{\beta_1 + 5/2}. \tag{61}$$

The choice of the power index $\beta_1$ comes from the condition of matching expansion (61) with the exact solution in the limit of $\overline{Z} \to \infty$. Neglecting terms proportional to $1/\overline{Z}$ in Eqs. (53) and (60) gives

$$\Phi_{11}(x)\big|_{\overline{Z}\to\infty} = \frac{1}{8x} + \frac{1}{12}. \tag{62}$$

It is easy to see that the values $\beta_1 = -1, -2, -3, \ldots$ satisfy our requirement. Calculations show that expansion (61) with $\beta_1 = -1$ has the fastest convergence with the number of polynomials. Table 98.II shows a summary of coefficients $\alpha^E_\sigma$ for a different ion charge $\overline{Z}$. Observe that the stress tensor has a very weak dependence on $\overline{Z}$ (3% variation in $\alpha^E_\sigma$ from $\overline{Z} = 1$ to $\overline{Z} = \infty$). One more function remains to be determined in the first approximation: the correction $\Phi_{12}$ to the symmetric part of the distribution function. This function belongs to the first type and can be found in the integral form using Eq. (51) with

$$\phi(x) = \left(\frac{3}{2} - x + \frac{3\sqrt{\pi}}{4\sqrt{x}}\right)\frac{\nu_{ei}}{3} \tag{63}$$

Table 98.II: Transport coefficients in the first approximation.

| $\overline{Z}$ | 1 | 2 | 3 | 4 | 5 | 10 | 30 | 80 | ∞ |
|---|---|---|---|---|---|---|---|---|---|
| $\alpha^T_{j1}$ | –1.39 | –2.1 | –2.57 | –2.91 | –3.16 | –3.87 | –4.59 | –4.89 | –5.09 |
| $\alpha^T_{q1}$ | –7.66 | –12.11 | –15.19 | –17.46 | –19.23 | –24.31 | –29.86 | –32.27 | –33.95 |
| $\alpha^T_{j2}$ | –1.99 | –2.34 | –2.54 | –2.67 | –2.77 | –3.01 | –3.25 | –3.34 | –3.39 |
| $\alpha^T_{q2}$ | –6.35 | –7.93 | –8.90 | –9.57 | –10.07 | –11.40 | –12.70 | –13.23 | –13.58 |
| $\alpha^E_\sigma$ | 1.029 | 1.027 | 1.023 | 1.020 | 1.017 | 1.010 | 1.004 | 1.002 | 1.000 |

and $\Phi = \Phi_{12}$. The integration gives[8]

$$\Phi_{12}(x) = \overline{Z}\left\{-\tilde{C}_2 + C_2 x - \frac{\sqrt{\pi}}{12}\int_1^x \frac{dt\sqrt{t}(x-t)}{\left[\gamma(3/2,t)\right]^2}\right\}, \quad (64)$$

where $C_2$ and $\tilde{C}_2$ are determined from the condition of zero contribution of $\Phi_{12}$ to the electron density and temperature,

$$\int_0^\infty dx e^{-x}\sqrt{x}\Phi_{12}(x) = 0, \quad \int_0^\infty dx e^{-x}x^{3/2}\Phi_{12}(x) = 0. \quad (65)$$

Conditions (65) yield $C_2 = 0.721$ and $\tilde{C}_2 = 0.454$. Note two misprints in $\Phi_{12}$ reported in Ref. 8 [the different sign in front of the integral and $(x - t)$ instead of $(1 - t)$ inside the integral]. The correction to the symmetric part in the distribution function comes mainly from balancing the inverse bremsstrahlung heating $\sqrt{\pi/x}\,\nu_{ei}/3\left(v_E^2/v_T^2\right)$ with the electron–electron collisions $\delta J_{ee}$. Since $\delta J_{ee} \sim \nu_{ei}/\overline{Z}$, function $\Phi_{12}$ becomes proportional to the average ion charge $\overline{Z}$, as shown in Eq. (64). As emphasized in Ref. 8, the symmetric correction $\Phi_{12}$ gives the dominant contribution to the heat flux in the second-order approximation.

**Second-Order Approximation**

Correction $\psi_2$ to the distribution function in the second approximation satisfies the following equation:[8]

$$\left(x-\frac{5}{2}\right)\frac{\nabla \mathbf{j}^{(1)}}{en} - \left(x-\frac{3}{2}\right)\frac{2\nabla \mathbf{q}^{(1)}}{3nT} + \frac{v^2}{3\nu_{ei}}\left[\Phi_{13}\nabla^2 \ln T\right.$$

$$\left. + \Phi_{14}\nabla\left(\nabla \ln nT - \frac{e\mathbf{E}_0}{T}\right)\right]$$

$$+ \mathbf{v}\frac{\nabla v_E^2}{v_T^2}\left[\Phi_{12} + \frac{1}{3}\left(\Phi_{13}+\Phi_{14}\right) + \frac{1}{2} - \frac{x}{6}\right]$$

$$+ \frac{v_i \partial_{r_k}\left(\mathbf{v}_E^2\right)_{ik}}{10 v_T^2}\left(8x\Phi_{11} - x\right) - \frac{e}{\nu_{ei}T}\Phi_{14}\mathbf{v}\partial_t \mathbf{E}_0$$

$$+ \frac{\left(\mathbf{v}^2\right)_{ij}}{\nu_{ei}}\left[\Phi_{13}\frac{\partial^2 \ln T}{\partial r_i \partial r_j} + \Phi_{14}\partial_{r_i}\left(\partial_{r_j}\ln nT - \frac{eE_{0j}}{T}\right)\right]$$

$$+ \left(\mathbf{v}^3\right)_{ijk}\frac{\partial_{r_k}\left(\mathbf{v}_E^2\right)_{ij}}{v_T^4}\left(\Phi_{11} - \frac{1}{8}\right) = \delta J_{ei}\left[\psi_2\right] + \delta J_{ee}\left[\psi_2\right]. \quad (66)$$

A general solution of Eq. (66) can be written as

$$\psi_2 = \Phi_{20}\frac{\left(\mathbf{v}^3\right)_{ijk}\partial_{r_k}\left(\mathbf{v}_E^2\right)_{ij}}{v_T^4\nu_{ei}} + \Phi_{21}\frac{v_i\partial_{r_j}\left(\mathbf{v}_E^2\right)_{ij}}{\nu_{ei}v_T^2}$$

$$+\Phi_{22}\frac{\mathbf{v}\nabla v_E^2}{v_T^2\nu_{ei}} + \frac{\left(\mathbf{v}^2\right)_{kj}}{\nu_{ei}^2}\left\{\Phi_{23}\left(\frac{\partial^2 \ln T}{\partial r_k \partial r_j} - \frac{1}{3}\delta_{jk}\nabla^2 \ln T\right)\right.$$

$$\left. + \Phi_{24}\left[\frac{\partial}{\partial r_k}\left(\partial_{r_j}\ln nT - \frac{eE_{0j}}{T}\right) - \frac{1}{3}\delta_{jk}\nabla\left(\nabla \ln nT - \frac{e\mathbf{E}_0}{T}\right)\right]\right\}$$

$$-\Phi_{25}\frac{e}{\nu_{ei}T}\mathbf{v}\partial_t \mathbf{E}_0$$

$$+\frac{v_T^2}{\nu_{ei}^2}\left[\Phi_{26}\nabla^2 \ln T + \Phi_{27}\nabla\left(\nabla \ln nT - \frac{e\mathbf{E}_0}{T}\right)\right]. \quad (67)$$

The electric current and the heat flux in the second order take the form

$$j_i^{(2)} = env_T\lambda_e\left[\alpha_{j1}^E\frac{\partial_{r_k}\left(\mathbf{v}_E^2\right)_{ik}}{v_T^2} + \alpha_{j2}^E\frac{\partial_{r_i}v_E^2}{v_T^2}\right.$$

$$\left. - \alpha_{j3}^E\frac{e\lambda_e}{v_T T}\partial_t E_{0i}\right], \quad (68)$$

$$q_i^{(2)} = nTv_T\lambda_e\left[\alpha_{q1}^E\frac{\partial_{r_k}\left(\mathbf{v}_E^2\right)ik}{v_T^2} + \alpha_{q2}^E\frac{\partial_{r_i}v_E^2}{v_T^2}\right.$$

$$\left. -\alpha_{q3}^E\frac{e\lambda_e}{v_T T}\partial_t E_{0i}\right]. \quad (69)$$

Coefficients $\alpha^E_{j(q)}$ are calculated using the following relations:

$$\alpha^E_{j1(2,3)} = \frac{4}{3\sqrt{\pi}}\int_0^\infty dx x^{3/2} e^{-x} \Phi_{21(2,5)}(x), \tag{70}$$

$$\alpha^E_{q1(2,3)} = \frac{4}{3\sqrt{\pi}}\int_0^\infty dx x^{5/2} e^{-x} \Phi_{21(2,5)}(x). \tag{71}$$

Next, we find functions $\Phi_{21}$, $\Phi_{22}$, and $\Phi_{25}$. These functions are of the second type; therefore, to obtain them we solve Eq. (52) with

$$\phi = \frac{x}{10}\left(8\Phi_{11} - 1\right), \quad \text{for } \Phi = \Phi_{21}/\nu_{ei}, \tag{72}$$

$$\phi = \Phi_{12} + \frac{1}{3}\left(\Phi_{13} + \Phi_{14}\right) + \frac{1}{2} - \frac{x}{6}, \quad \text{for } \Phi = \Phi_{22}/\nu_{ei}, \tag{73}$$

$$\phi = \Phi_{14}, \quad \text{for } \Phi = \Phi_{25}/\nu_{ei}. \tag{74}$$

Following the method described in the previous section, functions $\Phi_{21}$, $\Phi_{22}$, and $\Phi_{25}$ are expanded in series (57). The exact solution for $\Phi_{21}$ as $\bar{Z} \to \infty$ becomes

$$\Phi_{21}\big|_{\bar{Z}\to\infty} = -\frac{2x^{3/2}}{15\sqrt{\pi}}\left(1 - \frac{x}{3}\right); \tag{75}$$

thus $\beta$ takes the values $\beta = 3/2 - k$ with $k = 0, 1, 2, \ldots$. The fastest convergence of the coefficients $\alpha^E_{j1}$ and $\alpha^E_{q1}$ is obtained with $\beta = 1/2$. A summary of $\alpha^E_{j1}$ and $\alpha^E_{q1}$ for different ion charge $\bar{Z}$ is given in Table 98.III. Next, we find the function $\Phi_{22}$. The exact matching of the polynomial expansion (57) with the exact solution $\Phi_{22}$ for $\bar{Z} \to \infty$,

$$\Phi_{22}\big|_{\bar{Z}\to\infty} = -\frac{4x^{3/2}}{3\sqrt{\pi}}\Phi_{12}, \tag{76}$$

cannot be done since $\Phi_{12}$ does not have a polynomial structure [see Eq. (64)]. It is easy to show, however, that $\Phi_{12}(x \to 0) \sim 1/\sqrt{x}$ and $\Phi_{12}(x \to \infty) \sim x^{5/2}$. Therefore, the expansion of $\Phi_{22}$ with $\beta = 1$ reproduces the asymptotic limits for $x << 1$ and $x >> 1$. Taking $\beta = 1$ and keeping $N = 5$ terms in expansion (57) gives values of $\alpha^E_{j2}$ and $\alpha^E_{q2}$, which are reported in Table 98.III. Observe that these coefficients become quite large for $\bar{Z} >> 1$. To find the remaining coefficients in the heat flux and electric current, we solve the equation for the function $\Phi_{25}$. In the limit of $\bar{Z} \to \infty$, the function $\Phi_{25}$ becomes

$$\Phi_{25}\big|_{\bar{Z}\to\infty} = -\Phi_{14}\big|_{\bar{Z}\to\infty}\frac{4x^{3/2}}{3\sqrt{\pi}} = \frac{16}{9\pi}x^3; \tag{77}$$

thus, $\beta$ = 3, 2, 1… matches the polynomial expansion (57) with the exact solution in the limit of $\bar{Z} \to \infty$. Calculations show that $\beta = 1$ requires a minimum number of polynomials in expansion (57) to achieve the desired accuracy. The values of $\alpha^E_{j3}$ and $\alpha^E_{q3}$ are summarized in Table 98.III. Next, we

Table 98.III: Transport coefficients in the second approximation.

| $\bar{Z}$ | 1 | 2 | 3 | 4 | 5 | 10 | 30 | 80 | ∞ |
|---|---|---|---|---|---|---|---|---|---|
| $\alpha^E_{j1}$ | –0.03 | –0.01 | 0.00 | 0.02 | 0.03 | 0.06 | 0.09 | 0.10 | 0.11 |
| $\alpha^E_{q1}$ | –0.03 | 0.07 | 0.16 | 0.23 | 0.30 | 0.49 | 0.73 | 0.83 | 0.90 |
| $\alpha^E_{j2}$ | 4.05 | 8.54 | 13.07 | 17.51 | 21.86 | 42.30 | 116.3 | $\bar{Z}$ 3.66 | $\bar{Z}$ 3.48 |
| $\alpha^E_{q2}$ | 19.7 | 48.3 | 80.0 | 113.0 | 146.6 | 314.1 | 960.9 | $\bar{Z}$ 31.7 | $\bar{Z}$ 31.3 |
| $\alpha^E_{j3}$ | 4.69 | 7.21 | 9.07 | 10.51 | 11.67 | 15.15 | 19.18 | 21.00 | 22.28 |
| $\alpha^E_{q3}$ | 16.77 | 28.75 | 38.45 | 46.39 | 52.99 | 74.05 | 100.6 | 113.3 | 122.5 |

combine the electric current and the thermal flux in the first and second approximations. The result is

$$\mathbf{j}_i = en v_T \lambda_e \left[ \alpha_{j1}^T \partial_{r_i} \ln T + \alpha_{j2}^T \left( \partial_{r_i} \ln nT - \frac{eE_{0i}}{T} \right) + \alpha_{j1}^E \frac{\partial_{r_k} \left( \mathbf{v}_E^2 \right)_{ik}}{v_T^2} + \alpha_{j2}^E \frac{\partial_{r_i} v_E^2}{v_T^2} - \alpha_{j3}^E \frac{e\lambda_e}{v_T T} \partial_t E_{0i} \right], \quad (78)$$

$$\mathbf{q}_i = nT v_T \lambda_e \left[ \alpha_{q1}^T \partial_{r_i} \ln T + \alpha_{q2}^T \left( \partial_{r_i} \ln nT - \frac{eE_{0i}}{T} \right) + \alpha_{q1}^E \frac{\partial_{r_k} \left( \mathbf{v}_E^2 \right)_{ik}}{v_T^2} + \alpha_{q2}^E \frac{\partial_{r_i} v_E^2}{v_T^2} - \alpha_{q3}^E \frac{e\lambda_e}{v_T T} \partial_t E_{0i} \right]. \quad (79)$$

Imposing a condition of zero current $\mathbf{j} = 0$ and also assuming $t_E \nu_{ei} << \alpha_{j3}^E / \alpha_{j2}^T$ (where $t_E$ is the time scale of $\mathbf{E}_0$ variation) define the slowly varying component of the electric field $\mathbf{E}_0$,

$$\frac{eE_{0i}}{T} = \partial_{r_i} \ln nT + \frac{\alpha_{j1}^T}{\alpha_{j2}^T} \partial_{r_i} \ln T + \frac{\alpha_{j1}^E}{\alpha_{j2}^T} \frac{\partial_{r_k} \left( \mathbf{v}_E^2 \right)_{ik}}{v_T^2} + \frac{\alpha_{j2}^E}{\alpha_{j2}^T} \frac{\partial_{r_i} v_E^2}{v_T^2}. \quad (80)$$

Substituting $\mathbf{E}_0$ from Eq. (80) into Eq. (79) gives the heat flux in laser-produced plasmas,

$$\mathbf{q}_i = nT v_T \lambda_e \left[ \beta^T \partial_{r_i} \ln T + \beta_1^E \frac{\partial_{r_i} v_E^2}{v_T^2} + \beta_2^E \frac{\partial_{r_k} \left( \mathbf{v}_E^2 \right)_{ik}}{v_T^2} \right], \quad (81)$$

where

$$\beta^T = \alpha_{q1}^T - \alpha_{q2}^T \alpha_{j1}^T / \alpha_{j2}^T,$$

$$\beta_1^E = \alpha_{q2}^E - \alpha_{q2}^T \alpha_{j2}^E / \alpha_{j2}^T,$$

and

$$\beta_2^E = \alpha_{q1}^E - \alpha_{q2}^T \alpha_{j1}^E / \alpha_{j2}^T$$

can be represented with the following fitting formulas:

$$\beta^T = -\frac{128}{3\pi} \frac{\overline{Z} + 0.24}{\overline{Z} + 4.20},$$

$$\beta_1^E = 17.31\, \overline{Z}\, \frac{\overline{Z}^2 + 14.04\, \overline{Z} + 2.41}{\overline{Z}^2 + 14.34\, \overline{Z} + 29.5}, \quad (82)$$

$$\beta_2^E = 0.45 \frac{\overline{Z} - 0.29}{\overline{Z} + 3.47}. \quad (83)$$

In addition, the coefficients in the electric field $E_0$ can be fitted as follows:

$$\frac{\alpha_{j1}^T}{\alpha_{j2}^T} = 1.50\ \frac{\overline{Z} + 0.52}{\overline{Z} + 2.26},$$

$$\frac{\alpha_{j1}^E}{\alpha_{j2}^T} = -\ 0.03\ \frac{\overline{Z} - 2.63}{\overline{Z} + 3.22}, \quad (84)$$

$$\frac{\alpha_{j2}^E}{\alpha_{j2}^T} = -1.03\, \overline{Z}\, \frac{\overline{Z} + 8.54}{\overline{Z} + 3.82}.$$

Coefficients $\beta^T$ and $\alpha_{j1}^T / \alpha_{j2}^T$ agree with previously published results.[1,11,13]

Next, we discuss the validity of the derived transport coefficients. As shown earlier, the main contribution to the second-order heat flux comes from the correction $\Phi_{12}$ to the symmetric part of the distribution function. The function $\Phi_{12}$ is given in the integral form by Eq. (64) and has the following asymptotic behavior for small and large velocities:

$$\Phi_{12}(x \to 0) = -\frac{\overline{Z}}{4}\sqrt{\frac{\pi}{x}}, \tag{85}$$

$$\Phi_{12}(x \to \infty) = -\overline{Z}\,\frac{4}{45\sqrt{\pi}}\,x^{5/2}. \tag{86}$$

The validity condition of the Chapman–Enskog method[10] $|\Phi_{12}|v_E^2/v_T^2 << 1$ breaks down for

$$x < \overline{Z}^2\,\frac{\pi}{16}\,\frac{v_E^4}{v_T^4} \tag{87}$$

and

$$x > \frac{3}{\overline{Z}^{2/5}}\left(\frac{v_T}{v_E}\right)^{4/5}. \tag{88}$$

According to Eq. (71), the main contribution to the heat flux comes from the superthermal electrons [which correspond to the maximum in the function $x^{5/2}e^{-x}\Phi(x)$]. Therefore, the limit (87) imposes no restrictions on the applicability of the derived results. The electron distribution function for the subthermal electrons, nevertheless, is different from the limit (85). As derived in Refs. 14 and 15, the inverse bremsstrahlung heating modifies the distribution of the cold electrons to

$$f_0(v << v_T) = \frac{n}{(2\pi)^{3/2}v_T^3}\,\exp\left(-\frac{1}{v_T^2}\int_0^v \frac{u^4\,du}{u^3 + V_L^3}\right), \tag{89}$$

where $V_L = \left(\sqrt{\pi/8}\;\overline{Z}v_E^2 v_T\right)^{1/3}$ is the Langdon velocity.[16] To check the limitations due to the second condition (88), we find that the maximum of

$$x^{5/2}e^{-x}\Phi_{22} \sim x^{5/2}e^{-x}x^{3/2}\Phi_{12} \sim x^{13/2}e^{-x}$$

corresponds to $x_{\max} \simeq 13/2$. This limits the applicability of the Chapman method to $v_E^2/v_T^2 < 0.2/\overline{Z}$. Even though the modulus of $\Phi_{12}$ becomes larger than unity for large $x$ [see Eq. (88)], we can show that

$$f_0^{\text{int}} = f_M\,\exp\left[1 + \frac{v_E^2}{v_T^2}\Phi_{12}(x)\right] \tag{90}$$

is a good approximation to the symmetric part of the distribution function even for $x \to \infty$. For such a purpose, we find the asymptotic behavior of the function that satisfies the following equation:

$$\partial_t f_0 = J_{ee}(f_0, f_0). \tag{91}$$

We look for a solution of Eq. (91) in the form $f_0 = Ae^{\Psi}$, where $\Psi = F(v_T^2)g(v^2)$ and $A$ is a normalization constant. The temperature dependence is combined in function $F$, and velocity dependence is in $g$; then, the time derivative of $f_0$ becomes

$$\partial_t f_0 = f_0 F' v_T^2 g\,\frac{\partial_t T}{T} = f_0 F' g\,\frac{v_E^2 \nu_{ei}}{3}, \tag{92}$$

where we substituted $\partial_t T/T = \left(v_E^2/v_T^2\right)\nu_{ei}/3$ due to the inverse bremsstrahlung heating. The electron–electron collision integral reduces in this case to

$$J_{ee} = \frac{16\pi e^4\Lambda}{3m^2 v}\,F\,\frac{\partial}{\partial v^2}\left[f_0 I\left(v^2\right)\right], \tag{93}$$

$$I\left(v^2\right) = 4\pi\int_0^v dv' v'^4 f_0(v')\left[g'\left(v^2\right) - g'\left(v'^2\right)\right] + 4\pi v^3\int_v^\infty dv' v' f_0(v')\left[g'\left(v^2\right) - g'\left(v'^2\right)\right]. \tag{94}$$

In the limit of $v \to \infty$, $I$ becomes

$$I \simeq g'\left(v^2\right)4\pi\int_0^\infty dv' v'^4 f_0(v') = 3g'\left(v^2\right)nv_T^2,$$

and Eq. (91) takes the form

$$g'' + Fg'^2 = \overline{Z}\,\frac{vv_E^2}{v_T^5}\,\frac{F'}{F}\,\frac{g}{18\sqrt{2\pi}}. \tag{95}$$

Next, we make an assumption $g'' << g'^2$, which will be verified *a posteriori*. In this case the solution of Eq. (95) becomes

$$g = \frac{2}{225\sqrt{2\pi}}\, v^5 \frac{F'}{F^2} \frac{\overline{Z} v_E^2}{v_T^5}. \tag{96}$$

Observe that the condition $g'' << g'^2$ is satisfied in the limit of large velocity. The function $g$, by definition, does not depend on temperature; this yields for $F$

$$\frac{F'}{F^2} = C\left(v_T^2\right)^{5/2}, \quad F = \frac{\tilde{C}}{v_T^7}, \tag{97}$$

where $C$ and $\tilde{C}$ are constants. The distribution function $f_0$ depends on the product $F\left(v_T^2\right) g\left(v^2\right)$, which, according to Eqs. (96) and (97), takes the form

$$F\left(v_T^2\right) g\left(v^2\right) = -\frac{7\overline{Z}}{225\sqrt{2\pi}} \frac{v_E^2 v^5}{v_T^7}. \tag{98}$$

Using Eq. (98), the asymptotic limit of the symmetrical part of the distribution function reduces to

$$f_0\left(x >> 1\right) \sim \exp\left(-0.07\, \overline{Z}\, \frac{v_E^2}{v_T^2} x^{5/2}\right). \tag{99}$$

The latter equation must be compared to $f_0^{\text{int}}$ in the limit $x \to \infty$ [see Eq. (90)],

$$f_0^{\text{int}}\left(x >> 1\right) \sim \exp\left(-0.05\, \overline{Z}\, \frac{v_E^2}{v_T^2} x^{5/2}\right). \tag{100}$$

Thus, we can conclude that the function in the form (90) is a good approximation to the distribution function for thermal and superthermal electrons.

In conclusion, we have derived the transport coefficients, including the thermal and ponderomotive terms for an arbitrary ion charge. The modification of the thermal transport due to the ponderomotive effects near the critical surface and laser turning point will be discussed in a forthcoming publication.

## ACKNOWLEDGMENT

This work was supported by the U.S. Department of Energy Office (DOE) of Inertial Confinement Fusion under Cooperative Agreement No. DE-FC03-92SF19460, the University of Rochester, and the New York State Energy Research and Development Authority. The support of DOE does not constitute an endorsement by DOE of the views expressed in this article.

## REFERENCES

1. L. Spitzer, Jr. and R. Härm, Phys. Rev. **89**, 977 (1953).
2. R. C. Malone, R. L. McCrory, and R. L. Morse, Phys. Rev. Lett. **34**, 721 (1975).
3. I. B. Bernstein, C. E. Max, and J. J. Thomson, Phys. Fluids **21**, 905 (1978).
4. P. Mora and R. Pellat, Phys. Fluids **22**, 2408 (1979).
5. I. P. Shkarofsky, Phys. Fluids **23**, 52 (1980).
6. V. L. Ginzburg, *Propagation of Electromagnetic Waves in Plasmas*, edited by W. L. Sadowski and D. M. Gallik (Gordon and Breach, New York, 1961).
7. V. I. Perel' and Ya. M. Pinskii, Sov. Phys.-JETP **27**, 1014 (1968).
8. A. V. Maxsimov, V. P. Silin, and M. V. Chegotov, Sov. J. Plasma Phys. **16**, 331 (1990).
9. V. N. Goncharov and V. P. Silin, Plasma Phys. Rep. **21**, 48 (1995).
10. S. Chapman and T. G. Cowling, *The Mathematical Theory of Non-Uniform Gases; An Account of the Kinetic Theory of Viscosity, Thermal Conduction and Diffusion in Gases*, 3rd. ed. (Cambridge University Press, Cambridge, England, 1970).
11. S. I. Braginskii, in *Reviews of Plasma Physics*, edited by Acad. M. A. Leontovich (Consultants Bureau, New York, 1965), Vol. 1.
12. N. N. Lebedev and R. A. Silverman, *Special Functions and Their Applications*, rev. English ed. (Dover Publications, New York, 1972).
13. E. M. Epperlein and M. G. Haines, Phys. Fluids **29**, 1029 (1986).
14. A. V. Maksimov *et al.*, JETP **86**, 710 (1998).
15. V. P. Silin, Phys.-Usp. **45**, 955 (2002).
16. A. B. Langdon, Phys. Rev. Lett. **44**, 575 (1980).

# Effects of Nonuniform Illumination on Implosion Asymmetry in Direct-Drive Inertial Confinement Fusion

Attaining ignition and high gain in inertial confinement fusion (ICF) requires that deuterium–tritium (DT)–filled capsules be spherically imploded to high temperature and density.[1–3] "Hot-spot" ignition, where a capsule is compressed so as to form two different regions—a small mass of low-density, hot (~10-keV) fuel at the center surrounded by a larger mass of high-density, low-temperature fuel—is the leading method envisioned to achieve this goal. Shock coalescence "ignites" the hot spot, and a burn wave propagates into the main fuel region. Success requires a symmetric implosion because significant deviation from spherical symmetry will result in shock dynamics that do not lead to ignition. In the direct-drive approach to ICF, where implosion occurs in response to a large number of high-power, individual laser beams illuminating the surface of a capsule, the requirement for spherical implosion imposes severe constraints on the uniformity of the laser drive[1–3] and on the sphericity of the capsule.

Illumination nonuniformities, coupled with initial capsule imperfections, lead to distortions in the compressed capsule. High-mode-number perturbations ($\ell > 10$) are primarily imprinted by nonuniformities within individual laser beams.[4,5] During both the acceleration and deceleration phases, these perturbations are amplified by Rayleigh–Taylor (RT) instabilities and grow exponentially until reaching saturation at amplitudes of $\sim 4R/\ell^2$ ($R$ is the capsule radius); thereafter, they grow linearly.[6] Low-mode-number asymmetries ($\ell \leq 10$) result primarily from either drive-pressure asymmetry, due to nonuniformity in on-target laser intensity, or capsule fabrication asymmetry.[4,5] These secular modes grow linearly throughout the entire implosion, largely due to Bell–Plesset (BP)–related convergence effects.[7]

A major effort has been made in current ICF research to reduce target illumination nonuniformity and capsule imperfections. Characterization of these efforts requires the measurement of any deviations from spherical symmetry in the assembled capsule mass, or areal density ($\rho R$).[8] Previous work relied on numerical simulations to predict the conditions under which asymmetries may develop and on x-ray imaging to provide information about emission symmetry.[9] Quantitative experimental information about $\rho R$ asymmetries has not been available, however, until recent experiments[10–11] on OMEGA[12] using novel charged-particle spectrometry techniques.[13] These experiments have resulted in the first studies of low-mode-number $\rho R$ asymmetries at the time of fusion burn for direct-drive spherical implosions (the diagnostic technique is sensitive to structure with mode numbers $\ell \lesssim 5$). From these experiments we conclude that changes in laser-intensity distributions result in changes in $\rho R$ asymmetries, while capsule imperfections do not seem to be a dominant factor under current conditions.[14] In this article we present new studies showing quantitatively, for the first time, how the amplitude of $\rho R$ asymmetries is directly correlated with the amplitude of asymmetries in time-averaged, on-target laser intensity $I$ for ablatively driven implosions. The resulting scaling law is based on both theoretical implications of capsule convergence and experimental data and has implications for future work on the National Ignition Facility (NIF)[1] as well as on OMEGA. The terminology that will be used is that $\langle \rho R \rangle$ and $\langle I \rangle$ are averages over angle, $\delta\rho R$ and $\delta I$ are deviations from the average at a given angle, and $\langle \delta\rho R \rangle$ and $\langle \delta I \rangle$ are rms averages over angle.

Illumination asymmetries on OMEGA are generated by several sources. First, there are differences in the time-integrated energies delivered by the 60 individual laser beams, which can be characterized by an rms beam energy imbalance $\sigma_b$ that tends to be in the range $\sigma_b \lesssim 3\%$.[15] The beams, however, overlap on the capsule surface, and the overlap reduces the net energy nonuniformity to a value $\sigma_e$ that can be estimated from a typical measured beam profile shape and the theoretical positions of the individual beam centers: $\sigma_e \sim 0.8\%$ to 1.5% rms. The total illumination nonuniformity on the capsule surface is higher than $\sigma_e$ because of other contributing factors and can be estimated as $\langle \delta I \rangle / \langle I \rangle \approx \sqrt{\sigma_e^2 + \sigma_s^2 + \sigma_p^2 + \sigma_0^2}$. The component $\sigma_s$, typically ~1% rms,[16] is due to deviations of individual beam shape profiles from that assumed in calculating $\sigma_e$. The component $\sigma_p$ (typically ~1.9% rms[16]) results from errors in the pointing of individual laser beams, and $\sigma_0$ (typically ~1% rms[16]) is an additional contribution from any

offset of the capsule center from the center of the target chamber ($\sigma_0$ is ~0.2 times the offset in $\mu$m[16]). Target offset results in drive asymmetry with strong $\ell = 1$ and 2 modes. This is demonstrated in Fig. 98.5, which displays a two-dimensional (2-D) simulation from the hydrodynamic code *DRACO*, incorporating the measured beam imbalance and other nominal experimental conditions for an implosion with 50-$\mu$m offset from target chamber center (TCC). The simulation indicates a strong correlation between drive asymmetry and $\rho R$ asymmetry, which will be addressed empirically below. These low-mode capsule perturbations cannot be smoothed by the effects of lateral energy flow in the form of transverse thermal conduction[17] because the scale length of the perturbations is typically much longer than the separation between the critical surface and the ablation surface.

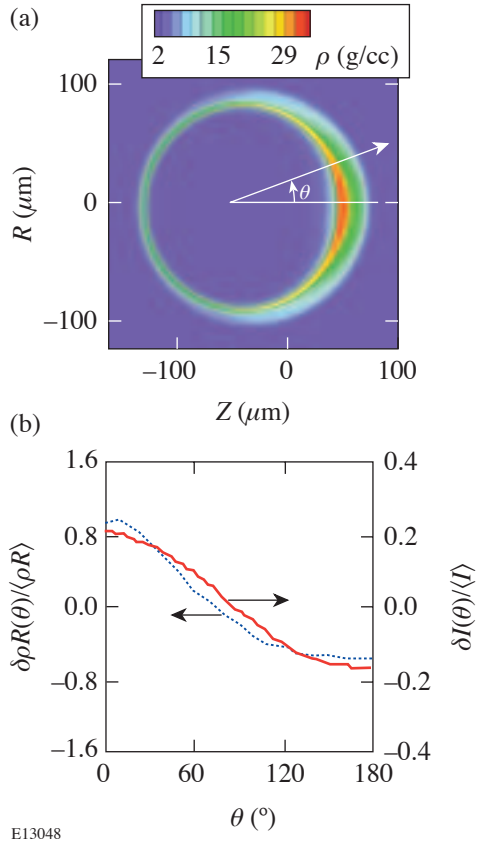


Figure 98.5
(a) Density contours at a time of peak burn (~1.9 ns) for an implosion of a capsule offset by 50 $\mu$m from TCC, simulated using the 2-D code *DRACO* for conditions of shot 26646 (23 kJ of laser energy in a 1-ns square pulse applied to a capsule with 15 atm of $D_2$ in a 20-$\mu$m CH shell). (b) The target offset results in drive asymmetry with strong $\ell$ =1 and 2 modes, which generates a correlated $\rho R$ asymmetry.

The amplitude of asymmetries in $\rho R$ is quantitatively correlated with the amplitude of asymmetries in time-averaged, on-target laser intensity $I$. Both theoretical and experimental approaches have been used to understand the correlation. Theoretically, a scaling law for predicting how measured $\rho R$ asymmetries relate to $\langle \delta I \rangle / \langle I \rangle$ can be derived from considerations of implosion dynamics, assuming that $\rho R$ asymmetries are seeded by the illumination asymmetries and modified due to effects of capsule convergence. The growth rates of low-$\ell$-number perturbations due to RT instabilities are small $\left(\propto \sqrt{\ell}\right)$. To first order, the angular variations in acceleration rates ($g$) during both acceleration and deceleration phases of an implosion can be written $\langle \delta g \rangle / \langle g \rangle \approx \langle \delta V_{\rm imp} \rangle / \langle V_{\rm imp} \rangle$ (Ref. 1), where $V_{\rm imp} = V_{\rm imp}(t)$ is the capsule implosion velocity. Starting with $\left(R_0 - R\right) \approx V_{\rm imp} t_{\rm imp}$ and considering implosion dynamics, one obtains

$$-\frac{\langle \delta R \rangle}{\langle R \rangle} \approx \frac{\langle \delta V_{\rm imp} \rangle}{\langle V_{\rm imp} \rangle}\left(C_r - 1\right). \tag{1}$$

In this expression, $C_r$ is the convergence ratio

$$C_r \equiv R_0 / \langle R \rangle \approx \sqrt{\langle \rho R \rangle / f\, \rho_0\, R_0},$$

where $\rho_0$ and $R_0$ are the initial shell density and radius and $f$ is the fraction of shell mass not ablated (which can be estimated from "burnthrough" experiments[18]). One obtains $-\langle \delta R \rangle / \langle R \rangle \approx 1/2 \langle \delta \rho R \rangle / \langle \rho R \rangle$. $V_{\rm imp}$ is a function of laser intensity on target for direct-drive implosions with

$$V_{\rm imp} \propto I^{1/3} \ln\left(m_0 / m\right),$$

where $m(m_0)$ is the payload (initial) capsule mass determined by $dm/dt \propto I^{\alpha}$ ($\alpha$ is a constant).[1,19,20] Substituting these relations into Eq. (1) and keeping terms of first order in $\langle \delta I \rangle / \langle I \rangle$, the resultant scaling has the form

$$\langle \delta \rho R \rangle / \langle \rho R \rangle \approx B\left(C_r - 1\right) \langle \delta I \rangle / \langle I \rangle,$$

where $B$ is a coefficient of the order of 1 that depends weakly on the payload mass. This result is analogous to the BP effect for incompressible fluids, which predicts that the growth of $\delta \rho R$ is proportional to capsule convergence and in-flight shell thickening. The above discussion includes only 1-D effects.

Two-dimensional (2-D) effects, such as lateral mass flow, can modify the convergence-driven asymmetry growth, resulting in a lower value of $B$ for high-$\ell$-number asymmetries with ratios of perturbation wavelength ($\lambda$) to in-flight shell thickness ($\Delta$) of the order of 1 or less. To avoid this theoretical complication, we use experimental data to determine $B$. In addition, since initial asymmetries in capsule structure due to fabrication imperfections (with rms amplitude $\sigma_C$) should grow in the same manner during convergence, we would expect that

$$\left(C_r - 1\right)^{-2}\left(\frac{\langle \delta\rho R\rangle}{\langle \rho R\rangle}\right)^2 \approx a^2\sigma_C^2 + B^2\left(\frac{\langle \delta I\rangle}{\langle I\rangle}\right)^2, \qquad (2)$$

where $a$ is an unknown coefficient. Experimental verification of the form of this equation, and a value for $B$, will be found below.

Experiments were conducted on OMEGA with 60 beams of frequency-tripled (0.35-$\mu$m) UV light driving the targets directly. The total laser energy was ~23 kJ for 1-ns square pulses or ~18 kJ for shaped pulses. Individual beams were smoothed using single-color-cycle, 1-THz, 2-D smoothing by spectral dispersion (SSD) and polarization smoothing (PS) using birefringent wedges.[5] The room-temperature capsules had plastic (CH) shells with 20-$\mu$m nominal thickness and were filled with 18 atm of $D^3He$ or 15 atm of $D_2$ gas. Each imploded cryogenic capsule had an 80- to 100-$\mu$m $D_2$-ice layer inside an ~5-$\mu$m CH shell.[21,22] The primary[23] or secondary protons[10] generated from $D^3He$ reactions ($D+{}^3He \rightarrow \alpha + p$) were measured. These protons are energetic enough to easily penetrate the CH shell or $D_2$-ice layer, but they interact strongly enough with the capsule plasma that their energy loss is a direct measure of $\rho R$ for each spectrometer line of sight:

$$\rho R = \int_{E_0}^{E} \rho\left(dE/dx\right)^{-1} dE$$

[see (Ref. 24)]. Because the shell (CH or $D_2$ ice) has a lower temperature, higher density, and higher mass than the gas, the measured $\rho R$ and $\rho R$ asymmetry are dominated by $\rho R_{\text{shell}}$.

$\rho R$ asymmetry can be seen in sample $D^3He$ proton spectra from a single shot (25221), shown in Fig. 98.6. The measured mean proton energy losses $\Delta\langle E_p\rangle$ varied from 1.1 to 2.2 MeV, leading to a variation in $\rho R$ from about 35 to 70 mg/cm$^2$. Under current conditions a number of sources of $\rho R$ asymmetry typically contribute, with no single source dominating. When an effort is made to maintain the same capsule and laser conditions from shot to shot, the spatially averaged $\langle \rho R\rangle$ remains relatively constant, as shown in Fig. 98.7. Although contiguous implosions often show similar angular variations in $\delta\rho R$,[10,11] there are small, random variations from shot to shot and a tendency for the angular variations to become uncorrelated over a long shot series.

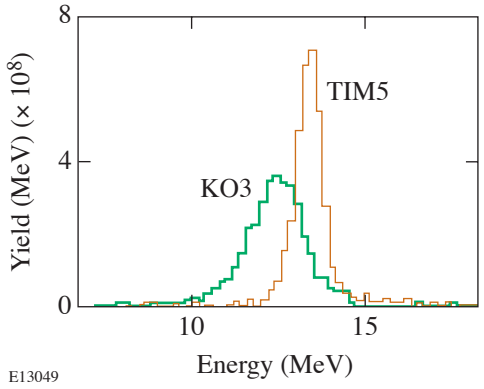


Figure 98.6
Proton spectra were measured simultaneously at seven different diagnostic ports for shot 25221. Two of the spectra are shown here, labeled with the port ID. Substantial asymmetries in the mean downshifted energy indicate $\rho R$ asymmetry.

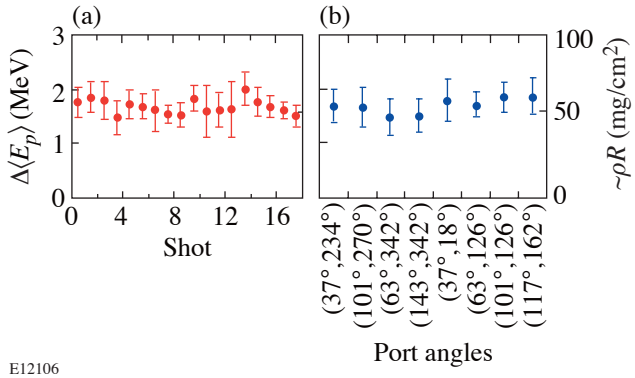


Figure 98.7
(a) Measured $\Delta\langle E_p\rangle$ and inferred $\rho R$ for individual shots that were nominally identical, averaged over different port locations, plotted versus time over a two-week time interval. (b) Measured $\Delta\langle E_p\rangle$ and inferred $\rho R$ at different port angles $(\theta,\varphi)$, averaged over the same shots over a two-week interval. The "error bars" are not measurement uncertainties but standard deviations of all measurements represented by a given, plotted average.

For the shots under study here, the values of $\langle \delta\rho R\rangle/\langle \rho R\rangle$ and $\langle \delta I\rangle/\langle I\rangle$ were tabulated and are plotted in Fig. 98.8. The data were fit to the two-parameter function

$$\left(C_r - 1\right)^{-1}\langle \delta\rho R\rangle/\langle \rho R\rangle = \sqrt{A^2 + B^2\left(\langle \delta I\rangle/\langle I\rangle\right)^2};$$

this is equivalent to Eq. (2) with $A^2 = \left\langle a^2\sigma_C^2\right\rangle$, but $A^2$ can also be thought of as including the average effect of any other unknown source of asymmetry not correlated with $\langle \delta I\rangle/\langle I\rangle$. As discussed in the figure caption, the data are well fit by this function using a value of $B \approx 1/2$, indicating that the contribution of $\langle \delta I\rangle/\langle I\rangle$ to $\langle \delta\rho R\rangle/\langle \rho R\rangle$ is

$$\frac{\langle \delta\rho R\rangle}{\langle \rho R\rangle} \approx \frac{1}{2}\left(C_r - 1\right)\frac{\langle \delta I\rangle}{\langle I\rangle}. \tag{3}$$

The value $B$ = 1/2 in Eq. (3) was determined almost exclusively by the high $\langle \delta I\rangle/\langle I\rangle$, high $\langle \delta\rho R\rangle/\langle \rho R\rangle$ data points in Fig. 98.8. Most of these points correspond to large capsule offset, where illumination asymmetries are dominated by $\ell$ = 1 and $\ell$ = 2; the others correspond to cases with some laser beams turned off, where $\langle \delta I\rangle/\langle I\rangle$ was also dominated by low-$\ell$ structure. $B$ may be somewhat smaller for higher modes due to the effects of lateral mass flow; this will be the subject of future work. The data used here correspond to capsules with similar payload masses, but the derivation of Eq. (2) indicates that (logarithmic) dependence on payload mass should be very weak.[1] In addition, only one fill pressure was used in the room-temperature capsules (18 atm), but data from other experiments[11] with the much lower fill pressure of 4 atm are consistent with Eq. (3) (although all of these data fall in the low $\langle \delta I\rangle/\langle I\rangle$, low $\langle \delta\rho R\rangle/\langle \rho R\rangle$ grouping of Fig. 98.8). Of particular interest is the fact that Eq. (3) seems equally valid for both room-temperature, CH-shell capsules and cryogenic capsules, even though these two types of capsules have very different theoretical susceptibilities to the RT instability.[1] The convergence-driven growth is probably more important than RT effects for the low modes under study here. (High-mode-number RT instabilities do have indirect effects on the growth of these low modes because they cause fuel–shell mix, which decreases $C_r$ and thereby decreases the growth of $\delta\rho R$.) This is particularly important for lower fill pressures, where $C_r$ would be expected to be larger but is not; experiments show that $C_r$ is nearly the same for 4-atm capsules as for 18-atm capsules.[25] The data demonstrate that the growth of these low-mode asymmetries is driven primarily by convergence. Whereas different pulse shapes (adiabats), drive energies, or payload masses may result in different asymmetry amplitudes, the primary differences are likely to be due to the size of $C_r$ rather than the size of the coefficient 1/2 in Eq. (3) or even the breakdown of the scaling itself. We conclude that the coefficient 1/2 in Eq. (3) may be slightly different in different ablative-drive contexts, but probably not by much.

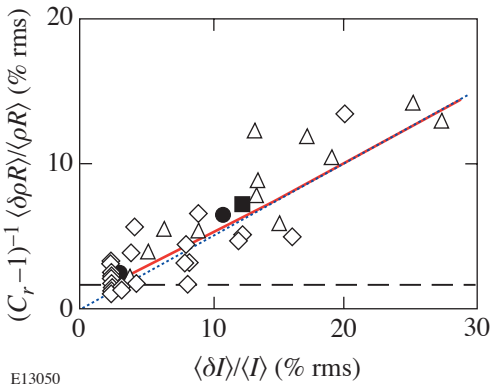


Figure 98.8
Plot of $y \equiv \left(C_r - 1\right)^{-1}\langle \delta\rho R\rangle/\langle \rho R\rangle$ versus $x \equiv \langle \delta I\rangle/\langle I\rangle$ for the shots described in the text. The solid line represents a least-squares fit of the data to the function $y(x) = \sqrt{A^2 + B^2x^2}$, where $A$ = 1.63±0.33 and $B$ = 0.50±0.03; the reduced $\chi^2$ was 1.24. The dotted line represents the contribution of $\langle \delta I\rangle/\langle I\rangle$, while the dashed line represents the mean contribution of all other sources of asymmetry. Open diamonds correspond to room-temperature capsules with plastic shells, while triangles correspond to cryogenic capsules; it is notable that the two types of data are fairly consistent with each other. Taken separately, the plastic-shell data give $B$ = 0.41±0.05 and the cryogenic data give $B$ = 0.55±0.04. In most cases, values of $\langle \delta I\rangle/\langle I\rangle > 3\%$ were due to offsets of capsules from the target chamber center. Solid circles (20-$\mu$m CH shell) and a solid square (26-$\mu$m CH shell) are from 2-D simulations and show good agreement with the data and with Eq. (3).

Other evidence supports the scaling of Eq. (3). As shown in Fig. 98.8, it is compatible with 2-D simulations for two different shell thicknesses (20 and 26 $\mu$m). This shows that the 1-D arguments used to derive Eq. (3), and also the arguments given for the weak dependence on payload mass, are compatible with 2-D simulations. The weak dependence on payload mass is experimentally shown through comparisons of the data shown here with recent results with 26-$\mu$m-shell capsules,[26] which also indicates that the scaling applies at all angles, applies for modes $\ell$ = 1 and $\ell$ = 2 individually, and applies at separate times during the implosion.

The scaling of Eq. (3) is useful for estimating behavior in future experiments. On OMEGA, the performance of cryogenic implosions has been shown to be diminished when target offsets cause low-mode asymmetries.[21,22] Another example is

cone-capsule, fast-ignition experiments on OMEGA,[27] where there is no laser illumination on part of the capsule (essentially an $\ell = 1$ mode). For future indirect-drive experiments at the NIF, low-mode symmetry is an important design issue.[1] Since very high values of $C_r$ (~30 to 40) are required for ignition,[1] Eq. (3) implies that even small amounts of drive asymmetry can disrupt implosion dynamics. Although the experimental data used in this article are from direct-drive implosions, the scaling for indirect drive should theoretically be similar because the drive pressure scales with $I$ in a similar way;[1] direct experimental evidence is currently being sought in ongoing indirect-drive experiments at OMEGA.[28] Another NIF illumination scheme under consideration is polar direct drive (PDD),[29] in which laser beams arranged in a six-ring configuration normally used for indirect drive will be used for direct drive; although this configuration will be optimized as much as possible, it will involve significant low-mode illumination asymmetry, and it is important to know how serious that will be for implosion performance. Equation (3) can be used in these cases to estimate constraints on $\langle \delta I \rangle / \langle I \rangle$ if we know the upper limit of $\langle \delta \rho R \rangle / \langle \rho R \rangle$ that an imploded capsule can tolerate, although in some cases the criteria for ignition have been stated in terms of the symmetry of the hot, compressed core[1] rather than the symmetry of total $\rho R$. Current work is underway to study the relationship between core symmetry and total $\rho R$ symmetry in indirect-drive implosions.[28]

In summary, we have performed the first experiments to systematically study $\rho R$ asymmetries and their relationship with laser illumination asymmetries for direct-drive capsule implosions on OMEGA. A scaling law relating $\langle \delta \rho R \rangle / \langle \rho R \rangle$ to $\langle \delta I \rangle / \langle I \rangle$ has been found, and it has critical implications for future work on the National Ignition Facility (NIF) as well as on OMEGA.

## ACKNOWLEDGMENT

This work was supported in part by the U.S. Department of Energy Contract #DE-FG03-99SF21782, LLE subcontract #PO410025G, LLNL subcontract #B313975, the U.S. Department of Energy Office of Inertial Confinement Fusion under Cooperative Agreement No. DE-FC03-92SF19460, and the New York State Energy Research and Development Authority.

## REFERENCES

1. J. D. Lindl, Phys. Plasmas **2**, 3933 (1995).

2. S. W. Haan *et al*., Phys. Plasmas **2**, 2480 (1995).

3. S. E. Bodner, D. G. Colombant, J. H. Gardner, R. H. Lehmberg, S. P. Obenschain, L. Phillips, A. J. Schmitt, J. D. Sethian, R. L. McCrory, W. Seka, C. P. Verdon, J. P. Knauer, B. B. Afeyan, and H. T. Powell, Phys. Plasmas **5**, 1901 (1998).

4. R. L. McCrory, R. E. Bahr, R. Betti, T. R. Boehly, T. J. B. Collins, R. S. Craxton, J. A. Delettrez, W. R. Donaldson, R. Epstein, J. Frenje, V. Yu. Glebov, V. N. Goncharov, O. Gotchev, R. Q. Gram, D. R. Harding, D. G. Hicks, P. A. Jaanimagi, R. L. Keck, J. Kelly, J. P. Knauer, C. K. Li, S. J. Loucks, L. D. Lund, F. J. Marshall, P. W. McKenty, D. D. Meyerhofer, S. F. B. Morse, R. D. Petrasso, P. B. Radha, S. P. Regan, S. Roberts, F. Séguin, W. Seka, S. Skupsky, V. Smalyuk, C. Sorce, J. M. Soures, C. Stoeckl, R. P. J. Town, M. D. Wittman, B. Yaakobi, and J. D. Zuegel, Nucl. Fusion **41**, 1413 (2001).

5. D. D. Meyerhofer, J. A. Delettrez, R. Epstein, V. Yu. Glebov, V. N. Goncharov, R. L. Keck, R. L. McCrory, P. W. McKenty, F. J. Marshall, P. B. Radha, S. P. Regan, S. Roberts, W. Seka, S. Skupsky, V. A. Smalyuk, C. Sorce, C. Stoeckl, J. M. Soures, R. P. J. Town, B. Yaakobi, J. D. Zuegel, J. Frenje, C. K. Li, R. D. Petrasso, D. G. Hicks, F. H. Séguin, K. Fletcher, S. Padalino, M. R. Freeman, N. Izumi, R. Lerche, T. W. Phillips, and T. C. Sangster, Phys. Plasmas **8**, 2251 (2001).

6. S. W. Haan, Phys. Rev. A **39**, 5812 (1989).

7. M. S. Plesset, J. Appl. Phys. **25**, 96 (1954).

8. R. D. Petrasso, C. K. Li, M. D. Cable, S. M. Pollaine, S. W. Haan, T. P. Bernat, J. D. Kilkenny, S. Cremer, J. P. Knauer, C. P. Verdon, and R. L. Kremens, Phys. Rev. Lett. **77**, 2718 (1996).

9. B. Yaakobi, V. A. Smalyuk, J. A. Delettrez, F. J. Marshall, D. D. Meyerhofer, and W. Seka, Phys. Plasmas **7**, 3727 (2000).

10. F. H. Séguin, C. K. Li, D. G. Hicks, J. A. Frenje, K. M. Green, R. D. Petrasso, J. M. Soures, D. D. Meyerhofer, V. Yu. Glebov, C. Stoeckl, P. B. Radha, S. Roberts, C. Sorce, T. C. Sangster, M. D. Cable, S. Padalino, and K. Fletcher, Phys. Plasmas **9**, 2725 (2002); F. H. Séguin, C. K. Li, J. A. Frenje, S. Kurebayashi, R. D. Petrasso, F. J. Marshall, D. D. Meyerhofer, J. M. Soures, T. C. Sangster, C. Stoeckl, J. A. Delettrez, P. B. Radha, V. A. Smalyuk, and S. Roberts, Phys. Plasmas **9**, 3558 (2002).

11. C. K. Li, F. H. Séguin, J. A. Frenje, R. D. Petrasso, R. Rygg, S. Kurebayashi, B. Schwartz, R. L. Keck, J. A. Delettrez, J. M. Soures, P. W. McKenty, V. N. Goncharov, J. P. Knauer, F. J. Marshall, D. D. Meyerhofer, P. B. Radha, S. P. Regan, T. C. Sangster, W. Seka, and C. Stoeckl, Phys. Plasmas **10**, 1919 (2003).

12. T. R. Boehly, D. L. Brown, R. S. Craxton, R. L. Keck, J. P. Knauer, J. H. Kelly, T. J. Kessler, S. A. Kumpan, S. J. Loucks, S. A. Letzring, F. J. Marshall, R. L. McCrory, S. F. B. Morse, W. Seka, J. M. Soures, and C. P. Verdon, Opt. Commun. **133**, 495 (1997).

13. F. H. Séguin, J. A. Frenje, C. K. Li, D. G. Hicks, S. Kurebayashi, J. R. Rygg, B.-E. Schwartz, R. D. Petrasso, S. Roberts, J. M. Soures, D. D. Meyerhofer, T. C. Sangster, J. P. Knauer, C. Sorce, V. Yu. Glebov, C. Stoeckl, T. W. Phillips, R. J. Leeper, K. Fletcher, and S. Padalino, Rev. Sci. Instrum. **74**, 975 (2003).

14. This is because there is often a great deal of similarity in the asymmetries of contiguous shots, while capsule imperfections would be expected to vary randomly from shot to shot.

15. We have ignored the fact that the individual laser beams may have slightly different time histories, resulting in a small time-dependent power imbalance, as discussed in Ref. 5.

16. F. J. Marshall, J. A. Delettrez, R. Epstein, R. Forties, R. L. Keck, J. H. Kelly, P. W. McKenty, S. P. Regan, and L. J. Waxer, Phys. Plasmas **11**, 251 (2004).

17. M. H. Emery *et al.*, Phys. Rev. Lett. **48**, 253 (1982).

18. J. Delettrez, D. K. Bradley, and C. P. Verdon, Phys. Plasmas **1**, 2342 (1994).

19. W. M. Manheimer, D. G. Colombant, and J. H. Gardner, Phys. Fluids **25**, 1644 (1982).

20. B. Yaakobi, T. Boehly, P. Bourke, Y. Conturie, R. S. Craxton, J. Delettrez, J. M. Forsyth, R. D. Frankel, L. M. Goldman, R. L. McCrory, M. C. Richardson, W. Seka, D. Shvarts, and J. M. Soures, Opt. Commun. **39**, 175 (1981).

21. T. C. Sangster, J. A. Delettrez, R. Epstein, V. Yu. Glebov, V. N. Goncharov, D. R. Harding, J. P. Knauer, R. L. Keck, J. D. Kilkenny, S. J. Loucks, L. D. Lund, R. L. McCrory, P. W. McKenty, F. J. Marshall, D. D. Meyerhofer, S. F. B. Morse, S. P. Regan, P. B. Radha, S. Roberts, W. Seka, S. Skupsky, V. A. Smalyuk, C. Sorce, J. M. Soures, C. Stoeckl, K. Thorp, J. A. Frenje, C. K. Li, R. D. Petrasso, F. H. Séguin, K. A. Fletcher, S. Padalino, C. Freeman, N. Izumi, J. A. Koch, R. A. Lerche, M. J. Moran, T. W. Phillips, and G. J. Schmid, Phys. Plasmas **10**, 1937 (2003).

22. P. W. McKenty, T. C. Sangster, M. Alexander, R. Betti, R. S. Craxton, J. A. Delettrez, L. Elasky, R. Epstein, A. Frank, V. Yu. Glebov, V. N. Goncharov, D. R. Harding, S. Jin, J. P. Knauer, R. L. Keck, S. J. Loucks, L. D. Lund, R. L. McCrory, F. J. Marshall, D. D. Meyerhofer, S. P. Regan, P. B. Radha, S. Roberts, W. Seka, S. Skupsky, V. A. Smalyuk, J. M. Soures, K. A. Thorp, M. Wozniak, J. A. Frenje, C. K. Li, R. D. Petrasso, F. H. Séguin, K. A. Fletcher, S. Padalino, C. Freeman, N. Izumi, J. A. Koch, R. A. Lerche, M. J. Moran, T. W. Phillips, G. J. Schmid, and C. Sorce, "Direct-Drive Cryogenic Target Implosion Performance on OMEGA," to be published in Physics of Plasmas.

23. C. K. Li, D. G. Hicks, F. H. Séguin, J. A. Frenje, R. D. Petrasso, J. M. Soures, P. B. Radha, V. Yu. Glebov, C. Stoeckl, D. R. Harding, J. P. Knauer, R. L. Kremens, F. J. Marshall, D. D. Meyerhofer, S. Skupsky, S. Roberts, C. Sorce, T. C. Sangster, T. W. Phillips, M. D. Cable, and R. J. Leeper, Phys. Plasmas **7**, 2578 (2000).

24. C. K. Li and R. D. Petrasso, Phys. Rev. Lett. **70**, 3059 (1993).

25. C. K. Li, F. H. Séguin, J. A. Frenje, S. Kurebayashi, R. D. Petrasso, D. D. Meyerhofer, J. M. Soures, J. A. Delettrez, V. Yu. Glebov, P. B. Radha, F. J. Marshall, S. P. Regan, S. Roberts, T. C. Sangster, and C. Stoeckl, Phys. Rev. Lett. **89**, 165002 (2002).

26. F. H. Séguin, R. D. Petrasso, J. A. Frenje, C. K. Li, J. R. Rygg, C. Stoeckl, P. B. Radha, J. A. Delettrez, V. Yu. Glebov, D. D. Meyerhofer, T. C. Sangster, and J. M. Soures, Bull. Am. Phys. Soc. **47**, 144 (2002); F. H. Séguin, J. R. Rygg, J. A. Frenje, C. K. Li, R. D. Petrasso, J. A. Delettrez, V. Yu. Glebov, V. N. Goncharov, R. L. Keck, J. P. Knauer, F. J. Marshall, P. W. McKenty, D. D. Meyerhofer, T. C. Sangster, V. A. Smalyuk, J. M. Soures, and S. P. Hatchett, Bull. Am. Phys. Soc. **48**, 57 (2003).

27. C. Stoeckl, J. A. Delettrez, T. C. Sangster, R. B. Stephens, S. P. Hatchett, J. A. Frenje, C. K. Li, F. H. Séguin, S. Fujioka, H. Shiraga, and K. A. Tanaka, Bull. Am. Phys. Soc. **48**, 298 (2003).

28. C. K. Li *et al.*, Bull. Am. Phys. Soc. **48**, 57 (2003).

29. S. Skupsky, J. A. Marozas, R. S. Craxton, R. Betti, T. J. B. Collins, J. A. Delettrez, V. N. Goncharov, P. W. McKenty, P. B. Radha, T. R. Boehly, J. P. Knauer, F. J. Marshall, D. R. Harding, J. D. Kilkenny, D. D. Meyerhofer, T. C. Sangster, and R. L. McCrory, "Polar Direct Drive on the National Ignition Facility," to be published in Physics of Plasmas.

# Convective Stimulated Brillouin Scattering (SBS) in One- and Two-Ion Plasmas

## Introduction

Stimulated brillouin scattering (SBS) is the decay of an incident (pump) light wave into a frequency-downshifted (Stokes) light wave and an ion-acoustic (sound) wave.[1] It is important in inertial confinement fusion (ICF) experiments because it scatters laser light away from the target, which reduces the laser energy that is available to drive the compression of the nuclear fuel.[2]

Unabated SBS results in a complete transfer of energy from the pump wave to the Stokes (and sound) wave(s); however, such a transfer is not observed in experiments. Several mechanisms can saturate SBS: The first and most important one is the Landau damping[3] of sound waves. This is a linear phenomenon and, hence, can be significant even for small sound-wave amplitudes. Heikkinen,[4] Rozmus,[5] and Cohen[6] have discussed a wide variety of ion-acoustic nonlinearities. Hydrodynamic effects such as daughter-wave generation and nonlinear phase shifts can limit SBS significantly if the sound-wave amplitude is large enough. Finally, if the Stokes intensity becomes comparable to the pump intensity, the effects of pump depletion become significant. Our goal is to compare these processes in one- and two-ion plasmas. Our model of sound waves consists of mass and momentum conservation equations for the ion fluids (two of each for two-ion plasmas), together with the inertionless electron-fluid equation and the Poisson equation. The results of kinetic theory[7–9] were used to calculate phenomenological damping coefficients. Beating the pump with Stokes waves creates a low-frequency ponderomotive force that drives the sound wave. In this article the exact partial differential equation for a light wave is not solved; instead, an approximate ordinary differential equation is used for the amplitude of the ponderomotive force. Neglecting the transient dynamics of the ponderomotive force is a good approximation because the group velocity of light is much higher than the group velocity of sound.

A one-dimensional model is used to simulate backward scattering. The first part of this article is devoted to SBS in a one-ion plasma. In this case it is easier to understand underlying physical processes and to find an approximate analytical solution of the model equations. A numerical solution was obtained by a code developed at LLE. To verify numerical results, the model equations were linearized, the exact dispersion equation was found, and it was solved numerically. The solution obtained through this method was compared to a numerical solution of linearized equations at different values of pump intensities and damping coefficients. The next step was to solve numerically the nonlinear equation for ponderomotive force along with the linear ion-fluid equation. That allowed us to quantify the effects of pump depletion. The latter solution was then compared to a solution of an exact nonlinear set of equations, which showed the effect of ion-acoustic nonlinearities. The same steps were repeated to simulate SBS in two-ion plasmas. The effects of Landau damping, pump depletion, and ion-acoustic nonlinearities are shown separately for fast and slow sound waves. SBS was simulated for carbon and hydrocarbon plasmas with parameters typical for experiments on the OMEGA laser system.

## SBS in One-Ion Plasmas

1. Model Equations

The equations governing the ion-fluid motion are similar to the equations for undriven sound waves.[10] Specifically, each ion species is governed by a continuity equation

$$\partial_t n_i + \partial_x \left( n_i v_i \right) = 0 \tag{1}$$

and a momentum equation

$$m_i n_i \left( \partial_t + v_i \partial_x \right) v_i = -Ze\, n_i \partial_x \phi - \partial_x p_i, \tag{2}$$

where $n_i$ is the ion (number) density, $v_i$ is the ion velocity, $m_i$ is the ion mass, $Ze$ is the ion charge, $p_i$ is the ion pressure, and $\phi$ is the electrostatic potential. One can use an adiabatic equation of state for ions under the assumption that the ion-acoustic wave phase velocity is much larger than the ion thermal velocity. It follows from the adiabatic equation of state

that

$$\partial_x p_i = 3n_{i0}T_i\left(n_i/n_{i0}\right)^2\partial_x\left(n_i/n_{i0}\right), \tag{3}$$

where $T_{i0}$ is the equilibrium ion temperature and $n_{i0}$ is the equilibrium ion density. By substituting Eq. (3) into Eq. (2), one finds that

$$m_i n_i\left(\partial_t + v_i\partial_x\right)v_i$$

$$= -Zen_i\partial_x\phi - 3n_{i0}T_{i0}\left(n_i/n_{i0}\right)^2\partial_x\left(n_i/n_{i0}\right). \tag{4}$$

The electrostatic potential is governed by the Poisson equation

$$\partial_{xx}\phi = 4\pi e\left(n_e - Zn_i\right). \tag{5}$$

With the ponderomotive term added,[1] the electron-fluid momentum equation is

$$\partial_t v_e = e\partial_x\phi/m_e - \partial_x\left(ea_\perp/m_e c\right)^2/2 - \partial_e p_e/n_e m_e, \tag{6}$$

where $a_\perp$ is the vector potential of a light wave. Because the electron thermal velocity is much higher than the phase velocity of the sound waves, one can use the isothermal equation of state

$$p_e = n_e T_e \tag{7}$$

for the electron fluid. By substituting Eq. (7) into Eq. (6) and neglecting electron inertia, one finds that

$$\partial_x n_e/n_e = e\partial_x\phi/T_e - e\partial_x d/T_e, \tag{8}$$

where the ponderomotive potential $d = a_\perp^2 e/2m_e c^2$. The integral of Eq. (8) is

$$n_e = n_{e0}\exp\left(e\phi/T_e - ed/T_e\right), \tag{9}$$

where $n_{e0}$ is equilibrium electron density. One can simplify the manipulation of equations by rewriting them in dimensionless variables. It is clear from Eq. (9) that one should measure the potentials in units of $T_e/e$ and the electron density in units of $n_{e0}$. It is clear from Eq. (4) that one should measure the ion density in units of $n_{i0}$ (equilibrium ion density). It follows from Eq. (5) and the normalization of the potentials that one should measure distance ($x$) in units of the electron Debye length $\lambda_{\mathrm{De}} = \left(T_e/4\pi n_{e0}e^2\right)^{1/2}$. If one measures time ($t$) in units of the inverse ion-plasma frequency $\omega_{\mathrm{pi}}^{-1} = \left(m_i/4\pi Zn_{e0}e^2\right)^{1/2}$, the corresponding speed unit is the ion-sound speed $c_s = \left(ZT_e/m_i\right)^{1/2}$. By making these changes in Eqs. (1), (4), (5), and (9), one obtains the dimensionless equations

$$\partial_t N_i + \partial_x\left(N_i V_i\right) = 0, \tag{10}$$

$$\left(\partial_t + V_i\partial_x\right)V_i + \partial_x\Phi + \theta N_i\partial_x N_i = 0, \tag{11}$$

$$\partial_{xx}^2\Phi + N_i - N_e = 0, \tag{12}$$

$$N_e - \exp\left(\Phi - D\right) = 0, \tag{13}$$

where $\theta = 3T_i/ZT_e$. The dimensionless ponderomotive potential is given by

$$D = A_\perp^2, \tag{14}$$

where $A_\perp = ea_\perp/\left(2m_e T_e c^2\right)^{1/2}$ is the dimensionless vector potential of a light wave. Physically $A_\perp$ is the transverse electron quiver velocity divided by the electron thermal velocity. Equations (10)–(13) describe a sound wave in plasma. The equation for the vector potential of a light wave in a plasma was derived from the Maxwell equations:[1]

$$\left(\partial_{tt}^2 - c^2\partial_{xx}^2\right)A_\perp = -4\pi e^2 n_e A_\perp/m_e. \tag{15}$$

The vector potential $A_\perp$ can be written as

$$A_\perp = \left[A\exp\left(-i\omega_0 t\right) + \text{c.c.}\right]/2, \tag{16}$$

where $A$ is the slowly varying amplitude and $\omega_0$ is the pump frequency. Slowly varying amplitude $A$ satisfies[5]

$$2i\left(n_c Z m_e / n_{e0} m_i\right)^{1/2} \partial_t A$$

$$+ c^2 m_e / T_e \partial_{xx}^2 A + n_c / n_{e0} a = A n_e / n_{e0}, \quad (17)$$

where $n_c = m_e \omega_0^2 / \left(4\pi e^2\right)$ is the critical density. The slowly varying amplitude can be expressed as the sum of two components:

$$A = A_0 \exp\left(ik_0 x\right) + A_1 \exp\left(ik_1 x - i\omega_1 t\right), \quad (18)$$

where $A_{0(1)}$ is the pump (Stokes)-wave amplitude, $k_{0(1)}$ is the pump (Stokes)-wave number, and $\omega_1$ is the frequency difference between the pump and Stokes waves. If the SBS gain length is large compared to the wavelengths of pump and Stokes waves, the envelope approximation is valid. By substituting Eq. (18) into Eq. (17) and using envelope approximation, one finds that

$$\left(\partial_t A_0 / v_0 + \partial_x A_0\right) \exp\left(ik_0 x\right)$$

$$= -i\gamma A_1 \overline{N_e} \exp\left[i\left(k_1 + k_2\right)x - i\left(\omega_1 + \omega_2\right)t\right]/2, \quad (19)$$

$$\left(-\partial_t A_1^* / v_0 + \partial_x A_1^*\right) \exp\left(-ik_1 x + i\omega_1 t\right)$$

$$= -i\gamma A_0^* \overline{N_e} \exp\left[i\left(-k_0 + k_2\right)x - i\omega_2 t\right]/2, \quad (20)$$

where $\overline{N_e}$ is the first Fourier harmonic of the electron-density fluctuations, $v_0$ is the group velocity of the pump wave, $k_2(\omega_2)$ is the wave number (frequency) of the undriven sound wave, and the coupling constant $\gamma = T_e / \left(k_2 m_e c^2\right)$. In the context of SBS, the plasma response is important only near resonance. For three-wave processes the resonance conditions are

$$\omega_1 + \omega_2 = 0, \quad (21)$$

$$k_0 - k_1 - k_2 = 0. \quad (22)$$

The undriven sound-wave frequency $\omega_2$ and wave number $k_2$ satisfy the dispersion relation[10]

$$\omega_2 = k_2\left[\left(1 + k_2^2\right) + \theta\right]^{1/2}. \quad (23)$$

By using Eqs. (21) and (22), one can reduce Eqs. (19) and (20) to

$$\partial_t A_0 / v_0 + \partial_x A_0 = -i\gamma A_1 \overline{N_e}/2, \quad (24)$$

$$-\partial_t A_1^* / v_0 + \partial_x A_1^* = -i\gamma A_0^* \overline{N_e}/2. \quad (25)$$

Because the light-wave group velocity is much higher than the sound-wave group velocity, the intrinsic relaxation time is much shorter than the SBS gain time. Consequently, the time derivatives in Eqs. (24) and (25) can be neglected, in which case the equations reduce to

$$\partial_x A_0 = -i\gamma A_1 \overline{N_e}/2, \quad (26)$$

$$\partial_x A_1^* = -i\gamma A_0^* \overline{N_e}/2. \quad (27)$$

By substituting Eq. (16) into Eq. (14) one finds that

$$D = \left[A^2 \exp\left(-2i\omega_0 t\right) + A^{*2} \exp\left(2i\omega_0 t\right) + 2|A|^2\right]/4. \quad (28)$$

The first two terms on the right-hand side of Eq. (28) are nonresonant and can be omitted, thus one obtains

$$D = |A|^2 / 2. \quad (29)$$

By substituting Eq. (18) into Eq. (29) and neglecting nonresonant terms, one finds that

$$D = \left[A_0 A_1^* \exp\left(ik_2 x - i\omega_2 t\right) + \text{c.c.}\right]/2. \quad (30)$$

It follows from Eq. (30) that the Fourier harmonic of the ponderomotive potential is

$$\overline{D} = A_0 A_1^*. \quad (31)$$

By differentiating Eq. (31) and substituting $\partial_x A_{0,1}$ from Eqs. (26) and (27), one obtains

$$\partial_x \overline{D} = -i\gamma \overline{N_e} \left(4\left|\overline{D}\right|^2 + C\right)^{1/2} \Big/ 2, \tag{32}$$

where the integration constant $C = \left(\left|A_0\right|^2 + \left|A_1\right|^2\right)^2 - 4\left|\overline{D}\right|^2$. One can calculate $C$ at the left boundary ($x = 0$) and express it in terms of two physical parameters: the pump intensity $I = \left|A_0(0)\right|^2$ and the reflectivity $R = \left|A_1(0)\right|^2 \Big/ \left|A_0(0)\right|^2$:

$$C = \left[I(1-R)\right]^2. \tag{33}$$

The physical laser intensity $I_l = c\left(k_0\left|a_0\right|\right)^2 \Big/ (8\pi)$, from which it follows that the normalized intensity

$$I = \left(I_l e^2 \lambda_0^2\right) \Big/ \left(\pi m_e T_e c^3\right).$$

If $I_l$ is measured in W/cm$^2$, $\lambda_0$ is measured in $\mu$m, and $T_e$ is measured in keV, then

$$I \approx 2 \times 10^{-16}\, I_l \lambda_0^2 / T_e\,. \tag{34}$$

By adding phenomenological damping terms to Eqs. (11) and (12) and ponderomotive potential terms to Eqs. (13) and (14), one obtains

$$\partial_t N_i + \partial_x\left(N_i V_i\right) + \zeta\left(N_i - 1\right) = 0, \tag{35}$$

$$\left(\partial_t + V_i \partial_x\right) V_i + \partial_x \Phi + \theta N_i \partial_x N_i + \zeta V_i = 0, \tag{36}$$

$$\partial_{xx}^2 \Phi + N_i - \exp\left\{\Phi - \Re\left[\overline{D}\exp\left(ik_2 x - i\omega_2 t\right)\right]\right\} = 0, \tag{37}$$

$$N_e - \exp\left\{\Phi - \Re\left[\overline{D}\exp\left(ik_2 x - i\omega_2 t\right)\right]\right\} = 0, \tag{38}$$

where $\Re(f)$ denotes the real part of $f$. Equations (35)–(38), (32), and (33) form a complete set that self-consistently describes SBS.

We used the following initial and boundary conditions: the plasma is undisturbed initially and remains so at the left boundary ($x = 0$); SBS is seeded by a finite-amplitude Stokes wave at the right boundary ($x = L$). We used $\left|A_1(L)\right|^2 = 10^{-6} I$, which corresponds to

$$\left|\overline{D}(L)\right|^2 = 10^{-3} I. \tag{39}$$

2. Numerical Scheme

Our code uses the MacCormack (MC) method[11] to solve the ion-fluid Eqs. (35) and (36), written in conservation form. MC is a two-step method: at the first step the values of the ion density and velocity are predicted using the first-order forward difference scheme associated with Eqs. (35) and (36):

$$N_{ij}^{\overline{k+1}} = N_{ij}^k - c\left[\left(N_i V_i\right)_{j+1}^k - \left(N_i V_i\right)_j^k\right] - \delta t \zeta\left(N_{ij}^k - 1\right), \tag{40}$$

$$V_{ij}^{\overline{k+1}} = V_{ij}^k - c\left[\left(V_i^2/2 + \Phi + \theta N_i^2/2\right)_{j+1}^k - \left(V_i^2/2 + \Phi + \theta N_i^2/2\right)_j^k\right] - \delta t \zeta V_{ij}^k. \tag{41}$$

In Eqs. (40) and (41), the subscript $j$ denotes the position $j\delta x$, the superscript $k$ denotes the time $k\delta t$, and $c = \delta t/\delta x$ is the convection number.

With $N_{ij}^{\overline{k+1}}$ known, the predicted values of the electrostatic potential $\Phi_j^{\overline{k+1}}$, electron density $N_{ej}^{\overline{k+1}}$ and ponderomotive potential $D_j^{\overline{k+1}}$ can be determined by solving Eqs. (32), (33), (37), and (38) iteratively. First, Eq. (37) is solved using the ponderomotive potential obtained in the previous iteration (previous time step for the first iteration). Equation (37) is solved using the Newton iteration method, which was described in detail in Ref. 10. The values of the electrostatic potential obtained from Eq. (37) are used in Eq. (38) to calculate the electron density $N_e$. The discrete Fourier transform[12] is used to calculate the first harmonic of $N_e$. Fourier transform actually gives the values of the first harmonic averaged over one wavelength; thus, Eq. (32) has to be solved on a grid whose points are separated by exactly one wavelength. Linear interpolation was used to calculate the values of ponderomotive potential between those grid points:

$$\overline{D}(x) = \overline{D}\left(x_l\right) + \left[\overline{D}\left(x_r\right) - \overline{D}\left(x_l\right)\right]\left(x - x_1\right)/\lambda_2\,, \tag{42}$$

where $x_l$ and $x_r$ are left and right grid points and $\lambda_2$ is the sound wavelength. The square of the ponderomotive potential amplitude in Eq. (32) also has to be averaged over one wavelength: $\langle \overline{D}^2 \rangle = \int_{x_l}^{x_r} \overline{D}(x)^2 dx / \lambda_2$. By using formula (42) for $\overline{D}(x)$ and integrating, one obtains

$$\left\langle \overline{D}^2 \right\rangle = \left\{ \left|\overline{D}(x_l)\right|^2 + \left|\overline{D}(x_r)\right|^2 + \Re\left[\overline{D}(x_l)\right]\Re\left[\overline{D}(x_r)\right] + \Im\left[\overline{D}(x_l)\right]\Im\left[\overline{D}(x_r)\right] \right\} / 3, \tag{43}$$

where $\Im(f)$ denotes the imaginary part of $f$.

A straightforward numerical scheme is then used to solve Eq. (32):

$$\overline{D}_c(x_l) = \overline{D}_c(x_r) + i\gamma\lambda_2 \overline{N_e} \left( 4\left\langle \overline{D}^2 \right\rangle_p + C \right)^{1/2} \Big/ 2. \tag{44}$$

The values of $\langle \overline{D}^2 \rangle_p$ and $C_p$ obtained in the previous iteration (previous time step for the first iteration) are used to calculate $\overline{D}_c$ in the current iteration. The values of $\overline{D}_c$ are calculated from right to left because the value of $\overline{D}$ at the right boundary is fixed [Eq. (39)]. The values of $\overline{D}_c$ are then used in Eq. (33) to calculate $R_c$ and $C_c$. Subsequently, Eq. (37) is solved using the values of ponderomotive potential obtained in the previous iteration. These iterations are repeated until the convergence condition

$$\left| \left( R_c - R_p \right) / R_p \right| < \epsilon \tag{45}$$

is satisfied. At the second step of the MC method, spatial derivatives are evaluated using the first-order forward-difference approximation based on the predicted values of the density, velocity, and electrostatic potential. Corrected values of density and velocity are obtained by averaging the spatial derivatives calculated at the first and second steps:

$$N_{i_j}^{k+1} = N_{i_j}^k - c\left[ \left(N_i V_i\right)_{j+1}^k - \left(N_i V_i\right)_j^k + \left(N_i V_i\right)_j^{\overline{k+1}} - \left(N_i V_i\right)_{j-1}^{\overline{k+1}} \right] / 2 - \delta t \left[ \xi\left(N_{i_j}^k - 1\right) + \xi\left(N_{i_j}^{\overline{k+1}} - 1\right) \right] / 2, \tag{46}$$

$$V_{i_j}^{k+1} = V_{i_j}^k - c\left[ \left(V_i^2/2 + \Phi + \theta N_i^2/2\right)_{j+1}^k - \left(V_i^2/2 + \Phi + \theta N_i^2/2\right)_j^k + \left(V_i^2/2 + \Phi + \theta N_i^2/2\right)_j^{\overline{k+1}} - \left(V_i^2/2 + \Phi + \theta N_i^2/2\right)_{j-1}^{\overline{k+1}} \Big/ 2 - \delta t \left[ \xi V_{i_j}^k + \xi V_{i_j}^{\overline{k+1}} \right] / 2. \tag{47}$$

The iterations described at the first step are repeated at the second step to calculate the corrected values of the electrostatic potential $\Phi_j^{k+1}$, electron density $N_{ej}^{k+1}$, and ponderomotive potential amplitude $\overline{D}_j^{k+1}$. The MC method is of second-order accuracy in both time and space and is conditionally stable.[11] The Courant stability condition for the MC scheme applied to the sound-wave equations is derived in Ref. 10.

The sound-wave equations are solved on a spatial interval that is longer than the interaction length of the sound and light waves. To prevent the reflection of the sound wave from the right boundary, the spatial interval includes an extra region in which the sound wave is strongly damped and not driven.

## 3. Linear Regime of SBS

By linearizing Eqs. (35)–(38), one finds that

$$\partial_t N_i^{(1)} + \partial_x V_i^{(1)} + \xi N_i^{(1)} = 0, \tag{48}$$

$$\partial_t V_i^{(1)} + \partial_x \Phi + \theta \partial_x N_i^{(1)} + \xi V_i^{(1)} = 0, \tag{49}$$

$$\partial_{xx}^2 \Phi^{(1)} + N_i^{(1)} - N_e^{(1)} = 0, \tag{50}$$

$$N_e^{(1)} - \Phi^{(1)} + D^{(1)} = 0, \tag{51}$$

where $N_i^{(1)} = N_i - 1$, $N_e^{(1)} = N_e - 1$, $V_i^{(1)} = V_i$, $\Phi^{(1)} = \Phi$, and $D^{(1)} = D$. By substituting

$$y^{(1)} = \left[ \tilde{y} \exp\left(-\sigma x + ik_2 x - i\omega_2 t\right) + \text{c.c.} \right],$$

where $\sigma$ is the spatial growth rate, and differentiating, one obtains the linear equations

$$(i\omega - \zeta)\tilde{N}_i - (ik - \sigma)\tilde{V}_i = 0, \tag{52}$$

$$(i\omega - \zeta)\tilde{V}_i - (ik - \sigma)\left(\tilde{\Phi} + \theta\tilde{N}_i\right) = 0, \tag{53}$$

$$(ik - \sigma)^2\tilde{\Phi} + \tilde{N}_i - \tilde{N}_e = 0, \tag{54}$$

$$\tilde{N}_e - \tilde{\Phi} + \tilde{D} = 0, \tag{55}$$

in which $\omega$ and $k$ are the frequency and wave number of the undriven sound wave (the subscript 2 was omitted for simplicity). By solving Eqs. (52)–(55) one finds that

$$\tilde{N}_e \Big/ (ik - \sigma)^2 = \left\{1 - 1\Big/\left[\theta(ik - \sigma)^2 - (i\omega - \zeta)^2\right]\right\}\left(\tilde{N}_e + \tilde{D}\right). \tag{56}$$

Linearization of the light-wave equation is equivalent to neglecting pump depletion

$$\partial_x \overline{D} = -i\gamma\, I\overline{N_e}/2. \tag{57}$$

One can rewrite Eq. (57) in terms of $\tilde{D} = \overline{D}\exp(-\sigma x)$ and $\tilde{N}_e = \overline{N}_e \exp(-\sigma x)$:

$$\tilde{D} = \tilde{N}_e i\gamma I/(2\sigma), \tag{58}$$

It follows from Eqs. (56) and (58) that

$$1/(ik - \sigma)^2 = \left\{1 - 1\Big/\left[\theta(ik - \sigma)^2 - (i\omega - \zeta)^2\right]\right\}\left[1 + i\gamma I/(2\sigma)\right]. \tag{59}$$

By using the sound-wave dispersion relation (23) and neglecting terms of second and higher order in $\sigma/k$ and $\delta/\omega$, one can reduce Eq. (59) to

$$\sigma = -\gamma Ik/4\sigma + \eta\left(c_2\zeta - \theta\sigma\right), \tag{60}$$

where phase velocity $c_2 = \omega/k$ and $\eta = (1 + k^2)^2$. Equation (60) is a quadratic equation and can be solved analytically. The spatial growth rates are given by

$$\sigma_{\pm} = \frac{\eta c_2\zeta \pm \left[\eta^2 c_2^2\zeta^2 - \gamma Ik(1 + \eta\theta)\right]^{1/2}}{2(1 + \eta\theta)}. \tag{61}$$

By using boundary conditions for the ion density $N^{(1)}(0) = 0$, ponderomotive potential $D(L) = D_0 \cos(kx - \omega t)$, and Eq. (58), one finds that

$$D = D_0 \frac{\exp\left(-\sigma_+ x\right)/\sigma_+ - \exp\left(-\sigma_- x\right)/\sigma_-}{\exp\left(-\sigma_+ L\right)/\sigma_+ - \exp\left(-\sigma_- L\right)/\sigma_-} \times \cos\left(kx - \omega t\right), \tag{62}$$

$$N_i = 1 + 2D_0\left(1 + k^2\right)\frac{\exp\left(-\sigma_+ x\right) - \exp\left(-\sigma_- x\right)}{\exp\left(-\sigma_+ L\right)/\sigma_+ - \exp\left(-\sigma_- L\right)/\sigma_-} \times \sin\left(kx - \omega t\right)/(\gamma I). \tag{63}$$

Equation (60) has real solutions for growth rates $\sigma$ only if

$$\zeta^2 > \gamma Ik(1 + \eta\theta)/(\eta c_2)^2. \tag{64}$$

When the ion-acoustic damping is weak, condition (64) is violated and there is no physically meaningful solution for $\sigma$. For this case the linear SBS equations predict absolute instability.[13] There is no steady-state solution of linear SBS equations in this case. The only saturation mechanisms in the case of weak ion-acoustic damping are nonlinear effects such as pump depletion and hydrodynamic nonlinearities. We consider convective SBS with strong ion-acoustic damping. In this case nonlinear effects can also be important, but even in the linear

regime SBS can be saturated by damping. For very strong damping

$$\zeta^2 >> \gamma Ik. \tag{65}$$

By neglecting the second- and higher-order powers of $\gamma Ik/\zeta^2$ in the Maclaurin expansion of formula (61), one obtains

$$\sigma_+ \approx \frac{\eta c_2 \zeta}{1+\eta\zeta} - \frac{\gamma Ik}{4\eta c_2 \zeta}, \tag{66}$$

$$\sigma_- \approx \frac{\gamma Ik}{4\eta c_2 \zeta}. \tag{67}$$

If condition (65) is satisfied, then $\sigma_+ >> \sigma_-$ and $\exp(-\sigma_+ x) << \exp(-\sigma_- x)$. Neglecting $\exp(-\sigma_+ x)$, one can reduce Eq. (62) to

$$D \approx D_0 \exp\left[G(L-x)\right] \cos\left(kx - \omega t\right), \tag{68}$$

where $G = \gamma Ik/4\eta c_2 \zeta$ is the well-known convective growth rate.

To assess the accuracy of the analytical approximations, we chose typical parameters and solved Eq. (59) numerically. There are up to eight solutions for $\sigma$, but only two of them have $\left|\Re(\sigma)\right| >> \left|\Im(\sigma)\right|$ and are relevant to SBS. For future reference we will refer to the solution obtained by the method described above as the combined solution.

We modeled SBS in a carbon plasma ($Z = 6$) with parameters that are typical of ICF experiments on the OMEGA laser system: $\lambda_0 = 0.35\ \mu$m, $I_L = 10^{15}$ W/cm$^2$, $T_e/T_i = 4$, $T_e = 1$ keV, and $n_{0e}/n_{cr} = 0.1$. We used kinetic theory[14] to evaluate the Landau damping rate

$$\zeta/\omega = \frac{(\pi/8)^{1/2}}{\left(1+k^2\right)} \times c_s \left[\left(\frac{m_e Z}{m_i}\right)^{1/2} + \left(\frac{T_e Z}{T_i}\right)^{3/2} \exp\left(-c_s^2 \frac{T_e Z}{2T_i}\right)\right]. \tag{69}$$

For the OMEGA parameters listed above, the Landau damping rate $\zeta/\omega \approx 3.5\%$.

The numerical (steady-state) solution of Eqs. (48)–(51) and (57) is compared to the analytical and combined solutions in Fig. 98.9. SBS in carbon plasma was simulated for the OMEGA-like parameters listed above. The three solutions agree perfectly. The reflectivity ($R_N$) obtained through direct numerical solution of Eqs. (48)–(51) and (57) = 20.6%. The reflectivity ($R_{A,C}$) obtained through analytical and combined solution = 20.8%. Relative difference $\left(R_{A,C} - R_N\right)/R_N = 0.9\%$.

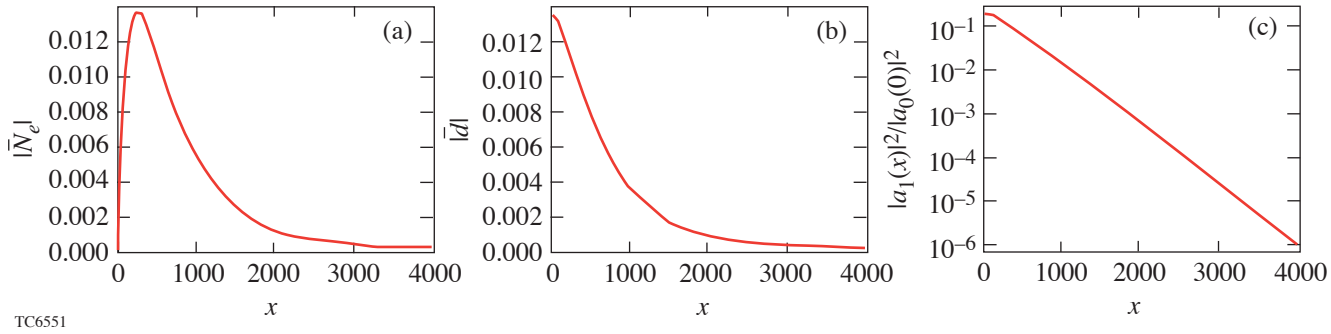


Figure 98.9
(a) First harmonic of electron density; (b) ponderomotive potential amplitude; (c) Stokes-wave intensity normalized to pump-wave intensity versus distance for steady state of SBS. Solutions of linearized equations [(48)–(51), (57)] describing SBS obtained through different methods are compared. Dotted lines represent numerical solution. Dashed lines represent combined solution obtained by numerical solution of Eq. (59). Solid lines represent analytical solution. All three solutions are indistinguishable. Simulation parameters are $\lambda_0 = 0.35\ \mu$m, $I_L = 10^{15}$ W/cm$^2$, $T_e/T_i = 4$, $T_e = 1$ keV, and $n_{0e}/n_{cr} = 0.1$.

4. Nonlinear Saturation

Convective SBS can be significantly reduced by nonlinear effects when the reflectivity is big enough. Pump depletion can be taken into account by solving the nonlinear light-wave equations (32) and (33). The effects of hydrodynamic nonlinearities can be determined by solving the nonlinear ion-fluid and Poisson equations (35)–(38). Different effects such as nonlinear phase shift[15] and generation of higher-order ion-wave harmonics of sound wave[4,5,16] were studied analytically. Our goal is to compare the effects of pump depletion and hydrodynamic nonlinearities on the saturation of SBS at OMEGA-like parameters. To separate the effects of pump depletion and hydrodynamic nonlinearities we numerically solved the nonlinear light-wave equations coupled with the linear sound-wave equations (48)–(51). This partially nonlinear solution was compared to the linear solution, based on Eqs. (48)–(51) and (57), and to the numerically obtained fully nonlinear solution, based on Eqs. (32), (33), and (35)–(38). All three solutions are shown in Figs. 98.10 and 98.11. Simulation parameters are the same as those used in the previous section.

Steady-state reflectivities are as follows: linear reflectivity $R_{LN} = 20.6\%$, partially nonlinear reflectivity $R_{PN} = 7.8\%$, fully nonlinear reflectivity $R_{FN} = 6.3\%$. Pump depletion reduces reflectivity by 60%. Ion-acoustic nonlinearities reduce reflectivity by 20%.

It is straightforward to express the pump intensity in terms of ponderomotive potential amplitude and constant of integration $C$. By using Eq. (31) and the definition of $C$, one finds that

$$|A_0|^2 = \left[\left(C + 4|\bar{D}|^2\right)^{1/2} + C^{1/2}\right]\Big/2. \qquad (70)$$

To show the effect of pump depletion we plotted the pump intensity based on the partially nonlinear solution. The pump-wave intensity normalized to the input pump intensity is shown as a function of distance in Fig. 98.12. The pump

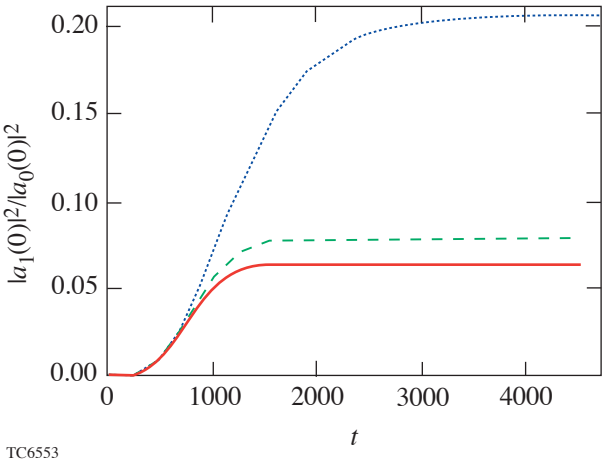


Figure 98.11
Reflectivities versus time. Dotted line represents numerical solution of linearized equations (48)–(51) and (57). Dashed line represents numerical solution of partially nonlinear equations (32), (33), and (48)–(51). Solid line represents numerical solution of fully nonlinear equations (32), (33), and (35)–(38). Simulation parameters are the same as in Fig. 98.9.

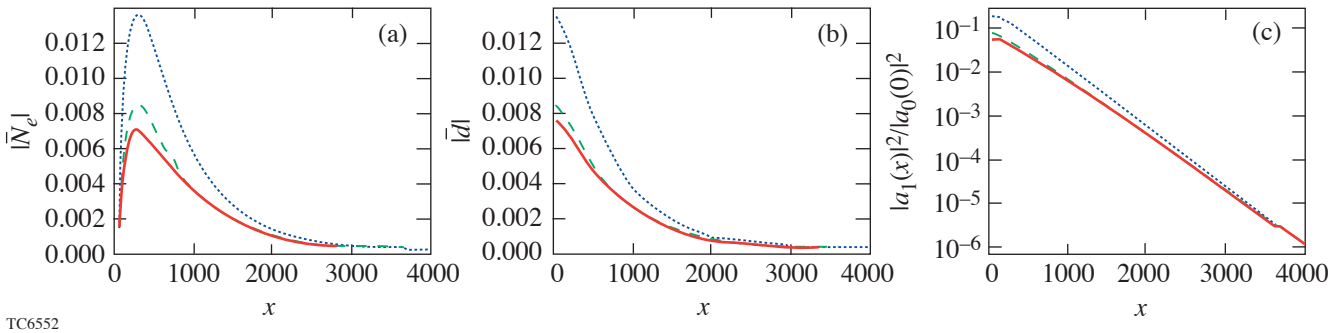


Figure 98.10
(a) First harmonic of electron density; (b) ponderomotive potential amplitude; (c) Stokes-wave intensity normalized to pump wave intensity versus distance for steady state of SBS. Dotted lines represent numerical solution of linearized equations (48)–(51) and (57). Dashed lines represent numerical solution of partially nonlinear equations (32), (33), and (48)–(51). Solid lines represent numerical solution of fully nonlinear equations (32), (33), and (35)–(38). Simulation parameters are the same as in Fig. 98.9.

intensity decreases on a scale length of several wavelengths. As one would expect, output pump intensity

$$|A_0(L)|^2 / I = 1 - R_{\mathrm{PN}} + |A_1(L)|^2 / I.$$

To show the higher-order harmonic generation, we plotted the discrete Fourier spectra of the electron density near its maximum. The absolute values of the harmonic amplitudes are shown in Fig. 98.13. The second and third harmonics can have significant amplitudes, whereas the fourth and higher harmonics are negligibly small.

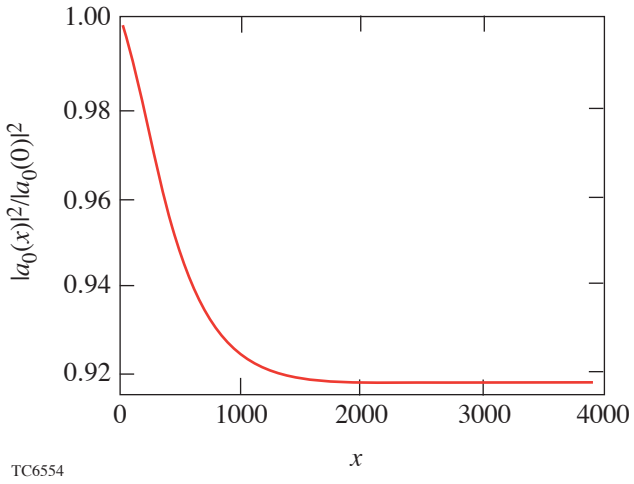


Figure 98.12
Pump-wave intensity normalized to input pump intensity versus distance for steady state of SBS. Simulation parameters are the same as in Fig. 98.9.

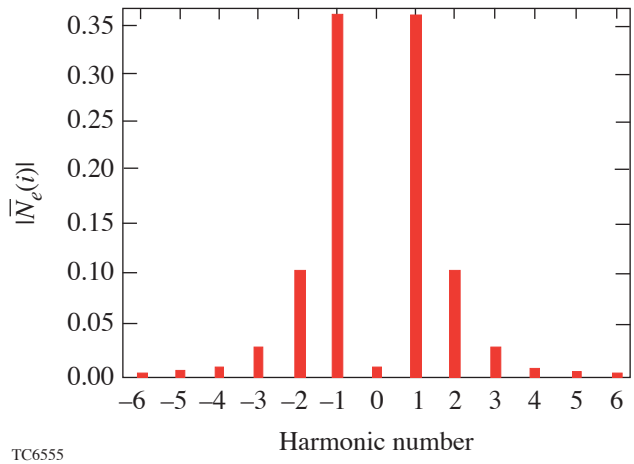


Figure 98.13
Fourier spectra of electron density near the point where it has maximal amplitude for steady state of SBS. Simulation parameters are the same as in Fig. 98.9.

## SBS in Two-Ion Plasmas

1. Model Equations

The equations governing the ion-fluid motion are the same as those for undriven sound waves.[17] For each ion species $s$, the mass and momentum conservation equations are

$$\partial_t n_s + \partial_x \left( n_s v_s \right) = 0, \tag{71}$$

$$m_s n_s \left( \partial_t + v_s \partial_x \right) v_s + Z_s e n_s \partial_x \phi - \partial_x p_s = 0, \tag{72}$$

where $n_s$ is the ion density, $v_s$ is the ion velocity, $m_s$ is the ion mass, $Z_s e$ is the ion charge, $p_s$ is the ion pressure, and $\phi$ is the electrostatic potential. A detailed comparison of fluid and kinetic models of sound waves in two-ion plasmas is described in Ref. 9. In particular it shows that a fluid model with self-consistent values of adiabatic exponents approximates the kinetic phase velocities of the sound waves with an accuracy close to the accuracy of the fluid model with adiabatic exponents equal to 3 for both ion species. If one assumes adiabatic exponents equal to 3 for both ion species, one finds that

$$\partial_x p_s = 3 n_{s0} T_{s0} \left( n_s / n_{s0} \right)^2 \partial_x \left( n_s / n_{s0} \right), \tag{73}$$

where $T_{s0}$ is the equilibrium ion temperature and $n_{s0}$ is the equilibrium ion density. One can easily modify Eq. (73) for a polytropic equation of state. By substituting Eq. (73) into Eq. (72), one finds that

$$m_s n_s \left( \partial_t + v_s \partial_x \right) v_s$$

$$+ Z_s e n_s \partial_x \phi 3 n_{s0} T_{s0} \left( n_s / n_{s0} \right)^2 \partial_x \left( n_s / n_{s0} \right) = 0. \tag{74}$$

The evolution of the electrostatic potential is governed by the Poisson equation

$$\partial_{xx} \phi = 4\pi e \left( n_e - \sum_s Z_s n_s \right). \tag{75}$$

One can simplify the manipulation of these equations by normalizing $n_s$ to $n_{s0}$, $n_e$ to $n_{e0}$, and $u_s$ to the sound speed of a reference species $r$. By rewriting Eqs. (71), (74), and (75) in the dimensionless form and adding phenomenological damping terms, one obtains

$$\partial_t N_s + \partial_x\left(N_s V_s\right) + \zeta\left(N_s - 1\right) = 0, \tag{76}$$

$$\left(\partial_t + V_s\partial_x\right)V_s + \beta_s\partial_x\Phi + \theta_s N_s\partial_x N_s + \zeta V_i = 0, \tag{77}$$

$$\partial_{xx}^2\Phi - N_e + \sum_s \alpha_s N_s = 0, \tag{78}$$

where $\theta_s = 3T_s/Z_r T_e\, m_r/m_s$, $\alpha_s = Z_s n_{s0}/n_{e0}$ is the ion charge-to-density ratio, and $\beta_s = Z_s m_r/Z_r m_s$ is the ion charge-to-mass ratio. Distance is measured in units of the electron-Debye length $\lambda_D = \left(T_e/4\pi e^2 n_{e0}\right)^{1/2}$, and time is measured in units of the reference ion-plasma period $1/\omega_{pi} = \left(m_r/4\pi Z_r e^2 n_{e0}\right)^{1/2}$. The equations for the electron density and ponderomotive potential amplitude are the same as those for the one-ion case: Eqs. (32), (33), and (38). We used the same initial and boundary conditions as in the one-ion case.

2. Numerical Scheme

A modified version of the numerical scheme described in the one-ion section was used to simulate SBS in two-ion plasmas. The mass- and momentum-conservation equations for each ion species are solved to evaluate the density $N_s$ and velocity $V_s$ of each of the ion fluids. Next, the Poisson equation (78) with a weighted sum of the light- and heavy-ion charge densities is used to calculate the electrostatic potential $\Phi$. Equations (78), (33), (37), and (38) are solved using the iterative procedure described in the one-ion section. The Courant stability condition for the MC scheme applied to the sound-wave equation in two-ion plasmas is given in Ref. 17.

3. Linear Regime of SBS

By linearizing Eqs. (76)–(78), one finds that

$$\partial_t N_s^{(1)} + \partial_x V_s^{(1)} + \zeta N_s^{(1)} = 0, \tag{79}$$

$$\partial_t V_s^{(1)} + \beta_s\partial_x\Phi + \theta_s\partial_x N_s^{(1)} + \zeta V_s^{(1)} = 0, \tag{80}$$

$$\partial_{xx}^2\Phi^{(1)} + \sum_s \alpha_s N_s^{(1)} - N_e^{(1)} = 0. \tag{81}$$

By substituting $y^{(1)} = \left[\tilde{y}\exp\left(-\sigma x + ik_2 x - i\omega_2 t\right) - c.c.\right]$ into Eqs. (79)–(81) and differentiating, one obtains the linear algebraic equations

$$\left(i\omega - \zeta\right)\tilde{N}_s - \left(ik - \sigma\right)\tilde{V}_s = 0, \tag{82}$$

$$\left(i\omega - \zeta\right)\tilde{V}_s - \left(ik - \sigma\right)\beta_s\left(\tilde{\Phi} + \theta_s\tilde{N}_s\right) = 0, \tag{83}$$

$$\left(ik - \sigma\right)^2\tilde{\Phi} + \sum_s \alpha_s\tilde{N}_s - \tilde{N}_e = 0. \tag{84}$$

The undriven sound-wave frequency $\omega$ and wave number $k$ satisfy the dispersion relation[17]

$$1 + k^2 = \sum_s \alpha_s\beta_s k^2\Big/\left(\omega^2 - \theta_s k^2\right). \tag{85}$$

The analysis of an undriven sound wave in two-ion plasmas was described in detail in Ref. 17. Two types of sound waves exist in such plasmas: a fast wave (fa), with phase speed in the range

$$c_{fa}^2 > \theta_l^2, \tag{86}$$

and a slow wave (sl), with phase speed in the range

$$\theta_h^2 < c_{sl}^2 < \theta_l^2, \tag{87}$$

where the indices $l$ and $h$ denote the lighter and heavier ions, respectively. Equation (85) is biquadratic and can be solved analytically. The frequencies are given by

$$\omega_{fa,sl}^2 = k^2\Big\{\mu_l + \theta_l^2 + \mu_h + \theta_h^2 \pm \left[\left(\mu_l + \theta_l^2 - \mu_h - \theta_h^2\right)^2 + 4\mu_l\mu_h\right]^{1/2}\Big\}\Big/2, \tag{88}$$

where $\mu_s = \alpha_s\beta_s/\left(1 + k^2\right)$. In Eq. (88) the plus sign is associated with the fast wave and the minus sign is associated with the slow wave. Both sound waves can be driven and participate in SBS. We artificially separated SBS from the fast and the slow sound waves by choosing the beat frequency of ponderomotive potential. Fast- or slow-wave SBS is modeled by driving the sound wave by ponderomotive potential, which has a corresponding frequency.

By combining Eqs. (82)–(84), (55), and (58), one finds that

$$1/(ik-\sigma)^2 = \left\{1-\sum_s \alpha_s\beta_s/\left[\theta_s(ik-\sigma)^2-(i\omega-\zeta)^2\right]\right\}\left[1+i\gamma I/(2\sigma)\right]. \quad (89)$$

As one should expect, the one-ion limit of Eq. (89) coincides with Eq. (59). Following the envelope-approximation procedure described in the one-ion section, we simplified Eq. (89) by substituting the undriven sound-wave frequencies given by Eq. (88) into Eq. (89) and neglecting second- and higher-order powers of $\sigma/k$ and $\zeta/\omega$. The result is

$$\sigma = -\gamma Ik/4\sigma + \sum_s \alpha_s\beta_s\left(c_2\zeta-\theta_s\sigma\right)/\left(c_2^2-\theta_s\right)^2. \quad (90)$$

Equation (90) is quadratic and can be solved analytically. The growth rates are given by

$$\sigma_{1,2} = \frac{c_2\zeta\sum_s\chi_s}{2\left(1+\sum_s\chi_s\theta_s\right)} \pm \frac{\left[\left(c_2\zeta\sum_s\chi_s\right)^2-\gamma Ik\left(1+\sum_s\chi_s\theta_s\right)\right]^{1/2}}{2\left(1+\sum_s\chi_s\theta_s\right)}, \quad (91)$$

where $\chi_s = \alpha_s\beta_s/\left(c_2^2-\theta_s\right)^2$.

As in the one-ion case, this approximate analytical solution was compared to the exact numerical solution of Eq. (89). Just as in the one-ion case, there are up to eight numerical roots of Eq. (89), but only two of them have $|\Re(\sigma)| >> |\Im(\sigma)|$ and are relevant to SBS. The solution obtained by the numerical solution of the analytically derived equation for $\sigma$ is also referred to as the combined solution.

The comparison of the approximate analytical solution to the exact numerical solution of Eq. (89) showed that in the case of a strong Landau damping $(\zeta/\omega \gtrsim 0.1)$, neglecting second-order powers of $\zeta/\omega$ leads to a significant error in the growth-rate values.

We modeled SBS from fast and slow waves in hydrocarbon (CH) plasma ($\alpha_l$ = 1/7, $\alpha_h$ = 6/7, $\beta_l$ = 1, $\beta_h$ = 1/2), with parameters that are typical of ICF experiments on OMEGA: $\lambda_0 = 0.35$ $\mu$m, $I_L = 2\times10^{15}$ W/cm$^2$, $T_e/T_l = T_e/T_h = 4$, $T_e$ = 1 keV, $n_{0e}/n_{cr} = 0.4$.

A detailed kinetic analysis of sound waves in two-ion plasmas is described in Refs. 7–9. We used the expression given in Ref. 9 for the Landau-damping rates:

$$\frac{\zeta_{fa(sl)}}{\omega_{fa(sl)}} = c_{fa(sl)}\frac{(\pi/8)^{1/2}}{1+\nu+k^2}\left[\left(\frac{m_eZ_r}{m_i}\right)^{1/2} + \sum_s \alpha_s\beta_s\left(\frac{3}{\theta_s}\right)^{3/2}\exp\left(-\frac{3c_{fa(sl)}^2}{2\theta_s}\right)\right], \quad (92)$$

where $\nu = 0$ for the fast wave and $\nu = 3\alpha_l/\theta_l$ for the slow wave. Coefficient $\nu$ reflects the reduction of the slow-wave damping rate by the light-ion Debye-screening factor. For the parameters listed above, the light-ion contribution to the Landau-damping rate ($\zeta_l$) dominates for both fast and slow waves and $\zeta_l/\omega \approx 0.13$. The heavy-ion contribution for the fast wave is negligibly small $\left(\zeta_h/\omega \approx 10^{-6}\right)$ because the phase velocity of the fast wave is much closer to the thermal velocity of the light ions than to the thermal velocity of the heavy ions. The phase velocity of the slow wave lies between the thermal velocities of the light and heavy ions. For the stated parameters, the heavy-ion contribution to the slow-wave Landau-damping rate is significant $\left(\zeta_h/\omega \approx 0.013\right)$, but smaller than the light-ion contribution. The electron contribution ($\zeta_e$) is significant for both waves. For the fast wave $\zeta_e/\omega \approx 0.01$, whereas for the slow wave $\zeta_e/\omega \approx 0.005$. The relative damping rates of fast and slow waves turn out to be close $\left(\zeta_{fa}/\omega_{fa} \approx 0.138,\ \zeta_{sl}/\omega_{sl} \approx 0.148\right)$. By definition the fast-wave frequency is higher than the slow-wave frequency, so the absolute damping rate of the fast wave, $\zeta_{fa} \approx 0.03$, is higher than the absolute damping rate of the slow wave, $\zeta_{sl} \approx 0.02$.

The combined solution, which was found by solving Eq. (89) numerically, was compared to the analytical solution of the envelope approximation of Eq. (89) and to the direct numerical stationary solution of Eqs. (79)–(81), (51), and (57). The numerical, combined, and analytical solutions of these equations are shown in Figs. 98.14 and 98.15 for fast- and slow-wave SBS, respectively. SBS in hydrocarbon plasma was simulated for the OMEGA-like parameters listed above. As in

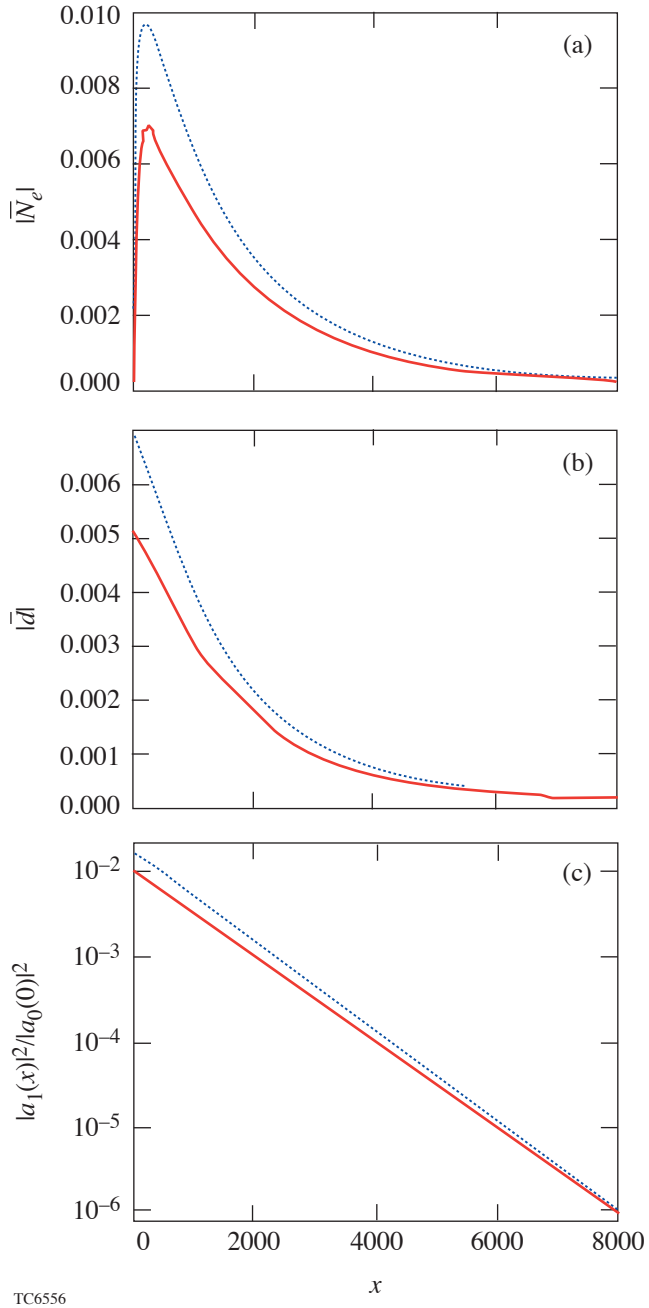


Figure 98.14
(a) First harmonic of electron density; (b) ponderomotive potential amplitude; (c) Stokes-wave intensity normalized to pump-wave intensity versus distance for steady state of fast-wave SBS. Solutions of linearized equations (51), (57), and (79)–(81) obtained through different methods are compared. Dotted lines represent numerical solution. Dashed lines represent combined solution obtained by numerical solution of Eq. (89). Solid lines represent analytical solution. Numerical and combined solutions are indistinguishable. Simulation parameters are $\lambda_0 = 0.35$ $\mu$m, $I_L = 2 \times 10^{15}$ W/cm$^2$, $T_e/T_l = T_e/T_h = 4$, $T_e = 1$ keV, and $n_{0e}/n_{cr} = 0.4$.

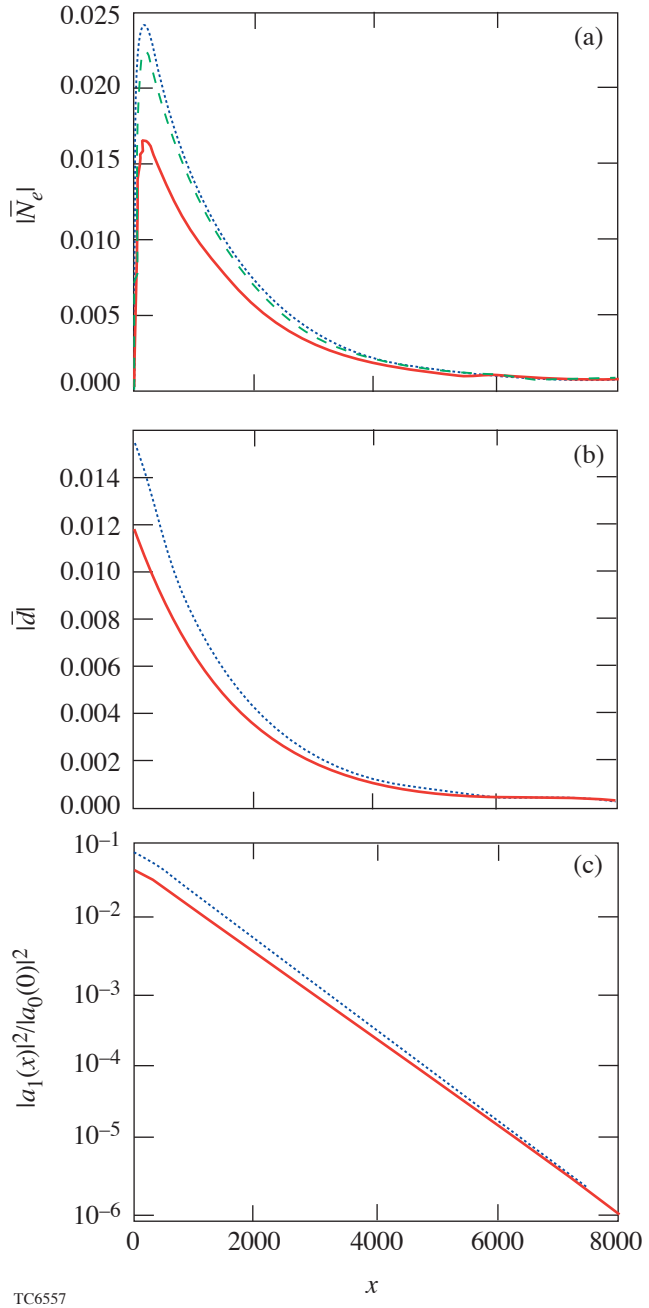


Figure 98.15
(a) First harmonic of electron density; (b) ponderomotive potential amplitude; (c) Stokes-wave intensity normalized to pump-wave intensity versus distance for steady state of slow-wave SBS. Solutions of linearized equations (51), (57), and (79)–(81) obtained through different methods are compared. Dotted lines represent numerical solution. Dashed lines represent combined solution obtained by numerical solution of Eq. (89). Solid lines represent analytical solution. Numerical and combined solutions for ponderomotive potential amplitude and Stokes-wave intensity are indistinguishable. Simulation parameters are the same as in Fig. 98.14.

the one-ion case, the numerical and combined solutions almost coincide. The fast-wave reflectivity obtained from the numerical solution is $R_N = 1.89\%$. The fast-wave reflectivity obtained from the combined solution is $R_C = 1.88\%$. The relative difference is $(R_C - R_N)/R_N = 0.2\%$. Fast-wave reflectivity obtained from the analytical solution is $R_A = 1.05\%$. The relative difference is $(R_A - R_N)/R_N = 44\%$. The slow-wave steady-state reflectivity obtained from the numerical solution is $R_N = 8.29\%$. The slow-wave reflectivity obtained from the combined solution is $R_C = 8.27\%$. The relative difference is $(R_C - R_N)/R_N = 0.25\%$. Slow-wave reflectivity obtained from the analytical solution is $R_A = 4.88\%$. The relative difference is $(R_A - R_N)/R_N = 41\%$. For both types of SBS the agreement between the numerical and combined solutions again proves the validity of the computational results. Landau-damping rates in CH plasmas are high for both fast and slow sound waves $(\zeta/\omega \simeq 0.14)$, which explains why analytical approximations are inaccurate in both cases. For the stated parameters, the Landau damping of the fast wave is stronger than that of the slow wave: $(\zeta_{fa} - \zeta_{sl})/\zeta_{sl} \approx 0.5$. The SBS growth rate is inversely proportional to the damping rate. This fact explains why the fast-wave SBS reflectivity is lower than the slow-wave SBS reflectivity: $R_{fa}/R_{sl} \approx 0.23$.

The first harmonics of the light- and heavy-ion densities ($\bar{N}_l$ and $\bar{N}_h$) in fast- and slow-wave SBS are shown in Figs. 98.16 and 98.17. Linear analysis of sound waves in two-ion plasmas shows that for fast wave $0 < \bar{N}_h/\bar{N}_l < 1$ and for

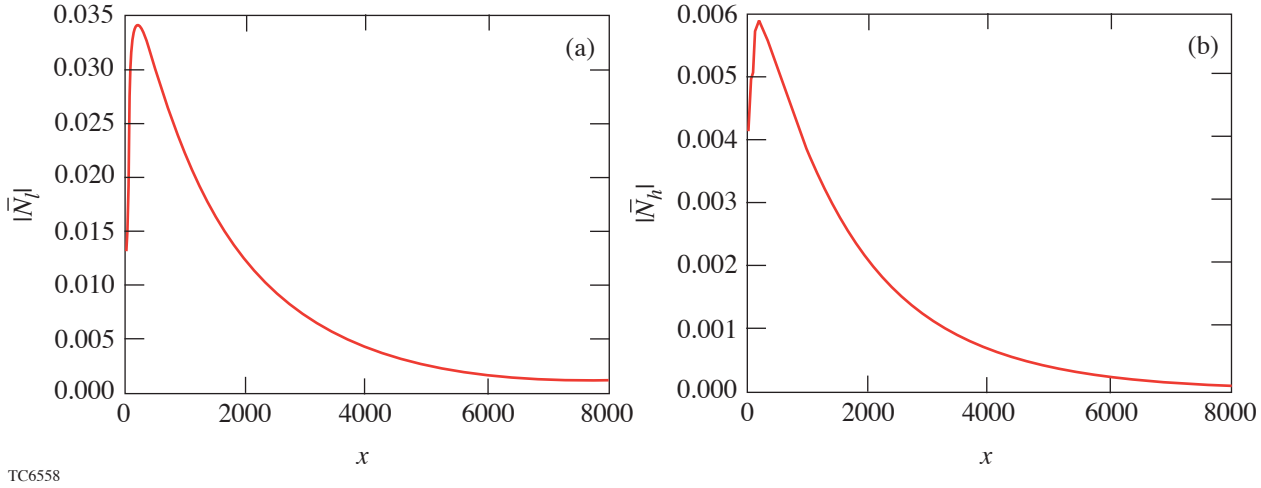


Figure 98.16
(a) First harmonic of light-ion and (b) heavy-ion densities versus distance for steady state of fast-wave SBS. Simulation parameters are the same as in Fig. 98.14.

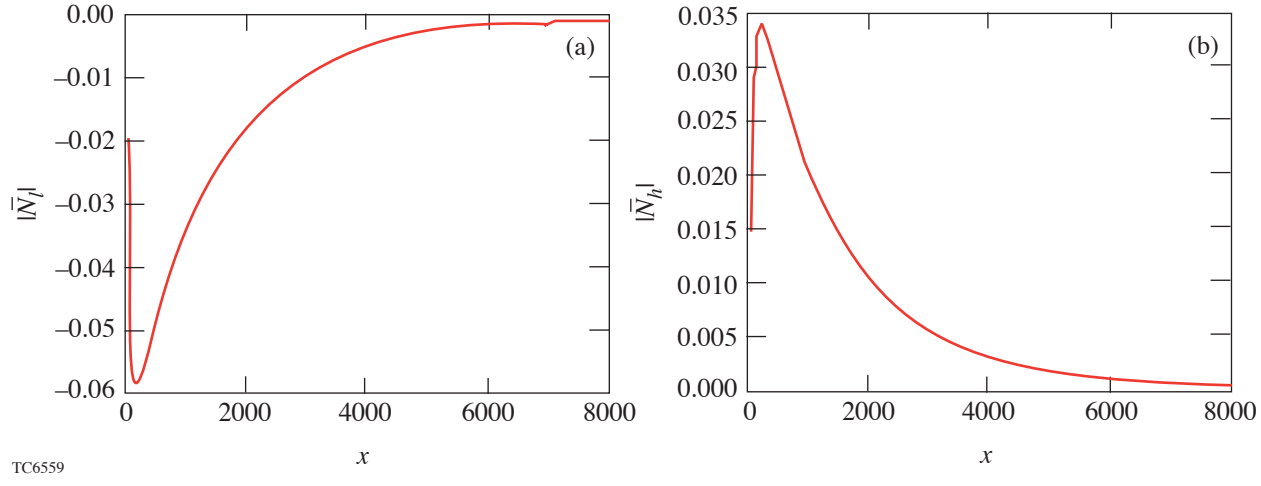


Figure 98.17
(a) First harmonic of light-ion and (b) heavy-ion densities versus distance for steady state of slow-wave SBS. Simulation parameters are the same as in Fig. 98.14.

slow wave $\overline{N}_h/\overline{N}_l < 0$.[17] Heavy ions are less mobile than light ions. Their density and velocity perturbations in the high-frequency field of the fast sound wave are smaller than the light-ion perturbations. The negative density ratio is a key feature of the slow sound wave. In the slow wave, light ions shield the electrostatic potential of the heavy ions and, hence, reduce the restoring force. The lower restoring force means lower frequency. At such low frequencies, heavy-ion perturbations are comparable to the light-ion perturbations.

4. Nonlinear Saturation

Figures 98.18–98.21 show the effects of hydrodynamic nonlinearities and pump depletion on the saturation of fast- and slow-wave SBS. The simulation parameters were listed in **Linear Regime of SBS** (p. 82). Similar to the one-ion case, the linear solution based on Eqs. (79)–(81), (51), and (57) was compared to the partially nonlinear solution based on Eqs. (79)–(81), (51), (32), and (33) and to the numerically obtained fully nonlinear solution, based on Eqs. (32), (33), and (76)–(78). This allowed us to separate the effects of hydrodynamic nonlinearities and pump depletion.

Steady-state reflectivities of fast-wave SBS are as follows: linear reflectivity $R_{LN} = 1.89\%$, partially nonlinear reflectivity $R_{PN} = 1.66\%$, and fully nonlinear reflectivity $R_{FN} = 1.6\%$. Pump depletion reduces reflectivity by 12%. Ion-acoustic nonlinearities reduce reflectivity by 3.8%.

Steady-state reflectivities of slow-wave SBS are as follows: linear reflectivity $R_{LN} = 8.29\%$, partially nonlinear reflectivity $R_{PN} = 5.09\%$, and fully nonlinear reflectivity $R_{FN} = 5.06\%$. Pump depletion reduces reflectivity by 39%. Ion-acoustic nonlinearities reduce reflectivity by 0.6%.

Nonlinear steepening of fast and slow sound waves was investigated in Ref. 17. In CH plasmas, the fast wave steepens much more than the slow wave. Wave steepening can be considered the generation of higher-order harmonics. Stronger steepening means that the amplitudes of the higher-order harmonics are bigger. These observations explain the difference in the effect of hydrodynamic nonlinearities on the saturation of fast- and slow-wave SBS. The reflectivity of slow-wave SBS is bigger than that of the fast-wave SBS. Consequently, the amplitude of the fast sound wave is smaller than that of the slow sound wave. On the other hand, if the fast- and slow-wave amplitudes were comparable, hydrodynamic nonlinearities would affect the fast-wave SBS much more than the slow-wave SBS. If the slow-wave reflectivity is much

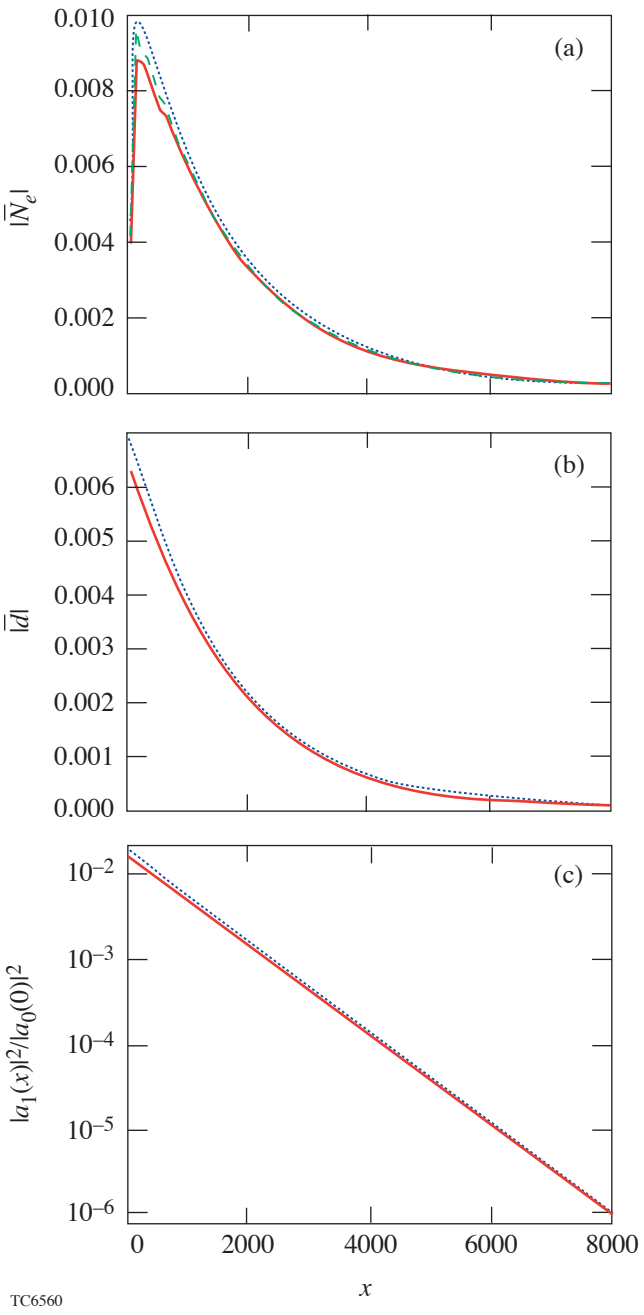


Figure 98.18
(a) First harmonic of electron density; (b) ponderomotive potential amplitude; (c) Stokes-wave intensity normalized to pump-wave intensity versus distance for steady state of fast-wave SBS. Dotted lines represent numerical solution of linearized equations (51), (57), and (79)–(81). Dashed lines represent numerical solution of partially nonlinear equations (32), (33), (51), and (79)–(81). Solid lines represent numerical solution of fully nonlinear equations (32), (33), and (76)–(78). Simulation parameters are the same as in Fig. 98.14.

higher than the fast-wave reflectivity, the slow-wave amplitude is much bigger than the fast-wave amplitude, in which case the effects of hydrodynamic nonlinearities can be more important for the slow wave than the fast wave. For the stated simulation parameters, the slow-wave reflectivity is not much higher than the fast-wave reflectivity $\left(R_{\mathrm{fa}} \approx 1\%,\ R_{\mathrm{sl}} \approx 5\%\right)$. In this case, hydrodynamic nonlinearities affect the fast-wave SBS more strongly than slow-wave SBS. Hydrodynamic nonlinearities reduce the fast-wave reflectivity by 3.8%, whereas they only reduce the slow-wave reflectivity by 0.6%

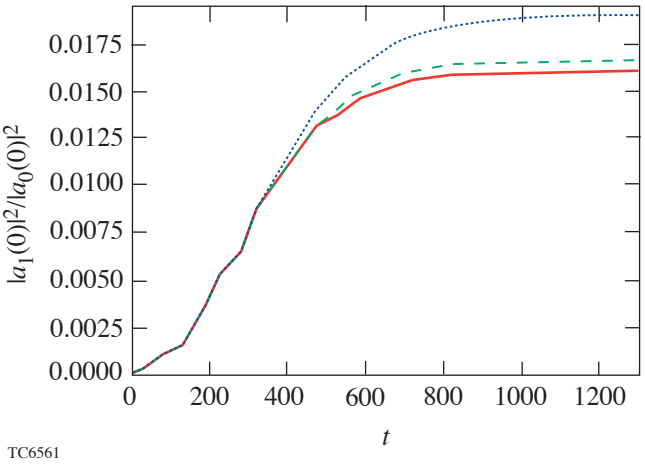


Figure 98.19
Reflectivities versus time for fast-wave SBS. Dotted lines represent numerical solution of linearized equations (51), (57), and (79)–(81). Dashed lines represent numerical solution of partially nonlinear equations (32), (33), (51), and (79)–(81). Solid lines represent numerical solution of fully nonlinear equations (32), (33), and (76)–(78). Simulation parameters are the same as in Fig. 98.14.

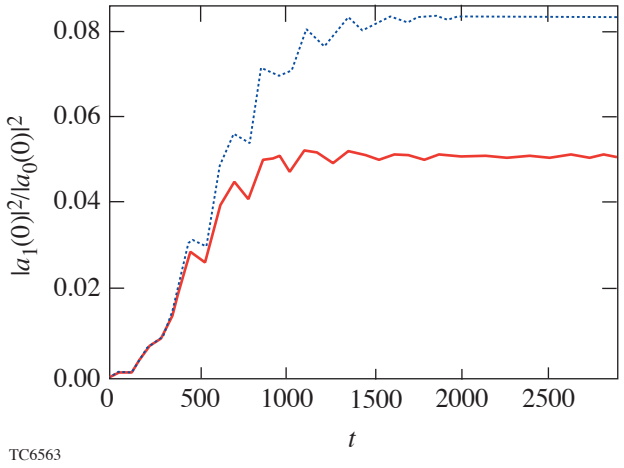


Figure 98.21
Reflectivities versus time for slow-wave SBS. Dotted lines represent numerical solution of linearized equations (51), (57), and (79)–(81). Dashed lines represent numerical solution of partially nonlinear equations (32), (33), (51), and (79)–(81). Solid lines represent numerical solution of fully nonlinear equations (32), (33), and (76)–(78). Simulation parameters are the same as in Fig. 98.14.

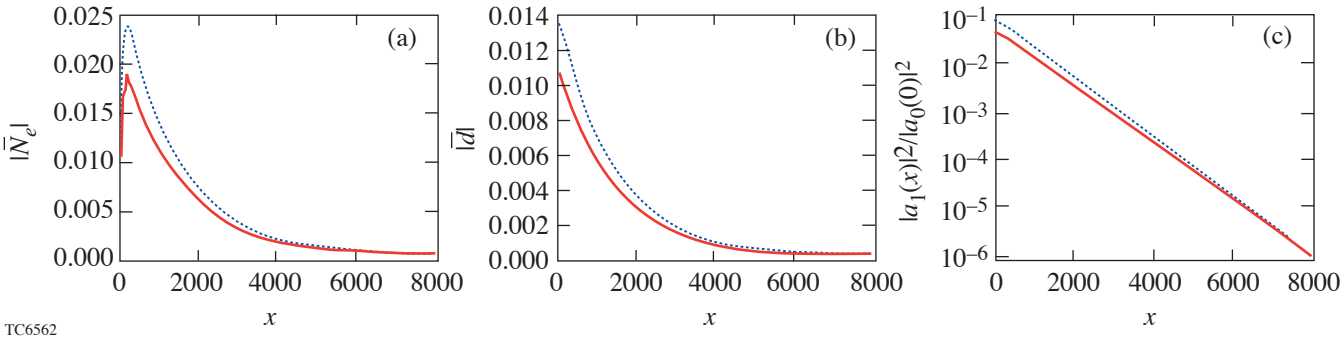


Figure 98.20
(a) First harmonic of electron density; (b) ponderomotive potential amplitude; (c) Stokes-wave intensity normalized to pump-wave intensity versus distance for steady state of slow-wave SBS. Dotted lines represent numerical solution of linearized equations (51), (57), and (79)–(81). Dashed lines represent numerical solution of partially nonlinear equations (32), (33), (51), and (79)–(81). Solid lines represent numerical solution of fully nonlinear equations (32), (33), and (76)–(78). Simulation parameters are the same as in Fig. 98.14.

The pump-wave intensities in fast- and slow-wave SBS are plotted as functions of distance in Figs. 98.22 and 98.23, respectively. Pump intensities are normalized to input pump intensity. The output pump intensity

$$\left|A_0(L)\right|^2 / I = 1 - R_{\mathrm{PN}} + \left|A_1(L)\right|^2 / I .$$

Light scattering by the slow sound wave decreases the pump intensity much more than scattering by the fast sound wave because the reflectivity of slow-wave SBS is higher than that of fast-wave SBS.

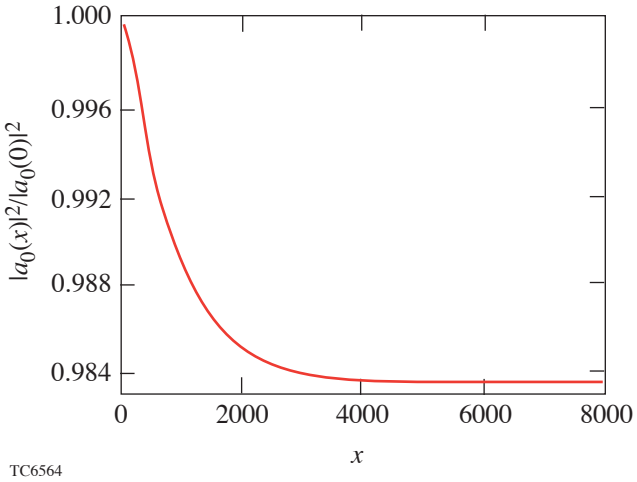


Figure 98.22
Pump-wave intensity normalized to input pump intensity versus distance for steady state of fast-wave SBS. Simulation parameters are the same as in Fig. 98.14.

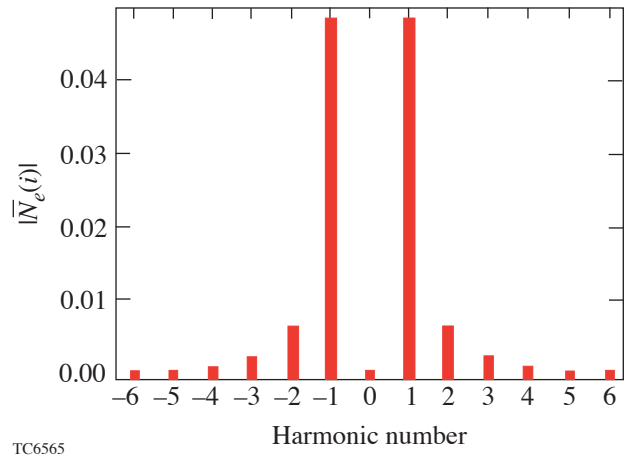


Figure 98.23
Fourier spectra of electron density near the point where it has maximal amplitude for steady state of fast-wave SBS. Simulation parameters are the same as in Fig. 98.14.

Higher-order harmonic generation is demonstrated by plotting discrete Fourier spectra of electron density near the point where it has maximal amplitude. The absolute values of the steady-state harmonics associated with the fast- and slow-wave SBS are shown in Figs. 98.24 and 98.25, respectively. The second- and higher-order harmonics are small in both the fast and slow sound waves because the amplitudes of both sound waves are small. The higher-order harmonics of fast-

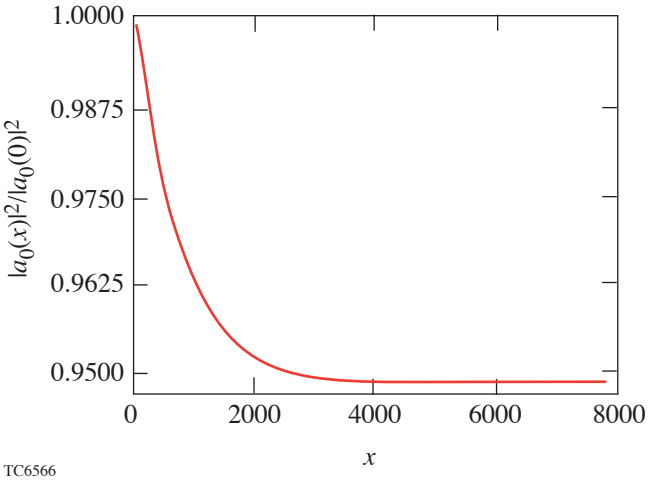


Figure 98.24
Pump-wave intensity normalized to input pump intensity versus distance for steady state of slow-wave SBS. Simulation parameters are the same as in Fig. 98.14.

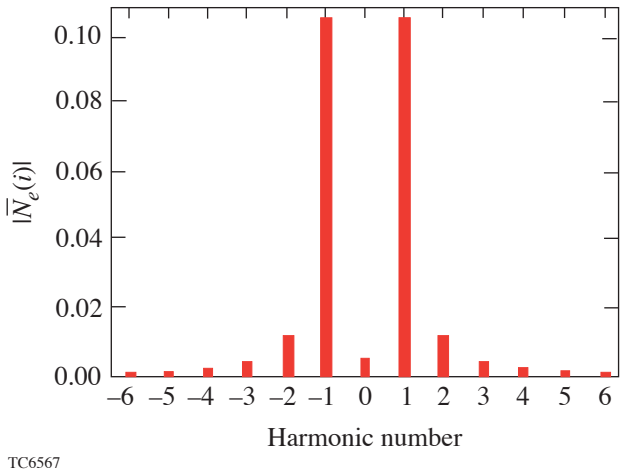


Figure 98.25
Fourier spectra of electron density near the point where it has maximal amplitude for steady state of slow-wave SBS. Simulation parameters are the same as in Fig. 98.14.

wave SBS are larger than the higher-order harmonics of slow-wave SBS because in CH plasmas the fast wave steepens much more than the slow wave. Consequently the effects of hydrodynamic nonlinearities on both the fast- and slow-wave SBS are small. They are noticeable for the fast-wave SBS but negligible for the slow-wave SBS.

**Summary**

A fluid model with phenomenological damping terms was used to study convective SBS in one- and two-ion plasmas. The Landau-damping rates were evaluated using formulas from kinetic theory. A fluid code was developed and tested by comparing its predictions to analytical formulas for SBS in the linear regime. SBS was simulated in carbon and hydrocarbon (CH) plasmas with OMEGA-like parameters. Two types of sound waves (fast and slow) exist in two-ion plasmas, each of which can participate in SBS. SBS from fast and slow sound waves were separated by choosing the beat frequency of the ponderomotive potential. The fast-wave reflectivity is lower than the slow-wave reflectivity because the Landau damping of the fast wave is stronger than the Landau damping of the slow wave. Effects of hydrodynamic nonlinearities and pump depletion on saturation of SBS in one- and two-ion plasmas were compared. The pump depletion significantly reduces reflectivity in one- and two-ion plasmas. The hydrodynamic nonlinearities are important for the SBS in one-ion carbon plasmas and noticeable for the fast-wave SBS in two-ion CH plasmas, but negligible for the slow-wave SBS.

Acknowledgment

The authors would like to thank D. D. Meyerhofer, W. Seka, J. Myatt, V. N. Goncharov, K. Vagin, I. Kuzora, and S. Urupin for fruitful discussions on this topic. This work was supported by the Department of Energy (DOE) Office of Inertial Confinement Fusion, under Cooperative Agreement No. DE-FC03-92SF19460, the University of Rochester, the New York State Research and Development Authority, and the Civilian Research and Development Foundation, under Award No. RP1-2268. The support of DOE does not constitute an endorsement by DOE of the views expressed in this article.

REFERENCES

1. W. L. Kruer, *The Physics of Laser-Plasma Interactions*, Frontiers in Physics, Vol. 73, edited by D. Pines (Addison-Wesley, Redwood City, CA, 1988), Chap. 4, pp. 37–43.

2. R. L. McCrory and J. M. Soures, in *Laser-Induced Plasmas and Applications*, edited by L. J. Radziemski and D. A. Cremers (Marcel Dekker, New York, 1989), pp. 207–268.

3. N. A. Krall and A. W. Trivelpiece, *Principles of Plasma Physics* (San Francisco Press, Inc., San Francisco, 1986).

4. J. A. Heikkinen, S. J. Karttunen, and R. R. E. Salomaa, Phys. Fluids **27**, 707 (1984).

5. W. Rozmus *et al.*, Phys. Fluids B **4**, 576 (1992).

6. B. I. Cohen *et al.*, Phys. Plasmas **4**, 956 (1997).

7. B. D. Fried, R. B. White, and T. K. Samec, Phys. Fluids **14**, 2388 (1971).

8. H. X. Vu, J. M. Wallace, and B. Bezzerides, Phys. Plasmas **1**, 3542 (1994).

9. E. A. Williams, R. L. Berger, R. P. Drake, A. M. Rubenchik, B. S. Bauer, D. D. Meyerhofer, A. C. Gaeris, and T. W. Johnston, Phys. Plasmas **2**, 129 (1995).

10. M. V. Kozlov and C. J. McKinstrie, Laboratory for Laser Energetics Report No. 321, NTIS document No. DOE/SF/19460-385, University of Rochester (2001). Copies may be obtained from the National Technical Information Service, Springfield, VA 22161.

11. J. D. Hoffman, *Numerical Methods for Engineers and Scientists* (McGraw-Hill, New York, 1992).

12. W. H. Press *et al.*, *Numerical Recipes in FORTRAN: The Art of Scientific Computing*, 2nd ed. (Cambridge University Press, Cambridge, England, 1992).

13. N. M. Kroll, J. Appl. Phys. **36**, 34 (1965); A. V. Maximov *et al.*, Phys. Plasmas **7**, 4227 (2000).

14. C. J. McKinstrie, R. E. Giacone, and E. A. Startsev, Phys. Plasmas **6**, 463 (1999).

15. V. V. Kurin and G. V. Permitin, Sov. J. Plasma Phys. **8**, 365 (1982).

16. S. J. Karttunen and R. R. E. Salomaa, Phys. Lett. A **72**, 336 (1979).

17. M. V. Kozlov and C. J. McKinstrie, Phys. Plasmas **9**, 3783 (2002).

# Imprint Efficiency Measurements in Laser-Driven Plastic Foils Using Beams with Different Angles of Incidence

## Introduction

The goal of the direct-drive approach to inertial confinement fusion (ICF)[1,2] is to uniformly implode a spherical target with deuterium–tritium (DT) fuel using a large number of overlapped laser beams. A combination of high temperature and high areal density ($\rho R$) in the DT fuel at peak compression is necessary to ignite the target and achieve high gain.[1–3] The most-significant factor that limits the implosion performance is the unstable growth of target perturbations. As a result of this growth, the fuel temperature and compression may be reduced, leading to a reduction in the thermonuclear yield. The target perturbations in direct-drive ICF include existing imperfections of the inner and outer target surfaces and are dominated by modulations seeded (or imprinted) by the spatial laser nonuniformities;[4–29] therefore, understanding and controlling laser imprinting are crucial to the success of direct-drive ICF.

Spatial modulations in laser intensity are imprinted into the target in the first few hundred picoseconds of the drive. As the laser light is applied to the target, the pressure created by the target ablation launches a shock wave that compresses the target.[30,31] Any nonuniformities in the laser drive modulate the ablation pressure. The modulations in surface acceleration provide the seeds for hydrodynamic instabilities. Later, as a large volume of plasma develops, the laser modulations decouple from the target surface, smoothing the ablation pressure. The imprinted front-surface (or ablation-surface) perturbations continue to evolve as the shock-driven Richtmyer–Meshkov (RM) instability causes the modulations to grow; the ablation stabilizes this growth.[18,32] As a result, the ablation-surface nonuniformities oscillate during the shock propagation to the rear surface of the target. The amplitude and frequency of these oscillations are defined by the modulation wavelength, the sound speed, the ablation, and the expanding (or "blowoff") plasma velocities.[32] Because the shock is launched by a modulated laser drive, the shock front is also distorted. The amplitude of this distortion oscillates as it propagates through the target with a frequency determined by the modulation wavelength and the drive intensity.[30,31] When the shock front reaches the rear surface of the target, it sends the rarefaction wave back to the ablation surface; shortly thereafter, the target starts to accelerate. During the acceleration phase, the ablation-surface modulations grow exponentially due to Rayleigh–Taylor (RT) instability.[2,3]

A number of techniques have been developed to reduce laser imprinting in direct-drive ICF facilities. A combination of distributed phase plates (DPP's),[33] polarization smoothing (PS),[34] and smoothing by spectral dispersion (SSD)[35] is employed on the OMEGA laser.[36] Induced spatial incoherence (ISI)[37] is used on the NIKE laser system. Partially coherent light (PCL)[38] in combination with random-phase plates is used on the GEKKO-XII laser facility. Targets with foam-buffered layers, high-$Z$ overcoat, and a combination of the two have been demonstrated to reduce imprinting.[5–7,11,16,20,23–25,27–29]

The first measurements[5] of laser-imprinted modulations were performed using a side-on geometry, where the diagnostic x rays penetrate a planar target in the direction perpendicular to its motion. Almost all subsequent imprinting studies were performed using a face-on geometry where the diagnostic x rays penetrate the target in the direction along its motion, allowing more-quantitative measurements of target perturbations. Face-on radiography is sensitive to variations in the target density thickness, or areal density ($\rho R$), which includes not only the ablation-front modulations (existing or laser imprinted), $\delta\left[\rho R_{\mathrm{abl}}(t)\right]$ at time $t$, but also any shock-front modulation in the bulk of the target, $\delta\left[\rho R_{\mathrm{sh}}(t)\right]$:

$$\delta\left[\rho R(t)\right] = \delta\left[\rho R_{\mathrm{abl}}(t)\right] + \delta\left[\rho R_{\mathrm{sh}}(t)\right]. \qquad (1)$$

Early imprint experiments[8–10,12,14,15,17–19] were performed at or before shock breakout on the rear surface of the target (before the onset of the RT growth), when the ablation- and shock-front modulations are of the same order of magnitude, $\delta\left[\rho R_{\mathrm{abl}}(t)\right] \cong \delta\left[\rho R_{\mathrm{sh}}(t)\right]$. Intended to be measurements of the ablation-surface imprinted perturbations (initial seed for the RT instability), the resulting areal-density modulations also included the shock-front perturbations.[30,31] Later experiments

observed shock-front and ablation-surface evolutions during shock transit before the beginning of the RT growth.[30,31,39–41]

To quantify imprinted modulation levels, imprint efficiency measurements[10,14,26] have used the acceleration-phase RT growth to magnify the ablation-front modulations in order to separate them from the shock-front modulations. Figure 98.26 (from Ref. 34) schematically presents the idea behind these experiments using simulations by the 2-D code *ORCHID*.[42] The solid curve shows the evolution of the areal-density modulation of an initially smooth target driven by a laser having a single-mode intensity modulation at 60-$\mu$m spatial wavelength, while the dotted curve shows the evolution of the single-mode, 60-$\mu$m-wavelength, preimposed perturbation driven by a spatially perfect laser. The solid curve starts at zero and rises as imprinting begins, while the dotted curve starts at its preimposed level. The RT growth (starting at ~400 ps) amplifies the imprinted and imposed ablation-front perturbations in the same manner and, when ablation-front modulations become higher than shock-front modulations, $\delta\left[\rho R_{\mathrm{abl}}(t)\right] > \delta\left[\rho R_{\mathrm{sh}}(t)\right]$, the areal-density evolutions become similar (dotted and solid curves are parallel after 0.5 ns). The equivalent surface amplitude of imprinting at a particular mode number $k$ is defined by extrapolating (dashed curve) the temporal evolution of the imprinted modulation (solid curve) back to $t = 0$ using the behavior of the preimposed mode (dotted curve):

$$\eta_{\mathrm{imp}}(k,t=0) = \eta_{\mathrm{pre}}(k,t=0) \times \left\{\delta\left[\rho R_{\mathrm{imp}}(k,t)\right] \Big/ \delta\left[\rho R_{\mathrm{pre}}(k,t)\right]\right\}, \qquad (2)$$

where $\eta_{\mathrm{pre}}(k,t=0)$ is the initial amplitude of the preimposed modulation and $\delta\left[\rho R_{\mathrm{imp}}(k,t)\right]$ and $\delta\left[\rho R_{\mathrm{pre}}(k,t)\right]$ are the measured areal-density modulations of imprinted and imposed perturbations during linear RT growth, respectively. This technique is valid when (1) the amplitudes of imprinted and preimposed modulations are in the linear regime of the RT growth, and (2) the measurements are taken when the ablation-front modulations are large enough to dominate the measurements. The imprint efficiency $E(k)$ was defined[10,14] as the initial amplitude of equivalent surface modulation $\eta_{\mathrm{imp}}(k,t=0)$, normalized to the relative laser modulation $\delta I(k)/I$, that produced it:

$$E(k) = \eta_{\mathrm{imp}}(k,t=0) \Big/ \left[\delta I(k)/I\right]. \qquad (3)$$

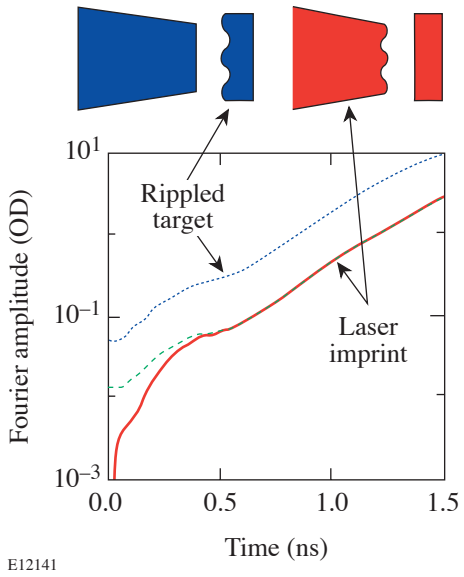


Figure 98.26
Definition of the equivalent surface amplitude using an *ORCHID* simulation of a single-mode, 60-$\mu$m-wavelength, imprinted modulation (solid curve) calibrated to a preimposed (dotted curve) modulation (from Ref. 34). The equivalent surface amplitude of imprinting at a particular mode number $k$ is defined by extrapolating (dashed curve) the temporal evolution of the imprinted modulation (solid curve) back to $t = 0$, using the behavior of the preimposed mode (dotted curve) and Eq. (2).

In direct-drive implosions, a spherical shell is illuminated by a large number of overlapping laser beams. Each beam diameter is roughly equal to that of the target; therefore, different parts of the beam irradiate the target at different angles of incidence: the central part of the beam is nearly normally incident to the target, while the outer parts of the beam irradiate the target at oblique angles. As a result it is important to investigate the effect of the beam angle of incidence on imprint efficiency. Recently, the imprint efficiency measurements for three different angles of incidence were performed for the first time in targets and laser intensities relevant to the spherical implosion program on OMEGA.[43] This article presents details of the techniques and analysis of the imprint efficiency measurements and is considered complimentary to Ref. 43.

## Experimental Configuration

Figure 98.27(a) shows schematically the experimental configuration, previously used in a number of experiments.[20–22,26,34] The 20-$\mu$m-thick plastic targets were irradiated by 351-nm laser light at ~2 × $10^{14}$ W/cm$^2$ using seven overlapped beams with a 3-ns square pulse shape on the

OMEGA laser system.[36] The imprint efficiencies at 60-$\mu$m spatial wavelength were with and without 0.2-THz SSD.[35] Targets with preimposed, single-mode, two-dimensional, 60-$\mu$m sinusoidal perturbations were used to determine the imprint efficiency: one target with 0.125-$\mu$m initial amplitude and the other with 0.05-$\mu$m initial amplitude. The temporal growth of target perturbations was measured using x-ray, face-on radiography. The targets were backlit with x rays produced by a uranium backlighter located 9 mm away from the driven foil and irradiated at ~$1 \times 10^{14}$ W/cm$^2$ using 12 additional beams. X rays transmitted through the target and a 3-$\mu$m-thick aluminum debris shield (located between the backlighter and the driven foil) were imaged by the 8-$\mu$m pinhole array on a framing camera filtered with 6 $\mu$m of aluminum.[20–22] This yielded the highest sensitivity for the average photon energy of ~1.3 keV. The distance between the target and the pinhole array was 2.5 cm, and the magnification was 14.4. The framing camera recorded eight images in each shot with a temporal resolution of ~80 ps and a spatial resolution in a target plane of ~10 $\mu$m.[44] The framing camera images were captured on Kodak T-Max 3200 film, which was digitized with a 20-$\mu$m-sq scanning aperture. The measured target optical depth (which is proportional to the target areal density) is the natural logarithm of the intensity-converted images of a target.

Figure 98.27(b) shows the laser-beam configuration. Six beams (numbers 34, 36, 38, 41, 43, and 49) were incident at 23° to a target normal, while one beam (number 48) was incident at 48° to a target normal. The 23° beams had DPP's[33] and PS.[34] An equivalent-target-plane image of one such beam is shown in Fig. 98.28(a). These beams had a broadband spectrum of modulations with the smallest features having spatial wavelengths of ~2.5 $\mu$m. Beam 48 [shown in Fig. 98.28(b)], incident at a more-oblique 48° angle, had 2-D, 60-$\mu$m-wavelength intensity modulations (together with several higher harmonics) to distinguish it from the 23° beams. The beam modulations were oriented along the direction of its propagation, so the imprinted target modulations had the same wavelengths as the laser modulations. The 2-D laser modulations were used to

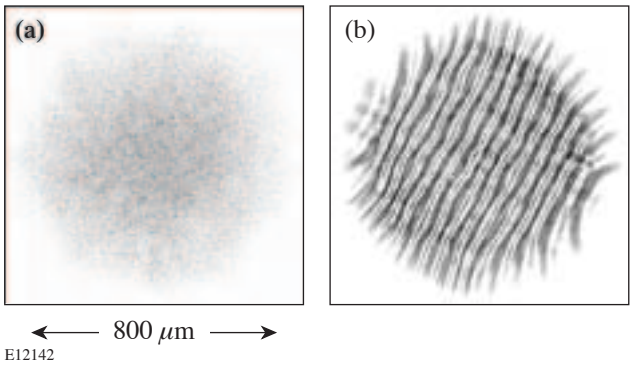


Figure 98.28
Beam images of the (a) 23° beam having 3-D broadband perturbations and (b) 48° beam having 2-D, 60-$\mu$m-wavelength perturbation.

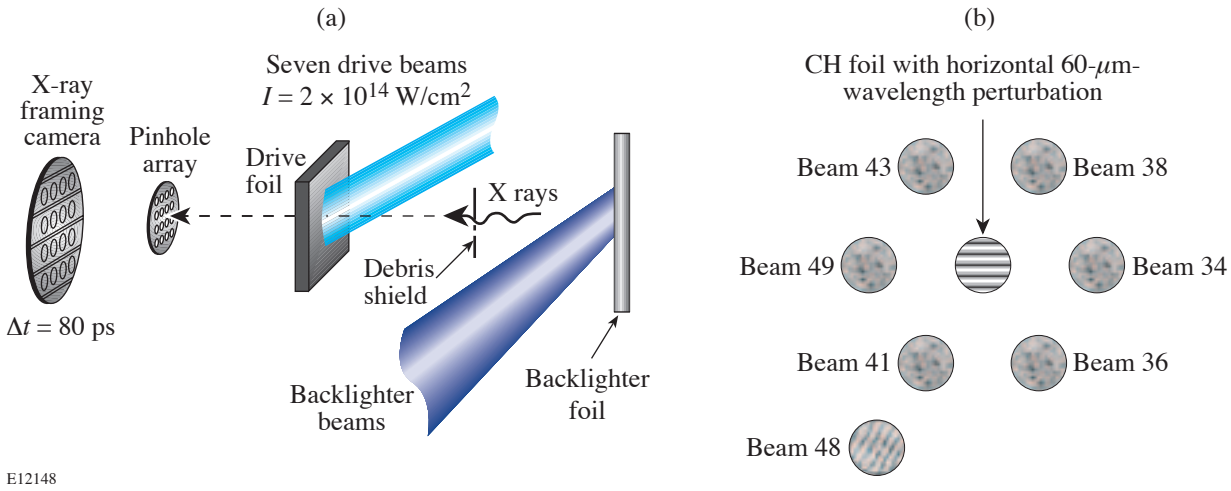


Figure 98.27
(a) Experimental configuration (from Ref. 22); (b) beam and target configuration. Diagonal 2-D perturbations at 60-$\mu$m wavelength come from beam 48 incident at 48° to a target normal, while 3-D broadband perturbations come primarily from beams 34, 36, 38, 41, 43, and 49 incident at 23° to the target normal. The target has a horizontal, preimposed, single-mode, 60-$\mu$m-wavelength perturbation used for calibration.

separate perturbations caused by the 48° beam from the 3-D broadband modulations caused by the 23° beams in the radiogram of the driven target. Figure 98.29(a) shows the profile of the relative intensity incident on the target (averaged in the direction along the 2-D perturbations), calculated using measured beam intensities [Figs. 98.28(a) and 98.28(b)] and taking into account experimentally measured beam energies, effects of beam overlap, and obliquity angles. Figure 98.29(b) presents the Fourier amplitude of this lineout showing the laser perturbations at 60-$\mu$m wavelength (together with the higher harmonics) clearly distinguishable from the other broadband laser modulations. The laser modulations were analyzed in nine different square areas (with a box size of $L = 300$ $\mu$m, the same size as in the target x-ray radiographs shown later) of ~800-$\mu$m laser spots, and it was found that the modulations were reasonably constant across the laser-spot size. The amplitudes of relative laser modulations at a spatial frequency of 17 mm$^{-1}$ (corresponding to a spatial wavelength of 60 $\mu$m) were 6.3±0.4% for the two-dimensional modulation (from the 48° beam) and 0.54±0.09% for the broadband modulations (from the 23° beams), as calculated in the nine different areas.

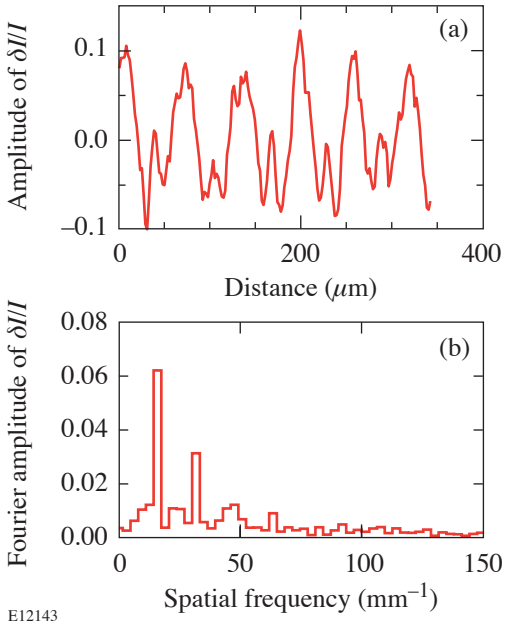


Figure 98.29
(a) Profile of the relative intensity incident on the target averaged in the direction along the 2-D laser perturbations. (b) Fourier amplitude of this profile showing the laser perturbations at a spatial frequency of 17 mm$^{-1}$ (corresponding to the 60-$\mu$m wavelength) together with the higher harmonics clearly distinguishable from the other broadband laser modulations.

## Experimental Results

Figure 98.30(a) presents one of the eight images of target optical-depth modulations taken at ~1.9 ns after the beginning of the laser drive for the shot without SSD. The corresponding Fourier-space image of the target optical-depth modulations is shown in Fig. 98.30(b). Two-dimensional perturbations, imprinted from the 48° beam, are diagonal across the real-space image; they have distinctive first- and second-harmonic peaks in the Fourier-space image. The preimposed, 60-$\mu$m-wavelength perturbation is horizontal in the real-space image; therefore it has two vertical peaks in the Fourier-space image. The 3-D features in the real-space image are imprinted from the broadband perturbations of 23° beams; these perturbations are located in the broad area of the Fourier-space image. The profiles of the 2-D imprinted and preimposed modulations are presented in the Fig. 98.31. Figure 98.31(a) shows the optical-depth profile of the 2-D imprinted modulation averaged along the modulations, while Fig. 98.31(b) shows the profile of the 2-D preimposed modulation, averaged along the horizontal direction. The higher optical depth corresponds to thinner areas of the targets, or bubbles, while the lower optical depth corresponds to thicker target areas, or spikes. The profile of the imprinted optical-depth modulation resembles the profiles of the laser modulation [compare Figs. 98.29(a) and 98.31(a)].

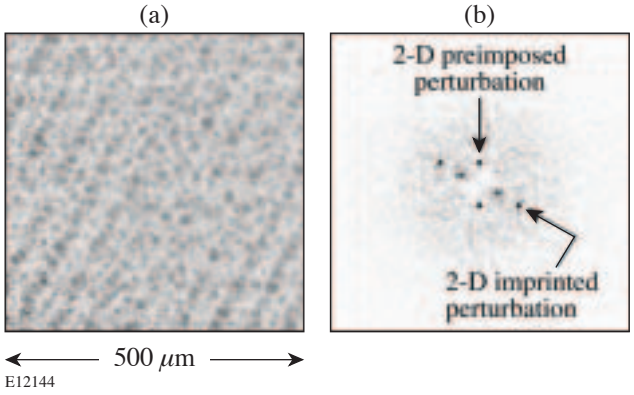


Figure 98.30
(a) Image of the target optical-depth modulations taken at ~1.9 ns after the beginning of the laser drive for the shot without SSD. (b) Fourier-space image of the target optical-depth modulations showing peaks for a diagonal 2-D, 60-$\mu$m wavelength and its second-harmonic imprinted modulations, and 2-D, 60-$\mu$m-wavelength, preimposed modulations in the vertical direction.

Figure 98.32 summarizes the results of the measured growth for all 60-$\mu$m-wavelength perturbations with imprinted modulations shown in Fig. 98.32(a) and preimposed modulations in Fig. 98.32(b) for two shots with and without SSD. Two-dimensional imprinted modulations from the 48° beam are

shown by the upper data (diamonds) in Fig. 98.32(a), and 3-D broadband modulations from the 23° beams are shown by the lower data (squares). The amplitudes of imprinted modulations are separated by about 0.5 ns in shots with and without SSD [Fig. 98.32(a)]. This is because the SSD reduces the initial amplitudes of imprinted modulations by a factor of ~2.5, and it takes longer for the RT growth to bring them to the same levels as for the shot without SSD. The initial amplitudes of preimposed modulations were 0.125 $\mu$m and 0.05 $\mu$m for the shots without and with SSD, respectively.

To satisfy the conditions for imprint efficiency measurements described in the **Introduction**, the growth measurements of 60-$\mu$m-wavelength perturbations were performed in the linear regime of RT instability. To confirm that the measured modulations were below the RT saturation levels, ablation-front amplitudes $\eta(k,t)$ were estimated from the measured optical-depth modulations OD$(k,t)$, the measured undriven target attenuation length $\lambda_{\text{eff}}$ = 10 $\mu$m, and the calculated (1-D hydrocode *LILAC*)[45] target compression $C_p \sim 3$, $\eta(k,t) = \text{OD}(k,t) \times \lambda_{\text{eff}} / C_p$. The amplitudes of 2-D, single-mode perturbations were calculated to be below 1 $\mu$m at all times for both shots (the 2-D saturation amplitude for the $\lambda$ = 60-$\mu$m wavelength is $S_{2\text{-D}}$ = 6 $\mu$m), and the amplitudes of 3-D, broadband perturbations were calculated to be below 0.1 $\mu$m in the square analysis area with a size of $L$ = 300 $\mu$m [the 3-D saturation amplitude[46,21] for the $\lambda$ = 60-$\mu$m wavelength is $S_{3\text{-D}} = \lambda^2/(2\pi^2 L) \cong 0.3\,\mu\text{m}$]. All measurements were performed 1.0 ns after the beginning of the drive, when the growth of imprinted and preimposed modulations was similar. All three types of target modulations (2-D imprinted, 2-D preimposed, and 3-D imprinted) at 60-$\mu$m wavelength grow with similar growth rates for each shot, as shown in Fig. 98.32. The solid lines in Fig. 98.32 show exponential fits to the experimental data. The inferred growth rates were 1.7±0.2 ns$^{-1}$, 1.5±0.2 ns$^{-1}$, and 1.6±0.2 ns$^{-1}$ for the 2-D imprinted, 2-D preimposed, and 3-D imprinted modulations, respectively, for the shot without SSD. The corresponding growth rates for the shot with SSD are 1.7±0.3 ns$^{-1}$, 2.0±0.3 ns$^{-1}$, and 2.1±0.3 ns$^{-1}$.

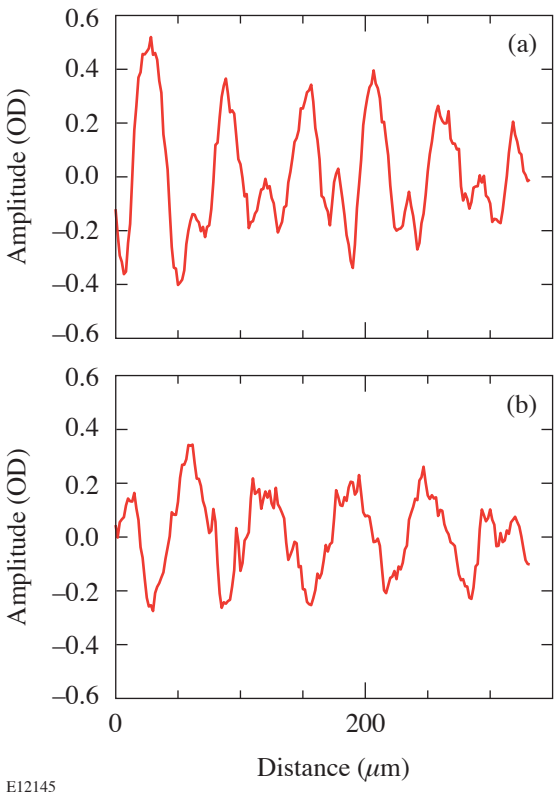


Figure 98.31
Optical-depth profiles of (a) the 2-D imprinted modulation and (b) the 2-D preimposed modulation taken at ~1.9 ns after the beginning of the laser drive.

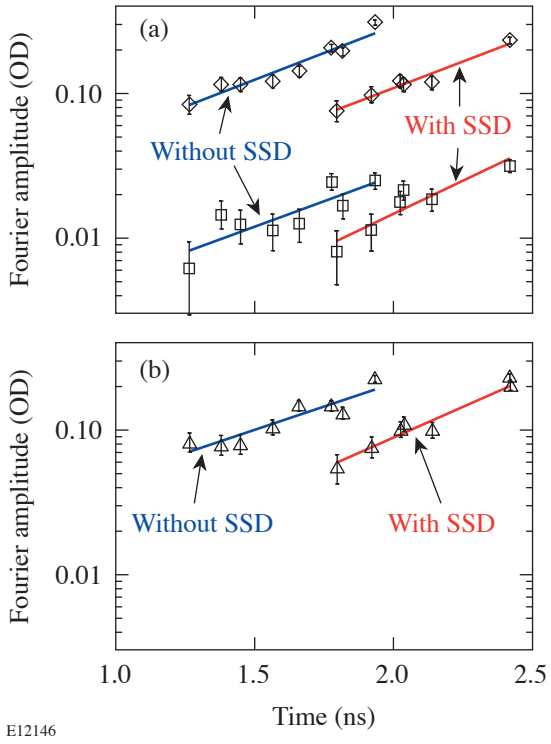


Figure 98.32
Fourier amplitudes of optical-depth modulations as a function of time for (a) 2-D imprinted modulations (diamonds, upper data), 3-D broadband modulations (squares, lower data), and (b) the 2-D preimposed modulations (triangles). Data with SSD comes later than the data without SSD.

The surface equivalent amplitude of an imprinted 2-D, 60-$\mu$m-wavelength perturbation from a 48° beam was $\eta_{\text{imp 2-D}}(t = 0) = 0.16\pm0.01$ $\mu$m, from Eq. (2). The initial modulation amplitude of 2-D preimposed modulation $\eta_{\text{pre 2-D}}(t = 0) = 0.125$ $\mu$m, and the ratios of measured optical-depth modulations at various times,

$$\delta\left[\rho R_{\text{imp 2-D}}(k,t)\right] \Big/ \delta\left[\rho R_{\text{pre 2-D}}(k,t)\right],$$

taken from Figs. 98.32(a) and 98.32(b). The surface equivalent amplitude of 3-D imprinted, 60-$\mu$m-wavelength perturbations from 23° beams was $\eta_{\text{imp 3-D}}(t = 0) = 0.016\pm0.001$ $\mu$m. The imprint efficiencies at 60-$\mu$m wavelength for 48° and 23° beams were $E_{48°} = 2.5\pm0.2$ $\mu$m and $E_{23°} = 3.0\pm0.3$ $\mu$m, respectively, as calculated using Eq. (3) and relative laser modulations $[\delta I(k)/I]_{48°} = 6.3\pm0.4\%$ for the 48° beam and $[\delta I(k)/I]_{23°} = 0.54\pm0.04\%$ for the 23° beams at a spatial wavelength of 60 $\mu$m. As shown in Ref. 43, the imprint efficiency for more-oblique beams is lower because these beams see an effectively longer length of plasma on the way to the ablation surface than the less-oblique beams; therefore, plasma smoothing is more effective for larger-angle-of-incidence beams.[43] Figure 98.32(a) shows the effect of SSD on imprint reduction. The imprinting amplitudes (of 23° and 48° beams) are reduced by a factor of ~2.5 at a spatial wavelength of 60 $\mu$m.

**Conclusions**

The first measurements of imprint efficiency for laser beams incident at two different angles (23° and 48°) to a target normal have been presented. The measurements were performed at a spatial wavelength of 60 $\mu$m with and without smoothing by spectral dispersion (SSD). The imprinted amplitudes were calibrated with preimposed, 60-$\mu$m-wavelength perturbations during the linear phase of RT growth. The measured imprint efficiencies at the spatial wavelength of 60 $\mu$m were 2.5±0.2 $\mu$m for the beam with a 48° angle of incidence and 3.0±0.3 $\mu$m for the beams with a 23° angle of incidence. The SSD reduced modulations by a factor of ~2.5 at the same spatial wavelength.

## ACKNOWLEDGMENT

This work was supported by the U.S. Department of Energy Office of Inertial Confinement Fusion under Cooperative Agreement No. DE-FC03-92SF19460, the University of Rochester, and the New York State Energy Research and Development Authority. The support of DOE does not constitute an endorsement by DOE of the views expressed in this article.

## REFERENCES

1. J. Nuckolls *et al.*, Nature **239**, 139 (1972).
2. S. E. Bodner, D. G. Colombant, J. H. Gardner, R. H. Lehmberg, S. P. Obenschain, L. Phillips, A. J. Schmitt, J. D. Sethian, R. L. McCrory, W. Seka, C. P. Verdon, J. P. Knauer, B. B. Afeyan, and H. T. Powell, Phys. Plasmas **5**, 1901 (1998).
3. J. D. Lindl, *Inertial Confinement Fusion: The Quest for Ignition and Energy Gain Using Indirect Drive* (Springer-Verlag, New York, 1998), Chap. 6, pp. 61–82.
4. M. H. Emery *et al.*, Phys. Fluids B **3**, 2640 (1991).
5. M. Desselberger *et al.*, Phys. Rev. Lett. **68**, 1539 (1992).
6. M. Desselberger *et al.*, Phys. Rev. Lett. **74**, 2961 (1995).
7. M. Dunne *et al.*, Phys. Rev. Lett. **75**, 3858 (1995).
8. R. J. Taylor *et al.*, Phys. Rev. Lett. **76**, 1643 (1996).
9. D. H. Kalantar, M. H. Key, L. B. Da Silva, S. G. Glendinning, J. P. Knauer, B. A. Remington, F. Weber, and S. V. Weber, Phys. Rev. Lett. **76**, 3574 (1996).
10. S. G. Glendinning, S. N. Dixit, B. A. Hammel, D. H. Kalantar, M. H. Key, J. D. Kilkenny, J. P. Knauer, D. M. Pennington, B. A. Remington, R. J. Wallace, and S. V. Weber, Phys. Rev. E **54**, 4473 (1996).
11. R. G. Watt, D. C. Wilson, R. E. Chrien, R. V. Hollis, P. L. Gobby, R. J. Mason, R. A. Kopp, R. A. Lerche, D. H. Kalantar, B. MacGowan, M. B. Nelson, T. Phillips, P. W. McKenty, and O. Willi, Phys. Plasmas **4**, 1379 (1997).
12. R. J. Taylor *et al.*, Phys. Rev. Lett. **79**, 1861 (1997).
13. C. J. Pawley *et al.*, Phys. Plasmas **4**, 1969 (1997).
14. S. V. Weber, S. G. Glendinning, D. H. Kalantar, M. H. Key, B. A. Remington, J. E. Rothenberg, E. Wolfrum, C. P. Verdon, and J. P. Knauer, Phys. Plasmas **4**, 1978 (1997).
15. D. H. Kalantar, M. H. Key, L. B. Da Silva, S. G. Glendinning, B. A. Remington, J. E. Rothenberg, F. Weber, S. V. Weber, E. Wolfrum, N. S. Kim, D. Neely, J. Zhang, J. S. Wark, A. Demir, J. Lin, R. Smith, G. J. Tallents, C. L. S. Lewis, A. MacPhee, J. Warwick, and J. P. Knauer, Phys. Plasmas **4**, 1985 (1997).
16. H. Azechi *et al.*, Phys. Plasmas **4**, 4079 (1997).
17. E. Wolfrum *et al.*, Phys. Plasmas **5**, 227 (1988).
18. A. L. Velikovich *et al.*, Phys. Plasmas **5**, 1491 (1998).
19. S. G. Glendinning, S. N. Dixit, B. A. Hammel, D. H. Kalantar, M. H. Key, J. D. Kilkenny, J. P. Knauer, D. M. Pennington, B. A. Remington, J. Rothenberg, R. J. Wallace, and S. V. Weber, Phys. Rev. Lett. **80**, 1904 (1998).

20. R. G. Watt, J. Duke, C. J. Fontes, P. L. Gobby, R. V. Hollis, R. A. Kopp, R. J. Mason, D. C. Wilson, C. P. Verdon, T. R. Boehly, J. P. Knauer, D. D. Meyerhofer, V. Smalyuk, R. P. J. Town, A. Iwase, and O. Willi, Phys. Rev. Lett. **81**, 4644 (1998).

21. V. A. Smalyuk, T. R. Boehly, D. K. Bradley, V. N. Goncharov, J. A. Delettrez, J. P. Knauer, D. D. Meyerhofer, D. Oron, and D. Shvarts, Phys. Rev. Lett. **81**, 5342 (1998).

22. V. A. Smalyuk, T. R. Boehly, D. K. Bradley, V. N. Goncharov, J. A. Delettrez, J. P. Knauer, D. D. Meyerhofer, D. Oron, D. Shvarts, Y. Srebro, and R. P. J. Town, Phys. Plasmas **6**, 4022 (1999).

23. D. G. Colombant *et al.*, Phys. Plasmas **7**, 2046 (2000).

24. V. N. Goncharov, S. Skupsky, T. R. Boehly, J. P. Knauer, P. McKenty, V. A. Smalyuk, R. P. J. Town, O. V. Gotchev, R. Betti, and D. D. Meyerhofer, Phys. Plasmas **7**, 2062 (2000).

25. A. J. Schmitt *et al.*, Phys. Plasmas **8**, 2287 (2001).

26. T. R. Boehly, V. N. Goncharov, O. Gotchev, J. P. Knauer, D. D. Meyerhofer, D. Oron, S. P. Regan, Y. Srebro, W. Seka, D. Shvarts, S. Skupsky, and V. A. Smalyuk, Phys. Plasmas **8**, 2331 (2001).

27. M. Nishikino *et al.*, Phys. Plasmas **9**, 1381 (2002).

28. M. Nakai *et al.*, Phys. Plasmas **9**, 1734 (2002).

29. S. P. Obenschain *et al.*, Phys. Plasmas **9**, 2234 (2002).

30. T. Endo *et al.*, Phys. Rev. Lett. **74**, 3608 (1995).

31. R. Ishizaki and K. Nishihara, Phys. Rev. Lett. **78**, 1920 (1997).

32. V. N. Goncharov, Phys. Rev. Lett. **82**, 2091 (1999).

33. Y. Lin, T. J. Kessler, and G. N. Lawrence, Opt. Lett. **20**, 764 (1995).

34. T. R. Boehly, V. A. Smalyuk, D. D. Meyerhofer, J. P. Knauer, D. K. Bradley, R. S. Craxton, M. J. Guardalben, S. Skupsky, and T. J. Kessler, J. Appl. Phys. **85**, 3444 (1999).

35. S. P. Regan, J. A. Marozas, J. H. Kelly, T. R. Boehly, W. R. Donaldson, P. A. Jaanimagi, R. L. Keck, T. J. Kessler, D. D. Meyerhofer, W. Seka, S. Skupsky, and V. A. Smalyuk, J. Opt. Soc. Am. B **17**, 1483 (2000).

36. T. R. Boehly, D. L. Brown, R. S. Craxton, R. L. Keck, J. P. Knauer, J. H. Kelly, T. J. Kessler, S. A. Kumpan, S. J. Loucks, S. A. Letzring, F. J. Marshall, R. L. McCrory, S. F. B. Morse, W. Seka, J. M. Soures, and C. P. Verdon, Opt. Commun. **133**, 495 (1997).

37. R. H. Lehmberg and S. P. Obenschain, Opt. Commun. **46**, 27 (1983).

38. H. Nakano *et al.*, J. Appl. Phys. **73**, 2122 (1993).

39. Y. Aglitskiy *et al.*, Phys. Rev. Lett. **87**, 265001 (2001).

40. Y. Aglitskiy *et al.*, Phys. Rev. Lett. **87**, 265002 (2001).

41. Y. Aglitskiy *et al.*, Phys. Plasmas **9**, 2264 (2002).

42. R. L. McCrory and C. P. Verdon, in *Computer Applications in Plasma Science and Engineering*, edited by A. T. Drobot (Springer-Verlag, New York, 1991), Chap. 11, pp. 291–325.

43. V. A. Smalyuk, J. A. Delettrez, S. B. Dumanis, R. Epstein, V. Yu. Glebov, D. D. Meyerhofer, P. B. Radha, T. C. Sangster, C. Stoeckl, N. C. Toscano, J. A. Frenje, C. K. Li, R. D. Petrasso, F. H. Séguin, and J. H. Koch, "Hot-Core Characterization of the Cryogenic $D_2$ Target at Peak Neutron Production in Direct-Drive Spherical Implosion," to be submitted to Physical Review Letters.

44. V. A. Smalyuk, T. R. Boehly, D. K. Bradley, J. P. Knauer, and D. D. Meyerhofer, Rev. Sci. Instrum. **70**, 647 (1999).

45. J. Delettrez, R. Epstein, M. C. Richardson, P. A. Jaanimagi, and B. L. Henke, Phys. Rev. A, Gen. Phys. **36**, 3926 (1987).

46. M. J. Dunning and S. W. Haan, Phys. Plasmas **2**, 1669 (1995).

# Stopping of Directed Energetic Electrons in High-Temperature Hydrogenic Plasmas

A basic problem in plasma physics is the interaction and energy loss of energetic charged particles in plasmas.[1–4] This problem has traditionally focused on ions (i.e., protons, alphas, etc.), either in the context of heating and/or ignition in, for example, inertial confinement fusion (ICF)[3–6] or the use of these particles for diagnosing implosion dynamics.[7] More recently, prompted in part by the concept of fast ignition for ICF,[8] scientists have begun considering energy deposition from relativistic fast electrons in deuterium–tritium (DT) plasmas.[8–13] Tabak *et al.*[8] used, for example, the energy deposition of Berger and Seltzer,[14] which is based on the continuous slowing down of electrons in cold matter. This treatment, though quite similar to electrons slowing in plasmas, does not include the effects of scattering. Deutsch *et al.*[9] addressed this issue by considering the effects of scattering off the background ions;[16,17] they ignored scattering due to background electrons.

In another important context in ICF, researchers addressed the issue of fuel preheat due to energetic electrons (~50 to 300 keV),[5,18,19] the consequence of which is to elevate the fuel adiabat to levels that would prohibit ignition. This article shows that scattering effects could be significant for quantitative evaluations of preheat.

The starting point for these calculations is the relativistic elastic differential cross sections for electrons scattering off fully ionized ions of charge $Z$ (Refs. 20–22) and off the neutralizing bath of electrons,[21,23,24] which are approximated as

$$\left(\frac{d\sigma}{d\Omega}\right)^{\mathrm{ei}} \approx \frac{Z^2}{4}\left(\frac{r_0}{\gamma\beta^2}\right)^2 \frac{1}{\sin^4\theta/2}, \tag{1}$$

$$Z\left(\frac{d\sigma}{d\Omega}\right)^{\mathrm{ee}} \approx Z\frac{(\gamma+1)^2}{\left(2\sqrt{(\gamma+1)/2}\right)^4}\left(\frac{r_0}{\gamma\beta^2}\right)^2 \frac{1}{\sin^4\theta/2}, \tag{2}$$

where $\beta = v/c, \gamma = \left(1-\beta^2\right)^{-1/2}$, and $r_0 = e^2/m_0c^2$ is the classical electron radius. The relative importance of electron scattering is implied from the ratio

$$\Re = Z\left(\frac{d\sigma}{d\Omega}\right)^{\mathrm{ee}} \Big/ \left(\frac{d\sigma}{d\Omega}\right)^{\mathrm{ei}} \approx \frac{4(\gamma+1)^2}{\left(2\sqrt{(\gamma+1)/2}\right)^4}\frac{1}{Z}. \tag{3}$$

For a hydrogenic plasma ($Z$ = 1) and for $\gamma \lesssim 10$, $\Re \sim 1$, indicating that the electron component is equally important. As best we can tell, the electron-scattering component has been largely ignored since it was typically assumed, usually justifiably, that ion scattering dominates. This will not be the case, however, for problems discussed here, for relativistic astrophysical jets,[25] or for many of the present high-energy laser–plasma experiments[26] for which $Z \sim 1$ and $\gamma \lesssim 10$.

To calculate the effects of multiple scattering, a Boltzmann-like diffusion equation is used:[27]

$$\frac{\partial f}{\partial s} + \mathbf{v}\cdot\nabla f = n_i \int \left[f(\mathbf{x},\mathbf{v}',s) - f(\mathbf{x},\mathbf{v},s)\right]\sigma\left(|\mathbf{v}-\mathbf{v}'|\right)d\mathbf{v}', \tag{4}$$

where $f$ is the angular distribution function of the scattered electrons, $n_i$ is the number density of plasma ions of charge $Z$, $\mathbf{x}$ is the position where scattering occurs, and $\sigma = \sigma_{\mathrm{ei}} + Z\sigma_{\mathrm{ee}}$ is the total scattering cross section, where $\sigma_{\mathrm{ei}} = \int \left(d\sigma/d\Omega\right)^{\mathrm{ei}} d\Omega$ and $\sigma_{\mathrm{ee}} = \int \left(d\sigma/d\Omega\right)^{\mathrm{ee}} d\Omega$. Equation (4) is solved in cylindrical coordinates with the assumption that the scattering is azimuthally symmetric. The solution that satisfies the boundary conditions is[27,28]

$$f(\theta,s) = \frac{1}{4\pi}\sum_{\ell=0}^{\infty}(2\ell+1)P_\ell(\cos\theta)\exp\left[-\int_0^s \sigma_\ell(s')ds'\right], \tag{5}$$

where $P_\ell(\cos\theta)$ is a Legendre polynomial. Using orthogonality and projecting the $\ell = 1$ term,

$$\langle\cos\theta\rangle = \int f(\theta,s)P_1(\cos\theta)d\Omega = \exp\left[-\int_0^s \sigma_1(s')ds'\right]$$

$$= \exp\left[-\int_{E_0}^{E} \sigma_1(E)\left(\frac{dE}{ds}\right)^{-1} dE\right], \quad (6)$$

where $\langle\cos\theta\rangle$, a function of the residual electron energy, is a measure of the mean deflection resulting from multiple scattering,[29] and relates $dE/ds$ to $dE/dx$ through

$$\frac{dE}{dx} = \langle\cos\theta\rangle^{-1}\frac{dE}{ds}, \quad (7)$$

where $dE/ds$ is the stopping power along the path while $dE/dx$ is the linear energy stopping power. In the above,

$$S(E) = \int_0^s ds' = \int_{E_0}^{E}\left(\frac{dE}{ds}\right)^{-1} dE, \quad (8)$$

and

$$\sigma_1(E) = 2\pi n_i\int_0^\pi\left(\frac{d\sigma}{d\Omega}\right)(1-\cos\theta)\sin\theta d\theta, \quad (9)$$

where $\sigma_1$ is the diffusion cross section (or transport cross section) that characterizes the loss of directed electron velocity through scattering.[2] Equations (1) and (2) are substituted into Eq. (9), and, after a standard change of variables, the integrations are taken from $b_{\min}^{ei}$ or $b_{\min}^{ee}$ to $\lambda_D$, where $\lambda_D$ is the Debye length,[30] and $b_{\min}^{ei}\left(b_{\min}^{ee}\right)$ is the larger of $b_{\text{quantum}}^{ei}\left(b_{\text{quantum}}^{ee}\right)$ and $b_\perp^{ei}\left(b_\perp^{ee}\right)$ (Ref. 31). $b_{\text{quantum}}^{ei}$ and $b_{\text{quantum}}^{ee}$ are approximately the electron deBroglie wavelength, and $b_\perp^{ei} = Zr_0/\gamma\beta^2$ and

$$b_\perp^{ee} \approx 2(\gamma+1)r_0\Big/\left[\left(2\sqrt{(\gamma+1)/2}\right)^2\gamma\beta^2\right]$$

are the impact parameters for 90° scattering of electrons off ions ($e\rightarrow i$) or electrons off electrons ($e\rightarrow e$). Thus

$$\sigma_1(E) = \sigma_1^{ei}(E) + Z\sigma_1^{ee}(E)$$

$$= 4\pi n_i\left(\frac{r_0}{\gamma\beta^2}\right)^2\left[Z^2\ln\Lambda^{ei} + \frac{4(\gamma+1)^2}{\left(2\sqrt{(\gamma+1)/2}\right)^4}Z\ln\Lambda^{ee}\right], \quad (10)$$

where the arguments of the Coulomb logarithm are $\Lambda^{ei} = \lambda_D/b_{\min}^{ei}$ and $\Lambda^{ee} = \lambda_D/b_{\min}^{ee}$ (Ref. 29). Since these Coulomb logarithms are used in this and later calculations, they are shown in Fig. 98.33.

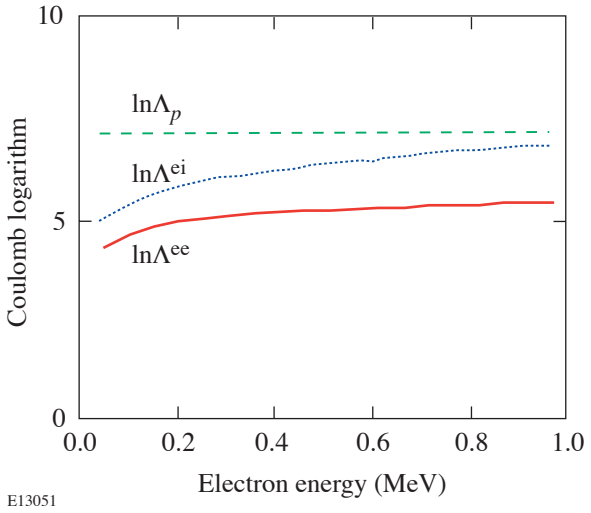


Figure 98.33
The Coulomb logarithms for incident 1-MeV electrons interacting with a DT plasma ($\rho = 300$ g/cm$^3$; $T_e = 5$ keV). For the background plasma, the Coulomb logarithm $\ln\Lambda_p$, relevant to plasma transport processes (e.g., electrical and thermal conductivity), is about 7.

The stopping power in Eq. (6) consists of contributions from binary interactions with plasma electrons and from plasma oscillations. The binary contribution is[32]

$$\left(\frac{dE}{ds}\right)_b = -n_i Z(\gamma-1)m_0c^2\int_{\varepsilon_{\min}}^{\varepsilon_{\max}}\varepsilon\left(\frac{d\sigma}{d\varepsilon}\right)d\varepsilon, \quad (11)$$

where the differential energy loss cross section is from Møller[23]

$$\frac{d\sigma}{d\varepsilon} = \frac{2\pi r_0^2}{(\gamma-1)\beta^2} \times \left[\frac{1}{\varepsilon^2} + \frac{1}{(1-\varepsilon)^2} + \left(\frac{\gamma-1}{\gamma}\right)^2 - \frac{2\gamma-1}{\gamma^2\varepsilon(1-\varepsilon)}\right], \quad (12)$$

and $\varepsilon$ is the energy transfer in units of $(\gamma-1)m_0c^2$. The lower integration limit reflects the minimum energy transfer that occurs when an incident electron interacts with a plasma electron at $\lambda_D$, i.e., $\varepsilon_{\min} = 2\gamma r_0^2/\left[\lambda_D(\gamma-1)\right]^2$. The upper limit occurs for a head-on collision, for which $\varepsilon_{\max} = 0.5$.

The contribution from plasma oscillations, which reflects the response of the plasma to impact parameters larger than $\lambda_D$,[31] is

$$\left(\frac{dE}{ds}\right)_c = -\frac{4\pi r_0^2 m_0 c^2 n_i Z}{\beta^2} \ln\left(\frac{1.123\beta}{\sqrt{2kT_e/m_0c^2}}\right), \quad (13)$$

where relativistic effects are included. Consequently,

$$\frac{dE}{ds} = -\frac{2\pi r_0^2 m_0 c^2 n_i Z}{\beta^2}\left\{\ln\left[\frac{(\gamma-1)\lambda_D}{2\sqrt{2\gamma}\,r_0}\right]^2 + 1 + \frac{1}{8}\left(\frac{\gamma-1}{\gamma}\right)^2 - \left(\frac{2\gamma-1}{\gamma}\right)\ln 2 + \ln\left(\frac{1.123\beta}{\sqrt{2kT_e/m_0c^2}}\right)^2\right\}. \quad (14)$$

Figure 98.34 illustrates this relationship [Eq. (6)], where the incident electron ($E_0 = 1$ MeV) continuously changes direction as it loses energy. When $\langle\cos\theta\rangle$ equals one $e$-folding, $|\theta| \approx 68°$ and $E/E_0 \approx 0.1$, at which point the incident electron has lost memory of its initial direction.

We iterate upon this process, important for low-energy electrons, until the electrons are thermalized with the background plasma, which has the cumulative effect of bending the path of the electrons away from their initial direction. Figure 98.35 illustrates the enhancement of $dE/dx$ for scattering off ions and for scattering off ions plus electrons.

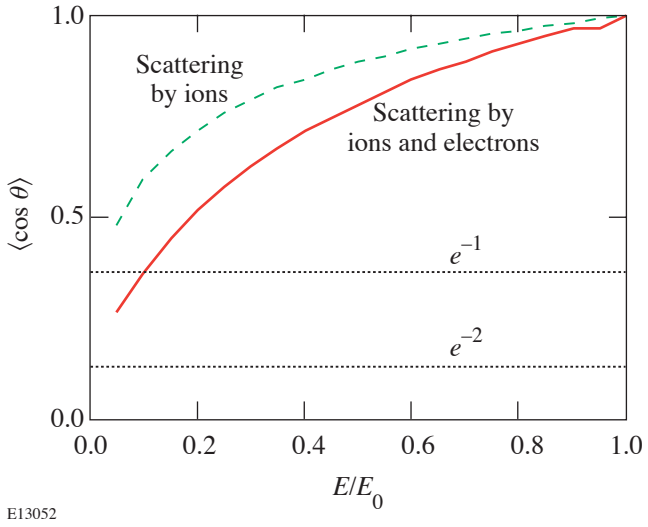


Figure 98.34
The mean deflection angle $\langle\cos\theta\rangle$ is plotted against the fraction of the residual energy in a DT plasma for $e \rightarrow i$ and for $e \rightarrow i + e$ scattering (1-MeV electrons with $\rho = 300$ g/cm$^3$; $T_e = 5$ keV). When $\langle\cos\theta\rangle$ equals one $e$-folding, corresponding to $|\theta| \approx 68°$ and $E/E_0 \approx 0.1$, the incident electron has lost memory of its initial direction.

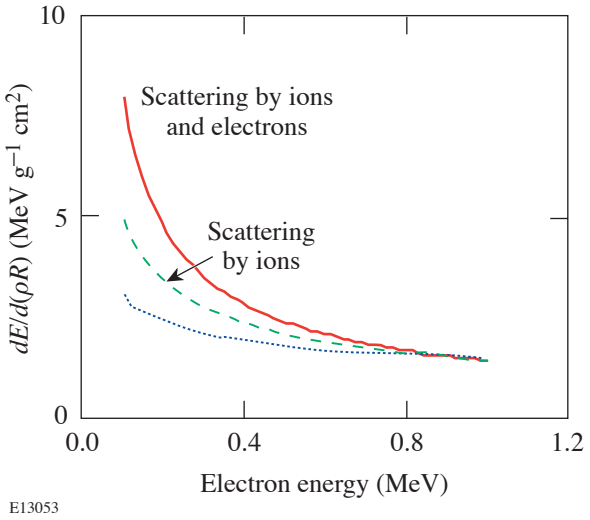


Figure 98.35
Stopping power for linear-energy transfer and continuous slowing down are plotted as functions of the electron energy for incident 1-MeV electrons in a DT plasma ($\rho = 300$ g/cm$^3$; $T_e = 5$ keV). Enhancement of $dE/dx$ (solid line) over $dE/ds$ (dotted line) is a consequence of the effects of multiple scattering.

This effect is further illustrated in Fig. 98.36, where the corresponding set of curves for range ($R$) and penetration ($\langle X_p \rangle$) with and without the electron scattering contributions are shown for electrons with $E_0 = 0.1$–$10$ MeV.

$$R = \int_0^R ds' = \int_{E_0}^{\sim kT} \left(\frac{dE}{ds}\right)^{-1} dE, \tag{15}$$

and

$$\langle X_p \rangle \approx \sum_{n=0} e^{-n} \int_{E_n}^{E_{n+1}} \langle \cos\theta \rangle \left(\frac{dE}{ds}\right)^{-1} dE, \tag{16}$$

where $E_0$ is the initial energy; $E_1$, $E_2$.... correspond to the electron energies at the first, second.... $e$-folding of $\langle \cos\theta \rangle$ (see Fig. 98.34); $R$ is the total path length the electron traverses as it scatters about and eventually thermalizes; and $\langle X_p \rangle$ is the distance along the *initial* electron trajectory that it eventually reaches. Contributions from electron and ion scattering are shown in Fig. 98.36.

Three other points are worth noting: First, the temperature and density dependence are weak, i.e., a factor-of-10 reduction in either temperature or density results in only ~10% reduction in the penetration. Second, as the initial electron energy decreases, the effects of scattering become more pronounced [Fig. 98.36(c)]—an effect, very similar in nature, that is also seen in the scattering of energetic electrons in metals.[34] Third, for a given electron energy, scattering effects decrease slightly as the target plasma temperature decreases, i.e., the path of the electron straightens slightly as the target plasma temperature drops. For example, when the target plasma temperature changes from 5.0 to 0.5 keV ($\rho$ = 300 g/cm$^3$), the ratio $R/\langle X_p \rangle$ is reduced by ~5% for 1-MeV electrons.

By calculating of the penetration as a function of energy loss, the energy deposition can be evaluated (Fig. 98.37). In addition to the differences in total penetration with and without scattering contributions, it is seen that the linear-energy transfer increases near the end of its penetration (i.e., an effective Bragg peak), an effect that is seen more weakly with just ion scattering. Such differences may need to be considered in quantitatively modeling the energy deposition of relativistic electrons for fast ignition and for critically assessing ignition requirements.[35] It is also interesting, and a consequence of

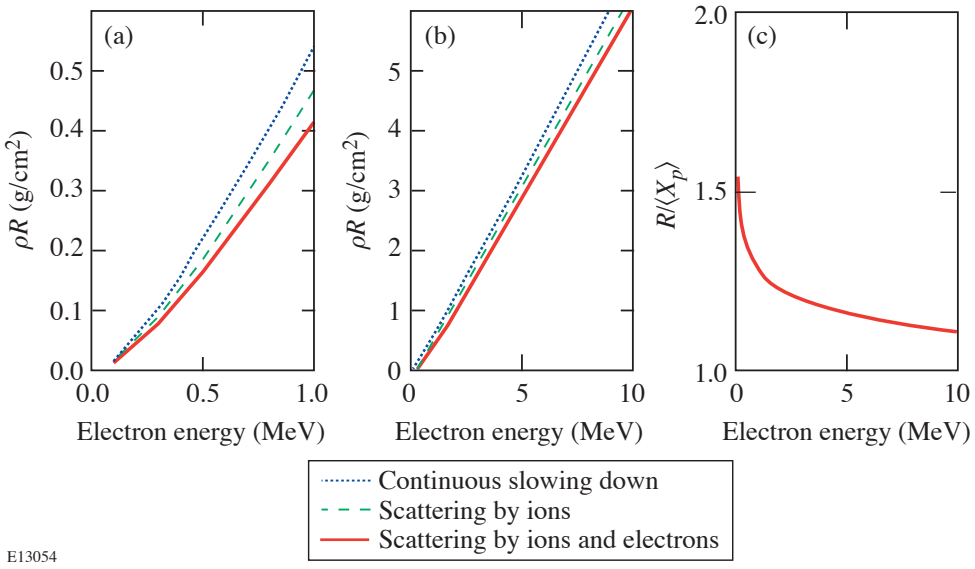


Figure 98.36
The range (dotted line) and penetration for (a) 0.1- to 1-MeV electrons and (b) 1- to 10-MeV electrons in a DT plasma ($\rho = 300$ g/cm$^3$; $T_e = 5$ keV). The penetration is shown for scattering off ions and for scattering off ions plus electrons. A factor-of-10 reduction in either the temperature or density results in only ~10% reduction in the penetration. (c) The ratio of range to penetration for 0.1- to 10-MeV electrons. As the initial electron energy decreases, the effects of multiple scattering become more pronounced, and the penetration is further diminished with respect to the range.

selecting 1-MeV electrons [Figs. 98.36 and 98.37], that the effects of scattering reduce the penetration from 0.54 to 0.41 g/cm$^2$; this latter value is close to the range of 3.5-MeV alphas, 0.3 g/cm$^2$, which is required for hot-spot ignition in a 10-keV plasma.[3–6]

Finally, in order to explore the importance of electron-on-electron multiple scattering in a hydrogenic setting, and since definitive stopping power experiments in plasmas are extremely difficult, we propose that experiments be undertaken in which a monoenergetic electron beam, with energy between 0.1 and 1.0 MeV, scatters off thin layers of either $D_2$ or $H_2$ ice, where the thickness of the ice layer is between ~100 and 1000 $\mu$m, the appropriate thickness depending on the exact electron energy. Although there are differences in the scattering calculations for cold, condensed hydrogenic matter and a hydrogenic plasma, there is reason to believe that the *relative* importance of the electron-to-electron and the electron-to-ion multiple scattering terms will be approximately the same for both states of matter.

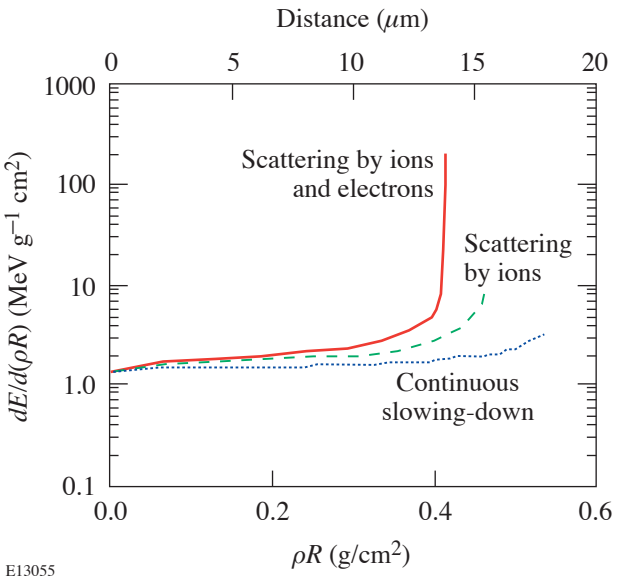


Figure 98.37
The stopping power for 1-MeV electrons, plotted as a function of the electron penetration, for a DT plasma with $\rho = 300$ g/cm$^3$ and $T_e = 5$ keV. The three curves correspond to three different models. As a result of the scattering effects, the energy transfer increases notably near the end of the penetration (i.e., an effective Bragg peak). For these 1-MeV electrons, the effects of scattering reduce the penetration from 0.54 g/cm$^2$ to 0.41 g/cm$^2$ (Ref. 33).

**Summary**

The energy loss and penetration of energetic electrons into a hydrogenic plasma has been analytically calculated, and the effect of scattering off ions and electrons is treated from a unified point of view. In general, scattering enhances the electron linear-energy transfer along the initial electron direction and reduces the electron penetration. Energy deposition increases near the end of its range. These results should have relevance to "fast ignition" and to fuel preheat in inertial confinement fusion, specifically to energy deposition calculations that critically assess quantitative ignition conditions.

## ACKNOWLEDGMENT

This work was supported in part by the U.S. Department of Energy Contract #DE-FG03-99SF21782, LLE subcontract #PO410025G, LLNL subcontract #B313975.

## REFERENCES

1. L. Spitzer, *Physics of Fully Ionized Gases*, 2nd rev. ed., Interscience Tracts on Physics and Astronomy (Interscience, New York, 1962).
2. B. Trubnikov, *Review of Plasma Physics* (Consultants Bureau, New York, 1965).
3. S. Skupsky, Phys. Rev. A, **16**, 727 (1977); G. S. Fraley *et al.*, Phys. Fluids **17**, 474 (1974).
4. C. K. Li and R. D. Petrasso, Phys. Rev. Lett. **70**, 3059 (1993).
5. J. D. Lindl, *Inertial Confinement Fusion: The Quest for Ignition and Energy Gain Using Indirect Drive* (Springer-Verlag, New York, 1998); references therein.
6. J. D. Lindl, R. L. McCrory, and E. M. Campbell, Phys. Today **45**, 32 (1992).
7. R. D. Petrasso, J. A. Frenje, C. K. Li, F. H. Séguin, J. R. Rygg, B. E. Schwartz, S. Kurebayashi, P. B. Radha, C. Stoeckl, J. M. Soures, J. Delettrez, V. Yu. Glebov, D. D. Meyerhofer, and T. C. Sangster, Phys. Rev. Lett. **90**, 095002 (2003); V. A. Smalyuk, P. B. Radha, J. A. Delettrez, V. Yu. Glebov, V. N. Goncharov, D. D. Meyerhofer, S. P. Regan, S. Roberts, T. C. Sangster, J. M. Soures, C. Stoeckl, J. A. Frenje, C. K. Li, R. D. Petrasso, and F. H. Séguin, Phys. Rev. Lett. **90**, 135002 (2003); F. H. Séguin, J. A. Frenje, C. K. Li, D. G. Hicks, S. Kurebayashi, J. R. Rygg, B.-E. Schwartz, R. D. Petrasso, S. Roberts, J. M. Soures, D. D. Meyerhofer, T. C. Sangster, J. P. Knauer, C. Sorce, V. Yu. Glebov, C. Stoeckl, T. W. Phillips, R. J. Leeper, K. Fletcher, and S. Padalino, Rev. Sci. Instrum. **74**, 975 (2003).
8. M. Tabak *et al.*, Phys. Plasmas **1**, 1626 (1994).
9. C. Deutsch *et al.*, Phys. Rev. Lett. **77**, 2483 (1996); *ibid.* **85**, 1140 (2000).
10. S. Atzeni, Phys. Plasmas **6**, 3316 (1999).

11. M. H. Key, M. D. Cable, T. E. Cowan, K. G. Estabrook, B. A. Hammel, S. P. Hatchett, E. A. Henry, D. E. Hinkel, J. D. Kilkenny, J. A. Koch, W. L. Kruer, A. B. Langdon, B. F. Lasinski, R. W. Lee, B. J. MacGowan, A. MacKinnon, J. D. Moody, M. J. Moran, A. A. Offenberger, D. M. Pennington, M. D. Perry, T. J. Phillips, T. C. Sangster, M. S. Singh, M. A. Stoyer, M. Tabak, G. L. Tietbohl, M. Tsukamoto, K. Wharton, and S. C. Wilks, Phys. Plasmas **5**, 1966 (1998).

12. For the case of fast ignition, numerical simulations[13] indicate that the electron transport is highly filamented due to Weibel instability,[15] which occurs at early times when beam density $n_b$ is comparable to critical density $n_c$. Plasma heating can be characterized by collective beam stopping due to coalescence of current filaments and related ion dynamics. Subsequently, however, as these electrons enter the dense plasma region where $n_e/n_b >> 1$, the interaction can be envisioned as the linear superposition of individual, isolated electrons interacting with plasma, which is the focus of this article.

13. M. Honda, J. Meyer-ter-Vehn, and A. Pukhov, Phys. Rev. Lett. **85**, 2128 (2000); L. Gremillet, G. Bonnaud, and F. Amiranoff, Phys. Plasmas **9**, 941 (2002).

14. M. J. Berger and S. M. Seltzer, in *Studies in Penetration of Charged Particles in Matter*, Nuclear Science Series, Committee on Nuclear Science, Report 39, Publication 1133 (National Academy of Sciences—National Research Council, Washington, DC, 1964), pp. 205–268; L. Pages *et al*., At. Data **4**, 1 (1972), and references therein. These results are very close to that of the range calculation of this article.

15. E. S. Weibel, Phys. Rev. Lett. **2**, 83 (1959).

16. H. H. Hubbell, Jr. and R. D. Birkhoff, Phys. Rev. A, **26**, 2460 (1982).

17. C. Deutsch *et al*. have a factor-of-2 error in the electron continuous-slowing-down stopping power [Eq. (3) of Ref. 9]; in both their erratum and the original paper, this leads to about a factor-of-2 overestimate in the electron range [Figs. 1(a) and 2(a) of Ref. 9 and erratum].

18. M. D. Rosen *et al*., Phys. Rev. A **36**, 247 (1987).

19. B. Yaakobi, C. Stoeckl, T. Boehly, D. D. Meyerhofer, and W. Seka, Phys. Plasmas **7**, 3714 (2000).

20. N. F. Mott, M. A. Gonville, and C. College, Proc. R. Soc. Lond. A, Math. Phys. Sci. **CXXXV**, 429 (1932).

21. R. D. Evans, *The Atomic Nucleus*, International Series in Pure and Applied Physics (McGraw-Hill, New York, 1955).

22. Only the first term has been kept in this differential cross section. This approach is equivalent to the first-order Born approximation (the second term has an order of $\alpha Z$, $\alpha = 1/137$, the fine-structure constant). For heavy elements, the *e-i* cross section will need to be corrected.

23. C. Møller, Ann. Physik (Leipz) **14**, 531 (1932).

24. Since small-angle scattering dominates, we have neglected terms that are not associated with this process. Furthermore, this expression is approximately accurate only for $\gamma \lesssim 10$.

25. P. A. Hughes, ed. *Beams and Jets in Astrophysics*, Cambridge Astrophysics Series (Cambridge University Press, Cambridge, England, 1991).

26. A. Pukhov, Z. M. Sheng, and J. Meyer-ter-Vehn, Phys. Plasmas **6**, 2847(1999), and references within.

27. H. W. Lewis, Phys. Rev. **78**, 526 (1950), and references therein.

28. S. Goudsmit and J. L. Saunderson, Phys. Rev. **57**, 24 (1940); *ibid*. **58**, 36; H. A. Bethe, Phys. Rev. **89**, 1256 (1953).

29. Since $\sigma_1(E)(dE/ds)^{-1} \propto \nu_D(E)/\nu_E(E)E$, where $\nu_D(\nu_E)$ is the rate of scattering (energy loss), deflection from initial direction is a function of the ratios of these frequencies. Furthermore, since both $\sigma_1$ and $dE/ds$ have nearly the same dependence on $\ln\Lambda$, a consequence that is is sufficiently large (i.e., ~5), any sensitive dependence on the Coulomb logarithm nearly cancels out.

30. For plasmas such as discussed herein, the Debye screening length is the standard approximation for the cutoff.[1,2]

31. J. D. Jackson, *Classical Electrodynamics*, 2nd ed. (Wiley, New York, 1975).

32. E. Rohrlich and B. C. Carlson, Phys. Rev. **93**, 38 (1954).

33. In Deutsch *et al*., their penetration is about four times smaller than their range for 1-MeV electrons [Figs. 1(a) and 2(a) of Ref. 9 and erratum]. Even including electron-scattering effects, the results of the present article indicate a penetration that is only a factor of 1.32 smaller than the range of 1-MeV electrons. As best we can tell, the approach of Deutsch *et al*. is unjustified since they invoke an approximation by P. C. Hemmer and I. E. Farquhar [Phys. Rev. **168**, 294 (1968); see Eq. (67) and discussion], which is valid only for small angle deflections and small energy loss. This approximation is invalid in the present context of large deflections and total energy loss.

34. K.-H. Weber, Nucl. Instrum. Methods **25**, 261 (1964).

35. Whether considering fast ignition or electron preheat, the distribution of electron energies about their mean will smear out the energy deposition, making it more uniform.

# Operation of a Single-Photon–Counting X-Ray CCD Camera Spectrometer in a Petawatt Environment

## Introduction

Single-photon–counting x-ray CCD (charge-coupled device) spectrometers are frequently used in ultrashort-pulse laser experiments, mostly for *K*-shell spectroscopy.[1–3] For single-photon counting, the incident x-ray flux is attenuated such that the probability that two x-ray photons hit a single pixel is small. Consequently, the pixel value of each readout pixel is proportional to the deposited energy from the incident x-ray photon. If the x-ray energy is not too high (<100 keV), a significant fraction of the x-ray photons deposit all their energy in one pixel. In this case, a histogram of the pixel values provides a good approximation of the incident x-ray spectrum. This technique has the advantage of requiring almost no alignment and the potential of providing absolute x-ray flux information. Consequently single-photon–counting x-ray CCD spectrometers are also used in astronomical satellites,[4,5] where an extensive set of calibration and characterization data exists. For the satellite data, the low number of incident photons is the biggest issue, whereas in ultrashort-pulse laser experiments, photon counts are generally very high. Signal-to-background issues, especially in a high-energy petawatt environment, become dominant.[3] Shielding strategies against background x rays must be carefully chosen to obtain high-quality spectra. In this article, results from a recent experimental campaign at the petawatt facility of the Rutherford Appleton Laboratory (RAL) are presented showing successful strategies to improve the signal-to-background ratio.

## Experimental Setup

The single-photon–counting x-ray spectrometer consists of a Spectral Instruments Series 800 Camera using a 2-k × 2-k-pixel, back-thinned CCD chip with a pixel size of 13.5 $\mu$m.[6] The CCD was cooled to –35°C to reduce the dark current, and the images were recorded with 16-bit resolution.

The camera was mounted 3.8 m from the target outside the target chamber on a 1-m vacuum tube. Mounting the camera in air and using thin vacuum windows was not possible because the x rays of interest—Cu *K*-shell radiation at ~8 keV—are strongly absorbed in air. The RAL petawatt target chamber is very well shielded with 10 cm of lead on three sides and on top. The side where the access doors are located is unshielded but backed by a curtain shield of 10 cm of lead and 60 cm of concrete (Fig. 98.38). The CCD camera was shielded against x rays scattered from structures close to the target with up to four lead collimators of 10-cm length inside the target chamber and the vacuum tube (inner shielding). The CCD camera housing was surrounded by up to 10 cm of lead to shield against x rays from the sides and the back of the CCD (outer shielding). A matched *K*-edge filter was used to attenuate the *K*-shell signal to maintain single-photon counting. Figure 98.39 shows the transmission of the 150 $\mu$m Cu filter used for Cu *K*-shell spectroscopy. Compared to a simple high-pass filter against the thermal radiation from the target, a *K*-edge filter attenuates the spectrum above the lines of interest, thus improving the signal-to-background ratio.

The targets were irradiated with 1053-nm pulses from the RAL Vulcan petawatt laser, which delivers up to ~500 J in ~1 ps in a 60-cm-diam beam.[7,8] These pulses are focused with an *f*/3 off-axis parabola to a focal spot of ~10-$\mu$m FWHM. Losses in the compressor and aberrations generally

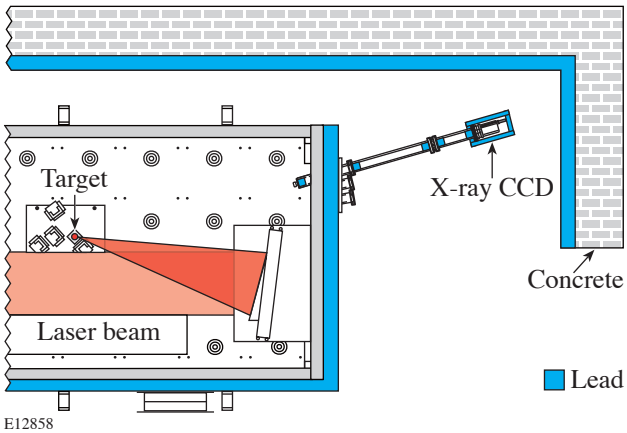


Figure 98.38
Setup of the single-photon–counting x-ray CCD at the RAL petawatt facility, showing the target-area shielding and the CCD shielding.

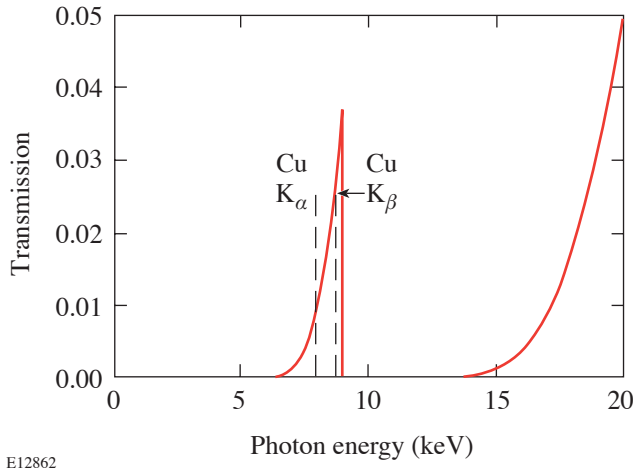


Figure 98.39
A matched *K*-edge filter was used to improve the signal-to-background ratio (150 $\mu$m Cu for Cu *K*-shell spectroscopy shown). The positions of the Cu $K_\alpha$ and $K_\beta$ lines are indicated in the graph.

limit the focusable energy to <50% of the laser energy. Consequently, the maximum intensity on target was estimated to be ~$2 \times 10^{20}$ W/cm$^2$.

### Optimizing the Shielding

A series of experiments were conducted to optimize the inner and outer shields and to assess the relative importance of the x-ray background from structures close to the target that reach the CCD from its face and fluorescence and scattered photons that reach the CCD from the side or back.

Figure 98.40(a) shows the histogram from a 20-$\mu$m-thick Cu target irradiated with an ~250-J, 1-ps pulse, at $1 \times 10^{20}$ W/cm$^2$ using 10-cm inner shielding and no outer shielding. Figure 98.40(b) shows the *K*-shell spectrum after background subtraction. The energy scale is inferred from the published energies of Cu $K_\alpha$ = 8.05 keV and Cu $K_\beta$ = 8.90 keV. The third line visible in the spectrum is identified as the $He_\alpha$ line of Cu at 8.36 keV.

The high background seen in these experiments distorts the spectrum and makes it almost impossible to discern the Cu $K_\beta$ line.

Adding 5 cm of lead as outer shielding around the CCD camera dramatically improves both the background and the quality of the spectrum as shown in Fig. 98.41. This indicates that most of the background is coming from either Compton-scattered primary x rays or x-ray fluorescence in the structures around the CCD. The spectrum shows the Cu $K_\beta$ line

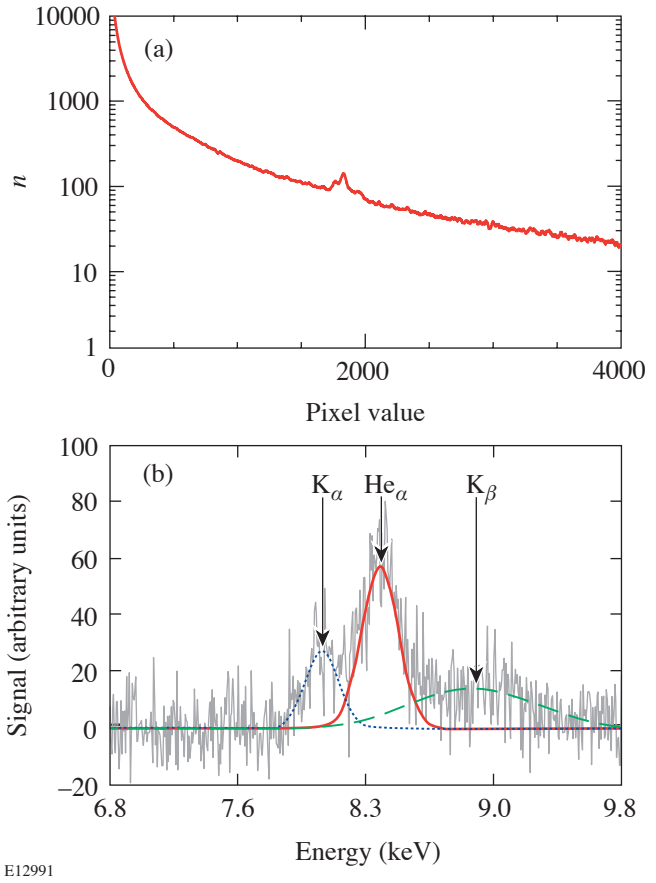


Figure 98.40
CCD histogram (a) and *K*-shell spectrum (b) from a 20-$\mu$m-thick Cu target irradiated with a ~250-J, 1-ps laser pulse, at $1 \times 10^{20}$ W/cm$^2$ using 10-cm inner shielding and no outer shielding.

clearly separated, and the Cu $K_\alpha$ and the He-like feature can be easily distinguished.

Increasing the laser energy by a factor of 2 results in a dramatically increased background. Even improving the inner shielding to 40 cm and the outer shielding to 10 cm does not prevent the background from rising by about a factor of 3 (see Fig. 98.42). Fortunately in this experiment the x-ray flux also rose by almost a factor of 3 and the spectrum is still well resolved. A new, fourth line is seen in the spectrum, which is identified as Cu $Ly_\alpha$ at 8.64 keV.

### Summary and Conclusions

Efficient shielding is required to obtain high-quality x-ray spectra from a single-photon–counting x-ray CCD spectrometer in a petawatt environment. Shielding the direct line of sight against x rays from structures close to the target was not sufficient to decrease the background. Only by shielding the

CCD camera from all sides with 10 cm of lead was it possible to reduce the background to a level low enough to be able to obtain high-quality spectra even at 500-J laser energy. Scaling the shielding to even higher laser energies or intensities could be difficult given the significant rise in background from 250-J to 500-J energy.

## ACKNOWLEDGMENT

This work was supported by the U.S. Department of Energy Office of Inertial Confinement Fusion under Cooperative Agreement No. DE-FC03-92SF19460, the University of Rochester, and the New York State Energy Research and Development Authority. The support of DOE does not constitute an endorsement by DOE of the views expressed in this article.

## REFERENCES

1. F. N. Beg *et al.*, Phys. Plasmas **4**, 447 (1997).
2. F. Ewald, H. Schwoerer, and R. Sauerbrey, Europhys. Lett. **60**, 710 (2002).
3. K. Yasuike *et al.*, Rev. Sci. Instrum. **72**, 1236 (2001).
4. M. Nishiuchi *et al.* in *EUV, X-Ray, and Gamma-Ray Instrumentation for Astronomy IX*, edited by O. H. Siegmund and M. A. Gummin (SPIE, Bellingham, WA, 1998), Vol. 3445, pp. 268–277.
5. M. Nishiuchi *et al.*, Nucl. Instrum. Methods Phys. Res. **436**, 79 (1999).
6. Spectral Instruments, Tucson, AZ 85745.
7. C. B. Edwards *et al.*, in the *25th International Congress on High-Speed Photography and Photonics*, edited by C. Cavailler, G. P. Haddleton, and M. Hugenschmidt (SPIE, Bellingham, WA, 2003), Vol. 4948, pp. 444–451.
8. C. N. Danson *et al.*, in *Inertial Fusion Sciences and Applications 2001*, edited by K. A. Tanaka, D. D. Meyerhofer, and J. Meyer-ter-Vehn (Elsevier, Paris, 2002), pp. 479–483.

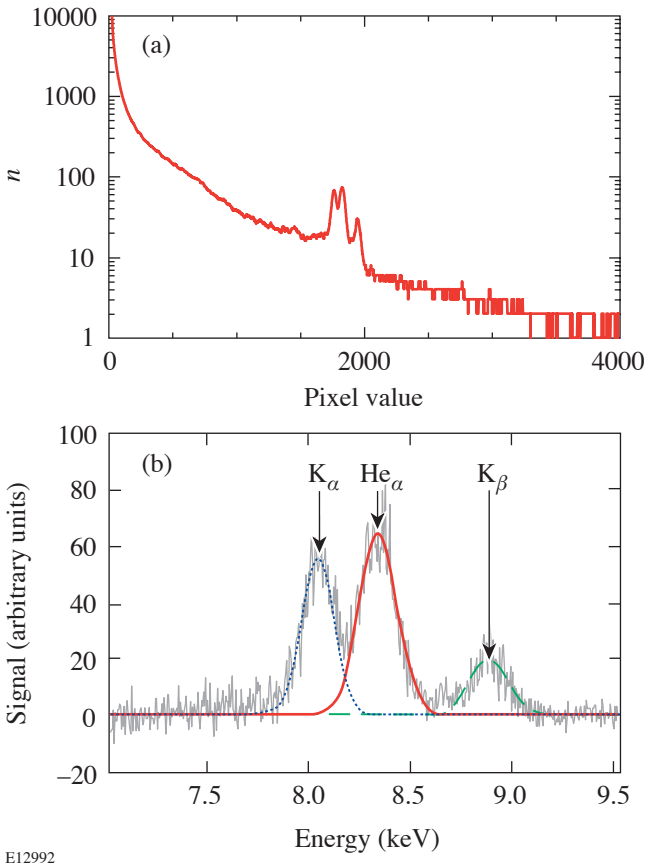


Figure 98.41
CCD histogram (a) and *K*-shell spectrum (b) from a 20-$\mu$m-thick Cu target irradiated with an ~250-J, 1-ps laser pulse, at $1 \times 10^{20}$ W/cm$^2$ using 10-cm inner shielding and 5-cm outer shielding.

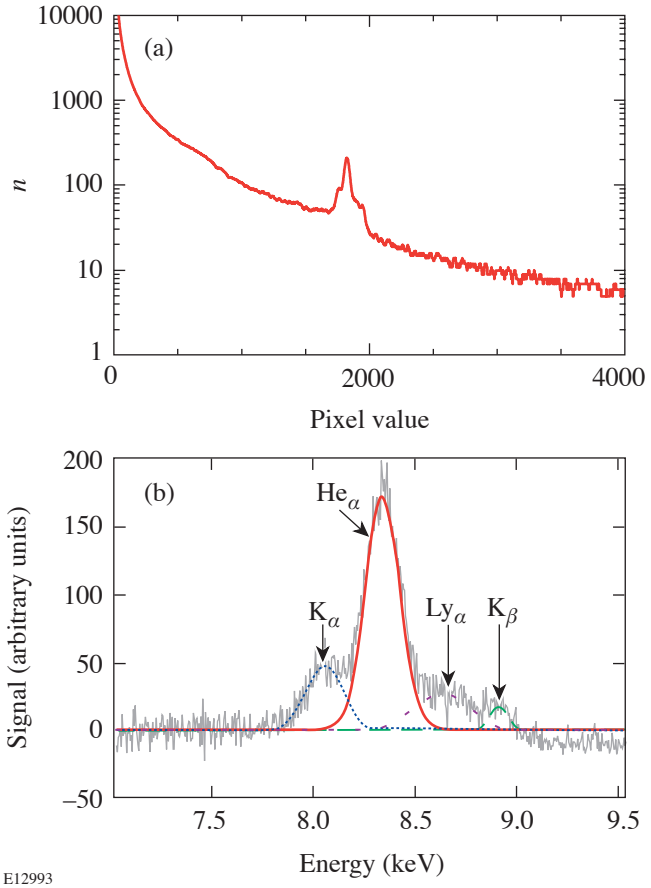


Figure 98.42
CCD histogram (a) and *K*-shell spectrum (b) from a 20-$\mu$m-thick Cu target irradiated with an ~500-J, 1-ps laser pulse, at $1 \times 10^{20}$ W/cm$^2$ using 40-cm inner shielding and 10-cm outer shielding.

# Theory of Laser-Induced Adiabat Shaping in Inertial Fusion Implosions: The Relaxation Method

**Introduction**

In recent years it has been theoretically shown that the stability of inertial fusion implosions can be significantly improved by shaping the entropy inside the shell. The optimum adiabat shape in the shell consists of a profile that is monotonically decreasing from the outer to the inner surface. Large values of the adiabat on the outer shell surface increase the ablation velocity $V_a$, which follows a power law of the outer-surface adiabat $\alpha_{\text{out}}$,

$$V_a \sim \alpha_{\text{out}}^{3/5}, \tag{1}$$

while low adiabat values on the inner surface lead to improved ignition conditions and larger burn fraction. A more-detailed history and target design implications of adiabat shaping can be found in the introduction of Ref. 1, which is mostly devoted to the adiabat shape induced by a strong decaying shock. Shaping by a decaying shock[1,2] requires a very strong prepulse, followed by a low-intensity foot of the main pulse, to launch a strong shock, which decays inside the shell shortly after the prepulse is turned off. The decaying shock (DS) leaves behind a monotonically decreasing adiabat profile, which follows a power law of the mass coordinate

$$\alpha = \alpha_{\text{in}}\left(\frac{m_{\text{shell}}}{m}\right)^{\Delta_{\text{DS}}}, \tag{2}$$

where $m$ is the mass calculated from the outer surface, $m_{\text{shell}}$ is the total shell mass, and $\Delta_{\text{DS}}$ varies between 1.06 and 1.13 depending on the prepulse duration. Two-dimensional simulations[2] of all-DT, OMEGA-sized capsule implosions have confirmed that DS adiabat targets exhibit significantly reduced Rayleigh–Taylor growth on the ablation surface during the acceleration phase with respect to the flat-adiabat targets. Comparisons between flat- and shaped-adiabat targets are typically carried out by designing the flat- and shaped-adiabat pulses to generate identical adiabats on the inner shell surface.

A different technique aimed at shaping the adiabat is the so-called shaping by relaxation (or RX shaping) described in Ref. 3. The relaxation technique uses a less-energetic prepulse than the DS technique. The RX prepulse is used to launch a shock that may or may not decay inside the shell. In both cases, the prepulse is turned off before the prepulse shock reaches the shell's inner surface. Since the prepulse is followed by a complete power shutoff, the outer portion of the shell expands outward, generating a relaxed density profile, while the prepulse shock travels inside the shell. The prepulse shock is not intended to greatly change the shell adiabat even though it may cause a significant adiabat modification. The main adiabat shaping occurs later in time when the foot of the main pulse starts, driving a strong shock up the relaxed density profile. The main shock first encounters the low-density portion of the relaxed profile, setting it on a very high adiabat. The adiabat develops a monotonically decreasing profile as a result of the increasing pre-shock density. Figure 98.43 shows a plot of the

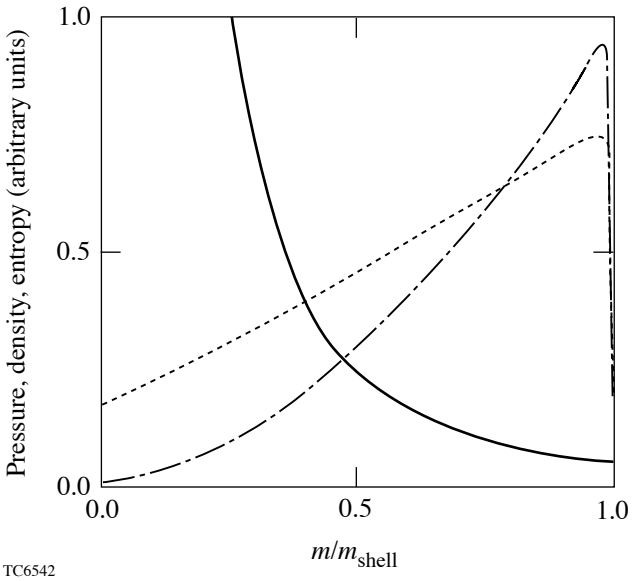


Figure 98.43
Pressure (dashed), density (dot–dashed), and adiabat (solid) profiles generated by a strong shock supported by constant pressure propagating through a relaxed density profile.

pressure, density, and entropy profiles generated by a strong shock propagating through a relaxed density profile. Observe that the adiabat profile is strongly shaped with large values on the outer shell surface and low values on the inner shell surface. To produce a monotonically decreasing adiabat profile, it is important to design the laser pulse so that the prepulse and main shock merge at the inner shell surface. The RX adiabat-shaping technique can be viewed as a two-step process: the prepulse and power shutoff are needed to generate the relaxed density profile, following which the foot of the main pulse shapes the adiabat.

In this article, a detailed hydrodynamic analysis of the relaxed profile generation as well as the shock propagation through these profiles is carried out.

**The General Model**

The general gasdynamic model governing the hydrodynamic motion of a compressible gas is greatly simplified by adopting a Lagrangian frame of reference where the independent spatial coordinate is the mass. In planar geometry, the mass coordinate is defined as the mass per unit area calculated from the outer shell surface:

$$m = \int_0^{\bar{x}} \rho(\bar{x}',0)\,d\bar{x}', \tag{3}$$

where $\rho(\bar{x},0)$ is the initial density and $\bar{x}$ is the initial spatial location of the fluid elements.

In this coordinate, the outer shell surface is represented by $\bar{x} = 0$ and $m = 0$. In spherical geometry, Eq. (3) should be replaced by $m = \int_0^{\bar{r}} \bar{r}'^2 \rho(\bar{r}',0)\,d\bar{r}'$. For simplicity, we carry out the calculation for the case of an ideal gas with adiabatic index $\gamma$ and neglect convergence effects on the basis that the adiabat shaping occurs when the inner shell surface has not yet moved and the initial aspect ratio is sufficiently large that the shell can be approximated with a uniform slab.

In the Lagrangian frame and away from the shock front, the planar equations of motion for the shocked material can be written in the following conservative form:

$$\frac{\partial u}{\partial m} - \frac{\partial}{\partial t}\frac{1}{\rho} = 0, \tag{4}$$

$$\frac{\partial u}{\partial t} + \frac{\partial P}{\partial m} = 0, \tag{5}$$

$$p = S(m)\rho^{\gamma}, \tag{6}$$

where $u$, $P$, $\rho$, and $S(m)$ are the velocity, pressure, density, and entropy, respectively. The function $S(m)$ is referred to as the adiabat and depends exclusively on the Lagrangian coordinate. At the shock front, the physical quantities must satisfy the Hugoniot conditions, which in the strong shock regime can be written in the following simple form:

$$\left[\rho_{\mathrm{ps}}\right]_{m_{\mathrm{sh}}} = \frac{\gamma+1}{\gamma-1}\left[\rho_0\right]_{m_{\mathrm{sh}}}, \tag{7}$$

$$\left[u_{\mathrm{ps}}\right]_{m_{\mathrm{sh}}} = \frac{2}{\gamma-1}\frac{\dot{m}_{\mathrm{sh}}}{\left[\rho_{\mathrm{ps}}\right]_{m_{\mathrm{sh}}}}, \tag{8}$$

$$\dot{m}_{\mathrm{sh}} = \sqrt{\frac{(\gamma-1)}{2}\left[P_{\mathrm{ps}}\rho_{\mathrm{ps}}\right]_{m_{\mathrm{sh}}}}, \tag{9}$$

where $P_{\mathrm{ps}}$ represents the post-shock pressure, $\rho_{\mathrm{ps}}$ is the post-shock density, $u_{\mathrm{ps}}$ is the post-shock velocity, and $\rho_0$ is the initial unshocked density. Here, $m_{\mathrm{sh}}$ is the mass coordinate corresponding to the shock location. More details on the Lagrangian model used here can be found in Ref. 1.

**The Generation of the Relaxed Profiles**

When a square laser prepulse precedes the main laser pulse, a pressure pulse is applied to the shell's outer surface, launching a uniform shock followed by a rarefaction wave, which causes a relaxation of the pressure and density profiles. Since the leading edge of the rarefaction wave travels faster than the shock, it eventually catches the shock unless the shock reaches the inner shell surface before interacting with the rarefaction wave. Two different relaxed profiles are generated depending on whether or not the rarefaction leading edge catches the prepulse shock inside the shell. If the shock and rarefaction do not merge in the shell, the resulting relaxed profiles are said to be of the "first kind" while merging leads to relaxed profiles of the "second kind."

It is convenient to define with subscript $p$ the prepulse quantities, $P_p$, $\rho_p$, $S_p$, $a_p$, and $u_p$, representing the induced pressure, compressed density, adiabat, sound speed, and flow velocity while the uniform laser prepulse of duration $\Delta t_p$ is applied. Using the prepulse quantities, we define the following set of dimensionless quantities and coordinates:

$$\hat{\rho} \equiv \frac{\rho}{\rho_p}, \quad \hat{P} \equiv \frac{P}{P_p}, \quad \hat{u} \equiv \frac{u}{a_p}, \tag{10}$$

$$\hat{S} = \frac{S}{S_p}, \quad z = \frac{m}{m_*}, \quad \tau = \frac{t}{\Delta t_*}, \tag{11}$$

where

$$\Delta t_* = \frac{\Delta t_p}{\sqrt{2\gamma/(\gamma-1)}-1}, \tag{12}$$

$$m_* = \Delta t_* \rho_p a_p = \Delta t_* \sqrt{\gamma P_p \rho_p}. \tag{13}$$

Here $\Delta t_*$ is the travel time of the rarefaction wave before catching the shock, and $m_*$ is the areal density undertaken by the rarefaction wave's leading edge before catching the prepulse shock. Furthermore, $\tau = 0$ is defined as the time when the laser prepulse is terminated and the rarefaction wave is launched. It follows that $\tau = 1$ represents the shock–rarefaction interaction time.

These dimensionless variables can be used to rewrite the Lagrangian equations of motion in the convenient form

$$\frac{\partial \hat{u}}{\partial z} = \frac{\partial \hat{\rho}^{-1}}{\partial \tau}, \tag{14}$$

$$\gamma \frac{\partial \hat{u}}{\partial \tau} = -\frac{\partial \hat{P}}{\partial z}, \tag{15}$$

$$\hat{P} = \hat{S}(z)\hat{\rho}^{\gamma}. \tag{16}$$

Observe that Eqs. (14)–(16) can be combined into the following single equation:

$$\gamma \frac{\partial^2}{\partial \tau^2}\frac{1}{\hat{\rho}} + \frac{\partial^2}{\partial z^2}\hat{S}(z)\hat{\rho}^{\gamma} = 0, \tag{17}$$

which can be solved for $\hat{\rho}$ once $\hat{S}$ is known. There is no general solution of the equations of motion after the rarefaction wave is launched; however, one can consider two limiting cases resulting in two different relaxed profiles. The first is the case when the rarefaction wave catches the shock at the shell's rear surface. This case is characterized by values of $m_* = m_{\text{shell}}$. The second is the case when the rarefaction wave quickly catches the shock near the outer surface, causing the shock to decay throughout most of the shell. This case requires a small $m_*$ satisfying $m_* < m_{\text{shell}}$. We will consider these two cases separately.

1. Relaxed Profiles of the First Kind: Rarefaction and Shock Merge at the Rear Surface of the Shell: $m_* = m_{\text{shell}}$

In this case, the relaxed density and pressure profiles are the ones generated by the rarefaction wave, whose functional forms can be obtained from Ref. 1 or from most textbooks on compressible flow. In the mass coordinate, the density profile can be written in the following simple form:

$$\rho(z < \tau) = \rho_p \left(\frac{z}{\tau}\right)^{\frac{2}{\gamma+1}} = \rho_p \left(\frac{m}{m_{\text{rf}}}\right)^{\frac{2}{\gamma+1}}, \tag{18}$$

where $m_{\text{rf}} = a_p \rho_p t$ represents the trajectory of the rarefaction wave's leading edge. For $z > \tau$, the density is uniform and equal to the post-shock density $\rho = \rho_p$.

2. Relaxed Profiles of the Second Kind: Rarefaction Catches the Shock Inside the Shell: $m_* < m_{\text{shell}}$

In this case, the derivation of the relaxed profiles is significantly more complicated since there is no exact solution of the equations of motion after the rarefaction wave catches the prepulse shock. After the rarefaction wave reaches the shock at $z = 1$, the latter decays, leaving behind a relaxed profile with two distinct spatial shapes in the regions $0 < m < m_*$ and $m_* < m < m_s^p$, where $m_s^p$ is the location of the prepulse shock. In the dimensionless variable $z = m/m_*$, those two regions are $0 < z < 1$ and $1 < z < z_s^p$, where $z_s^p \equiv m_s^p / m_*$.

a. The region $z < 1$. One could speculate that the profiles in the region $0 < z < 1$ have a similar shape to the ones generated by the rarefaction wave, $\rho \sim z^{2/\gamma+1}$; however, this assumption does not take into account a second profile relaxation occurring when a sound wave travels backward down the rarefaction-wave profile right after the rarefaction wave catches the shock. The solution in the regions $0 < z < 1$ must satisfy Eq. (17) and the boundary conditions at $z = 0$ and $z = 1$. At $z = 0$, the vacuum boundary condition requires that $\rho(z = 0) = 0$. At $z = 1$, both the pressure and its gradient must be continuous to prevent separation of the continuous medium requiring that

$$P\left(z=1^{-},\tau\right)=P\left(z=1^{+},\tau\right),$$
$$\frac{dP}{dz}\left(z=1^{-},\tau\right)=\frac{dP}{dz}\left(z=1^{+},\tau\right). \tag{19}$$

It would be unrealistic to hope that a simple power law in $z$ would exactly satisfy the equations of motion and the boundary conditions; however, one could attempt to look for an approximate solution behaving as a power law of the mass coordinate

$$\hat{\rho}\approx\overline{\rho}(\tau)z^{\alpha}, \tag{20}$$

which, by construction, satisfies the boundary conditions at $z = 0$. Substituting Eq. (20) into Eq. (17) with $\hat{S}=1$ leads to the following two conditions:

$$\frac{d^2}{d\tau^2}\frac{1}{\overline{\rho}}+\alpha\left(\alpha\gamma-1\right)\overline{\rho}^{\gamma}\approx 0, \tag{21}$$

$$F_1(\alpha)\equiv\frac{\alpha\left(\gamma+1\right)}{2}\approx 1. \tag{22}$$

Note that the symbol ≈ has been used to indicate that the function (20) is meant to represent an approximate rather than an exact solution. To solve Eq. (21), one needs two initial conditions for $\overline{\rho}$ and $d\overline{\rho}/d\tau$ at $\tau=1^{+}$ just after the rarefaction wave interacts with the shock. While the initial condition for the density at $z = 1$ is trivial,

$$\overline{\rho}\left(\tau=1^{+}\right)=1, \tag{23}$$

the condition on the time derivate at $\tau = 1^{+}$ is rather complicated. The exact derivation of $\hat{\rho}'(1,1)$ is described in Ref. 1 and leads to Eq. (56) of Ref. 1, which reads as

$$\left[\frac{d\overline{\rho}}{d\tau}\right]_{\tau=1^{+}}=-\frac{6/\left(\gamma+1\right)}{\frac{3}{2}+\sqrt{\frac{\gamma}{2\left(\gamma-1\right)}}+\sqrt{\frac{\gamma-1}{2\gamma}}}. \tag{24}$$

It is worth mentioning that the initial condition on the density spatial profile at $\tau = 1$ requires that the function $\hat{\rho}(\tau=1,z)\approx\overline{\rho}(1)z^{\alpha}$ reproduces the rarefaction-wave solution $\hat{\rho}(1,z)=z^{2/\gamma+1}$, thus requiring that the power index $\alpha$ satisfies $\alpha-2/(\gamma+1)\approx 0$. This condition is identical to Eq. (22) and does not represent an additional condition. Note that a simple analytical solution of Eq. (21) is the following power law:

$$\overline{\rho}(\tau)=\left[\frac{2\left(\gamma-1\right)}{\alpha\left(\gamma+1\right)^2\left(\alpha\gamma-1\right)}\right]^{\frac{1}{\gamma+1}}\frac{1}{\tau^{\frac{2}{\gamma+1}}}. \tag{25}$$

Equation (25) satisfies the initial conditions (23) and (24) only if the following conditions are met:

$$F_2(\alpha)\equiv\left[\frac{2\left(\gamma-1\right)}{\alpha\left(\gamma+1\right)^2\left(\alpha\gamma-1\right)}\right]^{\frac{1}{\gamma+1}}\approx 1, \tag{26}$$

$$F_3(\alpha)\equiv\frac{1}{3}\left[\frac{2\left(\gamma-1\right)}{\alpha\left(\gamma+1\right)^2\left(\alpha\gamma-1\right)}\right]^{\frac{1}{\gamma+1}}\times\left(\frac{3}{2}+\sqrt{\frac{\gamma}{2\left(\gamma-1\right)}}+\sqrt{\frac{\gamma-1}{2\gamma}}\right)\approx 1. \tag{27}$$

To test Eq. (20) against the remaining boundary conditions (19) at $z = 1$, one needs to determine the solution for $z > 1$ carried out in the next section. In any case, the condition (22) implies that $\alpha\approx 2/\left(\gamma+1\right)$, indicating that the density profile shape is little changed by the second relaxation occurring after the shock–rarefaction merging.

b. The region $1 < z < z_s^p$. As mentioned earlier, the shock decays for $z > 1$, $\tau > 1$. The entropy profile left behind by the decaying shock is calculated in Ref. 1 and approximately follows a power law of the Lagrangian coordinate $m$ (or $z$):

$$\hat{S}(z)\simeq\frac{1}{z^{\delta}}, \tag{28}$$

where $\delta\simeq 1.31$ when the effects of ablation are neglected and the spatial range is limited to $z < 10$. Typically, the range $1 < z < 10$ includes most (if not all) of the ICF RX target

designs for both OMEGA-like as well as NIF-like capsules. However, if $z > 10$, the shock decay becomes self-similar and the power-law index asymptotically approaches the value $\delta \simeq 1.275$. The residual ablation pressure leads to a somewhat slower decay and can be accounted for through a lower $\delta$ (approximately 17% lower) as indicated in Ref. 1. In the self-similar solution, the density is a function of the coordinate

$$\xi = \frac{z}{z_s^p}, \tag{29}$$

where $z_s^p$ is the trajectory of the decaying shock, satisfying the Hugoniot condition

$$\dot{z}_s^p = \sqrt{\frac{\gamma - 1}{2\gamma}\frac{1}{\left(z_s^p\right)^\delta}}. \tag{30}$$

Equation (30) can be easily integrated with the initial condition $z_s^p(1) = 1$, leading to the following form of the decelerating shock trajectory:

$$z_s^p(\tau) = \left[1 + \left(1 + \frac{\delta}{2}\right)\sqrt{\frac{\gamma - 1}{2\gamma}}(\tau - 1)\right]^{\frac{2}{2+\delta}}. \tag{31}$$

The density $\hat{\rho}(\xi)$ does not follow a power law. Instead it must satisfy a complicated second-order differential equation derived by substituting Eqs. (16) and (28) into (17), leading to

$$\xi\frac{d}{d\xi}\left[1 + \frac{\delta}{2} + \xi\frac{d}{d\xi}\right]\frac{1}{\hat{\rho}} + \frac{2}{\gamma - 1}\frac{d^2}{d\xi^2}\frac{\hat{\rho}^\gamma}{\xi^\delta} = 0. \tag{32}$$

Equation (32) cannot be exactly integrated; however, one can again attempt to look for an approximate solution in the form of a power law of the self-similar coordinate

$$\hat{\rho} \approx \xi^\mu, \tag{33}$$

which approximately satisfies not only Eq. (32) but also the boundary by conditions at $z = 1$ [Eqs. (19)] and at the shock front $z = z_s^p$. In order for the simple power law (33) to approximate the solution of Eq. (32), the power index $\mu$ must satisfy the following conditions obtained upon substitution of (33) into (32):

$$G_1(\mu) \equiv \frac{\mu(\gamma + 1)}{\delta + 2} \approx 1, \tag{34}$$

$$G_2(\mu) \equiv \frac{\mu(\gamma - 1)\left(1 + \frac{\delta}{2} - \mu\right)}{2(\mu\gamma - \delta)(\mu\gamma - \delta - 1)} \approx 1. \tag{35}$$

The boundary conditions at the shock front are provided by the Hugoniot conditions that determine $\hat{\rho}$ and $d\hat{\rho}/d\xi$ at $\xi = 1$. Note that the density gradient can be obtained from Eqs. (35b) and (36) of Ref. 1 for $\xi = 1$, yielding the following condition:

$$\frac{d\hat{\rho}}{d\xi}(\xi = 1) = \frac{3\delta}{\gamma + 1}. \tag{36}$$

While the Hugoniot condition on the density $\hat{\rho}(1) = 1$ is trivially satisfied by $\hat{\rho} = \xi^\mu$, the condition on $d\hat{\rho}/d\xi$ requires that

$$G_3(\mu) \equiv \frac{\mu(\gamma + 1)}{3\delta} \approx 1. \tag{37}$$

The next step is to verify that Eq. (33) used for $z > 1$ satisfies Eqs. (19) at $z = 1$. Since the entropy is continuous at $z = 1$, the first of Eq. (19) requires that the density be continuous; therefore $\hat{\rho}\left(z = 1^-, \tau\right) \approx \hat{\rho}\left(z = 1^+, \tau\right)$, yielding

$$\overline{\rho}(\tau) \approx \frac{1}{\left[z_s^p(\tau)\right]^\mu}. \tag{38}$$

Then, using the continuity of the density and Eqs. (28) and (33) into the second of Eq. (19), one finds the condition

$$H(\alpha, \mu) \equiv \frac{\gamma\alpha + \delta}{\gamma\mu} \approx 1. \tag{39}$$

The last step is to find the two power indices $\alpha$ and $\mu$ in such a way that all the conditions [Eqs. (22), (26), (27), (34), (35), (37), and (39)] are met and that Eq. (38) is approximately satisfied for any time $\tau$ limited by $z_s^p(\tau) \le 10$ representing the range of interest for ICF capsule design.

c. Determination of the power indices. The power indices $\alpha$ and $\tau$ can be determined by plotting the conditions

$$G_1(\mu) \approx 1, \quad G_2(\mu) \approx 1, \quad G_3(\mu) \approx 1, \tag{40}$$

$$F_1(\alpha) \approx 1, \quad F_2(\alpha) \approx 1, \quad F_3(\alpha) \approx 1, \tag{41}$$

$$H(\alpha, \mu) \approx 1, \tag{42}$$

and determining $\alpha$ and $\mu$ so that all such conditions are approximately satisfied. Figure 98.44 shows the plot of three functions $G_1$, $G_2$, and $G_3$ that depends exclusively on the power index $\mu$ for a given $\gamma = 5/3$ and $\delta \simeq 1.315$. Observe that all the $G$-functions exhibit a zero near $\mu \simeq 1.45$, which can be considered as an approximate solution of all the Eqs. (40). After determining $\mu$, the $F$-functions are plotted together with the function $H$ versus the parameter $\alpha$ (Fig. 98.45), clearly indicating that $\alpha \simeq 0.75$ is an approximate solution of all Eqs. (41) and (42). The last step is to verify that Eq. (38) is approximately satisfied for any time $\tau$ and for $z_s^p \le 10$. First, it is easily found from Eq. (31) that the condition $z_s^p \le 10$ requires $\tau \le 61$. Second, we plot both sides of Eq. (38) versus time for $\tau \le 61$ (Fig. 98.46) and realize that both functions are approximately equal over the range of interesting times.

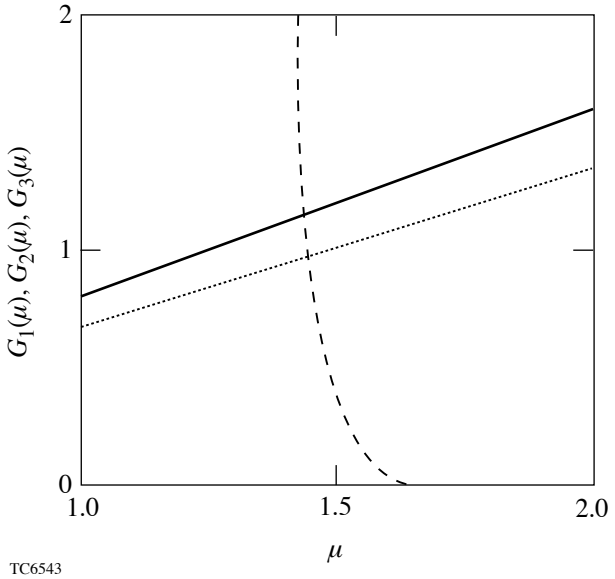


Figure 98.44
The functions $G_1(\mu)$ (solid), $G_2(\mu)$ (dashed), and $G_3(\mu)$ (dotted) are all approximately equal to 1 at $\mu = 1.45$.

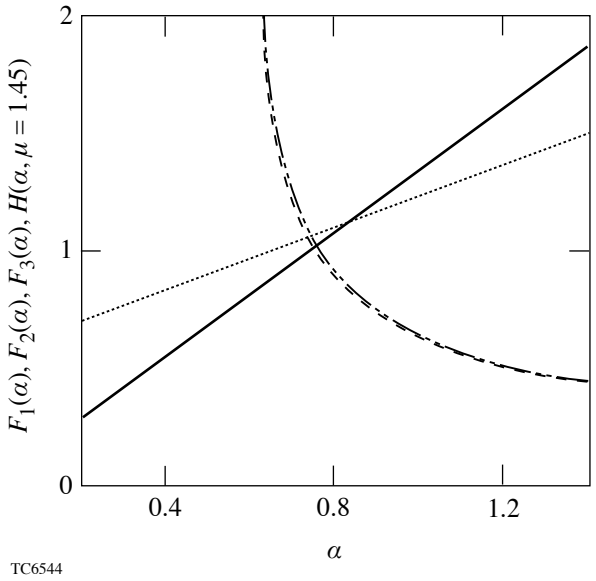


Figure 98.45
The functions $F_1(\alpha)$ (solid), $F_2(\alpha)$ (dashed), $F_3(\alpha)$ (dashed–double-dotted), and $H(\alpha,\mu = 1.45)$ (dotted) are all approximately equal to 1 at $\alpha = 0.75$.

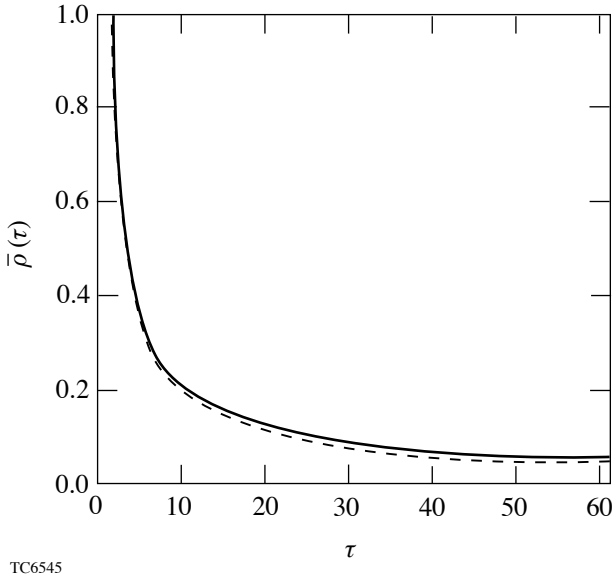


Figure 98.46
The analytic solution of Eqs. (21), (23), and (24) for $\bar{\rho}(\tau)$ given by Eq. (25) (solid) is compared to the approximate solution for $\bar{\rho}(\tau)$ given by Eq. (38) using $\mu = 1.45$ (dashed). The plot indicates good agreement between the two functional forms of $\bar{\rho}(\tau)$.

In summary, all the equations of motions and boundary conditions for $\tau > 1$ are approximately satisfied by simple power laws of the Lagrangian coordinate $z$, leading to the following solutions for $\gamma = 5/3$:

$$\rho\,(z<1) \approx \rho_p \left(\frac{z}{\tau}\right)^{3/4} = \rho_p \left(\frac{m}{m_{\rm rf}}\right)^{3/4}, \qquad (43)$$

$$\rho\left(1<z<z_s^p\right) \approx \rho_p \left(\frac{z}{z_s^p(\tau)}\right)^{1.45} = \rho_p \left(\frac{m}{m_s^p(\tau)}\right)^{1.45}, \qquad (44)$$

where $m_s^p$ represents the trajectory of the prepulse shock $m_s^p = z_s^p m_*$ and $m_{\rm rf} = a_p \rho_p t$. Here $t = 0$ represents the end of the prepulse. This concludes the calculation of the relaxed profiles. The next step is to determine the adiabat shape induced by the main shock propagating through the relaxed profiles of the first and second kind described by Eqs. (18) and [(43), (44)], respectively.

**Main Shock Propagation Through the Relaxed Profiles**

Before the prepulse shock reaches the rear surface, the main shock is launched by the foot of the main laser pulse and supported by the applied pressure $P_f$, which is assumed constant during the main shock propagation. The adiabat shaping occurs when the main shock travels up the relaxed density profile, shocking material with increasing density to lower and lower adiabats. The main shock is typically a strong shock in the sense that the ratio of pressures across the shock front is much larger than unity. Using the strong-shock form of the Hugoniot relations leads to a great simplification of the hydrodynamic analysis and is often accurate for the main shock propagation. However, it is important to emphasize that some of the strong-shock Hugoniot relations are accurately satisfied only for a very large pressure jump. For instance, the density jump across a strong shock with $Z = \left(P_2 - P_1\right)/P_1 >> 1$ is

$$\frac{\rho_2}{\rho_1} = \frac{\gamma+1}{\gamma-1} - \frac{4\gamma}{(\gamma-1)^2}\frac{1}{Z} + O\left(\frac{1}{Z^2}\right). \qquad (45)$$

Observe that even for large $Z$, the first-order corrections can be significant due to the large coefficient $-4/(\gamma-1)^2$. For instance, in a gas with $\gamma = 5/3$, this coefficient is –15 and the leading order term is 4, thus indicating that the $1/Z$ correction is small only when $Z >> 15/4$. Another implication of a strong main shock is the fact that the shocked material evolves on the time scale of its own sound speed, which scales as $\sqrt{P_M}$, where $P_M$ is the main shock pressure. Instead, the relaxed profiles evolve on a slower time scale of the order of the prepulse shock sound speed, which scales as $\sim \sqrt{P_p}$. It follows that in the limit of $\sqrt{P_M/P_p} >> 1$, one can neglect the dynamics of the relaxed profiles during the main shock propagation. In other words, one can regard the relaxed profiles as frozen in time while the main shock propagates through. Obviously, the corrections due to a finite $\sqrt{P_M/P_p}$ may be large and need to be estimated.

For the sake of simplicity, we will first proceed by neglecting the finite main shock strength correction, assume that the relaxed profiles are frozen, and determine the lowest-order solution. The finite shock strength effects will be estimated later as corrections to the lowest-order solution.

Effects of mass ablation and residual ablation pressures, though important, are also neglected in this article, and the calculation focuses on the ideal case of a strong shock supported by a constant applied pressure traveling up a relaxed density profile described by the power laws (18) or [(43), (44)].

1. Shock Propagation Through a Relaxed Profile of the First Kind

As indicated earlier in **Relaxed Profiles of the First Kind** (p. 108), the density profile generated by a rarefaction wave before its interaction with the prepulse shock is described by a simple power law of the areal density $\rho = \left(m/m_{\rm rf}\right)^{\alpha}$ with $\alpha = 2/(\gamma+1) = 0.75$. Here $m_{\rm rf} = a_p \rho_p t$ is the location of the rarefaction leading edge. If the main shock is much stronger than the prepulse shock, then the relaxed profile may be considered as frozen in time during the fast main shock propagation. Since both shocks must merge at the shell's inner surface, the fast main shock is launched when the prepulse shock is approaching the inner shell surface. One can therefore approximate $m_{\rm rf} \approx m_{\rm shell}$ to lowest order in the inverse shock strength.

a. The approximation of a static relaxed profile. Introducing the new variable $\zeta \equiv m/m_{\rm rf} \approx m/m_{\rm shell}$, the relaxed profile can be represented by the simple power law

$$\rho = \rho_p \zeta^{\alpha}, \quad \alpha = \frac{2}{\gamma+1}, \qquad (46)$$

with $0 < \zeta < 1$. To simplify the analysis, we introduce another dimensionless variable related to the main shock location:

$$\xi = \frac{m}{m_s^M} = \frac{\zeta}{\zeta_s^M}, \tag{47}$$

where both $m_s^M$ and $\zeta_s^M$ represent the main shock location in their respective coordinates. Obviously, $0 < \xi < 1$ with $\xi = 1$ representing the shock position. The profiles left behind by the main shock can be written in terms of the variables $\zeta$ and $\xi$ in the following form:

$$\rho = \frac{\rho_M \zeta^\alpha}{\Phi(\xi)^{1/\gamma}}, \quad S = \frac{S_M}{\zeta^{\gamma\alpha}}, \tag{48}$$

$$P = \frac{P_M}{\Phi(\xi)}, \quad u = a_M \frac{U(\xi)}{\zeta^{\alpha/2}}, \tag{49}$$

where

$$\rho_M \equiv \rho_p (\gamma + 1)/(\gamma - 1),$$

$$P_M = S_M \rho_M^\gamma,$$

$$a_M \equiv \sqrt{\gamma P_M / \rho_M},$$

and $\Phi(\xi)$, $U(\xi)$, and $S_M$ need to be determined. By inspection of Eqs. (48) and (49), it is clear that by setting $\Phi(1) = 1$, the pressure immediately behind the shock is $P_M$. Furthermore, using the Hugoniot condition for the post-shock velocity, one can immediately deduce that $U(1) = \sqrt{2/\gamma(\gamma - 1)}$. Substituting Eqs. (48) and (49) into the equations of motion and using the Hugoniot condition for the shock velocity,

$$\dot{m}_s^M = \sqrt{\frac{\gamma - 1}{2} p_M \rho_M \left(\zeta_s^M\right)^\alpha}, \tag{50}$$

it is straightforward to derive the two equations governing $\Phi$ and $U$:

$$\xi \sqrt{\frac{\gamma - 1}{2\gamma}} \frac{d\Phi^{1/\gamma}}{d\xi} - \frac{\alpha}{2} \frac{U}{\xi^{1-(\alpha/2)}} + \xi^{\alpha/2} \frac{dU}{d\xi} = 0, \tag{51}$$

$$\sqrt{\frac{\gamma(\gamma - 1)}{2}} \xi^{1-(\alpha/2)} \frac{dU}{d\xi} - \frac{d}{d\xi} \frac{1}{\Phi} = 0, \tag{52}$$

which need to be solved with the initial conditions $\Phi(1) = 1$ and $U(1) = \sqrt{2/\gamma(\gamma - 1)}$. The unknown $S_M$ can be determined by requiring that the solution of Eqs. (51) and (52) reproduces the applied pressure $P_f$ at $m = 0$. Using Eq. (49), one finds the following expression for $S_M$ and the pressure behind the shock $P_M$:

$$S_M = \frac{P_f \Phi(0)}{\rho_M^\gamma}, \quad P_M = P_f \Phi(0). \tag{53}$$

Observe that the pressure behind the shock is constant throughout the shock propagation. An approximate yet quite accurate solution of Eqs. (51) and (52) can be found by using the following ansatz:

$$\Phi(\xi) \approx \frac{\Phi(0)}{1 + \xi[\Phi(0) - 1]}. \tag{54}$$

Substituting Eq. (54) into (52) and using the boundary condition for the velocity at the shock front yields

$$U(\xi) \approx \sqrt{\frac{2}{\gamma(\gamma - 1)}} \left\{ \left[ 1 - \frac{1}{\Phi(0)} \right] \frac{2}{\alpha} \left( \xi^{\alpha/2} - 1 \right) + 1 \right\}. \tag{55}$$

The functions (54) and (55) must approximately satisfy Eq. (51), which can be rewritten upon substitution of the two functions as

$$\left[ 2 - \alpha - \frac{2}{\Phi(0)} \right] \frac{1}{\xi^{1-(\alpha/2)}} \approx \frac{\gamma - 1}{\gamma} \frac{\Phi(0) - 1}{\Phi(0)} \xi \Phi(\xi)^{(\gamma+1)/\gamma}. \tag{56}$$

Observe that since $\alpha < 2$, the left-hand side of Eq. (56) is singular for $\xi \to 0$ while the right-hand side is regular. It follows that Eq. (56) can be satisfied only when $2 - \alpha - 2/\Phi(0) \approx 0$, leading to

$$\Phi(0) \approx \frac{2}{2 - \alpha} = \frac{\gamma + 1}{\gamma} = 1.6. \tag{57}$$

The numerical solution of Eqs. (51) and (52) yields $\Phi(0) \simeq 1.68$ in good agreement with the analytic derivation. Figure 98.47 compares the numerically derived functions $\bar{p} \equiv \Phi(0)/\Phi(\xi)$ (representing the pressure profile) and $\bar{u} \equiv U(\xi)/\xi^{\alpha/2}$ (representing the velocity profile) with the analytic solutions from Eqs. (54), (57), and (55). Observe that the pressure increases approximately linearly before the shock, while the velocity profile is approximately flat. The shock pressure is amplified about 1.6 to 1.7 times with respect to the applied pressure. This amplification is due to the slowing down of the shocked material against the shock front. The shock-front velocity decreases in time as a power law. It can be easily derived by first determining the shock trajectory in the mass coordinate through Eq. (50) and then substituting the post-shock velocity $u_{\rm ps}$ calculated at the shock front [Eq. (49) at $\xi = 1$ and $m = m_s^M$ ] into the shock relation

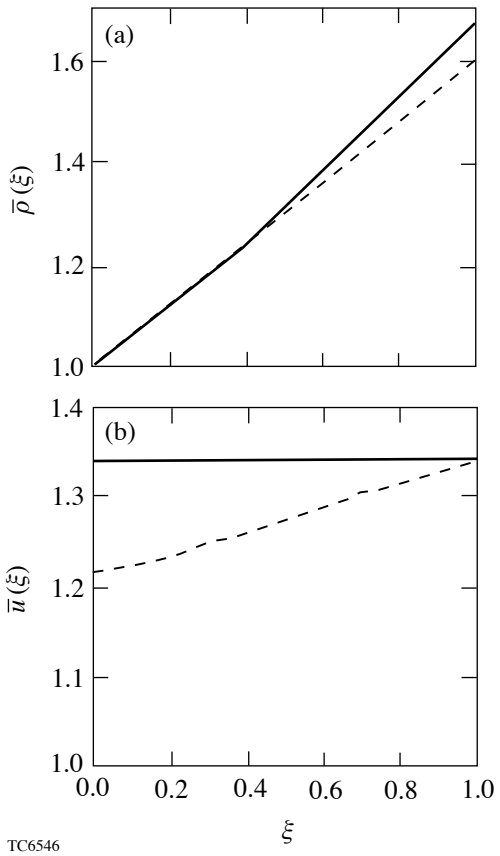


Figure 98.47
The numerical (solid) and analytic (dashed) solutions of the self-similar (a) pressure profiles $\bar{p}(\xi)$ and (b) density profile $\bar{\rho}(\xi)$ are shown to be in relatively good agreement.

$$U_{\rm shock} = \left[(\gamma+1)/2\right] u_{\rm ps}.$$

This leads to the following expression for the shock velocity:

$$U_{\rm shock} = \frac{a_M \sqrt{\dfrac{(\gamma+1)^2}{2\gamma(\gamma-1)}}}{\left[\sqrt{\dfrac{\gamma-1}{2\gamma}}\,\dfrac{2-\alpha}{2}\,\dfrac{\rho_M a_M t}{m_{\rm shell}}\right]^{\alpha/(2-\alpha)}}, \tag{58}$$

which decreases as $1/t^{0.6}$ for $\alpha = 2/(\gamma+1) = 0.75$.

Furthermore, as indicated by Eqs. (48) and (53), the entropy profile behind the main shock follows a simple power law of the mass coordinate

$$S(m) = \frac{P_f \Phi(0)}{{\rho_M}^{\gamma}} \left(\frac{m_{\rm shell}}{m}\right)^{\gamma\alpha}, \tag{59}$$

where the rarefaction leading edge $m_{\rm rf}$ has been taken near the inner surface at $m_{\rm rf} = m_{\rm shell}$ and $\alpha = 2/(\gamma+1)$. Indeed, it is important to require that the main shock, the rarefaction leading edge, and the prepulse shock merge at the target's rear surface, leading to $m_{\rm rf} \simeq m_{\rm shell} \simeq m_*$. This timing requirement is discussed in the **Introduction** (p. 106), where the optimized adiabat shaping procedure is described. Figure 98.48 shows the simulated adiabat profile generated by a strong shock driven by a 26-Mbar applied pressure traveling up a relaxed target with a density profile represented by the following power law:

$$\rho = \rho_p \left[\frac{(1-\alpha)\rho_p x}{m_{\rm shell}}\right]^{\frac{\alpha}{1-\alpha}}, \tag{60}$$

where $0 < x < m_{\rm shell}/(1-\alpha)\rho_p$ is the spatial coordinate. Observe that the profile in Eq. (60) requires that $\alpha < 1$ to avoid singularities at $x = 0$ (here $\alpha = 0.75$). Note Eq. (60) can be easily rewritten in terms of the mass coordinate $m$ leading to $\rho = \rho_p (m/m_{\rm shell})^{\alpha}$, which is identical to Eq. (18) with $m_{\rm rf} = m_{\rm shell}$. The solid curve of Fig. 98.48 represents the adiabat from the 1-D simulation, while the dashed curve is obtained from the analytic theory in Eq. (59). Observe that the two adiabat profiles are virtually identical, indicating excellent agreement between theory and simulations.

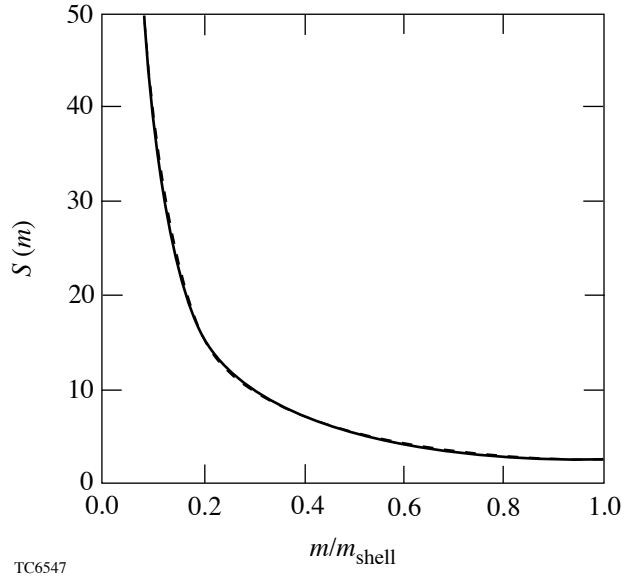


Figure 98.48
A comparison of the simulated (solid) and analytically calculated [Eq. (59)] (dashed) adiabat shapes generated by propagating a shock supported by a constant 26-Mbar pressure through a density profile of the first kind shows excellent agreement.

b. Corrections due to dynamic relaxed profiles/finite shock strength. The analytic theory above has been derived in the limit of a relaxed profile that is stationary during the shock propagation. However, the profile varies in time as the leading edge of the rarefaction wave travels toward the shell's inner surface. Because of these changes, the resulting adiabat profile left behind by the main shock is somewhat shallower than the one predicted by Eq. (59). One can estimate the effects of dynamic profiles on the adiabat shape by assuming that the relaxed profile changes slightly over the main shock propagation interval. The dynamic corrections to the entropy profiles can be estimated by determining the entropy at the shock front located at $m_s^M(t)$:

$$S\left(m_s^M\right) = \frac{P_{\rm ps}^M}{\left(\rho_{\rm ps}^M\right)^\gamma}, \tag{61}$$

where $P_{\rm ps}^M$ and $\rho_{\rm ps}^M$ are the post-shock pressure and density at the main shock front, respectively. It is obvious that if one can rewrite the right-hand side of Eq. (61) as a function of the shock position, then the entropy profile is given by the RHS with $m_s^M$ replaced by $m$. The post-shock density in Eq. (61) can be rewritten in terms of the pre-shock density at the shock front $\rho_{\rm bs}^M$ including the linear corrections in the inverse shock strength:

$$\rho_{\rm ps}^M \simeq \frac{\gamma+1}{\gamma-1}\rho_{\rm bs}^M\left[1-\frac{4\gamma}{\gamma^2-1}\frac{P_p}{P_M}\left(\frac{m_s^M}{m_{\rm shell}}\right)^{\gamma\alpha}\right], \tag{62}$$

where the post-shock pressure used to calculate the correction of order $P_p/P_M$ has been taken equal to the zeroth-order solution $P_M$. Because of the large numerical coefficient $4\gamma/\left(\gamma^2-1\right)$, the first-order correction in the inverse shock strength shown in Eq. (62) needs to be retained. Another important correction is in the pre-shock density $\rho_{\rm bs} = \rho_p\left(m/m_{\rm rf}\right)^\alpha$, which varies in time due to the evolution of the rarefaction leading edge $m_{\rm rf}$, which can be written as

$$m_{\rm rf} = m_{\rm shell} - a_p\rho_p\left(\Delta t_s^M + t_f - t\right), \tag{63}$$

where $\Delta t_s^M$ is the travel time of the main shock through the shell and $t_f$ is the beginning time of the laser foot when the main shock is launched. Observe that the second term on the right-hand side represents the correction to $m_{\rm rf}$ and is small as long as the main shock is strong. This can be quantified by calculating $\Delta t_s^M$ after integrating Eq. (50) and setting $m_{\rm rf} \simeq m_{\rm shell}$ into the variable $\zeta$. A straightforward calculation yields

$$\Delta t_s^M \simeq \sqrt{\frac{2\gamma}{\gamma-1}}\frac{2}{2-\alpha}\frac{m_{\rm shell}}{\rho_M a_M} \tag{64}$$

and $\left(t-t_f\right)/\Delta t_s^M = \left(m_s^M/m_{\rm shell}\right)^{1-\alpha/2}$. Substituting Eq. (64) into (63) leads to the following equation for the rarefaction leading edge in terms of the main shock location:

$$m_{\rm rf} = m_{\rm shell}\left\{1-\frac{2}{2-\alpha}\sqrt{\frac{2\gamma}{\gamma+1}\frac{P_p}{P_M}}\left[1-\left(\frac{m_s^M}{m_{\rm shell}}\right)^{\frac{2-\alpha}{2}}\right]\right\}. \tag{65}$$

Observe that the correction to $m_{\rm rf}$ is of the order of $\sqrt{P_p/P_M}$ as indicated in the introduction of **Main Shock Propagation Through the Relaxed Profiles** (p. 112) and can be significant even for a strong main shock. It follows that the post-shock density used in Eq. (61) can be rewritten, including the relevant corrections, in the following form:

$$\rho_{\rm ps}^M = \rho_M \left(\frac{m_s^M}{m_{\rm shell}}\right)^{\alpha} \times \frac{1-\dfrac{4\gamma}{\gamma^2-1}\dfrac{P_p}{P_M}\left(\dfrac{m_s^M}{m_{\rm shell}}\right)^{\gamma\alpha}}{\left\{1-\dfrac{2}{2-\alpha}\sqrt{\dfrac{2\gamma}{\gamma+1}\dfrac{P_p}{P_M}}\left[1-\left(\dfrac{m_s^M}{m_{\rm shell}}\right)^{\frac{2-\alpha}{2}}\right]\right\}^{\alpha}}. \quad (66)$$

The next step is the calculation of the dynamic correction to the post-shock pressure in Eq. (62). While the exact calculation of such corrections can be cumbersome, a fairly good approximation can be obtained by assuming that the post-main-shock pressure profile is linear in the mass coordinate:

$$P \approx P_f\left[1 + A(t)\frac{m}{m_s^M(t)}\right], \quad (67)$$

where $A(t)$ needs to be determined. It is important to notice that in the static relaxed profile case, $A(t)$ was previously determined to be approximately constant with $A(t) \approx A_0 \approx \alpha/(2-\alpha)$ It follows that the dynamic corrections will lead to a change in $A(t)$, which can be rewritten as a small correction to $A_0$ such as

$$A(t) = A_0 + \delta A(t) + \cdots, \quad (68)$$

where $\delta A << A_0$ needs to be determined. An important dynamic correction enters the Hugoniot relations for the velocity jump across the main shock

$$u_{\rm ps}^M = u_{\rm bs}^M + \sqrt{\frac{2}{\gamma+1}\frac{P_{\rm ps}^M}{\rho_{\rm bs}^M}}, \quad (69)$$

where $u_{\rm bs}^M$ is the pre-shock velocity at the shock front given by the standard rarefaction-wave solution

$$u_{\rm bs}^M = a_p\left[\frac{\alpha}{1-\alpha}\left(\frac{m_s^M}{m_{\rm rf}}\right)^{1-\alpha} + \sqrt{\frac{2}{\gamma(\gamma-1)}} - \frac{2}{\gamma-1}\right]. \quad (70)$$

Observe that $u_{\rm bs}$ represents a correction of the order of $\sqrt{P_p/P_M}$ in the Hugoniot relation [Eq. (69)] and can be evaluated using the lowest-order form of $m_{\rm rf} \simeq m_{\rm shell}$. Instead, the pre-shock density $\rho_{\rm bs}^M = \rho_b\left(m_s^M/m_{\rm rf}\right)^{\alpha}$ in Eq. (69) needs to include the lowest-order corrections for $m_{\rm rf}$ given in Eq. (65). Conservation of momentum requires that the acceleration balances the pressure gradient at the shock front leading to

$$\frac{\partial u_{\rm ps}^M}{\partial t} = -\left(\frac{\partial P}{\partial m}\right)_{m_s^M}. \quad (71)$$

Substituting Eqs. (67)–(70) into (71) yields the following ordinary differential equation for $\delta A$:

$$\frac{d}{d\eta}\left(\eta^{2-\alpha}\delta A\right) = -\frac{2\alpha}{2-\alpha}\sqrt{\frac{P_b}{P_M}} \times \left[\sqrt{\frac{2\gamma}{\gamma+1}} + \sqrt{2\gamma(\gamma+1)}\right]\eta^{2-\frac{3\alpha}{2}}, \quad (72)$$

where $\eta \equiv m_s^M/m_{\rm shell}$. Equation (72) can be integrated using the initial condition that $\delta A\left(m_s^M = 0\right) = 0$, leading to the following final form of the post-shock pressure at the shock front:

$$P_{\rm ps}^M = P_M\left\{1 - \frac{2\alpha}{3(2-\alpha)}\sqrt{\frac{P_p}{P_M}} \times \left[\sqrt{\frac{2\gamma}{\gamma+1}} + \sqrt{2\gamma(\gamma+1)}\right]\eta^{1-\frac{\alpha}{2}}\right\}. \quad (73)$$

Observe that the corrections due to finite main shock strength cause the main shock pressure to decrease as the shock propagates through the dynamic relaxed profile. This clearly leads to a gentler decrease in entropy.

The last step is to substitute Eqs. (66) and (73) into (61) and derive the final form of the adiabat shape:

$$S(m) = S_{\text{in}}\left(\frac{m_{\text{shell}}}{m}\right)^{\frac{2\gamma}{\gamma+1}} \frac{\chi\left(\dfrac{m}{m_{\text{shell}}}\right)}{\chi(1)}, \tag{74}$$

where

$$S_{\text{in}} = c_0 \frac{(\gamma-1)^{2\gamma}\chi(1)}{\gamma(\gamma+1)^{2\gamma-1}} \frac{P_f}{\rho_0^{\gamma}} \tag{75}$$

is the entropy on the inner shell surface, $c_0 = 1.68/1.6 = 1.05$ is a corrective factor to account for the analytical approximation used in Eq. (54), and $\rho_0$ is the initial shell density.

The function $\chi(x)$ represents the corrections due to the finite main shock strength

$$\chi(x) = \left[1 - \frac{2\sqrt{2}}{3}\frac{\gamma+2}{\gamma+1}\sqrt{\frac{P_p}{P_f}}x^{\frac{\gamma}{\gamma+1}}\right] \times \frac{\left[1 - \sqrt{\dfrac{2P_p}{P_f}}\left(1 - x^{\frac{\gamma}{\gamma+1}}\right)\right]^{\frac{2\gamma}{\gamma+1}}}{\left[1 - \dfrac{4\gamma^2}{(\gamma+1)^2(\gamma-1)}\dfrac{P_p}{P_f}x^{\frac{2\gamma}{\gamma+1}}\right]^{\gamma}}, \tag{76}$$

where the relation $\alpha = 2/(\gamma+1)$ has been used and $P_p/P_f$ is the ratio of the prepulse pressure to the pressure of the foot of the main pulse. This concludes the analysis of the main shock propagation through a relaxed profile of the first kind. The next step is to investigate the main shock propagation through relaxed profiles of the second kind and determine the resulting adiabat shape.

## 2. Shock Propagation Through a Relaxed Profile of the Second Kind

In the case of a short prepulse, the rarefaction wave catches the shock at $m = m_*$ before the inner surface ($m < m_{\text{shell}}$), and the shock decays until it reaches the inner surface at $m = m_{\text{shell}}$. As described in **Relaxed Profiles of the Second Kind** (p. 108), the relaxed profile for $\gamma = 5/3$ is well-approximated by two power laws of the mass coordinate: $\rho \sim m^{0.75}$ for $m < m_*$ and $\rho \sim m^{1.45}$ for $m_* < m < m_{\text{shell}}$. The analysis of the main shock propagation through such a profile is vastly more complicated with respect to the case of the single power-law profile discussed in **Shock Propagation Through a Relaxed Profile of the First Kind** (p. 112). An approximate analytic solution can be found, however, by assuming that the pressure profile behind the main shock is linear in the mass coordinate. Similar to the case of profiles of the first kind, we will first consider the approximation of infinite main shock strength and static relaxed profiles. The corrections due to the finite shock strength and dynamic profiles are estimated *a posteriori* as small perturbations of the zeroth-order solution.

a. The approximation of a strong shock and a static relaxed profile. In the static case, the relaxed profile in the region $m < m_*$ is identical to the profile of the first kind, leading to a pressure profile behind the shock that linearly increases about 60% with respect to the applied foot pressure $P_f$. Once the main shock enters into the second region $m_* < m < m_{\text{shell}}$, an exact analytic solution cannot be found. A careful analysis of the numerical simulation indicates, however, that the pressure profile behind the shock remains approximately linear in the mass coordinate. In contrast with the behavior in the first region, however, the shock-front pressure is not constant while the pressure at $m_*$ varies slightly around the value $\omega P_f$ with $\omega \simeq 1.5$ to 1.6 for $\gamma = 5/3$. Thus, it makes sense to look for a solution of the hydrodynamic equation with a linear pressure profile of the following form:

$$P_{\text{ps}}(m > m_*) \approx \omega(\gamma) P_{\text{foot}}\left[1 + D(t)\left(\frac{m}{m_*} - 1\right)\right], \tag{77}$$

where $\omega(\gamma)$ is a constant that must be chosen to reproduce the pressure at the time when the main shock reaches $m_*$. Using the results of the previous section for the main shock propagation for $m < m_*$, one can conclude that

$$\omega(\gamma) \approx \frac{\gamma+1}{\gamma}. \tag{78}$$

Similar to the analysis in **Shock Propagation Through a Relaxed Profile of the First Kind** (p. 112), Eq. (77) can be substituted into the momentum equation at the shock front $\left[\partial_t u_{\text{ps}} = -(\partial_m P)\right]_{m_s^M}$, where the post-shock velocity at the

shock front is given by the Hugoniot relation

$$u_{\rm ps}^{M} = \sqrt{2P_{\rm ps}^{M}/(\gamma+1)\rho_{\rm bs}^{\rm M}}$$

with the pre-shock density at the shock front given by

$$\rho_{\rm bs}^{M} = \rho_p\left(\frac{m_s^M}{m_{\rm shell}}\right)^{\mu}, \tag{79}$$

where the prepulse shock location $m_{\rm sh}^{p}$ has been assumed to have reached the inner shell surface so that $m_s^p \simeq m_{\rm shell}$. As in **Shock Propagation Through a Relaxed Profile of the First Kind** (p. 112), $u_{\rm ps}^{M}$ and $P_{\rm ps}^{M}$ represent the post-shock velocity and pressure at the main shock front. The resulting shock-front momentum equation can be simplified by using the main shock trajectory $m_s^M(t)$ as the time coordinate and by using the shock mass velocity $\dot{m}_s^M = \sqrt{(\gamma+1)P_{\rm ps}^{M}\rho_{\rm bs}^{M}/2}$. A straightforward manipulation of the momentum equation leads to the following simple differential equation for $D$:

$$\frac{dD}{dz_s^M}\left(z_s^M-1\right)+3D-\frac{\mu}{z_s^M}\left[1+D\left(z_s^M-1\right)\right]=0, \tag{80}$$

where $D = D\left[z_s^M\right]$ and $z_s^M \equiv m_s^M(t)/m_*$. It is important to note that the only nonsingular solution of Eq. (80) has the simple form

$$D(x)=\frac{2\left(x^{\mu}-1\right)+\mu(x-3)(x-1)-\mu^2(x-1)^2}{(\mu-2)(\mu-1)(x-1)^3}. \tag{81}$$

The pressure at the shock fronts can be determined from Eq. (77) upon substitution of Eq. (81), leading to

$$P_{\rm ps}^{M}\left(m_s^M\right)\approx\omega(\gamma)P_f\left[1+D\left(\frac{m_s^M}{m_*}\right)\left(\frac{m_s^M}{m_*}-1\right)\right], \tag{82}$$

representing a growing function of $m_s^M$ reaching the asymptotic value of 3.6 for $m_s^M >> m_*$. The entropy behind the shock can be easily calculated by substituting the pressure and density at the shock front into the definition of the entropy:

$$S\left(m_s^M\right)=\frac{P_{\rm ps}^{M}\left(m_s^M\right)}{\left[\rho_{\rm ps}^{M}\left(m_s^M\right)\right]^{\gamma}}. \tag{83}$$

Using Eqs. (77), (81), and (82) into (83) leads to the following form of the entropy:

$$S_{\infty}\left(m_* < m \le m_{\rm shell}\right)=\frac{\omega(\gamma)P_f}{\rho_M^{\gamma}}$$

$$\times\left(\frac{m_{\rm shell}}{m}\right)^{\gamma\mu}\left[1+D\left(\frac{m}{m_*}\right)\left(\frac{m}{m_*}-1\right)\right], \tag{84}$$

where $\rho_M = \rho_p(\gamma+1)/(\gamma-1)$ and the subscript $\infty$ indicates that Eq. (84) is valid only for infinite main shock strength. Figure 98.49 shows a comparison of the predicted adiabat profile of Eq. (84) (dashed) with the simulated adiabat profile (solid) generated by a strong shock driven by a 26-Mbar applied pressure traveling up a static, relaxed target with a density profile given by $\rho = \rho_M(m_*/m_{\rm shell})^{\mu}(m/m_*)^{\alpha}$ for $m \le m_*$, and $\rho = \rho_M(m/m_{\rm shell})^{\mu}$ for $m_* < m \le m_{\rm shell}$. Here, $m_*/m_{\rm shell}$ is chosen to be 0.05. The theory again shows excellent agreement with the simulation.

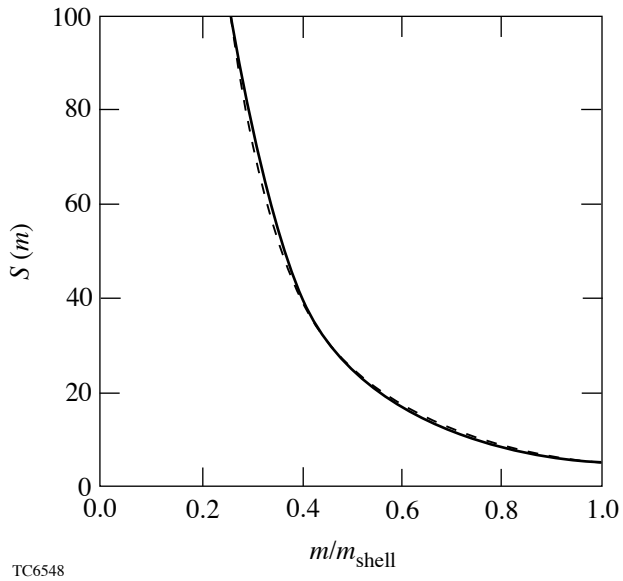


Figure 98.49
A comparison of the simulated (solid) and analytically calculated [Eq. (84)] (dashed) adiabat shape generated by propagating a shock supported by a constant 26-Mbar pressure through a density profile of the second kind shows excellent agreement.

It is interesting to observe that the linear approximation for the pressure profile leads to a flat velocity profile as shown by substituting Eq. (77) into the momentum equation, yielding

$$u(m,t) = u_{\rm ps}^{M}(t). \tag{85}$$

The density behind the shock can be determined from the pressure and the entropy through the relation $\rho = (p/S)^{1/\gamma}$. Upon substitution of the density, the mass conservation equation [Eq. (4)] can be solved for the velocity profile, leading to

$$u(m,t) = u_{\rm ps}^{M}\left[1 - G\left(z, z_s^M\right)\right], \tag{86}$$

where $z = m/m_*$ and

$$G\left(z, z_s^M\right) = \frac{\gamma - 1}{2\gamma}\frac{dD\left(z_s^M\right)}{dz_s^M}$$

$$\times \int_{z_s^M}^{z} \frac{(x-1)\left[1 + D(x)(x-1)\right]^{1/\gamma}}{\left[1 + D\left(z_s^M\right)(x-1)\right]^{(\gamma+1)/\gamma}}\left(\frac{z_s^M}{x}\right)^{\mu} dx. \tag{87}$$

Observe that the two velocity profiles obtained from the momentum and mass conservation equations are approximately equal in magnitude as long as $|G| << 1$. The value $G$ can be estimated after replacing $z$ with $\eta z_s^M$ and by plotting $G\left(\eta z_s^M, z_s^M\right)$ for $1/z_s^M < \eta < 1$ for different values of $z_s^M$. Figure 98.50 shows the value of $G$ for $z_s^M$ = 2, 5, 10, 20, indicating that $G$ does not exceed 0.21 for typical values of $z_s^M \le 20$. It follows that the linear pressure profile of Eq. (77), the flat velocity profile of Eq. (85), and the entropy profile of Eq. (84) are accurate approximations of the solution to the hydro equations.

b. Corrections due to dynamic relaxed profiles/finite shock strength. To determine the correction to the adiabat shape due to the finite shock strength and the dynamic evolution of the relaxed profile during the main shock propagation, one needs to calculate the main shock position in terms of the prepulse shock location. Both the main shock $m_s^M$ and the prepulse shock positions $m_s^p$ are governed by the Hugoniot relations

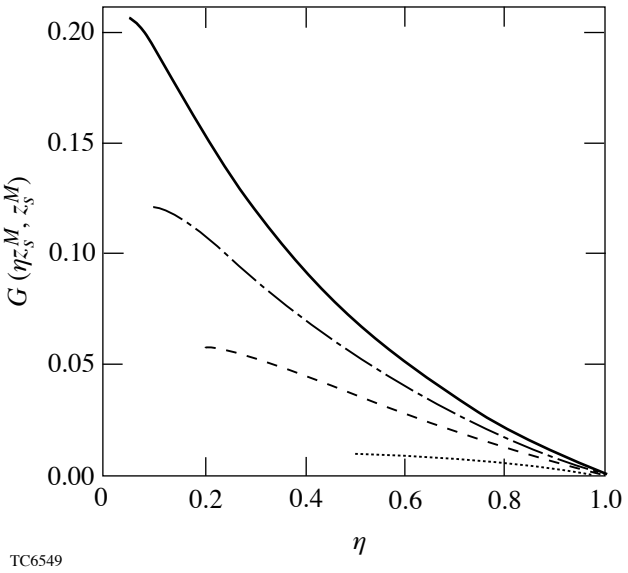


Figure 98.50
Plots of $G\left(\eta z_s^M, z_s^M\right)$ for $z_s^M$ = 2, 5, 10, 20 (dotted, dashed, dash–dotted, and solid lines, respectively) show that $G$ does not exceed 0.21 for typical values of $z_s^M \le 20$.

$$\dot{m}_s^M = \sqrt{\frac{\gamma - 1}{2} P_f \rho_M \left(\frac{m_s^M}{m_s^p}\right)^{\mu}\left[1 + D\left(z_s^M\right)\left(z_s^M - 1\right)\right]}, \tag{88}$$

$$\dot{m}_s^p = \sqrt{\frac{\gamma - 1}{2} P_p \rho_p \left(\frac{m_*}{m_s^p}\right)^{\delta}}, \tag{89}$$

where $\delta \simeq 1.315$. Replacing the time variable with $m_s^p(t)$ into Eq. (88) leads to the following algebraic equation relating the main and the prepulse shock location:

$$\left(z_s^p\right)^{\beta} - z_{\rm shell}^{\beta} = \beta\sqrt{\frac{2(\gamma-1)}{\gamma+1}\frac{P_p}{\omega(\gamma)P_f}}$$

$$\times\left[\sigma\left(z_s^M\right) - \sigma\left(z_{\rm shell}\right)\right], \tag{90}$$

where $\beta = (\delta - \mu + 2)/2$, $z_s^p = m_s^p/m_*$, $z_{\rm shell} = m_{\rm shell}/m_*$, and

$$\sigma(\xi) = \sqrt{\frac{(\mu-2)\xi^{1-\mu} - (\mu-1)\xi^{2-\mu} + 1}{(\mu-2)(\mu-1)}}. \qquad (91)$$

It is important to recognize that Eq. (90) has been derived using the condition that $z_s^p = z_{\text{shell}}$ when $z_s^M = z_{\text{shell}}$. This is an essential constraint requiring that both the prepulse and main shock merge on the shell's inner surface. Observe that Eq. (90) can be used to find $z_s^p$ in terms of $z_s^M$. An analytic form of $z_s^M$ in terms of $z_s^p$ can also be found by approximating $\mu \simeq 1.45$ and reducing Eq. (90) to a second-order algebraic equation for $z_s^M$.

Similar to the analysis in **Shock Propagation Through a Relaxed Profile of the First Kind** (p. 112), we estimate the dynamic corrections to the entropy profile by rewriting the entropy at the main shock front:

$$S\left(z_s^M\right) = \left(\frac{z_s^p}{z_s^M}\right)^{\mu\gamma} \frac{P_{\text{ps}}^M\left(z_s^M, t\right)}{\rho_M^\gamma}. \qquad (92)$$

Since we did not find an exact solution of the post-shock pressure for the static case, it is not worth calculating small corrections to an already inexact solution. Nevertheless, we retain the corrections due to the dynamic evolution of the relaxed profile. These corrections require including the time dependence of $z_s^p$ in the pre-shock density. We speculate that the largest corrections to the entropy are likely to come from such dynamic effects. This consideration is supported by the large power index $\mu\gamma \simeq 2.4$ for $z_s^p$ in Eq. (92) and the finite shock strength corrections of the order of $\sqrt{P_p/P_f}$ in Eq. (92) for $z_s^p$. It follows that the dynamic corrections to the entropy profile can be determined by substituting $z_s^p$ from Eq. (90) into Eq. (92) and by replacing $z_s^M$ with $z = m/m_*$. A straightforward manipulation leads to the following form of the entropy profile:

$$S(m) = S_\infty(m)\left\{1 - \beta\left(\frac{m_*}{m_{\text{shell}}}\right)^\beta \sqrt{\frac{2(\gamma-1)}{(\gamma+1)\,\omega(\gamma)}\frac{P_p}{P_f}}\right.$$

$$\left. \times \left[\sigma\left(\frac{m_{\text{shell}}}{m_*}\right) - \sigma\left(\frac{m}{m_*}\right)\right]\right\}^{\frac{\gamma\mu}{\beta}}, \qquad (93)$$

where $S_\infty$ is given in Eq. (84). Observe that dynamic corrections to the adiabat shape lead to a shallower profile.

**Conclusion**

We have derived analytical forms of the relaxation adiabat shapes for (1) the case where the prepulse is long enough that the rarefaction wave catches the prepulse shock at the rear surface of the shell, and (2) the case of short prepulses, where the mass undertaken by the unattenuated prepulse shock is less than the total mass of the shell. The analytic relaxation adiabat profiles derived here are in excellent agreement with simulation. In addition, we have shown that relaxation designs with short prepulses lead to steeper adiabat gradients than decaying shock designs. The effects of mass ablation and residual ablation pressure on relaxation adiabat shapes will be analyzed in a future article.

ACKNOWLEDGMENT

This work was supported by the U.S. Department of Energy Office of Inertial Confinement Fusion under Cooperative Agreement No. DE-FC03-92SF19460, the University of Rochester, and the New York State Energy Research and Development Authority. The support of DOE does not constitute an endorsement by DOE of the views expressed in this article.

**Appendix A: Relaxed Density Profiles in Real Space**

A better understanding of the relaxed profile shape can be obtained by converting the profile functions from the Lagrangian coordinate $m$ to the spatial coordinate $x$. Equation (3) relating the mass to the initial density is also valid if the initial density is replaced by the density at time $t$ as long as the lower limit and upper limit of integration are the trajectory of the outer surface $x_{\text{out}}(t)$ and the trajectory of generic fluid element $x(t)$. It follows that the conversion between mass and real space is straightforward once the relation between $m$ and $x$ is rewritten in the differential form

$$\frac{dm}{dx} = \rho(x,t). \qquad (A1)$$

Equation (A1) is then used to rewrite the profiles of the first kind [Eq. (18)] and second kind [Eqs. (43) and (44)] in real space.

1. Relaxed Profiles of the First Kind

In the case where the shock and rarefaction merge at the inner shell surface, one can substitute Eq. (A1) into (18) and find the density profile shape in real space:

$$\rho = \rho_p\left[\frac{\gamma-1}{\gamma+1}\frac{x - x_{\text{out}}}{a_p t}\right]^{\frac{2}{\gamma-1}}, \qquad (A2)$$

where $x_{out}$ is the trajectory of the outer shell surface coinciding with the trailing edge of the rarefaction wave moving away from the shell with the escape velocity $2a_p/(\gamma-1)$. The range of $x$ in Eq. (A2) is limited by the trailing and leading edge of the rarefaction wave. Since the leading edge travels inside the shell with the sound speed, the range of $x$ is limited by $x_{out} < x < x_{out} + a_p t$. Note that $t = 0$ at the time when the prepulse ends and the rarefaction is launched. Equation (A2) indicates that, in real space, the density profile is a simple power law of the distance from the rarefaction trailing edge. The leading edge of the rarefaction wave reaches the prepulse shock at the inner shell surface ($m_* = m_{shell}$) at the time

$$t_{shell} = \frac{m_{shell}}{\left(a_p \rho_p\right)} = \frac{\gamma-1}{\gamma+1}\frac{d_{shell}}{a_p}, \tag{A3}$$

where $d_{shell}$ is the initial shell thickness and $m_{shell} = \rho_0 d_{shell}$ is the total shell mass. At this time, the density profile is simply

$$\rho\left(t = t_{shell}\right) = \rho_p\left(\frac{x - x_{out}}{d_{shell}}\right)^{\frac{2}{\gamma-1}}. \tag{A4}$$

Note that the profile extends over a distance equal to the uncompressed shell thickness $d_{shell}$ and approaches the compressed density $\rho_p$ on the shell's inner surface located at $x_{in} = x_{out} + d_{shell}$.

2. Relaxed Profiles of the Second Kind

By defining with $x_*(\tau)$ the trajectory of the Lagrangian point corresponding to the fluid element where the prepulse shock and rarefaction wave interact (i.e., $m = m_*$), and with $x_s^p(\tau)$ the location of the prepulse shock after the interaction, the spatial density profile for the region $x_*(\tau) < x < x_s^p(\tau)$ can be obtained by substituting Eq. (A1) into Eq. (44), leading to

$$\rho = \rho_p\left[\frac{1}{1 + 4\left(\mu-1\right)\left(1 - x/x_s^p\right)}\right]^{\frac{\mu}{\mu-1}}, \tag{A5}$$

where $\mu = 1.45$ for $\gamma = 5/3$. By defining with $\bar{x}_* \equiv x_*(1)$ the initial position inside the shell of the shock–rarefaction interaction point, it is straightforward to show that

$$x_s^p(\tau) = \bar{x}_* z_s^p(\tau), \tag{A6}$$

$$x_*(\tau) = \bar{x}_* z_s^p(\tau)\left[1 + \frac{1 - z_s^p(\tau)}{4\left(\mu-1\right)}\right], \tag{A7}$$

where $z_s^p$ is given in Eq. (31). Equation (A5) represents the spatial density profile of the shell portion between the shock–rarefaction merging point and the shock front. The density profile of the remaining portion between the shock–rarefaction merging point and the outer shell surface is described by Eq. (43) and in real space can again be determined by integrating Eq. (43) upon substitution of Eq. (A1). The result is similar to the density profile of the first kind and yields

$$\rho = \rho_p\left(\frac{\gamma-1}{\gamma+1}\frac{x - x_{out}}{a_p t}\right)^{\frac{2}{\gamma-1}}. \tag{A8}$$

It is important to emphasize that the density profiles [Eqs. (43) and (44)] are approximate solutions; therefore, the profiles [Eqs. (A5) and (A8)] are also approximate solutions. The location of the rarefaction trailing edge (or outer shell surface) cannot be exactly calculated because it is affected by the sound waves traveling down from the point of shock–rarefaction interaction. An approximate form of $x_{out}$ can be derived by requiring that the density is continuous at $x = x_*(\tau)$, thus setting Eq. (A8) equal to Eq. (A5) at $x_*(\tau)$. This leads to the following form of $x_{out}$:

$$x_{out} = x_*(\tau) - \bar{x}_* \frac{a_p \tau}{z_s^p(\tau)^{\frac{\mu(\gamma-1)}{2}}}. \tag{A9}$$

Observe that, in real space, the density profile is represented by two very different functions of $x$: Eq. (A5) describes the profile behind the shock, and Eq. (A8) describes the profile behind the rarefaction–shock merging point.

REFERENCES

1. K. Anderson and R. Betti, Phys. Plasmas **10**, 4448 (2003).

2. V. N. Goncharov, J. P. Knauer, P. W. McKenty, P. B. Radha, T. C. Sangster, S. Skupsky, R. Betti, R. L. McCrory, and D. D. Meyerhofer, Phys. Plasmas **10**, 1906 (2003).

3. K. Anderson and R. Betti, Phys. Plasmas **11**, 5 (2004).

# Using Nuclear Data and Monte Carlo Techniques to Study Areal Density and Mix in $D_2$ Implosions

## Introduction

Maximizing the hot-fuel areal density ($\rho R_{hot}$) and understanding the effects of mix upon it are fundamental issues of inertial confinement fusion (ICF).[1–3] One method used to estimate $\rho R_{hot}$ of $D_2$-filled capsule implosions is to measure the yields of secondary protons ($Y_{2p}$) and/or secondary neutrons ($Y_{2n}$) relative to the primary neutron yield ($Y_{1n}$).[4–12] These secondary particles result from sequential reactions in which the energetic primary products of reactions

$$D + D \rightarrow n(2.45\ \text{MeV}) + {}^3\text{He}(0.82\ \text{MeV}), \tag{1}$$

$$D + D \rightarrow p(3.02\ \text{MeV}) + T(1.01\ \text{MeV}) \tag{2}$$

undergo fusion reactions with thermal deuterons in the fuel:

$${}^3\text{He}(\le 0.82\ \text{MeV}) + D \rightarrow p(12.5 - 17.4\ \text{MeV}) + {}^4\text{He}(6.6 - 1.7\ \text{MeV}), \tag{3}$$

$$T(\le 1.01\ \text{MeV}) + D \rightarrow n(11.9 - 17.2\ \text{MeV}) + {}^4\text{He}(6.7 - 1.4\ \text{MeV}). \tag{4}$$

These processes produce secondary particles with spectra spread over significant energy intervals due to the kinetic energy of the primary reactants. The secondary-particle yields are typically two to three orders of magnitude lower than the primary yield, and the ratios $Y_{2n}/Y_{1n}$ and $Y_{2p}/Y_{1n}$ (which are linearly dependent on $\rho R_{hot}$ in certain plasma regimes) can each be used to infer a value of $\rho R_{hot}$ for implosions of $D_2$-filled capsules in both direct- and indirect-drive experiments.[12–15] In those studies, the simple "hot-spot" and/or the "uniform" models were used to relate these ratios to $\rho R_{hot}$. Although these simple models have been widely used to infer a value of $\rho R_{hot}$, they have some serious limitations that can result in misinterpretation and errors (as described in the next section); one manifestation of these problems is often disagreement between the proton- and neutron-inferred values of $\rho R_{hot}$ calculated from experimental data (see Fig. 98.51). These deviations are related to a combination of mix, temperature profile, and the difference between the cross section for secondary reactions (3) and (4). These factors can cause secondary protons and neutrons to be produced in different regions of the compressed capsules (Fig. 98.52). In addition,

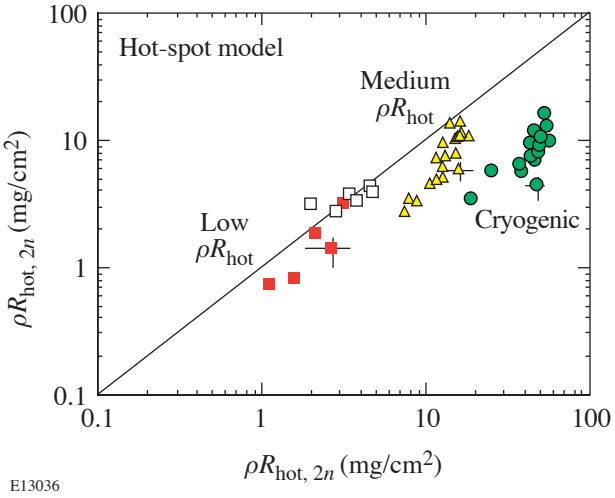


Figure 98.51
Secondary-proton- and secondary-neutron-implied values of $\rho R_{hot}$ are compared for implosions of low $\rho R_{hot}$ (squares), medium $\rho R_{hot}$ (triangles), and cryogenic (circles) capsules on OMEGA. For low-$\rho R_{hot}$ implosions, the values of $\rho R_{hot}$ inferred from secondary protons and neutrons using the simple hot-spot model agree well. It is also shown that values of $\rho R_{hot}$ are larger for implosions with ~12-kJ laser energy (open squares) than for implosions with ~23-kJ laser energy (closed squares). For these dramatically overdriven implosions, it is possible that the effects of mix are coming back into play, as indicated by the observation that $\rho R_{hot,2n}$ is larger than $\rho R_{hot,2p}$. For implosions with larger $\rho R_{hot}$, however, the values inferred from secondary neutrons are always larger than the values from secondary protons. The error bars shown are typical of each type of implosion; they include uncertainties in the measurements and in the assumed values of the density.

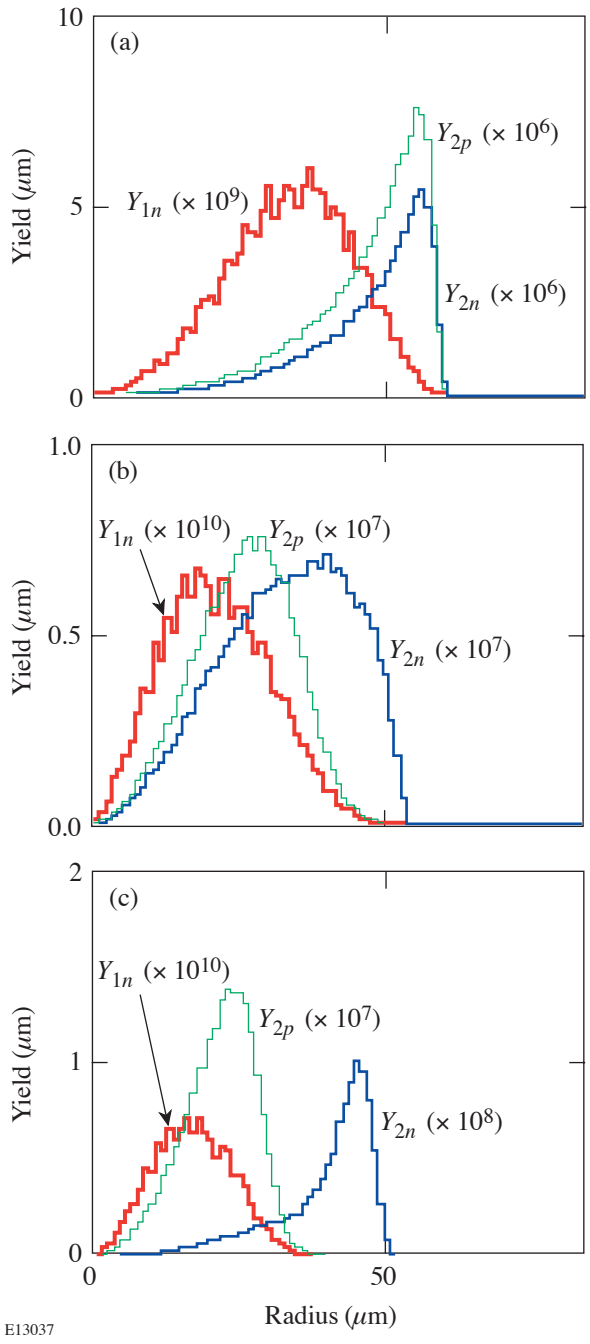


Figure 98.52
Calculated radial distributions of primary- and secondary-birth positions per unit length for (a) low-$\rho R$ implosion 30981, (b) medium-$\rho R$ implosion 27443, and (c) cryogenic implosion 28900. For low-$\rho R$ implosions, where $\rho R_{2p}$ and $\rho R_{2n}$ agree reasonably well, birth positions of secondary protons and neutrons are virtually identical. For medium-$\rho R$ and cryogenic implosions, however, where $\rho R_{2n}$ is always larger than $\rho R_{2p}$, secondary neutrons are produced in more outer regions compared to secondary protons. Note that calculated radial distributions of primary birth rates per unit volume (as opposed to unit radius) are shown in Figs. 98.60–98.62 for these three implosions.

others have noted some puzzling issues with recent secondary-neutron measurements in indirect-drive implosions on OMEGA.[16] In that work, the authors observed a factor-of-3-larger $Y_{2n}/Y_{1n}$ ratio and a narrower secondary-neutron spectrum than predicted for these low-convergence implosions (where mix should be relatively unimportant). In contrast, for high-convergence implosions, they found better agreement between measured and predicted $Y_{2n}/Y_{1n}$ values.

In previous work,[12] high-resolution secondary-proton spectra were obtained during experiments on OMEGA.[17] The yields were used with measured neutron yields to estimate $\rho R_{\text{hot}}$ with the hot-spot and uniform models, and it was shown that the $Y_{2p}/Y_{1n}$-inferred $\rho R_{\text{hot}}$ was often lower than the $Y_{2n}/Y_{1n}$-inferred $\rho R_{\text{hot}}$. This was attributed to the effects of fuel–shell mix, and it was suggested that the two inferences might be considered lower and upper limits, respectively. In this article, that work is extended to cover a wider range of implosion types and to include Monte Carlo simulations that allow a detailed study of the implications of more-realistic models of the compressed core on the secondary production. The following sections (1) describe the hot-spot and uniform models and their limitations, (2) describe the experiments and the range of measured parameters, (3) describe a Monte Carlo program that will model the implosions to understand how particle production occurs, (4) discuss results from both experiments and Monte Carlo calculations, with an emphasis on how $\rho R_{\text{hot}}$ is related to the yields of primary and secondary particles, and (5) summarize the results.

## Primary and Secondary Products

The hot-spot and uniform models have been commonly used to relate $Y_{2p}/Y_{1n}$ and $Y_{2n}/Y_{1n}$ to $\rho R_{\text{hot}}$. The hot-spot model assumes that an imploded capsule is a sphere of uniform density and temperature and that all primary reactions occur at the very center of the capsule. A fraction of the primary $^3$He (tritons) fuse with thermal deuterons, producing secondary protons (neutrons) as they move radially outward. As the primary particles travel through the D plasma, they lose energy, and the probability for producing secondary particles along the path varies greatly since the secondary D$^3$He and DT fusion cross sections ($\sigma_{\text{D}^3\text{He}}$ and $\sigma_{\text{DT}}$) are strong functions of the primary $^3$He and T energies [Fig. 98.53(a)].[18] $\sigma_{\text{D}^3\text{He}}$ peaks at ~0.65 MeV, close to the $^3$He birth energy (0.8 MeV), while $\sigma_{\text{DT}}$ peaks at ~0.18 MeV, significantly lower than the triton birth energy (1.0 MeV). As a result, secondary protons are mainly produced near the $^3$He birth position, while secondary neutrons are mainly produced farther away from the triton birth position [see Fig. 98.53(b)]. This information is used to calcu-

late $\rho R_{\text{hot}}$ from $Y_{2p}/Y_{1n}$ and $Y_{2n}/Y_{1n}$, and the resulting dependencies are shown in Fig. 98.54 for D plasmas with different temperatures and densities. The ratios each saturate at different values of $\rho R_{\text{hot}}$ for different temperatures and densities because the primary $^3$He and tritons generally have significantly different ranges in the plasma. If either particle stops before leaving the fuel, it will not sample the entire $\rho R_{\text{hot}}$, and the implied value of $\rho R_{\text{hot}}$ underestimates the actual value. $Y_{2p}/Y_{1n}$ does not depend on temperature until it starts to saturate, while $Y_{2n}/Y_{1n}$ is sensitive to temperature well below the saturation level. Therefore, without a reasonable estimate of plasma temperature, $Y_{2n}/Y_{1n}$ cannot be used to accurately infer $\rho R_{\text{hot}}$.

The uniform model assumes that the primary particles are produced uniformly in a sphere of constant density and temperature. The $Y_{2p}/Y_{1n}$ and $Y_{2n}/Y_{1n}$ dependencies show similar behavior to the hot-spot model. The primary difference is that values of $\rho R_{\text{hot}}$ implied by the uniform model are always larger than values from the hot-spot model because the mean path length of primary particles in the D plasma is shorter by 25% in the uniform model, when saturation has not occurred. The simulations described in the **Results** section (p. 128) indicate that the hot-spot model gives more-meaningful values of $\rho R_{\text{hot}}$ than the uniform model; therefore, the hot-spot model will be used throughout the remainder of this article.

Both models have limitations that can introduce errors into the analysis of $\rho R_{\text{hot}}$. These include the saturation of $Y_{2p}$ and $Y_{2n}$ and the uncertainty introduced by the temperature dependence of $Y_{2n}$. The shapes of temperature and density profiles and the presence of fuel–shell mix[20–22] can have substantial impact on secondary-particle production. In reality, the temperature is highest and the density is lowest at the center of the implosion. As the temperature decreases and the density increases, the rate of energy loss of primary particles becomes larger. This typically causes a reduction of the secondary-proton production rate and an enhancement of the secondary-neutron production rate [see Fig. 98.53(a)]. Fuel–shell mix

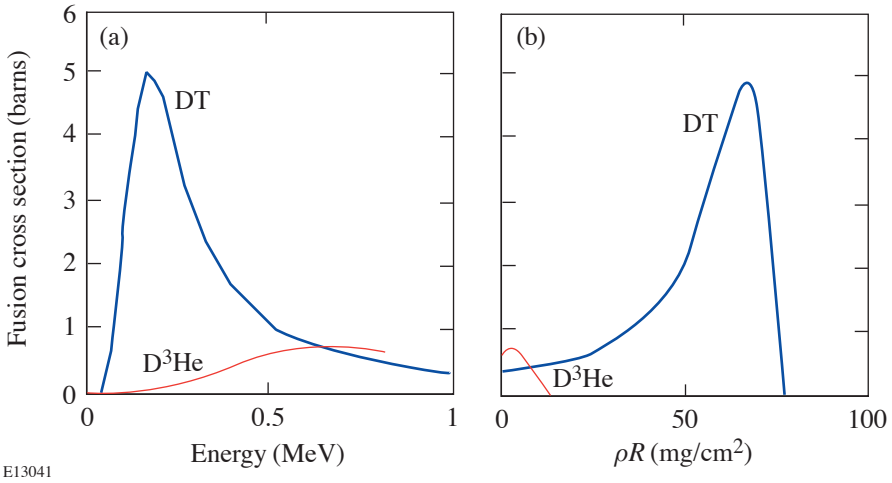


Figure 98.53
(a) Dependence of the secondary D$^3$He (DT) reaction cross section on the energy of the primary $^3$He (T) in a cold D plasma.[18] The D$^3$He-reaction cross section is peaked close to the birth energy of $^3$He, while the DT-reaction cross section peaks dramatically after T has lost most of its energy. (b) As a result, secondary protons are created close to the birth points of primary $^3$He (here defined as $\rho R$ = 0), while secondary neutrons are produced away from the birth points of primary T ($\rho R$ = 0). Although this plot is for a 1-g/cc, 3-keV D plasma, it looks similar for plasmas with different densities and temperatures.

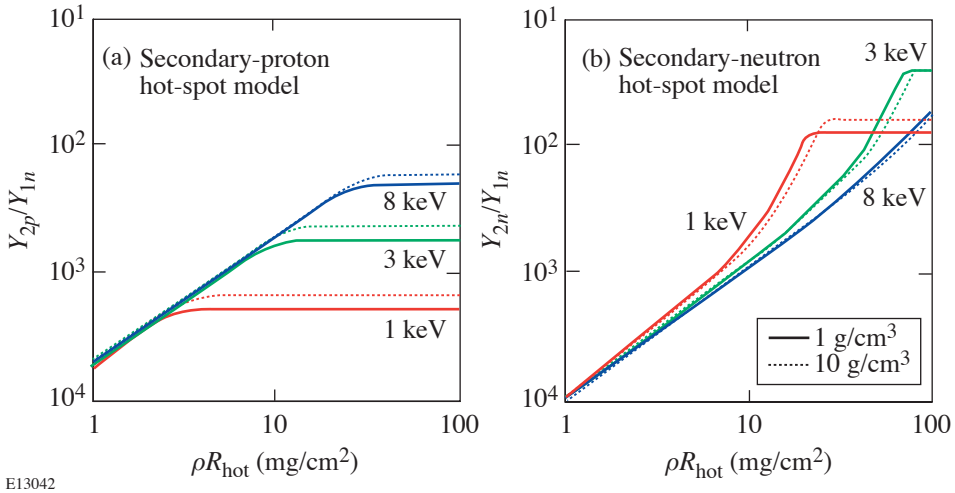


Figure 98.54
(a) $Y_{2p}/Y_{1n}$ and (b) $Y_{2n}/Y_{1n}$ as functions of $\rho R_{\text{hot}}$ for a 1-, 3-, and 8-keV D plasma of 1 g/cc (solid line) and 10 g/cc (dotted line) using the hot-spot model. The energy losses of primary $^3$He and T were calculated according to Ref. 19, and the fusion cross sections were calculated according to Ref. 18. $Y_{2p}/Y_{1n}$ is temperature independent until it reaches the saturation levels. In contrast, $Y_{2n}/Y_{1n}$ is temperature dependent well below saturation levels.

lowers the temperature in the mix region, which increases the energy loss rate and results in a further reduction of the secondary-proton production rate and an enhancement of the secondary-neutron production rate. Shell material mixed into the fuel can directly affect secondary production by increasing the energy lost by T and $^3$He after traveling through a given amount of D, due to the higher effective charge of the shell material mixed in.

**Experiments**

In the direct-drive experiments described here, distributed phase plates,[23] polarization smoothing using birefringent wedges,[24] and 1-THz, two-dimensional smoothing by spectral dispersion[25] were applied to smooth the OMEGA laser beams in order to enhance implosion uniformity and the nuclear reaction rate. Three types of capsules were used to study implosions with a wide range of areal densities: Low-$\rho R_{\text{hot}}$ implosions were studied using thin (~3-$\mu$m) glass ($SiO_2$) shells filled with ~15 atm of $D_2$. Some of these capsules were irradiated with a 1-ns square pulse delivering 23 kJ of on-target energy, while others were irradiated with a shorter (600- to 800-ps) pulse with on-target energy of ~12 kJ.[26] Medium- and large-$\rho R$ implosions were studied using capsules with thick (~20-$\mu$m) plastic (CH) shells filled with ~15 atm of $D_2$ and cryogenic capsules with an ~100-$\mu$m layer of $D_2$ ice enclosed within a 3- to ~5-$\mu$m-thick CH shell, respectively. They were all irradiated with 1-ns square pulses, delivering 23 kJ of on-target energy.

Charged-particle data were collected with two types of spectrometers: Wedged-range-filter proton spectrometers[12,27] provided secondary-proton spectra from up to six different directions simultaneously. These spectra were used to calculate the yield and mean energy of secondary protons. Two magnet-based charged-particle spectrometers[27] provided the spectra of primary protons and tritons for low-$\rho R$ implosions. Neutron data were obtained from three diagnostics: Neutron time-of-flight detectors[28] provided primary- and secondary-neutron yields as well as primary-neutron-yield–averaged ion temperature $\left(\langle T_i \rangle_{Y_{1n}}\right)$, and a neutron temporal diagnostic[29] measured the peak primary-neutron production time and the DD burn duration. In addition, secondary-neutron spectra were obtained from the 1020-scintillator array[30] on some of the more-recent implosions.

The data from each implosion then include the five quantities $Y_{1n}$, $Y_{2n}$, $Y_{2p}$, $\langle T_i \rangle_{Y_{1n}}$, and $\langle E_{2p} \rangle$, which will be matched to simulations in the next section. In addition, the spectral energy distributions of the secondary protons (and sometimes secondary neutrons) will be compared with the simulations. The yields and $\langle T_i \rangle_{Y_{1n}}$, together with a realistic plasma density, can also be used to determine what the simple hot-spot and uniform models imply for values of $\rho R^{\text{expl}}_{\text{hot},2p}$ and $\rho R^{\text{expl}}_{\text{hot},2n}$ (where the superscript "exp1" refers to the use of the measured $\langle T_i \rangle_{Y_{1n}}$ as the characteristic ion temperature).

**Monte Carlo Simulations**

A Monte Carlo program was developed to model the experiments described in the previous section. This allows us to use more-realistic temperature and density profiles than those in the hot-spot and uniform models. The burn-averaged ion temperature profile $[T_i(r)]$ and the shell (or cold fuel, for cryogenic capsules) density profile $[\rho_{\text{cold}}(r)]$ are assumed to have super- or sub-Gaussian profiles, and the six input parameters are $T_{i0}, T_{iw}, T_{ip}, S_{r0}, S_w$, and $S_p$ characterizing the temperature and density profiles

$$T_i(r) = T_{i0} \exp\left[-\left(r/T_{iw}\right)^{T_{ip}}\right] \tag{5}$$

and

$$\rho_{\text{cold}}(r) = \rho_{\text{cold0}} \exp\left\{-\left[\left(r - S_{r0}\right)/S_w\right]^{S_p}\right\}. \tag{6}$$

These parameters are varied to produce simulated particle production that best fits the measured data for each implosion. The hot-fuel density profile $[\rho_{\text{hot}}(r)]$ is calculated assuming that the plasma is isobaric out to the peak shell pressure region; with this constraint, $\rho_{\text{cold0}}$ is then adjusted to conserve the fuel mass. (The initial fuel mass is calculated based on the initial fuel pressure and the size of the capsule.)

For computational purposes, each primary particle is assumed to produce a secondary particle, and a spectrum of particles per unit energy $dN_2/dE$ is obtained. Since only a small fraction of the primary particles actually undergo secondary reactions, the secondary yield and spectrum need to be normalized according to $Y_2 = \langle P_2 \rangle Y_1$ and

$$dY_2/dE \approx \langle P_2 \rangle Y_1 \left(dN_2/dE\right)/N_2;$$
$$\langle P_2 \rangle \equiv \left\langle \int n_{\text{D}}(l)\sigma_{\text{sec}}(l)\,dl \right\rangle$$

is the probability of primary-to-secondary conversion, calculated in the program as the primary-yield–weighted mean value of the line integral of the D number density ($n_{\text{D}}$) times the secondary fusion cross section ($\sigma_{\text{sec}}$) for all possible primary-particle trajectories. The primary-particle production is determined by the density and temperature profiles. The particles are followed along their trajectories through the capsule until

they either escape or lose all of their energy. The energy loss is calculated, as briefly described in the next paragraph, in order to obtain $\sigma_{sec}$ along paths of primary particles. The probability of a secondary fusion reaction is calculated along the path of the primary particle; then the birth position, direction, and energy of the secondary particle are calculated. The radial distributions of the primary- and secondary-particle birth positions are recorded as well to illustrate the effects of profiles and fuel–shell mix.

The energy loss of charged particles in plasmas is strongly dependent upon the velocity of the particle. Depending on the relative magnitude of the particle velocity $v_p$ and the thermal velocity $v_{th}$ of the background electrons, the plasma can be described as "cold" ($v_p >> v_{th}$), "warm" ($v_p \sim v_{th}$), or "hot" ($v_p << v_{th}$). The theory described in Ref. 19 predicts that the plasma-stopping power reaches a maximum when $v_p \approx v_{th}$, which was also demonstrated for the first time in Ref. 39. The general form for the charged-particle energy loss per unit distance, $dE/dx$, in fully ionized plasmas is given by[19]

$$-\frac{1}{Z^2}\frac{dE}{dX} = \left(\frac{\omega_p e}{v_p}\right)^2 G\left(\frac{v_p^2}{v_{th}^2}\right)\ln\Lambda, \qquad (7)$$

where $\omega_p = \left(4\pi n_e e^2/m_e\right)^{1/2}$ is the electron-plasma frequency, $Z$ is the projectile charge number, $v_p$ is the velocity of the particle, $v_{th} = \left(2T/m_e\right)^{1/2}$ is the thermal velocity of the plasma electrons, and $\ln\Lambda$ is the Coulomb logarithm; $n_e$, $e$, and $m_e$ are the electron density, charge, and mass, respectively. $G\left(v_p/v_{th}\right)$ is the Chandrasekhar function, which peaks at $v_p/v_{th} \approx 1$, and explains why the stopping power reaches a maximum when $v_p \approx v_{th}$. The formulation given above applies to both plasma-electron stopping and plasma-ion stopping, where the latter, for the conditions of interest here, is about 10% of the stopping by electrons.

Since the model is static, the primary yield is calculated by multiplying the burn profile by the burn duration (full width at half maximum of the neutron-production rate); therefore, the error in the measurement of the burn duration is included in the error of the primary yield. $\langle E_{2p}\rangle$ is calculated from the secondary-proton spectrum, and $\langle T_i\rangle_{Y_{1n}}$ is determined in the region where the primary particles are produced.[31] Each of the six input parameters is varied over a large range, initially using large steps to identify the region of small $\chi^2$. This region is then more carefully explored using finer grids; as a result, the six-dimensional parameter space is explored completely. For each set of model parameters, the predicted values of the experimentally measured quantities are calculated and the quality of agreement with the data from a particular implosion is characterized with the total $\chi^2$, which takes into account uncertainties in the experimental measurements. For each implosion, it is found that multiple local minima exist within the space of model parameters but there is one clear region with the smallest values of $\chi^2$. Errors in the values of individual model parameters are then estimated by asking how much they can be changed without causing the total $\chi^2$ to increase by more than 1. Although the widths and shapes of secondary-proton spectra are not used as fit criteria, it will be seen that the predicted spectra match the measured spectra quite well; this fact provides extra confidence that the best-fit-model parameters are realistic.

The characteristics of the best-fit model for each implosion were used to determine how realistic the hot-spot-model inferred values of $\rho R_{hot}$ are. Values of $Y_{2p}/Y_{1n}$, $Y_{2n}/Y_{1n}$, $\langle T_i\rangle_{Y_{1n}}$, and plasma density from the simulations were used to infer $\rho R^{sim1}_{hot,2p}$ and $\rho R^{sim1}_{hot,2n}$ according to Fig. 98.54 (the superscript "sim1" indicates that $\langle T_i\rangle_{Y_{1n}}$ was used as the characteristic ion temperature). The values of $\rho R^{sim2}_{hot,2p}$ and $\rho R^{sim2}_{hot,2n}$ were calculated assuming that the appropriate temperatures are averages weighted by secondary yields $\langle T_i\rangle_{Y_{2p}}$ and $\langle T_i\rangle_{Y_{2n}}$, respectively. These values were then compared with $\rho R^{int}_{hot} \equiv \int \rho_D dr$, integrated over the hot-fuel region.

**Results**

1. Low-Areal-Density Implosions

For low-$\rho R_{hot}$ implosions, the primary $^3$He and T traverse the entire hot-fuel region, and the values of $\rho R_{hot}$ inferred from secondary protons and neutrons using the hot-spot (or uniform) model generally agree with each other and usually give a reasonable estimate of the actual value of $\rho R_{hot}$. This is shown experimentally by the square points in Fig. 98.51, which compares values of $\rho R^{exp1}_{hot,2p}$ and $\rho R^{exp1}_{hot,2n}$. These values were inferred according to Fig. 98.54 assuming a D plasma with a temperature of $\langle T_i\rangle_{Y_{1n}}$ keV and a density of 1.5 g/cc (obtained from a typical best-fit simulation, as discussed below). Figure 98.51 also illustrates that $\rho R^{exp1}_{hot,2p}$ and $\rho R^{exp1}_{hot,2n}$ are larger for implosions with lower (~12 kJ) on-target laser energy (open squares) than for implosions with full (~23 kJ) laser energy (closed squares). This could be explained by a larger amount of glass shell being ablated away in full-energy implosions, resulting in less material to drive the fuel inward[32,33] (Fig. 98.55). In addition, these values of $\rho R^{exp1}_{hot}$ from $D_2$ implosions with full laser energy show reasonable agreement with values from similar thin-glass-shell DT

implosions,[34,12] for which the knock-on method[35] was used to determine the $\rho R_{\text{hot}}$.

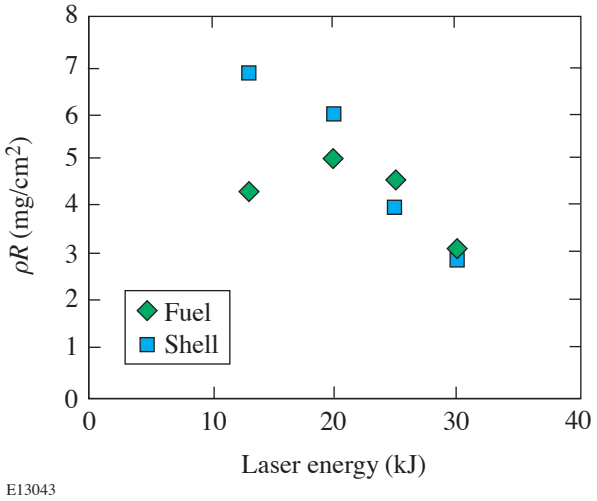


Figure 98.55
One-dimensional clean *LILAC* simulations for low-$\rho R$ implosion 30981 indicate that hot-fuel $\rho R$ starts to decrease as the capsule is significantly overdriven. This trend agrees with measurements where $\rho R_{\text{hot}}$ is lower for full-laser-energy–driven (~23-kJ), thin-glass-shell capsules than for low-laser-energy–driven (~12-kJ) capsules (Fig. 98.51).

For implosion 30981, which involved a 3.1-$\mu$m glass shell filled with 14.7 atm of $D_2$ gas, Fig. 98.56(a) shows simulated density and temperature profiles from the best-fit simulation. Figure 98.56(b) shows radial distributions of the primary- and secondary-particle-birth positions; secondary protons and neutrons are produced in virtually identical regions of the capsule. In addition, a high plasma temperature and a low $\rho R_{\text{hot}}$ result in similar values of $\rho R_{\text{hot}}^{\text{sim1}}$ inferred from the simulated secondary yields. Values of $\rho R_{\text{hot}}^{\text{sim1}}$ are inferred using the hot-spot model and assuming a plasma temperature of $\langle T_i \rangle_{Y_{1n}}$ keV and a plasma density of 1.5 g/cc (obtained from simulation). In addition, values of $\rho R_{\text{hot}}^{\text{sim1}}$ agree with $\rho R_{\text{hot}}^{\text{int}}$ obtained from the fuel-density profile shown in Fig. 98.56(a); this indicates that the small amount of fuel–shell mix in this type of implosion does not have much impact on the accuracy of the simple model. Results of the simulation along with measured data are summarized in Table 98.IV.

Simulated secondary spectra are in good agreement with measured spectra as shown in Figs. 98.56(c) and 98.56(d). The measured secondary-proton spectrum is an average of five spectra obtained simultaneously at different angles from implosion 30981.

2. Medium-Areal-Density Implosions

Correctly inferring the value of $\rho R_{\text{hot}}$ is more difficult for implosions of capsules with thick plastic shells because $Y_{2p}$ reaches saturation when $\rho R_{\text{hot}}$ is sufficiently large, and $Y_{2n}$ is enhanced in the presence of increased fuel–shell mix. The triangles in Fig. 98.51 show that the values of $\rho R_{\text{hot},2p}^{\text{exp1}}$ are often smaller than the values of $\rho R_{\text{hot},2n}^{\text{exp1}}$, as previously reported in Ref. 12. Values of $\rho R_{\text{hot},2p}^{\text{exp1}}$ and $\rho R_{\text{hot},2n}^{\text{exp1}}$ are inferred assuming a temperature of $\langle T_i \rangle_{Y_{1n}}$ keV and a D plasma with a density of 2 g/cc.

Figure 98.57(a) shows the temperature and density profiles that result in the best fit to the measured data for implosion 27443 (19.4-$\mu$m plastic shell filled with 15 atm of $D_2$ gas), and Fig. 98.57(b) shows the resulting radial distributions of primary- and secondary-particle-birth positions. About 32% of the initial CH mass remains, and ~1.3 $\mu$m of the initial CH layer has mixed into the fuel (which is similar to the amount of mix reported in Refs. 20–22).[36] The $^3$He are ranged out before traversing the entire fuel region. Figure 98.57(b) also illustrates an enhancement of $Y_{2n}$ by fuel–shell mix; the increased energy loss of T per unit $\rho R_{\text{hot}}$, due to the cooler, dense shell material, results in an enhanced DT fusion cross section (Fig. 98.53), which causes $Y_{2n}/Y_{1n}$ to overestimate $\rho R_{\text{hot}}^{\text{int}}$. In addition, $Y_{2n}/Y_{1n}$ is more sensitive to temperature in this $\rho R_{\text{hot}}$ range; using $\langle T_i \rangle_{Y_{1n}}$, which is always higher than $\langle T_i \rangle_{Y_{2n}}$, results in a larger inferred value of $\rho R_{\text{hot}}$.

Simulated yields and additional parameters characterizing the implosion are summarized and compared with measurements in Table 98.V. This table shows that the values of $\rho R_{\text{hot}}^{\text{sim1}}$ implied by secondary protons and neutrons are smaller and larger than the value of $\rho R_{\text{hot}}^{\text{int}}$, respectively. The hot-spot model was used to obtain values of $\rho R_{\text{hot}}$ using $\langle T_i \rangle_{Y_{1n}}$ keV for the temperature and assuming the density of the D plasma was 2 g/cc.

The simulated secondary-proton spectrum is compared with the measured spectrum in Fig. 98.57(c). The measured secondary-proton spectrum is an average of three spectra simultaneously obtained at different angles from implosion 27443 and shows more downshift than spectra from the low-$\rho R_{\text{hot}}$ implosions. The widths of the secondary-proton and secondary-neutron spectra [Fig. 98.57(d)] are slightly narrower than in the previous case because the average energy of the primary particle, at the time it undergoes secondary fusion, is smaller.[12]

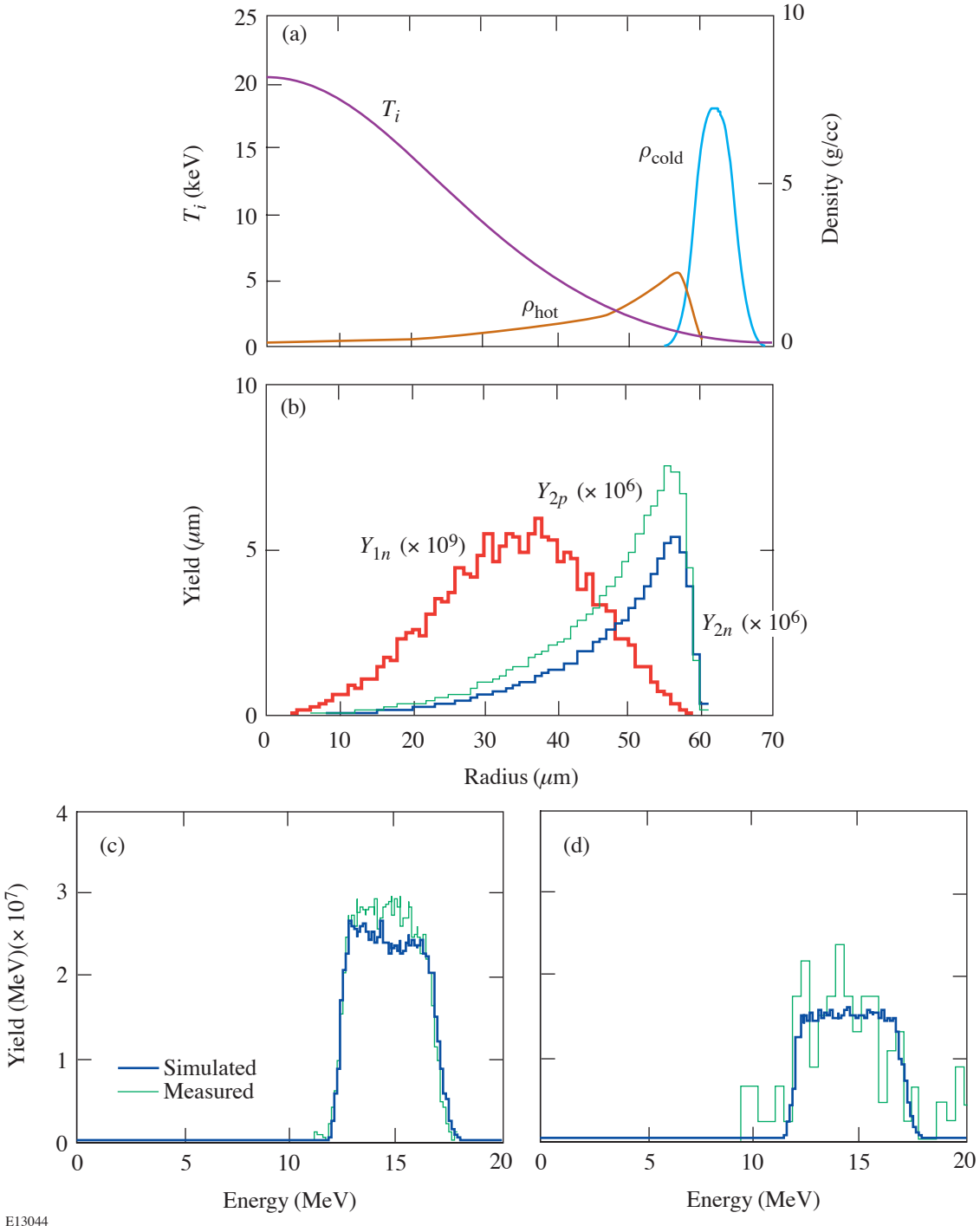


Figure 98.56

Parameters from the best-fit Monte Carlo simulation of shot 30981 (3.1-$\mu$m $SiO_2$ shell filled with 14.7 atm of $D_2$). (a) $T_i(r)$ and $\rho(R)$. Fuel mass is fully conserved, while 11% of the shell mass remains. (b) Radial distributions of the birth positions of primary and secondary particles indicate that secondary protons and neutrons are produced in a virtually identical region of the capsule. (c) Measured and simulated secondary-proton and (d) secondary-neutron spectra. Note that the shape and width of the simulated proton spectrum are very similar to those of the measured spectrum, even though these were not part of the fitting procedure. The difference in simulated and measured secondary yields is within the measurement uncertainties. Measured and simulated values of implosion characteristics are summarized in Table 98.IV. Figure 98.60 indicates how the radial profiles of $T_i$ and $\rho$ can change without changing too much the quality of the fit to the data.

Table 98.IV: Measured and simulated values of yields and $\rho R$ for OMEGA implosion 30981. Experimental data were fitted by adjusting $\rho(R)$ and $T_i(r)$. Total $\chi^2$ along with parameters specifying the cold ($SiO_2$) temperature and density Gaussian profiles [peak temperature ($T_{i0}$), 1/*e* radius ($T_{iw}$), power of the exponent ($T_{ip}$), peak density radius ($S_{r0}$), 1/e radius ($S_w$), and power of the exponent ($S_p$)] are also listed. $\rho R_{\text{cold}} = \int \rho_{\text{cold}} dr$, integrated radially over the $SiO_2$ shell region, and $\rho R_{\text{hot}} = \int \rho_{\text{D}} dr$, integrated radially over the hot-fuel region of the simulated profiles. Values of $\rho R_{\text{hot},2n}$ and $\rho R_{\text{hot},2p}$ were deduced using measured and simulated yield ratios assuming a 1.5±1-g/cc [obtained from Fig. 98.56(a)] D plasma at $\langle T_i \rangle_{Y_{1n}}$ ±0.5 keV.

| **Shot 30981** | | |
|---|---|---|
| | **Measured** | **Simulated** |
| $Y_{1n}$ | $(1.5\pm0.15) \times 10^{11}$ | $(1.5+0.23–0.18) \times 10^{11}$ |
| $Y_{2n}/Y_{1n}$ | $(5.1\pm0.98) \times 10^{-4}$ | $(5.1+1.1–0.57) \times 10^{-4}$ |
| $Y_{2p}/Y_{1n}$ | $(7.9\pm1.1) \times 10^{-4}$ | $(7.6+1.0–0.96) \times 10^{-4}$ |
| $\langle E_{2p} \rangle$(MeV) | 14.47±0.1 | 14.64+0.14–0.16 |
| $\langle T_i \rangle_{Y_{1n}}$(keV) | 8.2±0.5 | 8.2+0.7–0.5 |
| | | |
| $\chi^2$ | … | 0.1 |
| $T_{i0}$ (keV) | … | 20.5+2.5–10 |
| $T_{iw}$ ($\mu$m) | … | 34+14–4 |
| $T_{ip}$ | … | 2+5–0 |
| $S_{r0}$ ($\mu$m) | … | 62+6–10 |
| $S_w$ ($\mu$m) | … | 3.5+3–3.3 |
| $S_p$ | … | 2.5+7.5–2 |
| | | |
| $\rho R_{\text{cold}}$ (mg/cm$^2$) | … | 4.5+4.3–4.2 |
| $\rho R_{\text{hot}}$ (mg/cm$^2$) | … | 3.7+0.8–0.4 |
| | | |
| $\rho R_{\text{hot},2n}$ (mg/cm$^2$) | 4.6+0.9–1.2 | 4.6+1.0–0.6 |
| $\rho R_{\text{hot},2p}$ (mg/cm$^2$) | 4.3+0.6–0.8 | 4.1±0.5 |

3. Cryogenic Implosions

For cryogenic implosions, the interpretation of inferred values of $\rho R_{\text{hot}}$ is even more subtle since there is a high-temperature, low-density fuel region and a low-temperature, high-density fuel region. If most of the secondary particles are produced only in the hot-fuel region, $Y_2/Y_{1n}$ can be used to infer $\rho R_{\text{hot}}$. On the other hand, if secondary particles are produced mainly in the inner part of the cold-fuel region, the inferred $\rho R$ is larger than $\rho R_{\text{hot}}$, but smaller than $\rho R_{\text{total}}$. (Even the more-penetrating T cannot traverse the entire cold-fuel region since the range of T in an 8-g/cc, 1-keV D plasma is ~15 mg/cm$^2$, and we usually calculate $\rho R_{\text{total}} > 40$ mg/cm$^2$ from the downshift of the average secondary-proton energy for cryogenic implosions.) Figure 98.51 shows that values of $\rho R_{\text{hot}}$ implied by measured $Y_{2n}/Y_{1n}$ are always larger than values from measured $Y_{2p}/Y_{1n}$ for those implosions (values were inferred assuming a $\langle T_i \rangle_{Y_{1n}}$ keV, 3-g/cc D plasma).

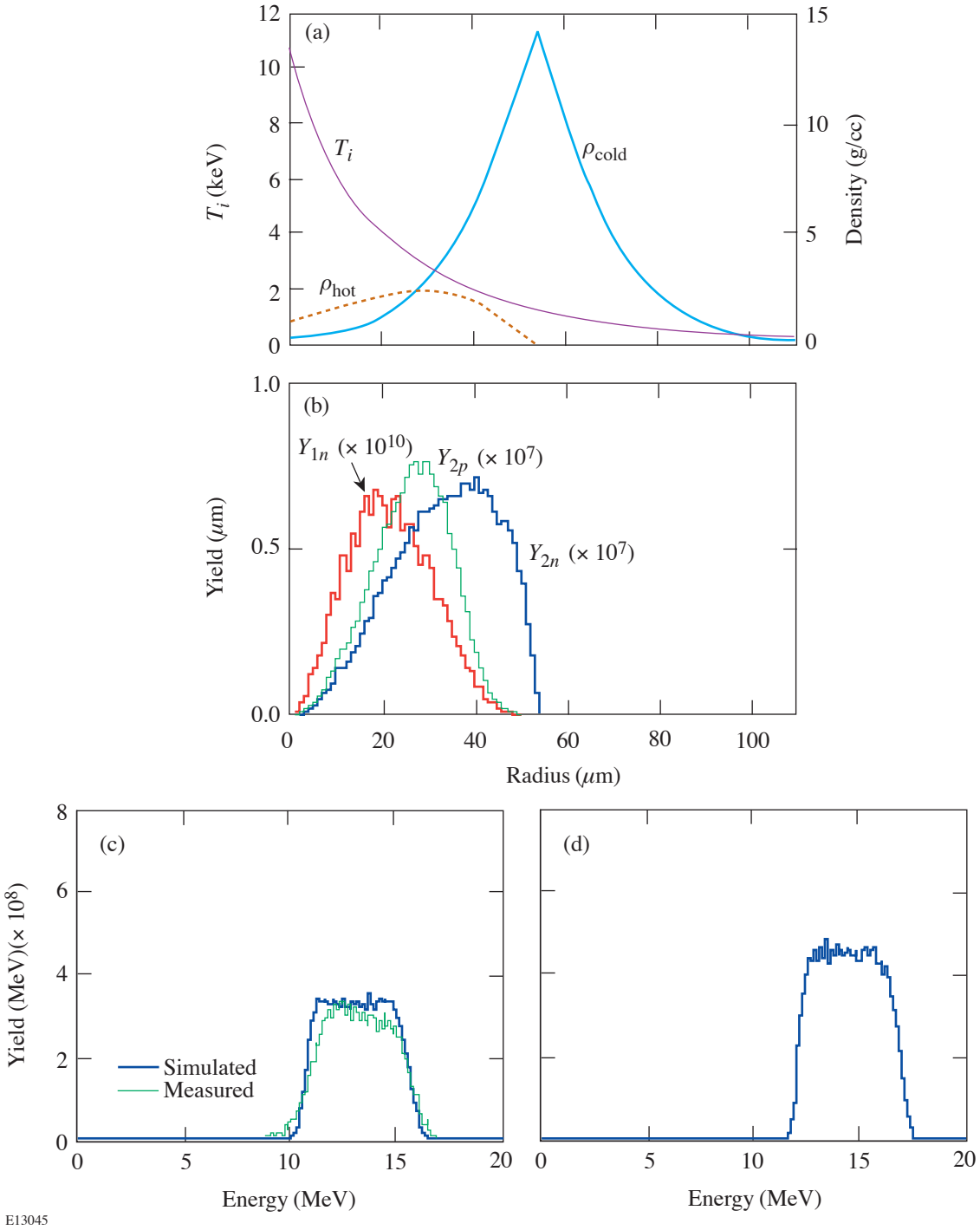


Figure 98.57

Best-fit parameters from the Monte Carlo simulation for shot 27443, which involved a 19.4-$\mu$m CH shell filled with 15 atm of $D_2$. (a) $T_i(r)$ and $\rho(r)$. Fuel mass is fully conserved, while 32% of the shell mass remains. (b) Radial distributions of the birth positions of primary and secondary particles show that secondary-proton production is diminished, while secondary-neutron production is enhanced in the region of significant fuel–shell mix. This causes secondary protons to underestimate and secondary neutrons to overestimate the actual value of $\rho R_{hot}$. (c) Measured and simulated secondary-proton spectra are compared, and (d) simulated secondary-neutron spectrum is shown. The secondary-proton spectra show more energy downshift, and the width of the secondary spectra are slightly narrower than the low $\rho R_{hot}$ case because the average primary particle energy is smaller at the time of secondary reaction. Measured and simulated values of implosion characteristics are listed in Table 98.V, while other fits are illustrated in Fig. 98.61.

Table 98.V: Measured and simulated values of implosion characteristics for OMEGA implosion 27443. Values $\rho R_{\text{hot}}$ were calculated assuming a 2±1-g/cc D plasma at $\langle T_i \rangle_{Y_{1n}}$ ±0.5 keV. Results from simulation indicate that the $\rho R_{\text{hot},2p}$ underestimates and $\rho R_{\text{hot},2n}$ overestimates the actual value.

| **Shot 27443** | | |
|---|---|---|
| | **Measured** | **Simulated** |
| $Y_{1n}$ | (1.5±0.15) × $10^{11}$ | (1.6+0.1–0.25) × $10^{11}$ |
| $Y_{2n}/Y_{1n}$ | (1.5±0.24) × $10^{-3}$ | (1.4+0.16–0.12) × $10^{-3}$ |
| $Y_{2p}/Y_{1n}$ | (1.0±0.14) × $10^{-3}$ | (1.0+0.1–0.15) × $10^{-3}$ |
| $\langle E_{2p} \rangle$(MeV) | 13.1±0.1 | 13.07+0.1–0.11 |
| $\langle T_i \rangle_{Y_{1n}}$(keV) | 4.1±0.5 | 4.1+0.2–0.4 |
| | | |
| $\chi^2$ | … | 0.5 |
| $T_{i0}$ (keV) | … | 11+0–5.5 |
| $T_{iw}$ ($\mu$m) | … | 20+18–0 |
| $T_{ip}$ | … | 0.8+1.2–0 |
| $S_{r0}$ ($\mu$m) | … | 54±2 |
| $S_w$ ($\mu$m) | … | 16+2–6 |
| $S_p$ | … | 1.2+0–0.2 |
| | | |
| $\rho R_{\text{cold}}$ (mg/cm$^2$) | … | 42.3+3.9–2.1 |
| $\rho R_{\text{hot}}$ (mg/cm$^2$) | … | 8.9+1–0.4 |
| | | |
| $\rho R_{\text{hot},2n}$ (mg/cm$^2$) | 12.8±1.9 | 11.6+1.2–1 |
| $\rho R_{\text{hot},2p}$ (mg/cm$^2$) | 5.0±0.7 | 5.2+0.5–0.7 |

Radial profiles of temperature and density calculated for implosion 28900 (89-$\mu$m $D_2$-ice layer inside a 5.1-$\mu$m CH shell) are shown in Fig. 98.58(a), and simulated and measured spectra are shown in Figs. 98.58(c) and 98.58(d). As indicated in Fig. 98.58(d) and Fig. 98.59, the secondary-neutron spectrum is much narrower than the secondary-neutron spectra from Figs. 98.56(d) and 98.57(d) because the primary T are, on average, less energetic when they fuse with thermal D.[12] Measurements of secondary-neutron spectra from more-recent cryogenic implosions also show the same characteristics.

The radial distributions of the primary- and secondary-birth positions shown in Fig. 98.58(b) indicate that secondary protons and neutrons are born mainly in the hot- and cold-fuel regions, respectively. Therefore, the $\rho R$ obtained from secondary protons gives an estimate of $\rho R_{\text{hot}}$, while the secondary-neutron yield provides a lower limit on $\rho R_{\text{total}}$. In this type of implosion, effects of mix or exchange of hot and cold fuel play significant roles in determining the radial distribution of secondary-birth positions.

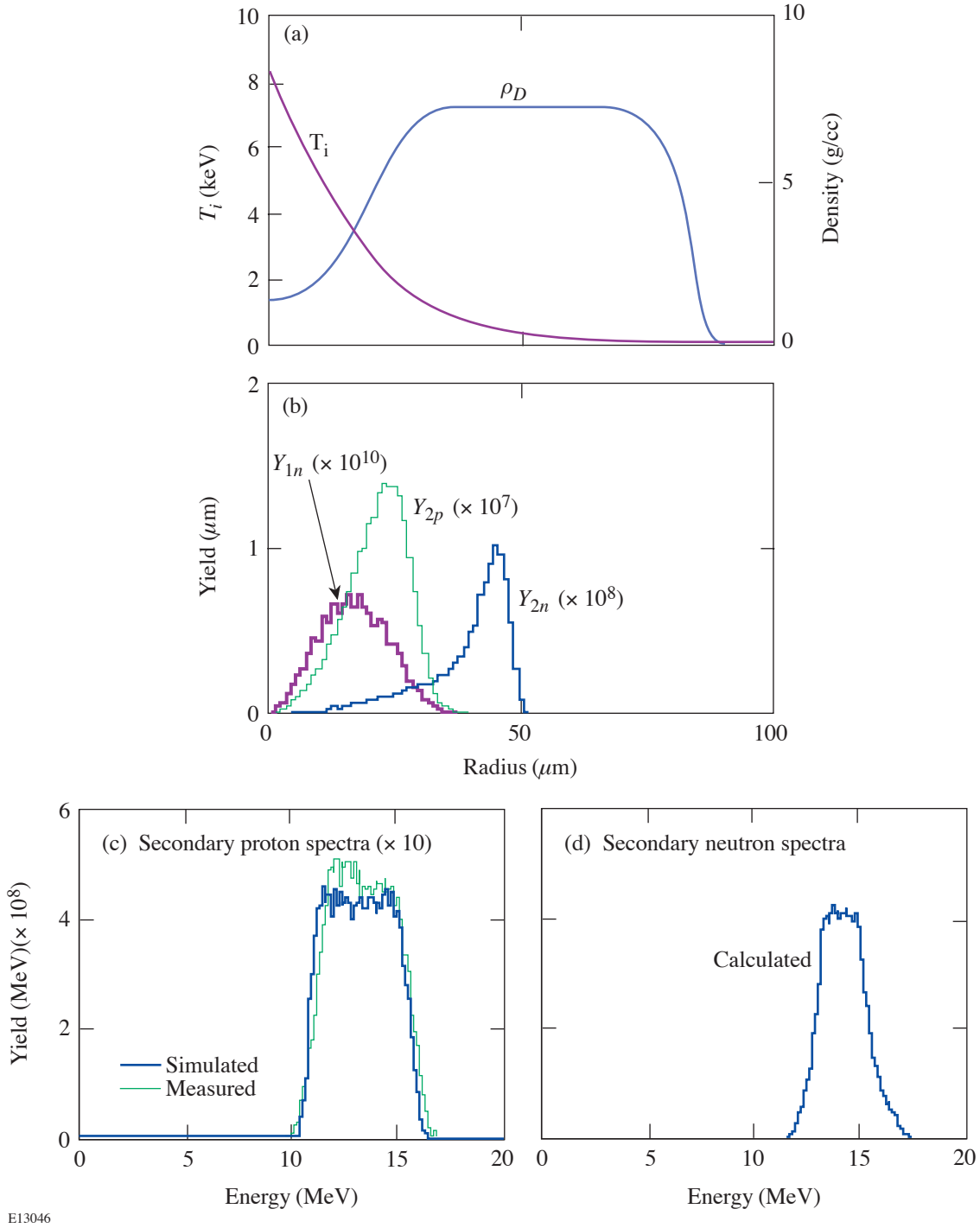


Figure 98.58
(a) Simulated profile of shot 28900 (cryogenic capsule with a 5.1-$\mu$m CD shell and 89-$\mu$m $D_2$-ice layer), which gives the best fit to the measurement; 31% of the total mass remains. (b) Radial distributions of the birth points of primary and secondary particles show that most of the secondary protons are produced in the hot-fuel region, while secondary neutrons are mainly produced in the cold-fuel region. (c) Measured and simulated secondary-proton spectra. (d) Simulated secondary neutron spectrum is narrower than the spectra in Figs. 98.56(d) and 98.57(d) because primary T are less energetic at the time they undergo secondary reactions; $\rho R$ of cold fuel is large enough to stop primary T [Fig. 98.58(b)], and the cross section increases as T loses energy [Fig. 98.53(a)]. Important implosion characteristics are summarized in Table 98.VI, while other fits are illustrated in Fig. 98.62.

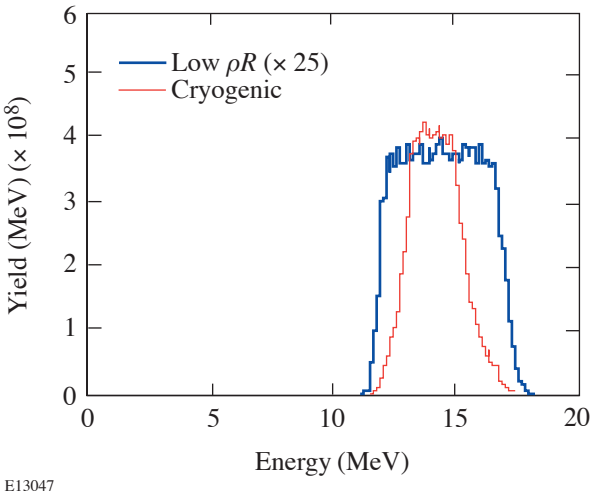


Figure 98.59
The simulated secondary-neutron spectrum is narrower than the spectra in Figs. 98.56(d) and 98.57(d) because the primary T are less energetic at the time they undergo secondary reactions; $\rho R$ of cold fuel is large enough to stop primary T [Fig. 98.58(b)], and the cross section increases as T loses energy [Fig. 98.53(a)]. Note that detailed analysis of secondary-neutron spectra was used to study areal density in Ref. 10.

Simulated values of yields and other important implosion characteristics are compared with measured results in Table 98.VI. The secondary-neutron, hot-spot-model–inferred $\rho R^{\text{sim1}}$ is close to $\rho R^{\text{int}}_{\text{total}}$, but this does not mean that the hot-spot model describes the implosion accurately. The agreement is an accidental consequence of using the wrong temperature $\langle T_i \rangle_{Y_{1n}}$, which samples the hotter central region rather than the cooler fuel region where most of the secondary neutrons are produced.

This implosion has also been analyzed using a combination of x-ray and neutron measurements, without the use of secondary-proton data. These results are discussed in Ref. 37. While the best-fit profiles were somewhat different, they agree within the uncertainties of the two simulation techniques.

**Conclusions**

The hot-spot and uniform models have been used to infer the areal density of the hot-fuel region ($\rho R_{\text{hot}}$) of $D_2$ implosions, but disagreements between the values of $\rho R_{\text{hot}}$ inferred from secondary-proton and secondary-neutron yields have often been observed, indicating limitations in these models. Results from direct-drive experiments on the OMEGA laser system and Monte Carlo simulations provided a deeper understanding of the relationship between $\rho R$, the capsule structure, and secondary-particle production. Experiments show that values of $\rho R_{\text{hot}}$ inferred from the ratios of secondary-proton and neutron-to-primary neutron yields ( $Y_{2p}/Y_{1n}$ and $Y_{2n}/Y_{1n}$ ) using the hot-spot model agree well for low-$\rho R_{\text{hot}}$ implosions (thin-glass-shell capsules), and simulations indicate that they give a good estimate of the actual value of $\rho R_{\text{hot}}$. The results from implosions of $D_2$-filled, thin-glass shells also show reasonably good agreement with results from implosions of similar capsules filled with DT gas. For thick-plastic-shell-capsule implosions, where the $\rho R_{\text{hot}}$ of an implosion becomes sufficiently large, $Y_{2p}/Y_{1n}$ underestimates $\rho R_{\text{hot}}$ since the primary $^3$He are ranged out before sampling the entire hot-fuel region. In addition, fuel–shell mix increases the rate of energy loss of $^3$He and causes $Y_{2p}/Y_{1n}$ to further underestimate $\rho R_{\text{hot}}$. The fuel–shell mix also causes $Y_{2n}/Y_{1n}$ to overestimate $\rho R_{\text{hot}}$ by slowing down the primary T, thereby increasing the secondary DT fusion reaction cross section. As a result, values of $\rho R_{\text{hot}}$ for medium $\rho R_{\text{hot}}$ capsules inferred from $Y_{2p}/Y_{1n}$ and $Y_{2n}/Y_{1n}$ using the hot-spot model should be interpreted as estimates of the lower and upper limits on the actual $\rho R_{\text{hot}}$, respectively. For cryogenic capsules, secondary protons are produced mainly in the hot-fuel region, and the proton-implied value of $\rho R$ provides a good estimate of the hot-fuel $\rho R$. In contrast, secondary neutrons are mostly produced in the inner part of the cold-fuel region, and the neutron-implied $\rho R$ gives a lower limit on the total $\rho R$ when calculated correctly using the average temperature and density of the secondary-neutron birth point. Naive use of the simple hot-spot or uniform model, with a burn-averaged temperature, often results in inaccurate inference of $\rho R_{\text{hot}}$. A more-thorough analysis, such as the use of complete data sets and simulations to determine the secondary-birth positions and the effects of mix, as presented herein, or the use of detailed analysis of secondary-neutron spectra both from experiments and simulations,[10] is required in order to obtain a realistic estimate of $\rho R_{\text{hot}}$.

Table 98.VI: Measured and simulated values of implosion characteristics for OMEGA implosion 28900. $\rho R_{\text{total}} = \int \rho_D dr$, integrated radially over the entire simulated profiles; $\rho R_{\text{hot}}$ is defined as the $\rho R$ that includes 90% of primary production. Values of $\rho R_{\text{hot}}$ were calculated assuming a 3.0±1.5-g/cc D plasma at $\langle T_i \rangle_{Y_{1n}}$ ±0.5 keV. Results from the simulation suggest that the value of $\rho R_{\text{hot},2p}$ provides a good estimate of $\rho R_{\text{hot}}$. Secondary-neutron implied $\rho R_{\text{hot}}$ is similar to $\rho R_{\text{total}}$, but this is because the value of the temperature used to infer $\rho R_{\text{hot}}$ is too large. If the temperature of the cold-fuel region (1 keV instead of 3.6 keV) were used, a much smaller and physical value of $\rho R_{\text{hot}}$ would be implied.

| **Shot 28900** | | |
|---|---|---|
| | **Measured** | **Simulated** |
| $Y_{1n}$ | (1.2±0.12) × $10^{11}$ | (1.3+0.12–0.14) × $10^{11}$ |
| $Y_{2n}/Y_{1n}$ | (9.4±1.4) × $10^{-3}$ | (9.1+1.0–1.1) × $10^{-3}$ |
| $Y_{2p}/Y_{1n}$ | (1.8±0.26) × $10^{-3}$ | (1.6+0.0–0.2) × $10^{-3}$ |
| $\langle E_{2p} \rangle$(MeV) | 13.31±0.10 | 13.28+0.5–0.11 |
| $\langle T_i \rangle_{Y_{1n}}$(keV) | 3.6±0.5 | 3.5+0.6–0.3 |
| | | |
| $\chi^2$ | … | 0.6 |
| $T_{i0}$ (keV) | … | 8.5+9.5–2.5 |
| $T_{iw}$ ($\mu$m) | … | 18+10–8 |
| $T_{ip}$ | … | 1.2+0.6–0.4 |
| $S_{r0}$ ($\mu$m) | … | 52+22–2 |
| $S_w$ ($\mu$m) | … | 32+16–12 |
| $S_p$ | … | 9+≥1–7.5 |
| | | |
| $\rho R_{\text{total}}$ (mg/cm$^2$) | … | 48.2+3.2–6.0 |
| $\rho R_{\text{hot}}$ (mg/cm$^2$) | … | 7.9+0.2–1.7 |
| | | |
| $\rho R_{\text{hot},2n}$ (mg/cm$^2$) | 49.8+5.0–6.9 | 48.0+4.9–4.0 |
| $\rho R_{\text{hot},2p}$ (mg/cm$^2$) | 9.3+1.9–1.5 | 7.8+0.5–0.6 |

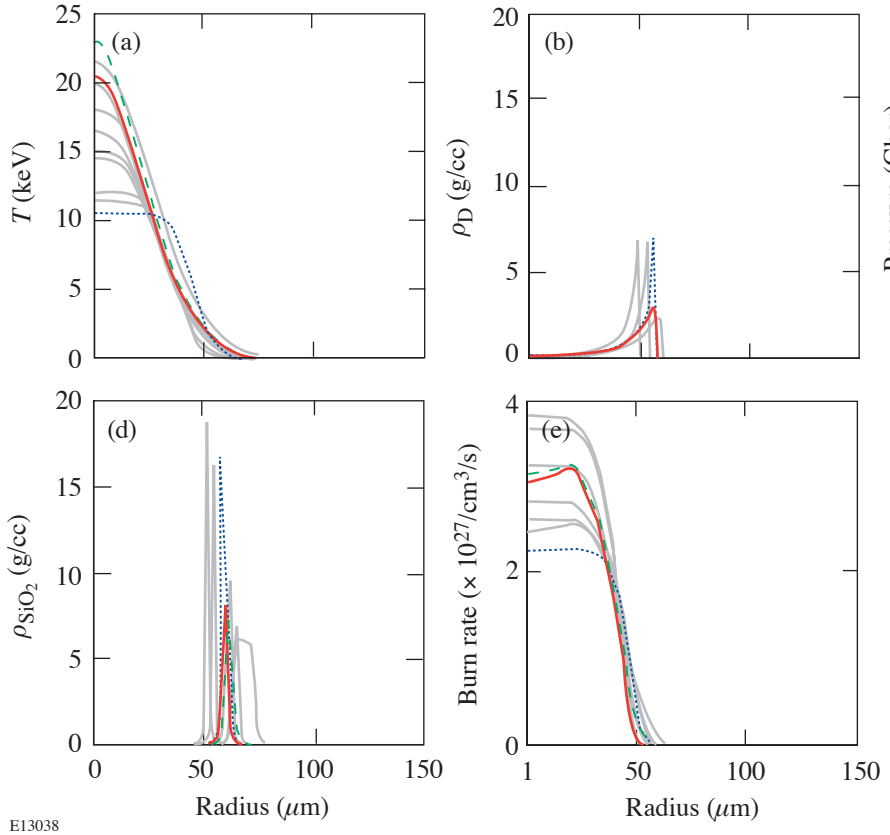


Figure 98.60
Samples of (a) temperature, (b) and (d) density, (c) pressure, and (e) burn profiles that produced fits to the data that were not as good as the best fit for implosion 30981. Solid lines represent the best-fit profiles; dashed and dotted lines represent the fits having the highest and lowest peak temperature, respectively, in the group of fits for which the total $\chi^2$ is within one of its minimum values (gray lines).

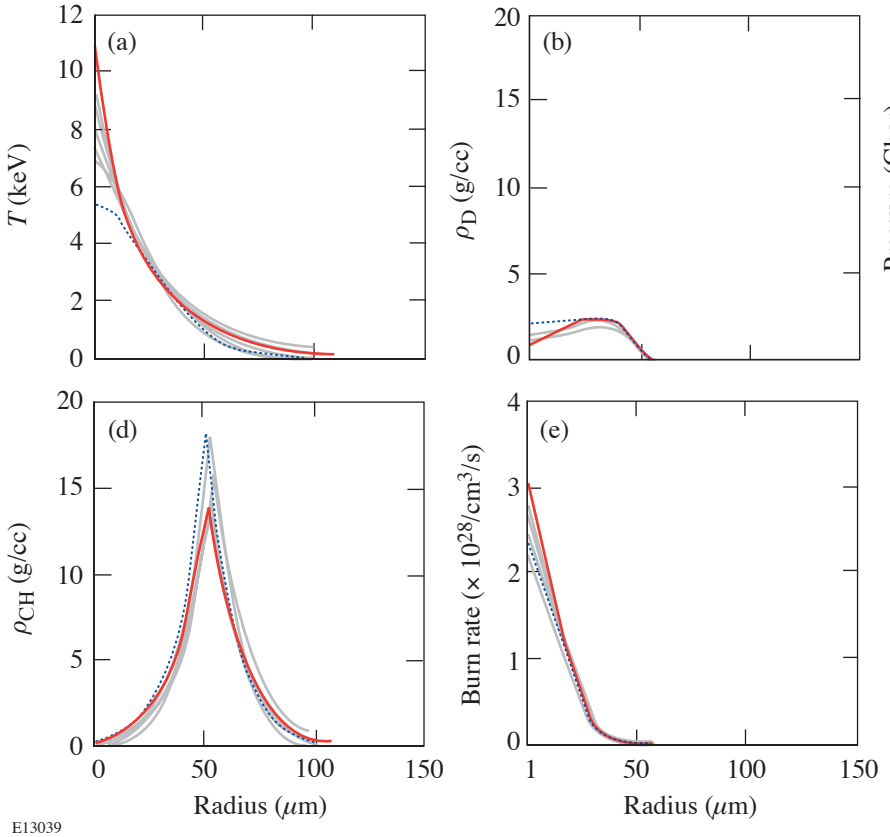


Figure 98.61
Samples of (a) temperature, (b) and (d) density, (c) pressure, and (d) burn profiles that produced fits to the data that were not as good as the best fit for implosion 27443 (as described in the caption of Fig. 98.60). The width of the burn profile is narrower than the width for implosion 30981, indicating more compression.

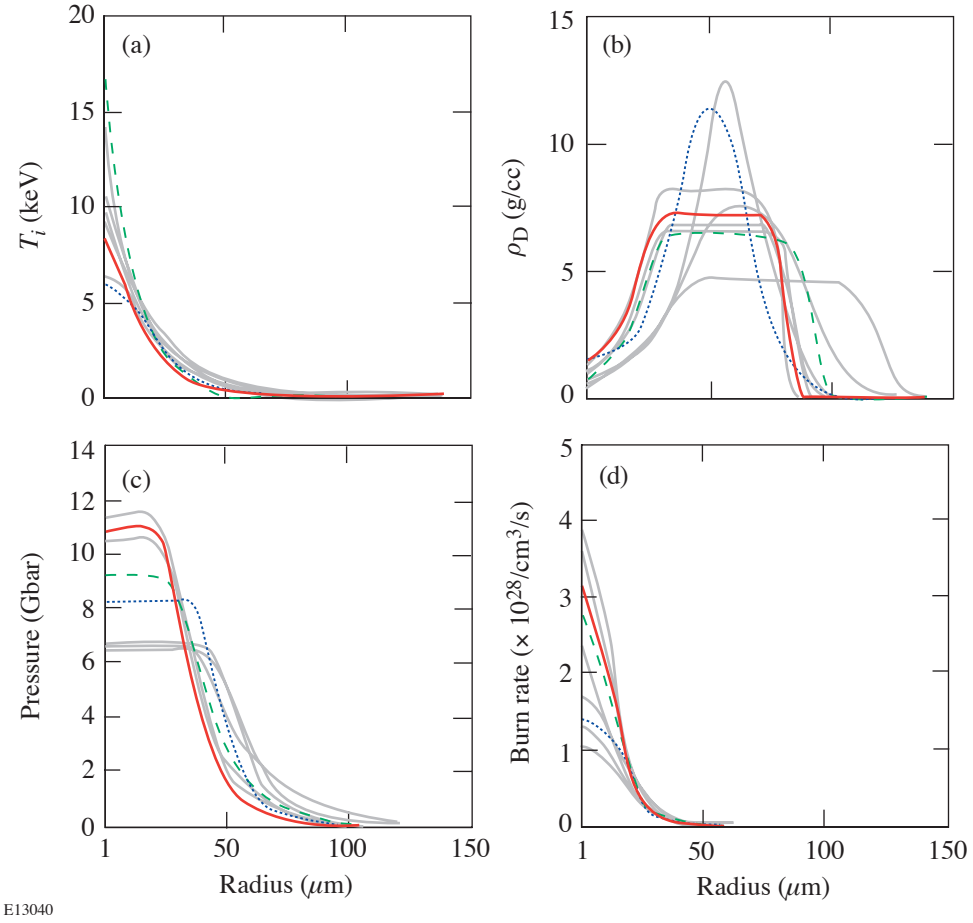


Figure 98.62
Samples of (a) temperature, (b) density, (c) pressure, and (d) burn profiles that produced fits to the data that were not as good as the best fit for implosion 28900 (as described in the caption of Fig. 98.60). The width of the burn profile is narrower than the width for implosion 30981, indicating more compression.

## ACKNOWLEDGMENT

The work was performed in part at LLE's National Laser Users' Facility (NLUF) and was supported in part by the U.S. DOE (grant DE-FG03-03SF22691), US DOE DP/NNSA (Cooperative Agreement DE-FG03-03NA00058), LLE (subcontract 412160-001G), and LLNL (subcontract B504974).

## REFERENCES

1. S. W. Haan *et al*., Phys. Plasmas **2**, 2480 (1995).
2. J. D. Lindl, R. L. McCrory, and E. M. Campbell, Phys. Today **45**, 32 (1992).
3. J. D. Lindl, Phys. Plasmas **2**, 3933 (1995).
4. H. D. Campbell and F. H. Southworth, in *1st Topical Meeting on the Technology of Controlled Nuclear Fusion* (American Nuclear Society, Hinsdale, IL, 1974), pp. 75–76.
5. E. G. Gamalii *et al*., JETP Lett. **21**, 70 (1975).
6. S. Skupsky and S. Kacenjar, J. Appl. Phys. **52**, 2608 (1981).
7. T. E. Blue and D. B. Harris, Nucl. Sci. Eng. **77**, 463 (1981).
8. T. E. Blue *et al*., J. Appl. Phys. **54**, 615 (1983).
9. H. Azechi, M. D. Cable, and R. O. Stapf, Laser Part. Beams **9**, 119 (1991).
10. M. D. Cable and S. P. Hatchett, J. Appl. Phys. **62**, 2233 (1987).
11. H. Azechi *et al*., Appl. Phys. Lett. **49**, 555 (1986).
12. F. H. Séguin, C. K. Li, D. G. Hicks, J. A. Frenje, K. M. Green, R. D. Petrasso, J. M. Soures, D. D. Meyerhofer, V. Yu. Glebov, C. Stoeckl, P. B. Radha, S. Roberts, C. Sorce, T. C. Sangster, M. D. Cable, S. Padalino, and K. Fletcher, Phys. Plasmas **9**, 2725 (2002).
13. P. Amendt, R. E. Turner, and O. L. Landen, Phys. Rev. Lett. **89**, 165001 (2002).
14. T. C. Sangster, J. A. Delettrez, R. Epstein, V. Yu. Glebov, V. N. Goncharov, D. R. Harding, J. P. Knauer, R. L. Keck, J. D. Kilkenny, S. J. Loucks, L. D. Lund, R. L. McCrory, P. W. McKenty, F. J. Marshall, D. D. Meyerhofer, S. F. B. Morse, S. P. Regan, P. B. Radha, S. Roberts, W. Seka, S. Skupsky, V. A. Smalyuk, C. Sorce, J. M. Soures, C. Stoeckl, K. Thorp, J. A. Frenje, C. K. Li, R. D. Petrasso, F. H. Séguin, K. A. Fletcher, S. Padalino, C. Freeman, N. Izumi, J. A. Koch, R. A. Lerche, M. J. Moran, T. W. Phillips, and G. J. Schmid, Phys. Plasmas **10**, 1937 (2003).
15. C. Stoeckl, C. Chiritescu, J. A. Delettrez, R. Epstein, V. Yu. Glebov, D. R. Harding, R. L. Keck, S. J. Loucks, L. D. Lund, R. L. McCrory, P. W. McKenty, F. J. Marshall, D. D. Meyerhofer, S. F. B. Morse, S. P. Regan, P. B. Radha, S. Roberts, T. C. Sangster, W. Seka, S. Skupsky, V. A. Smalyuk, C. Sorce, J. M. Soures, R. P. J. Town, J. A. Frenje, C. K. Li, R. D. Petrasso, F. H. Séguin, K. Fletcher, S. Padalino, C. Freeman, N. Izumi, R. Lerche, and T. W. Phillips, Phys. Plasmas **9**, 2195 (2002).
16. R. E. Turner, P. A. Amendt, O. L. Landen, L. J. Suter, R. J. Wallace, H. E. Dalhed, B. A. Hammel, and V. Glebov, Bull. Am. Phys. Soc. **47**, 328 (2002).
17. T. R. Boehly, D. L. Brown, R. S. Craxton, R. L. Keck, J. P. Knauer, J. H. Kelly, T. J. Kessler, S. A. Kumpan, S. J. Loucks, S. A. Letzring, F. J. Marshall, R. L. McCrory, S. F. B. Morse, W. Seka, J. M. Soures, and C. P. Verdon, Opt. Commun. **133**, 495 (1997).
18. S. Glasstone and R. H. Lovberg, *Controlled Thermonuclear Reactions: An Introduction to Theory and Experiment* (Van Nostrand, Princeton, NJ, 1960).
19. C. K. Li and R. D. Petrasso, Phys. Rev. Lett. **70**, 3059 (1993).
20. P. B. Radha, J. Delettrez, R. Epstein, V. Yu. Glebov, R. Keck, R. L. McCrory, P. McKenty, D. D. Meyerhofer, F. Marshall, S. P. Regan, S. Roberts, T. C. Sangster, W. Seka, S. Skupsky, V. Smalyuk, C. Sorce, C. Stoeckl, J. Soures, R. P. J. Town, B. Yaakobi, J. Frenje, C. K. Li, R. Petrasso, F. Séguin, K. Fletcher, S. Padalino, C. Freeman, N. Izumi, R. Lerche, and T. W. Phillips, Phys. Plasmas **9**, 2208 (2002).
21. C. K. Li, F. H. Séguin, J. A. Frenje, S. Kurebayashi, R. D. Petrasso, D. D. Meyerhofer, J. M. Soures, J. A. Delettrez, V. Yu. Glebov, P. B. Radha, F. J. Marshall, S. P. Regan, S. Roberts, T. C. Sangster, and C. Stoeckl, Phys. Rev. Lett. **89**, 165002 (2002).
22. S. P. Regan, J. A. Delettrez, F. J. Marshall, J. M. Soures, V. A. Smalyuk, B. Yaakobi, V. Yu. Glebov, P. A. Jaanimagi, D. D. Meyerhofer, P. B. Radha, W. Seka, S. Skupsky, C. Stoeckl, R. P. J. Town, D. A. Haynes, Jr., I. E. Golovkin, C. F. Hooper, Jr., J. A. Frenje, C. K. Li, R. D. Petrasso, and F. H. Séguin, Phys. Rev. Lett. **89**, 085003 (2002).
23. Y. Lin, T. J. Kessler, and G. N. Lawrence, Opt. Lett. **20**, 764 (1995).
24. T. R. Boehly, V. A. Smalyuk, D. D. Meyerhofer, J. P. Knauer, D. K. Bradley, R. S. Craxton, M. J. Guardalben, S. Skupsky, and T. J. Kessler, J. Appl. Phys. **85**, 3444 (1999).
25. S. Skupsky, R. W. Short, T. Kessler, R. S. Craxton, S. Letzring, and J. M. Soures, J. Appl. Phys. **66**, 3456 (1989).
26. Short laser pulses (<1 ns) imploding thin-glass-shell capsules prevent significant nuclear production while the laser is on. This is important if $\rho R_{\text{total}}$ is to be studied because the capsule can be charged to a significant potential relative to the target chamber wall due to laser–plasma interactions. The potential can cause an upshift of measured proton energies,[35,38,39] making it difficult to determine how much energy the protons lost while leaving the capsule (necessary for calculating $\rho R_{\text{total}}$). The potential decays away rapidly after the laser is turned off, so it does not affect measurements of protons from implosions in which the nuclear burn occurs after the pulse (such as those involving thick-plastic-shell or cryogenic capsules[35]). This affects only the study of $\rho R_{\text{total}}$; measurements of yields are unaffected by capsule potentials.
27. F. H. Séguin, J. A. Frenje, C. K. Li, D. G. Hicks, S. Kurebayashi, J. R. Rygg, B.-E. Schwartz, R. D. Petrasso, S. Roberts, J. M. Soures, D. D. Meyerhofer, T. C. Sangster, J. P. Knauer, C. Sorce, V. Yu. Glebov, C. Stoeckl, T. W. Phillips, R. J. Leeper, K. Fletcher, and S. Padalino, Rev. Sci. Instrum. **74**, 975 (2003).

28. M. A. Russotto and R. L. Kremens, Rev. Sci. Instrum. **61**, 3125 (1990).

29. R. A. Lerche, D. W. Phillion, and G. L. Tietbohl, Rev. Sci. Instrum. **66**, 933 (1995).

30. V. Yu. Glebov, C. Stoeckl, S. Roberts, T. C. Sangster, J. A. Frenje, R. D. Petrasso, R. A. Lerche, and R. L. Griffith, Bull. Am. Phys. Soc. **48**, 342 (2003).

31. Primary-neutron-yield-weighted average ion temperature is calculated by two methods, each yielding a virtually identical temperature. First, the product of the temperature and the primary neutron birth rate per unit length at each radius is integrated and divided by the primary neutron yield. Second, the primary neutron spectrum is calculated, and the width of the spectrum is used to obtain an ion temperature.

32. J. D. Lindl, *Inertial Confinement Fusion: The Quest for Ignition and Energy Gain Using Indirect Drive* (Springer-Verlag, New York, 1998).

33. M. D. Rosen and J. H. Nuckolls, Phys. Fluids **22**, 1393 (1979).

34. M. J. Canavan, MIT, private communication (2004); herein the laser energy was ~30 kJ for these DT implosions.

35. C. K. Li, F. H. Séguin, D. G. Hicks, J. A. Frenje, K. M. Green, S. Kurebayashi, R. D. Petrasso, D. D. Meyerhofer, J. M. Soures, V. Yu. Glebov, R. L. Keck, P. B. Radha, S. Roberts, W. Seka, S. Skupsky, C. Stoeckl, and T. C. Sangster, Phys. Plasmas **8**, 4902 (2001).

36. P. B. Radha *et al.*,[20] C. K. Li *et al.*,[21] and S. P. Regan *et al.*[22] reported ~1 $\mu$m, ~0.5 $\mu$m, and ~0.4 $\mu$m of the initial shell layer mixed into the fuel, respectively.

37. V. A. Smalyuk, J. A. Delettrez, S. B. Dumanis, R. Epstein, V. Yu. Glebov, D. D. Meyerhofer, P. B. Radha, T. C. Sangster, C. Stoeckl, N. C. Toscano, J. A. Frenje, C. K. Li, R. D. Petrasso, F. H. Séguin, and J. H. Koch, "Hot-Core Characterization of the Cryogenic $D_2$ Target at Peak Neutron Production in Direct-Drive Spherical Implosion," submitted to Physical Review Letters.

38. D. G. Hicks, C. K. Li, F. H. Séguin, J. D. Schnittman, A. K. Ram, J. A. Frenje, R. D. Petrasso, J. M. Soures, D. D. Meyerhofer, S. Roberts, C. Sorce, C. Stoeckl, T. C. Sangster, and T. W. Phillips, Phys. Plasmas **8**, 606 (2001).

39. D. G. Hicks, C. K. Li, F. H. Séguin, A. K. Ram, J. A. Frenje, R. D. Petrasso, J. M. Soures, V. Yu. Glebov, D. D. Meyerhofer, S. Roberts, C. Sorce, C. Stöckl, T. C. Sangster, and T. W. Phillips, Phys. Plasmas **7**, 5106 (2000).

# Two-Dimensional Simulations of Plastic-Shell, Direct-Drive Implosions on OMEGA

## Introduction

In direct-drive inertial confinement fusion (ICF),[1] nominally identical beams of a laser are incident on a nearly spherically symmetric target. The target's outer surface ablates, driving the shell inward like a rocket. The shell first accelerates and then, shortly after the laser drive is turned off, coasts before decelerating toward peak compression; disassembly then follows. The goal is to implode the target, resulting in sufficiently high temperatures and densities to propagate a self-sustaining burn wave through the target, giving rise to energetic neutrons with a total energy greater than the laser energy. Ignition target designs require layers of cryogenic deuterium–tritium (DT) ice[2] and relatively high laser energies such as those available on the National Ignition Facility (NIF).[3] To provide an understanding of target dynamics, a large number of implosions on the 60-beam OMEGA laser[4] have been devoted to warm capsules,[5–8] which include plastic (CH) shells filled with deuterium ($D_2$) gas. While a number of papers have been written on the experimental results from CH-shell implosions on OMEGA,[5–8] the range of nonuniformity wavelengths that influence fusion yields has been an outstanding question.

In this article, a detailed analysis of the CH-shell implosions using one- and two-dimensional simulations and analytical modeling is performed. The goal of this work is to identify, by using the hydrodynamic code *DRACO*,[9] the nonuniformity seeds that influence target performance. Mechanisms that influence yields are also identified. In addition, comparisons to experimental results are presented.

Imperfect illumination and target roughness seed the nonuniformity growth in direct-drive implosions. The incident laser irradiation on the target includes nonuniformities that result from energy and power imbalances between beams and from nonuniformities within each beam. While the former will be shown to result in long-wavelength ($\ell < 10$, where $\ell = 2\pi R/\lambda$ is the Legendre mode number, $R$ is the target radius, and $\lambda$ is the nonuniformity wavelength) perturbations that lead to an overall deformation of the shell, the latter manifest themselves in the intermediate-wavelength ($10 < \ell < 50$) and short-wavelength ($\ell > 50$) nonuniformities that may lead to shell breakup during the acceleration phase as well as a disruption in final fuel assembly.

Nonuniformities grow due to the Rayleigh–Taylor (RT) instability[10] during the acceleration phase of the implosion. The RT growth rates are smaller than classical values due to the ablative effects.[10–13] Nevertheless, the RT growth factors of the short-wavelength modes in the thin shells are large enough to compromise shell integrity during the acceleration phase. Shell breakup results in degradation in the shell's compressibility, which leads to a reduction in the final core temperature and density and consequently a reduction in the neutron-production rates.

Nonuniformity growth during the coasting and deceleration phases of the implosions is seeded by feedthrough to the inner surface of the shell. As will be shown later in the text, the fuel–pusher interface distortions grow significantly during the coasting phase because of convergent effects (Bell–Plesset growth).[14,15] Further, truncation of the neutron-production rate occurs due to the flow of fuel into the colder bubbles at the $D_2$–CH interface during shell deceleration. Truncation is also caused by the increased heat conduction out of the core due to the larger surface area caused by shell distortions.

This article is organized as follows: (1) one-dimensional and multidimensional hydrodynamic modeling are described; (2) overall shell dynamics is discussed; (3) the four phases of the implosion (shock transit, acceleration, coasting, and deceleration) are analyzed in the context of single-mode growth; (4) multidimensional simulations of beam-to-beam imbalances and single-beam nonuniformity are described, and the combined effects of all nonuniformity sources are discussed; and (5) conclusions are presented.

**Radiation-Hydrodynamics Modeling**

The one-dimensional (1-D) target dynamics discussed in this article is modeled using the code *LILAC*,[16] which has been described extensively in the literature and is not discussed any further.

Multidimensional behavior (2-D) of plastic targets is modeled using the code *DRACO*.[9] *DRACO* is a one-, two-, and three-dimensional arbitrary Lagrangian Eulerian (ALE) code based on a structured mesh. The implosions described here are simulated in one and two dimensions. The compressible hydrodynamic scheme is based on the work by Amsden *et al*.[17] Shocks are treated using the scheme of Wilkins.[18] Several artificial grid-smoothing algorithms are available to control numerical grid distortions (bowties and herringbone distortions). These are based on Refs. 17–19; only Ref. 19 is used in this work.

In a purely Lagrangian mode, interfaces between materials are maintained at cell edges; however, a significant growth of perturbations results in a severely distorted grid. As a result, the grid must be "rezoned" for the simulation to proceed. The new grid can be constructed using several prescriptions. While some grid movement options are heuristically derived, others are based on Winslow-regridding–type[20] schemes. *DRACO* allows for cells with mixed materials resulting from this grid rezoning. Rezoning is possible through a first-order (donor-cell) or a direction-split second-order scheme.[21] Material interfaces are reconstructed before every rezoning step using a scheme based on Young's method,[22] which has been extended to allow for the distorted Lagrangian cells. In this scheme, the interface between materials in a cell is represented by a straight line; the slope of this line is obtained through the gradient of the fractional volumes occupied by the material in the neighboring cells.

The pressure in each mixed-material cell is obtained by adding the partial pressures of the constituent cell materials. A single temperature for the materials in the cell is obtained using the prescription described in Ref. 23. While this interface tracking scheme cannot be used to model turbulent regimes,[22] it has been used to model the highly nonlinear growth of buried layers that burn through to the corona.[9]

Various physical processes, such as heat conduction, radiation transport, etc., are treated using an operator splitting procedure. *DRACO* includes the deposition of laser energy through ray tracing and inverse bremsstrahlung. Both normal-incidence laser energy deposition and the ray-trace approach are used in this work. Since normal incidence does not include refractive energy losses, it can significantly overestimate the energy coupled to the target. Consequently, the laser pulse shape is iteratively adjusted in 1-D simulations to provide the same overall dynamics of the implosion, including shock-breakout times, the final convergence of the shell, ablation velocities, density scale lengths, etc., as obtained with a full ray trace. This modified pulse shape is used in two-dimensional (2-D) simulations involving modes ≥20. Spherically symmetric 2-D simulations with this modified pulse shape compare very well with 1-D simulations using a full ray trace. For simulations that include only long-wavelength modes, we use a refractive ray trace. This ray trace uses a quasi-1-D scheme, where rays are not allowed to cross angular sector boundaries. This scheme accounts for refractive losses reasonably accurately when the distortions are of relatively long wavelengths. In this technique, an angular spectrum describing the distribution of energy with angle of incidence is launched from a chosen surface each time step. This distribution takes into account both the single-beam ray distribution and beam overlap. In the limit of a spherically symmetric problem, this approach yields the same results as a full ray trace.

Several equation-of-state options (ideal gas, *SESAME*,[24] Thomas–Fermi,[25] and QEOS[26]) are available; the analytic Thomas–Fermi formulation is used for the simulations described in this work. Heat conduction and multigroup diffusive radiation transport are included. Tabular opacities assuming local thermal equilibrium are used for the materials while in unmixed cells. An ion-number weighted opacity is used in mixed cells for radiation transport. Radiation transport is solved in parallel across several processors.

The simulations use the "group-parallel" approach where each energy group is solved on one processor and the resulting radiation energy density is broadcast to all other processors. Four radiation groups, reduced from very fine opacity tables,[27] are included in all the calculations in this work. The choice of the four energy groups is optimally made to closely match the 1-D dynamics corresponding to 48 energy groups. The parallel scientific library, PetSc,[28] is used to solve the diffusion equation via a preconditioned conjugate-gradient scheme. Message Passing Interface (MPI)[29] is used to communicate between processors.

Particle production from nuclear reactions is calculated using Ref. 30. Alpha-particle transport and depletion of fuel material for modeling ignition are included in *DRACO* but are not necessary in simulating OMEGA target implosions.

*DRACO* has been tested extensively against analytic problems (shock-tube problems, blast-wave problems, etc.), against other codes (*LILAC*,[17] *ORCHID*[31]), and against the ICF post-processor described in Ref. 32 for single-mode growth. Good agreement is obtained with the known solutions for all the problems considered.[9]

**Shell Dynamics**

This work focuses on targets with plastic (CH) shells filled with $D_2$ gas. Two cases are considered (Fig. 99.1): (1) a 20-$\mu$m-thick CH shell with 15 atm of $D_2$ with a convergence ratio CR ~ 13 (CR is defined as the ratio of the initial radius to the compressed radius of the fuel–shell interface at the peak of the neutron production); (2) a 27-$\mu$m-thick CH shell with 15 atm of $D_2$ (CR ~ 12). A 1-ns square pulse with ~23 kJ of energy is used to irradiate these targets with full beam smoothing [two-dimensional smoothing by spectral dispersion[33] (2-D SSD) with polarization smoothing (PS)[34]]. Case (1) has been chosen to illustrate implosion dynamics (Fig. 99.2). The laser pulse and shell acceleration history are shown in Fig. 99.2(a). The magnitude of the gradient of the natural logarithm of the pressure, $|\partial \ln P/\partial r|$, is shown in Fig. 99.2(b). The dark lines correspond to shock trajectories. The dashed line is the trajectory of the fuel–shell interface. Since the rise time of the laser is relatively fast (~200 ps), a strong shock is driven into the target, setting the shell material on a high adiabat, $\alpha \sim 5$, defined as the ratio of the pressure at a given density to the cold Fermi pressure at that density. The rarefaction wave launched at the breakout of the shock (at ~0.4 ns) from the shell reaches the ablation surface, where a compression wave is consequently launched into the target. At this time the shell starts to accelerate inward as indicated by the negative acceleration in Fig. 99.2(a). The compression wave travels down the decreasing density gradient and breaks out of the shell as a shock (at ~0.8 ns). Both shocks meet in the gas (at ~1 ns) before reaching the center. The four main phases of the implosion are shown in Fig. 99.2(a). The acceleration phase occurs after shock transit and continues until shortly after the laser pulse turns off (at ~1.4 ns), at which time the shell starts traveling with a constant velocity (coasting phase). Deceleration of the shell begins when the shock reflects from the center and returns to the shell (at ~1.75 ns). This impulsive deceleration is followed by a period of continuous deceleration due to pressure buildup in the gas [Fig. 99.2(a)].

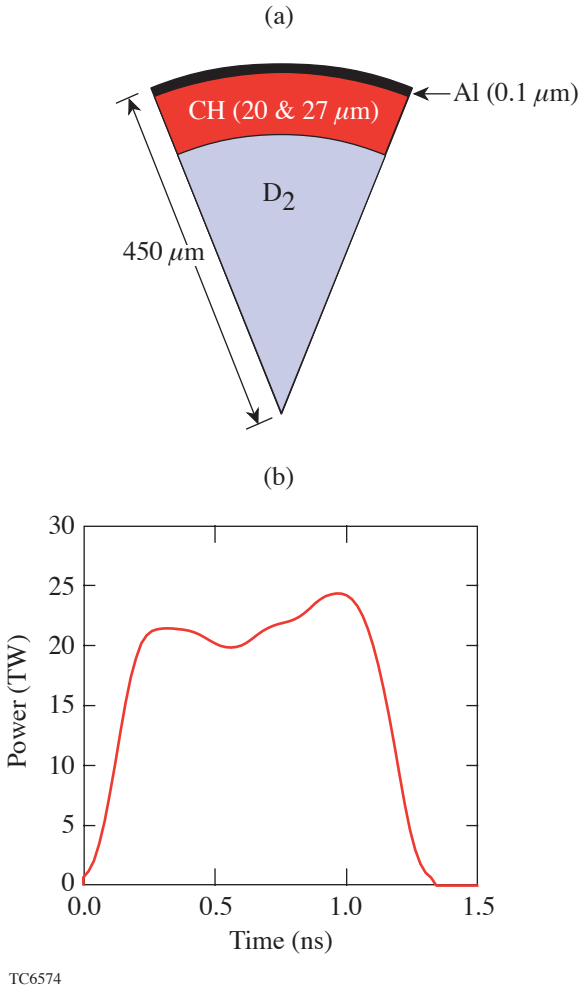


Figure 99.1
(a) Plastic-shell targets of two thicknesses—20 $\mu$m and 27 $\mu$m—with $D_2$ fills were considered in this work. (b) The pulse shape (1-ns square) used to irradiate these targets sets the shell on a relatively high adiabat (~5).

Shock breakout is later in the thicker, 27-$\mu$m implosion (at ~0.5 ns compared to ~0.4 ns). The more-massive, 27-$\mu$m-thick shell moves more slowly during the coasting phase than the 20-$\mu$m-thick CH shell. It therefore coasts for a longer time (~650 ps compared to ~350 ps). The shell's convergence ratio for the coasting phase, defined as the ratio of the shell radius at the beginning and end of the coasting phase, is 3.0 for the thicker shell compared to 2.2 for the thinner shell.

**Single-Mode Simulations**

In this section, the evolution of nonuniformities through single-mode simulations is described. The seeding of nonuniformities is described in "Shock Transit." The growth during the three phases—acceleration, coasting, and deceleration—is described in subsequent subsections.

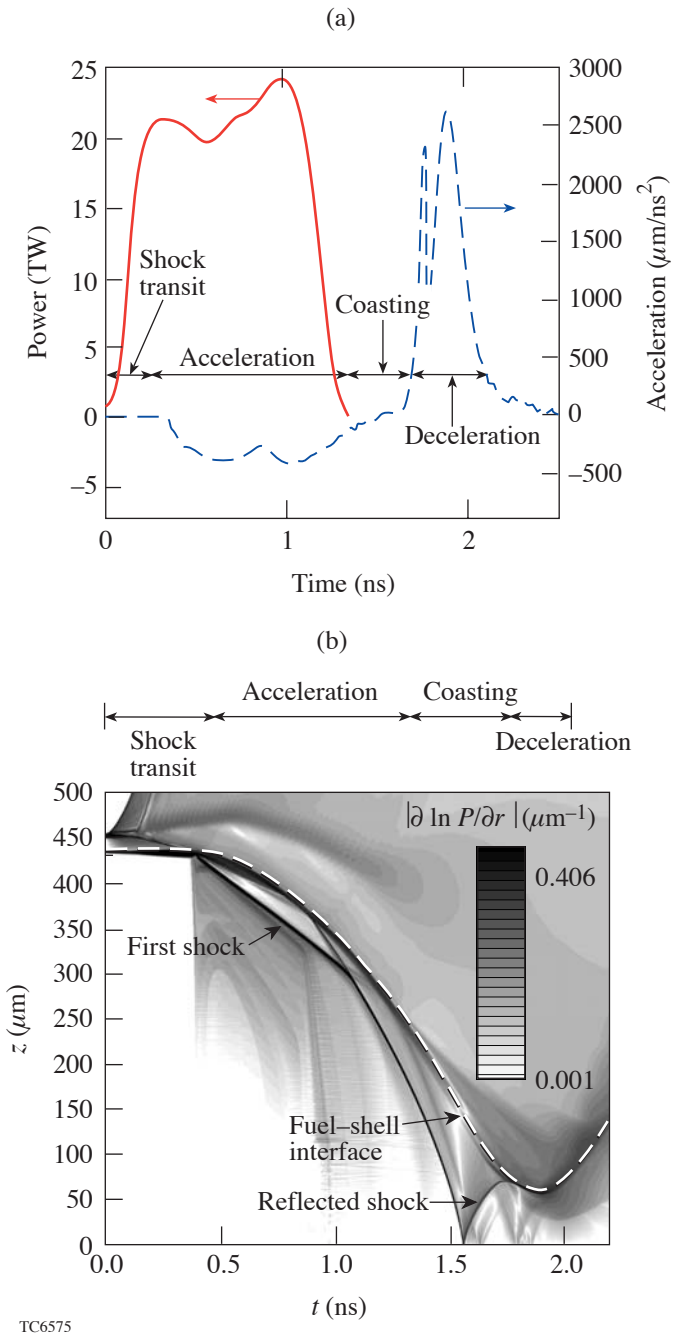


Figure 99.2
(a) Acceleration and laser pulse shape history (1-ns square) for the 20-$\mu$m CH shell irradiated with a 1-ns square pulse at 23 kJ of energy. (b) Contour plot of the magnitude of the gradient of the natural log of pressure for the target in (a). The darker contours correspond to shock trajectories. The dashed line is the trajectory of the fuel–shell interface. Also shown is the duration of the four phases of the implosion (shock-transit, acceleration, coasting, and deceleration).

1. Shock Transit

As mentioned in the last section, a strong shock is launched into the shell at the beginning of the pulse. Since there is no significant acceleration of the ablation front during the shock propagation through the shell, the shell nonuniformities are not susceptible to Rayleigh–Taylor instability. The perturbations, however, grow during this phase because of nonuniform laser illumination (power imbalance, beam mistiming, and single-beam nonuniformities or laser imprint). The initial outer-surface roughness, in general, can be amplified as well by Richtmyer–Meshkov[35] instability at the ablation front; such a growth, however, is totally stabilized by ablation.[36] As a result, the mode spectrum due to the initial outer-surface roughness does not significantly change during shock transit.

First, the evolution of long-wavelength modes seeded by power imbalance among the 60 OMEGA beams is described. This imbalance is due to beam mispointing, different beam shapes, beam mistiming, and energy imbalance between beams. The resultant laser illumination amplitudes due to all these sources are shown in Fig. 99.3 for the dominant modes. The tilt that might be introduced to each beam pulse shape is not included in these calculations. Azimuthal asymmetries in each phase plate are also not modeled. The perturbation amplitude for a given mode is obtained by overlapping and decomposing

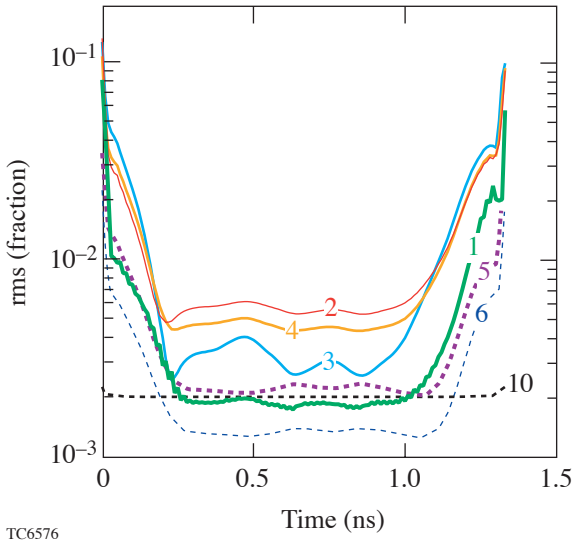


Figure 99.3
Modal amplitudes of the dominant modes due to beam imbalances as a function of time. The early-time large amplitudes correspond to beam mistiming. The values at the peak of the pulse (0.2 ns to 1.1 ns) are due to energy imbalance between beams, beam mispointing, and differences in spot shapes.

the 60-beam energies on a sphere into spherical harmonics. The amplitude of the corresponding Legendre mode is obtained by adding all the $m$-mode amplitudes in quadrature. The phase of the mode is chosen to be that of the $m = 0$ spherical harmonic. The large perturbation amplitudes of the Legendre modes correspond to the beginning of the laser pulse and are mainly due to beam mistiming (~12-ps rms). Once the peak intensity is reached, the nonuniformity reaches its asymptotic value corresponding to the energy imbalance in the beams (beam energies of the 60 OMEGA beams from a typical shot are used to apply energy imbalance), beam mispointing (~24-$\mu$m rms),[37] and differences in beam shapes (~11-$\mu$m rms in super-Gaussian radius and ~0.6% rms in super-Gaussian exponent). These values are typical of OMEGA. The target is assumed to be at the target chamber center. (Typically on OMEGA, plastic shells are within 5 $\mu$m of target chamber center at shot time.) Mode numbers 2 and 4 have the largest amplitudes as indicated by Fig. 99.3. Mode number 10 is due to the 60-beam OMEGA geometry.

A model that describes the seeding of the ablation surface due to the long-wavelength nonuniformities is described in Appendix A. This sharp-boundary model relates the modal amplitudes at the fuel–shell interface to the modulation in drive pressure, which in turn is related to the modulations in laser intensity using the "cloudy-day" model.[38] Here, the results of this model are compared with the full 2-D simulation involving modes up to 10. The modal amplitudes of the $D_2$–CH interface at the onset of the acceleration phase are shown in Fig. 99.4 for the 20-$\mu$m-thick implosion. These are obtained by decomposing the interface perturbations from the 2-D simulation into Legendre modes (solid circles). The amplitudes obtained from the model (x's) are also shown in Fig. 99.4. The results of the simulation are reproduced well by the simple model.

Next, the evolution of target nonuniformities caused by single-beam modulations (laser imprint) is described. Since laser imprint stays in the linear regime during shock transit, the mode spectrum is calculated by carrying out a series of single-mode, 2-D simulations up to the beginning of the acceleration phase. Imprint simulations are performed by imposing a 1% single-mode modulation in the laser illumination. 1-THz, 2-D SSD[32] is applied to the perturbation amplitudes. SSD is modeled nondeterministically. Each mode is characterized by a coherence time given by $t_c = \left[\Delta\nu \sin\left(n_c \pi \ell / \ell_{\max}\right)\right]^{-1}$, where $\ell_{\max} = 2\pi R_0/\delta$ is the mode number corresponding to half the speckle size $\delta$ ($\delta = 2.35$ $\mu$m for the OMEGA system), $R_0$ is the initial outer shell radius, $\Delta\nu$ is the SSD bandwidth, and $n_c$ is the number of color cycles on the laser system. The phase of the mode is chosen randomly every coherence time (the "flipping" approximation). This scheme mimics the average response of the target to the laser modulations. Averaged over time $T$, the single-beam rms nonuniformity, for a constant-intensity laser pulse, decreases as $\sqrt{t_c/T}$. For each mode in the simulation, the sequence of phases corresponds to a discrete two-state random walk. The number of the statistically independent phase sequences is limited by a finite maximum angular spread $\Delta\theta$ of the light propagating through the laser. The averaged mode amplitude cannot be reduced by SSD to levels below the asymptotic limit. This limit is inversely proportional to the square root of the number of statistically independent speckle patterns $N_{\text{stat}}(\lambda) = \left(4S^x_{\max}/\lambda\right)\left(4S^y_{\max}/\lambda\right)$, where $\lambda = 2\pi R_0/\ell$ is the nonuniformity wavelength, $S^{x(y)}_{\max} = F\Delta\theta^{x(y)}$ is the maximum spatial shift in the $x(y)$ direction, $F$ = 180 cm is the focal length, and $\Delta\theta^x$ = 50 $\mu$rad and $\Delta\theta^y$ = 100 $\mu$rad for the OMEGA laser system. The asymptotic limits are modeled in the flipping approximation by selecting only $N_{\text{stat}}$ independent choices for the sign of the nonuniformity amplitude. The average over a large number of runs will then correspond to the expected response of the target to the single mode. The calcu-

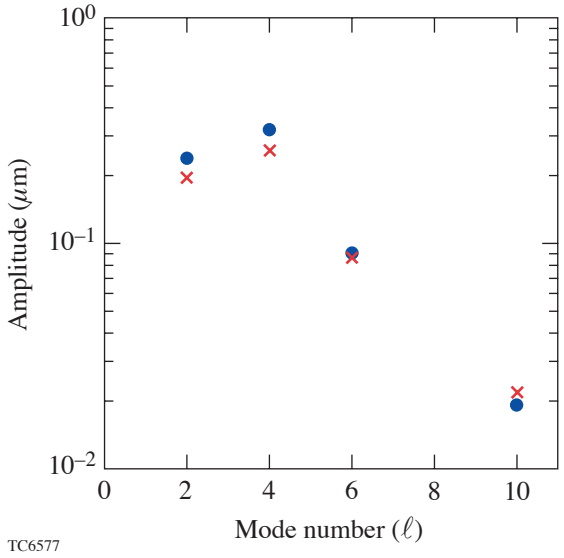


Figure 99.4
Single-mode amplitudes of the fuel–shell interface at the beginning of acceleration from a 2-D simulation for the 20-$\mu$m-thick CH implosion (solid circles). The values obtained from the model described in Appendix A are also shown (x's). The "cloudy-day" model relates the amplitudes at the fuel–shell interface to modulation in laser drive. Good agreement between the simulations and model indicates that the seeding of the interface is well understood.

lated ablation-front amplitude at the beginning of the acceleration phase $\eta_{\%}$ is a decaying function of the mode number $\ell$.[39] This is due to both the shorter decoupling time and the stronger dynamic overpressure stabilization of the higher-$\ell$ modes. When the effect of SSD is included, the imprint efficiency scales linearly with the mode wavelength. For the plastic shells driven by a 1-ns square pulse with 1-THz, 2-D SSD, the numerical calculations give the following ablation-front amplitude per 1% laser nonuniformity:

$$\eta_{\%} \simeq 6\times 10^{-5}\left(6.7+2\pi R_0/\ell\right), \tag{1}$$

where the initial shell radius $R_0$ and $\eta_{\%}$ are in microns. To calculate the mode spectrum at the ablation front due to the laser imprint, amplitude $\eta_{\%}$ is multiplied by $\sigma_{\text{rms}}$ of the laser nonuniformity of a particular mode.

Calculation of the laser $\sigma_{\text{rms}}(\ell)$ includes the effects of the distributed phase plates (DPP's).[40–42] Laser beams are phase converted by being passed through the DPP's on the OMEGA laser. The DPP's improve the focused single-beam uniformity by removing the large-scale beam structure with a higher imprint efficiency [see Eq. (1)], leaving intensity profiles with a well-controlled envelope modulated by fine-scale speckle with a lower imprint efficiency. An analytical model that describes this fine speckle[43] is used to model the static single-beam nonuniformity in 2-D simulations in which the $\ell$-mode nonuniformity is given as

$$\sigma^2_{\text{rms}}(\ell) = \frac{16\ell}{\pi\ell^2_{\max}}\left[\cos^{-1}\left(\frac{\ell}{\ell_{\max}}\right) - \frac{\ell}{\ell_{\max}}\sqrt{1-\left(\frac{\ell}{\ell_{\max}}\right)^2}\right]. \tag{2}$$

This mode spectrum was confirmed experimentally in Ref. 44. The illumination nonuniformity given by Eq. (2) is shown in Fig. 99.5 as a function of mode number. Note that the laser nonuniformity amplitudes increase initially as a function of mode number (up to $\ell \sim 600$), opposite to the decay in the imprint efficiency with the wave number [Eq. (1)].

Polarization smoothing further reduces the amplitude by a factor of $\sqrt{2}$.[34] Further reduction in modal amplitudes is obtained with beam overlap. This reduction factor is obtained by comparing the result of overlapping 60 OMEGA beams on a sphere with the single-beam DPP amplitudes. A reduction factor of $\sqrt{12}$ reproduces the resultant overlapped amplitude pattern on a sphere. Overall amplitudes in the *DRACO* simulation are correspondingly reduced. The resulting imprint spectrum (dotted line) at the ablation front is plotted in Fig. 99.6. Figure 99.6 also shows the ablation-surface amplitude due to imprint from one multimode *DRACO* simulation up to mode number 200 (solid line). The multimode simulation

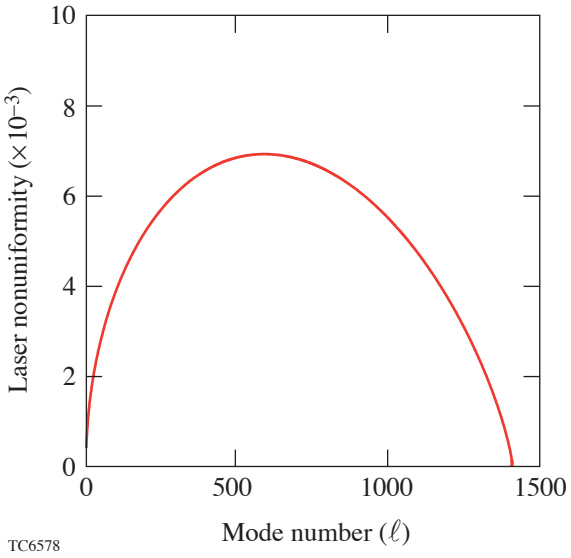


Figure 99.5
Nonuniformity spectrum due to phase-plate speckle. This nonuniformity peaks around $\ell \sim 600$.

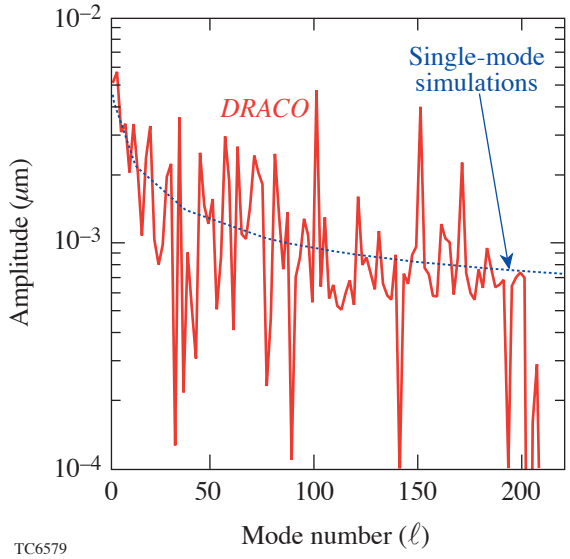


Figure 99.6
Imprint spectrum from single-mode simulations (dotted line) and multimode simulation (solid line). The good agreement confirms linear behavior of imprint. Note that imprint efficiency decreases with increasing mode number. This is opposite in behavior to the laser nonuniformity (Fig. 99.5).

shows variations in the imprint spectrum due to the nondeterministic scheme used to model SSD. Good agreement, on average, between the two calculations confirms the linear behavior of imprint prior to shell acceleration.

The seeding due to all three nonuniformity sources is compared in Figs. 99.6 and 99.7. The contribution of the ablation-surface nonuniformity from power imbalance and surface roughness[45] is shown in Fig. 99.7. The comparison of this spectrum with Fig. 99.6 shows that the main contribution to the low-$\ell$ modes comes from beam imbalances. Surface roughness has a smaller contribution at low $\ell$. Laser imprint dominates the intermediate ($10 < \ell < 50$)- and high-$\ell$-mode seeding (not shown).

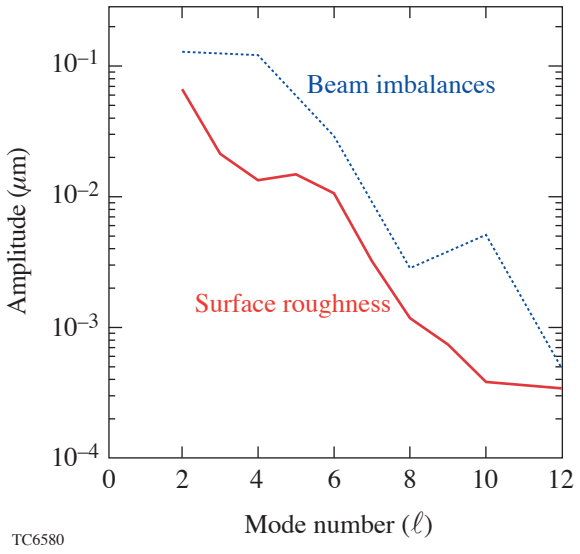


Figure 99.7
Long-wavelength perturbations at the ablation surface due to beam imbalances (dotted line) and surface roughness (solid line) at the start of acceleration. Beam imbalances provide the larger contribution to long-wavelength nonuniformity seeds.

2. Acceleration Phase

The two main sources of perturbation growth during the acceleration phase are (1) the RT instability caused by the opposite directions of the pressure and density gradients at the ablation front and (2) the secular growth due to the asymmetries in the laser drive. The latter growth is important only for low-$\ell$ modes where the wavelength is much longer than the distance between the laser deposition region and the ablation front (conduction zone). Shorter-wavelength drive nonuniformities are smoothed out by the thermal conduction in the conduction zone (the cloudy-day effect). In addition, the RT growth rate increases with mode number; therefore, secular growth becomes negligible at the shorter wavelengths.

The relative importance of the secular growth versus the RT growth for different long-wavelength modes is illustrated in Appendix B using a simple model. The model indicates that the final amplitudes at the end of the acceleration phase caused by secular growth alone are significantly smaller than when RT growth is also included. This suggests that power balance is extremely important during the period of shock transit when the seeds for RT growth are established. During acceleration, beam imbalances are less important because the resulting secular growth is dominated by RT growth. This is confirmed by the results of the simulations shown in Fig. 99.8. In simulation 1 (solid line), beam imbalance is turned off at the start of acceleration, whereas in simulation 2 (dotted line), it is retained throughout the laser pulse. The ablation-surface amplitudes vary by less than 20%, confirming that beam balance is important primarily during shock transit.

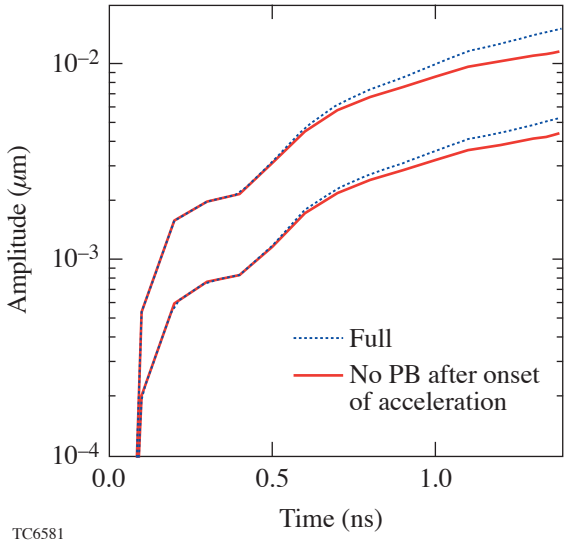


Figure 99.8
Amplitudes of the $D_2$–CH interface versus time for mode numbers 2 and 4 for beam imbalances throughout the pulse (dotted) and beam imbalances imposed on target only until the start of acceleration (solid). The small effect of beam imbalances during the acceleration phase indicates that long-wavelength modes are seeded primarily during shock transit.

Next, evolution of the intermediate ($10 < \ell < 50$)- and short-wavelength modes ($\ell > 50$) is considered. The main seed of these modes comes from the single-beam nonuniformity (laser imprint). The initial spectrum of imprint perturbations at the ablation surface is peaked at the low-$\ell$ modes (Fig. 99.6). The RT growth rate, however, increases with the mode number,

shifting the spectrum maximum during acceleration toward shorter wavelengths. It is well known that mass ablation significantly reduces RT growth rate compared to the classical limit.[11–13] As shown in Ref. 44, a rather complicated expression for the growth rate can be fitted with much simpler formulas:

$$\gamma = \alpha_1 \sqrt{kg} - \beta_1 k V_a, \quad Fr >> 1, \tag{3}$$

$$\gamma = \alpha_2 \sqrt{\frac{kg}{1+kL_m}} - \beta_2 k V_a, \quad Fr << 1, \tag{4}$$

where $Fr = V_a^2 / (gL_0)$ is the Froude number, $L_0$ is the characteristic thickness of the ablation front, $L_m$ is the minimum density-gradient scale length, and $V_a$ is the ablation velocity defined as the mass ablation rate divided by the shell density. The coefficients $\alpha_{1,2}$ and $\beta_{1,2}$ are functions of the Froude number and the effective power index for thermal conduction $\nu$. The dispersion formulas described in Eqs. (3) and (4) have been verified experimentally in Ref. 45 for CH. For the 20-$\mu$m-thick plastic shell considered in this article, the time-averaged acceleration, ablation velocity, ablation-front thickness, and power index, respectively, are $g = 320$ $\mu$m/ns$^2$, $V_a = 3.2$ $\mu$m/ns, $L_0 = 0.18$ $\mu$m, $L_m = 0.72$ $\mu$m, and $\nu = 1$; therefore, the Froude number is small, $Fr = 0.18$, and Eq. (4) can be used to calculate the RT growth rate. The fitting procedure described in Ref. 44 gives the following coefficients: $\alpha_2 = 0.94$ and $\beta_2 = 1.50$. Growth rates from single-mode simulations (solid circles in Fig. 99.9) compare very well with this analytic formula (dotted line in Fig. 99.9). Each simulation point in Fig. 99.9 is a single-mode simulation with a small amplitude perturbation to the laser nonuniformity, such that the mode growth remains in the linear regime during the acceleration. Equation (4) also indicates that the cutoff occurs at very high $\ell$ modes, $\ell_c = 1220$, and the growth rate does not decrease significantly even for mode numbers as high as $\ell \sim 600$ for these plastic ablators. Modes above $\ell \sim 600$, however, have a much smaller initial amplitude and experience nonlinear saturation. Their contribution to the total nonuniformity budget, therefore, is insignificant.

It is instructive to point out the stabilizing role of the radiation. Reabsorption of the emission from the corona by the shell raises the shell adiabat near the ablation front, leading to adiabat shaping by radiation in the shell. This increases the ablation velocity (from ~2.2 $\mu$m/ns to ~3.2 $\mu$m/ns) and the density-gradient scale length (from $L_m = 0.1$ $\mu$m to 0.7 $\mu$m). Since the density is much sharper when the radiation transport is turned off, the Froude number increases, $Fr = 0.7$ (compare to $Fr = 0.18$ with radiation). Fitting the growth rate gives the following result: $\gamma_{\mathrm{NoRad}} = 0.92\sqrt{kg/(1+kL_m)} - 1.59\ kV_a$. The cutoff mode number in this case increases from $\ell_c = 1200$ to $\ell_c = 4000$, and the growth rate of mode $\ell = 200$ increases from $\gamma = 7.8$ ns$^{-1}$ to 10.1 ns$^{-1}$. The growth rates for the cases with and without radiation transport are summarized in Fig. 99.9.

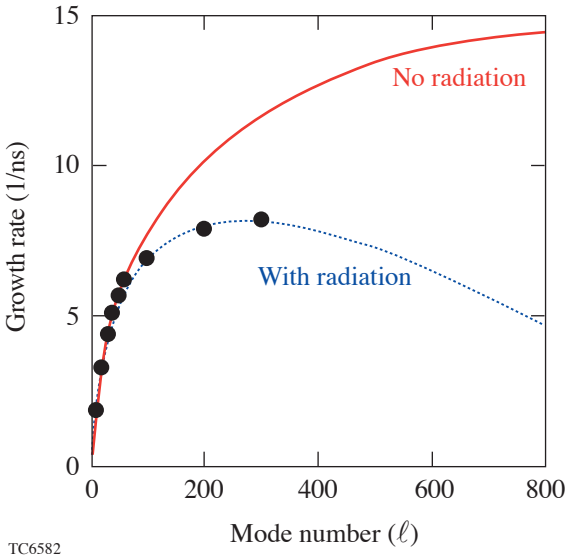


Figure 99.9
Good agreement is obtained with simulated single-mode growth rates (solid circles) and the Betti formula for plastic (dotted line). Also shown is the Betti formula for growth rates when radiation transport is not included in the simulation (solid line). Reabsorption of radiation from the corona plays an important role in stabilizing the growth of perturbations at the ablation surface.

The results from single-mode simulations using the realistic imprint amplitudes caused by the use of phase plates are shown in Fig. 99.10. SSD and polarization smoothing are applied to smooth the nonuniformity over time. Since beam smoothing is modeled nondeterministically, the average of several simulations is used for the ablation-surface amplitude. Each simulation point in Fig. 99.10 is the ablation-surface amplitude obtained from the average of five simulations with the error bar representing the standard deviation of these five simulations. It can be seen that modes up to at least 400 contribute to the ablation-surface nonuniformity. A full 2-D simulation would require, therefore, at least 400 modes to realistically model shell stability during the acceleration phase.

The more-massive, 27-$\mu$m-thick plastic shell accelerates less ($g$ = 240 $\mu$m/ns$^2$) and consequently has lower growth

rates. The nonuniformity seeds at the end of the acceleration phase from feedthrough are, therefore, also smaller at the $D_2$–CH interface.

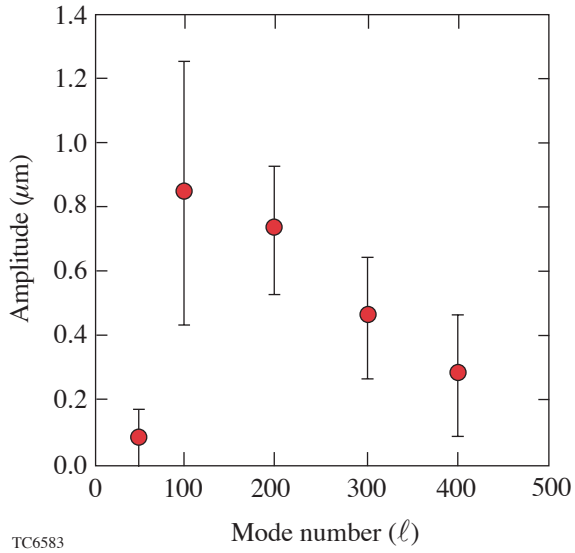


Figure 99.10
Single-mode amplitudes at the end of the acceleration phase. The solid circles are averages of five simulations, each with a different choice of random number seed for the nondeterministic SSD model. The error bars represent the standard deviation of the amplitude across the five simulations. The relatively large values of $\ell = 400$ indicate that such short wavelengths will contribute significantly to the ablation-surface nonuniformity.

## 3. Coasting Phase

Shortly after the laser drive is turned off, the shell stops accelerating and starts to coast with a spatially averaged velocity that is constant in time. The coasting phase lasts until the main shock reflects from the center and begins to interact with the incoming shell. Even though the shell perturbations are not subject to the RT instability while the shell coasts inward, the perturbations are still amplified by Bell–Plesset growth. This growth is due to convergence and scales approximately as $\eta \sim (\rho r^2)^{-1}$. Since the shell coasts inward, the shell radius decreases and the perturbation amplitude grows. Furthermore, both the front and back surfaces of the shell and the $D_2$–CH interface expand (in the frame of reference moving with the shell) with the local sound speed, leading to a decrease in the density that further amplifies the perturbations. In general, the equation governing the perturbation evolution in the absence of acceleration has a weak mode-number dependence.[32] Simulations, however, show a strong $\ell$-dependence of the Bell–Plesset growth, especially for long- and intermediate-wavelength modes (see Fig. 99.11). Such dependence is due to the differences in long- and short-wavelength growth prior to the coasting phase. Since the low-$\ell$ RT growth rate scales as a square root of the mode number $\ell$, the longer-wavelength perturbations have lower RT growth rates during shell acceleration. Therefore, at the end of the pulse, the velocity perturbation at the $D_2$–CH interface is proportional to the square root of the mode number. To illustrate how mode dependence appears in the convergence growth, we adopt the simplest model for the perturbation evolution during the coasting phase:[15]

$$\frac{d}{dt}\left[\frac{d\left(\rho r^2 \eta\right)}{dt}\frac{1}{\rho r}\right] = 0. \tag{5}$$

Integrating Eq. (5) twice with the initial conditions $\eta(t=0) = \eta_0$ and $d\eta/dt\,(t=0) = \eta_0' \simeq \sqrt{\ell/R_0 g}\,\eta_0$ gives the perturbation growth factor

$$\frac{\eta}{\eta_0} = C_c^2\left[\frac{\rho_0}{\rho} + \left(-\frac{2V_{\text{imp}}}{\rho R_0^2} + \sqrt{\frac{\ell g}{R_0}}\frac{1}{\rho R_0}\right)\int_0^t \rho(t')r(t')\,dt'\right], \tag{6}$$

where $C_c$ is the shell convergence ratio during the coasting phase, $R_0$ is the shell radius at the end of the acceleration phase, $\rho_0$ is the density at the end of the acceleration phase, and $V_{\text{imp}}$ is the implosion velocity. Equation (6) shows that the longer-

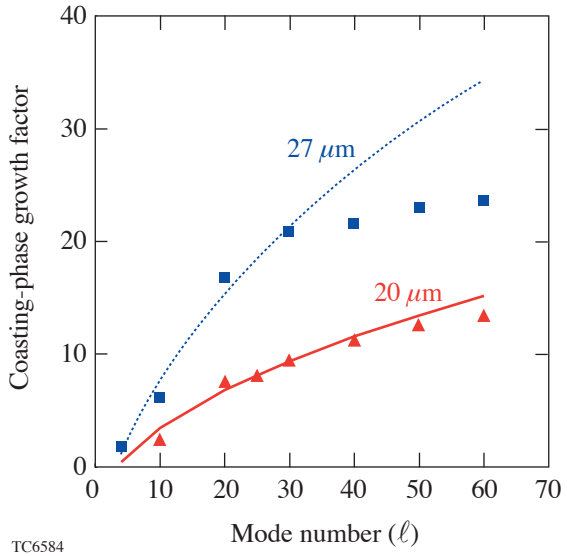


Figure 99.11
Single-mode growth factors for the coasting phase for the 20-$\mu$m-thick (triangles) and 27-$\mu$m-thick (squares) CH implosions. The lines are $\sim\sqrt{\ell}$ - fit to the growth factors for $\ell < 30$. Growth factors clearly saturate for $\ell > 30$ for the 27-$\mu$m-thick CH shell.

wavelength modes experience smaller growth factors, in agreement with the results of simulations (see Fig. 99.11). The behavior of shorter wavelengths ($\ell > 50$), however, is different from Eq. (6). The perturbations at the $D_2$–CH interface for such modes decouple from the unstable ablation front during shell acceleration when $\Delta_{int}\ell/r$ becomes greater than unity, where $\Delta_{int}$ is the distance between the ablation front and the interface. After decoupling, the interface ripple starts to oscillate with increasing amplitude due to the convergence effects. The growth factor for such modes is defined as the ratio of the interface amplitude at the end of shell coasting to the amplitude maximum during the acceleration phase; then, $\eta_0' \neq \sqrt{\ell/rg}\,\eta_0$ and $\ell$-dependence of the solution of Eq. (5) becomes much weaker than $\sqrt{\ell}$. This is confirmed in Fig. 99.11, which shows a clear saturation of the growth factors after $\ell \sim 30$ for the 27-$\mu$m-thick implosion. The lines in Fig. 99.11 are a $\sqrt{\ell}$ fit to the growth factor for $\ell < 30$. For the 20-$\mu$m-thick implosion, this saturation is less apparent. The 27-$\mu$m shell moves slower during the acceleration phase; hence, it coasts for a longer time ($C_c = 2.2$ for 20-$\mu$m shell and $C_c = 3.0$ for 27-$\mu$m shell). This leads to larger coasting-phase growth factors in thicker shells. It is important to note that the larger $D_2$–CH growth factors during coasting partially compensate for the smaller nonuniformity seeds at the start of the coasting phase for the thicker, 27-$\mu$m implosion. At shell stagnation, therefore, the interface distortions exhibit very little sensitivity to shell thickness.

## 4. Deceleration Phase

The coasting phase is followed by shell deceleration when the main shock reflected from the center begins to propagate outward inside the shell. The shell at the deceleration phase is defined as the high-density portion of the CH material (according to a standard definition, the shell is bounded by the $\rho_{max}/e$ points on both sides from the position of the maximum density $\rho_{max}$; also Fig. 99.12). The fuel, together with the inner lower-density, high-temperature CH, forms the hot spot. As the shell converges and temperature inside the hot spot increases, the heat front advances outward and ablates the colder portion of the shell. Therefore, the mass of the higher-temperature hot spot increases during the deceleration phase. This is similar to the hot-spot formation in cryogenic ignition designs.[46] The main difference between cryogenic implosions and the gas-filled plastic implosions is that the hot spot in a cryogenic target consists only of the fuel, while the plastic implosions have two materials—fuel and CH. Since there is a mismatch in the average ion charge $Z$ of the two materials, the density and thermal conductivity are discontinuous across the material interface. The density jump is easily obtained from the pressure continuity condition across the interface in the absence of radiative effects. The total pressure of the ionized gas is $p = \rho T/A$, where $T$ is the temperature, $A = m_i/(1+Z)$, and $m_i$ is the average ion mass. Since the heat flux is continuous across the interface, the temperature must be continuous as well; therefore, the jump in density becomes

$$\frac{\rho_{CH}}{\rho_{DD}} = \frac{m_{CH}}{m_{DD}}\frac{1+Z_{DD}}{1+Z_{CH}}. \tag{7}$$

Substituting $m_{CH} = 6.5\ m_p$, $m_{DD} = 2m_p$, $Z_{CH} = 3.5$, and $Z_{DD} = 1$ into Eq. (7) gives $\rho_{CH}/\rho_{DD} = 1.44$, which leads to the Atwood number $A_T = 0.18$. Here, $m_p$ is the proton mass. Such a density jump across the material interface creates conditions for the RT growth. There are two RT unstable regions during the deceleration phase: (1) the classically unstable CH–$D_2$ interface with $A_T = 0.18$ and (2) the rear surface of the shell. Density profiles at peak neutron production are shown in Fig. 99.12 to illustrate this point. The simulation without radiative effects (solid) shows two distinct regions of instability: the fuel–shell interface with an Atwood number of 0.18 and a less-steep density gradient leading up to the peak density. While the first region is unstable for all mode numbers, the growth rate at the second region is significantly reduced by the density-gradient scale length and mass ablation. With radiative effects included in the calculation (dotted), however, the effective Atwood number at the interface significantly increases to

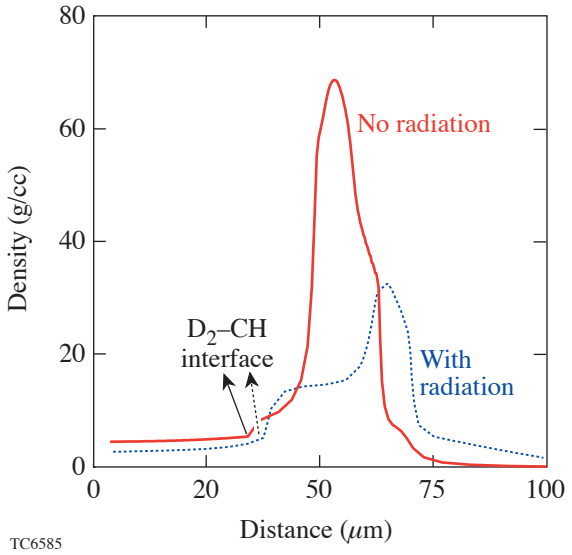


Figure 99.12
Density profiles at peak neutron production from a 1-D simulation with (dotted) and without (solid) radiation transport. Radiation plays an important role during deceleration by raising the effective Atwood number for long and intermediate wavelengths.

~0.5 from the relatively small value of 0.18. This effect is due to the ablation of the colder shell material. As the shell material ablates and is heated by the thermal conduction from the core, the bremsstrahlung radiation increases. The radiation losses lead to additional cooling and compression of the blowoff CH. The simulation with radiation transport in Fig. 99.12 (dotted line), at peak neutron production, has a larger $A_T$ compared to the simulation without radiation (solid line). As a consequence of this increased Atwood number, there is an increase in the RT instability growth rate for long and intermediate wavelengths. The RT instability creates a lateral flow of the fuel along the interface that moves the fuel from the hotter spike region into the colder bubbles. This leads to an effective cooling of the fuel and degradation in the neutron production rate. Such a mechanism of the neutron-yield truncation is dominant for the thicker shell, which is stable enough during the acceleration phase to maintain its integrity.

As mentioned earlier, the main shock reflected from the target center starts to propagate across the shell at the beginning of the deceleration phase. The material behind the shock stagnates, transferring the shell's kinetic energy into the internal energy of the hot spot. It is easy to understand intuitively that the larger momentum flux of the shell material across the shock results in higher hot-spot stagnation pressure. To estimate the dependence of the final hot-spot pressure $P_f$ on the shell's parameters, we use the continuity conditions across the shock propagating inside the shell, which moves with implosion velocity $V_{\rm imp}$ and has density $\rho_{\rm sh}$. In the shock-front frame of reference, the mass-flow continuity reads as

$$\rho_c U_2 = \rho_{\rm sh} U_1, \tag{8}$$

where $U_1$ and $U_2$ are the fluid velocities ahead and behind the shock and $\rho_c$ is the compressed density behind the shock. Since the material behind the shock stagnates in the laboratory frame of reference, $U_2 = U_s$ and $U_1 = V_{\rm imp} + U_s$, where

$$U_s \simeq \sqrt{\frac{\gamma+1}{2}\frac{P_f}{\rho_{\rm sh}}} \tag{9}$$

is the shock velocity in the strong-shock limit and $\gamma = 5/3$ is the ratio of specific heats. Combining Eqs. (8) and (9) and using $\rho_c \simeq 4\rho_{\rm sh}$ gives

$$P_f \sim \rho_{\rm sh} V_{\rm imp}^2 \sim \frac{E_{\rm kin}}{R_{\rm hs}^2 \Delta_{\rm sh}}. \tag{10}$$

At shell stagnation, the kinetic energy of the shell $E_{\rm kin} = M_{\rm sh} V_{\rm imp}^2 / 2$ is transferred into the internal energy of the hot spot $2/3\, P_f R_{\rm hs}^3$. Equation (10) shows that the stagnation radius is proportional to the shell thickness $R_{\rm hs} \sim \Delta_{\rm sh}$; therefore, the final pressure of the compressed fuel is larger for a "compact" shell with higher density and smaller shell thickness for a given shell kinetic energy. In other words, the kinetic energy of the converging shell heats the hot spot more efficiently in shells with larger compressibility (smaller entropy). Comparing 20- and 27-$\mu$m shells, we conclude that the stagnation radius of the thicker shell is larger; thus the final pressure and the neutron-production rate are smaller. On the other hand, if one compares the shell that remains integral during the acceleration phase with a shell whose stability is severely compromised by RT growth, the integral shell has a lower entropy and smaller shell thickness. It, therefore, stagnates at a smaller radius reaching a higher hot-spot pressure and temperature. This leads to a larger neutron-production rate in the integral shell in comparison with the significantly distorted shell.

The larger shell thickness in the implosion with compromised shell integrity also implies that the rate at which neutron production decreases should be less steep during shell disassembly. Between the time of peak neutron production and peak compression, the neutron rate decreases due to the falling temperature in the gas. The subsequent decrease in the neutron-production rate occurs due to shell disassembly. If the shell is thicker, disassembly occurs later in the implosion as follows: The time between the interaction of the reflected shock (which is very similar for both integral and severely distorted shells) and when the shock breaks out of the shell is given by $t_s = \Delta_{\rm sh}/U_s$. From Eqs. (9) and (10), $U_s \simeq \sqrt{E_{\rm kin}/R_{\rm hs}^2 \Delta_{\rm sh} \rho_{\rm sh}}$. Since $E_{\rm kin}$ is very similar between the integral shell and severely distorted shell implosion (only a small portion of the total energy goes into lateral flow in the distorted shell implosion) and mass $\left(\propto R_{\rm hs}^2 \Delta_{\rm sh} \rho_{\rm sh}\right)$ is conserved, the shock velocity is very similar in both cases; therefore, $t_s \propto \Delta_{\rm sh}$ and is longer for the thicker shell, and disassembly is delayed. Consequently, neutron production falls less steeply in the implosion where shell stability is compromised than in the implosion with an integral shell.

**Multimode Simulations**

1. Effects of Beam-to-Beam Imbalances

We now turn to multimode simulations using *DRACO*. As mentioned in the **Shock Transit** section (p. 142), imbalances between beams result in long-wavelength modes on target. Even modes between 2 and 10 are used to simulate the effect of low-order modes using the amplitudes in Fig. 99.3. The

power in odd modes is added in quadrature to the even-mode amplitudes. Figure 99.13 shows the fuel–shell interface amplitudes versus time for the dominant modes in the simulation for the 20-$\mu$m-thick shell implosion. The initially unperturbed interface acquires a perturbation shortly after shock breakout around 0.4 ns. When the compression wave returns to the interface, it causes another jump in the perturbation around 0.8 ns. Significant growth is simulated after this time due to the feedthrough of the perturbation from the ablation surface and the convergent Richtmyer–Meshkov instability. Modes 6 and up start oscillating shortly after the end of the acceleration phase as they decouple from the ablation surface. The reflected shock from the center returns to the interface around 1.75 ns, when $\ell = 4$ changes phase. Rayleigh–Taylor growth occurs shortly after that as the shell continuously decelerates toward stagnation.

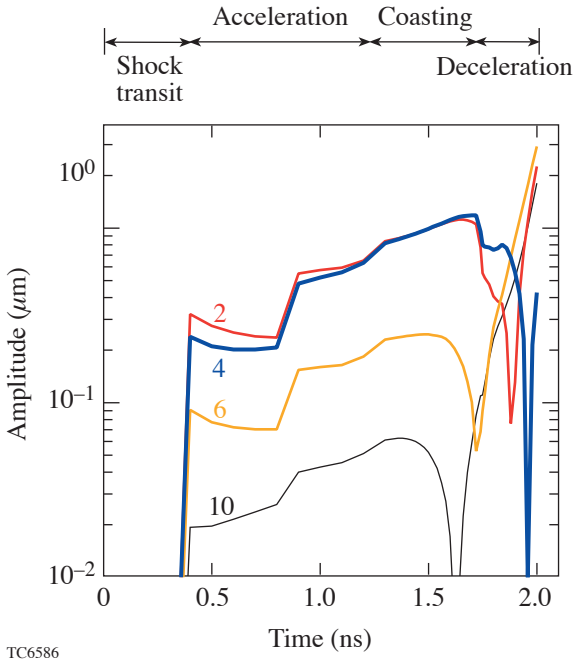


Figure 99.13
Modal amplitudes versus time at the fuel–shell interface for the low-order multimode simulation (due to beam imbalances) of a 20-$\mu$m-thick CH shell. The interface becomes perturbed shortly after shock breakout around 0.4 ns. A second jump in the amplitude is modeled at ~0.8 ns when the second shock breaks out of the shell. Shorter wavelengths such as modes 6 and 10 decouple during the coasting phase when they change phase. Longer wavelengths (modes 2 and 4) change phase when the shock returns to the interface at ~1.75 ns.

The yield is only marginally affected by low-order modes with 2-D simulation, resulting in ~95% of the 1-D yield for the 20-$\mu$m-thick shell and ~94% of 1-D for the 27-$\mu$m-thick shell.

Figure 99.14 shows the density contours at peak neutron production for the 20-$\mu$m-thick implosion. The $D_2$–CH interface is marginally distorted. Areal-density variations of ~23% at peak neutron production (for both shell thicknesses) are simulated.

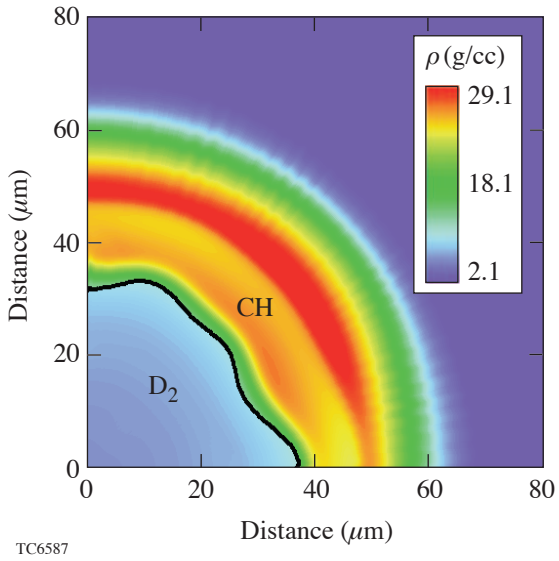


Figure 99.14
Density contours at peak neutron production from a multimode simulation including only low-$\ell$ modes ($\ell < 10$) for the 20-$\mu$m-thick CH implosion. An areal-density variation of 23% is calculated at this time in the implosion. The solid line corresponds to the $D_2$–CH interface.

The marginal effect of low-order modes is consistent with the experimental beam-balancing work described in Ref. 37. In that work, on-target beam balance was changed in a controlled manner; the estimated decrease in the amplitude of these modes was between 30%–50%. While a decrease in areal-density variations was observed, only a marginal difference was observed in absolute neutron yields.

### 2. Effects of Single-Beam Nonuniformity

Single-beam nonuniformity influences intermediate- and short-wavelength seeds on target. As mentioned earlier, modes up to at least 400 are required to realistically model shell stability. A full 2-D simulation including the effects of power imbalance would then require modes between 2 and 400. Resolving mode 400 in such a simulation requires a large number of computational zones—far beyond the scope of this work. We illustrate the effect of laser imprint on shell stability by performing simulations with a smaller set of modes. The simulations include beam-smoothing techniques modeled as

described in the **Acceleration Phase** section (p. 145). Figure 99.15(a) shows a plot of density contours at the end of the acceleration phase from a simulation that includes even modes up to $\ell = 200$ for the 20-$\mu$m-thick CH shell. The shortest wavelength in this simulation is resolved using 14 cells, resulting in a $200 \times 700$ zone simulation. Since odd modes are not included in the simulation, their power is added in quadrature to the amplitudes of the even modes. The shell indicated by the high-density regions is considerably distorted with portions of the shell at less than solid densities. The peak-to-valley variation in the center-of-mass radius is calculated to be 6.6 $\mu$m at the end of the acceleration phase, significantly greater than the 1-D shell thickness of ~5 $\mu$m. It is expected that shell distortion will increase only when even-shorter wavelengths are included in the calculation. Therefore, short wavelengths play an important role in increasing the adiabat of the shell by introducing additional degrees of freedom for the fluid flow. This will influence the compressibility of the shell and, therefore, neutron yields. In comparison, the 27-$\mu$m-thick implosion [Fig. 99.15(b)] has an integral shell at the end of the acceleration phase with a peak-to-valley amplitude of 3.4 $\mu$m in the center-of-mass radius compared to a shell thickness of ~6.8 $\mu$m. The effect of the still-shorter wavelengths not included in the calculation ($\ell > 200$) can be estimated using a RT postprocessor[31] to the 1-D simulation. This postprocessor indicates that the thicker, 27-$\mu$m-thick shell remains integral during the acceleration phase while the stability of the 20-$\mu$m-thick shell is severely compromised.

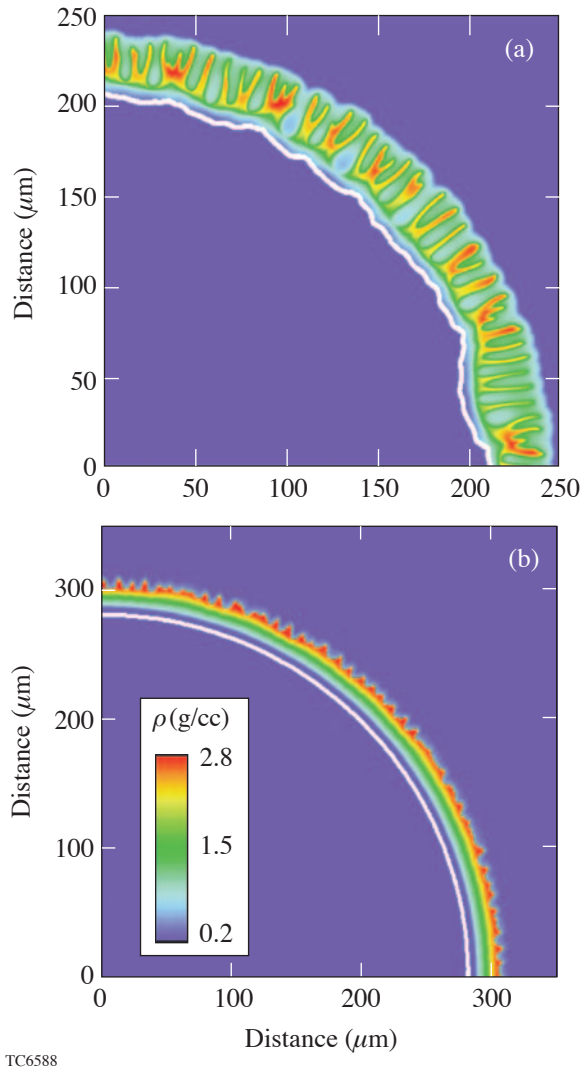


Figure 99.15
Density contours at the end of the acceleration phase for (a) a 20-$\mu$m-thick CH shell and (b) a 27-$\mu$m-thick CH shell from a multimode simulation of laser imprint. The solid lines correspond to the $D_2$–CH interface. Note that the shell (indicated by the higher-density contours) is significantly more distorted for the 20-$\mu$m implosion than the 27-$\mu$m implosion.

Due to the large number of computational cells in these simulations, it is extremely challenging to reliably simulate these implosions until peak compression. Instead, we assess the effect of the various nonuniformity sources by simulations that include only a few modes but represent reasonably well the shell's stability. The goal of these simulations is to identify the mechanisms that influence neutron yields. More-detailed comparisons with experimental observables will be performed in the future.

### Combined Effects of All Sources of Nonuniformity

Simulations that include a few modes are useful to shed light on which modes influence target performance. The mode ranges are divided into three regions: long wavelengths ($\ell \leq 10$), intermediate wavelengths ($10 \leq \ell \leq 50$), and shorter wavelengths that include all the higher mode numbers. In the **Effects of Beam-to-Beam Imbalances** section (p. 149), it has been pointed out that low-order modes ($\ell \leq 10$) alone have a marginal influence on target performance. We consider simulations involving two modes corresponding to mode numbers 4 and 20 that combine the effect of long and intermediate wavelengths. These simulations and those described later are performed on a 45° wedge. The initial amplitude for each mode is chosen from the amplitudes added in quadrature of a range of mode numbers (from the DPP spectrum for $\ell = 20$ using modes between 15 and 40 as the mode range and from the initial power balance and surface-roughness data for modes $2 < \ell < 10$ for mode $\ell = 4$). The neutron-production rate is shown in Fig. 99.16(a) for the 20-$\mu$m-thick implosion and Fig. 99.16(b) for the 27-$\mu$m-thick implosions. The rate from

the two-mode simulations (dotted line) deviates from the 1-D simulation, and the burn truncates relative to 1-D. This is the case for both thicknesses. The two-mode simulation illustrates the mechanisms for yield reduction through burn truncation. The RT and RM growth at the fuel–shell interface results in the flow of fuel into the colder bubbles, decreasing the yield. This is illustrated in Fig. 99.17, where the fluid velocity vectors (arrows) in the frame moving radially with the fluid are overlaid on the contour plot of ion temperature at peak neutron production. This result is shown from a single-mode simulation of mode number 20, where this mode has the same initial amplitude as the previous two-mode simulation. Due to heat conduction, the temperature contours are more spherically symmetric than the material interface (solid line). As the vectors indicate, fuel flows into the colder bubbles. This truncates the neutron-production rate. The second mechanism for the truncation of the neutron rate occurs because of the distortion of the high-density shell. The increased surface area enhances heat conduction out of the core, cooling the fuel and decreasing the yield. These mechanisms for the truncation of neutron yield cannot be included in 1-D mix models that have been used previously to model these implosions.[6,8,49] It is also to be noted that the single intermediate-mode simulation has a yield relative to 1-D of 78% (for both thicknesses). The addition of long wavelengths ($\ell = 4$) reduces this value to 55% for the 20-$\mu$m-thick shell and 61% for the 27-$\mu$m-thick shell. Thus, the combination of the low and intermediate modes has a greater effect on yield than each range of modes alone.

To investigate the role of the shorter wavelengths on yield, we perform a three-mode simulation including mode numbers 4, 20, and 200. In this simulation, modes 4 and 20 have the

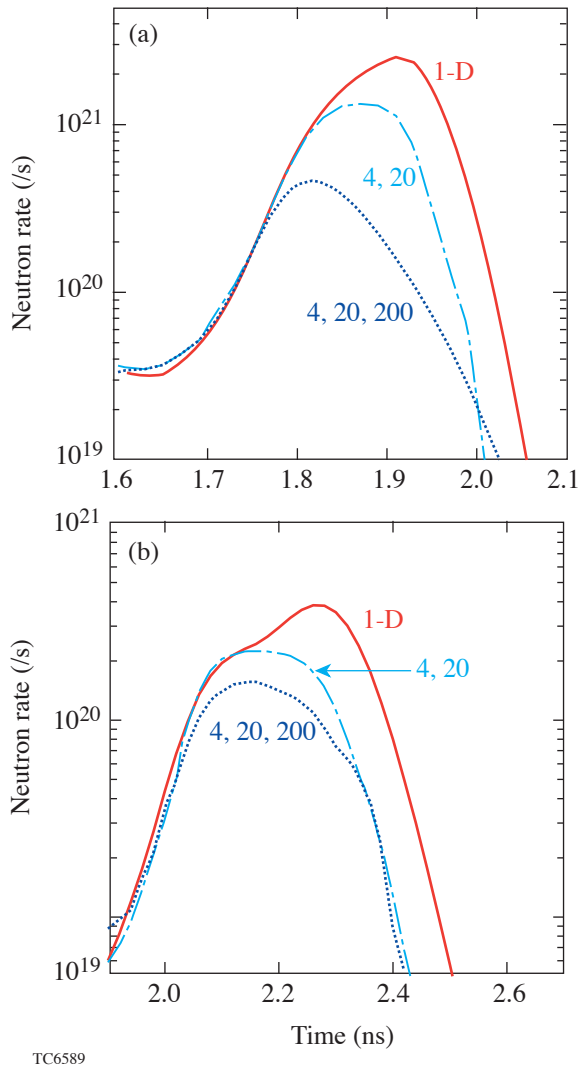


Figure 99.16
Neutron-production rates from the simulation including only low- and intermediate-mode numbers (dashed–dotted line) and the simulation including short wavelengths (dotted line) compared to 1-D (solid line) for (a) the 20-$\mu$m-thick CH shell and (b) the 27-$\mu$m-thick CH shell. Note that the addition of mode 200 in the simulation including short wavelengths results in a less-steep fall of the neutron production rate for the 20-$\mu$m implosion and retains burn truncation for the 27-$\mu$m case.

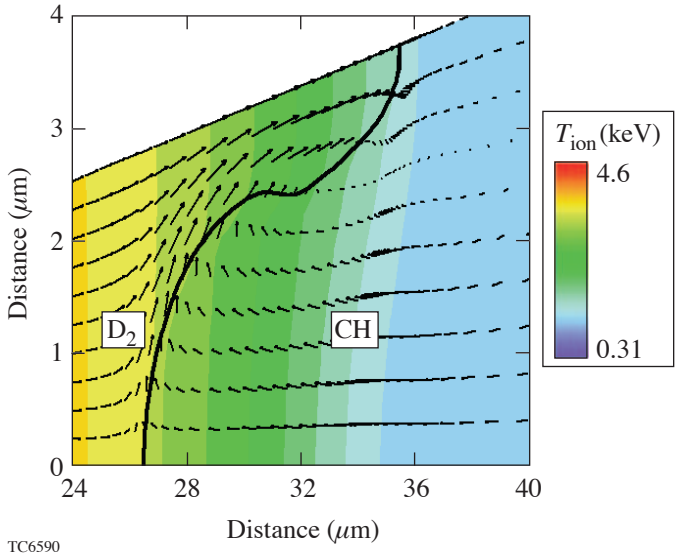


Figure 99.17
Fluid velocity vectors in a frame moving radially with the fluid overlaid on a contour plot of ion temperature at peak neutron production for the 20-$\mu$m-thick CH shell. The simulation, from a single-mode perturbation, illustrates one mechanism for burn truncation. As the velocity vectors indicate, fuel flows into the colder bubbles due to RT growth resulting in burn truncation.

same amplitude as the simulation discussed earlier. The amplitude for mode $\ell = 200$ is chosen by adding in quadrature the power between modes 100 and 300. Contours of mass density for the two shell thicknesses are shown at peak neutron production in Fig. 99.18. The significant shell distortion corresponds to the intermediate mode $\ell = 20$. Even though the growth rate at the $D_2$–CH interface is highly nonlinear for the short wavelength ($\ell = 200$), the bubble amplitude is, at most, 1 $\mu$m. Larger mixing widths (~20 $\mu$m) have been inferred based on spherically symmetric 1-D mix models.[6,8] Since 1-D mix models need to account for the increased volume due to long-wavelength distortions, it is very likely that they overestimate the mixing length. An order of magnitude estimate for the mixing length can be obtained as follows: since a hydrodynamic code such as *DRACO* cannot follow materials into the turbulent regime, we consider the amplitude of the short wavelength as a "mix thickness." The simulated thickness is consistent with expectations from turbulent mixing. The turbulent-mixing layer grows self-similarly with a mixing thickness $h$, given by Ref. 50:

$$h = \alpha A_T g t^2, \tag{11}$$

where $\alpha$ is a dimensionless constant.

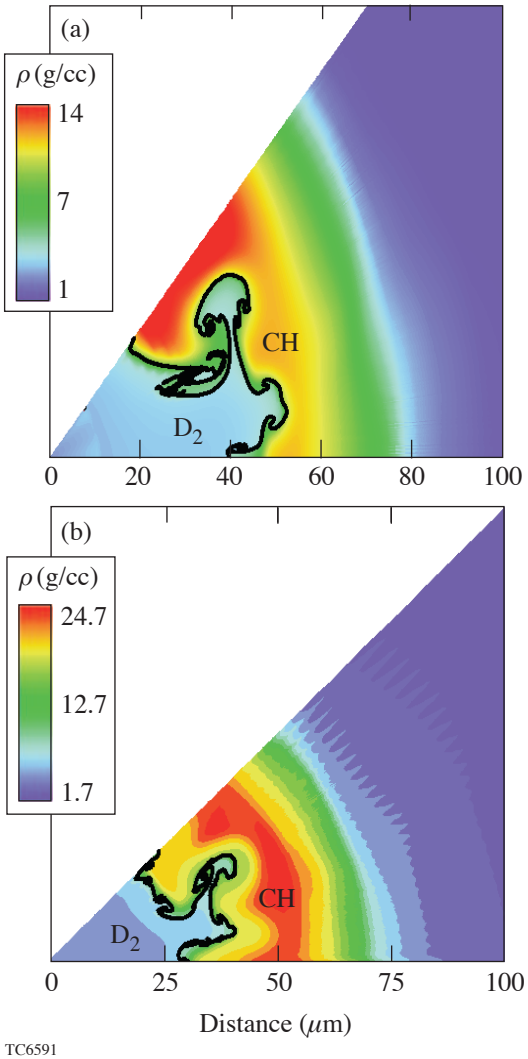


Figure 99.18
Density contours for simulations including short wavelengths at peak neutron production for (a) the 20-$\mu$m-thick CH shell and (b) the 27-$\mu$m-thick CH shell. The solid line is the fuel–shell interface. The short wavelengths ($\ell \sim 200$) have an amplitude of ~1 $\mu$m, consistent with estimates of mixing thicknesses from turbulence observations.[48]

As described in the **Deceleration Phase** section (p. 148), bremsstrahlung cooling increases CH density in the hot spot. Consequently, the Atwood number varies continuously during the deceleration phase, reaching a maximum value of 0.5. The increased density, however, does not significantly alter the perturbation growth rate of short wavelengths due to the stabilizing effects of the density-gradient scale length and thermal conduction. Taking $A_T = 0.18$ for the $D_2$–CH interface gives $\alpha = 0.05$ (Ref. 48), which leads to $h = 0.9$ $\mu$m. This compares favorably with the amplitude of $\ell = 200$ inferred from simulation. In previous work, homogenous mixing of $D_2$ and CH[6–8,49] has been inferred from experimental observables such as secondary neutron ratios,[6,8] argon spectral lines,[7] $D^3He$ yields in $^3$He-filled CD shells,[6,8] etc. Primary neutron yields have not been used directly to determine the presence of turbulence. The relatively small turbulent mixing layer (compared to the overall deformation of the interface due to intermediate mode numbers) suggests that the experimentally inferred turbulence plays a small role in determining primary neutron yields.

The simulations including $\ell = 200$ also indicate an interesting trend in neutron production when compared to the simulations including only low and intermediate modes (Fig. 99.16). For both shell thicknesses, the peak in the neutron-production rate deviates earlier. For the 20-$\mu$m-thick shell, however, neutron production does not decrease as steeply as the previous two-mode simulation. For the 27-$\mu$m-thick shell, the neutron-production history is very similar in width to the two-mode simulation. This difference in trends can be explained as follows: The shell is integral for the 27-$\mu$m-thick shell and the density and temperature distribution compare favorably with 1-D [this is shown in Fig. 99.19(b)]. The solid black line is the

1-D result, whereas the other two lines correspond to radial lineouts from the simulations (dashed–dotted at 36° and dotted at 0°). For the 20-$\mu$m-thick shell, the profiles from the 2-D simulation are significantly different from 1-D [Fig. 99.19(a)]. The peak densities are much lower, and the shell has a wider extent due to the increased adiabat from shell breakup during acceleration. This profile results in delayed stagnation as the shock takes much longer in this case to reach the back of the shell [see the **Deceleration Phase** section (p. 148)]. This delayed shell disassembly results in a persistence of neutron production compared to the simulation including only low and intermediate modes. Figures 99.19(c) and 99.19(d) show the corresponding radial temperature lineouts from the simulation. The lower temperature in the 27-$\mu$m implosion [Fig. 99.19(d)] is caused by shell distortion and increased heat flow from the core. The 20-$\mu$m implosion [Fig. 99.19(c)], in addition, shows lower temperature caused by the decreased compression. The yields relative to 1-D are 21% for the 20-$\mu$m-thick CH shell compared to 47% for the 27-$\mu$m-thick CH shell. Experimentally, the yields relative to 1-D are

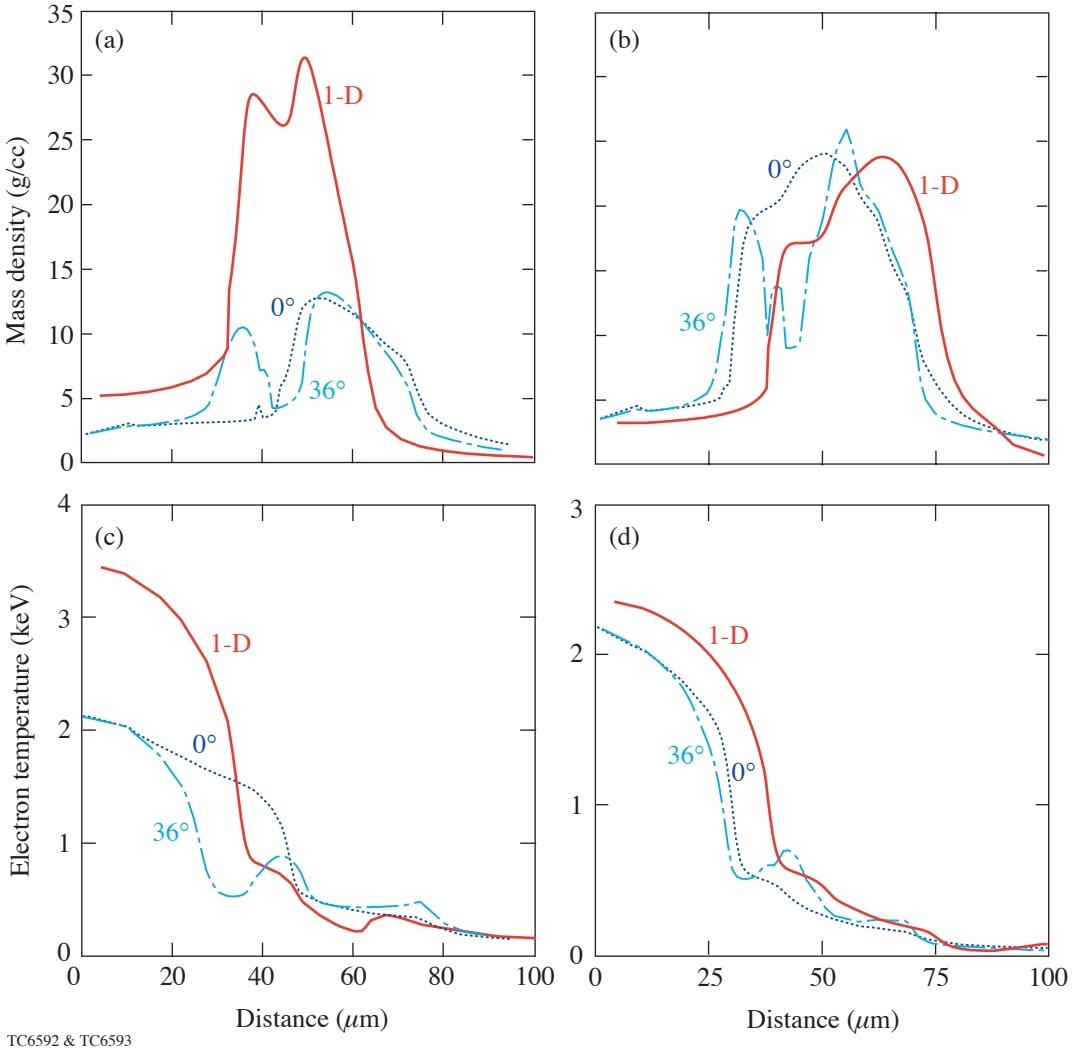


Figure 99.19
Radial lineouts of density from the simulation including short wavelengths for (a) the 20-$\mu$m-thick CH shell and (b) the 27-$\mu$m-thick CH shell at two different polar angles [0° (dotted) and 36° (dashed–dotted)], compared to the 1-D simulation (solid line). Note that the thinner shell has significantly lower densities compared to 1-D. The shell is considerably thicker for the 20-$\mu$m implosion. Radial lineouts of temperature are shown for (c) the 20-$\mu$m implosion and (d) the 27-$\mu$m implosion. All lineouts are at peak neutron production in 1-D. The temperatures in the core are lower than 1-D due to enhanced heat conduction out of the distorted core (both thicknesses) and the overall lower compression in the 20-$\mu$m-thick implosion.

~40% and ~45% for the 20-$\mu$m and 27-$\mu$m thicknesses, respectively. Since mode $\ell$ = 200 has a larger effect on the 20-$\mu$m implosion, the smaller yield relative to 1-D in the simulation for the 20-$\mu$m implosion points to an overestimate of the initial amplitude of $\ell$ = 200 in the simulation.

Similar trends in neutron-production rates are observed in experiments. Figure 99.20 shows the neutron-production rates from experiment (dotted line), and the 1-D simulation (solid line), for the 20-$\mu$m-thick implosion [Fig. 99.18(a)] and the 27-$\mu$m-thick implosion [Fig. 99.18(b)]. Since absolute timing in these experiments was unknown, the 1-D rates are overlaid on the experimental rates by aligning the rise times of the two neutron-rate curves. For the thinner shell, the experimental burnwidth is closer to 1-D, whereas for the thicker, more-stable shell, the burnwidth is truncated compared to 1-D. This trend persists: a still thicker shell (33 $\mu$m) shows increased burn truncation, and even thinner shells (15 $\mu$m) indicate a widening of the neutron-production history. The 2-D simulation of the 20-$\mu$m implosion shows a slower fall of the neutron-production rate compared to the experimentally observed rate. This is likely due to the larger value for the initial amplitude of the $\ell$ = 200 mode in the simulation compared to that in the experiment.

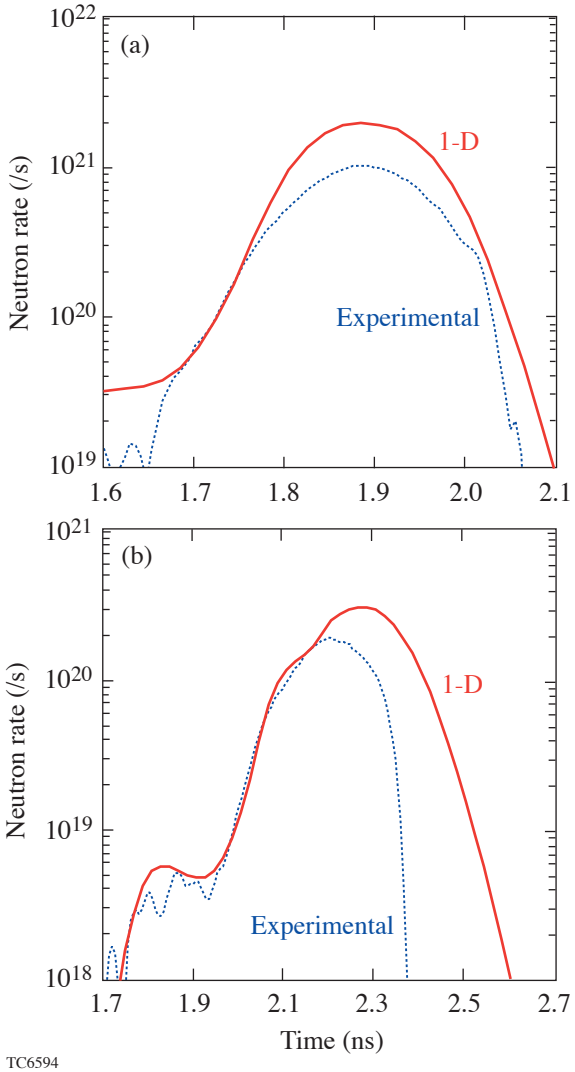


Figure 99.20
Comparison of calculated (1-D) neutron rates (solid line) with experiment (dotted) for (a) the 20-$\mu$m-thick implosion (shot number 30628) and (b) the 27-$\mu$m-thick implosion (shot number 22088). Burn truncation is evident for the 27-$\mu$m-thick implosion. Neutron production rate persists and is almost as wide as 1-D for the 20-$\mu$m-thick implosion.

In summary, the combination of intermediate and low modes significantly influences yields, which manifests itself as burn truncation in the neutron-production rates. The short wavelengths significantly affect shell stability for the thinner shells and can consequently influence stagnation. This in turn widens the burnwidth and also influences yields. For the thicker shells, the burnwidth does not change significantly with the addition of short-wavelength modes. In both cases, the neutron rates deviate earlier from 1-D with the addition of short wavelengths in simulation.

## Conclusions

One-dimensional dynamics of plastic-shell implosions of two different thicknesses irradiated by a smooth laser is discussed. Seeding and evolution of nonuniformities are discussed for the different phases of the implosion. We show that during the acceleration phase, modes up to at least ~400 should contribute to shell stability. Multimode simulations using the code *DRACO* indicate that the shell stability in the implosion of a 20-$\mu$m-thick plastic shell is significantly compromised due to Rayleigh–Taylor instability during the acceleration phase, whereas the 27-$\mu$m-thick shell is only marginally distorted. Long-wavelength multimode simulations indicate that imbalances between the laser beams have a small effect on target yields. Intermediate modes appear to influence yields significantly. Short wavelengths result in qualitatively different behavior between the two shell thicknesses: widening the burnwidth for the thinner shell and marginally influencing burnwidth for the thicker shell. This trend in neutron-production rates is also observed in experiment. Future work will include detailed comparisons of charged-particle spectra with experimental observations, an additional analysis to relate

small-scale mix thicknesses to observations of homogenous mixing in experiments, and the comparison of x-ray images of the compressed core with experiments.

ACKNOWLEDGMENT

This work was supported by the U.S. Department of Energy Office of Inertial Confinement Fusion under Cooperative Agreement No. DE-FC52-92SF19460, the University of Rochester, and the New York State Energy Research and Development Authority. The support of DOE does not constitute an endorsement by DOE of the views expressed in this article. This work has been supported in part by LLE (subcontract PO412163G) with the University of Wisconsin for the implementation of the PetSc Libraries in *DRACO*.

## Appendix A: Seeding of the Long-Wavelength Modes due to Drive Asymmetry

The nonuniformities in laser intensity result in asymmetries in drive pressure $\Delta P$. To relate the ablation pressure and laser-intensity nonuniformities $\Delta I$, we adopt the "cloudy-day" model.[38] Using the scaling $P \sim I^{2/3}$ yields the following relation:

$$\frac{\Delta P}{P} \simeq \frac{2}{3}\frac{\Delta I}{I}e^{-kD_c} \equiv \frac{2}{3}\tilde{I}, \tag{A1}$$

where $D_c$ is the size of the conduction zone (the distance between the ablation front and critical surface) and $k$ is the wave number. For the set of experiments described in this article, the conduction zone grows linearly in time, $D_c = V_c t$ with $V_c \simeq 68$ $\mu$m/ns. Since the laser intensity is spatially modulated, the shocks driven by the peaks in the laser illumination travel faster than the shocks launched at the intensity minimums; therefore, the shock and ablation fronts get distorted. This distortion growth can be estimated for long-wavelength modes using the following simple model: The shock velocity, in the strong-shock limit, is proportional to the square root of the drive pressure $P$:

$$U_s \simeq \sqrt{\frac{\gamma+1}{2}\frac{P}{\rho_0}}, \tag{A2}$$

where $\rho_0$ is the initial (undriven) shell density and $\gamma$ is the ratio of specific heats ($\gamma = 5/3$ for the monoatomic ideal gas). Modulations in the drive pressure distort the shock front according to

$$\frac{d\eta_s}{dt} = \Delta U_s = \frac{dU_s}{dP}\Delta P_s \simeq \frac{2}{\sqrt{5}}c_s\frac{\Delta P}{P}, \tag{A3}$$

where $c_s$ is the sound speed of the shock-compressed shell, $\Delta P_s$ is the pressure modulation at the shock, and $\eta_s$ is the shock-front modulation. We approximate $\Delta P$ in the latter equation with the modulation at the ablation front [Eq. (A1)]. Such an approximation is justified only for the long-wavelength modes when the lateral fluid motion can be neglected. The distortion in the ablation front is caused by the perturbations in the post-shock velocity $U_{\rm ps} = -\rho_0/\rho U_s$, where $U_{\rm ps}$ is calculated in the shock frame of reference. Such perturbations are due to (1) modulations in the shock velocity, $-(\rho_0/\rho)\Delta U_s$; (2) modulations $\Delta\rho$ in the shock-compressed density, $(\rho_0/\rho)(\Delta\rho/\rho)U_s$; and (3) modulations in the position of the shock front. It can be shown that the density modulation right behind the shock is small for strong shocks ($\Delta\rho/\rho \sim M_s^{-2}\,\Delta P/P$, where $M_s$ is the shock Mach number) and can be neglected. The resulting modulation in the post-shock velocity takes the form

$$\Delta U_{\rm ps} \simeq (\rho_0/\rho - 1)\Delta U_s = \frac{3}{4}\Delta U_s. \tag{A4}$$

Since ablative stabilization and lateral flow can be neglected for the long-wavelength modes, $d\eta_a/dt = \Delta U_{\rm ps}$. Integrating the latter equation gives the ablation-front modulation $\eta_a$:

$$\eta_a(t) \simeq \frac{1}{\sqrt{5}}\int_0^t dt'\tilde{I}(t')c_s(t'),\ \eta_s = \frac{4}{3}\eta_a. \tag{A5}$$

It is also important to determine the modulation in the CH–gas interface $\eta_{\rm int}$ at the beginning of the acceleration phase. The modulation at the interface is seeded by the perturbed shock. As soon as the shock breaks out of the shell, the rear surface starts to expand with the velocity $3\,c_s$ (Ref. 51) with respect to the shock-compressed material. Therefore, the amplitude of the CH–gas interface takes the value $\eta_{\rm int} = 3\,c_s\delta t$, where $\delta t = \eta_s/U_s$ is the shock transit time across the modulation amplitude. Using the strong shock limit, one obtains $\eta_{\rm int} 3\sqrt{5}\,\eta_s/4$. Taking into account the relation between $\eta_s$ and $\eta_a$ yields $\eta_{\rm int} = \sqrt{5}\eta_a$. As shown in Ref. 52, the gas–CH interface is unstable during the rarefaction-wave (RW) propagation through the shell. Since such a growth is linear in time and proportional to the modulation wave number, there is very little change in the amplitude of the fuel–pusher interface between the shock breakout and the beginning of the acceleration phase. To determine the mode amplitudes at the beginning of the acceleration phase, we integrate Eq. (A5) using the laser nonuniformity profiles shown in Fig. 99.3. The spectrum thus obtained is plotted in Fig. 99.4 and compared against the results of the full 2-D power-balance simulation. Observe that the simple model reproduces the results of simulations very well. To calculate the initial conditions for the RT growth, in addition to the initial

amplitude, we must calculate the perturbed front velocity $\eta_a'$. This velocity has two components: the first is given by Eqs. (A3) and (A4), and the second is due to the rippled RW breakout at the ablation front. Indeed, when the first shock reaches the rear surface, the RW is launched toward the ablation front. The RW travels with the local sound speed $c_s$; therefore, if the shock amplitude is $\eta_s$, the rarefaction amplitude then becomes $\eta_{\mathrm{RW}} = c_s\left(\eta_s/U_s\right) = \sqrt{5}\eta_s/4$. The phase of the modulation in the rarefaction head is opposite to the phases of the rear-surface and ablation-front perturbations. Upon reaching the ablation front, the leading edge of the RW establishes the pressure gradient, accelerating the front. Since the peaks of the RW break out at the ablation front prior to the valleys, the ablation-front ripple gains an additional velocity perturbation $\delta v = g\delta t$, where $g$ is the acceleration and $\delta t = \eta_{\mathrm{RW}}/c_s = \sqrt{5}/3\left(\eta_a/c_s\right)$. Combining the two contributions, the initial ripple velocity takes the form

$$\frac{d\eta_a}{dt}\left(t_0\right) = \tilde{I}\left(t_0\right)\frac{c_s}{\sqrt{5}} + \frac{\sqrt{5}g}{3c_s}\eta_a\left(t_0\right), \tag{A6}$$

where $t_0$ is the time at the beginning of acceleration phase. Equations (A5) and (A6) show that the ablation-front amplitude changes slope at $t = t_0$. Substituting $g = c_s^2/\left(\gamma\Delta_{\mathrm{sh}}\right)$ into Eq. (A6) and also approximating $\eta_a\left(t_0\right) \sim \langle\tilde{I}\rangle_{\mathrm{sh}}\left(c_s/U_{\mathrm{sh}}\right)4\Delta_{\mathrm{sh}}$, we can rewrite Eq. (A6) as

$$\eta_a'\left(t_0\right) \sim \tilde{I}\left(t_0\right)\frac{c_s}{\sqrt{5}} + \left\langle\tilde{I}\right\rangle_{\mathrm{sh}}\frac{c_s}{\sqrt{5}}. \tag{A7}$$

The second term on the right-hand side of Eq. (A7) is proportional to the laser nonuniformity averaged over the shock transit time, $\langle\tilde{I}\rangle_{\mathrm{sh}}$. Taking into account that beam mistiming significantly increases $\tilde{I}$ at the beginning of the pulse (during the pulse rise), $\langle\tilde{I}\rangle_{\mathrm{sh}}$ becomes much larger than $\tilde{I}\left(t_0\right)$ (in most cases by a factor of 5). This conclusion is valid for a large variety of target designs, including the ignition design, since the laser reaches its peak intensity prior to the acceleration phase. One must keep in mind, however, that Eq. (A6) assumes sharp interfaces of the CH–gas boundary and the ablation front. In reality the radiation preheat relaxes the density at the CH–gas interface prior to the first shock breakout. In addition, the ablation front has a finite thickness. These effects cause deviations of the initial condition from simple estimates [Eqs. (A5) and (A7)]. Comparison with the results of 2-D simulations, however, shows that finite interface thickness effects do not significantly modify the perturbation amplitudes (Fig. 99.4).

## Appendix B: Growth of Long-Wavelength Modes During the Acceleration Phase

The equation describing the perturbation growth for the long-wavelength modes (ablation effects are neglected) during the acceleration phase can be written as[32]

$$\frac{d}{dt}\left(\frac{1}{\rho r}\frac{d}{dt}\rho r^2\eta\right) - \ell g\eta = \ell\frac{\Delta P}{\rho} = \ell\frac{2}{3}\frac{\delta I}{I}\left(\frac{r}{r_c}\right)^{\ell} g\Delta_{\mathrm{sh}}, \tag{B1}$$

where $\Delta P$ is the drive-pressure nonuniformity, $r$ is the shell radius, $g$ is the shell acceleration, $\rho$ is the shell density, $\Delta_{\mathrm{sh}}$ is the shell thickness, $r_c$ is the position of the average laser-deposition surface, and $\eta$ is the ablation-front modulation amplitude. The factor $\left(r/r_c\right)^{\ell}$ is due to the cloudy-day effect. Equation (B1) is subject to the initial conditions (A5) and (A6). The shell thickness is $\Delta_{\mathrm{sh}}$ = 5 $\mu$m for the 20-$\mu$m shell and $\Delta_{\mathrm{sh}}$ = 6.8 $\mu$m for the 27-$\mu$m shell. During this phase of the implosion, the shell density remains approximately constant, so we can cancel $\rho$ in Eq. (B1). For simplicity we assume constant shell acceleration $r = r_0 - gt^2/2$. To compare a relative importance of the RT growth versus the secular growth during the shell acceleration, we compare $\ell g\eta$ with the right-hand side of Eq. (B1). The lower limit of this term is

$$\min\left(\ell g\eta\right) = \ell g\eta\left(t_0\right) \simeq \ell g\left\langle\tilde{I}\right\rangle_{\mathrm{sh}}\frac{\Delta_0}{\sqrt{5}}\frac{c_s}{U_{\mathrm{sh}}} = \ell g\Delta_{\mathrm{sh}}\left\langle\tilde{I}\right\rangle_{\mathrm{sh}}, \tag{B2}$$

where $\Delta_{\mathrm{sh}}$ is the in-flight shell thickness (which is approximately four times smaller than the initial thickness $\Delta_0$) and $\langle\tilde{I}\rangle_{\mathrm{sh}}$ is the intensity modulation averaged over the shock-propagation time. Comparing the latter expression with the right-hand side of Eq. (B1), we observe that $\Delta P/\rho << g\eta$ during the acceleration phase. The latter inequality is satisfied for very long wavelengths ($\ell$ < 10) because $\langle\tilde{I}\rangle I_{\mathrm{sh}} >> \tilde{I}\left(t_0\right)$ due to beam mistiming early in the pulse. Shorter wavelengths ($\ell$ > 10), on the other hand, experience a large attenuation due to thermal smoothing in the conduction zone; therefore, the right-hand side of Eq. (B1) is also small for such mode. Thus, we can conclude that the secular growth during the acceleration phase is much smaller than the RT amplification of the initial amplitude and velocity of the ablation-front modulation. This growth can be estimated using the WKB solution of the homogeneous part of Eq. (B1) with the following initial conditions:

$$\eta_0 = \left\langle\tilde{I}\right\rangle_{\mathrm{sh}}\Delta_{\mathrm{sh}}, \quad \eta_0' = \frac{c_s}{\sqrt{5}}\left[\tilde{I}\left(t_0\right) + \left\langle\tilde{I}\right\rangle_{\mathrm{sh}}\right]. \tag{B3}$$

Using results of Ref. 31, the solution takes the form

$$\eta_a = C_r^{5/4}\left[\eta_0 \cosh\Psi + \eta_0' \sqrt{\frac{r_0}{(\ell+2)g}} \sinh\Psi\right], \qquad \text{(B4)}$$

where $\Psi = \sqrt{2(\ell+2)}\arcsin\sqrt{1-C_r^{-1}}$ and $C_r$ is the convergence ratio during the acceleration phase. During the acceleration phase, the convergence ratio of the 20-$\mu$m shell and the 27-$\mu$m shell is $C_r = r_0/r \simeq 1.7$ and $C_r \simeq 1.4$, respectively, where $r_0 = 430\ \mu$m is the ablation-front radius at the beginning of the shell acceleration. The dominant role of the RT growth over the secular growth is confirmed by the results of *DRACO* simulation. Figure 99.8 shows a plot of the perturbation amplitude with full power imbalance (dashed–dotted line) and with the power imbalance turned off (solid line) during the acceleration phase.

## REFERENCES


1. J. Nuckolls *et al*., Nature **239**, 139 (1972).
2. C. P. Verdon, Bull. Am. Phys. Soc. **38**, 2010 (1993).
3. M. D. Campbell and W. J. Hogan, Plasma Phys. Control. Fusion **41**, B39 (1999).
4. T. R. Boehly, D. L. Brown, R. S. Craxton, R. L. Keck, J. P. Knauer, J. H. Kelly, T. J. Kessler, S. A. Kumpan, S. J. Loucks, S. A. Letzring, F. J. Marshall, R. L. McCrory, S. F. B. Morse, W. Seka, J. M. Soures, and C. P. Verdon, Opt. Commun. **133**, 495 (1997).
5. D. D. Meyerhofer, J. A. Delettrez, R. Epstein, V. Yu. Glebov, V. N. Goncharov, R. L. Keck, R. L. McCrory, P. W. McKenty, F. J. Marshall, P. B. Radha, S. P. Regan, S. Roberts, W. Seka, S. Skupsky, V. A. Smalyuk, C. Sorce, C. Stoeckl, J. M. Soures, R. P. J. Town, B. Yaakobi, J. D. Zuegel, J. Frenje, C. K. Li, R. D. Petrasso, D. G. Hicks, F. H. Séguin, K. Fletcher, S. Padalino, M. R. Freeman, N. Izumi, R. Lerche, T. W. Phillips, and T. C. Sangster, Phys. Plasmas **8**, 2251 (2001).
6. P. B. Radha, J. Delettrez, R. Epstein, V. Yu. Glebov, R. Keck, R. L. McCrory, P. McKenty, D. D. Meyerhofer, F. Marshall, S. P. Regan, S. Roberts, T. C. Sangster, W. Seka, S. Skupsky, V. Smalyuk, C. Sorce, C. Stoeckl, J. Soures, R. P. J. Town, B. Yaakobi, J. Frenje, C. K. Li, R. Petrasso, F. Séguin, K. Fletcher, S. Padalino, C. Freeman, N. Izumi, R. Lerche, and T. W. Phillips, Phys. Plasmas **9**, 2208 (2002).
7. S. P. Regan, J. A. Delettrez, F. J. Marshall, J. M. Soures, V. A. Smalyuk, B. Yaakobi, V. Yu. Glebov, P. A. Jaanimagi, D. D. Meyerhofer, P. B. Radha, W. Seka, S. Skupsky, C. Stoeckl, R. P. J. Town, D. A. Haynes, Jr., I. E. Golovkin, C. F. Hooper, Jr., J. A. Frenje, C. K. Li, R. D. Petrasso, and F. H. Séguin, Phys. Rev. Lett. **89**, 085003 (2002).
8. C. K. Li, D. G. Hicks, F. H. Séguin, J. Frenje, R. D. Petrasso, J. M. Soures, P. B. Radha, V. Yu. Glebov, C. Stoeckl, J. P. Knauer, F. J. Marshall, D. D. Meyerhofer, S. Skupsky, S. Roberts, C. Sorce, T. C. Sangster, T. W. Phillips, and M. D. Cable, Rev. Sci. Instrum. **72**, 864 (2001).
9. D. Keller, T. J. B. Collins, J. A. Delettrez, P. W. McKenty, P. B. Radha, B. Whitney, and G. A. Moses, Bull. Am. Phys. Soc. **44**, 37 (1999).
10. Lord Rayleigh, Proc. London Math Soc. **XIV**, 170 (1883); G. Taylor, Proc. R. Soc. London Ser. A **201**, 192 (1950).
11. S. E. Bodner, Phys. Rev. Lett. **33**, 761 (1974).
12. H. Takabe *et al*., Phys. Fluids **28**, 3676 (1985).
13. R. Betti, V. N. Goncharov, R. L. McCrory, P. Sorotokin, and C. P. Verdon, Phys. Plasmas **3**, 2122 (1996).
14. G. I. Bell, Los Alamos National Laboratory, Los Alamos, NM, Report LA-1321 (1951).
15. M. S. Plesset, J. Appl. Phys. **25**, 96 (1954); D. L. Book and S. E. Bodner, Phys. Fluids **30**, 367 (1987); Laboratory for Laser Energetics LLE Review **94**, 81, NTIS document No. DOE/SF/19460-485 (2003). Copies of the last item may be obtained from the National Technical Information Service, Springfield, VA 22161.
16. M. C. Richardson, G. G. Gregory, R. L. Keck, S. A. Letzring, R. S. Marjoribanks, F. J. Marshall, G. Pien, J. S. Wark, B. Yaakobi, P. D. Goldstone, A. Hauer, G. S. Stradling, F. Ameduri, B. L. Henke, and P. Jaanimagi, in *Laser Interaction and Related Plasma Phenomena*, edited by H. Hora and G. H. Miley (Plenum Press, New York, 1986), Vol. 7, pp. 179–211.
17. A. A. Amsden, H. M. Ruppel, and C. W. Hirt, Los Alamos National Laboratory, Los Alamos, NM, Report LA-8095 (1980).
18. M. L. Wilkins, J. Comput. Phys. **36**, 281 (1980).
19. G. Maenchen and S. Sack, in *Methods in Computational Physics*, edited by B. Alder, S. Fernbach, and M. Rotenberg, Fundamental Methods in Hydrodynamics (Academic Press, New York, 1964), Vol. 3, pp. 181–210.
20. A. M. Winslow, J. Comput. Phys. **2**, 149 (1967); S. Atzeni and A. Guerrieri, Laser Part. Beams **9**, 443 (1991); J. U. Brackbill and J. S. Saltzman, J. Comput. Phys. **46**, 342 (1982).
21. B. van Leer, J. Comput. Phys. **23**, 276 (1977).
22. D. L. Youngs, in *Numerical Methods for Fluid Dynamics*, edited by K. W. Morton and M. J. Baines (Academic Press, London, 1982), pp. 273–285.
23. D. J. Benson, Comput. Methods Appl. Mech. Eng. (Netherlands) **99**, 235 (1992).
24. S. P. Lyon and J. D. Johnson, Los Alamos National Laboratory, Los Alamos, NM, Report LA-UR-92-3407 (1992).
25. A. R. Bell, Rutherford Appleton Laboratory, Chilton, Didcot, Oxon, England, Report RL-80-091 (1980).
26. R. M. More, K. H. Warren, D. A. Young, and G. B. Zimmerman, Phys. Fluids **31**, 3059 (1988).
27. W. F. Huebner *et al*., Los Alamos National Laboratory, Los Alamos, NM, Report LA-6760-M (1977).

28. S. Balay *et al.*, in *Modern Software Tools for Scientific Computing*, edited by E. Arge, A. M. Bruaset, and H. P. Langtangen (Birkhäuser, Boston, 1997), Chap. 8, pp. 163–202.

29. MPI Version 1.2 Standard for IRIX—A Communication Language for Parallel Processing (2001).

30. L. M. Hively, Nucl. Fusion **17**, 873 (1977).

31. R. L. McCrory and C. P. Verdon, in *Inertial Confinement Fusion*, edited by A. Caruso and E. Sindoni (Editrice Compositori, Bologna, Italy, 1989), pp. 83–124.

32. V. N. Goncharov, P. McKenty, S. Skupsky, R. Betti, R. L. McCrory, and C. Cherfils-Clérouin, Phys. Plasmas **7**, 5118 (2000).

33. S. Skupsky, R. W. Short, T. Kessler, R. S. Craxton, S. Letzring, and J. M. Soures, J. Appl. Phys. **66**, 3456 (1989).

34. T. R. Boehly, V. A. Smalyuk, D. D. Meyerhofer, J. P. Knauer, D. K. Bradley, R. S. Craxton, M. J. Guardalben, S. Skupsky, and T. J. Kessler, J. Appl. Phys. **85**, 3444 (1999).

35. R. D. Richtmyer, Commun. Pure. Appl. Math. **XIII**, 297 (1960); V. A. Andronov *et al.*, Sov. Phys.-JETP **44**, 424 (1976).

36. V. N. Goncharov, Phys. Rev. Lett. **82**, 2091 (1999).

37. F. J. Marshall, J. A. Delettrez, R. Epstein, R. Forties, R. L. Keck, J. H. Kelly, P. W. McKenty, S. P. Regan, and L. J. Waxer, Phys. Plasmas **11**, 251 (2004).

38. S. E. Bodner, J. Fusion Energy **1**, 221 (1981).

39. V. N. Goncharov, S. Skupsky, T. R. Boehly, J. P. Knauer, P. McKenty, V. A. Smalyuk, R. P. J. Town, O. V. Gotchev, R. Betti, and D. D. Meyerhofer, Phys. Plasmas **7**, 2062 (2000).

40. C. B. Burckhardt, Appl. Opt. **9**, 695 (1970).

41. Y. Kato *et al.*, Phys. Rev. Lett. **53**, 1057 (1984).

42. Laboratory for Laser Energetics LLE Review **65**, 1, NTIS document No. DOE/SF/19460-117 (1995). Copies may be obtained from the National Technical Information Service, Springfield, VA 22161.

43. R. Epstein, J. Appl. Phys. **82**, 2123 (1997).

44. S. P. Regan, J. A. Marozas, J. H. Kelly, T. R. Boehly, W. R. Donaldson, P. A. Jaanimagi, R. L. Keck, T. J. Kessler, D. D. Meyerhofer, W. Seka, S. Skupsky, and V. A. Smalyuk, J. Opt. Soc. Am. B **17**, 1483 (2000).

45. R. C. Cook, R. L. McEachern, and R. B. Stephens, Fusion Technol. **35**, 224 (1999).

46. R. Betti, V. N. Goncharov, R. L. McCrory, and C. P. Verdon, Phys. Plasmas **5**, 1446 (1998).

47. J. P. Knauer, R. Betti, D. K. Bradley, T. R. Boehly, T. J. B. Collins, V. N. Goncharov, P. W. McKenty, D. D. Meyerhofer, V. A. Smalyuk, C. P. Verdon, S. G. Glendinning, D. H. Kalantar, and R. G. Watt, Phys. Plasmas **7**, 338 (2000).

48. R. Betti, K. Anderson, V. N. Goncharov, R. L. McCrory, D. D. Meyerhofer, S. Skupsky, and R. P. J. Town, Phys. Plasmas **9**, 2277 (2002).

49. D. C. Wilson, C. W. Cranfill, C. Christensen, R. A. Forster, R. R. Peterson, H. M. Hoffman, G. D. Pollak, C. K. Li, F. H. Séguin, J. A. Frenje, R. D. Petrasso, P. W. McKenty, F. J. Marshall, V. Yu. Glebov, C. Stoeckl, G. J. Schmid, N. Izumi, and P. Amendt, Phys. Plasmas **11**, 2723 (2004).

50. G. Dimonte, Phys. Plasmas **6**, 2009 (1999).

51. L. D. Landau and E. M. Lifshitz, *Fluid Mechanics*, 2nd ed., Course of Theoretical Physics, Vol. 6 (Butterworth-Heinemann, Newton, MA, 1987), p. 36.

52. J. G. Wouchuk and R. Carretero, Phys. Plasmas **10**, 4237 (2003).

# Formation of Deuterium-Ice Layers in OMEGA Targets

When the OMEGA Cryogenic Target Handling System (CTHS) became operational in July 2000, it was the culmination of a seven-year engineering effort to build the infrastructure needed to produce cryogenic inertial confinement fusion (ICF) targets. These targets are used for implosion experiments that are a one-third scale of the experiments to be performed on the National Ignition Facility (NIF). These experiments allow issues that affect the quality of the implosion, such as the hydrodynamic stability and laser imprint, to be correlated to the laser performance and target specifications.

This article discusses the process of forming a cryogenic target—specifically, how to make a 0.9-mm-diam shell of deuterium ice constrained in a thin-walled plastic shell. The process differs from that developed for earlier cryogenic systems in many aspects: (1) there is sufficient deuterium mass to form thick-walled (100-$\mu$m) shells; (2) the deuterium is permeated into the plastic shell, eliminating the need for a filling tube, which can perturb the thermal environment and influences the process; (3) the system possesses all of the engineering features needed to deliver a target for implosion, so the effect of those features are included in the process demonstrated to make cryogenic targets; and (4) the CTHS system can also produce cryogenic NIF-sized targets, which will allow the cryogenic processes to be demonstrated on full-sized ignition targets, even if the targets are too massive to be imploded on OMEGA in meaningful experiments. Schematics of OMEGA- and NIF-scale, direct-drive cryogenic targets are shown in Fig. 99.21. The OMEGA cryogenic target is a 0.9-mm-diam plastic shell with a 3-$\mu$m wall that is diffusion filled to a maximum pressure of 1500 atm. This gas density equates to a solid-deuterium wall thickness of up to 130 $\mu$m—one-third scale of a NIF direct-drive-ignition target.

## Overview of the Process Used to Make Cryogenic Targets

The process of transforming a plastic shell containing liquid deuterium into a cryogenic ICF target where a uniformly thick wall of deuterium ice adjoins the inner plastic wall is referred to as "layering."

Initially, an empty plastic shell is at vacuum and room temperature inside a pressure vessel. A hydrogen-isotope gas (deuterium presently and a deuterium–tritium mixture in the future) is added to the vessel until the pressure is approximately 1000 atm (depending on the desired ice thickness and shell dimensions). For any pressure ramp lower than the ratio of the shell's buckle pressure to the permeation rate (typically 1 atm per minute), the hydrogen gas will diffuse through the plastic without buckling the shell. Once the plastic shell

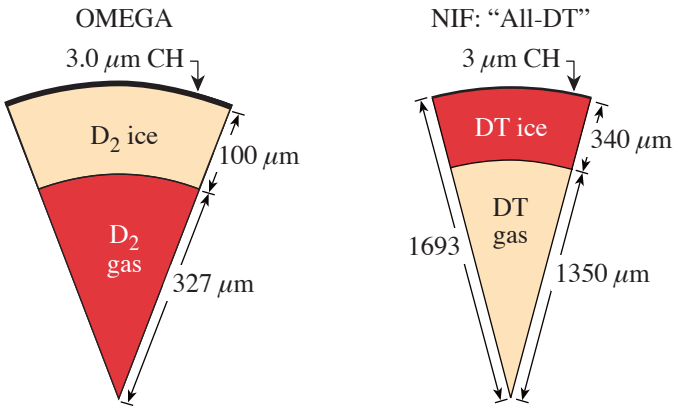


Figure 99.21
Schematic showing the dimensions of direct-drive targets for use on OMEGA and the NIF.

contains sufficiently dense hydrogen gas (~0.1 g/cm$^3$), it is gradually cooled: the liquid phase first appears at the critical point (38 K) and the solid forms at the triple point (18.72 K). At 18.72 K the hydrogen fuel is a solid "lump" with a vapor pressure of less than 200 Torr. The plastic shell is removed from the pressure vessel and transferred, inside a cryostat, to the mobile cryostat that transports the target to the OMEGA target chamber. The latter cryostat has two critical components: (a) a 2.5-cm-inner-diam isothermal copper shell that is placed around the target and (b) the "life-support" equipment required to sustain the target at all times.

When the target is centered inside the isothermal copper shell (called the *layering sphere*), it is bathed in infrared light at a wavelength that is absorbed by the deuterium. The combination of volumetric heating from the IR light and the isothermal boundary at the layering sphere creates a temperature gradient within the deuterium: the deuterium is warmest where it is thickest and closest to the center of the sphere. In minimizing this temperature gradient, the ice/liquid redistributes itself on the inside surface of the plastic shell. Eventually the ice forms a contiguous shell wall with an isothermal inner surface. The goal is a uniform-thickness deuterium-ice wall with a root-mean-square (rms) thickness variation of less than 1 $\mu$m.

The metric for the ice-layer quality is the roughness of the inner surface, which is equated to the ice-wall-thickness uniformity; however, the suitability of this value as a proxy for ice-thickness uniformity depends on the sphericity of the outer deuterium wall and, hence, the plastic shell, which defines the geometry. Typically, a plastic shell possesses an eccentricity of 0.1 $\mu$m to 0.5 $\mu$m and the wall thickness varies by <0.2 $\mu$m—values that can affect the ice-thickness uniformity and cause the ice roughness and thickness uniformity to differ. For a uniformly thick plastic shell with an isothermal outer surface, the ice shell will be uniformly thick if the radial thermal conductance is constant around the target. Under these optimal circumstances, any roughness on the inner surface of the ice will be due to the crystalline structure of the ice. In practice, such higher-spatial-frequency roughness is overwhelmed by low-mode roughness caused by imperfections in the target and asymmetries in the layering sphere.

Four years' experience in producing cryogenic targets identifies the elimination of the low-mode ice roughness as the major challenge to producing high-quality implosion targets. The highest-quality ice layers have an rms roughness of 1.2 $\mu$m, averaged over the entire surface (see Fig. 99.22). More typically, the roughness averages 3 $\mu$m to 6 $\mu$m, although values as great as 8 $\mu$m to 10 $\mu$m also occur. This article analyzes potential causes for the low-mode roughness and provides experimental data quantifying the effect of the perturbations on the roughness magnitude. Thermal and ray-tracing models make explicit how sensitive the ice roughness is to its environment. This allows a better understanding of the required level of control from the cryogenic equipment and provides better direction for improving the equipment.

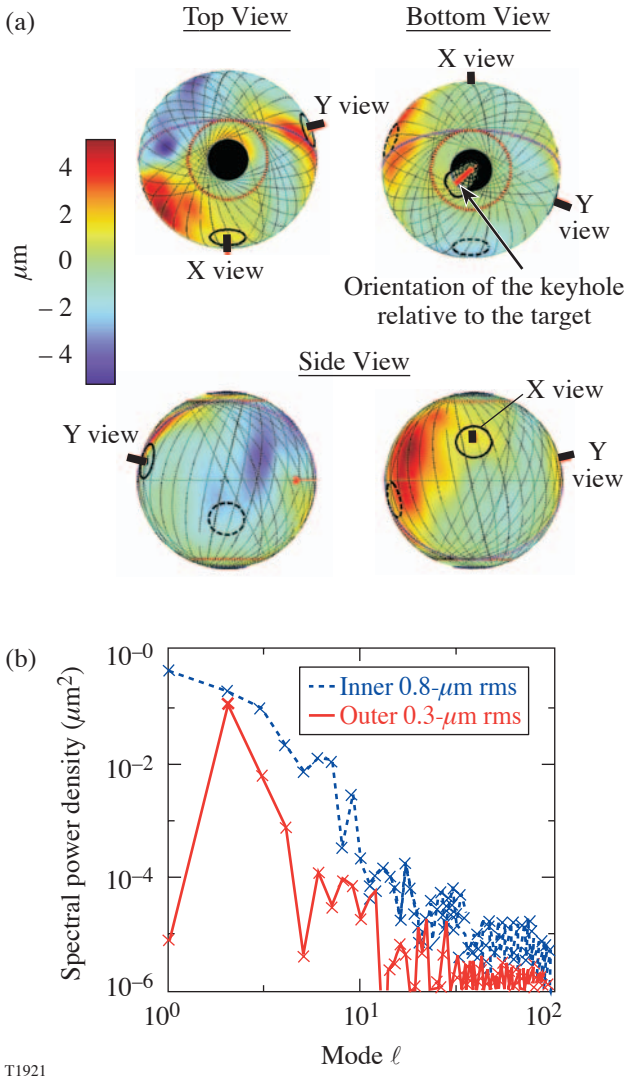


Figure 99.22
(a) Four views of the surface of an 80-$\mu$m-thick, 880-$\mu$m-diam spherical ice layer. The shading shows the variation in thickness of the ice. The 3-D profile is compiled from 50 2-D views. (b) Two-dimensional power spectra of the inner ice surface and the outer plastic surface.

## Introduction

The concept of layering was first demonstrated by radioactively inducing sublimation in solid tritium.[1] Subsequent work at Los Alamos National Laboratory (LANL) and Lawrence Livermore National Laboratory (LLNL) expanded the science and better quantified the process. This work relied on heat generated by the decay of a triton atom yielding a $^3$He nucleus, a beta electron, and an antineutrino with 18.6 keV of energy collectively. The average $\beta$ energy is 6 keV and equates to a volumetric heating rate of 51 kW/m$^3$ (0.977 W/mol, hereafter referenced as 1 $Q_{DT}$). Subsequent work at LLNL demonstrated that volumetric heating could also be achieved by radiatively heating the hydrogen-isotope ice using infrared illumination.[2] This method made it possible to "layer" nontritium hydrogen isotopes and is used to make the deuterium-ice layers studied and reported here.

An important difference between work reported here and earlier layering work is the geometry of the layering environment and the absence of a fill tube; earlier studies used geometries such as hemispheres, cylinders, and other surrogate geometries. These compromises simplified both filling the targets (a diffusion-filling capability is both complex and expensive) and diagnosing the layering process. However, the fill tube affected the thermal environment around the target, which affects the layering process itself. A protocol for a fill-tube-free layering method, and the resulting layer quality, is presented in the remaining sections, which (1) deal with the principles of the layering process, (2) examine the methodology of experimentally measuring the success of layering, (3) discuss how various parameters affect the layering process, and (4) present a summary and discussion.

## Layering Process

Experimentally, the process used to form a layer is straightforward: The target is centered in a 2.5-cm-diam, temperature-controlled, hollow sphere—the layering sphere (Fig. 99.23). The sphere contains helium gas to conduct the heat away from the target. The internal surface of the sphere is purposely roughened to form an "integrating sphere," which allows the target to be uniformly irradiated with infrared light at 3.16 $\mu$m, a frequency that corresponds to the strongest absorption band in the deuterium-ice [the $Q_1(1) + S_0(0)$ and $Q_1(0) + S_0(0)$ bands] molecular crystal,[3] in which each crystal-lattice site is occupied by one $D_2$ molecule.

There are two procedures for layering targets: One process starts with the target below the triple point (18.72 K) and a frozen lump of deuterium in the bottom of the target. Deuterium absorbs the IR light and becomes warmer than the plastic shell's outer surface. Solid deuterium sublimes from where it is thickest (and therefore hottest because of volumetric heating) and condenses where it is thinnest. In theory, the ice wall will become uniformly thick. In practice, there is an ~10- to 20-$\mu$m peak-to-valley variation in ice thickness formed by this method.

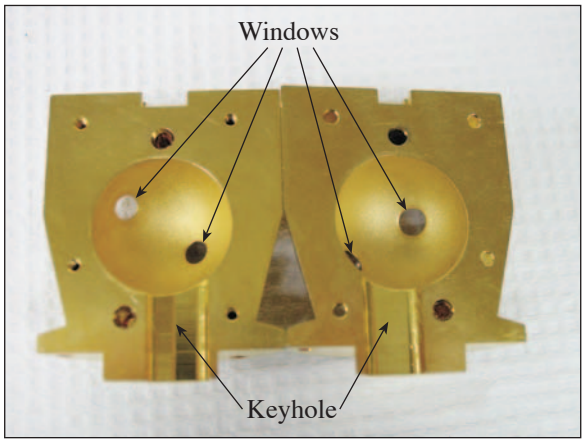


T1933

Figure 99.23
The two hemispheres that comprise the layering sphere are shown side by side. The "keyhole" opening at the base of the layering sphere is where the target is inserted and removed.

A second, more-successful method for forming a smooth ice layer starts with the deuterium in the liquid phase and then gradually cools the target through the triple point. The initial thermal environment *inside* the target is shown in Fig. 99.24. The temperature gradient along the interface between the gas and the liquid is determined by the helium gas pressure outside the target and the heat coupled into the deuterium. Properly executed, this process forms a single crystal within the melt that is first observed near the target's equator and then propagates azimuthally and vertically within the shell.

Figure 99.25 shows the same target produced using both methods. It demonstrates the importance of controlling the solidification rate: all parameters other than the temperature difference between the layering sphere and target, which controls the heat flux from the target (and hence the solidification rate), were kept constant; the same target was maintained in the identical position and orientation in the layering sphere, and the same volumetric heating rate was used. The smoother ice layer (2.5-$\mu$m rms) was produced at a temperature ~0.1 K

below the triple point; the second, rougher ice layer (4.3-$\mu$m rms) was produced at a temperature ~0.2 K below the triple point, in a faster solidification process. This difference in roughness can be attributed only to the intrinsic properties of the ice (the crystallographic structure and how well it attaches to the inner plastic wall). Both images show features that can be eliminated by carrying out the process still closer to the triple point (within 5 to 10 mK).

Ultimately, if the outer surface of the plastic capsule is isothermal, the ice will possess equivalent thickness everywhere if all of the following conditions are identical throughout the capsule: (1) heat conductance through the ice; (2) heat resistance at the ice/plastic interface; (3) heat conductance through the plastic; and (4) volumetric heating into the ice (and plastic). In the above comparison, the importance of the solidification rate on the resulting ice smoothness was demonstrated because only conditions (1) and (2) could vary. The effect of items (3) and (4) remained invariant because the plastic shell and its position in the layering sphere were the same.

One final consideration is to determine how precisely the solidification process must be controlled to achieve a "perfectly" uniform thick layer. The stochastic nature of the freezing process will always cause some variability to the layer quality, and this contribution to the overall roughness will become more important as extraneous, equipment-related perturbations to the ice are eliminated (examples include nonuniform heating or the position of the target in the layering sphere).

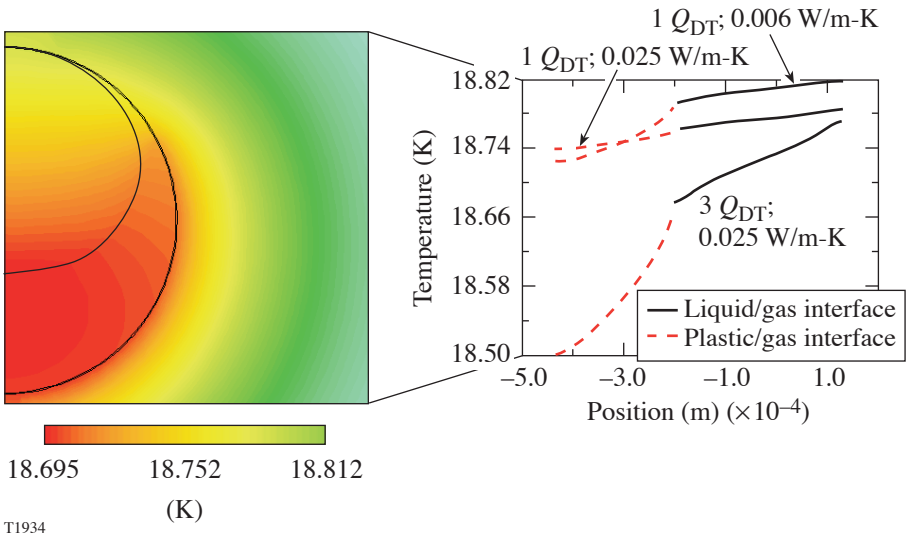


Figure 99.24
Temperature distribution inside a liquid-$D_2$–containing OMEGA target. Three different volumetric heat loads (1 and 3 $Q_{DT}$) and two different helium exchange gas pressures, which yield different thermal conductivities, are plotted.

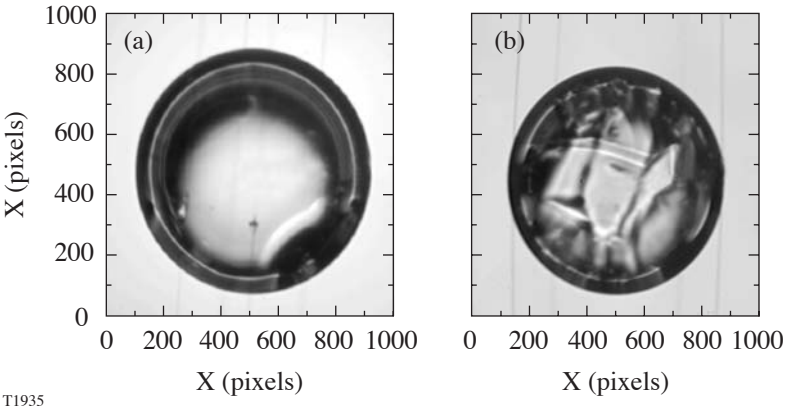


Figure 99.25
Image of the same target with two different ice layers. The first layer (a) is formed gradually at a temperature that is close to the triple-point temperature (within 0.1 K). The second layer (b) occurs when liquid is frozen instantaneously at a temperature and then allowed to layer.

**Characterizing the Ice Layer**

1. Experimental Configuration

The optical system used to measure the ice-layer roughness is shown in Fig. 99.26. The layering sphere has two pairs of opposing windows oriented along axes corresponding to the viewing axes in the OMEGA target chamber. The windows corresponding to the X- and Y-axis cameras are positioned 26.6° and 12° above and below the equator, respectively, and 110° apart.

The light-emitting diodes that back-illuminate the target are opposite the cameras. The diodes operate at 1 Hz and 0.15 A with a 30-ms to 300-ms exposure. The emission wavelength is 612 nm, i.e., in a spectral region where the deuterium (or tritium) ice does not absorb but where the plastic shell has broadband absorption of 5% to 10%. These exposure conditions permit a target image to be acquired in a sufficiently short period that vibration-induced blurring is minimized. Also, the brief exposure duration minimizes the heat load to the target. Based on measurements, and supported by calculations, the heat load to the target is <10 nW. Operating the diodes at a higher duty cycle and current can produce heat loads (in the plastic shell) that approach 0.1 $\mu$W, a value that is a significant fraction of the 10 $\mu$W to 30 $\mu$W deposited in an OMEGA target by IR radiation during layering. The effect of higher diode-radiation loads on a target is shown in Fig. 99.27. Here, in an extreme example, the diode is seen to deplete the 100-$\mu$m ice layer along the illumination axis. That such a drastic effect is induced at high illumination intensities underscores the need for minimizing any nonuniform heat load to the target, including loads from all optical systems associated with positioning the target in the target chamber as well as from the target existence detector.

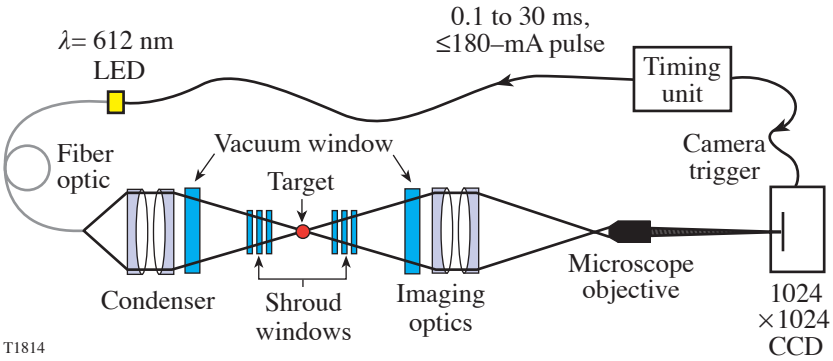


Figure 99.26
Schematic of the optical system used to acquire images of cryogenic targets.

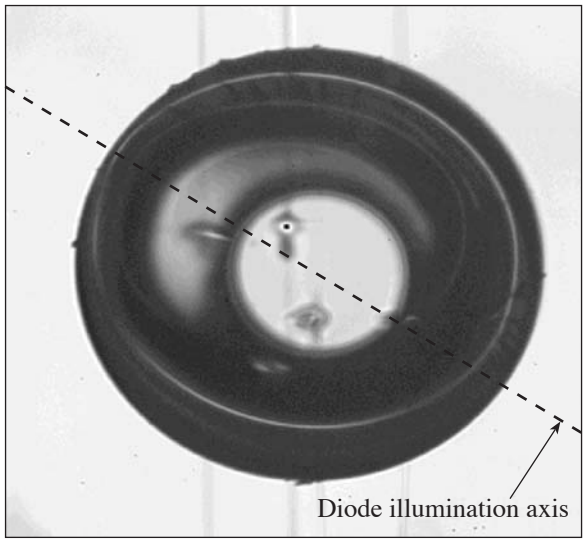


Figure 99.27
The ice layer is distorted (thinner) along the axis of the diode illumination used to backlight the target. The diode light (612 nm) was absorbed in the plastic to create localized hot spots.

## 2. Numerical Analysis

Backlighting the target provides an image as shown in Fig. 99.28. Notable are the outer limb of the plastic shell and narrow, concentric, circular, bright bands due to light reflecting off the inner ice surface. The brightest band is light reflected from the inner ice surface perpendicular to the illumination axis. Less-intense bands are reflections from different regions of the inner ice surface and may include multiple internal reflections. Only the brightest band is analyzed. The band may vary in intensity, or become discontinuous, due to either scattering centers in the ice (i.e., crystallographic features) or defects on the surface of the plastic shell that deflect light rays that would otherwise be captured by the viewing optics.

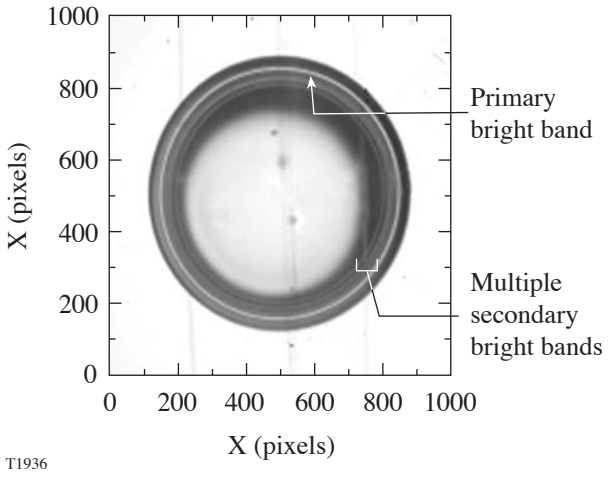


Figure 99.28
An example of a high-quality ice layer where both the primary bright band and multiple secondary bright bands are visible.

This technique, referred to more generally as *shadowgraphy,* yields a 2-D slice through the ice layer. Rotating the target and acquiring an image at each rotational position allows a 3-D tomographic image of the ice layer to be assembled.

The analysis algorithm calculates the center of the target from the outer limb of the plastic capsule and then determines the radial distance from the center to the inner ice surface. The variation in the distance is approximated using a Fourier cosine expansion. The coefficients of the expansion report the spectral power density in each mode. The layer roughness is calculated separately as an rms least-squares fit to the entire data set. The Fourier spectral decomposition better defines how the roughness is distributed. Phase information from the 2-D analysis is not used; that information is more easily visualized from the 3-D analysis.

The camera and optics provide a resolution of ~1.1 $\mu$m per pixel, and a total of ~350 pixels comprise the circumference of the bright band. Although the diffraction limit on the resolution is 3 $\mu$m to 4 $\mu$m, the statistics afforded by the large number of pixels allows the roughness to be determined with a precision better than 0.5 $\mu$m. This analysis assumes that the outer ice surface (the one contacting the plastic capsule) is perfectly circular, whereas the actual roughness ranges from 0.2 $\mu$m to 0.7 $\mu$m (as defined by the roughness and thickness uniformity of the plastic wall); clearly, as the ice roughness approaches the 1-$\mu$m goal, the existence of a 0.5- to 0.7-$\mu$m roughness due to the plastic will make the ice seem rougher than it really is. An example of this is shown in Fig. 99.29 where the ice roughness was 1.1 $\mu$m and the plastic roughness was 0.5 $\mu$m.

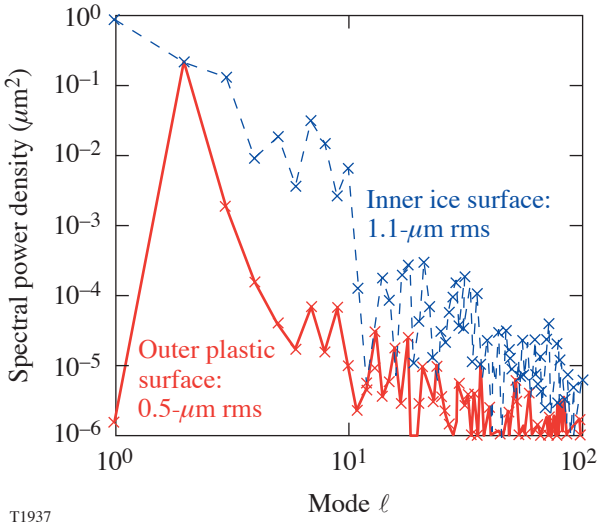


Figure 99.29
The power spectrum of a 100-$\mu$m ice layer shows that the smoothness is approaching the goal of 1-$\mu$m-rms roughness. The roughness is primarily in spectral modes 1 through 10, with comparatively little power in higher modes.

It is important to know the accuracy and repeatability of the analysis algorithm. Two methods were used to acquire this information: In the first method, a 1-mm sapphire ball with a measured ~0.05-$\mu$m-rms roughness (characterized using atomic force microscopy) was inserted into the layering sphere and the outer limb was analyzed with the optical system and software tools. The measured optical roughness was ~0.2 $\mu$m (rms), four times the roughness obtained using the more-accurate AFM technique. This suggests that the technique has an amplitude threshold below which the precision is increasingly dominated

by pixelated noise. In the second method, seven successive images of a target were acquired. Multiple ice layers were studied, and the difference between the average value of each data set of seven images and the actual value is shown in Fig. 99.30. A total of 382 data sets were analyzed and showed a repeatability of ±0.1 to 0.2 $\mu$m for most ice layers. Targets that vibrated significantly exhibited a greater variability in the roughness (up to 0.7-$\mu$m difference), despite the strobing effect of the pulsed illuminator. It is likely that different target views were imaged because a vibrating target also rotates slightly. These data suggest that a minimum of three and maximum of five images of each 2-D great circle be acquired in order to attain statistical confidence in the data.

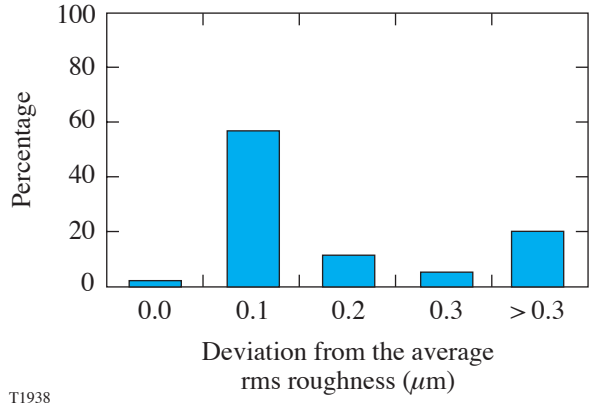


Figure 99.30
Histogram showing the variation of the inner ice surfaces' rms roughness from an average, as determined by the shadowgram analysis routine. The average rms roughness was calculated from seven repeat images of the same ice layer.

## Ice-Layer Quality

1. Solidification Process

At the start, deuterium is a liquid with its meniscus extending 3/4 of the way up the side of the capsule. Although it cannot be imaged, a thin, contiguous fluid layer should exist around the entire capsule since liquid hydrogen effectively wets plastics; the contact angle is zero.[4] The temperature is initially 0.05 K to 0.1 K above the triple point and is lowered by 0.2 K to begin solidification. A seed crystal appears first near the equator and expands vertically up the sides of the capsule. This behavior differs from that observed in targets containing fill tubes where a seed crystal is always present at the fill tube (at the top of the target) and the crystal grows from gas condensation.[5] Throughout the process, the target is thermally loaded by 3.16-$\mu$m radiation at a constant rate.

To fully solidify the target, the latent heat of fusion must be removed. In an OMEGA-scale target, this amounts to a total of ~2 mJ. The solidification time depends on the temperature difference between the target and the layering sphere and the helium gas that may be in one of two possible pressure regimes. Equation (1) applies to sufficiently high helium-gas pressure (*continuum* or *kinetic* regime), where heat flow is independent of pressure:[6]

$$Q = 2k\left(T_{\text{target}} - T_{\text{layering sphere}}\right) d_i d_o / \left(d_o - d_i\right), \qquad (1)$$

where $Q$ is the heat flow from the target to the layering sphere, $d_i$ is the diameter of the inner sphere, $d_o$ is the diameter of the layering sphere, and $k$ is the thermal conductivity of helium gas. In this application, the only variable parameter in Eq. (1) is the temperature of the layering sphere: the target will completely freeze in <1 s for a temperature gradient of 1 K between the target and the layering-sphere boundary. Since the goal is to slowly freeze the target to achieve a *single* seed crystal from which a single ice crystal can grow, the solidification rate depends strongly on (1) knowing precisely the layering-sphere temperature that *corresponds to the triple point in the target* and (2) maintaining the layering-sphere temperature marginally (10 mK) below this "triple-point-equivalent" value. Rapidly freezing the target forms a polycrystalline ice structure that makes it difficult to observe the bright band and to achieve a smooth ice layer [Fig. 99.25(b)].

This temperature differential can be ascertained by performing the inverse of freezing, i.e., *melting* the ice. Typical volumetric heat loads to the target range from 8 $\mu$W to 30 $\mu$W. (This value is determined by forming an ice layer using IR light, isolating the IR source, raising the temperature of the layering sphere and target to 18.72 K, and switching on the IR heat source again. The time required for the solid to melt provides an estimate of the heat load since the heat of fusion for deuterium and the mass in the target are accurately known.) These heat loads predict a steady-state temperature difference between the target and the layering sphere of the order of 0.05 K to 0.2 K; the actual temperature difference is 0.7 K to 2 K. Such a discrepancy points toward a helium-gas pressure in the layering sphere well below the continuum limit where thermal conduction depends on gas pressure. This situation is plausible since the gas path to the layering sphere is not leak-tight (an unavoidable "real-world" consequence of the equipment having to provide targets for implosion experiments, as opposed to a single-purpose, scientific test bed).

Equation (1) applies when the mean free path of the gas is significantly shorter (1/100th or less) than the distance between the target and the layering sphere. When the mean free path is of the same order, or larger, than the scale length (the Knudsen number >1), the gas is in the *transition or molecular regime*, and heat transport between the target and the layering sphere is described as[7,8]

$$Q = (a_o/4)\left[(\gamma+1)/(\gamma-1)\right]\sqrt{2R/\pi M} \times P\left(T_{\text{target}} - T_{\text{layering sphere}}\right)\Big/\sqrt{T_{\text{target}}}, \quad (2)$$

where $R$ is the universal gas constant, $P$ is the pressure, $M$ is the molecular weight, $\gamma$ is the ratio of the specific heat capacity at constant pressure and volume $\left(\gamma = C_p/C_v\right)$, and

$$a_o = \frac{a_1 a_2}{a_2 + \left(\frac{A_2}{A_1}\right)(1-a_2)a_1}, \quad (3)$$

where $a_1$ (or $a_2$) is the accommodation coefficient of helium at a surface, $A$ is the surface area, and 1 and 2 refer to the layering sphere and target, respectively.

Operating the layering process at a helium pressure below the continuum limit requires a lower temperature on the layering sphere to freeze the deuterium. This is to compensate for the diminished thermal transport through the gas. Figure 99.31(b) shows this effect.

A second effect of the low helium-gas pressure pertains to the temperature gradient that it establishes around the outside $(\theta,\phi)$ of the plastic shell, which increases the temperature gradient across the void space within the target (Fig. 99.24): the temperature gradient increases from 0.05 K to 0.11 K, for a heat load of 1 $Q_{\text{DT}}$, when the helium pressure is decreased from the continuum to the molecular regime. This temperature gradient is important since it affects the heat flux from the target and the dynamics of crystal growth. Typically, the OMEGA CTHS operates in the transitional region between the kinetic and molecular regimes.

While the target freezes, the ice temperature remains at, or very close to, the triple point temperature of 18.72 K. Once the latent heat of fusion is removed, the target continues to cool until it reaches a temperature where the IR heat load into the target is balanced by the heat flow out of the target. This temperature depends only on the temperature of the layering sphere, the helium-gas pressure, and the heat in the target. There are consequences for lowering this temperature in terms of strain experienced by the ice. The farther the final target temperature reaches below the triple point, the greater the ice strain (ice contracts by ~0.45%/K; contraction in the plastic is negligible over this range). The induced strain adds to any intrinsic strain due to the crystal contorting to the confines of the shell. Once the local strain exceeds the yield point (~0.2% strain),[9] the induced stress will cause the ice to fracture. The radial-thermal-conduction uniformity, and hence the ice-thickness uniformity, will be affected by where, and how extensively, the ice fractures.

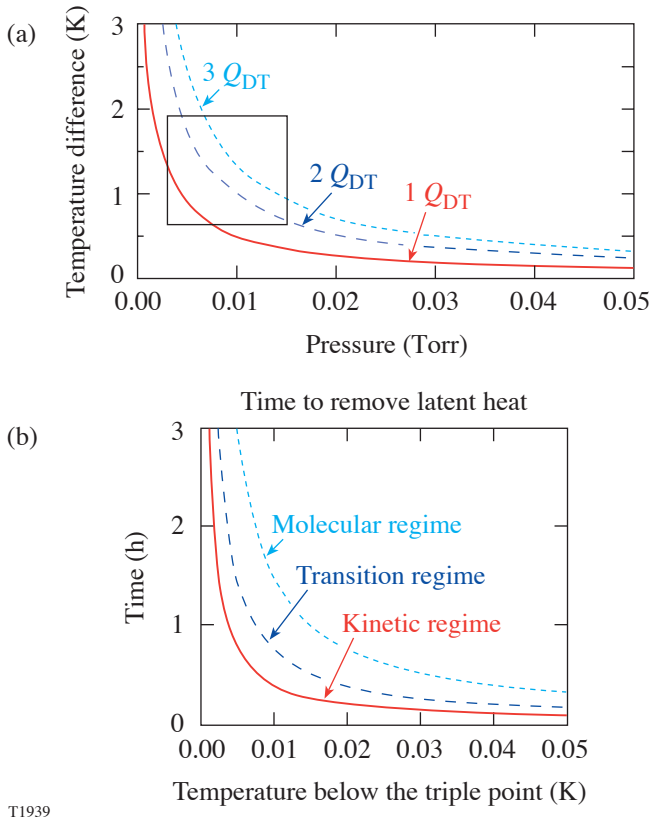


Figure 99.31
(a) The relationship between the helium-gas pressure and the temperature difference between the target and the layering sphere is shown for three heat loads (1, 2, and 3 $Q_{\text{DT}}$) (accommodation coefficient is 0.5). (b) The relationship between the time required to remove the latent heat from the target and the helium pressure and temperature gradient (between the target and the layering sphere). The inset box in (a) shows the typical region of operation.

2. Effect of the Solidification and Layering Process on the Resulting Ice Roughness

The solidification process is inherently stochastic. It depends on where a seed crystal forms, how many seeds form, and how quickly the resulting crystals grow and then interact. The resulting ice morphology, including facets or dislocations in the crystal structure, may influence the thermal-conduction path that in turn affects the final ice roughness.

To separate the effects of ice morphology and external perturbations on the ice roughness, and to quantify the inherent variability in the solidification process, a single target was repeatedly layered and melted using the identical protocol and configuration (the same IR heating power, helium-gas pressure, and target position). For each repetition, the liquid-containing target started at the same initial temperature, and layering was initiated using the same temperature decrement. The roughness of 11 separately formed ice layers is shown in a polar plot in Fig. 99.32. Each layer was rotated through 360°, and a 2-D image was acquired every 15°. The rms roughness of each great circle was plotted against the corresponding rotational angle. Three trends are noticeable: (1) The roughness of each great circle for a particular rotation shows good repeatability. The rms values are within ±1 μm of the average. (2) There is strong correlation between the roughness and the target's rotational orientation (±1-μm variability), and (3) there is significant variability in the roughness of each layer (±2 μm). This test was repeated using two different targets to determine if the rotational correlation was capsule dependent. The targets were layered, melted, and relayered three times with similar results (Fig. 99.33). Each layer's roughness repeated to within ±0.6 μm, and a similar azimuthal dependency of the roughness was observed. These data sug-

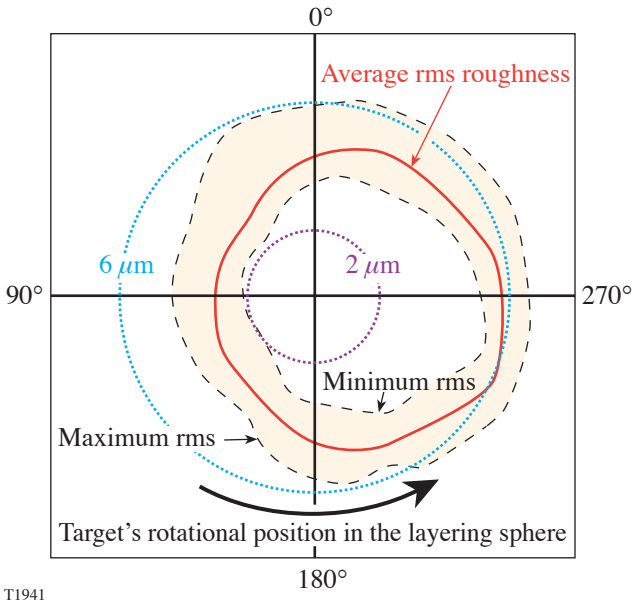


Figure 99.32
Polar plot showing the rms ice roughness of individual 2-D great circles through the target relative to the layering sphere. The average, minimum, and maximum roughness values of 11 different layers are shown for each 15° rotational angle.

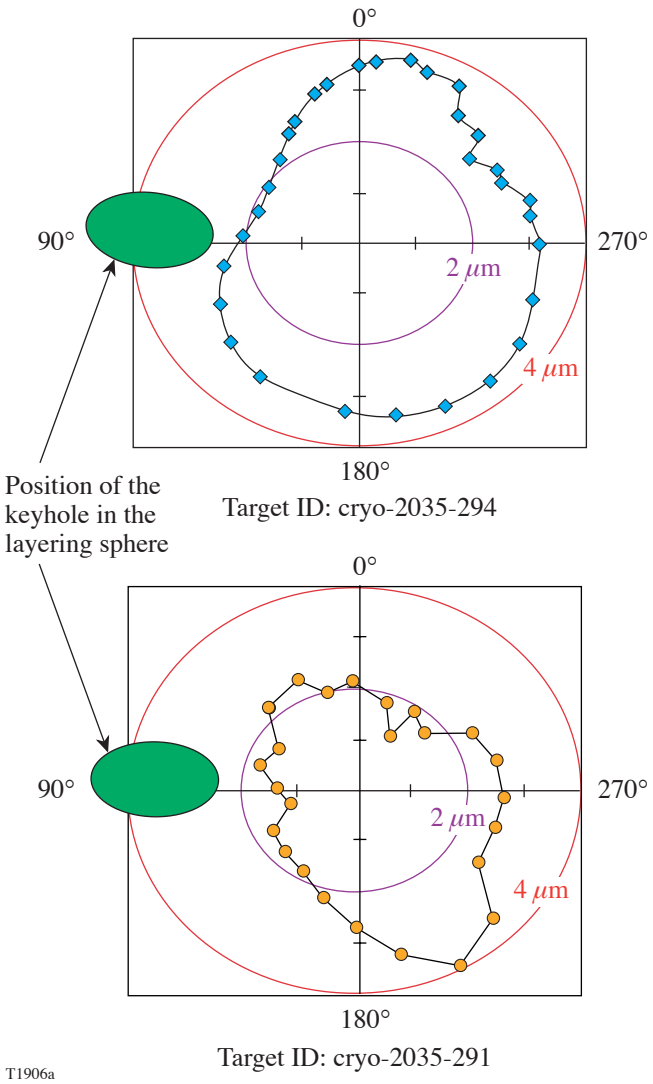


Figure 99.33
Polar plots showing the rms roughness of 2-D great circles relative to the layering sphere. Three separate ice layers were averaged for each plot. Each plot corresponds to a separate target.

gest the following: (1) the geometry of the layering sphere, not the plastic shell, is responsible for the azimuthal variation in roughness; and (2) the solidification and ice-layering process alone produced a variability of ±0.6- to 1-$\mu$m variability in the ice roughness.

Three-dimensional images of the ice-layer thickness of four of these layers (same target and layering conditions) are shown in Fig. 99.34. All layers have comparable roughness. The roughness distribution is similar: isolated regions of thicker ice are located at each target's equator and at varying azimuthal angles.

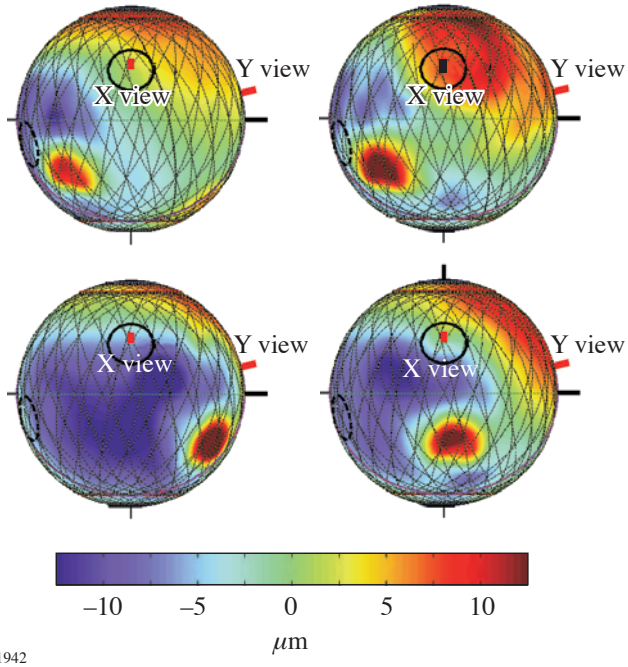


Figure 99.34
Three-dimensional plots of the ice thickness. Four separately formed ice layers in the same target are shown.

3. Effect of External Perturbations on the Ice-Layer Roughness

The environment surrounding the target will affect the ice-layer quality if there is insufficient control of the heat flows into and out of the target or if nonuniform illumination or thermal conditions exist. The stability of the heat flow *into* the target depends on the stability of the IR light source. The stability of the heat flow *out of* the target depends on a constant helium-gas pressure and constant temperature on the layering sphere. Uniform illumination of the target requires the layering sphere to perform as an integrating sphere to ensure uniform volumetric heating (no hot spots). Also, a uniform thermal boundary condition requires the layering sphere to be isothermal so that the outer surface of the plastic shell is isothermal *when* the ice is uniformly thick. The consequences of variations in any of these parameters are addressed next.

a. Stability of the IR source. The IR source is a pulsed optical parametric oscillator (OPO) supplied by Aculight, Inc. The pulse repetition rate is 30 kHz; the wavelength is tunable over the 2.9- to 3.3-$\mu$m range with a bandwidth of 10 nm. The IR light transits through a 60-ft optical fiber into the layering sphere. The layering sphere contains an indium antinomide (InSb) detector that measures the IR intensity and provides feedback for maintaining constant power. The maximum OPO output power is 200 mW, which is attenuated 60% to 80% by the fiber and coupling connectors. Of the 40 mW to 80 mW injected into the layering/integrating sphere, a maximum of 30 $\mu$W is coupled into the target. Reasons for this low efficiency are the low $Q$ of the integrating sphere (ray tracing suggests that a ray traverses the sphere fewer than 20 times before exiting) and the low absorption in the 100-$\mu$m ice layer (~4%).

The long-term stability of the OPO power is important since the target's temperature needs to be below, but as close as possible to, the triple point. This limits the crystal to growing from a single seed, slows the growth rate, and minimizes the volume contraction that occurs when solidification is completed. Any drift in the OPO output power over the layering period may melt the ice crystal. For example, consider a layered target that is 0.01 K below the triple point: a +1% drift (increase) in OPO power (corresponding to an 0.08-$\mu$W variation) equates to a 0.001-K change in the target's temperature if the helium pressure is in the continuum regime; however, if the pressure is below the continuum limit, the temperature may increase by up to 0.060 K, which would melt the ice. A negative drift in OPO power does not lower the target's temperature, which is clamped at the triple point until solidification is complete, but will cause an imbalance in the overall heat flow and hence the solidification rate. The parametric relationship between the change in the target's temperature and the heat load and helium pressure for a 1% increase in the OPO power is shown in Fig. 99.35. As the layering-sphere temperature is controlled to ±0.001 K, it is the stability of the OPO source that controls the stability of the target's temperature.

Typical data for the long-term power stability of the OPO are shown in Fig. 99.36. The OPO drifts by ±4% over a 24-h period. When operated under closed-loop control, the drift in

power diminishes to less than ±1%. Short-term power fluctuations involving energy change substantially less than the latent heat of fusion may not melt or flash freeze the deuterium. They may, however, affect the crystal formation, i.e., a 1-$\mu$W increase in power (equal to 4% of 3 $Q_{DT}$), which places the target temperature above the triple point, will cause the target to slump within 10 min and to melt within a half hour.

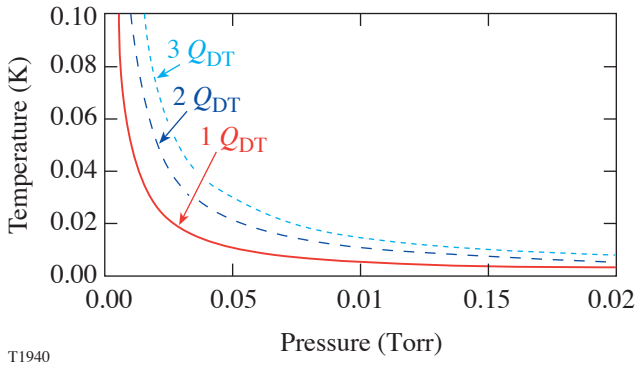


Figure 99.35
Graph showing the change in the target's temperature when the OPO power increases by 1%. The dependency of this response on different heat loads (1, 2, and 3 $Q_{DT}$) and helium-gas pressures is shown. The accommodation coefficient is 0.5.

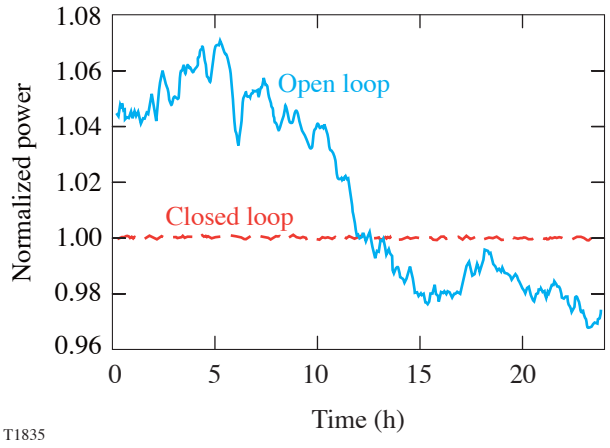


Figure 99.36
Plot showing the stability of the OPO when it is operated in closed-loop control and the magnitude of the drift when operated without feedback control.

b. Illumination uniformity of the layering sphere. As described earlier, the layering sphere containing the target is also the integrating sphere. The integrating feature is brought about by a purposely roughened, highly reflective Lambertian surface (gold coated) that is to provide a uniform IR intensity throughout the sphere. There are features, however, in the layering sphere that affect this illumination uniformity, including the four sapphire windows (~6-mm diam) and an entry hole at the base of the sphere used to insert and remove the target. The area of the entry hole is 2% to 3% of the total area and is the largest single feature affecting illumination uniformity. The effect of the shadow cast by this feature on the target was assessed by (1) tracing rays through the target to determine spatially where the heat was deposited in the ice, and (2) calculating how the resultant heat deposition affected the ice-layer thickness.

The ray-tracing calculation modeled only those rays that would originate from the "hole" region; rays originating elsewhere are uniformly distributed throughout the ice. The path of the rays through the ice was calculated from the refractive indices of the plastic, the ice, and the internal gas void, and the Fresnel coefficients when the angle of the ray relative to a surface was below a threshold.[10] The model was axisymmetric, and regions of the ice were zoned according to the ray density. Importantly, the ray density was not distributed isotropically (see Fig. 99.37). Because of the focusing effect of the ice, the density of rays at the target's rear surface is marginally greater than at the front surface. The largest variation in ray density was along a great circle perpendicular to the incident rays, but this was over a small area.

The assumed volumetric heat load into an axisymmetric thermal model of a cryogenic target was 8 $\mu$W (equivalent to the tritium decay energy in a DT target). Of this value, an average of 0.18 $\mu$W was subtracted from the target because of the absent rays that would have otherwise originated from the hole region. (This value is proportional to the ratio of the area of the hole to that of the entire surface.) The exact assignment of power into each zone was normalized to the ray density, where regions with the *highest* density of rays received the *largest reduction* in heat.

The resulting temperature profile on the internal ice surface was calculated using the computational fluid dynamic code FLUENT.[11] Simulating the ice-layering process manually, the ice-layer position was adjusted and the temperature distribution recalculated until the inner ice surface was isothermal.

The resulting ice-layer thickness is shown in Fig. 99.38. Spectral analysis of this great circle yields an ice roughness of ~4-$\mu$m rms.

Experimental evidence of this possible perturbation source is not straightforward since many competing sources can affect the ice-layer thickness. By examining only the smoothest targets, the contribution of other sources of roughness to the ice is reduced, which may allow the effect of the layering sphere to be more noticeable. Figures 99.39(a)–99.39(c) show a target with an average ice rms roughness of 1.2 $\mu$m (determined by averaging the roughness of 24 2-D great circles around a target) that possesses thinner ice facing the keyhole (bottom of the target) than at the rear surface (top of the target), which are the general locations predicted by the ray-tracing analysis. The light region in the image [Figs. 99.39(a)–99.39(c)] indicates a region of thicker ice and corresponds to the area where fewer rays coincide, possibly because of the shadow cast by the hole in the layering sphere.

The calculated ice thickness from the thermal model is shown in Fig. 99.39(d) for a 2-D great circle oriented along the same axis as the hole in the layering sphere. The volumetric heat load was obtained from the ray-trace calculation. The ice is thinnest where the target faces the hole (the darker hemisphere), and thicker opposite the hole. This pattern is similar to what is seen experimentally with the main difference being that the thick region of ice should be cylindrically symmetrical around the target's equator. While this is not conclusive evidence that the hole in the layering sphere is responsible for the observed ice-thickness variation, this possibility warrants a more-detailed study. Two limitations of the thermal model are that (1) it is only an axisymmetric model, not a 3-D model so that the modeled hole was circular, not of the more-complex

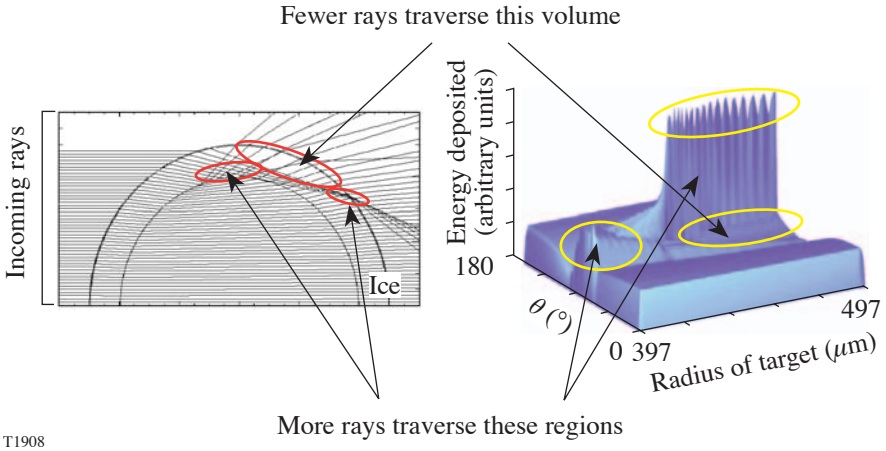


Figure 99.37
Ray trace through a symmetrical target showing where the IR energy is deposited in the ice. The focusing effect of the ice and internal reflection from the inner ice surface are responsible for the behavior. $Q$ is the volumetric heat load.

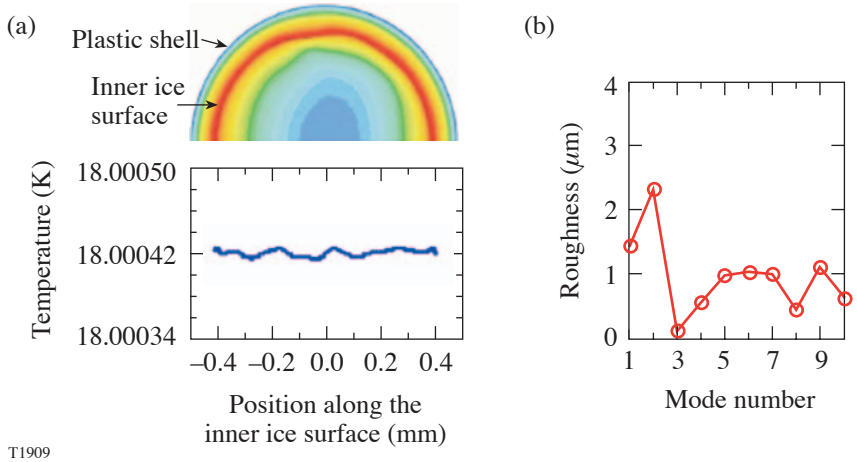


Figure 99.38
(a) Isotherms within an ice layer once the ice thickness is adjusted to account for the lack of illumination on the target (caused by the keyhole in the layering sphere). The associated power spectrum is shown in (b).

trapezoidal geometry of the actual hole, and (2) a constant-temperature thermal boundary condition was imposed on the outer surface of the target to provide sufficient grid (spatial) resolution for the calculation. This would exaggerate the ice thickness at the equator. The boundary condition should be on the layering sphere wall.

Lastly, the calculated 4-$\mu$m-rms roughness is greater than the roughness observed in any of the individual 2-D analyses of a target: this stems from the calculated 2-D great circle going through both the north and south poles—an orientation that cannot be viewed by either the X or Y viewing axes. Instead, the viewable 2-D great circles intersect only a portion of the great circle calculated above. The orientation of the ice-thickness distribution becomes apparent only after the 3-D surface is generated.

c. Stability of the target temperature and helium exchange gas. The temperature of the layering sphere is controlled to ±1 mK, using Cernox™ temperature sensors and heaters with a highly damped feedback-control algorithm. Fluctuations in target temperature are expected to be less than 1 mK, owing to the additional buffer provided by the low thermal diffusivity of the helium exchange gas. The effect of this temperature instability is insignificant compared to the effect of the power drift in the OPO, so much so that the temperature stability of the layering sphere does not affect the layering process.

It is important that the helium-gas pressure be stable for the duration of the layering. A variable heat flux would risk rapid freezing, the formation of multiple crystal growth sites, and the subsequent propagation of multiple crystals and facets. There is no experimental evidence that the gas pressure may vary.

An issue larger than the pressure stability is the lack of knowledge of the absolute pressure. This complicates, but does not compromise, the process by prolonging the time it takes to determine an optimal temperature setting on the layering sphere to commence layering. It may also be beneficial to be able to adjust the pressure in controlling temperature gradients around the target.

Furthermore, the accuracy of the target-temperature measurement depends also on the time available to make that determination. Experiments that freeze and melt the target at very slow rates (5 mK per two hours) ensure complete equilibration between the target's temperature and the temperature of the layering sphere, which compensates for the small heat-flow changes that occur relative to the latent heat of fusion. Under these conditions, it is possible to determine the target temperature to within 5 mK of its absolute value. Under such tight control, a geometrical effect comes into play: the liquid freezes at a slightly different temperature than the one at which the ice melts (because the slumped liquid layer covers only a portion of the plastic shell through which heat is removed).

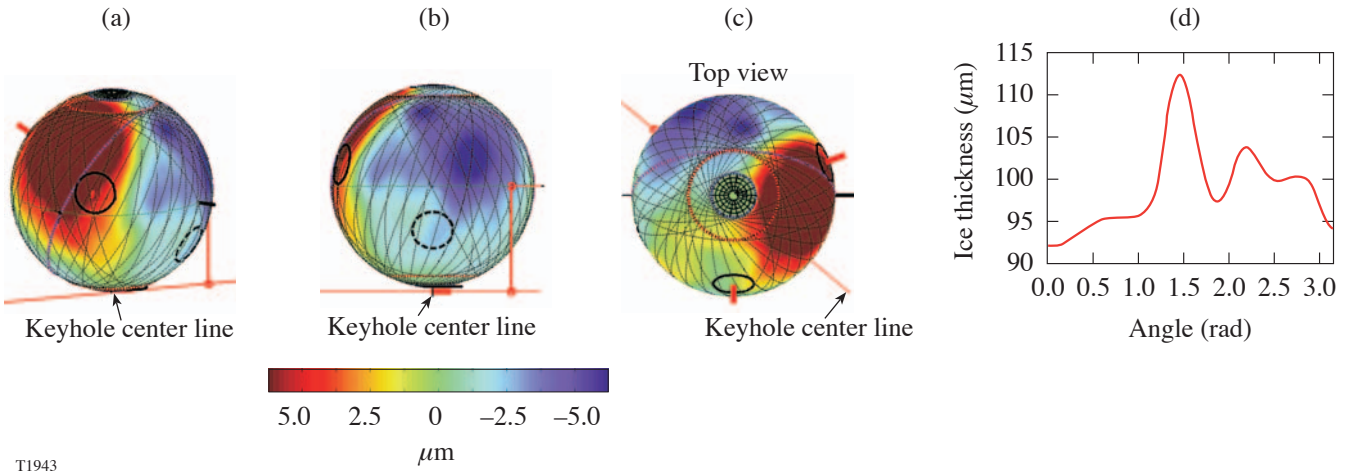


Figure 99.39
Images (a), (b), and (c) show the ice-thickness distribution in a target where the average ice rms roughness is 1.2 $\mu$m. The thickness variation along a great circle through the keyhole line is ~8 $\mu$m peak-to-valley. The calculated thickness variation, from the ray trace and thermal model, from the bottom of the target to the top and along the axis of the hole is shown in (d).

**Thermal Analysis**

The thermal environment within and around the target was modeled to quantify the thermal gradients that exist during the layering process. The results offered a better understanding of the layering process's sensitivity to extrinsically controllable and coupled parameters: IR power, gas pressure, and the temperature on the layering sphere. The primary motivation for this model was derived from an uncertainty about how accurately the solidification process can be controlled and what level of control was required for the desired ice-layer quality. Looking forward, such an analysis also helps to better determine the thermal requirements to refine cryogenic equipment.

4. Initial Phase of Forming the Ice Layer

The modeling results of the thermal environment at the initial stage of forming a layer are shown in Fig. 99.24: A melted target is centered in the layering sphere at a temperature slightly above the triple point. The temperature along the inner liquid surface varies between 0.05 K and 0.1 K, depending on the helium pressure. Based on actual experimental values, the model uses the following input parameters: The temperature on the layering sphere is 18.52 K, in accordance with the diminished helium-gas conductivity (0.006 W/m-K) due to the gas pressure being below the continuum limit. The heat load into the liquid and plastic is 1 $Q_{DT}$ (the amount of heat from an equimolar DT solution). Raising the heat coupled into the target to 3 $Q_{DT}$ raises the temperature gradient to 0.25 K.

With a 0.1-K temperature gradient around the target's external wall, and the average temperature of the target being within 0.005 K of the triple point, the liquid at the top of the target should form a crystal. If it does, the crystal should grow from this position. In practice, such a crystal growing from the top and propagating downward is not observed. Rather, the liquid around the equator of the target freezes first and a crystal grows upward (and in thickness) by vapor condensing on the crystal. Simultaneously, the crystal grows downward into the liquid melt, following classical solidification processes.

Multiple seed crystals form when the temperature decrement used to initiate freezing is large, and a low-quality, multifaceted, polycrystalline layer results. The parametric correlation between temperature difference, pressure, and heat flow from the target is shown in Fig. 99.31. The desirable operating pressure regime is in the flat portion of the curve, from 0.02 to 0.05 Torr, where the temperature gradient between the target and the wall of the layering sphere changes very little with temperature.

Even if slow solidification parameters, which favor single-crystal nucleation, and slow propagation are used, a layer will form within 1 h (Fig. 99.40). The rms roughness after that time is better than 10 $\mu$m.

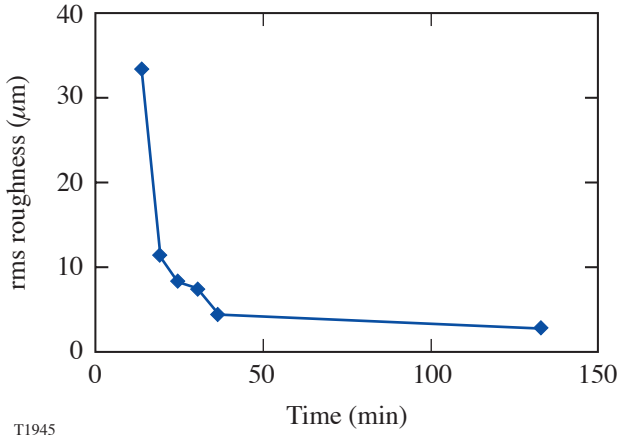


Figure 99.40
The time dependency of the ice-layer formation process indicates that an acceptably smooth ice layer can be achieved in under 3 h.

5. Final Phase of Forming the Ice Layer

Once the ice is mostly symmetrically distributed around the shell, only a small mass needs to be redistributed to create a uniform thickness. The time for this process depends on the sublimation rate, the temperature gradient along the ice/gas interface, and the diffusivity of the deuterium gas.

The sublimation rate depends on the difference between the gas pressure over the solid and the saturated vapor pressure. The pressure/temperature relationship for normal deuterium (near the triple point) is given by the equation[12]

$$P^{\text{vapor}} = \exp\left[19.192 - 177.48/T + 0.00663(T - 16.5\ \text{K})^2\right], \quad (4)$$

where $T$ is the temperature and the rate of sublimation is[13]

$$dm/dt = \left(P^{\text{vapor}} - P^{\text{saturated}}\right) S/\sqrt{2\pi MRT}, \quad (5)$$

where $m$ is mass, $P$ is the pressure, $M$ is the molecular mass, $R$ is the universal gas constant, $T$ is the temperature, and $S$ is the sticking coefficient, which is ~1 for vapor in equilibrium with its solid.

As the ice layer converges to a constant thickness, the temperature gradient along its internal surface decreases. This decreases the vapor pressure and density gradients across the gas void, slowing the layering process. For an ice layer with a peak-to-valley thickness variation of less than 5 $\mu$m, the temperature variation along the inner ice surface is less than 0.001 K. This corresponds to a gas-density variation of less than 0.001%. The density/temperature relationship is shown in Fig. 99.41.

Figure 99.40 shows the measured change in the layer roughness of one shell as it converges over time to a 1.8-$\mu$m final roughness. The heat load into this target was ~2 $Q_{DT}$. The process took <3 h; during the last ~100 min, the layer smoothed from 5 $\mu$m to 2 $\mu$m, corresponding to ~$10^{-6}$ of the total mass being redistributed. The associated temperature variation around the inner surface of the ice decreased from 1.4 mK to 0.15 mK (see Fig. 99.42; the range accounts for the uncertain helium-gas pressure, the converging thickness, and how well centered

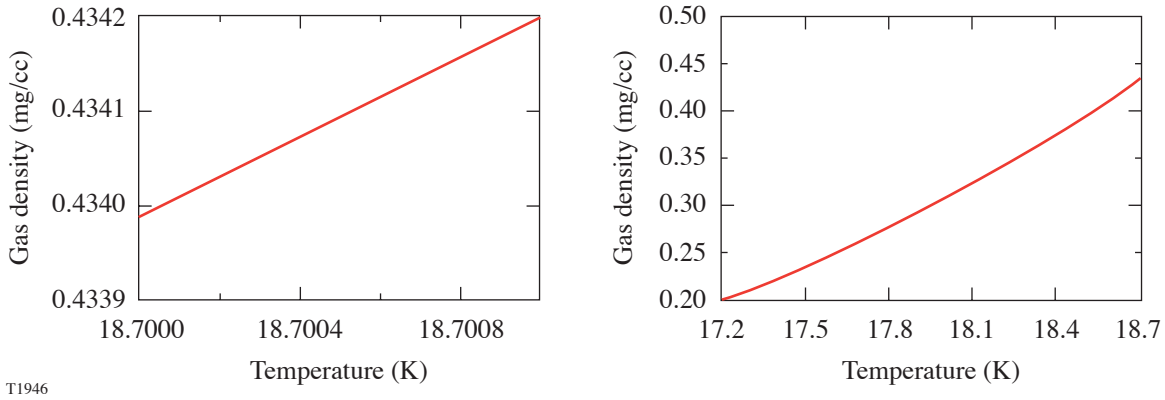


Figure 99.41
The relationship between the gas density and the temperature of the deuterium vapor.

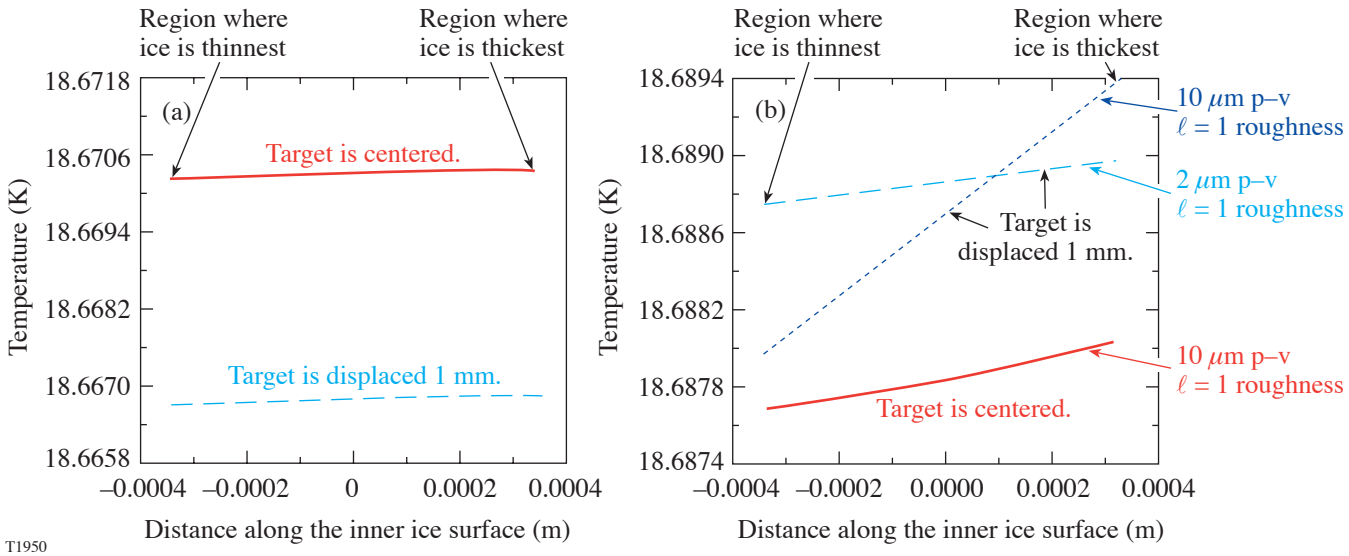


Figure 99.42
The temperature gradient on the inner ice surface is shown for varying conditions: (a) The ice layer has a 2-$\mu$m peak-to-valley (p–v) thickness variation, 1-$Q_{DT}$ volumetric heat load, and sufficient helium exchange gas for the system to be in the kinetic gas region. The effect of decentering the target by 1 mm in the layering sphere on the temperature gradient is negligible. (b) This shows the effect of higher roughness, higher heat loads (2 $Q_{DT}$), and lower gas pressures (thermal conductivity is 1/5 the continuum regime value) on the temperature gradient on the inner ice surface.

the target was in the layering sphere), and the gas density gradient decreased from 0.09% to 0.003%. This density gradient should produce a substantially faster layering time than is observed if gas phase diffusion was the rate-limiting step (the diffusion coefficient is $1.4 \times 10^{-6}$ m$^2$/s). Similarly, the $D_2$ pressure gradients should produce a faster layering rate than observed if the sublimation rate was the rate-limiting step. This infers that the density/pressure gradient is much lower than predicted for the measured ice thickness because the target is closer to an isothermal inner surface than the model predicts. This is achievable only if there is a variable thermal resistance around the target.

Historically, there has been an implicit assumption that the radial thermal resistance of the target is uniform for all ($\theta$, $\phi$) polar angles, and if it was nonuniform, the scale length would be sufficiently small for the consequences to be negligible. However, since the ice smoothness infrequently achieves the goal of 1-$\mu$m rms but more often is 2 to 3 $\mu$m, the validity of that assumption needs to be questioned. There are two parts to this evaluation: (1) the radial thermal resistance of the ice itself, and (2) the thermal resistance across the ice/plastic interface, which is not necessarily equal for all angles $\theta$ and $\phi$. Two other possibilities are addressed later: (a) the plastic-wall thickness may not be constant and hence contribute a variable-distance thermal path, and (b) the outer plastic surface may not be isothermal.

Given the geometry and size of the target, it is not possible to *measure* the thermal-resistance uniformity between the ice and the plastic, or within the ice itself. Its presence can only be inferred by eliminating other perturbations to the ice. Thermal conduction ($k$) is proportional to

$$k \sim C_s \rho_s U \lambda, \tag{6}$$

where $C_s$ is the crystal-lattice heat capacity, $\rho_s$ is the density, $U$ is the speed of sound, and $\lambda$ is the phonon mean-free path. Of these, the phonon mean-free path is the most likely to vary and is affected by (a) the temperature, which influences the phonon density and causes phonon–phonon scattering, (b) the crystal size since grain boundaries scatter phonons, and (c) the local density of deuterium in the molecular $J = 1$ rotational state ($J$ is the spin quantum number). At constant temperature, any variability would be caused by a disproportional distribution of either crystallite sizes or deuterium in the $J = 1$ rotational state (one-third of deuterium is in the $J = 1$ rotational state; the remainder is in the $J = 0$ state), which may occur if deuterium fractionates during the layering process (deuterium's triple point is 0.4 K lower if all the molecules are in the $J = 0$ state). While these are theoretically possible, they seem unlikely.

A second possibility for, and more likely the cause of, a variable thermal resistance is derived from the ice being partially detached from the plastic. If this occurred over a sufficiently wide cord length (of 100 $\mu$m or more), the thermal resistance between the inner ice surface and the plastic wall would rise appreciably, even if the gap thickness was very small (thermal conductivity of the gas is 2% that of the ice). The resulting higher ice temperature would cause the ice layer to thin in order to preserve an isothermal inner surface.

Figure 99.43 shows a cryogenic target with a pronounced gap between the ice and the plastic shell. This layer (~20-$\mu$m rms roughness) was obtained at a low heat load of ~0.2 $Q_{DT}$. Raising the heat load to 1 $Q_{DT}$ eliminated the gap, due to the intrinsic layering process, and improved the roughness to 6 to 8 $\mu$m. While similar voids were not visible at more-typical 1- to 3-$Q_{DT}$ heat loads, this is not proof that a thin delamination does not exist nor that any thermal resistance at the interface vanishes. It is possible that rapidly freezing a target causes precisely these delaminations, which makes it impossible to form high-quality layers. Figure 99.44 shows a thermal model and resulting ice-roughness power spectrum if a 1-$\mu$m-thick void with a length of 200 $\mu$m existed at the ice/plastic interface. The resulting rms roughness is 4 $\mu$m.

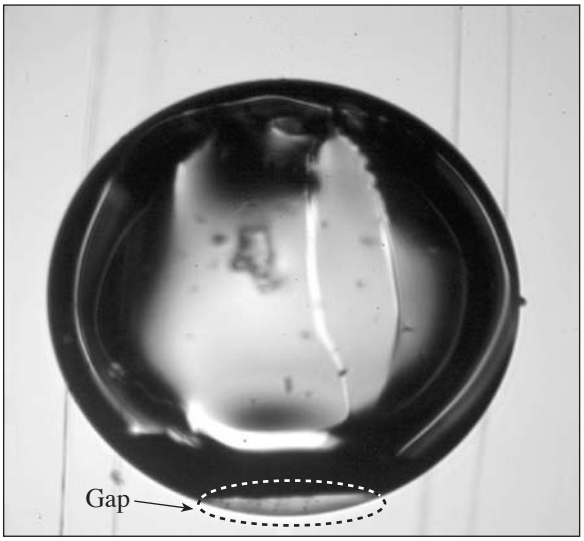


T1859

Figure 99.43
Image of a cryogenic target showing a gap between the plastic and the ice layer.

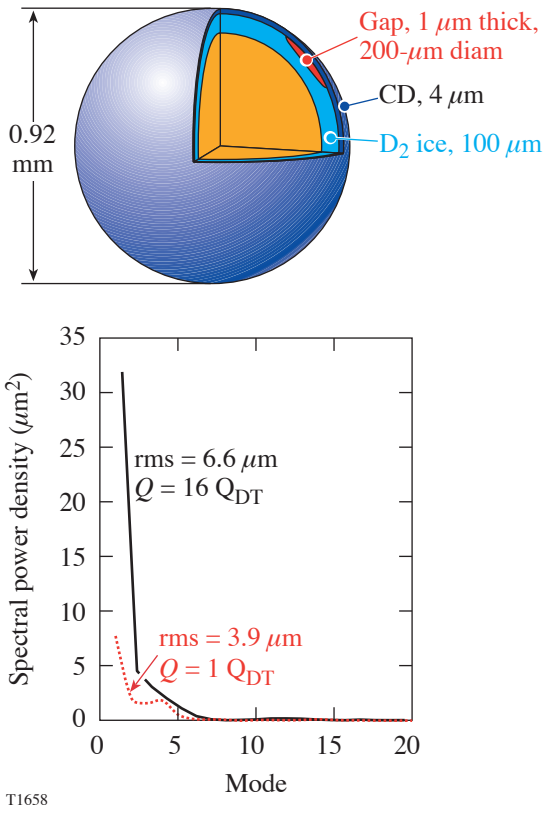


Figure 99.44
Thermal model showing the effect of a 1-$\mu$m-thick, 200-$\mu$m-diam gap between the ice and plastic on the uniformity of the ice layer.

Another method of affecting the inner ice temperature without changing the ice thickness is for the plastic wall to have variable thickness: if it is thicker on one side of the shell, it will provide a larger local thermal resistance that will make the inner ice surface warmer and will cause the ice layer to thin, relative to the opposing side, to maintain the isothermal property. For example, the thermal conductivity of plastic is one-tenth that of ice, so a 0.1-$\mu$m peak-to-valley nonconcentricity in the shell wall (the maximum allowable) would produce an ~1-$\mu$m peak-to-valley nonconcentricity in the ice wall. Table 99.I shows the effect of an extreme (0.75-$\mu$m) nonconcentricity in the wall of the plastic shell.

Lastly, the position of the target in the layering sphere during the solidification process may affect the eventual uniformity of the ice-layer thickness. It is possible that not centering a target in the layering sphere may result in the inner ice surface becoming isothermal before the ice is uniformly thick. This would occur if the side of the target with thicker ice was closer to the layering sphere. The following calculations investigate the sensitivity of the temperature gradient on the inner ice surface to the target's position in the layering sphere. A target with a 1-$\mu$m rough ice layer centered in the layering sphere will possess a temperature variation of 115 $\mu$K along the inner ice surface. Displacing the target by 1 mm within the layering sphere changes this variation by a maximum of 15 $\mu$K, depending on the alignment of the target's misplacement and ice-thickness variation. If the ice layer was perfectly smooth,

Table 99.I: The temperature gradient along the inner ice surface is calculated for different helium-gas thermal conductivities (due to low gas pressure), positional alignment in the layering sphere, and the effect of a nonconcentric plastic-shell wall.

| Peak-to-valley nonconcentricity ($\ell$ = 1 roughness) in the ice layer | Thermal conductivity of the helium exchange gas (W/m-K) | Position of the target in the layering sphere | |
|---|---|---|---|
| | | Centered | Displaced 1 mm from the center[a] |
| 2 $\mu$m | 0.025 | 0.115 mK | 0.10 to 0.13 mK |
| | | 0.190 mK[b] | |
| | 0.006 | 0.285 mK | 0.27 to 0.30 mK |
| 10 $\mu$m | 0.025 | | 0.55 to 0.60 mK |
| | 0.006 | | 1.42 to 1.44 mK |

[a]These values cover the maximum/minimum range that depends on how the ice thickness variation is oriented relative to the target position in the layering sphere.
[b]The plastic-shell wall possessed a 0.75-$\mu$m nonconcentricity.

the induced temperature gradient would be only 5 $\mu$K for a target displacement of 1 mm. At lower helium pressures (where we currently operate), the temperature gradient around the inner ice surface would be greater (285 $\mu$K), but the sensitivity to target position would be the same. Repeating the same calculation for a 10-$\mu$m peak-to-valley ice-thickness variation yields a similar proportional trend (see Table 99.I). It is desirable for the temperature variation on the inner ice surface for any ice-thickness variation to be as large as possible to maximize the layering driving force, and for the inner ice surface to be isothermal where the ice is uniformly thick. This will decrease the time it takes for the ice surface to become isothermal. In summary, these data suggest that misplacing the target by 1 mm from the center of the layering sphere will not affect the ability to form an ice layer with 1-$\mu$m-rms roughness.

The smoothest target obtained possessed an average ice roughness of 1.2-$\mu$m rms; it took 3 h for the liquid to form an ice layer with 1.5-$\mu$m-rms average roughness and an additional two days for it to decrease to 1.2 $\mu$m. This added time may reflect the gradual mass redistribution that accompanies a very small temperature gradient on the inner ice surface.

**Cooling Targets Below the Triple Point**

The internal gas density of a cryogenic target is required to be $\sim 0.2 \times 10^{-3}$ g/cm$^3$, corresponding to a temperature that is ~1.5 K below the triple point (Fig. 99.41). Cooling the target by this much densifies the ice but has no effect on the plastic. Because the ice is attached to the plastic, a strain of ~1% is induced either in the ice or at the interface between the ice and the plastic. This strain is in addition to existing strains that may have developed during solidification. The resulting stress may cause the ice to delaminate from the plastic, or if the adhesion is sufficiently great, the ice may rupture along existing crystallographic planes or defects. Both of these events can affect the ice roughness.

It has been conclusively determined from numerous experiments that the only possible method for meeting both the ice-quality and the sub-triple-point-temperature specification is to form an initial high-quality ice layer and then cool it. For a sufficiently slowly cooled target, the ice quality can be preserved. Figure 99.45(a) shows the results for two different but comparably smooth targets that were cooled at slow rates: 0.02 K and 0.03 K every 20 and 60 min, respectively. The slow rate allowed the strain that was induced during cooling to be relieved before further strain was incurred upon additional cooling. The target that was cooled at the faster rate experienced a marginal increase in roughness [Fig. 99.45(b)], while the second target was unaffected. It is premature to attribute the difference in behavior to the cooling ramps; this is the subject of further experiments. In a separate experiment a target that had roughened during cooling recovered its original smoothness when it was annealed for 18 h [Fig. 99.45(c)]. This behavior, however, does not always occur: the ice shows the same variable behavior that is seen when targets are repeatedly frozen, melted, and refrozen using identical conditions, a behavior that depends on the specifics of the ice crystal.

One expected consequence of decreasing the ice temperature is an increased likelihood for the ice surface to form facets that would generate a sawtooth-like texture and increase the high-frequency roughness. Experimentally, when increased roughness was measured, that roughness was primarily in the lower spectral modes, although the roughness also increased in modes up to 100 (Fig. 99.46). This outcome may be explained by structural changes occurring in the ice as it cools, changes that affect the radial thermal resistance of the ice around the target, which perturbs the isothermal condition on the inner ice surface that causes the ice to relayer. The subsequent ability of the ice to, in some instances, "anneal" these defects and to recover its original smoothness may depend on the type of defect that caused the initial perturbation to the ice.

**Effect of Ambient Radiation on the Cryogenic Target**

Removing the thermal shrouds exposes the cryogenic target to blackbody radiation from the target chamber, which is calculated from Plank's radiation law to be 0.0047 W. The effect of this heat load on the smoothness of the ice surface and the internal gas density determines the maximum time the target can be exposed before it has to be imploded.

The linear motor used to retract the thermal shrouds can achieve a velocity of 5 ms$^{-1}$ using a constant acceleration of 25 ms$^{-2}$. This corresponds to the target being exposed to ambient radiation for 0.05 s. The quality of the ice layer moments before implosion is determined using a high-resolution camera inside the target chamber to capture an image of the cryogenic target. The ice layer's smoothness does not appear to be degraded by this exposure time, which is encouraging; however, there is no way to measure the density (or temperature) of the gas in the center of the target. This information can be determined only by calculation. Should calculations also show that the rise in the density of the gas is sufficiently slow, it would be possible to slow the shroud's retraction. The extra time would allow any vibration in the target to be attenuated for longer, thereby allowing the target to be better centered in the target chamber.

Data from the camera inside the target chamber provided time-lapse images [Fig. 99.47(a)] that show how the cryogenic target behaves when the thermal shrouds are removed and the target is not imploded: first, the ice was observed to rotate inside the plastic shell (this occurred during the initial 2 s); then, as the liquid fraction increased, the ice/liquid slurry slumped (within 5 s) and melted after 10 s. The liquid continued to vaporize and the target exploded after 78 s. Immediately before the target exploded, it became transparent, indicating that the temperature had surpassed the critical point, which is the highest temperature where vapor and liquid coexist. Separate experiments determined that the temperature at which an OMEGA cryogenic target explodes is 43±1 K.

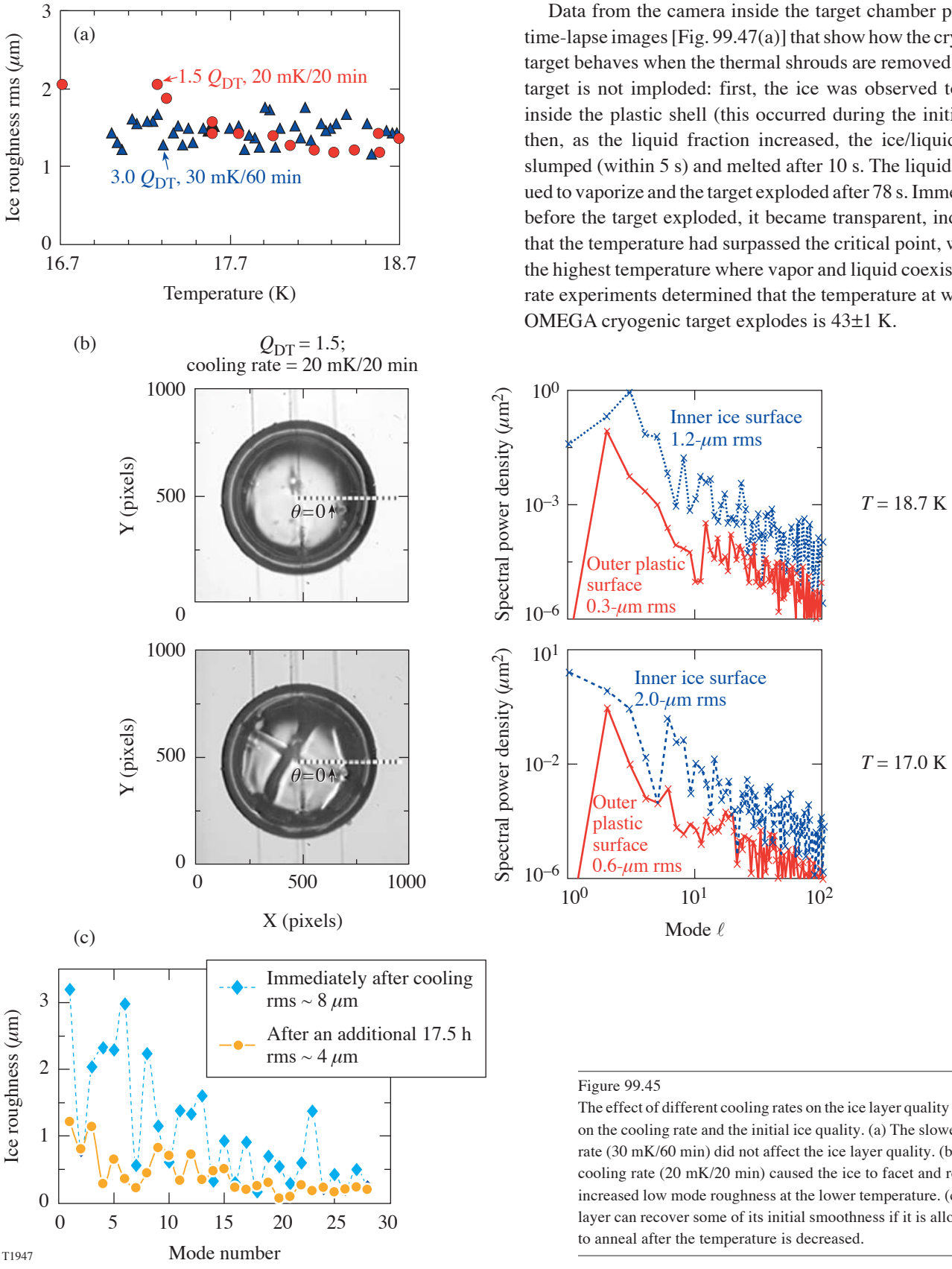


Figure 99.45
The effect of different cooling rates on the ice layer quality depended on the cooling rate and the initial ice quality. (a) The slower cooling rate (30 mK/60 min) did not affect the ice layer quality. (b) The fast cooling rate (20 mK/20 min) caused the ice to facet and resulted in increased low mode roughness at the lower temperature. (c) The ice layer can recover some of its initial smoothness if it is allowed time to anneal after the temperature is decreased.

The target contained $36 \times 10^{-6}$ g of deuterium, and the combined specific heat of the solid, liquid, and gas required to raise the temperature from 17 K to 43 K was 290 J/g (Ref. 14). Combining this value with the latent heats of fusion and vaporization yielded the total energy required to explode the target, ~0.014 J. These values suggest that the power coupled into the target was $1.7 \times 10^{-4}$ W, which was ~4% of the estimated 0.0047-W heat flux striking the target. Considering only the time required to melt the ice (10 s), and combining this with the latent heat of fusion for deuterium [50 J/g (Ref. 14)], the calculated heat deposited in the target was approximately $1.8 \times 10^{-4}$ W.

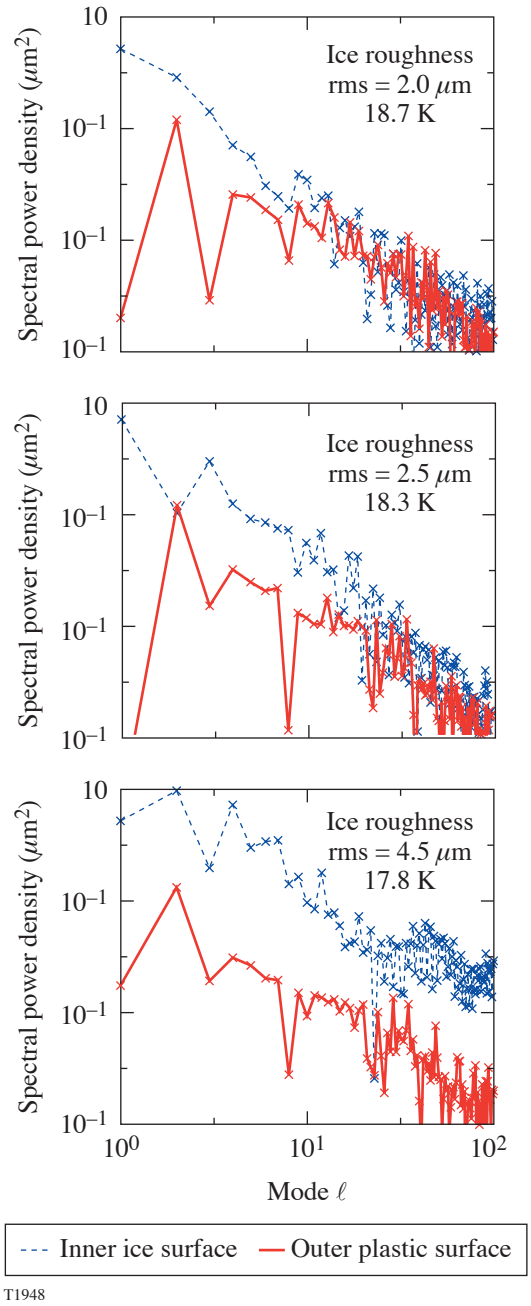


Figure 99.46
The change in the ice power spectrum is shown for a target that roughened when it was cooled.

A detailed thermal model of heat flow through the ice was used to determine how rapidly the temperature of the inner ice surface increased when the target was exposed to ambient radiation. This was done using the computational code FLUENT. For this model, the radiation heat load was coupled into the plastic shell wall alone, as deuterium ice and liquid absorb radiation over such a very limited spectral range (3.1± 0.3 μm) that the power coupled directly into the ice is negligible. The model included the temperature-dependent heat capacity of the solid and the latent heat of fusion for deuterium. The results reported are the time-dependent melt fraction of the ice, the temperature of the inner ice surface, and the heat flux to the inner ice surface. The time-dependent behavior of the ice layer is presented in Fig. 99.47(b) for comparison with the experimental data. In the simulation the ice layer was seen to melt closest to the plastic layer [Fig. 99.48(a)] and then slump on a time scale that was similar to that observed experimentally. This behavior gives confidence that the temperature calculations in the model are relevant.

The sequence of events that occurs once the target is exposed to ambient radiation can be described in more detail using the thermal model as a guide. Initially the ice is at 17 K with a very small radial temperature gradient (<0.1 K). When the shrouds are removed, the plastic absorbs radiation and heats rapidly since the heat capacity of the plastic at this temperature is extremely low (87 J/kg-K). The heat flux from the target to the surroundings is negligible since the target is in vacuum, so all of the heat conducts inward into the ice. The heat flux at the inner ice surface [Fig. 99.48(b)] reaches a peak at ~60 μW after 0.006 s and then decreases to <1 μW within 0.07 s. The behavior follows the radial temperature gradient: after 0.006 s has lapsed, the outer ice surface has reached the triple point (18.72 K) and cannot rise further until the ice is melted; meanwhile, the inner ice surface remained at 17 K. The delay time is due to the thermal diffusivity. Over the next 0.07 s, the outer ice surface remains at the triple point and the inner ice surface approaches the triple-point temperature. Once the inner surface is also at the triple-point temperature, the temperature gradient across the ice layer is negligible and

the heat flux is commensurately low. The time-dependent temperature profile of the inner ice surface is shown in Fig. 99.48(c). As the temperature of the inner ice surface increases, so does the saturated vapor pressure, and the heat flux determines how rapidly ice sublimes to maintain the equilibrium gas pressure. Fortunately, the low heat flux and sizeable latent heat of sublimation [367000 J/kg (Ref. 14)] limits how rapidly the gas density increases in the center of the target [Fig. 99.48(d)]. These data suggest that the gas density will not increase significantly over the sub-0.5 s exposure times when a target at a sub-triple-point temperature is exposed to 300-K radiation.

When a target 1.7 K below the triple point is heated back to the triple-point temperature, the deuterium ice experiences an ~1% volumetric expansion. Should this cause the ice to buckle instead of swelling uniformly, added roughness would be induced on the inner ice surface. Such roughness has not been observed in targets that were imaged in the target chamber, but that may only be because the spatial wavelength and amplitude of the roughness were beyond the resolution of the diagnostic. Ultimately, this effect may determine the allowable target exposure.

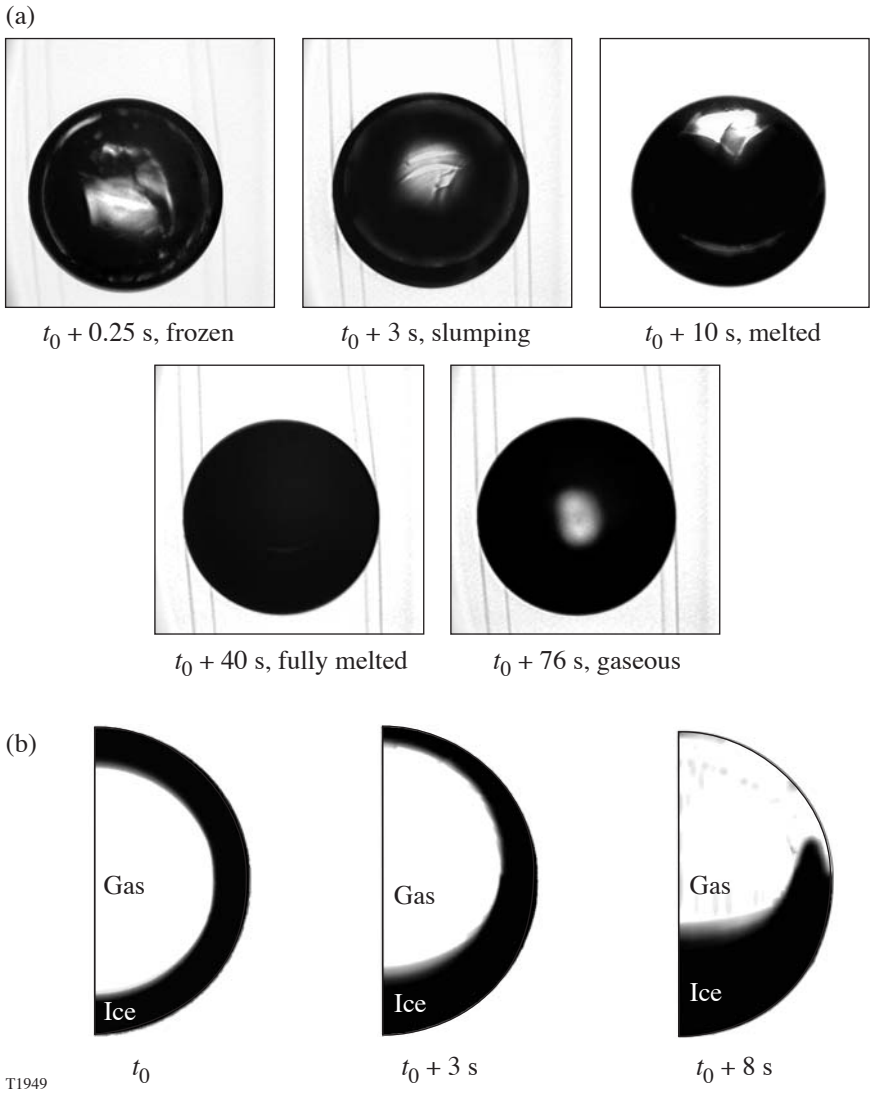


Figure 99.47
(a) Sequence of images showing the ice layer melting and slumping when the thermal shrouds were retracted; (b) calculated response of the ice when the shrouds are removed. The heat absorbed in the plastic caused the target to melt and slump in the same time period that was observed experimentally.

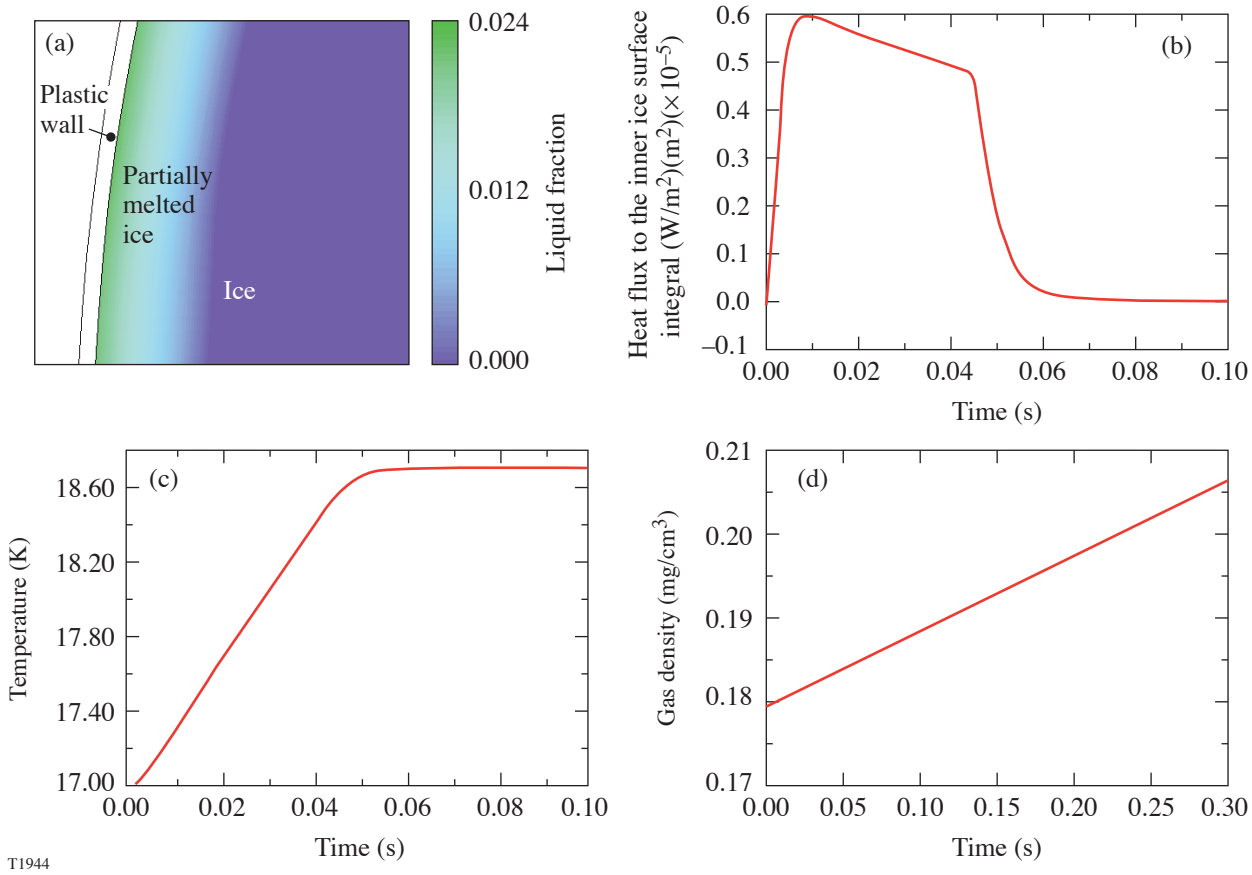


Figure 99.48
Calculated behavior of a cryogenic target when the thermal shroud is removed. (a) Liquid fraction of the outer region of a cryogenic target 0.1 s after being exposed to ambient radiation; (b) calculated heat flux to the inner ice surface; (c) rate of temperature increase of the inner ice surface; (d) density change of the gas in the center of the target.

**Summary and Conclusion**

High-quality cryogenic targets possessing an ice roughness averaging 1.2 $\mu$m for all modes, and for the entire surface, have been demonstrated. These values were achieved by controlling the thermal environment sufficiently to achieve a single initial ice crystal that subsequently grew slowly. A portion of this roughness may be attributable to the nonuniform irradiation of the target caused by the presence of the target-entry hole in the layering sphere. The correlation between this crystal growth phase and the extrinsically controllable parameters (heat flow into and out of the target) has been discussed in terms of the temperature environment within the target. These parameters provide guidelines for a more-complex protocol for controlling the solidification process.

The ice-layering process is controllable: the variability in ice roughness, when the same target is repeatedly layered and melted, is ±0.6 $\mu$m. The variability is attributed to intrinsic morphological features within the ice and at the ice/plastic-shell interface, which affects the uniformity of the thermal resistance. The layering process is shown to form a uniformly thick ice layer as evidenced by the ability to form very smooth ice (0.7- to 0.9-$\mu$m-rms roughness), albeit over a small cluster set of the 2-D great circles used to completely characterize a target.

It is possible to cool the target to 2 K below the triple point without changing the target's roughness; however, doing so requires a very slow cooling rate. The target's roughness is not

always unaffected even when using the slow cooling rate. When the roughness does change, it is primarily in the lower-order modes. Allowing the target to anneal for an extended period can reverse the roughening, but this does not guarantee that the smoothness will always recover. The variable behavior is attributed to structural changes that the ice undergoes during cooling and densification—changes that affect the radial thermal conductance sufficiently to influence the final ice thickness for which the inner ice surface must be isothermal.

## ACKNOWLEDGMENT

This work was supported by the U.S. Department of Energy Office of Inertial Confinement Fusion under Cooperative Agreement No. DE-FC52-92SF19460, the University of Rochester, and the New York State Energy Research and Development Authority. The support of DOE does not constitute an endorsement by DOE of the views expressed in this article.

## REFERENCES

1. J. K. Hoffer and L. R. Foreman, Phys. Rev. Lett. **60**, 1310 (1988).
2. G. W. Collins *et al.*, J. Vac. Sci. Technol. A **14**, 2897 (1996).
3. A. Crane and H. P. Gush, Can. J. Phys. **44**, 373 (1966).
4. R. J. Good and G. V. Ferry, in *Advances in Cryogenic Engineering*, edited by K. D. Timmerhaus (Plenum Press, New York, 1963), Vol. 8, pp. 306–310.
5. D. N. Bittner *et al.*, Fusion Technol. **35**, 244 (1999).
6. H. S. Carslaw and J. C. Jaeger, *Conduction of Heat in Solids*, 2nd ed. (Clarendon Press, Oxford, 1959).
7. E. H. Kennard, *Kinetic Theory of Gases, with an Introduction to Statistical Mechanics*, 1st ed. (McGraw-Hill, New York, 1938).
8. G. K. White, *Experimental Techniques in Low-Temperature Physics*, 2nd ed., Monographs on the Physics and Chemistry of Materials (Clarendon Press, Oxford, 1968).
9. D. N. Bol'shutkin, Yu. E. Stetsenko, and L. A. Alekseeva, Sov. Phys.-Solid State **12**, 119 (1970).
10. M. Wozniak, *2003 Summer Research Program for High School Juniors at the University of Rochester's Laboratory for Laser Energetics*, University of Rochester, Rochester, NY, Laboratory for Laser Energetics Report No. 332, NTIS document No. DOE/SF/19460-526 (2004). Copies may be obtained from the National Technical Information Service, Springfield, VA 22161.
11. Fluent USA Inc., Lebanon, NH 03766.
12. R. W. Powers, R. W. Mattox, and H. L. Johnston, J. Am. Chem. Soc. **76**, 5972 (1954).
13. D. S. Metzger and J. R. Gaines, Phys. Rev. **147**, 644 (1966).
14. P. C. Souers, *Hydrogen Properties for Fusion Energy* (University of California Press, Berkeley, 1986).

# KB-PJX: A TIM-Mountable Streaked Imager Based on a Versatile X-Ray Microscope Coupled to a High-Current Streak Tube

## Introduction

Experiments carried out on the OMEGA[1] laser place very stringent requirements on target-chamber diagnostics. For example, the development of early-time hydrodynamic instability measurements in inertial confinement fusion (ICF) targets involves x-ray radiographic techniques that require a diagnostic capable of detecting small perturbation amplitudes and high spatial frequencies. These are observed as variations in the areal density $\rho R$:

$$\rho R(x,y;t) = \int_0^{d(x,y;t)} \rho(x,y,R;t)\,dR, \qquad (1)$$

where, in the simple case of planar geometry, $d(x,y;t)$ is the target thickness (changing with time due to compression and ablation), $x$ and $y$ are the lateral coordinates, $R$ is the coordinate along the diagnostic line of sight, and $\rho$ is the evolving target density. A new x-ray diagnostic system (KB-PJX) has been developed, characterized, and fielded to measure small, high-spatial-frequency perturbations. It is re-entrant and can be mounted in any of the six OMEGA ten-inch manipulators (TIM's) arrayed around the target chamber, greatly increasing the available experimental configurations and reducing the time required for system adjustments.

The KB-PJX is a streaked imager based on the advanced PJX streak tube and a modular optical front end built around a relatively simple Kirkpatrick–Baez[2] (KB) microscope design. It consists of two mechanically distinct modules (Fig. 99.49): the PJX air bubble that houses the streak tube, the CCD and the PJX electronics, and a retractor housing the optical front end. The retractor (Fig. 99.50) makes it easy to service the optics while mounted in a TIM (operations such as replacement of the blast shield protecting the mirrors are common). It also provides a reference base that allows for precise optical coupling of the front end to the PJX. A kinematic mount engages when the retractor is fully extended and provides repeatability in the optical alignment with a precision better than 25 $\mu$m. Another advantage of a retractor module versus a more-permanent fixture is the possibility of replacing the default optical front end with another x-ray optic for some experiments. This design also provides a choice between single and multiple image modes, with the ability to dynami-

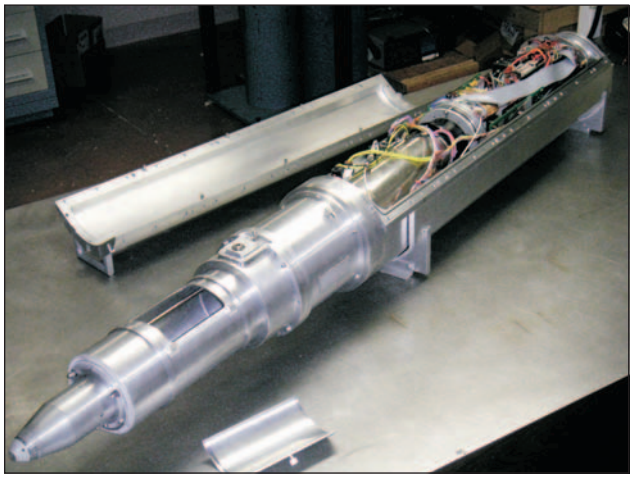

E13165

Figure 99.49
The KB-PJX diagnostic: the retractor in extended position and the PJX air bubble with the lid open.

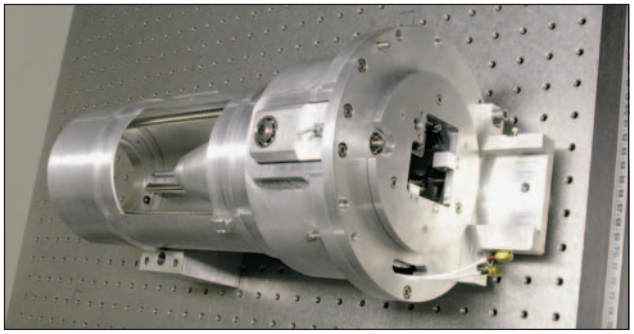

E12907

Figure 99.50
Front-end retractor housing the KB microscope. The side cover is removed to expose the microscope cone.

cally reconfigure for either option with minimal effort. This extends the utility of the streak camera, making its speed, resolution, and collection efficiency available for a broad range of experiments.

The following sections describe/discuss (1) the optical front end and its basic features, design advantages, and expandability; (2) the optical characterization of the microscope in its default configuration; (3) the PJX detector; (4) the resolving capabilities (both spatial and temporal) of the full system; and (5) the performance of the imager in OMEGA hydrodynamic-stability experiments that required high-throughput, high-resolution x-ray diagnostic. Finally, a new technique for measuring the mass ablation rate, a key parameter of the dynamics of ICF implosions, is presented. This method takes advantage of the KB-PJX's ability to provide a continuous high-resolution record of the evolving target areal density.

**Kirkpatrick–Baez (KB) Microscope**

The relative simplicity and optical characteristics[2,3] of a metal-coated KB x-ray microscope make it attractive for imaging high-temperature, laser-generated plasmas. Three implementations[3] of x-ray KB microscopes mounted in the target chamber of the OMEGA laser facility[1] were available prior to this work. All of them were fixed at their respective locations. The instrument described in this article is designed for deployment in an OMEGA TIM—an air-lock device, used to insert diagnostics into the vacuum chamber. Six nearly orthogonal TIM's are available on OMEGA, providing positioning flexibility and rapid reconfiguration of instrumentation for experiments. The microscope serving as the front end of the KB-PJX is a large-grazing-angle ($\theta_i = 2.1°$), four-mirror design (Fig. 99.51) that provides high throughput with a spatial resolution of less than 3 $\mu$m on axis.[4] The relatively large angle of incidence increases the optic's solid angle (~$3 \times 10^{-6}$ sr) and improves its resolution. The optimal resolution[5] of a single mirror in the assembly scales as

$$d_{\text{opt}} \sim \left( \frac{p\lambda^2}{\theta_i} \right)^{1/3}, \tag{2}$$

where $p$ is the object–mirror distance, $\lambda$ is the x-ray wavelength, and $\theta_i$ is the grazing angle. Details of the optical design, choice of coating process, angle of incidence, and mirror characterization are given in Ref. 4. The mirrors have spherical concave surfaces with radii of curvature $R$ = 4250 mm. The surface roughness and the optical figure have been measured in Ref. 4 to be within the specified ranges. The surface roughness after coating was ~4.4-Å rms, and the surface figure (deviation from the best-fit sphere) was measured through interferometry to be $<\lambda/40$ ($\lambda$ = 532 nm). The radius of curvature is sufficiently large (compared to mirror thickness along the optical axis) that each mirror obeys the thin-lens equation

$$\frac{1}{f} = \frac{1}{p} + \frac{1}{q} = \frac{2}{R\sin(\theta_i)}, \tag{3}$$

where $f$ is the focal distance and $p$ and $q$ are the object and image distances. For the KB-PJX geometry, $p$ = 90 mm, $q$ = 560 mm (magnification of about 6), and $f$ = 77.5 mm. These distances are measured from the center of assembly (the contact plane of the perpendicular mirrors), making $f$ an average value. The slight difference in focal distance for the front and back mirrors in a pair (which have different $p$'s and $q$'s) is compensated by a slight change in the incidence angle [see Eq. (3)].

The traditional method of assembling fixed KB x-ray mirrors is optical contacting, a technique yielding strength and longevity. This technique is not amenable to adjustment. Another option for mirror assembly is using special epoxy mixtures to glue the elements together, but any errors can be expensive to fix, especially when dealing with high-cost

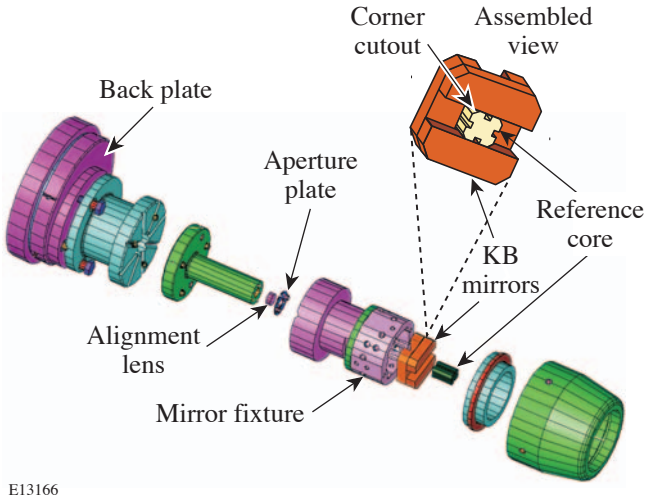


Figure 99.51
Assembled view of the microscope in the mounting mechanism. The mirrors are aligned against the reference core.

superpolished mirror elements. These methods provide robust assembly but limit the flexibility of the resulting optical systems, and fine-tuning their performance after assembly is difficult. The mechanical mirror mount used here allows for easy replacement or repositioning of the individual mirrors. Optimal mirror alignment is achieved by using a central reference core (the 10-mm-long, parylene-coated glass piece shown in Fig. 99.51) with the four Zerodur mirror elements pressed against it with ball plungers. The reference core is the most-unique feature of the optic's mechanical design. Its sides provide reference surfaces for the concave mirror faces, mitigating inaccuracies in the mirror element shape. The core was precisely machined to the specifications validated with numerical ray tracing. The assembly is built around a hollow Zerodur base. The front surface determines a reference plane along the optical axis and establishes the proper object distance for the microscope. An aluminum mirror fixture, mounted on this base as shown in Fig. 99.51, houses the mirror-core assembly and has screw holes for the ball plungers that provide fine mirror positioning and alignment by pressing each mirror against the reference core. Since Zerodur has one of the highest values for the Young's modulus (E = 91 GPa), available in a mirror material, the change of optical surface figure due to pressing stresses is not an issue. The estimated change in the surface figure, given the mirror element geometry and a maximum mounting force of 2.5 N is 0.7 nm, or about 20 times smaller than the acceptable surface figure. This assembly is resistant to vibrations and mechanical shocks associated with the operation of the TIM's. The rectangular profile of the central core provides for co-focusing of the mirrors in each imaging pair by introducing a small difference in the incidence angle (distance to optical axis) that compensates the difference in their position with respect to the object plane.[3] The glass core baffles the direct x rays not participating in image formation and is coated with parylene to reduce x-ray scattering. Both 1-D (reflections from a single mirror) and 2-D (two-mirror reflection) imaging modes are available from apertures in the mounting core. This is accomplished with the rectangular side grooves that define an aperture for single-reflection x rays and corner cutouts, defining apertures for double reflection (Fig. 99.51). For experiments where the photon signal levels are low, the microscope can be configured for use in the 1-D imaging mode with a streak camera as a detector and benefit from the $1/R$ ($R$ being the Ir coating reflectivity) increase in photon flux. Due to its relatively large solid angle,[4] the optic can be used with streak cameras even in the 2-D mode, with the added benefit of precise spatial alignment in the target field of view. A special film pack that mounts to the back of the retractor mechanism and sits at the image plane (i.e., the PJX photocathode location) is available to optimize the fine alignment in 2-D object space. A thin (200-$\mu$m) Ta aperture plate at the back of the optic provides further baffling. The size and position of the apertures on the plate are determined by the mode of operation (1-D, 2-D, single or multiple images). By choosing the appropriate plate, one limits the x rays to those forming the desired image(s). The apertures are large enough not to act as pinholes (~0.5 mm on average) and are equivalent to field stops. This system of easily replaceable aperture plates and thick glass core, when combined with the mirror reflectivity cutoff, acts as an efficient filter for scattered, high-energy x rays that can lower image contrast. The mirror reflectivity is maximized by using superpolished mirror substrates, manufactured by Research Electro-Optics[6] and iridium-coated at LLE. The quality of the deposited Ir film was verified by measuring the mirror's x-ray reflectivity at grazing incidence. By matching the measured reflectivity curve with that predicted by a numerical model,[7] the film density was estimated to be about 98% of the bulk material density. Near-bulk (22.42-g/cm$^3$) density of the iridium film is needed to achieve the optimal reflectivity that strongly depends on the electron number density. The film surface finish was characterized with an atomic force microscope (AFM). The measured surface roughness was used in the numerical fit to the reflectivity curve to determine the film density. With the Ir-coated mirrors in its current configuration, the microscope has a spectral window centered at about 1.5 keV with 0.4-keV FWHM. The finite width of the working energy band is provided by a Be blast shield, acting as a high-pass filter in combination with the cutoff in mirror reflectivity at the high-energy end. This cutoff can be estimated from the classical dispersion theory

$$E_c \sim \frac{he}{\theta_i}\sqrt{\frac{n_e}{\pi m_e}}\,, \tag{4}$$

where $n_e$ is the electron density in the coating, $m_e$ is the electron mass, $h$ is Plank's constant, $e$ is the electron charge (all units in cgs), and $\theta_i$ is the grazing angle in radians. For iridium, the total-reflection cutoff is $E_c \sim 2.36$ keV.

Replacing some or all of the mirror elements can extend or change the working energy band. To address different experimental requirements (an example is given later), the versatility of the KB-PJX will be extended by converting it into a high-photon-energy diagnostic with the addition of two new multilayer designs. These mirrors are designed to be drop-in replacements of the current metal-coated elements. The substrates are made with the same surface roughness and optical

figure as their soft-x-ray counterparts. They have the same geometric shape and work at the same angle of incidence. This simplifies the replacement of elements (or the whole assembly) and allows for dual band imaging, when multilayer and iridium-coated elements are mixed in the same assembly. Obtaining two simultaneous images from x rays in distinct energy bands can be very valuable in situations where large changes in the attenuation length occur within the field of view. The specifications of the new multilayer mirror elements are listed in Table 99.II, and their spectral response is compared to that of the soft-x-ray design in Fig. 99.52. The response is the product of the squared mirror reflectivity $R^2$ and the transmission through a standard 25-$\mu$m Be blast shield. The reflectivity cutoff $E_c$ discussed above, along with the absorption edge at 1.56 keV of the Al debris filter, determines the narrow spectral window of the Ir-coated mirror assembly. The reflectivity is calculated with a numerical algorithm[7] that uses the Fresnel equations and an analytic formula given by V. G. Kohn.[8] In

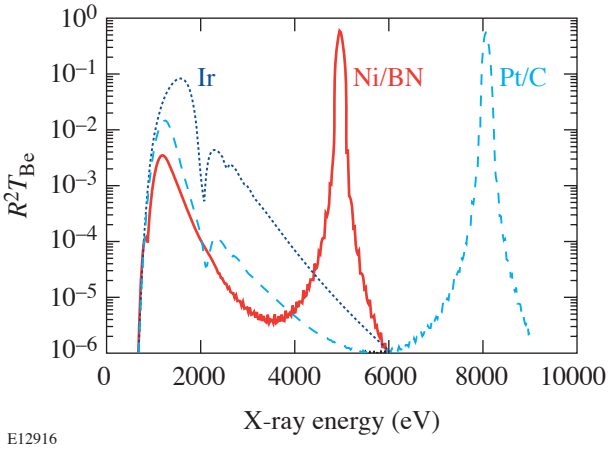


Figure 99.52
Comparison of the spectral windows of two new multilayer (Ni/BN and Pt/C) assemblies (tuned to work at 4.95 keV and 8.05 keV) with the response of the current Ir-coated mirrors.

Table 99.II, $d$ is the period (layer thickness) and $d_1/d$ is the thickness ratio of the metal layer to the period. The last column lists the x-ray energies for which these mirrors are tuned. As with previous designs,[9,10] the spectral windows of the multilayer elements are very narrow (<200-eV FWHM) since the Bragg condition $n\lambda = 2d \sin(\theta_i)$, determining the high reflectivity, is satisfied for a narrow band of wavelengths. This makes them good monochromators but limits the effective field of view of the optic by determining a preferential angle of incidence $\theta_i$. A solution to this limitation is to use graded layer thickness across the mirror surface. Despite its complexity and higher cost, this method is now used routinely with good results.[11] This challenge can also be solved by using a sufficiently broadband backlighter and using the dispersive properties of the mirrors (a range of $\lambda,\theta_i$ pairs that satisfy the Bragg condition will exist). The field of view will then be expanded by angularly dispersing the signal in spatial direction. Since the efficiency of high-energy, broadband backlighters is low, a compound backlighter that emits in several spectral lines must be used. This results in discrete, spatially dispersed signal regions within the expanded field of view. For example, a brass backlighter [75% Cu ($K_a$ = 8048 eV) and 25% Zn ($K_a$ = 8639 eV)] is a good candidate for the 8-keV region. To register comparable intensity levels in the two spatial regions (which will map into the central 400 $\mu$m of the field of view), a two-strip Zn-Cu backlighter can also be used (Fig. 99.53).

### Optic Characterization

After evaluating the reflectivity of each mirror,[4] the mirror assembly was placed in the retracting mechanism that houses the microscope during normal operation and provides proper coupling to the PJX streak tube. Fine alignment and resolution evaluation were performed under vacuum in an x-ray test chamber. A film pack loaded with Kodak direct exposure film (DEF) was placed at the image plane where the PJX photocathode would be located during normal operation. Several test exposures were taken using a tungsten target bombarded with

Table 99.II: Characteristics of the new, multiplayer, high-energy KB-PJX mirrors.

| Type | Layer | $D$ (nm) | Thickness Ratio $d_1/d$ | X-Ray Energy (keV) |
|---|---|---|---|---|
| Ni/BN | 60 | 3.5 | 0.4 | 4.95 |
| Pt/C | 100 | 2.13 | 0.37 | 8.05 |

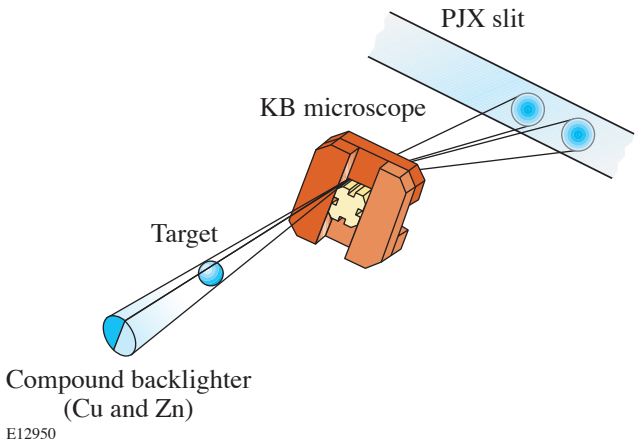


Figure 99.53
The field of view of a multilayer KB microscope is expanded by using a strip backlighter. The x rays are energy dispersed into two distinct regions at the image plane.

a 10-kV electron beam. Images of a 400-mesh grid as well as knife-edge images were acquired and analyzed to determine the system's modulation transfer function (MTF) and compare it with that predicted by numerical ray tracing[4] and the MTF of an 8-$\mu$m-pinhole array. Figure 99.54(a) shows a typical film image of a 400-mesh grid, digitized with a Perkin–Elmer photodensitometer with a 5-$\mu$m scanning aperture. A horizontal lineout through the image is shown in Fig. 99.54(b), where the profile was intensity converted using a semi-empirical formula[12] in the instrument spectral window centered around 1.5 keV. The MTF was calculated from both the grid images and an image of an opaque tantalum foil edge (knife edge). The edge response function (and the MTF, respectively) is treated independently for the two perpendicular directions determined by the grid lines. The MTF shown in Fig. 99.55 is averaged over the central 200 $\mu$m of the field of view and calculated by a method similar to that outlined in Ref. 3. After taking into account the system magnification $M = 6$, the diffraction MTF predicted by numerical ray tracing[4] was plotted on the same graph for comparison. It matches the shape of the edge MTF remarkably well. The slight deviations are most likely due to uncertainties in the determination of the line spread function from the edge data. It should be noted that the availability of a larger shadow region on the edge image provides for a more-accurate estimate of the transfer function for high spatial frequencies. Three MTF curves calculated from the edge image (for three different field positions) are shown on Fig. 99.56, along with the on-axis MTF of an 8-$\mu$m pinhole for comparison. In the central 600 $\mu$m of the field of view, the microscope has higher resolution than the pinhole. One can

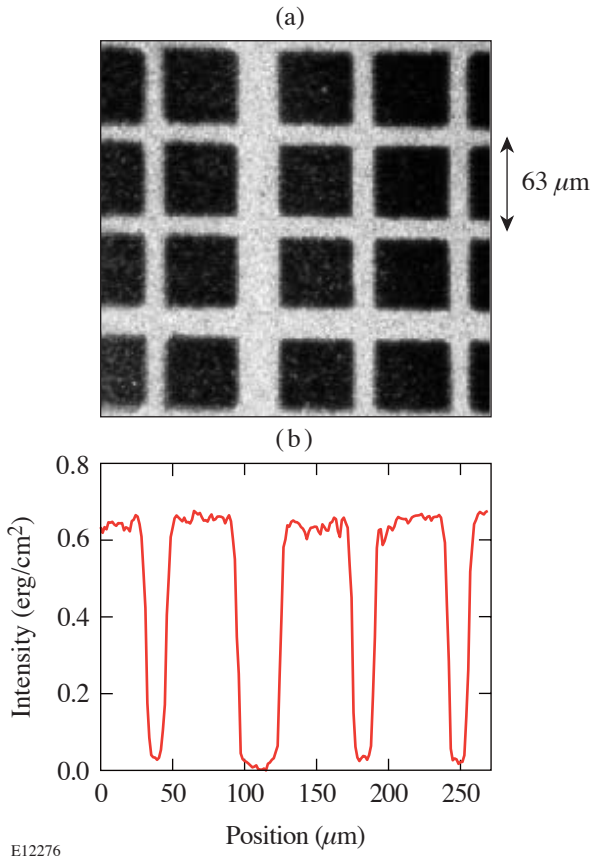


Figure 99.54
Film image (a) of a 400 LPI SEM grid and horizontal intensity profile (b) taken through the middle of it.

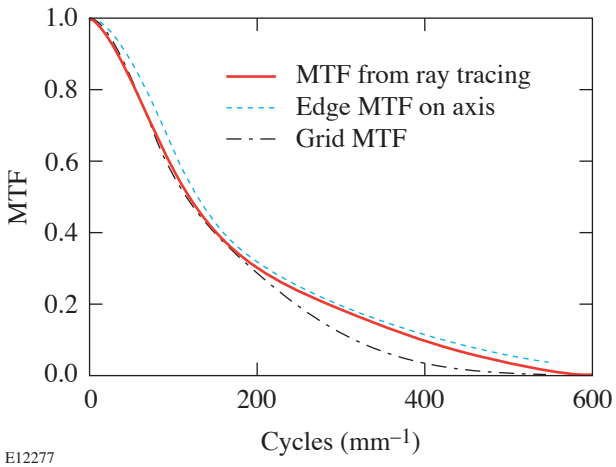


Figure 99.55
Modulation transfer function calculated from a grid image and vertical (perpendicular to the streak tube slit) knife edge.

also see the expected deterioration of resolution toward the edge of the field of view, where the resolution is comparable to the 8-$\mu$m pinhole.

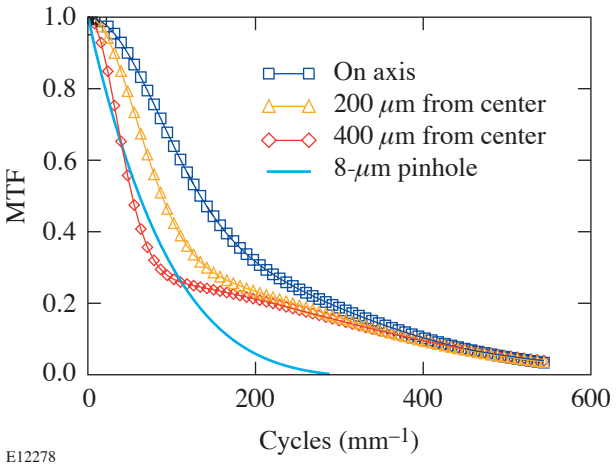


Figure 99.56
Modulation transfer functions calculated from an edge image at three different field positions are compared to the MTF of an 8-$\mu$m pinhole at a comparable magnification of 8×.

### PJX Streak Tube

The instrument's detector combines several state-of-the-art features that were previously not combined into a single detector. The PJX streak tube is the result of collaboration between the Commissariat à l'Énergie Atomique (CEA), Photonis (formerly Philips Photonique, located in Brive, France), and LLE. The final electron-optics design was completed by LLE. The streak tube is physically large—13 cm in diameter and 50 cm long. The camera is routinely operated with a 15-kV cathode–anode potential that can be increased to 25 kV. A quadrupole doublet, combined with three octupole correctors that minimize the aperture aberrations, focuses the accelerated photoelectrons. The phosphor screen is fiber-optic–coupled directly to a back-illuminated CCD and has a 24-mm × 24-mm output format. The CCD has a 13.5-$\mu$m individual pixel size. The system gain[13] is 150 CCD electrons per streak-tube electron, enabling single-electron detection with a signal-to-noise ratio (SNR) >3. There is no image intensifier in the camera, eliminating an additional source of noise. The streak tube can operate in either of two modes, determined by the polarity of the quadrupole doublet: in standard mode, the input slit size is 60 mm by 0.4 mm, with a demonstrated current-handling capability of 12.5 mA, while in inverse mode, the effective slit size is reduced to 6 mm by 0.09 mm with 1.5-mA peak current. In standard mode, the electron-optic spatial magnification is 0.4× and the temporal is 4×. Switching to inverse mode reverses the spatial and temporal direction magnifications. The streak tube is designed to mount in the OMEGA TIM enclosed in its own air bubble that houses the tube and the water-cooled CCD camera. The power, control, and communication electronics are internal to the air bubble, making the PJX a highly integrated self-contained instrument (Fig. 99.57). Cooling the CCD camera and power electronics that must operate inside the vacuum chamber is simplified by this design. A fan drives air circulation inside the bubble, and the heat is extracted through a chilled-water line. Communication to and from the camera is via an optical fiber. The PJX is a heatsink, not a heat source, inside the vacuum chamber. Other advantages of the air-bubble concept are better electromagnetic interference (EMI) shielding, the freedom to use vacuum-incompatible materials for high-voltage insulation, and the protection of many serviceable components from DT contamination.

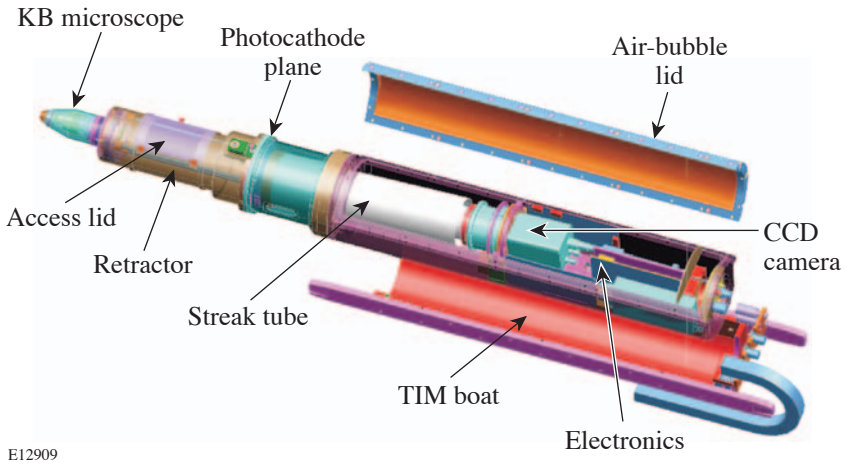


Figure 99.57
The PJX streak camera is kept at air in a "bubble" (shown with the lid open). This simplifies the cooling of both the CCD and power electronics.

The calculated time resolution of the PJX tube is less than 5 ps. The finite width $D$ of the line spread function divided by the sweep speed $v_{swp}$

$$\Delta t_{st} = \frac{D}{v_{swp}} \tag{5}$$

is one of the primary factors that determine this.

For the inverse mode and an 8-ns sweep, $\Delta t_{st}$ is 16-ps FWHM; it is proportionally less for faster sweep speeds. The energy dispersion of the secondary photoelectrons creates a spread in the transit time of the accelerated electrons,

$$\Delta t_{\varepsilon} = f\left[V(z), \vec{v}_0, x_0, y_0\right], \tag{6}$$

where $V(z)$ is the axial potential, $\vec{v}_0$ is the initial velocity vector of the secondary electrons, and $(x_0,y_0)$ is the initial point of emission. $\Delta t_{\varepsilon}$ has been calculated to be 1.26 ps on axis for the KBr photocathode, increasing to 3.0 ps for the extreme off-axis locations. Assuming Gaussian response curves, the FWHM of the combined temporal line-response function will then be given as the Gaussian convolution of the two effects:

$$\Delta t \cong \sqrt{\Delta t_{st}^2 + \Delta t_{\varepsilon}^2} \cong 16 \text{ ps}. \tag{7}$$

This value ($\Delta t \sim$ 16-ps FWHM) well represents the measured temporal resolution of the PJX in inverse mode. The number of time-resolution elements in the time window is ~300, based on a 50% contrast-ratio criterion.

It is currently difficult to measure the time-resolution limit of the PJX because of the lack of sufficiently short x-ray pulses at LLE. The resolution calculated in Eq. (7) was verified using 100-ps laser pulses available on OMEGA. A train of six 100-ps Gaussian, UV pulses separated by 1 ns illuminate a U backlighter to produce the x-ray pulses shown in Fig. 99.58(a) (recorded in inverse mode). Except for the first x-ray pulse, two overlapped OMEGA beams were used to generate each of the pulses. There are small aberrations away from the optical axis (center of the image), due to the spherically curved phosphor screen. This effect is characterized and corrected with an image-processing algorithm. A spatial average of the third x-ray pulse is shown in Fig. 99.58(b), along with the UV pulse that generated it. The time axis is calibrated, using a train of eight UV fiducial pulses fed into the camera with a fiber and recorded at the edge of the photocathode. The solid curve is the actual x-ray pulse, convolved with the time response (line-spread function) of the PJX. It provides a measure of the streak camera's time resolution. The only other information currently available is the shape (dashed curve) of the UV laser pulse that generated the x rays; however, the time resolution of the P510 streak camera (that recorded those) is of the order of the calculated PJX resolution. Using the UV pulse information is further complicated by the time history of the conversion of UV light to x rays. A phenomenological x-ray–conversion formula, such as that from Ref. 14, can be used to relate the intensity $I_{UV}$ of UV light with the converted x-ray intensity $I_x$, using a power law $I_x \propto I_{UV}^{\gamma}$. With a value of $\gamma \sim 3.4$ as determined in Ref. 14 and using the FWHM $D_{UV}$ = 109 ps of the recorded UV backlighter pulse, the $\sigma$ parameter of the x-ray–converted UV Gaussian $I_x(t) \sim \exp\left[-(t-t_0)^2 / \left(2\sigma_{UVx}^2\right)\right]$ is given by

$$\sigma_{UVx} = \frac{\sigma_{UV}}{\sqrt{\gamma}} = \frac{D_{UV}}{2\sqrt{2\gamma \ln(2)}} \cong 25.1 \text{ ps}. \tag{8}$$

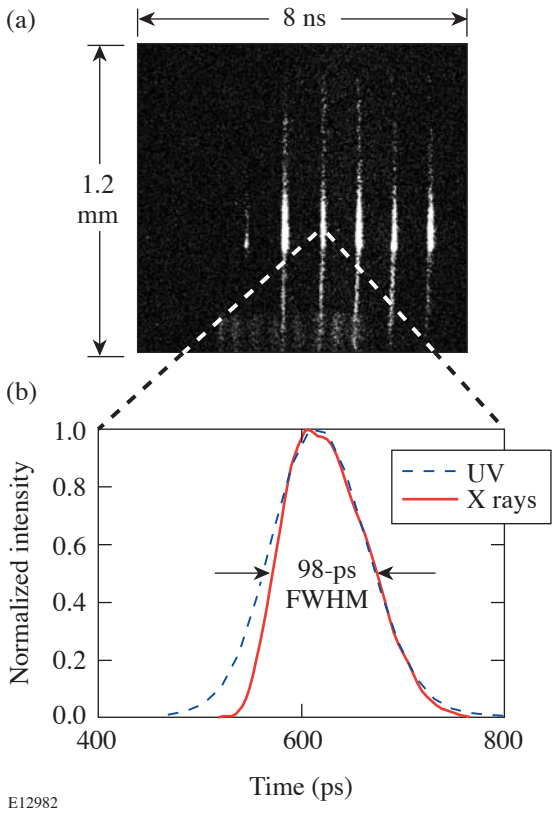


Figure 99.58
(a) A train of short backlighter pulses (100 ps) recorded with the KB-PJX in inverse mode and (b) spatial average of one such pulse and the generating UV pulse (dashed line).

The measured x-ray-intensity profile is fit by a combination of a Gaussian and an exponential decay function to account for the emission of x rays during the finite cooling time of the plasma. In Fig. 99.58(b), one can clearly see the asymmetry of the pulse due to this effect. The $\sigma$ value of the Gaussian is found from the fit to be $\sigma_x = 32$ ps. Because this pulse is a convolution of the PJX time-response function with the incident x-ray pulse, the width of the time-response function is

$$\sigma_{\mathrm{PJX}} = \sqrt{\sigma_x^2 - \sigma_{\mathrm{UV}x}^2} \cong 19.8 \pm 4.0 \text{ ps}, \tag{9}$$

where the main contribution to the uncertainty comes from the determination of the power index $\gamma$. This result is consistent with Eq. (7).

The point-spread function (PSF) of the PJX streak camera in inverse mode has been measured to be ~18 $\mu$m (versus 125 $\mu$m in standard mode) at the photocathode plane. This suggests that the camera and microscope will have a comparable effect on the resolution limit at the system magnification of 6×. The total point-spread function is a convolution of the two similar PSF's; therefore the resolution limit of the full instrument is expected to increase by a factor of $\sqrt{2}$ from the microscope resolution of 3 $\mu$m to 4.5 $\mu$m. The magnification of the electron optics is 4×, resulting in a total magnification of 24× to the CCD plane. The sharp edge of a Pt foil was imaged to measure the MTF of the complete KB-PJX system. The resulting MTF curve, as calculated from the edge data, is shown in Fig. 99.59. The curve was averaged over several time slices to improve the signal-to-noise ratio. For comparison, the MTF's of the microscope, calculated on axis and 200 $\mu$m away from it, are plotted. It was verified from the target-positioning images that the edge was located 150 to 200 $\mu$m off axis, which explains the good match between the edge MTF and the microscope curve at 200 $\mu$m from the center. The expected $\sqrt{2}$ widening of the system PSF as compared to the optic's alone is detectable in this comparison. In this configuration the KB-PJX was used in a series of hydrodynamic stability experiments[15] requiring high throughput (thick CH targets were driven with ten OMEGA beams) and high resolution. The instrument provided a continuous record of the evolving single-mode (typical wavelengths of 20 $\mu$m) areal-density perturbations at the ablation front of these targets.

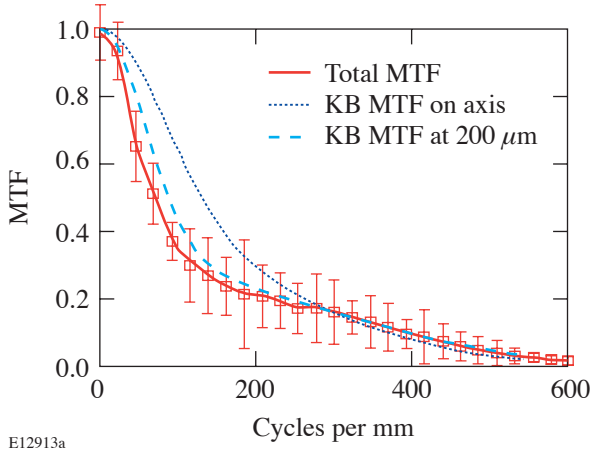


Figure 99.59
System MTF of the KB-PJX, calculated from its edge-response function and compared to the microscope MTF's at two field positions.

## OMEGA Experiments

This KB optic coupled to the PJX streak camera has been used successfully to measure the time evolution of the areal density of a perturbed planar target during shock transit (prior to the arrival of the rarefaction wave at the laser-illuminated surface). A sinusoidal perturbation is imposed on the side of the target illuminated by the laser. The goal of the experiment is to measure the evolution of the perturbations and to compare it to various models. A continuous record of the evolution of target areal density (modulated by the ablation-front mass perturbations) was obtained (Fig. 99.60), showing phase inversion in the single-mode perturbations as part of a period of their oscillatory evolution. The temporal oscillations at the laser-illuminated surface are faster for mass perturbations with a shorter wavelength. The oscillation frequency is given by[15]

$$\omega = kV_a\sqrt{\rho_a/\rho_{\mathrm{bl}}}, \tag{10}$$

where $k$ is the spatial modulation wave number, $\rho_a$ and $\rho_{\mathrm{bl}}$ are, respectively, the densities in the shock-compressed and blowoff plasma regions, and $V_a$ is the ablation velocity (defined as the mass ablation rate divided by the density $\rho_a$). This sets challenges for the diagnostics since one has to go to shorter wavelengths to observe a full oscillation before rarefaction breakout, when the onset of the Rayleigh–Taylor instability overpowers the oscillatory stabilization effect. Several limitations make a simple increase of the target thickness (i.e., shock transit time) impractical; these include (1) limits in backlighter photon flux, laser pulse duration (total energy) of the backlighter, and drive beams; and (2) limits in the target modulation depth driven by the requirement to have the single-mode perturbation amplitude much smaller than its wavelength in order to remain in the linear regime of evolution, etc. All of these factors are interdependent, restricting the parametric

space of the experiment. The KB-PJX, having both high spatial resolution and high throughput, is the appropriate diagnostic for these experiments. Compared to a previous experiment on the subject,[16] where part of an oscillation period for perturbation modes with wavelengths down to 30 $\mu$m was observed, the use of the KB-PJX allowed registering the evolution of perturbations with 20- and even 10-$\mu$m wavelengths, at the same target thickness and backlighter of equal or lower efficiency. In the experiments, CH targets were driven by ten of OMEGA's ultraviolet beams with a maximum intensity of $4\times10^{14}$ W/cm$^2$ on target in a 1.5-ns, fast-rise, flattop pulse. They were backlit with x rays produced by a U target, illuminated by another 11 OMEGA beams for 2 ns. A 25-$\mu$m-thick Be blast shield filtered the x-ray self-emission from the CH foils. The backlighter and target were separated by a 5-$\mu$m-thick Al debris shield, whose transmittance along with that of the Be foil and energy-dependent mirror reflectivity forms the working energy band, as shown in Fig. 99.52. The backlighter and driver pulse widths were chosen so that the camera registered the target areal density for the duration of the shock transit, up to the arrival of the rarefaction wave at the front of the compressed target. The streaked images, such as the one in Fig. 99.60, allow us to verify the theoretical models and validate the capabilities of the imager. The streaked microscope met its resolution and throughput requirements, making it possible to measure the perturbation oscillations.[15] Resolution estimates from recorded data confirm that the imager can resolve modulations with a characteristic wavelength of 5 to 7 $\mu$m and an optical depth above 0.05 (about twice the typical noise level). Currently, the optic is also being used together with the PJX streak tube in the development of a side-on radiographic technique[17] for equation-of-state (EOS) experiments.

**Mass-Ablation-Rate Measurements with the KB-PJX**

The ability of the KB-PJX to provide a continuous temporal record (with high time resolution) of the target's optical depth can be used in a novel technique to measure the time evolution of the mass ablation in an ICF target. The level of self-emission of the ablated hot plasma in a CH target driven by ten of OMEGA's beams was measured without backlighting, using only the x rays emitted from its hot corona and attenuated through the remainder of the target. The measured intensity profile $I_{SE}$ is shown in Fig. 99.61 along with the time history $I_{BL}$ of an undriven, backlit target and one from a target that is both driven and backlit. Due to ablation, the backlighter x rays see less optical depth at later times since the ablated material loses its opacity rapidly by heating up as it moves along the temperature gradient, away from the ablation front. The hot, low-density corona is approximately transparent to the 1.5-keV x rays up to the ablation front, where the largest temperature jump occurs. In time, the growing ablated mass reduces the total areal density of the target. Figure 99.61 shows an increasing difference between the intensity $I_D$ from the backlit and driven target (red curve) and the sum $I_{SE} + I_{BL}$ (blue curve) of intensities from the driven-only and backlit-only foils. Measuring the optical-depth evolution of the target material not yet ablated allows the mass-ablation rate to be inferred. Consider these three intensity terms as functions of time:

$$I_{BL}(t) = I^0_{BL}(t)e^{-\mu_0\rho_0 d_0} = I^0_{BL}(t)e^{-\mu_0 m_0}\ , \qquad (11)$$

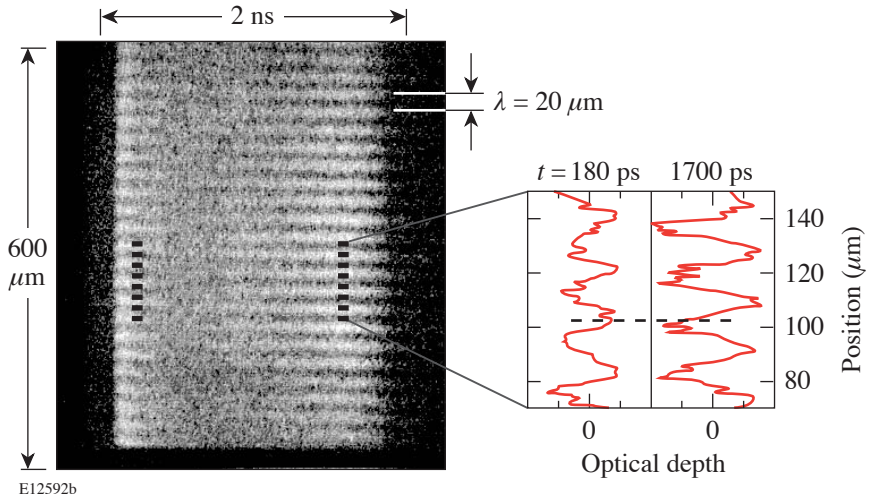


Figure 99.60
Streaked image of directly driven planar CH target with 60-$\mu$m thickness and single-mode ($\lambda = 20\ \mu$m) surface modulations on the front. Spatial profiles are shown at $t$ = 180 and 1700 ps, respectively.

$$I_D(t) = I_{SE}(t) + I^0_{BL}(t)e^{-\mu_0(m_0-\rho_0 U_s t)-\mu_c\left(\rho_0 U_s t-\int_0^t \dot{m}dt'\right)}. \quad (12)$$

In Eq. (12) the spectrally weighted mass absorption coefficient $\mu_c$ in the compressed region (in the second exponential term) is assumed to change very little from its uncompressed-target value $\mu_0$. The other approximation made in Eq. (12) is that the optical depth $\mu_{abl}m_{abl}$ of the ablated material is negligible (due to its low opacity). Both assumptions are supported by data from the 14000-group APL opacity tables,[18] for density and temperature profiles in the compressed and ablation regions, obtained from 1-D hydrodynamic simulations. Solving the last equation for the ablation rate yields

$$\dot{m}(t) = \frac{d(\Delta OD)}{\mu_0 dt} = \frac{d\left[\ln\dfrac{I_D(t)-I_{SE}(t)}{I_{BL(t)}}\right]}{\mu_0 dt}. \quad (13)$$

All of the intensities are measured and $\mu_0$—the mass absorption coefficient of the cold target—is also readily available. Even though the various intensities are measured in different shots, the results can be combined to estimate the mass ablation rate. The growing optical depth ΔOD of the ablated mass is shown in Fig. 99.62. Due to the intensity-pulse-shape dissimilarities, it is reasonable to get an average value of the time-dependent mass-ablation rate by fitting ΔOD with a straight line and determining its slope. The slope as determined from the fit is 0.77 ns$^{-1}$. Using the spectrally averaged attenuation length $\lambda = 12$ μm and the density of cold CH $\rho_0 = 1.06$ g/cm$^3$ to obtain $\mu_0 = (\rho_0\lambda)^{-1}$, one finds the ablation rate to be ~0.98 mg/(cm$^2$ ns), in line with the average value obtained from simulations, using the measured pulse shapes. A more-precise experiment can be performed if a single shot is used to record both $I_D$ and $I_{BL}$, while eliminating the target self-emission. This can be done if a high-energy backlighter is used in combination with the multilayer mirrors discussed in the **Kirkpatrick–Baez (KB) Microscope** section (p. 184). At 5 keV, for example, both the thicker target and the microscope's spectral window will filter out the soft-x-ray self-emission. A thicker target will be used since target thickness must be comparable to the spectrally weighted attenuation length (cold material) for maximum sensitivity to ablation. If the ablating target does not occupy the entire field of view, the intensity of the unattenuated backlighter can be recorded at the same time by recording part of the backlighter beam directly. This will allow the calculation of the mass-ablation-rate evolution curve from a single shot.

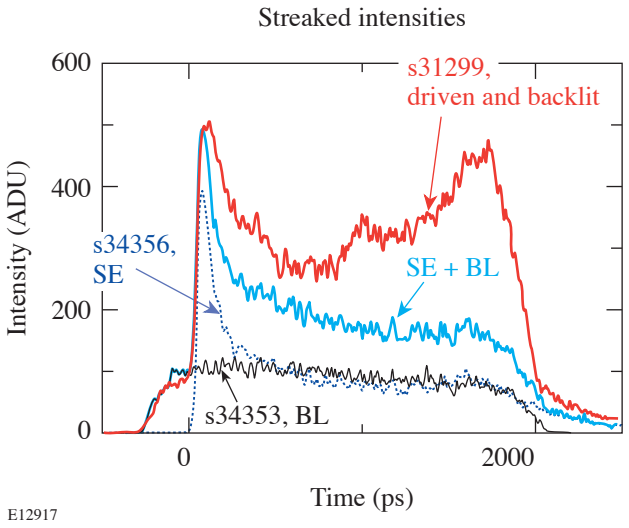


Figure 99.61
Intensity profiles of x rays transmitted through a 40-μm-thick CH target, which is driven and backlit (red curve), backlit only (black curve), and driven only (dotted curve). The sum of the thin solid and dotted lines (blue curve) does not match the solid, showing the effect of ablation.

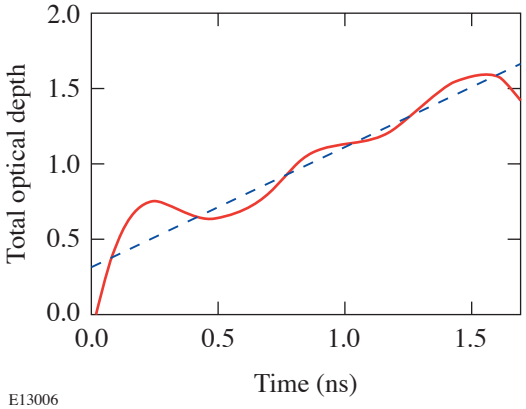


Figure 99.62
The difference in optical depth (ΔOD) (solid curve) grows due to mass ablation. An average value of the mass ablation rate is obtained by fitting the data with a straight line.

## Conclusions

This article, in combination with Ref. 4, has shown that the KB-PJX is a versatile instrument, well suited for ICF experiments that (1) need a high-throughput diagnostic with high temporal and spatial resolution in x-ray radiography configurations and (2) can be set up for different x-ray-energy ranges. The imager has high temporal (less-than-20-ps) and spatial (better-than-5-$\mu$m) resolution in inverse mode, while demonstrating high-current-handling capabilities, matching the throughput of the optical front end. The PJX streak tube has met the experimental requirements, matching or surpassing the projected spatial (~18-$\mu$m) and temporal (<20-ps) resolution, while delivering high peak current in both modes of operation.

## ACKNOWLEDGMENT

One of the authors (O. V. Gotchev) wishes to thank Dr. R. S. Craxton for his valuable comments on the opacity of CH plasma at various temperatures and densities. This work was supported by the U.S. Department of Energy Office of Inertial Confinement Fusion under Cooperative Agreement No. DE-FC52-92SF19460, the University of Rochester, and the New York State Energy Research and Development Authority. The support of DOE does not constitute an endorsement by DOE of the views expressed in this article.

## REFERENCES

1. T. R. Boehly, D. L. Brown, R. S. Craxton, R. L. Keck, J. P. Knauer, J. H. Kelly, T. J. Kessler, S. A. Kumpan, S. J. Loucks, S. A. Letzring, F. J. Marshall, R. L. McCrory, S. F. B. Morse, W. Seka, J. M. Soures, and C. P. Verdon, Opt. Commun. **133**, 495 (1997).
2. P. Kirkpatrick and A. V. Baez, J. Opt. Soc. Am. **38**, 766 (1948).
3. F. J. Marshall and Q. Su, Rev. Sci. Instrum. **66**, 725 (1995); F. J. Marshall, M. M. Allen, J. P. Knauer, J. A. Oertel, and T. Archuleta, Phys. Plasmas **5**, 1118 (1998).
4. O. V. Gotchev, P. A. Jaanimagi, J. P. Knauer, F. J. Marshall, D. D. Meyerhofer, N. L. Bassett, and J. B. Oliver, Rev. Sci. Instrum. **74**, 2178 (2003).
5. G. R. Bennett, Rev. Sci. Instrum. **70**, 608 (1999).
6. Research Electro-Optics, Inc., Boulder, CO 80301.
7. E. M. Gullikson, Center for X-Ray Optics, Materials Sciences Division, E.O. Lawrence Berkeley National Laboratory, available at http://cindy.lbl.gov/optical_constants/; B. L. Henke, E. M. Gullikson, and J. C. Davis, At. Data Nucl. Data Tables **54**, 181 (1993).
8. V. G. Kohn, Phys. Status Solidi B **187**, 61 (1995).
9. J. H. Underwood and T. W. Barbee, Jr., Appl. Opt. **20**, 3027 (1981); J. H. Underwood, T. W. Barbee, Jr., and C. Frieber, Appl. Opt. **25**, 1730 (1986).
10. F. J. Marshall and G. R. Bennett, Rev. Sci. Instrum. **70**, 617 (1999).
11. Osmic, Inc., Auburn Hills, MI 48326.
12. B. L. Henke *et al*., J. Opt. Soc. Am. B **3**, 1540 (1986).
13. S. Ghosh, R. Boni, and P. A. Jaanimagi, "Optical and X-Ray Streak Camera Gain Measurements," submitted to Review of Scientific Instruments.
14. F. J. Marshall, J. A. Delettrez, R. Epstein, R. Forties, R. L. Keck, J. H. Kelly, P. W. McKenty, S. P. Regan, and L. J. Waxer, Phys. Plasmas **11**, 251 (2004).
15. O. V. Gotchev, T. J. B. Collins, V. N. Goncharov, P. A. Jaanimagi, J. P. Knauer, and D. D. Meyerhofer, "Experiments on the Ablative Richtmyer–Meshkov Instability in Planar Direct-Drive Targets on OMEGA," to be submitted to Physics of Plasmas.
16. Y. Aglitskiy *et al*., Phys. Rev. Lett. **87**, 265001 (2001).
17. L. B. Da Silva *et al*., Phys. Rev. Lett. **78**, 483 (1997).
18. W. F. Huebner *et al*., Los Alamos National Laboratory, Los Alamos, NM, Report LA-6760-M (1977).

# A High-Energy, High-Average-Power Laser Using Nd:YLF Rods Corrected by Magnetorheological Finishing

## Introduction

Optical parametric chirped-pulse amplification[1,2] (OPCPA) is well suited for the front end of modern petawatt glass laser chains.[3] The broadband gain available with OPCPA at a wavelength of 1053 nm offsets the gain narrowing that occurs in large Nd-doped glass amplifiers.[4] It can be scaled to large energies,[5] in contrast to the practical limits imposed by the mode volume of a laser cavity in regenerative amplification. Lastly, the OPCPA process is prepulse free[6] and can produce gains of up to $10^9$ using a relatively simple optical system, which minimizes beam distortions.

Recently, we have shown that a high conversion efficiency of 30% and stable output energies[7] can be achieved in an OPCPA system using pump-laser pulses with uniform intensity profiles in both space and time. This significantly reduces the pump-laser energy requirements. Following this approach, an OPCPA system design[8] was proposed to amplify chirped pulses to more than 400 mJ while limiting the pump-laser requirement to approximately 1 J at a wavelength of 527 nm.

Several laser-amplifier architectures are capable of producing high pump-pulse energies. High-energy, *Q*-switched, unstable laser oscillators are commercially available and involve a relatively simple setup, but spatiotemporal coupling in the pump pulse limits the useful energy ultimately available for the OPCPA process, which in turn limits OPCPA conversion efficiency.[9] Master-oscillator, power-amplifier (MOPA) schemes utilizing amplifiers with progressively larger apertures cause large square-pulse distortions that pose a significant challenge when a temporally square output pulse is desired. More generally, amplification schemes that conjugate both high gain and large depletion of the gain medium limit the ability to control the pump-laser parameters. On the contrary, multipass geometries that utilize the full aperture of a gain medium avoid this difficulty since heavy gain saturation occurs only in the final passes. Multipass amplifiers also offer more-compact layouts and reduce pumping system complexity compared to linear MOPA systems.

Various active and passive multipass architectures offer unique advantages and disadvantages. Passive schemes with Faraday isolators or quarter-wave plates provide the simplest operational scheme but limit the number of passes in the gain medium. The number of passes in linear[10] and ring[11] laser-amplifier cavities can be selected by timing the *Q*-switching and cavity dumping with an intracavity Pockels cell, although this increases operational complexity. Angular multiplexing[12] eliminates the need for active switching but, as a result, is a less-flexible technique.

A limited number of gain media are suitable for high-energy laser applications. Among them, Nd:YAG was considered but not selected because of its high-stimulated emission cross section (low stored-energy density) and poor thermal behavior characteristics, such as a high thermal lensing effect and a high thermally induced stress birefringence. Nd:YLF operating at 1053 nm provides several advantages: First, a high saturation fluence (low-gain cross section) allows working at high laser fluence while minimizing pulse distortion. Second, strong static birefringence practically eliminates the impact of thermally induced stress birefringence, and Nd:YLF has a relatively weak thermal astigmatism. A final practical advantage is that it matches the gain peak of Nd-doped phosphate laser glasses, which permits employing a common front end for both pumping OPCPA systems and seeding large glass amplifiers used in large laser-fusion facilities. Unfortunately, the transmitted-wavefront quality of commercially available, large-aperture Nd:YLF laser rods was not previously sufficient for pumping an OPCPA system.

This article describes a multijoule laser amplifier based on a crystal large-aperture ring amplifier (CLARA) that is capable of producing high-energy pulses with the parameters required for a highly efficient OPCPA. The CLARA design uses 25.4-mm-diam Nd:YLF rods that can operate at a 5-Hz repetition rate because of their good thermal properties. Surface figure corrections were polished on one face of each CLARA rod using magnetorheological finishing (MRF)[13] to

compensate for the bulk inhomogeneities that cause the transmitted-wavefront errors. Correcting these errors increases the usable aperture of the Nd:YLF laser rods, which consequently increases the energy extraction from the laser rods. To our knowledge, this is the first reported application of MRF processing to correct the transmitted wavefront of a laser gain material.

The following sections (1) present the process and experimental realization of correcting the transmitted wavefront of a Nd:YLF laser; (2) describe the design of the CLARA laser amplifier, including an interferometric alignment technique that ensures that the MRF-corrected laser rods are properly aligned; (3) present experimental results demonstrating the benefits of the MRF correction on amplifier performance; and (4) discuss the potential applications of MRF to crystal laser material.

**Magnetorheological Finishing of Nd:YLF Rods**

Nd:YLF rods that are 25 mm in diameter represent the state of the art in crystal growth. Growing these laser rods with high optical-wavefront quality is extremely challenging, if not impossible. Even with the end-faces polished perfectly flat, up to several microns of wavefront distortion in the bulk crystal is typical. This makes these rods unsuitable for use in a high-energy laser system because these phase errors quickly turn into hot spots as the beam propagates. Additionally, large phase gradients introduced by the rod aberrations produce a beam divergence that phase-matches poorly in nonlinear optical processes, such as frequency doubling and OPCPA.

To overcome these limitations, surface figure corrections can be polished on one face of a laser rod using MRF to compensate for the bulk inhomogeneities that cause the transmitted wavefront errors, as shown schematically in Fig. 99.63. Correcting these errors increases the usable aperture of the Nd:YLF laser rods, which consequently increases the energy extraction.

The MRF process utilizes a small polishing spot formed on a rotating wheel carrying a ribbon of magnetorheological (MR) fluid that contains polishing abrasive, as shown in Fig. 99.64. As the ribbon of MR fluid passes between the poles of a powerful electromagnet, the MR fluid viscosity increases and distributes the polishing abrasive at the surface of the ribbon, where it produces a deterministic, two-dimensional removal-rate pattern. Once the removal-rate function for a material is characterized, a prescribed surface figure correction can be achieved by controlling the dwell time of the optic at each point on the surface as it moves under the wheel in

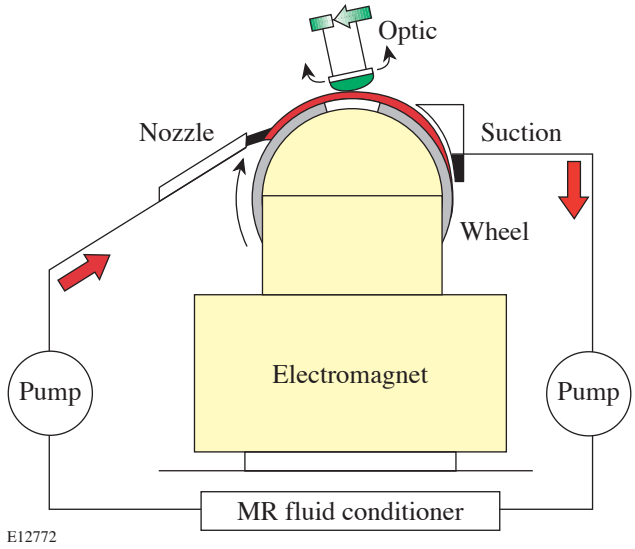


Figure 99.64
MRF principle. The MRF fluid is pumped to a rotating wheel that passes between the poles of a powerful electromagnet. In the magnetic field, the MRF fluid viscosity increases to a nearly solid consistency, which forms a sub-aperture polishing tool. After passing through the electromagnet, the MRF fluid is reconditioned and recycled.

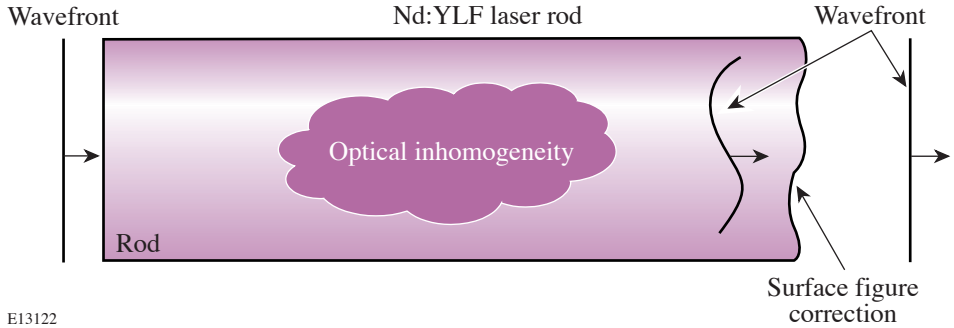


Figure 99.63
Transmitted-wavefront errors induced by bulk inhomogeneities in a Nd:YLF laser rod can be compensated by polishing a surface figure correction on one end-face of the rod.

either a raster or spiral pattern. Interferometry prior to an MRF polishing step measures the actual wavefront error of the sample, which is used to compute the MRF correction. Wavefront corrections converge quickly, usually requiring no more than two or three iterations.

Figure 99.65 shows the results of correcting a Nd:YLF laser rod. Initially, the transmitted-wavefront error for this laser rod was 0.60 $\lambda$ (at 1053 nm) in the desired 20-mm clear aperture. After several MRF iterations, this error was reduced to 0.11 $\lambda$. Table 99.III summarizes the results of correcting five different laser rods. Final wavefronts of ~$\lambda$/10 were generally achieved, except when the spatial structure of the initial wavefront error approached or exceeded the resolution of the MRF correction process.

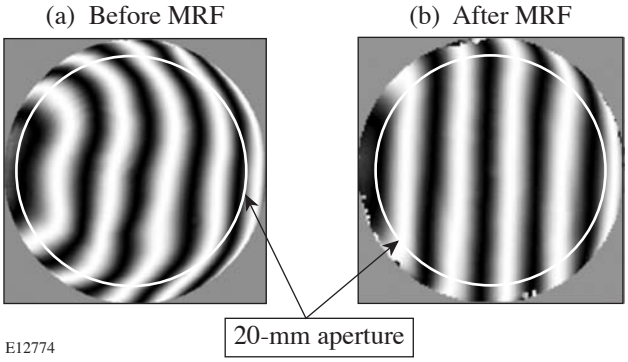


Figure 99.65
Interferograms for rod 2 show the transmitted-wavefront error (a) before and (b) after MRF correction. MRF corrections were applied to the central, 20-mm-diam circular region of the laser rod. The wavefront error was reduced from 0.60 $\lambda$ to 0.11 $\lambda$ (peak-to-valley at 1053 nm).

Table 99.III: Transmitted-wavefront distortion of 25-mm-diam Nd:YLF rods before and after MRF correction.

| Rod number | Wavefront before MRF (peak-to-valley) in waves at 1053 nm | Wavefront after MRF (peak-to-valley) in waves at 1053 nm |
|---|---|---|
| Rod 0 | 3.9 $\lambda$ | 0.06 $\lambda$ (15 × 15 mm$^2$) |
| Rod 1 | 1.5 $\lambda$ | 0.16 $\lambda$ |
| Rod 2 | 0.60 $\lambda$ | 0.11 $\lambda$ |
| Rod 3 | 0.92 $\lambda$ | 0.10 $\lambda$ |
| Rod 4 | 3.2 $\lambda$ | 0.10 $\lambda$ (18-mm diam) |

Several issues associated with wavefront-correcting Nd:YLF laser rods were identified: First, the measured transmitted-wavefront distortion in Nd:YLF is different for linearly polarized light aligned with the *c* axis (1047 nm) or *a* axis (1053 nm). As a result, MRF corrections are required for the specific polarization used for laser operation.

Second, the transmitted-wavefront quality of MRF-corrected laser rods depends on its alignment. Transmitted-wavefront error of a laser rod results from the accumulation of different optical phase delays across the aperture in the propagation direction. Since MRF corrections are applied on a single end-face to correct for bulk inhomogeneities distributed throughout the laser rod, the operational alignment of a corrected rod must match that used for the interferometric measurement upon which the MRF correction is applied. The orientation of the laser rod during the interferometry measurements of successive MRF iterations must be repeatable for the corrections to converge. This alignment repeatability ultimately limits the residual wavefront error that can be achieved, which depends on the initial wavefront error.

Figure 99.66 shows the measured alignment sensitivity of three MRF-corrected laser rods. The transmitted-wavefront error was measured as a function of rod orientation using a Zygo GPIxps interferometer. The rods were first aligned with a tip-tilt stage to achieve the minimum transmitted-wavefront error, corresponding to the MRF-correction alignment orientation. The peak-to-valley transmitted-wavefront error was measured for a range of misalignment angles. Transmitted-wavefront errors better than $\lambda$/4 were obtained for angular misalignment of rods #2 and #3 not exceeding ±10 mrad, while a narrower range of ±4 mrad was observed for rod #4 since its initial wavefront quality was poorer. Given that alignment accuracy better than ±1 mrad can be achieved by standard alignment techniques, diffraction-limited performance is expected.

It is important to note that the MRF-correction process cannot address transmitted amplitude distortions that can arise from inclusions or scattering sites in the bulk material, or depolarization in a polarization-sensitive scheme such as a *Q*-switched laser cavity. To avoid these problems, a careful selection of the best Nd:YLF boules is required.

**Experimental Setup**

The laser system, including both the low-energy front end and the CLARA amplifier, is presented schematically in Fig. 99.67. Seed pulses are generated in a diode-pumped,

single-longitudinal-mode Nd:YLF laser[14] producing ~100-nJ, 100-ns pulses at 1053 nm at a 300-Hz repetition rate. The output of the oscillator is temporally shaped using an aperture-coupled-strip-line (ACSL) pulse-shaping system[15] that precompensates for the square-pulse distortion occurring in the amplifier. Timing jitter of this pulse shape with respect to an external timing reference signal is approximately 15-ps rms. The temporally shaped pulse is subsequently amplified from ~50 pJ to 3 mJ in a diode-pumped, Nd:YLF regenerative amplifier.[16] In addition to providing excellent spatial beam quality and energy stability, square-pulse distortion in this amplifier is relatively weak (0.8:1), which minimizes the dynamic range requirements of the pulse-shaping system. After the regenerative amplifier, the laser beam is up-collimated to 15 mm (FWHM) before spatially shaping the beam to a super-Gaussian profile with a serrated-tooth apodizer.[17]

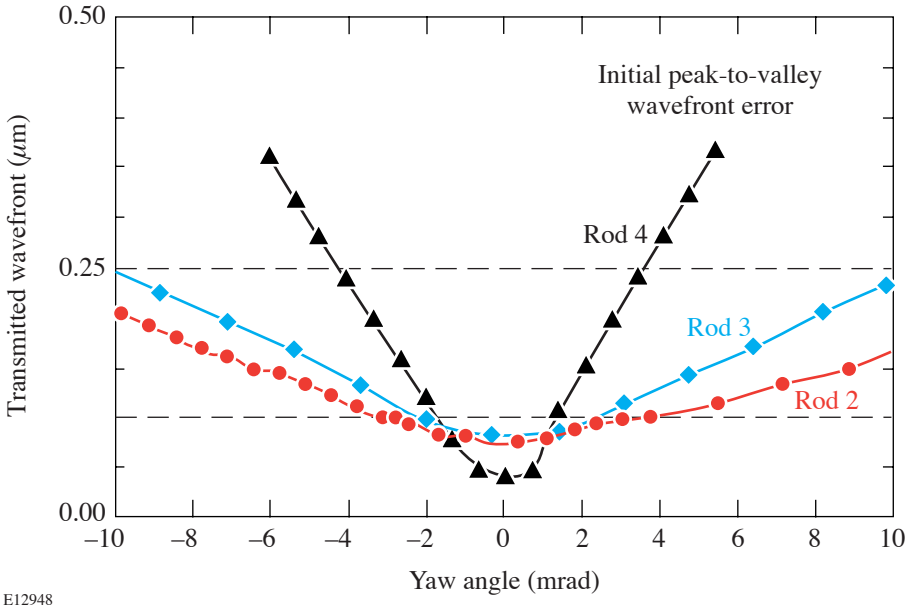


Figure 99.66
The transmitted-wavefront error of MRF-corrected rods is sensitive to its orientation. Optimum performance is achieved when the alignment matches the orientation used during measurements to perform the MRF correction. Increased alignment sensitivity is observed for rods with larger initial wavefront errors.

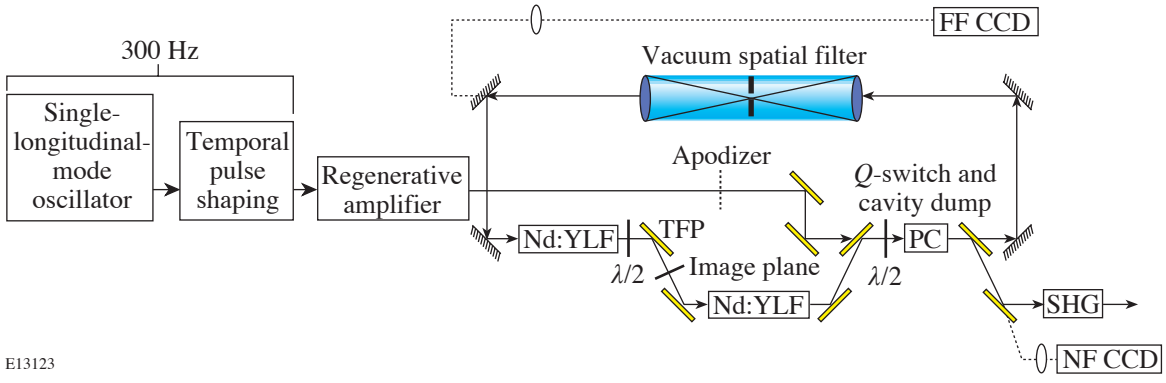


Figure 99.67
Experimental setup. The low-energy part includes a single-longitudinal-mode oscillator, the pulse-shaping system, and the regenerative amplifier. The CLARA setup includes the serrated-tooth apodizer, the CLARA ring, alignment cameras (NF CCD and FF CCD), and the frequency-conversion crystal. TFP: thin-film polarizer; SHG: frequency-doubling crystal; PC: Pockels cell; $\lambda/2$: half-wave plate.

Amplification to high pulse energies is accomplished using a CLARA amplifier, shown in Fig. 99.67. The CLARA architecture is based on a *Q*-switched, cavity-dumped, self-imaging laser cavity. After the pulse is injected through the intracavity Pockels-cell switch, the external apodizer location is imaged to a location between the two laser rods by a telephoto vacuum spatial filter. The spatial filter also image-relays the beam through successive round-trips in the cavity. Two 110-mm-long, 25.4-mm-diam, Nd:YLF, MRF-corrected laser rods are loaded into custom flash-lamp–pumped heads from Continuum with four flash lamps that achieve a single-pass small signal gain of approximately 3× per head. A pair of thin-film polarizers optically isolate the two laser heads to avoid parasitic lasing of the system on the higher-gain, 1047-nm gain transition. Orienting the 1053-nm gain axes of the two Nd:YLF laser rods at 90° cancels residual thermal astigmatism, leaving only a weak defocus that is easily accommodated by the beam-transport system. A 25.4-mm-aperture Pockels cell *Q*-switches the laser cavity and sets the number of round-trips in the 7-m (21-ns) round-trip cavity.

As described above, an MRF-corrected laser rod must be operated with an orientation identical to that used for the correction process. This is achieved by using an interferometric alignment technique for the CLARA laser system that will minimize the total accumulated wavefront error per round-trip through the CLARA. To measure the CLARA transmitted wavefront, an interference pattern is generated between the CLARA output beam and the reference beam. A CCD (charge-coupled-device) camera that images the CLARA image plane (labeled NF CCD in Fig. 99.67) records the interference pattern. Wavefront retrieval is achieved by applying a spatial interferometric technique[18] based on the analysis of tilt fringes and implemented for real-time operation. To produce the reference beam, a half-wave plate is placed in the CLARA, just before the Pockels cell, splitting the laser beam into two beams. This wave plate (shown in Fig. 99.67) is usually removed during operation of the CLARA. One beam propagates through the CLARA and is ejected at the next pass on the polarizer; the other beam, which does not go through the CLARA, is used as a reference beam. In addition to spatial overlap, temporal overlap of the laser pulses is required to have a visible interference pattern. Practically, two output pulses are produced from the regenerative amplifier by intentionally mistiming the cavity dumping. Since the round-trip times of the CLARA and regenerative amplifier are nearly identical, a pulse that travels one round-trip inside the CLARA temporally overlaps with the following pulse on the thin-film polarizer used for injecting the pulses. With temporal and spatial overlap, the interference pattern can be seen in the near field. By adjusting the half-wave plate, the interference fringes' contrast is maximized. A LabVIEW image acquisition and analysis utility records the interference pattern and retrieves the wavefront error in real time. Using this measurement technique, the lens separation in the spatial filter is adjusted with submillimeter accuracy, and the MRF-corrected laser rods can be aligned with great accuracy.

A simple three-dimensional amplification model, based on the Frantz–Nodvik equation,[19] was used to optimize the CLARA. The finite lifetime of the lower level of the Nd:YLF, 1053-nm lasing transition is treated by assuming that the system behaves as a three-level system at each pass, but with exponential decay of the lower-level population between round-trips. Given a lower-level decay time of 21.6 ns (Ref. 20), a pulse of 2 ns, and a round-trip time of 21 ns, we believe the approximation is valid. The model predicts that best energy extraction is achieved for five or six round-trips for a small signal gain of 4 and 3 per rod, respectively, and an injected energy of about 1 mJ. The more round-trips, however, the more wavefront distortion, so we decided to operate the system with four round-trips, where the energy extraction is lower but wavefront distortion is minimized. In addition, less saturation also means lesser distortion of the pump-laser parameters.

After amplification in the CLARA with four round-trips, a second spatial filter down-collimates the beam to a 15 × 15-mm$^2$-aperture, 10-mm-thick-lithium-triborate (LBO), second-harmonic-generation (SHG) crystal with a nominal incident intensity of 1 GW/cm$^2$.

**Results**

Results from operating the CLARA with a 10-mm round beam and uncorrected Nd:YLF laser rods are shown in Fig. 99.68. The figure shows the intensity distribution of the beam in the far field at the OPCPA crystal, where its diameter has been reduced to roughly 2 mm. The measured far field shows a large angular divergence that is unsuitable for pumping phase-matched processes like SHG and OPCPA. Inversion symmetry observed in this image results from the inverted imaging produced by the intracavity spatial filter. As a result, the spatial phase function of the beam is symmetrical, leading to a symmetrical energy distribution in the far field. Figure 99.68(b) shows the corresponding CLARA far-field measurement using MRF-corrected laser rods, which illustrates the greatly improved divergence of this beam. Unfortunately, MRF corrections for these Nd:YLF laser rods were not applied for the correct polarization corresponding to the 1053-nm gain

transition; nonetheless, a dramatic reduction in the angular divergence is realized.

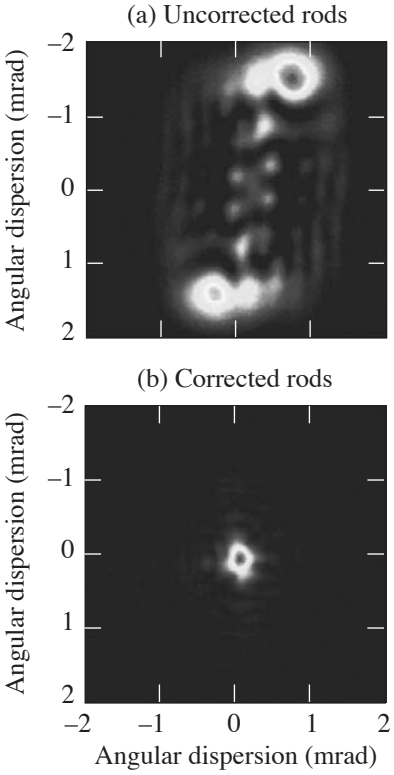


Figure 99.68
Pump-laser far-field distribution measured for a 2-mm beam used to pump an OPCPA preamplifier. (a) The divergence of the beam using uncorrected Nd:YLF rods is large and unsuitable for SHG and OPCPA. (b) Nearly diffraction limited divergence is achieved after MRF correcting the CLARA rods, although some residual divergence results from correcting the transmitted wavefront of the wrong polarization.

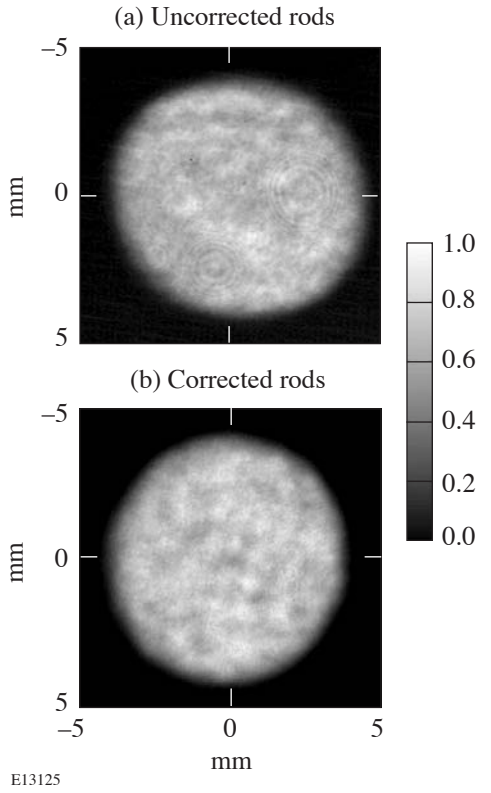


Figure 99.69
Near-field images of the laser beam, at $2\omega$, after frequency conversion. The dimensions reflect the beam size at this location, which is different from the beam size in the CLARA. (a) CLARA output beam with uncorrected rods and (b) CLARA output beam with MRF-corrected rods.

This improvement in the Nd:YLF laser rod quality increases the usable clear aperture and the stored energy available for extraction. Without MRF-corrected rods, it should be stressed that a 10-mm beam was the largest-diameter beam that could propagate through the amplifier without suffering huge spatial modulation or distortion. Figure 99.69 compares the CLARA output beam profile before and after the MRF correction for a similar input beam. The beam injected into the amplifier is limited by a circular tenth-order super-Gaussian apodizer that sets a 10-mm diameter (FWHM). The beam in Fig. 99.69(a) shows some important spatial distortion, which illustrates the maximum beam diameter that the system could support. The beam in Fig. 99.69(b) shows very little distortion, while the peak-to-mean value of the beam is improved from 49% to 41%. Except for beam distortion, which is important for an OPCPA system used as the front end of a larger system, the improvement in the near field is marginal, as may be expected for an imaged system.

The amplifier with MRF-corrected rods can amplify beams with a much larger area. Figure 99.70 shows spatial profiles of two larger beams amplified in the CLARA, when both (a) a round 17-mm-diam apodizer and (b) a square 14-mm-diam apodizer are used. The corresponding measured energies at 527 nm are 1.4 and 1.8 J, respectively, for a maximum average power of 9 W. In all cases, the SHG conversion efficiency using MRF-corrected rods exceeds 70%. The beam-intensity uniformity is 90% and 92% peak-to-mean for the round and square beams, respectively. The poorer beam-intensity uniformity could be explained by a beam extending slightly beyond the useful area of the rods and a poor matching of the input beam on the apodizer since the system was optimized for smaller-diameter beams. By carefully optimizing the input

beam diameter such that radial gain inversely matches the input beam's Gaussian shape at the apodizer, we believe near-top-hat conditions could be achieved.

The energy stability of the laser is remarkable. For instance, with large round beams, the energy stability is smaller than 0.5% rms over a 10,000-shot count at 5 Hz, as shown in Fig. 99.71 by the pulse energy versus shot number and the corresponding pulse-energy histogram. This excellent result for a flash-lamp–pumped system is attributed to the stable CLARA seed-pulse energy provided by the diode-pumped regenerative amplifier, strong simmering of the flash lamps, and heavy saturation of the SHG process.

## Discussion and Conclusion

The transmitted wavefront of a laser gain material has been corrected for the first time by magnetorheological finishing. Polishing a surface figure correction with MRF directly on one surface of 25.4-mm-diam Nd:LF laser rods compensates for bulk inhomogeneities. The results show a dramatic increase in the energy and wavefront-quality performance of the CLARA laser amplifier. The CLARA amplifier demonstrates a high average power of 9 W, which could be increased by 20% to 30% by increasing the number of passes in the amplifier and using laser rods with wavefront corrections correctly applied for the 1053-nm polarization.

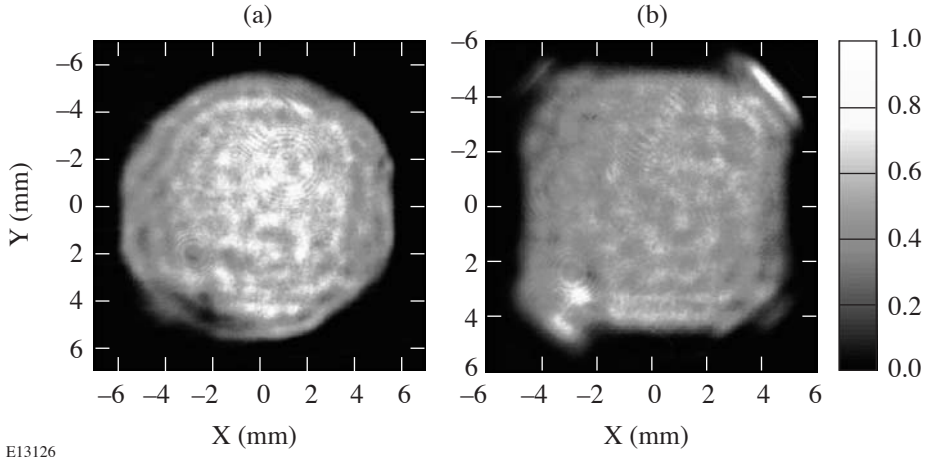


Figure 99.70
Larger beams can be amplified in the CLARA with MRF-corrected laser rods. Results with (a) a round, 17-mm-diam and (b) a square, 14-mm, 20th-order Gaussian spatial profile are demonstrated.

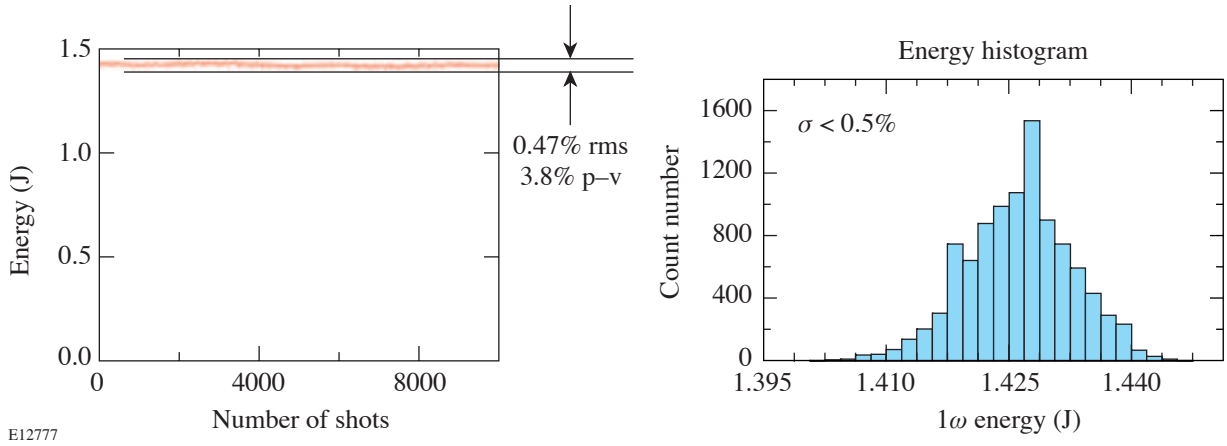


Figure 99.71
Energy stability at the output of the laser.

The MRF technique holds promise for additional applications, such as precompensating thermal aberrations and post-processing large-area laser crystals. Numerous techniques have been reported to mitigate thermal lensing in materials like Nd:YAG.[21,22] Since thermal lensing is a low-order error to the transmitted wavefront, MRF corrections to laser gain elements should easily statically precompensate for it without requiring any other elements in the laser cavity. It should be noted that MRF is probably not well-suited to small rods since edge effects and the finite MRF spot size become a problem with small areas. Efforts to produce large-area crystals of Yb:SFAP and Ti:sapphire are being pursued by diffusion bonding of smaller-aperture elements, but the transmitted-wavefront distortions are observed at the boundaries in such crystals. MRF wavefront corrections might solve this problem, as long as the wavefront gradients are not excessive.

In conclusion, use of a high-energy, high-average-power laser that is suitable for pumping an OPCPA-based front end for a petawatt laser system is demonstrated. Early results show a system that delivers 250-mJ pulses with 34% pump-to-signal energy conversion efficiency with a 10-mm round CLARA beam. This shows that the laser system is well suited to efficiently pumping a high-average-power OPCPA system. Further experiments are underway to use the full CLARA aperture and deliver >500-mJ OPCPA pulses.

## ACKNOWLEDGMENT

The authors thank VLOC for providing the Nd:YLF samples used to characterize the MRF process. This work was supported by the U.S. Department of Energy Office of Inertial Confinement Fusion under Cooperative Agreement No. DE-FC52-92SF19460, the University of Rochester, and the New York State Energy Research and Development Authority. The support of DOE does not constitute an endorsement by DOE of the views expressed in this article.

## REFERENCES

1. A. Dubietis, G. Jonusauskas, and A. Piskarskas, Opt. Commun. **88**, 437 (1992).
2. I. N. Ross *et al.*, Opt. Commun. **144**, 125 (1997).
3. H. Yoshida *et al.*, Opt. Lett. **28**, 257 (2003).
4. J. Collier *et al.*, Appl. Opt. **38**, 7486 (1999).
5. J. L. Collier *et al.*, "Progress Towards Petawatt Level OPCPA," to be published in *Inertial Fusion Sciences and Applications 2003*.
6. Y. Kitagawa *et al.*, IEEE J. Quantum Electron. **40**, 281 (2004).
7. L. J. Waxer, V. Bagnoud, I. A. Begishev, M. J. Guardalben, J. Puth, and J. D. Zuegel, Opt. Lett. **28**, 1245 (2003).
8. M. J. Guardalben, J. Keegan, L. J. Waxer, V. Bagnoud, I. A. Begishev, J. Puth, and J. D. Zuegel, Opt. Express **11**, 2511 (2003).
9. I. Jovanovic *et al.*, Appl. Opt. **41**, 2923 (2002).
10. V. Bagnoud, J. Luce, L. Videau, and A. Rouyer, Opt. Lett. **26**, 337 (2001).
11. A. Babushkin, J. H. Kelly, C. T. Cotton, M. A. Labuzeta, M. O. Miller, T. A. Safford, R. G. Roides, W. Seka, I. Will, M. D. Tracy, and D. L. Brown, in *Third International Conference on Solid State Lasers for Application to Inertial Confinement Fusion*, edited by W. H. Lowdermilk (SPIE, Bellingham, WA, 1999), Vol. 3492, pp. 939–943.
12. C. Le Blanc *et al.*, Opt. Lett. **18**, 140 (1993).
13. D. Golini, S. Jacobs, W. Kordonski, and P. Dumas, in *Advanced Materials for Optics and Precision Structures*, edited by M. A. Ealey, R. A. Paquin, and T. B. Parsonage, Critical Reviews of Optical Science and Technology (SPIE, Bellingham, WA, 1997), Vol. CR67, pp. 251–274.
14. A. V. Okishev and W. Seka, IEEE J. Sel. Top. Quantum Electron. **3**, 59 (1997).
15. M. D. Skeldon, Rev. Sci. Instrum. **71**, 3559 (2000).
16. A. V. Okishev, D. J. Battaglia, I. A. Begishev, and J. D. Zuegel, in *OSA TOPS Vol. 68, Advanced Solid-State Lasers*, edited by M. E. Fermann and L. R. Marshall, OSA Technical Digest (Optical Society of America, Washington, DC, 2002), pp. 418–422.
17. J. M. Auerbach and V. P. Karpenko, Appl. Opt. **33**, 3179 (1994).
18. M. Takeda, H. Ina, and S. Kobayashi, J. Opt. Soc. Am. **72**, 156 (1982).
19. L. M. Frantz and J. S. Nodvik, J. Appl. Phys. **34**, 2346 (1963).
20. J. D. Zuegel and W. Seka, IEEE J. Quantum Electron. **31**, 1742 (1995).
21. G. Vdovin and V. Kiyko, Opt. Lett. **26**, 798 (2001).
22. R. Weber, T. Graf, and H. P. Weber, IEEE J. Quantum Electron. **36**, 757 (2000).

# Prototypes of NIF Neutron Time-of-Flight Detectors Tested on OMEGA

## Introduction

The National Ignition Facility[1] (NIF) is a 2-MJ, 192-beam laser system currently under construction at Lawrence Livermore National Laboratory. One of the main missions of the NIF is to achieve thermonuclear ignition of fusion fuel in inertial confinement fusion (ICF).[2] In ICF experiments, primary neutrons are produced in two reactions:

$$\mathrm{D} + \mathrm{D} \rightarrow n(2.45\ \mathrm{MeV}) + {}^{3}\mathrm{He}, \tag{1}$$

$$\mathrm{D} + \mathrm{T} \rightarrow n(14.1\ \mathrm{MeV}) + \alpha. \tag{2}$$

Neutrons from reaction (1) are referred to as DD neutrons and neutrons from reaction (2) are referred to as DT neutrons.

Every large ICF laser facility, including Nova, OMEGA, and GEKKO, uses neutron time-of-flight (nTOF) systems to measure neutron yields and ion temperatures. Such nTOF systems are usually based on current-mode detectors consisting of a fast plastic scintillator optically coupled to a fast photomultiplier tube (PMT). A high-bandwidth transient digitizer records the signal. These systems, which are relatively inexpensive, have a large dynamic range and a fast time response. The nTOF detectors are reliable, and the information they record is fundamental to most ICF implosion experiments. It is for these reasons that the nTOF system was identified as a "core" diagnostic[3] for the NIF.

The 30-kJ, 60-beam OMEGA laser system[4] is currently the only facility that produces sufficient ICF neutrons for developing and testing prototype nTOF detectors for the NIF. Several nTOF detector prototypes have been built and tested on OMEGA. Based on the results of these tests, a set of nTOF detectors is proposed for use on the NIF to measure ion temperature and DD and DT neutron yields from $10^9$ to $10^{19}$.

## NIF nTOF Detector Requirements

The nTOF system for the NIF must measure ion temperatures of implosion targets, ranging from 1 to 50 keV for yields between $10^9$ and $10^{19}$ neutrons. The nTOF system must work in a harsh environment[5] of energetic neutrons, x rays, $\gamma$ rays, and high electromagnetic pulse (EMP) noise. The main objective of an nTOF system is to measure ion temperature. Because nTOF-detector signals are proportional to the number of neutrons detected, they are easily adapted for simultaneous use as a yield monitor.

The neutrons produced in fusion reactions (1) and (2) are monoenergetic. Center-of-mass motion of the reacting ions causes spectral broadening of these energy lines. Because ICF targets are nearly ideal point sources in both time (<100 ps) and space (<100 $\mu$m) and neutrons travel to a detector without collisions, neutron spectra can be measured using the time-of-flight technique. The arrival time at a detector corresponds to the energy of the neutron. The time spread $\Delta t$ of neutrons arriving at an nTOF detector is given by the following equations:[6]

$$\Delta t = 0.778 d\sqrt{T_i} \quad (\text{for DD}), \tag{3}$$

$$\Delta t = 0.122 d\sqrt{T_i} \quad (\text{for DT}), \tag{4}$$

where $\Delta t$ is the full width at half maximum (FWHM) in nanoseconds, $d$ is target-to-detector distance in meters, and $T_i$ is the ion temperature in keV. The width of a measured signal is the width of the time-of-flight spread added in quadrature with the detector response.[7] To minimize measurement error, the nTOF detector response (FWHM) should be much less than the neutron temporal broadening being measured. For scintillator- and PMT-based detectors, this requirement leads to the use of fast microchannel-plate (MCP) PMT's with time resolutions of a few hundred picoseconds (FWHM).

The scintillator used in an nTOF detector must also be fast. Bicron's[8] ultrafast BC-422 scintillator has a rise time of less than 20 ps[9] and an exponential decay constant of 1.4 ns. The quenched version of the scintillator, BC-422Q, has a two-component decay with time constants of about 0.6 and 5 ns. In addition, the nTOF detector-response function includes the transit time of the neutrons across the thickness of the scintillator. A scintillator thickness of 20 mm corresponds to a 0.92-ns transit time for DD neutrons and provides a good match between scintillator decay and transit time through the scintillator. The cables and digitizer also contribute to detector response. A cable with a 3-GHz bandwidth and a 1-GHz or faster oscilloscope contributes relatively small dispersion to temperature measurements.

X rays and $\gamma$ rays from an ICF implosion generate background[10] in nTOF detectors that can saturate a PMT and distort the neutron signal, causing errors in ion temperature and yield measurement. Shielding is therefore required to reduce the x-ray and $\gamma$-ray fluence entering PMT-based nTOF detectors. Lead-shielding thickness is limited to <30 mm to avoid neutron scattering that would appear as signal broadening in the detector. High-yield DT implosions create MeV $\gamma$ rays from $(n,\gamma)$ interactions in the target, target positioner, nearby diagnostics, and the target chamber walls. This $\gamma$-ray background is proportional to the DT neutron yield and will be very high at expected NIF yields. It is difficult to shield MeV $\gamma$ rays without also shielding the energetic neutrons. New techniques[10] like single-stage MCP PMT's and chemical-vapor-deposition (CVD) diamonds,[11] which are less sensitive to MeV $\gamma$ rays, are recommended for the NIF.

**nTOF Detector Locations on the NIF**

The optimum placement[12] of nTOF detectors is determined by a tradeoff between decreased time resolution at small distances from the target and a smaller statistical sample of detected neutrons at longer distances. It can be shown[13] that the number of neutrons needed to achieve a given statistical uncertainty should be a factor of 2 larger over that predicted by Poisson statistics. Therefore, in our design, we require at least 200 neutron interactions in the nTOF detectors to achieve 10% statistical uncertainty, which puts a restriction on detector location. Another requirement is that, at the lowest yields, the nTOF detector should provide a neutron signal with an amplitude five to ten times higher than the EMP noise of the system. The highest-measurable yield is determined by PMT saturation. The signal from a modern MCP PMT is linear to ~3 nC of integrated charge for low-repetition pulses. This was taken into account in estimating yield limits. A combination of the optimization[12] of the detector locations combined with background considerations provides several natural locations for nTOF detectors on the NIF.

Placing a detector outside the target chamber wall at 5 m from the target avoids vacuum interface and tritium contamination problems. A 5-m flight path is adequate for ion-temperature measurements. At this location the nTOF detector will not be affected by scattered neutrons and $(n,\gamma)$ interactions with the target chamber. The EMP noise at the OMEGA target chamber is 2 to 20 mV, depending on shot and detector design. The EMP noise at the NIF target chamber will most likely be higher; therefore, at least a 500-mV signal is required at the target chamber wall. This location should be used only for $D_2$ implosions and low-yield DT shots as described in the next section and Table 99.IV.

Another natural location for nTOF detectors is outside the NIF target bay shield wall against existing, predrilled holes. The 2-m-thick concrete walls of the target bay can be used as shielding against scattered neutrons and $\gamma$ rays. There are several such locations at the NIF where detectors can be placed 17 m to 20 m from the target. The digitizing oscilloscopes can be placed nearby, thereby shortening the signal and HV cables and decreasing EMP noise pickup. The EMP noise in this location should be much less of a problem than at the target chamber wall; therefore, the minimum signal requirement in this location is 100 mV.

The 20-m standoff distance is not adequate for pre-ignition and ignition targets producing $10^{17}$ to $10^{19}$ neutrons. Most of the nTOF detectors located 20 m from the target will saturate at such yields. The high neutron flux can also damage an oscilloscope and PC. Another location as far away from the target as possible with a clean flight path is needed for the ignition campaign. There is a line of sight at $\theta = 64°$ and $\phi = 275.62°$ with an opening in the target bay wall that exits outside the building just above the roof of the diagnostic building. The nTOF detectors can be installed on the roof of the diagnostic building at about 40 m from the target.

**OMEGA Performance Scaled to the NIF**

Three different types of fast detectors were used for the NIF nTOF prototype tests on OMEGA. The most-sensitive nTOF detector consists of a BC-422 scintillator coupled to a two-stage MCP PMT. The PMT has a response time of about 250 ps (FWHM), a gain up to $10^6$, and a 40-mm-diam photocathode. Detectors based on a two-stage MCP PMT are relatively sensitive to hard-x-ray and $\gamma$-ray background and are good for

relatively low ($10^9$ to $10^{11}$) neutron-yield NIF implosions, in which x-ray and $\gamma$-ray background is low as well. The first prototype has a 40-mm-diam, 20-mm-thick BC-422 scintillator coupled to a Photek[14] PMT240 PMT. To protect the prototype from the x-ray and $\gamma$-ray background inside the OMEGA Target Bay, it was heavily shielded on all sides by a thick lead housing (Fig. 99.72). The prototype was installed in the OMEGA Target Bay at 12.4 m from the target and connected by a 12-m-long LMR-400 cable to a 1-GHz Tektronix 684 oscilloscope. A Mini-Circuits model 15542 resistive splitter divides the detector signal between two oscilloscope channels with different sensitivity settings to increase the dynamic range of the recording system. The prototype was tested on $D_2$ implosions on OMEGA and calibrated against the standard suite of neutron diagnostics. Figure 99.73 shows a typical scope trace of the neutron signal taken for a shot yielding $1.2 \times 10^{11}$ DD neutrons and having a $T_i = 4.1$ keV. The measured signal was fitted by a convolution of a Gaussian and an exponential decay, as described in detail in Ref. 7. Scaled to the 5-m distance on the NIF chamber wall, this detector will have ~200 neutron interactions and produce a signal amplitude of 500 mV for a DD yield of $1 \times 10^9$ neutrons. This detector installed on the NIF target chamber wall will be sensitive to DD and DT neutron yields from $5 \times 10^8$ to $5 \times 10^{10}$. Using relations derived by Lerche,[12] it is estimated that, at 5 m, this detector can measure ion temperature with 15% accuracy for $10^9$ DD neutrons at 1 keV. Better than 10% accuracy is possible at higher yields or higher ion temperatures.

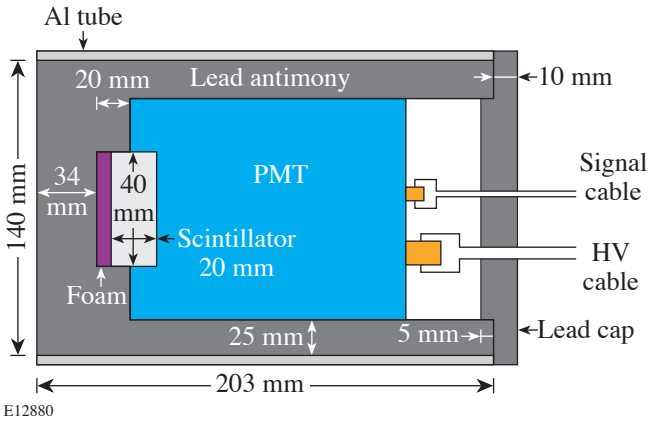


Figure 99.72
Schematic of the single-stage and two-stage MCP PMT nTOF prototypes tested on OMEGA at 12.4 m from the target.

Table 99.IV: Proposed set of nTOF detectors required for DD and DT temperature measurements for yields between $10^9$ and $10^{19}$ neutrons.

| N | Distance | Scintillator/ Wafer Size | Type | PMT | Yield Range |
|---|---|---|---|---|---|
| 1 | 5 m | 40 mm × 20 mm | BC-422 | 2 MCP | $1 \times 10^9$ to $5 \times 10^{10}$ |
| 2 | 5 m | 40 mm × 20 mm | BC-422 | 1 MCP | $1 \times 10^{10}$ to $5 \times 10^{11}$ |
| 3 | 5 m | 10 mm × 1 mm | CVD diamond | | $5 \times 10^{12}$ to $1 \times 10^{15}$ |
| 4 | 20 m | 40 mm × 20 mm | BC-422 | 1 MCP | $1 \times 10^{11}$ to $5 \times 10^{12}$ |
| 5 | 20 m | 40 mm × 20 mm | BC-422Q | 1 MCP | $1 \times 10^{12}$ to $1 \times 10^{14}$ |
| 6 | 20 m | 10 mm × 1 mm | CVD diamond | | $1 \times 10^{14}$ to $5 \times 10^{16}$ |
| 7 | 40 m | 10 mm × 5 mm | BC-422Q | 1 MCP | $1 \times 10^{14}$ to $1 \times 10^{16}$ |
| 8 | 40 m | 10 mm × 1 mm | CVD diamond | | $5 \times 10^{14}$ to $1 \times 10^{17}$ |
| 9 | 40 m | 2 mm × 0.5 mm | CVD diamond | | $2 \times 10^{16}$ to $1 \times 10^{19}$ |

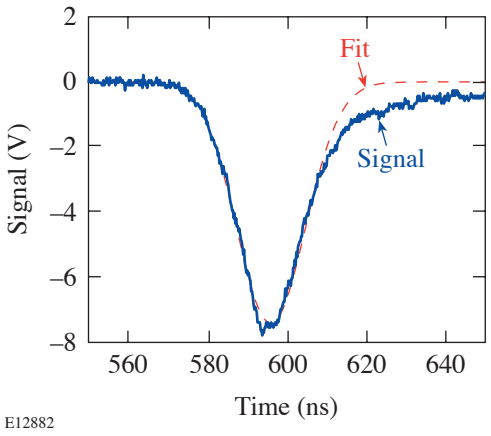


Figure 99.73
Neutron signal recorded for the two-stage MCP PMT prototype on $D_2$ shot 33949: yield = $1.2 \times 10^{11}$ and $T_i$ = 4.1 keV. The fit is a convolution of a Gaussian shape and a scintillator exponential decay.

The second nTOF detector designed for the NIF consists of a BC-422 or BC-422Q scintillator coupled to a single-stage MCP PMT. This PMT has a slightly faster response time of about 200 ps (FWHM), a gain up to $10^3$, and a 40-mm-diam photocathode. The single-stage MCP PMT is less sensitive (by a factor of about $10^3$) to x-ray and $\gamma$-ray background but has less gain by the same factor. Two versions of this detector were tested on OMEGA: The first version was designed to determine the maximum sensitivity achievable using a single-stage MCP Photek PMT140 PMT, coupled to a 20-mm-thick, 40-mm-diam BC-422 scintillator. It has 14-mm lead shielding in front and a 5-mm aluminum housing on all other sides. This prototype was tested on the OMEGA chamber wall, 1.65 m from the target, with DD implosions and calibrated against the standard neutron diagnostics. Figure 99.74 shows a typical oscilloscope trace of a neutron signal from this detector (DD yield of $6.7 \times 10^{10}$ neutrons and $T_i$ = 3.2 keV). This detector installed on the NIF target chamber wall will detect ~1900 neutron interactions and produce a 500-mV signal for a DD yield of $1 \times 10^{10}$ neutrons. The same detector installed outside the NIF target bay at 20 m from the target will have ~1700 neutron interactions and produce a 450-mV signal for a DD yield of $1 \times 10^{11}$.

The second version of the single-stage MCP PMT system was designed to test upper-yield limits of such detectors. This prototype had a 40-mm-diam, 20-mm-thick BC-422Q (1% benzephenone) quenched scintillator, coupled with a Photek PMT140 PMT, and operated at a gain of $5 \times 10^2$. The detector was placed in a lead housing identical to that shown in Fig. 99.72 and installed in the OMEGA Target Bay at 12.4 m from the target, next to the two-stage MCP PMT prototype. This prototype was tested with DT implosions and calibrated against copper activation measurements. A scope trace of a neutron signal is shown in Fig. 99.75 (DT neutron yield of $5.0 \times 10^{13}$ and $T_i$ = 9.7 keV). If this detector is installed outside the NIF target bay at 20 m from the target, it will be sensitive to DT yields from $10^{12}$ to $10^{14}$ neutrons.

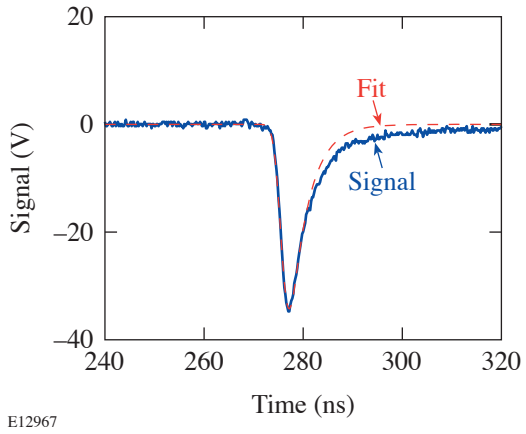


Figure 99.74
Neutron signal recorded for the singe-stage MCP PMT prototype on $D_2$ shot 33413: yield = $6.7 \times 10^{10}$ and $T_i$ = 3.2 keV. The fit is a convolution of a Gaussian shape and a scintillator exponential decay.

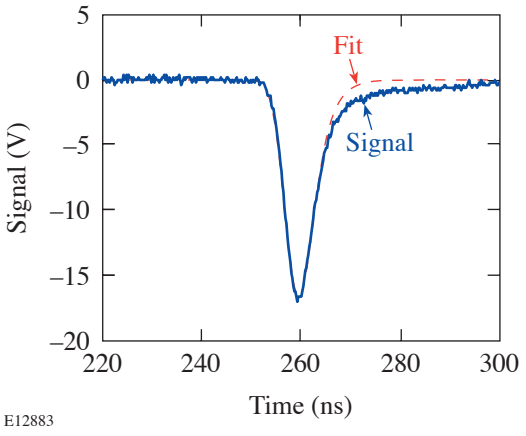


Figure 99.75
Neutron signal recorded for the single-stage MCP PMT prototype on DT shot 33797: yield = $5.0 \times 10^{13}$ and $T_i$ = 9.7 keV. The fit is a convolution of a Gaussian shape and a scintillator exponential decay.

The third prototype nTOF detector tested on OMEGA used a 10-mm-diam, 1-mm-thick CVD diamond wafer. Diamond detectors have low sensitivity[11] to hard-x-ray and $\gamma$-ray background and can be used at very-high DT yields. The CVD diamond detectors also have a larger dynamic range than PMT-based detectors. Such detectors[11] were previously tested inside the OMEGA target chamber. This time, the CVD diamond detector was installed outside the target chamber at 2.8 m from the target and biased at 1 kV. The CVD diamond prototype was tested with DT implosions and calibrated against copper activation. A typical scope trace is shown in Fig. 99.76 (DT yield of $5.0 \times 10^{13}$ and $T_i = 9.7$ keV). This detector installed on the NIF target chamber wall will be sensitive to DT neutrons over a yield range from $5 \times 10^{12}$ to $10^{15}$. The same detector installed outside the NIF target bay at 20 m from the target will be sensitive to DT yields between $10^{14}$ and $5 \times 10^{16}$ neutrons.

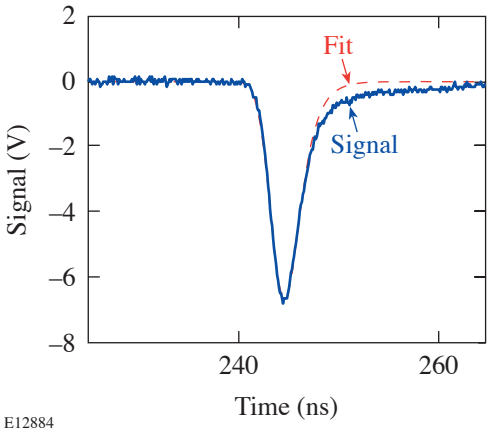


Figure 99.76
Neutron signal recorded for the CVD diamond prototype on DT shot 33797: $5.0 \times 10^{13}$ and $T_i = 9.7$ keV. The fit is a convolution of a Gaussian shape and an exponential decay.

For pre-ignition and ignition targets on the NIF, less-sensitive detectors are needed about 40 m from the target. Scaled detectors based on a single-stage MCP PMT and a CVD diamond detector are chosen for this purpose. The proposed set of nTOF detectors to measure ion temperature and DD and DT neutron yields between $10^9$ and $10^{19}$ is summarized in Table 99.IV.

The proposed set of detectors is a realistic, cost-effective approach to the NIF nTOF system and based on commercially available components. All of the nTOF detectors and components can be calibrated on OMEGA prior to installation and use on the NIF. The nTOF detector calibrations can be later cross checked against other yield-sensitive diagnostics, such as the PROTEX[15] and activation.[16]

## Conclusions

Neutron time-of-flight (nTOF) detectors are part of the NIF core diagnostic suite providing a measurement of ion temperature and yield. Several NIF nTOF detector prototypes have been built and tested with $D_2$ and DT implosions on OMEGA. Prototypes for low and moderate NIF neutron yields are based on fast plastic scintillators and fast photomultiplier tubes. A third prototype is based on a CVD diamond detector. A set of nTOF detectors is proposed for the NIF to measure ion temperature and DD and DT neutron yields between $10^9$ and $10^{19}$.

## ACKNOWLEDGMENT

This work was supported by the U.S. Department of Energy Office of Inertial Confinement Fusion under Cooperative Agreement No. DE-FC52-92SF19460, the University of Rochester, and the New York State Energy Research and Development Authority. The support of DOE does not constitute an endorsement by DOE of the views expressed in this article.

## REFERENCES

1. E. I. Moses, Fusion Sci. Technol. **44**, 11 (2003).
2. J. D. Lindl, *Inertial Confinement Fusion: The Quest for Ignition and Energy Gain Using Indirect Drive* (Springer-Verlag, New York, 1998).
3. T. J. Murphy, C. W. Barnes, R. R. Berggren, P. Bradley, S. E. Caldwell, R. E. Chrien, J. R. Faulkner, P. L. Gobby, N. M. Hoffman, J. L. Jimerson, K. A. Klare, C. L. Lee, J. M. Mack, G. L. Morgan, J. A. Oertel, F. J. Swenson, P. J. Walsh, R. B. Walton, R. G. Watt, M. D. Wilke, D. C. Wilson, C. S. Young, S. W. Haan, R. A. Lerche, M. J. Moran, T. W. Phillips, T. C. Sangster, R. J. Leeper, C. L. Ruiz, G. W. Cooper, L. Disdier, A. Rouyer, A. Fedotoff, V. Yu. Glebov, D. D. Meyerhofer, J. M. Soures, C. Stockl, J. A. Frenje, D. G. Hicks, C. K. Li, R. D. Petrasso, F. H. Séguin, K. Fletcher, S. Padalino, and R. K. Fisher, Rev. Sci. Instrum. **72**, 773 (2001).
4. T. R. Boehly, D. L. Brown, R. S. Craxton, R. L. Keck, J. P. Knauer, J. H. Kelly, T. J. Kessler, S. A. Kumpan, S. J. Loucks, S. A. Letzring, F. J. Marshall, R. L. McCrory, S. F. B. Morse, W. Seka, J. M. Soures, and C. P. Verdon, Opt. Commun. **133**, 495 (1997).

5. J. L. Bourgade, V. Allouche, J. Baggio, C. Bayer, F. Bonneau, C. Chollet, S. Darbon, L. Disdier, D. Gontier, M. Houry, H. P. Jacquet, J.-P. Jadaud, J. L. Leray, I. Masclet-Gobin, J. P. Negre, J. Raimbourg, B. Villette, I. Bertron, J. M. Chevalier, J. M. Favier, J. Gazave, J. C. Gomme, F. Malaise, J. P. Seaux, V. Yu. Glebov, P. Jaanimagi, C. Stoeckl, T. C. Sangster, G. Pien, R. A. Lerche, and E. Hodgson, "New Constraints for Plasma Diagnostics Development due to the Harsh Environment of MJ-Class Lasers," to be published in Review of Scientific Instruments.

6. H. Brysk, Plasma Phys. **15**, 611 (1973).

7. T. J. Murphy, R. E. Chrien, and K. A. Klare, Rev. Sci. Instrum. **68**, 610 (1997).

8. Saint-Gobain Crystals, Newbury, OH 44065.

9. R. A. Lerche, D. W. Phillion, and G. L. Tietbohl, in *Ultrahigh- and High-Speed Photography, Videography, and Photonics '93*, edited by P. W. Roehrenbeck (SPIE, Bellingham, WA, 1993), Vol. 2002, pp. 153–161.

10. V. Yu. Glebov, C. Stoeckl, T. C. Sangster, and G. J. Schmid, "Hard-X-Ray and $\gamma$ Background in Neutron Time-of-Flight Detectors on the NIF and LMJ," to be submitted to Review of Scientific Instruments.

11. G. J. Schmid, R. L. Griffith, N. Izumi, J. A. Koch, R. A. Lerche, M. J. Moran, T. W. Phillips, R. E. Turner, V. Yu. Glebov, T. C. Sangster, and C. Stoeckl, Rev. Sci. Instrum. **74**, 1828 (2003).

12. R. A. Lerche and B. A. Remington, Rev. Sci. Instrum. **61**, 3131 (1990).

13. T. J. Murphy *et al.*, Rev. Sci. Instrum. **72**, 850 (2001).

14. Photek Ltd., St. Leonards-on-Sea, United Kingdom.

15. M. J. Moran, V. Yu. Glebov, R. Rygg, and B.-E. Schwartz, "PROTEX: A Proton-Recoil Detector for ICF Fusion Neutrons," submitted to Review of Scientific Instruments.

16. G. W. Cooper and C. L. Ruiz, Rev. Sci. Instrum. **72**, 814 (2001).

# Subpicosecond Faraday Effect in $Cd_{1-x}Mn_xTe$ and Its Application in Magneto-Optical Sampling

## Introduction

Recent technological developments in electronics and optoelectronics have opened prospects for novel devices and digital circuits operating in the subpicosecond temporal regime.[1–5] As the operating speed of modern electrical devices increases, the problem of how to properly characterize them becomes progressively more difficult. Independent measurements of the voltage and the current transients are needed in order to get the full picture of the electromagnetic field distribution in the device or circuit under test and to be able to obtain the complex, frequency-dependent impedance characteristics of the tested element. Information on the voltage transient in the subpicosecond time range, corresponding to the device's THz operation rate, can be obtained using an electro-optical sampling (EOS) technique, based on a nonlinear optical crystal ($LiTaO_3$ in most cases) as the EO sensor.[6] Freeman[7,8] has recently developed a magneto-optical sampling (MOS) technique that is capable of directly measuring magnetic-field transients and, therefore, together with EOS, allows for the complete characterization of ultrafast devices and circuits. These previous realizations of MOS have been limited, however, to Tb-doped EuS[7] or garnet[8] crystals as the MO medium and could probe current pulses with experimentally demonstrated temporal resolution of the order of 10 ps at best. Part of the problem was that the implemented MO materials exhibited ferrimagnetic ordering,[9] leading to slow magnetization relaxation.

This article presents time-resolved studies of the Faraday effect in a diluted magnetic semiconductor $Cd_{1-x}Mn_xTe$ single crystal with $x > 0.5$, maintained at cryogenic (10 K) temperature. The $Cd_{0.38}Mn_{0.62}Te$ crystal has been implemented as the ultrafast MO transducer, allowing ultrafast current transients to be characterized with subpicosecond time resolution. Our MOS technique should also be applicable for accurate, time-resolved measurements of transient magnetic-field variations in modern spintronic devices.[10]

## Faraday Effect and Magneto-Optical Sampling

The $Cd_{1-x}Mn_xTe$ crystals are very suitable materials for MO applications, in general, and for MOS, in particular, since, especially at low temperatures, they exhibit very high Faraday rotation under externally applied magnetic fields.[11,12] Alignment of Mn spins in $Cd_{1-x}Mn_xTe$ due to the applied magnetic field leads to a large Zeeman splitting of the excitonic energy levels[13] through the strong *sp–d* exchange interaction between the Mn spins and carriers. In turn, this mechanism induces a magnetic-field–dependent birefringence in both optical circular polarization directions, ultimately resulting in the polarization rotation angle $\theta_F$ given by[9]

$$\theta_F = \frac{\omega}{2c}\left(n_+ - n_-\right)L = VBL, \tag{1}$$

where $\omega$ is the light angular frequency, $n_+(n_-)$ are the right (left) components of the index of refraction of the circularly polarized light within the MO material, $L$ is the optical beam magnetic-field $B$ interaction length, and $c$ is the speed of light. Equation (1) also shows that $\theta_F$ can be expressed as the product of the experimentally defined materials constant, so-called Verdet constant $V$, times $B$ and $L$. In the time domain, it is predicted that the Mn ion spin–spin interaction time decreases exponentially with increasing $x$ and reaches the subpicosecond range for $x > 0.5$.[14]

Figure 99.77 presents a schematic of our MOS experimental setup. The source of current pulses in our technique was a photoconductive LT-GaAs freestanding photoswitch capable of generating ~0.5-ps-wide electrical pulses.[15] The switch was integrated into a Ti/Au coplanar strip line (CSL) with 10-$\mu$m-wide metal strips with 10-$\mu$m separation, deposited on a transparent MgO substrate. The CSL was biased and could be shorted at one end in order to perform low-frequency $V$ measurements. A 0.5-mm-thick, optically polished platelet cut from a $Cd_{0.38}Mn_{0.62}Te$ single crystal was placed on top of the CSL and acted as the MO transducer. Our $Cd_{1-x}Mn_xTe$ crystals were grown using a modified Bridgeman method. The synthesized material of proper stoichiometry in the form of a polycrystalline powder was used as the source material for the final crystal growth. The quality of our crystals was verified

through extensive x-ray diffraction measurements.[16] The entire arrangement presented in Fig. 99.77 was placed inside a temperature-controlled optical helium cryostat, and the measurements were taken at 10 K.

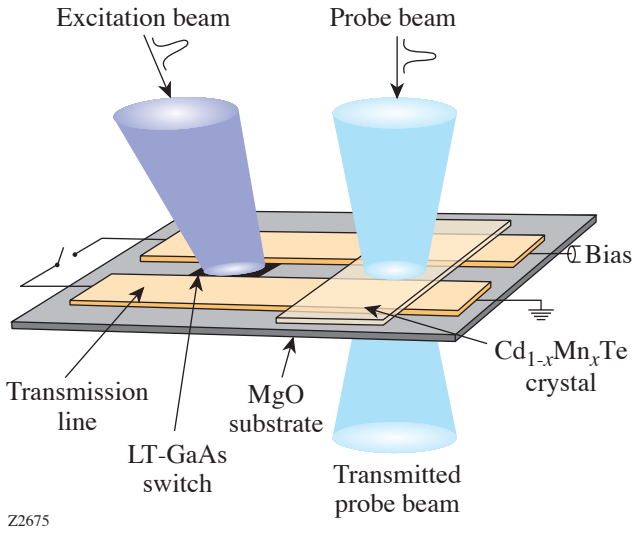


Figure 99.77
Schematic of the MOS setup, including the LT-GaAs freestanding photoswitch as an electrical pulse generator and the $Cd_{1-x}Mn_xTe$ crystal as an MO transducer. Both the switch and the transducer are integrated into a CSL fabricated on a transparent MgO substrate.

For our time-resolved Faraday rotation experiments, the LT-GaAs switch was excited by ~800-nm-wavelength, 100-fs-duration, 76-MHz-repetition-rate laser pulses generated by a commercial Ti:sapphire laser, while ~200-fs-wide probe pulses were generated by an optical parametric oscillator (OPO) with internal frequency doubling and their wavelengths covered the range from 570 nm to 615 nm. A 7:3 beam splitter was used to direct 70% of the optical energy to OPO; the remaining 30% was modulated by an acousto-optical modulator at 90 KHz and delivered to our LT-GaAs freestanding switch.[17] The linearly polarized femtosecond probe pulses from OPO traveled through the MO crystal between the metal CSL electrodes, about 300 $\mu$m away from the photoswitch. The CSL was connected to a bias source that charged the LT-GaAs switch. The polarizer and photodetector (not shown in Fig. 99.77) detected the polarization rotation of the transmitted probe light, which was displayed on a computer as a function of the excitation-probe delay time. The implemented two-color-beam approach allowed us to tune the probe-beam wavelength to reach the $Cd_{1-x}Mn_xTe$ maximum Faraday rotation, while, at the same time, exciting the LT-GaAs switch with the near-infrared (just above the bandgap) radiation. We could also maintain the excitation-probe synchronization needed for the sampling technique. Both the excitation and probe beams were focused to spots with an ~10-$\mu$m diameter.

## Experimental Results and Conclusions

At the first phase of our measurements, we measured the spectral characteristics of our $Cd_{0.38}Mn_{0.62}Te$ crystal response and determined the static MO effect. A 3-KHz sinusoidal voltage was applied to one end of the CSL with no light excitation on the LT-GaAs switch, so its resistance remained of the order of 1 MΩ and its presence in the circuit could be neglected. When the other end of the line was shorted (see Fig. 99.77), a 3-KHz current signal was induced in the CSL and the polarization rotation of the probe beam, passing through the $Cd_{0.38}Mn_{0.62}Te$ crystal and between the CSL lines, was observed because of the Faraday effect. In the opposite situation, i.e., when the left end of the CSL was opened, no polarization rotation of the probe beam was observed, excluding any possibility of the EO effect in our MO crystal. Open circles in Fig. 99.78 show the results of the above measurements in a form of the $V$ dependence on the probe-beam wavelength. We observe a broad local maximum centered at 593 nm, which corresponds to the earlier measured position of the exciton resonance in $Cd_{0.38}Mn_{0.62}Te$, although the significant (~6-nm) spectral width of our femtosecond probe

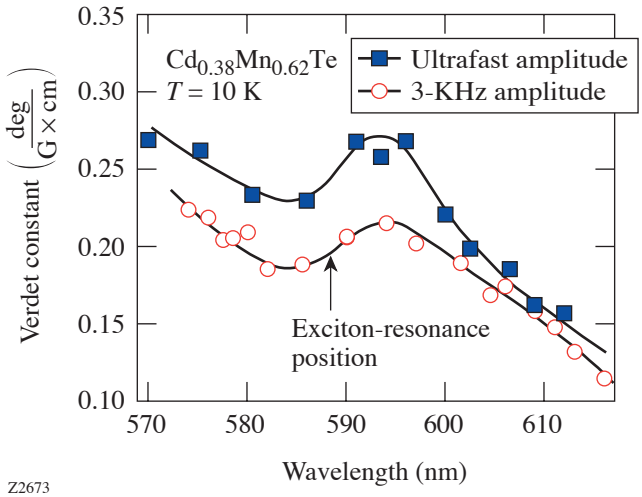


Figure 99.78
Spectral dependences of the transient (solid squares) and static (open circles) Verdet constant for a $Cd_{0.38}Mn_{0.62}Te$ single crystal measured using subpicosecond current pulses generated by the LT-GaAs switch and 3-KHz ac excitation. Both measurements were performed at 10 K in the tunability range of our OPO. The arrow shows the position of the exciton resonance. Solid lines are guides to the eye.

pulses did not allow us to resolve the resonance structure in detail. The $V$ value obtained at the 593-nm wavelength compares favorably to other MO materials reported in literature.[9] Finally, one can also notice the increase of $V$ at the bandgap edge below 580 nm. Faraday rotation experiments are not practical in this range due to the strong light absorption; however, one could try to implement the Kerr-effect–type measurements. We will discuss the MOS technique based on the Kerr effect in a separate publication.

When the excitation pulses were applied to the LT-GaAs switch, a train of subpicosecond electrical pulses was generated and propagated along the CSL. These electrical pulses induced the transient magnetic-field component in the CSL that coupled to our MO crystal and rotated the polarization of the transmitted probe beam. A 1.1-ps-wide magnetic pulse transient recorded using our MOS system for the probe-beam wavelength of 595 nm (corresponding to the maximum $V$ value in Fig. 99.78) is shown in Fig. 99.79. The pulse rise time, defined as the 0.9-to-0.1-amplitude time difference, was measured to be about 0.6 ps, and the decay time, obtained using exponential fittings, was 1.1 ps. The MOS signal amplitude scan, performed for different probe-beam wavelengths (closed squares in Fig. 99.78), showed that the transient $V$ value followed the low-frequency Verdet constant data. The latter confirms that the transient shown in Fig. 99.79 is due to the MO effect in $Cd_{1-x}Mn_xTe$, based on the ultrafast Mn ion spin–spin interaction.[14] We note, however, that within the exciton resonance range, the transient $V$ values are consistently ~30% larger than the static ones obtained using low-frequency excitation (open circles in Fig. 99.78). From the MOS transient signal-to-noise ratio, we estimated the sensitivity of our system as ~ 0.1 mA at 10 K. This resolution could be obtained after averaging 100 data scans with 0.3-s lock-in amplifier time constant.

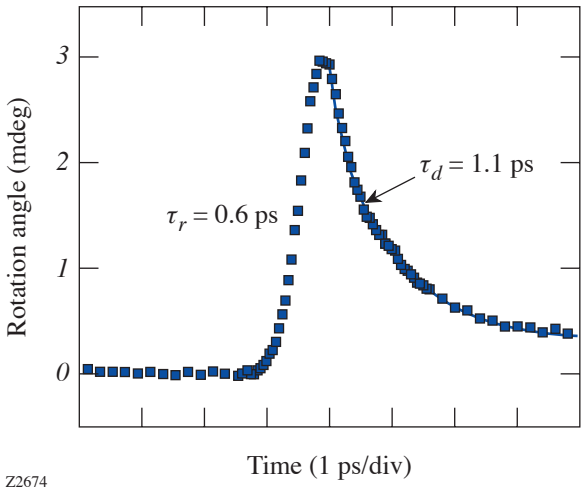


Figure 99.79
Time-resolved Faraday angle rotation as a function of time, measured using our MOS system. The probe-beam wavelength was 595 nm, and the experiment temperature was 10 K. Solid line is an exponential fit to the fall part of the signal.

To confirm the time dynamics of the MO effect in $Cd_{1-x}Mn_xTe$, we substituted the $LiTaO_3$ crystal for our MO crystal and performed the standard EOS testing at 10 K with the same LT-GaAs switch and CSL. The measured EOS response showed some additional oscillatory features due to apparent dielectric loading of the relatively large $LiTaO_3$ crystal, but the recorded MOS and EOS pulses exhibited essentially identical characteristic times. Since the response time of our $LiTaO_3$-based EOS system is 200 fs,[15] we can confirm that the response time of the cryogenic Faraday effect in $Cd_{1-x}Mn_xTe$ with $x > 0.5$ is of the order of a few hundred femtoseconds or less. The latter conclusion is in qualitative agreement with the data discussed in Ref. 14.

We have demonstrated subpicosecond dynamics of the Faraday effect in highly Mn-doped $Cd_{1-x}Mn_xTe$ at low temperatures and have implemented these crystals as MO transducers in the MOS system for time-resolved measurements of magnetic/current transients. The high sensitivity and subpicosecond temporal resolution of our MO sampler makes it practical for characterization of ultrafast current–driven (e.g., superconducting) devices and circuits. The presented sampler should also be very useful for testing the switching dynamics of spintronic logic elements. Finally, the $Cd_{1-x}Mn_xTe$ crystals should find applications as ultrafast MO modulators[18] for electrical-to-optical coupling of superconducting digital circuits.[19]

## ACKNOWLEDGMENT

This work has been funded by the NSF grant DMR-0073366 and the ONR grant N00014-00-1-0237. Additional support was provided by the NYSTAR grant through the Center for Electronic Imaging System at the University of Rochester.

## REFERENCES

1. M. M. Feiginov, Nanotechnology **11**, 359 (2000).

2. J. Mateos *et al.*, Nanotechnology **14**, 117 (2003).

3. K. Likharev, Phys. World **10**, 39 (1997).
4. P. Bunyk, K. Likharev, and D. Zinoviev, Int. J. High Speed Electron. Syst. **11**, 257 (2001).
5. R. Adam, M. Currie, C. Williams, R. Sobolewski, O. Harnack, and M. Darula, Appl. Phys. Lett. **76**, 469 (2000).
6. D. H. Auston and M. C. Nuss, IEEE J. Quantum Electron. **24**, 184 (1988).
7. M. R. Freeman, J. Appl. Phys. **75**, 6194 (1994).
8. A. Y. Elezzabi and M. R. Freeman, Appl. Phys. Lett. **68**, 3546 (1996).
9. A. K. Zvezdin and V. A. Kotov, *Modern Magnetooptics and Magneto-optical Materials* (Institute of Physics Publishing, Bristol, England, 1997).
10. S. A. Wolf *et al.*, Science **294**, 1488 (2001).
11. J. K. Furdyna, J. Appl. Phys. **64**, R29 (1988).
12. P. A. Wolff, in *Semiconductors and Semimetals*, edited by J. K. Furdyna and J. Kossut, Diluted Magnetic Semiconductors, Vol. 25 (Academic Press, Boston, 1988), Chap. 10, pp. 413–454.
13. D. D. Awschalom *et al.*, Phys. Rev. Lett. **55**, 1128 (1985).
14. T. Dietl *et al*. Phys. Rev. Lett. **74**, 474 (1995).
15. X. Zheng, Y. Xu, R. Sobolewski, R. Adam, M. Mikulics, M. Siegel, and P. Kordoš, Appl. Opt. **42**, 1726 (2003).
16. R. Rey-de-Castro, "Ultrafast Optical Properties and Applications of $Cd_{1-x}Mn_xTe$ Semimagnetic Semiconductors," Ph.D. thesis, University of Rochester, 2004.
17. R. Adam, M. Mikulics, A. Förster, J. Schelten, M. Siegel, P. Kordo□, X. Zheng, S. Wu, and R. Sobolewski, Appl. Phys. Lett. **81**, 3485 (2002).
18. R. Sobolewski and J.-R. Park, IEEE Trans. Appl. Supercond. **11**, 727 (2001).
19. R. Sobolewski, Supercond. Sci. Technol. **14**, 994 (2001).

# Simulation of Submicronmeter Metal–Semiconductor–Metal Ultraviolet Photodiodes on Gallium Nitride

## Introduction

Due to the high steady-state peak electron velocity[1–4] in gallium nitride (GaN) and the simplicity of fabrication, metal–semiconductor–metal photodiodes (MSM-PD's) fabricated on GaN have attracted intensive research effort. High-bandwidth, monolithic MSM devices have already been demonstrated.[5–8] Both Monte Carlo simulations[9] and experimental measurements[10] have shown that the intrinsic response time of the GaN MSM-PD's could be as fast as a few picoseconds. For practical applications, however, it is necessary to integrate the device into a fast package so that the photogenerated signal can be coupled out to standard timing instruments, such as a fast oscilloscope or a readout circuit. The packaging process will inevitably introduce a parasitic effect that limits the high-frequency performance of the devices. Our previous experimental results[5] showed the dominant role of the packaging fixture. To identify the performance-limiting factors and to design MSM-PD's with a required bandwidth and responsivity, it is essential to examine the dynamic behavior of the integrated unit including the photodiode and the packaging circuit.

In MSM-PD's, there are several design considerations in trying to improve their speed of response. Decreasing the interelectrode spacing has the beneficial effect of decreasing carrier-transit time (which decreases the response time), at the cost of an increase in the device capacitance (which increases the response time). To reduce the device capacitance, one can reduce the area of the interdigitated fingers. This requires a tighter focusing of the incident beam. Shrinking the total detector area would also increase the current density; thus the maximum total charge that can be delivered to the processing electronics must decrease. As a result, it is necessary to understand the behavior of UV MSM-PD's under a wide range of illumination levels. The transient behavior of infrared MSM-PD's subjected to optical pulse energies ranging from 0.01 to 316 pJ was reported recently.[11] The pulse broadening under high optical energy was attributed to the space-charge screening effect, which was studied in Refs. 12 and 13 for GaAs. However, theoretical simulations and experimental studies of the screening effect in GaN MSM-PD's under high illumination conditions have not appeared in the literature. This effect is part of our study and will be discussed in detail below.

## Simulation

The MSM device with 0.3-$\mu$m feature size and the broadband circuit to be simulated are the same as reported previously[5] (see Fig. 99.80). The circuit has a strip-line structure with the switch attached on a G-10 board. At first, we tried to model the entire assembly by an equivalent circuit with the lumped electric elements and then solve the circuit by using *SPICE*. This approach is simple and straightforward. The photocurrent, however, must be input as a parameter rather than calculated directly. Therefore the model cannot explore the opto-electronic process that occurs under optical illumination. Furthermore, this method cannot monitor the circuit effect and space-charge screening effect as discussed below.

To better understand the transient behavior of the device, we developed a more-complicated numerical simulation using a distributed-circuit approach.[14–16] Similar simulations have been used to describe the electric field in high-voltage photoconductive switches, although this is the first time they have been applied to an MSM photodiode. Instead of tracking the detailed carrier dynamics,[12,13] we assume that the optically generated electron-hole pairs are swept out (with negligible recombination) at rates determined by the field-dependence velocities.[1] The transient current and voltages are computed simultaneously and dynamically to produce the device temporal response. A major advantage of this approach is that it allows us to conveniently include the effect of the packaging circuit.

The simulation assumes a transverse electromagnetic wave propagation. This is an approximation that ignores modal dispersion and the discontinuity in the dielectric constant between the strip line and the air. The entire circuit, including the charge source, the transmission line, the semiconductor, and the load, was sliced into 1024 small cells along the equipotential lines. Each cell is modeled by discrete elements: resistors, capacitors, and inductors (see Fig. 99.80; $k$ is an even number) whose values are computed from the cell geometry.[17]

All of the cells have identical configurations and are linearly coupled to the two adjacent neighbors; therefore, we need to focus on solving only one such cell, and then the equations for the entire circuit can be mapped out. In each cell, only two unique nodes are considered: an "even" node and an "odd" node, as shown in Fig. 99.81, where $R_t$ is the resistance of the small cell, the value of which depends on the material properties of the location and is photosensitive in the active area of the device; $C_s$ is the capacitance across the resistance; $C_g$ is the capacitance between the cell and the ground; $L_s$ is the inductance of the cell; and $V_k$ is the potential at each node. When the Kirchhoff's law of current continuity is applied to these nodes, the equations of voltage and current can be obtained.

Several assumptions were made in deriving the circuit equations: (1) The Schottky contact in MSM-PD's is noninjecting; that is, no electron can flow from metal cell to semiconductor cell on the boundary between materials. (2) The gap between fingers is fully depleted, resulting in high resistivity; this is justified by noting that the flatband[18] voltage across the gap is calculated to be 0.25 V, much lower than the applied bias voltage of 5 V. (3) The optical illumination is spatially uniform across the finger spacing since the size of the spacing (0.3 $\mu$m) is much smaller than that of the active area (50 $\mu$m) and the focal spot (~10 $\mu$m). (4) The 2-D dependence of the electric field is neglected, and the electric field is uniform across the finger gap of the devices. This 1-D simulation appears to be a good approximation in estimating the device response time.

It is worthwhile to note that a more fundamental approach detailing the carrier dynamics has been done previously[12,13] using a numerical Poisson solver. In the simplified, distributed-circuit approach presented here, the entire package was modeled by discrete circuits. While it is straightforward to describe the rest of the circuit, it took some effort to build the accurate model for the interdigitated MSM photodiode so that

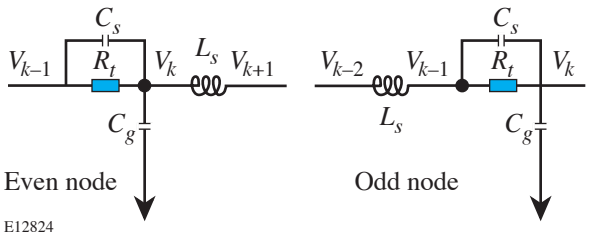


Figure 99.81
"Even" node and "odd" node of the lumped-element circuit. Here, $R_t$ is the resistance of the small cell, $C_s$ is the capacitance across the resistance, $C_g$ is the capacitance between the cell and the ground, $L_s$ is the inductance of the cell, and $V_k$ is the potential at each node.

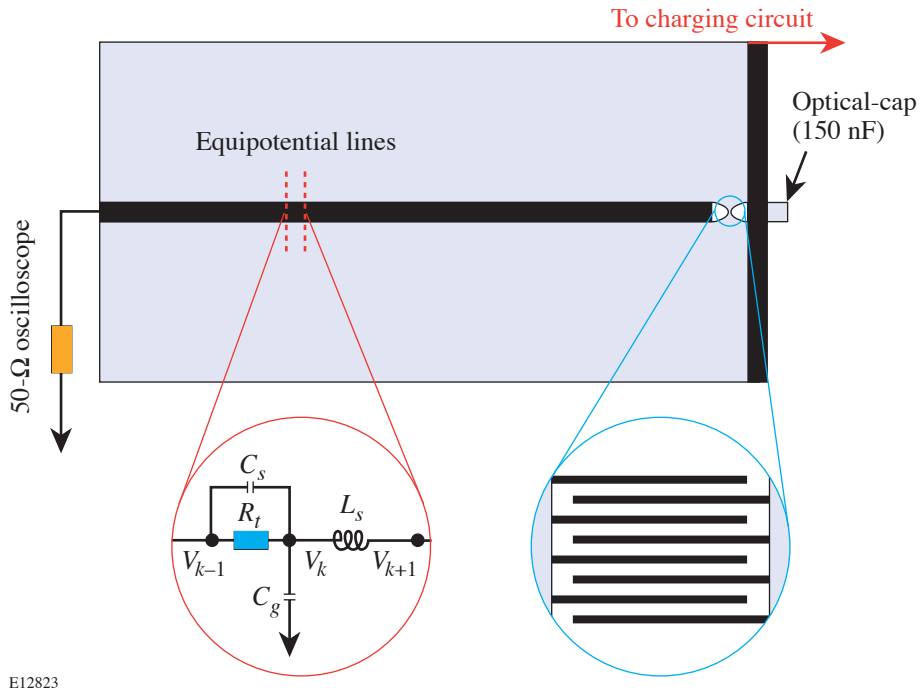


Figure 99.80
Top view of the broadband circuit designed for the MSM photodetectors. The one-dimensional transmission line was sliced into 1024 small cells along the equipotential lines and modeled as a lumped-element circuit as shown in the figure. To avoid an abrupt width change, a pad with a calculated curve tapers the transmission line down to the active area.

the 2-D structure can be degraded to a 1-D model. In the active region of the MSM photodiode, the gap between the finger electrodes was sliced into ten cells along the equipotential lines that follow the meandering shape of the fingers. When free carriers are generated optically in the gap, the carriers will move from one cell to the adjacent one under the external electric field. Transport perpendicular to the gap is ignored. Hence the time-dependent conductivity is 1-D between the finger electrodes. One concern about the 1-D model is that the electromagnetic waves may propagate along the fingers in real devices; however, the calculations show that the longest time for the electromagnetic wave to travel through the entire meander is less than 14 ps. This is small compared with the 40-ps rise time as shown below in the simulation results. Therefore, it is reasonable to ignore this propagation along the fingers and assume that the signal will travel from one finger electrode to the other finger electrode only so that the 1-D model is justified. The approach has an important advantage in that it allows the packaging circuit to be included in computing the response of the entire device assembly. A direct comparison with experimental results can then be made.

With the above assumptions, we can linearize the expressions for the currents and voltages in each cell. While the resistance in the metal transmission line is constant, the resistance in the semiconductor, which is a product of resistivity and length of the cell divided by the cross section of the cell, varies dynamically. The resistivity is calculated from the field-dependent expression

$$\rho(x,t)=\frac{1}{e\left[n(x,t)\mu_e(E)+p(x,t)\mu_h(E)\right]}(\Omega\,\mathrm{cm}), \qquad (1)$$

where the carrier densities $n$ and $p$ are calculated from the local optical intensity, absorption rate, and transport. The electron mobility $\mu_e$, a function of electric field, is given by Ref. 1, while the hole mobility $\mu_h$ is fixed at 30 $\mathrm{cm}^2$/Vs. After optical illumination, the electrons and holes separate under the influence of the applied electric field and are collected by electrodes. The changing electric field and carrier densities cause the resistance of the cell to evolve in time. This change of the resistance is coupled out to other cells by changing the values of the voltage and current in each node. The transient response of the detector is then computed according to the distributed-circuit model.[14]

With $V(t)$ as the voltage across the inductor at time $t$ and $V(t')$ as the voltage at the previous time $t'$, the currents at time $t$ and $t'$ in the inductor can be obtained by integrating $V(t)$ and $V(t')$ with the first-order Simpson's rule

$$\frac{1}{2}\left[V(t)+V(t')\right]=L_s\frac{dI}{dt}\approx\frac{L_s\left[I(t)-I(t')\right]}{\Delta t}, \qquad (2)$$

where $L_s$ is the inductance and $\Delta t = t - t'$. Similarly, the current at time $t$ in the capacitor can be written as

$$I(t)=C\frac{V(t)-V(t')}{\Delta t}, \qquad (3)$$

where $C$ is the capacitance of a section of line of length $\Delta x$. In the simulation, the even nodes and odd nodes each generate a different set of equations. By applying Kirchhoff's law of current continuity, the circuit equation for the even nodes is

$$\begin{aligned}
&V_k\left(\frac{C_g}{\Delta t}+\frac{\Delta t}{2L_S}+\frac{C_s}{\Delta t}+\frac{1}{R_t}\right)+V_{k+1}\left(-\frac{\Delta t}{2L_S}\right)\\
&+V_{k-1}\left(-\frac{C_s}{\Delta t}-\frac{1}{R_t}\right)\\
&=I'_k+V'_k\left(\frac{C_g}{\Delta t}-\frac{\Delta t}{2L_S}+\frac{C_s}{\Delta t}\right)+V'_{k+1}\left(\frac{\Delta t}{2L_S}\right)\\
&+V'_{k-1}\left(-\frac{C_s}{\Delta t}\right), \qquad (4)
\end{aligned}$$

where $k = 2n$ ($n$ changes from 1 to 1024), symbols with prime mean the variables at previous $t'$, and symbols without prime mean the variables at present time $t$. Similarly, for the odd nodes we have

$$V_{k-1}\left(\frac{\Delta t}{2L_S}+\frac{C_s}{\Delta t}+\frac{1}{R_t}\right)+V_{k-2}\left(-\frac{\Delta t}{2L_S}\right)$$

$$+V_k\left(-\frac{C_s}{\Delta t}-\frac{1}{R_t}\right)$$

$$=-I'_{k-1}+V'_{k-1}\left(-\frac{\Delta t}{2L_S}+\frac{C_s}{\Delta t}\right)+V'_{k-2}\left(\frac{\Delta t}{2L_S}\right)$$

$$+V'_k\left(-\frac{C_s}{\Delta t}\right). \tag{5}$$

The above questions are complex; however, they can be written in matrix format as follows:

$$\begin{pmatrix} A_1 & B_1 & & & & & & \\ C_2 & A_1 & B_2 & & & 0 & & \\ & \bullet & \bullet & \bullet & & & & \\ & & \bullet & \bullet & \bullet & & & \\ & & & \bullet & \bullet & \bullet & & \\ 0 & & & & \bullet & \bullet & B_{N-1} & \\ & & & & & C_N & A_N & \end{pmatrix}\begin{pmatrix} V_1 \\ V_2 \\ \bullet \\ \bullet \\ \bullet \\ \bullet \\ V_N \end{pmatrix}=\begin{pmatrix} -I'_1 \\ I'_2 \\ \bullet \\ \bullet \\ \bullet \\ \bullet \\ I'_N \end{pmatrix}$$

$$+\begin{pmatrix} A'_1 & B'_1 & & & & & & \\ C'_2 & A'_2 & B'_2 & & & 0 & & \\ & \bullet & \bullet & \bullet & & & & \\ & & \bullet & \bullet & \bullet & & & \\ & & & \bullet & \bullet & \bullet & & \\ & 0 & & & \bullet & \bullet & B'_{N-1} & \\ & & & & & C'_N & A'_N & \end{pmatrix}\begin{pmatrix} V'_1 \\ V'_2 \\ \\ \\ \\ \\ V'_N \end{pmatrix}, \tag{6}$$

where $N$ is equal to 2048 and the matrix elements are from the coefficients of the variables in Eqs. (4) and (5) and are defined as

$$A_i=\frac{C_g}{\Delta t}+\frac{\Delta t}{2L_S}+\frac{C_S}{\Delta t}+\frac{1}{R_t}$$

$$B_i=-\frac{\Delta t}{2L_S}$$

$$C_i=-\frac{C_S}{\Delta t}-\frac{1}{R_t}$$

$$\text{for } i=2n, \tag{7}$$

$$A'_i=\frac{C_g}{\Delta t}-\frac{\Delta t}{2L_S}+\frac{C_S}{\Delta t}$$

$$B'_i=\frac{\Delta t}{2L_S}$$

$$C'_i=-\frac{C_S}{\Delta t}$$

and

$$A_i=\frac{\Delta t}{2L_S}+\frac{C_S}{\Delta t}+\frac{1}{R_t}$$

$$B_i=-\frac{C_S}{\Delta t}-\frac{1}{R_t}$$

$$C_i=-\frac{\Delta t}{2L_S}$$

$$\text{for } i=2n-1. \tag{8}$$

$$A'_i=-\frac{\Delta t}{2L_S}+\frac{C_S}{\Delta t}$$

$$B'_i=-\frac{C_S}{\Delta t}$$

$$C'_i=\frac{\Delta t}{2L_S}$$

The initial values of current and voltage were determined from the dc-biased dark condition. These initial values were placed in matrix Eq. (6). The new values of voltage can then be solved. With the help of Eq. (2), the new values of current can be solved as well. Therefore, by iteration, the time response of the circuit can be numerically computed.

## Results and Discussion

In simulations, the model parameters were chosen to match the actual MSM-PD's previously tested.[5] The active area was $50 \times 50\ \mu m^2$, and the finger width and spacing were both 0.3 $\mu$m. For calculating the illumination on the detectors, we selected a Gaussian pulse with a full width at half maximum (FWHM) of 500 fs at a wavelength of 270 nm. Different illumination conditions with optical energies ranging from 0.01 pJ to 1 nJ were simulated. The results for optical pulse energies of 1, 6, 10, and 20 pJ are plotted in Fig. 99.82 with normalized amplitude. When the illumination level was lower than 1 pJ, the electric impulses delivered to the 50-Ω load had similar pulse shapes. The rising edge was dispersed by the transmission line and was typically 40 ps, which is longer than the optical pulse. The oscillations after the main peak were caused by the impedance discontinuities in the package. The shortest pulse width was 48 ps, which is a little shorter than our measured result of 60 ps for the same device as reported in Ref. 5. We attribute this discrepancy between simulation and measurement to parasitic effects not included in the simulation, such as the connector discontinuities and the fact that in a microstrip transmission the field is not truly transverse electromagnetic.

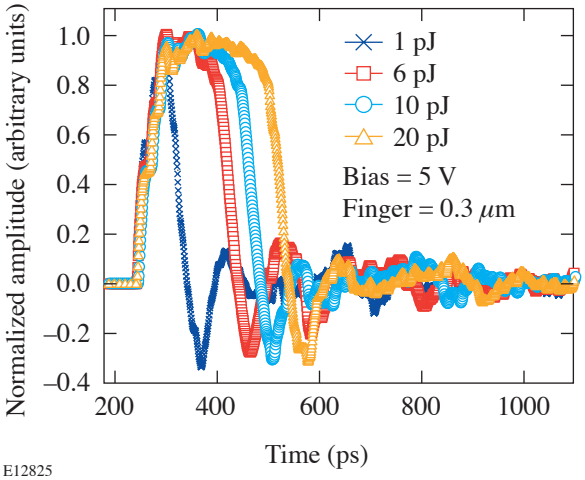


Figure 99.82
Simulated time responses of the detectors with different optical pulse energies of 1 pJ (×), 6 pJ (square), 10 pJ (circle), and 20 pJ (triangle) under 5-V bias. The amplitudes of the signal have been normalized to the peak values.

The most-distinguishing feature of the results is that the pulse width broadens markedly as the optical pulse energy increases. This trend is the same as observed in experiments.[5] This increase in pulse duration can be attributed to the screening of the dark electric field between the finger electrodes by the space-charge field induced by the separation of the photogenerated electrons and holes. Qualitatively, at high excitation intensity, carrier densities of both electrons and holes increase to the point when the normally depleted region of the detector now has a substantial conductivity that temporarily decreases the electric field. As a result, the carriers are now swept out at a lower speed, hence the slower detector response. This effect is essentially the same as was found in GaAs photodetectors reported in Refs. 12 and 13.

## Comparison with Experiments

The pulse broadening, under high-level illumination, was observed in both experiments[5] and simulations. In this section the pulse width's dependence on the total optical energy will be compared for the two cases. In our simulations, the external quantum efficiency was assumed to be 100%; that is, each photon generates a free electron and hole pair. To compare the simulated and experimental results at the same illumination level, it is necessary to modify the optical pulse energy in experiments according to the measured external quantum efficiency, defined as the ratio of the number of the electron-hole pairs and the incident photons. The number of electrons generated by the optical pulse was obtained by integrating the photoelectric current; the number of photons in each optical pulse was determined by dividing the measured average laser power by the repetition rate (82 MHz for a Ti:sapphire laser) and the energy of each photon. In the case of the highest input of 391 pJ, $\eta_{ex}$ was determined to be 1.77%. This factor was used to scale the experimental data. In Fig. 99.83, the simulated and measured FWHM's after the scaling are plotted together. With a single scaling factor, the experimental and simulated results are in close agreement.

Analysis of the data shows that the pulse width remains approximately constant until the optical energy exceeds a certain level (around 0.4 pJ) for both simulated results and scaled-experiment results. We can compute the photogenerated charge and compare its value to the stored charge in the device as follows: the capacitance of the MSM structure calculated to be 0.182 pF,[19] corresponding to a stored charge

of $9.1 \times 10^{-13}$ C (or, about $5.7 \times 10^{6}$ electrons) given 5-V bias. At an optical energy of 0.4 pJ, the depletion region would have a total carrier density equal to about 10% of the stored charge. This amount appears to be the threshold of the onset of the space-charge effect.

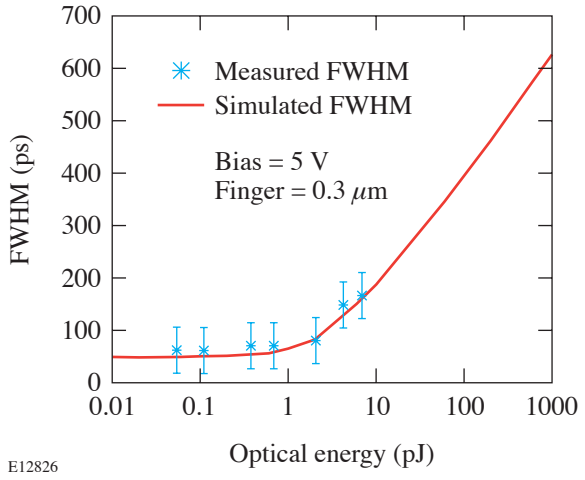


Figure 99.83
Comparison of FWHM's from stimulation and experiment. To compare them in the same illumination level, a single factor was used to scale down the optical energy in experiment.

## Summary

In summary, a GaN interdigitized-finger MSMPD with 0.3-$\mu$m finger width and spacing was packaged with a specially designed fast circuit. The entire assembly was simulated by a simplified, distributed-circuit approach so that the circuit effect can be conveniently monitored. The space-charge screening effect causing the broadening of the impulse response was discussed and compared with experimental results. After a single scaling factor of external quantum efficiency, theory and experiment were brought to a close agreement.

## ACKNOWLEDGMENT

This work was supported by the U.S. Department of Energy Office of Inertial Confinement Fusion under Cooperative Agreement No. DE-FC52-92SF19460, the University of Rochester, and the New York State Energy Research and Development Authority. The support of DOE does not constitute an endorsement by DOE of the views expressed in this article.

## REFERENCES

1. U. V. Bhapkar and M. S. Shur, J. Appl. Phys. **82**, 1649 (1997).
2. J. D. Albrecht *et al.*, J. Appl. Phys. **83**, 4777 (1998).
3. J. Kolnik *et al.*, J. Appl. Phys. **78**, 1033 (1995).
4. B. Gelmont, K. H. Kim, and M. Shur, J. Appl. Phys. **74**, 1818 (1993).
5. J. Li, W. R. Donaldson, and T. Y. Hsiang, IEEE Photonics Technol. Lett. **15**, 1141 (2003).
6. J. C. Carrano *et al.*, J. Electron. Mater. **28**, 325 (1999).
7. J. C. Carrano *et al.*, Appl. Phys. Lett. **73**, 2405 (1998).
8. D. Walker *et al.*, Appl. Phys. Lett. **74**, 762 (1999).
9. R. P. Joshi, A. N. Dharamsi, and J. McAdoo, Appl. Phys. Lett. **64**, 3611 (1994).
10. J. Li *et al.*, Appl. Phys. Lett. **84**, 2091 (2004).
11. K. Aliberti *et al.*, Appl. Phys. Lett. **80**, 2848 (2002).
12. S. V. Averine and R. Sachot, IEE Proc., Optoelectron. **147**, 145 (2000).
13. S. V. Averine and R. Sachot, Solid-State Electron. **44**, 1627 (2000).
14. L. Mu and W. R. Donaldson, in *Proceedings of the Ninth IEEE International Pulsed Power Conference*, edited by K. Prestwich and W. Baker (IEEE, New York, 1993), pp. 629–632.
15. L. E. Kingsley and W. R. Donaldson, IEEE Trans. Electron Devices **40**, 2344 (1993).
16. W. R. Donaldson and L. Mu, IEEE J. Quantum Electron. **30**, 2866 (1994).
17. B. C. Wadell, *Transmission Line Design Handbook* (Artech House, Boston, 1991).
18. S. M. Sze, D. J. Coleman, Jr., and A. Loya, Solid-State Electron. **14**, 1209 (1971).
19. Y. C. Lim and R. A. Moore, IEEE Trans. Electron Devices **ED-15**, 173 (1968).

# Overpressure Contact Printing and Its Applications in the Fabrication of Arrays of Magnetic Rings

The elastomeric property of poly(dimethylsiloxane) (PDMS) allows stamps made of this polymer to be widely used in replicating patterns with high fidelity through the conformal contact between the substrate and the stamp surfaces.[1–3] This unique property is also the origin of stamp deformations. Although the conformal contact is preferred in contact printing, the application of stamp deformations in nanofabrication is severely under investigated. Xia *et al*. were able to create patterns with size-reduced features by intentionally applying external forces to laterally deform the stamps during contact printing.[4] This article shows that not only can size reductions be achieved by applying pressure normal to the substrates during contact printing, but also new patterns different from those features on the stamps can be generated by this patterning approach. This method is referred to as overpressure contact printing (oCP). It is particularly worthwhile to mention that oCP is unique in the fabrication of new features while having the advantage of miniaturization.

As indicated, overpressure contact printing relies on the deformation of PDMS stamps. The mechanical properties of PDMS and the behaviors of PDMS stamps have been examined recently.[5,6] Delamarche *et al*. showed that the height-to-width ratios—the aspect ratios—of the relief structures on PDMS stamps need to be between about 0.2 and 2 in order to obtain defect-free printing. If the aspect ratio of the PDMS feature is too high, the roof of the feature may come into contact with a substrate under its own weight or under an external pressure. When the aspect ratios are too low, the relief structures are not able to withstand the stamp weight. The compressive forces of printing and the adhesion force between the stamp and the substrate can both cause the similar result.[5,7,8] This article will briefly describe the theoretical analysis of this deformation of PDMS.[8]

Figure 99.84(a) shows a basic geometry of a stamp that consists of periodic relief line features with height of $h$, feature width of $2w$, and trench width of $2a$. When pressure is applied to the stamp, several deformations occur, including in-plane lateral expansion, "sagging" of the trench, and relief feature from compression by the external stress. The in-plane expansion of the stamp could be minimized if a stiff backplane such as a glass plate on the elastomer is used since the Young's modulus of glass is much greater than that of PDMS. Because the strength of stress applied is typically of the order of the Young's modulus of PDMS, the Poisson expansion of the stamp bonded to the glass backplane can be several orders of magnitude lower than that of a stamp without a backplane and negligible.[8]

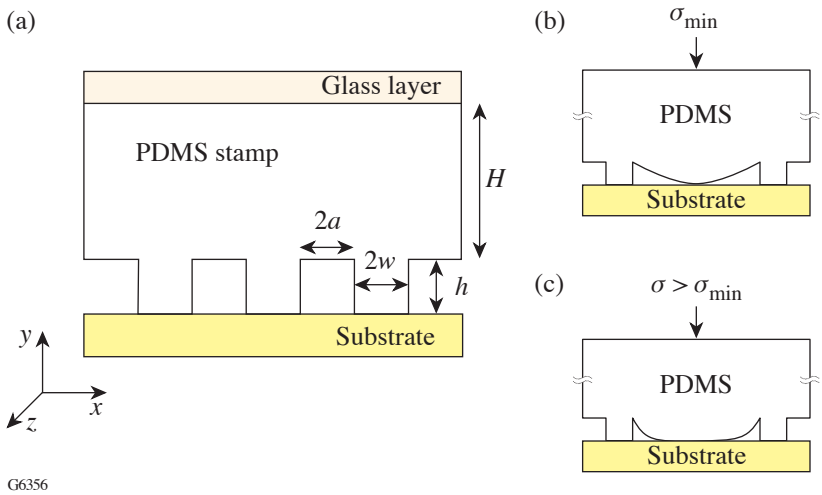


Figure 99.84
Illustrations of (a) the basic geometry of a PDMS stamp and stamps deformed into contact with substrates under (b) required minimum and (c) excess pressures.

Most elastomers are rubber elastic and incompressible with Poisson's ratio $v$ of approximately 0.5. The Young's modulus of PDMS depends strongly on the mixing ratios between prepolymer precursor and curing agent and the preparation conditions, such as curing time and temperature. The Young's modulus (E) and density of the PDMS material with different mixing ratios have been studied by examining the deflection of a single-side clamped PDMS cantilever beam.[6] To keep the mechanical properties of the PDMS consistent, a mixing ratio of 10:1 between the polymer and curing agent was used along with a curing temperature of 70°C overnight for all the stamps tested in this work. The Young's modulus of PDMS stamps prepared at these conditions is ~0.75 MPa as indicated by Armani *et al*.[6] For a qualitative analysis, the height of the stamp backbone is neglected because it is normally much greater than the height of the relief features, and the amount of pressure from the weight of the stamp is negligible as compared to the amount of pressure applied. With these assumptions, the model for promoted contact between the roof and substrates under external stress [Fig. 99.84(b)] can be simplified as follows:[8]

$$V_{\max} = \frac{4\sigma_{\min}}{\pi E^*}(w+a)\cosh^{-1}\left\{\sec\left[\frac{w\pi}{2(w+a)}\right]\right\}, \qquad (1)$$

where $V_{\max}$ is the maximum displacement of the roof by an applied minimum external stress $\sigma_{\min}$ and $E^* = E\Big/\left(1-v^2\right)$. All variables in the equation are known except external stress $\sigma$, which can be varied to give different degrees of contacts between the roof and the substrate [Fig. 99.84(c)].

This article further demonstrates the application of the oCP technique in creating FePt magnetic ring and anti-ring structures from microwell patterns of $Pt@Fe_2O_3$ nanoparticles. We are particularly interested in making arrays of these magnetic structures because such patterns are candidates for magnetic random access memory (MRAM).[9] In MRAM, it requires a reproducible switching mechanism from one cycle to the next. In this context, flux closure magnetic elements are favorable as compared to linear magnetic elements because of less dependence on the edge domain effect. For linear elements, the randomly magnetized edge domains form at the flat edges, which can prevent repeatable magnetic switching. On the contrary, the circular disks and rings with flux closure magnetization are more sustainable to edge roughness and, therefore, are suitable for device fabrication. In magnetic disks, however, a center vortex can form, and vortex displacement may lead to an irreproducible switching. A ring-shaped magnetic element can form a stable flux closure magnetization without the central vortex because of the geometry confinement of the ring.[9] A vertical magnetoresistive random access memory based on ring elements has been proposed recently.[9]

Nano-rings have been fabricated by *e*-beam lithography or nanoimprinting.[10–12] Although *e*-beam lithography can create ordered arrays of nano-rings with controllable diameter and thickness, the process is usually cumbersome and inaccessible to the majority of researchers. More recently, Scott *et al*. have successfully fabricated ordered arrays of magnetic rings by using controlled dewetting of polymeric percursors.[13] This technique is versatile and able to create ordered ring arrays of iron- and cobalt-containing polymers. Upon thermal treatment, the polymers can decompose and form magnetic ceramics. The combined dewetting and pyrolysis processes tend to lead, however, to the formation of local organization of the magnetic nanoparticles within the bands, while the continuity is pivotal for the rings to exhibit the unique flux closure magnetization mode. Here, an alternative technique to fabricate nano-rings in a controlled fashion using oCP is presented. The capability of the oCP technique is illustrated using self-assembled monolayers (SAM) on gold. The application of this method in making arrays of FePt rings from pLB films[14] of 4-nm $Pt@Fe_2O_3$ core–shell nanoparticles[15] is then described.

Gold substrates used in this research were made by depositing a 45-nm-thick gold layer onto silicon wafers using an *e*-beam evaporator. The ink was hexadecanethiol in an ethanol solution (~1 mM).[2] The PDMS patterns were replicated from photoresist (Shipley 1813) patterns on silicon following the standard procedures.[16] The height of the photoresist features made from this photoresist is expected to be 1.3 $\mu$m and was examined using a tapping-mode atomic force microscope (AFM, Digital Instrument, Nanoscope IIIa). In a typical procedure, the gold substrates and stamps were first cleaned with ethanol and dried under a stream of $N_2$ gas. A small amount of ink solution was then applied on the stamp surface using a cotton tip. The excess thiol solution was washed away with ethanol and dried with $N_2$ gas for 2 min. The stamp was then placed in contact with the gold substrate. To ensure conformal contact between the stamp and the substrate, and contact between the roof of the features and the substrate surface, pressure (~0.3 MPa) was applied normal to the substrate surface by using an iron block (3.2 kg/cm$^2$) during printing. The size of the stamp was typically $1 \times 1$ cm$^2$. The unprotected gold regions were removed by an aqueous etching solution consisting of $K_3Fe(CN)_6$ (0.01 M), $K_4Fe(CN)_6$ (0.001 M), $K_2S_2O_3$ (0.1 M), and KOH (1 M). The optimized duration for etching away 45 nm of gold was about 8.5 min. The etched

substrates were washed thoroughly with ethanol and deionized water and dried with $N_2$.

The ability to pattern $\gamma$-$Fe_2O_3$ (Ref. 17) and $Pt@Fe_2O_3$ nanoparticles[15,18] using the patterned Langmuir–Blodgett (pLB) technique[14,15] has been demonstrated. Both monolayer and multilayer depositions of nanoparticles are possible using the pLB technique through a layer-by-layer approach. This pLB technique has been used to pattern $Pt@Fe_2O_3$ core–shell nanoparticle arrays of rings and anti-rings in conjunction with oCP. The experimental procedure is shown in Fig. 99.85. In a typical procedure of making nanoparticle patterns, designed multilayers of Langmuir films of ~4-nm $Pt@Fe_2O_3$ nanoparticles were transferred onto a PDMS stamp of microwell pattern (10 $\mu$m). The nanoparticle-coated stamp was then contact printed on a plasma-cleaned Si wafer at a pressure of ~0.3 MPa for 2–3 s. The initial printing (oCP) generated the anti-ring pattern of nanoparticles [Fig. 99.85(a)], while removing the particles from the centers of the roofs of the wells that made contact with the substrate. The stamp was then carefully released from the substrate and used for a second printing under a pressure of ~0.3 MPa and a stamping time of 10 s. Arrays of ring structures could be obtained from the second printing, which is referred to as extended oCP [Fig. 99.85(b)].

Field-emission SEM images were obtained using a LEO 982 microscope. Tapping-mode AFM and magnetic-force microscope (MFM) images were collected using a Digital Instrument Nanoscope IIIa microscope. The magnetic tips (MFMR) were purchased from Nanosensors. The cantilevers are coated with cobalt alloy (40 nm thick) on the tip side and aluminum (30 nm thick) on the detector side. The tip radii are typically less than 50 nm. The tips are magnetized using a permanent magnet (field strength: ~0.2 Tesla) prior to MFM imaging. MFM images were obtained using the interleave mode at a lift scan height of 50 nm.

To demonstrate the oCP technique, gold microstructures were created on silicon starting from SAM of thiolate on gold surfaces. In this case, the SAM acted as an etching resist layer. Several line patterns with various height/width aspect ratios have been tested. The physical dimensions and their corresponding aspect ratios of some of the relief line patterns on the PDMS stamps used in this project are listed in Table 99.V. These numbers have been obtained from SEM and AFM characterizations of the photoresist masters and the PDMS stamps (Fig. 99.86). In oCP, the roof of the stamp is intentionally deformed to promote the contact with the substrate [Fig. 99.84(b)]. The minimum amount of pressure $\sigma_{min}$ required to make the initial contact between the roof of the stamp

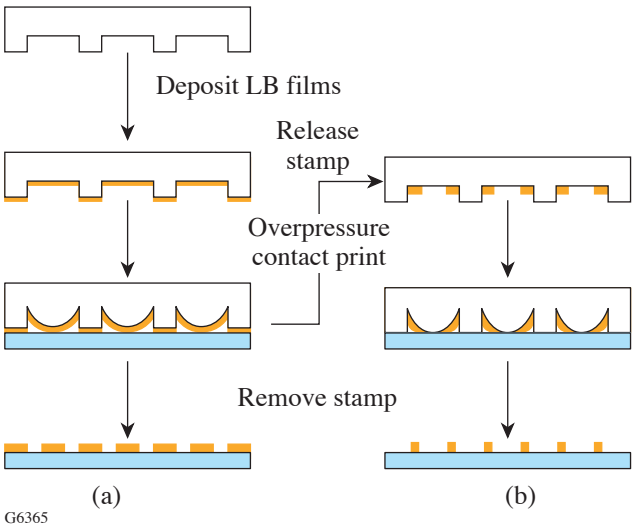


Figure 99.85
The experimental procedure for (a) overpressure and (b) extended overpressure contact printing.

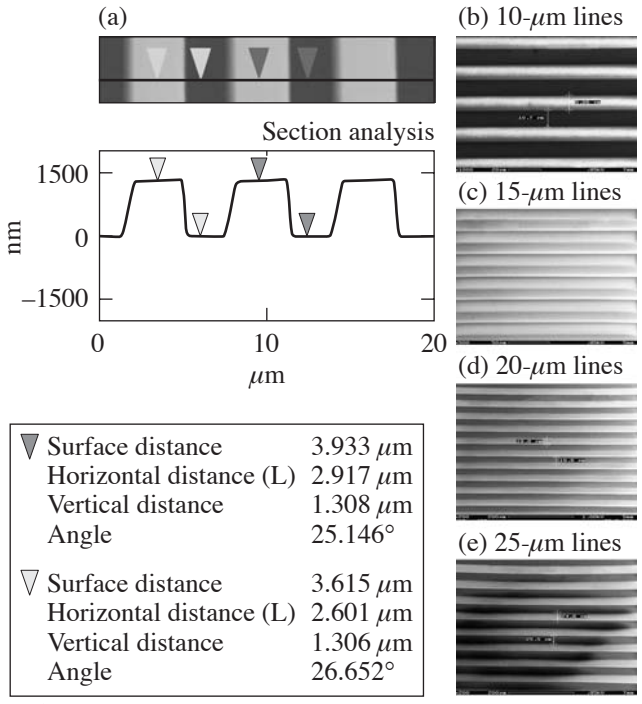


Figure 99.86
(a) AFM images and cross-section analyses showing the height (1.3 $\mu$m) of the PDMS stamps used in this work and [(b)–(e)] the SEM images of the photoresist masters of line patterns (10, 15, 20, and 25 $\mu$m) used in this study.

and the substrate was estimated for each of the stamps used based on the equation and data presented above; the results are listed in Table 99.V. The minimum pressures needed for the various stamps used were all below the Young's modulus of PDMS made at the current synthetic conditions (0.75 MPa)[6] and the amount of pressure applied (0.3 MPa). By applying pressure greater than the minimum, a higher degree of deformation can be obtained [Fig. 99.84(c)].

Figure 99.87 shows a series of SEM images of etched trenches on gold substrates fabricated by the oCP technique using the equally spaced line stamps presented in Table 99.V. The etched patterns consisted of arrays of gold lines separated by fine trenches (insets of Fig. 99.87). It is noticeable that the trenches between these lines were slightly uneven in width. This is most likely due to the unevenness of the weight when situated on top of the stamp. The contrast in SEM images of gold on silicon could also vary slightly. The light and dark line structures shown in Figs. 99.87(a) and 99.87(d) on both sides of the trenches were Au substrates resulting from the different etching resistance from the SAM's. During the initial oCP, the stamp was placed in intimate contact with the substrate where only the protruded structures on the stamp were able to contact the substrate [the lighter lines in Figs. 99.87(a) and 99.87(d)]. The roofs of the stamps were then brought into contact with the substrate by applying external pressure where coverage of thiolate on the Au substrate at the contact areas between the roof and the substrate (the darker lines) was different from feature regions. The difference between these two regions could be eliminated by controlling the etching conditions, as demonstrated in Figs. 99.87(b) and 99.87(c).

The sizes of the trenches made from each stamp of line patterns are summarized in Table 99.V. For a stamp with a roof height of 1.3 $\mu$m, the generated trenches have widths of about 1/10 or slightly less than 1/10 of those on the original patterns, when the applied pressure was ~0.3 MPa. For instance, a trench width of ~1 $\mu$m was fabricated by using a 10 × 10-$\mu$m–sized line stamp. The percentage of size reduction did not change

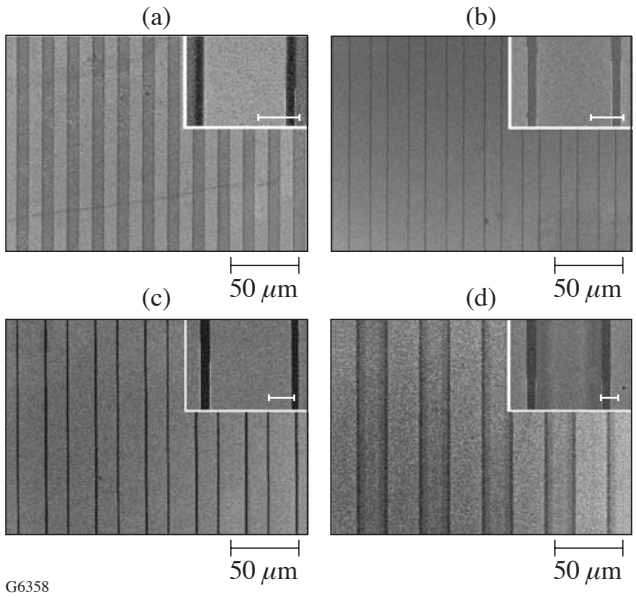


Figure 99.87
SEM images of trenches on surfaces of Au substrates fabricated using oCP from (a) 10 × 10-$\mu$m, (b) 15 × 15-$\mu$m, (c) 20 × 20-$\mu$m, and (d) 25 × 25-$\mu$m stamps. The scale bars in the insets are 5 $\mu$m.

Table 99.V: Dimensions and aspect ratios of the PDMS stamps of parallel lines used, the calculated minimum pressure for causing contacts between the roofs and substrates, the applied pressures, and the trench sizes fabricated in gold substrates using oCP.

| Width ($\mu$m) | | Height* $h$ ($\mu$m) | Aspect ratio ($h/w$) | $\sigma_{min}$** (MPa) | $\sigma_{applied}$ (MPa) | Trench size fabricated ($\mu$m) | | |
|---|---|---|---|---|---|---|---|---|
| Trench $2a$ | Feature $2w$ | | | | | Trench 1 | Trench 2 | Trench 3 |
| 10 | 10 | 1.30 | 0.13 | 0.13 | 0.3 | 0.99 | 1.09 | 1.0 |
| 15 | 15 | 1.30 | 0.087 | 0.87 | 0.3 | 1.01 | 1.30 | 1.2 |
| 20 | 20 | 1.30 | 0.065 | 0.065 | 0.3 | 1.48 | 1.80 | 1.6 |
| 25 | 25 | 1.30 | 0.052 | 0.052 | 0.3 | 2.31 | 2.32 | 2.3 |

*The height was estimated by AFM.
**Calculation was based on the equation given in the text.

substantially for patterns with line widths between 10 $\mu$m and 25 $\mu$m when the height of the roof was maintained the same and the features had height-to-width ratios varying between 0.052 and 0.13. All of these aspect ratios were smaller than the critical threshold value of 0.2 at which substantial external pressures is required to collapse the roof.[5] Our preliminary data indicate that the oCP technique can be extended to fabricate submicron and potentially nanometer-sized structures. Figure 99.88 shows an SEM image of submicron-sized trenches on the surface of the Au substrate fabricated from 1 × 1-$\mu$m line stamp with a height of ~0.5 $\mu$m using oCP technique. The average trench width was ~300 nm, although only a single trench per repeating unit has been produced. Careful design in stamp geometry is required for a systematic study in this size-reduced range.

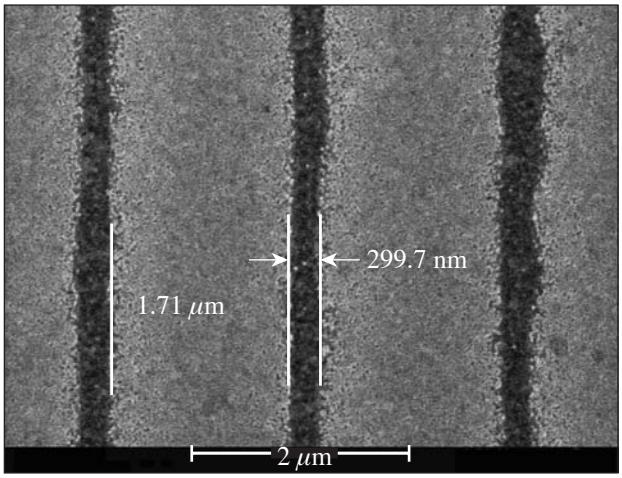


Figure 99.88
SEM image of submicron-sized trenches on the surface of Au substrate fabricated from 1 × 1-$\mu$m line stamps using oCP. Only a single trench per repeating unit has been produced.

The oCP technique was applied in patterning Pt@$Fe_2O_3$ core–shell nanoparticles to create anti-ring and ring structures. Langmuir films of ~4-nm Pt@$Fe_2O_3$ core–shell nanoparticles were transferred onto a PDMS stamp of well arrays (10 $\mu$m in well diameter with a well center-to-center distance of 15 $\mu$m). Overpressure and extended overpressure printing on plasma-cleaned Si substrates were used to obtain anti-ring and ring patterns, respectively. Figure 99.89 shows the SEM images of the single and arrays of fabricated anti-ring and ring patterns of Pt@$Fe_2O_3$ nanoparticles at different magnifications. The patterns were relatively uniform over a large area. The ring and anti-ring patterns obtained were not completely complimentary to each other. The average trench width of the anti-rings was ~1.3 $\mu$m, while the rings had an average line width of ~1.1 $\mu$m. Some of the rings were not completely closed loops or had variation in line width, which could be due to the rupture of the nanoparticulate films during contact printing. Similar defects at the inner and outer perimeters could be found for anti-ring patterns. This effect could be minimized by optimizing the thickness of the nanoparticulate films and using precise control in releasing the stamp.

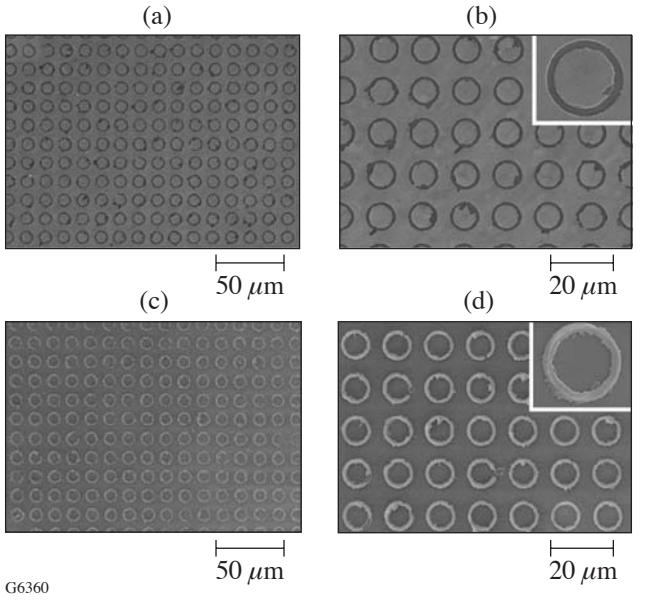


Figure 99.89
SEM images of [(a), (b)] anti-ring and [(c), (d)] ring patterns of Pt@$Fe_2O_3$ nanoparticles. Insets in (b) and (d) show the individual anti-ring and ring, respectively.

Tapping-mode AFM was used to examine the topology of the ring patterns made by extended oCP of Pt@$Fe_2O_3$ core–shell nanoparticles. Figures 99.90(a) and 99.90(b) show the three- (3-D) and two-dimensional (2-D) presentations of the ring structures of pLB films of Pt@$Fe_2O_3$ core–shell nanoparticles. The cross-section analysis shows that the rings had relatively uniform height [Fig. 99.90(c)]. The average height of the rings was ~285 nm, which corresponds to approximately 36 layers of nanoparticles. The number of layers in the rings was reasonable and further confirmed by measuring the height of six-layered unpatterned Pt@$Fe_2O_3$ nanoparticles to get an average thickness of a single particle layer. The AFM image and the cross-section analysis for an unpatterned six-layered film of Pt@$Fe_2O_3$ nanoparticles are shown in Fig. 99.91. The average thickness was 45 nm, which corresponds to a mono-

layer thickness of 7 to 8 nm. This value is reasonable since the 4-nm Pt@$Fe_2O_3$ core–shell nanoparticles are capped with oleic acid surfactants, which have a typical length of ~3 to 5 nm, depending on the configuration of hydrocarbon chains. The ruptured features observed in SEM were seen in the AFM image as well.

The patterned rings of Pt@$Fe_2O_3$ core–shell nanoparticles could be readily converted to face-centered tetragonal (fct) FePt alloy rings by thermal annealing in an atmosphere of 5% (*v*/*v*) hydrogen in argon at 450°C for 30 min.[15–19] Figures 99.92(a)–99.92(c) show the tapping-mode AFM images in 3-D and 2-D views and a cross-section analysis of the rings after the solid-state conversion. The average height of the patterns after annealing was approximately 140 nm. This value is reasonable considering the carbonization of surfactants and coalescence of nanoparticles upon annealing. The six-layered unpatterned film after the conversion had an average height of ~23 nm. Although the rings showed a large degree of shrinkage in height after the conversion, our cross-section analysis indicated that the line width of the ring did not show substantial broadening or shrinkage.

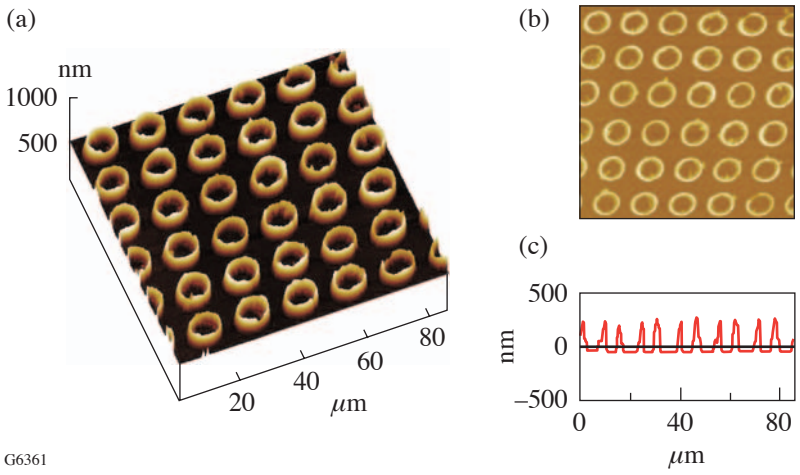


Figure 99.90
Tapping-mode AFM images of ring arrays of Pt@$Fe_2O_3$ nanoparticles: (a) 3-D representation, (b) 2-D representation, and (c) a cross-section analysis.

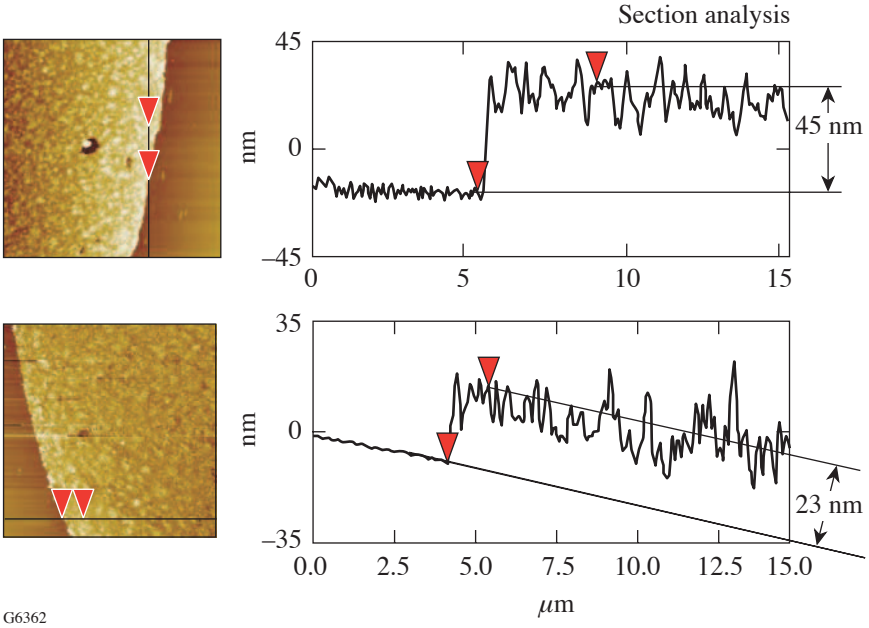


Figure 99.91
AFM images and their section analyses of six-layered unpatterned LB films of Pt@$Fe_2O_3$ core–shell nanoparticles (a) before and (b) after solid-state conversion.

MFM is a powerful tool to study magnetic properties of patterned structures.[20] In this technique, the topography contrast and magnetic interaction can be effectively separated by using tapping mode. As illustrated in Fig. 99.93(a), the phase contrast in an MFM image depends on the interaction of magnetic dipoles between the MFM tip coating layer and those of the substrate. Both low and high phase signals are possible for magnetic components on a substrate in comparison to nonmagnetic regions. The dark contrast indicates the magnetic repulsion between the tip and substrate, while the light-contrast region shows the attractive interaction. A relatively thick film was desired to have strong-enough magnetic signals for MFM characterization. Figure 99.93(b) shows the MFM study on the magnetization of the ring arrays characterized in Fig. 99.92. Both the tip and the substrate of FePt-magnetic ring on silicon have been premagnetized using a magnet (~0.2 to 0.25 Tesla). The magnetic response from the ring could be clearly visualized in the MFM image. The dark contrast indicated that the magnetic layer on the tip and the ring patterns repelled each other, which suggests that they were magnetized in the same direction.

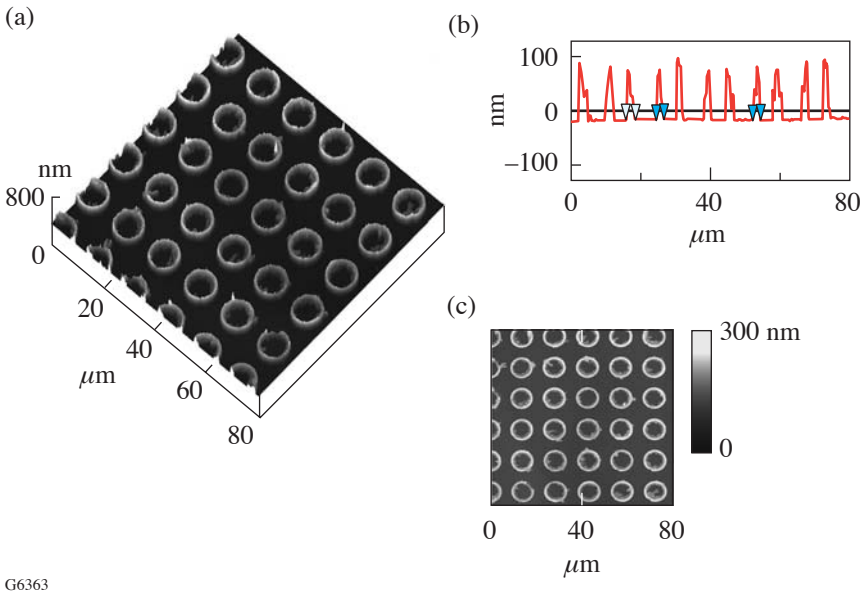


Figure 99.92
[(a)–(c)] Tapping-mode AFM images of FePt rings: (a) 3-D representation, (b) 2-D representation, and (c) cross-section analysis.

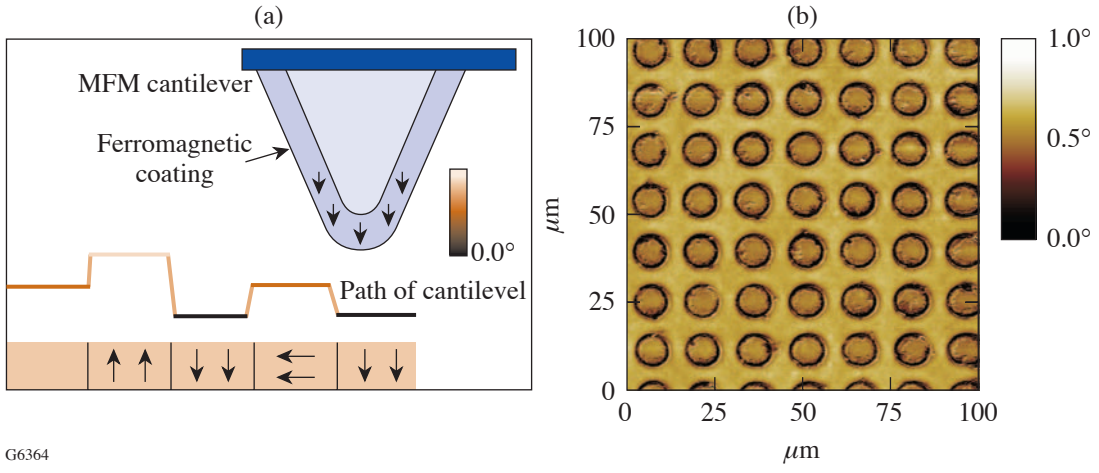


Figure 99.93
(a) An illustration of the magnetic interactions between MFM tip and patterned substrate and (b) MFM phase image of fct FePt magnetic rings made by extended oCP.

In conclusion, it has been demonstrated that a new patterning approach can be developed by controlling contact areas between the roof of an elastomeric stamp and the substrate surface to create size-reduced patterns. This technique is unique in that it offers a tool for making new patterns that may not exist on the original masters. The method is versatile and used to pattern self-assembled monolayers as well as thin films of nanoparticles. Fabrication of submicron-sized patterns is feasible with properly designed elastomeric stamps. The magnetic rings and anti-ring structures could have various novel applications, such as the study of magnetization reversal,[21] metastable states of magnetic rings,[12,22–24] and ring-based magnetic biological separations and manipulations.[25]

## ACKNOWLEDGMENT

This work was supported by the National Science Foundation and the U.S Department of Energy (DOE, DE-FC52-92SF19460) through the Laboratory for Laser Energetics at University of Rochester. We thank Mr. Justin Jiang of Harvard University for the gold substrates and Dr. Semyon Papernov (AFM and MFM) and Mr. Brian McIntyre (SEM) for help. The support of DOE does not constitute an endorsement by the DOE of the views expressed in this article.

## REFERENCES

1. Y. Xia *et al.*, Chem. Rev. **99**, 1823 (1999).
2. Y. Xia and G. M. Whitesides, Angew. Chem., Int. Ed. Engl. **37**, 550 (1998).
3. B. D. Gates *et al.*, Annu. Rev. Mater. Res. **34**, 339 (2004).
4. Y. Xia and G. M. Whitesides, Langmuir **13**, 2059 (1997).
5. E. Delamarche *et al.*, Adv. Mater. **9**, 741 (1997).
6. D. Armani, C. Liu, and N. Aluru, in *Twelfth IEEE International Conference on Micro Electro Mechanical Systems* (IEEE, Orlando, FL, 1999), pp. 222–227.
7. A. Bietsch and B. Michel, J. Appl. Phys. **88**, 4310 (2000).
8. C. Y. Hui *et al.*, Langmuir **18**, 1394 (2002).
9. J.-G. Zhu, Y. Zheng, and G. A. Prinz, J. Appl. Phys. **87**, 6668 (2000).
10. Y. Chen *et al.*, Microelectron. Eng. **57–58**, 405 (2001).
11. L. J. Heyderman *et al.*, J. Appl. Phys. **93**, 10,011 (2003).
12. F. J. Castaño *et al.*, Phys. Rev. B, Condens. Matter **67**, 184425 (2003).
13. S. B. Clendenning *et al.*, J. Mater. Chem. **14**, 1686 (2004).
14. Q. Guo *et al.*, J. Am. Chem. Soc. **125**, 630 (2003).
15. Q. Guo, X. Teng, and H. Yang, Adv. Mater. **16**, 1337 (2004).
16. H. Yang *et al.*, Adv. Mater. **13**, 54 (2001).
17. X. Teng and H. Yang, J. Mater. Chem. **14**, 774 (2004).
18. X. Teng *et al.*, Nano Lett. **3**, 261 (2003).
19. X. Teng and H. Yang, J. Am. Chem. Soc. **125**, 14,559 (2003).
20. X. Zhu and P. Grütter, MRS Bull. **29**, 457 (2004).
21. S. P. Li *et al.*, Phys. Rev. Lett. **86**, 1102 (2001).
22. M. Kläui *et al.*, Appl. Phys. Lett. **78**, 3268 (2001).
23. M. Kläui *et al.*, Appl. Phys. Lett. **84**, 951 (2004).
24. M. Steiner and J. Nitta, Appl. Phys. Lett. **84**, 939 (2004).
25. H. Lee *et al.*, Nano Lett. **4**, 995 (2004).

# Shock Propagation in Deuterium–Tritium–Saturated Foam

**Introduction**

Over the past few years there has been considerable interest regarding the use of foam shells in inertial confinement fusion (ICF)[1] targets. The original proposed use of plastic foam shells was as a matrix for liquid deuterium–tritium (DT) fuel.[2] More recently, in the designs of Colombant *et al.*,[3] foam has been proposed for use as an ablator material, in conjunction with an outer layer of a high-atomic-number material such as Pd. In these designs, the foam is preheated by radiation from the outer layer and has substantially higher ablation velocities, resulting in a more-stable outer surface. In other high-gain "wetted-foam" designs,[4] the foam is used primarily because it has a higher atomic number than DT. This results in greater absorption and increased laser-energy coupling, which in turn allows more fuel to be used without reduction in stability, resulting in higher gain. Sophisticated target designs for inertial fusion energy (IFE) that build on these techniques and use wetted-foam layers have been designed and tested computationally (see, for instance, Ref. 5 and references therein). Foam has also been suggested to reduce laser imprint in direct-drive ICF.[6]

Direct-drive ICF target designs use a pulse that drives at least two main shocks into the target. Target performance depends in part on the timing of these shocks. The first shock propagating through a foam layer encounters an inhomogeneous medium. It is important to know whether this will have any effect on the shock speed and resulting shock timing. In addition, inhomogeneities in the foam can feed through to the shell's inner surface,[7] and again to the outer surface, where they may potentially contribute to seeds of hydrodynamic instability during the deceleration and acceleration phases of the implosion (respectively).

The length scale of the foam inhomogeneities is a fraction of a micron; for one of the foams discussed here, the foam is fibrous, with a fiber radius of about 1/20 $\mu$m. A National Ignition Facility[8] direct-drive target radius is much larger, at least 1.5 mm, with a shell thickness of hundreds of microns. This large range of length scales makes it prohibitive to model foam inhomogeneities in a simulation of a target implosion. As a result, simulations of foam-target implosions must model the wetted foam as a homogeneous mixture.

To investigate the effects of foam microstructure, we have performed two-dimensional (2-D) hydrodynamic simulations of a shock propagating through a plastic foam saturated with DT ice. In these simulations, the microstructure of the foam filaments is resolved, allowing determination of its effects on shock behavior. ICF-relevant wetted-foam simulations modeling the foam microstructure have been performed previously by Phillips,[9] Hazak *et al.*,[10] Kotelnikov and Montgomery,[11] and Philippe *et al.*[12] Phillips considered an ICF-relevant case of a shock propagating through a random arrangement of plastic (CH) fibers filled with DT. He found that the shock-front perturbations were comparable in size to the fiber radius, and that the kinetic energy in the mixing region—the post-shock region in which the foam and DT are mixed and potentially homogenized—accounts for of the order of a few percent of the mean kinetic energy. Hazak *et al.* performed 2-D simulations of a shock propagating through a regular array of CH fibers, filled with liquid deuterium ($D_2$). They focused on the mix region behind the shock, deriving generalized jump conditions including fluctuations. Among other results, they found that the fluctuations result in an under-compression behind the shock, and that the jump to the under-compressed state cannot be modeled by a simple change in the ratio $\gamma$ of specific heats. Kotelnikov and Montgomery also simulated a regular array of fibers, saturated with cryogenic DT. In their simulations they made use of a kinetic-theory–based computational model. Like Hazak *et al.*, they found that the inhomogeneities result in a post-shock mixing region in which energy is temporarily stored in turbulent motion. Finally, Philippe *et al.* performed simulations of DT-saturated foams using an adaptive-mesh-refinement code and allowing random fiber placement. They focused on the effects of inhomogeneities on the shock speed for a low- and high-density foam. They found that for the high-density foam, the deviation in shock speed from the homogeneous value was about 1% and less than 0.3% for the low-density foam.

This problem has also been addressed in astrophysical contexts, where the ratio of the material densities is much larger. The role of clumps in augmentation of the Rayleigh–Taylor instability in supernova remnants was studied using hydrodynamic simulations by Jun.[13] More recently, Poludnenko *et al.*[14] have simulated the interaction of a shock with a layer of circular obstructions, or clumps, determining the critical inter-clump distance required for the transition to a non-interacting regime in which the clouds are destroyed by the shock independently of one another. They also discussed mass loading as well as the effects of finite layer thicknesses for the collection of circular obstructions.

In our simulations the shock passage through a random array of CH fibers separated by DT is simulated, and the time-averaged level of fluctuations is determined as a function of distance behind the shock front for quantities of interest. We define the decay length for a quantity as the inverse of the logarithmic derivative of the quantity's perturbations [see Eq. (1)]. We will show that the decay lengths are comparable to a micron for a wide range of foam densities. For shock propagation distances characteristic of ICF targets, the average post-mixing region conditions approach those given by the Rankine–Hugoniot jump conditions. We also address questions of feedthrough and feedout, showing that the stability of the shock front once it leaves the wetted-foam layer minimizes the effect of feedthrough.

In the following sections (1) the hydrodynamic code used and the simulations that were performed are described; (2) the interaction of a shock with a single circular obstruction is discussed; (3) the results of multifiber simulations and their implications are presented; (4) the role of the pusher (i.e., the inflow boundary conditions) is discussed; and (5) our conclusions are presented.

**Numerical Simulations**

The code used for these simulations, *AstroBEAR*,[15] is based on the adaptive-mesh-refinement (AMR) code *AMRCLAW*.[16] In the AMR approach, subregions of the computational domain are provided with higher resolution according to a refinement criterion such as the magnitude of the truncation error or the local gradients of the hydrodynamic variables. Because the entire simulation region is not simulated at the highest resolution, the AMR scheme typically provides much-reduced execution times. In this implementation of AMR, the code attempts to optimally gather the refined cells into rectangular subgrids in order to minimize the overhead associated with refinement, and subsequently the hydrodynamic equations are advanced in each grid and on every refinement level. The refinement criterion used in *AstroBEAR* is Richardson extrapolation, in which cells are flagged for refinement based on a local estimation of the integration error. *AstroBEAR* employs a fully nonlinear Riemann solver with the second-order-accurate Wave-Propagation Algorithm integration scheme of LeVeque.[17] A polytropic equation of state is used with a ratio of specific heats $\gamma = 5/3$ gas. Thermal and radiative energy transport are not modeled in these simulations. We expect that in a real target implosion these mechanisms will dissipate fluctuations in the post-shock mix region. The results of our simulations will thus overestimate the size of the post-shock mix region and underestimate the fluctuation decay rate behind the shock. The effects of radiation could in principle be imitated by elevating the initial fiber pressure to model the absorption by the fibers of radiation emitted from the corona.

*AstroBEAR* tracks multiple materials by solving separate continuity equations for each of the materials—the fiber material and the DT—which provides a measure of the level of mixing after the shock (this is referred to as volume-fraction contouring).[18] There is no interface construction at the boundary between the two materials. Instead, the mass of each material is maintained for a given cell. For instance, consider two adjacent cells, the left containing the first material at a higher pressure and the right the second material at a lower pressure. After one time step, the boundary between the two materials will have moved into the right cell, and at the end of that time step the right cell will be considered to contain a uniform mixture of both materials, with the appropriate fractions. Material interfaces experience some degree of smearing as a result. Shock-tube tests indicate that on the time scale of these simulations, the material interface is spread out over a distance approximately equal to the initial fiber radius. This method of material tracking is passive and in no way affects the hydrodynamics behind the shock, or the decay of perturbations in the mix region.

*AstroBEAR* solves the Euler equations, making no provision for turbulent motion. The Reynolds number is $\mathrm{Re} = UL/\nu$, where $U$ is a characteristic flow speed, $L$ is a characteristic length scale, and $\nu$ is the viscosity coefficient. For a shock in wetted foam, we may take for the length scale $L$ the fiber radius $a$ (~1/20 $\mu$m for the foam density of interest), and for the characteristic flow speed $U$ the post-shock flow speed $u$ (~30 km/s is a characteristic post-shock speed). Following Robey,[19] we may estimate the kinetic viscosity using the model of Clerouin *et al.*[20] The initial shock strength and electron and ion conditions for the high-gain, direct-drive, NIF

wetted-foam design described in Ref. 4, determined by 1-D simulations using *LILAC*,[21] give a Reynolds number of ~2800. This is below the value of 7700 typically taken as the critical value for the onset of turbulence. In our simulations no artificial viscosity is used, although a similar effect is obtained by splitting the contact discontinuity according to the scheme of Robinet *et al.*[22] This is done to prevent the growth of unphysical features (often referred to as "carbuncles"). Care has been taken to ensure that physical features are not damped.

As mentioned above, wetted-foam target designs, such as the one described in Ref. 4, take advantage of the higher laser absorption of plastic fiber than pure DT. In these designs a low-density plastic foam, which has a dry-foam density of ~140 mg/cc, is saturated with DT ice, e.g., $CH(DT)_4$, raising its density to 360 mg/cc. A typical direct-drive, NIF-scale target design consists of a shell of DT ice surrounded by a thin layer of plastic. In a wetted-foam design, an outer portion of the DT shell is replaced by wetted foam. The thickness of this layer is chosen so that the foam is entirely ablated by the laser pulse. In choosing the density of the foam, a balance must be struck between the increased absorption, which is greater for larger densities, and minimizing the radiative preheat of the inner-fuel layer of the DT ice, which is also greater for larger foam densities. As in many direct-drive target designs, the pulse consists of an initial intense picket, followed by a foot pulse, and then a drive pulse. The picket/foot combination launches the first shock into the shell, creating a greater adiabat in the ablator than in the inner-fuel layer. The second shock, launched by the more-intense drive pulse, is timed to meet the first shock inside the gas within the shell. The first shock is most relevant here since it is the only shock to encounter unshocked and unmixed wetted foam.

We have performed a number of simulations to investigate the effects of microstructure on shock propagation. The baseline simulation consists of an 8-$\mu$m × 0.8-$\mu$m simulation region filled with a mixture of DT (with a density of 0.253 g/cc) and randomly placed polystyrene (CH) fibers (with a density of 1.044 g/cc). The foam being simulated, resorcinol formaldehyde (RF), is a fibrous foam with fiber spacing of ~0.1 to 0.2 $\mu$m. For RF, denser foams generally have the same average center-to-center fiber separation, but with thicker fibers. We simulate a foam that has a random array of fibers with the same average density as a rectangular array of fibers with a unit cell size of $R = 0.2$ $\mu$m. This corresponds to an average nearest-neighbor distance of $d \sim 0.13$ $\mu$m (so the simulation size is ~60 $d$ × 6 $d$). The combination of fiber density and average density, for a given fiber spacing, determines the fiber radius: for $CH(DT)_4$ the fiber radius is $a \sim 0.0428$ $\mu$m. The dry-foam density $\rho_{dry}$ and wetted-foam density $\rho_{ave}$ are related by $\rho_{ave} = \rho_{dry} + \rho_{DT} - \rho_{dry}\rho_{DT}/\rho_{CH}$. The dry-foam density is given by $\rho_{dry} = \rho_{ch}\pi(a/R)^2$. In these simulations generally two levels of refinement, both ×4 (so that a cell being refined is replaced by 16 cells in a 4 × 4 grid), were used in addition to the base level. The cells have an aspect ratio of unity, with a resolution at the highest level of 800 cells/$\mu$m, and an equivalent simulation size at the highest resolution of 6400 × 640. This corresponds to about 68 cells across a fiber. We find negligible differences between 34 and 136 cells per fiber radius. This convergence is supported by a resolution scan performed using *AstroBEAR* by Poludnenko *et al.* [Ref. 23; see their Fig. 3(a)], who also found only small differences between 32 and 64 cells per fiber radius.

In addition to this simulation size, we have also performed simulations with a size of 0.2-$\mu$m transverse to the shock propagation direction, but with a 16-$\mu$m-simulation region length in the direction of shock propagation, in order to extend the size of the mixed region. The upper and lower boundary conditions in these simulations are periodic, so the central difference between these simulations is that in the thinner one the lateral distance between the fibers is always 0.2 $\mu$m.

If we take the ablation-driven shock to travel to the right, then the right simulation boundary condition is outflow, or zero-order extrapolation, and the left is inflow. The inflow conditions are given by the Rankine–Hugoniot conditions for the average pre-shock density and pressure and for a post-shock pressure of 8 Mbar. We refer to this as an "impedance-matched" boundary condition [other inflow boundary conditions are discussed in the **Results for Different Pushers** section (p. 237)]. The CH and DT are initially in pressure equilibrium with a pressure of 0.01 Mbar. The flow, being governed by the Euler equations, is independent of Mach number when in the strong-shock limit,[24] so that the results are not sensitive to the initial pressure.

### The Interaction of a Shock with a Single Fiber

The interaction of a shock with a single fiber (or circular obstruction) has been studied extensively as a hydrodynamic problem.[25,26] Additional physical elaborations have also been modeled, such as partial ionization[27] and magnetized obstructions (see, e.g., Ref. 28). Following Klein *et al.*,[24] the interaction of a shock with a fiber may be broken down into several distinct phases. If the flow were one-dimensional, a "forward" shock would propagate through the fiber, compressing and impulsively accelerating it, while a "reverse" bow shock would

be reflected back into the DT. Once the forward shock had crossed the fiber, a rarefaction wave would be sent back across the fiber, followed by a continuous period of acceleration that would continue until the fiber speed equaled that of the surrounding shocked DT.

Because the flow is two-dimensional, the fiber experiences several shocks: In addition to the main forward shock, other shocks are driven into the fiber from the sides as the shock in the DT moves around and past the fiber. Similarly, many rarefaction waves (RW's) are launched as each of these shocks breaks out of the fiber. These additional rarefaction waves result in expansion during this phase, both in the direction of and perpendicular to the direction of shock propagation. Finally, following the passage of these RW's, the fiber begins to accelerate. During this phase, the fiber is accelerated to the speed of the ambient (DT) fluid flow.

As described in Ref. 25, the passage of the shock generates, for a cylindrical fiber, two vortex lines behind the obstruction, and for a spherical obstruction a vortex ring is generated. These vortices and the vorticity generated by the shear flow as the fiber is accelerated mix the fiber and interfiber material. For a cylindrical obstruction and a normal shock (whose velocity vector is normal to its surface), the vortex lines are of equal magnitude and oppositely directed, so the total vorticity remains zero. If the shock is oblique, the symmetry is broken and net vorticity may be generated.

The fiber is subject to the Richtmyer–Meshkov instability as the shock first passes. As the fiber is accelerated to the speed of the post-shock DT, it is also subject to the Rayleigh–Taylor (RT) instability and, due to the shear at the fiber boundaries, the Kelvin–Helmholtz (KH) instability. In the case of a CH fiber and DT ambient fluid, the density ratio is $1.044\ \text{g cc}^{-1}/0.253\ \text{g cc}^{-1} \sim 4$. Both the RT and KH instabilities are more effective at mixing the fiber and ambient material when the ratio of fiber to ambient density is greater. Figure 100.1 shows the density at three times for a fiber of radius 0.0428 $\mu$m struck by a 3-Mbar shock, for a fiber-to-interfiber mass density ratio of 4:1. A measure of the fiber's mixing or destruction time may be made by determining the fraction of fiber material that lies outside the initial radius of the fiber from its center of mass (this is shown in Fig. 100.2). If we take the fiber destruction time as the time it takes for the flow to expel 75% of the fiber material from this region, we see that the fiber is destroyed in ~13 ps.

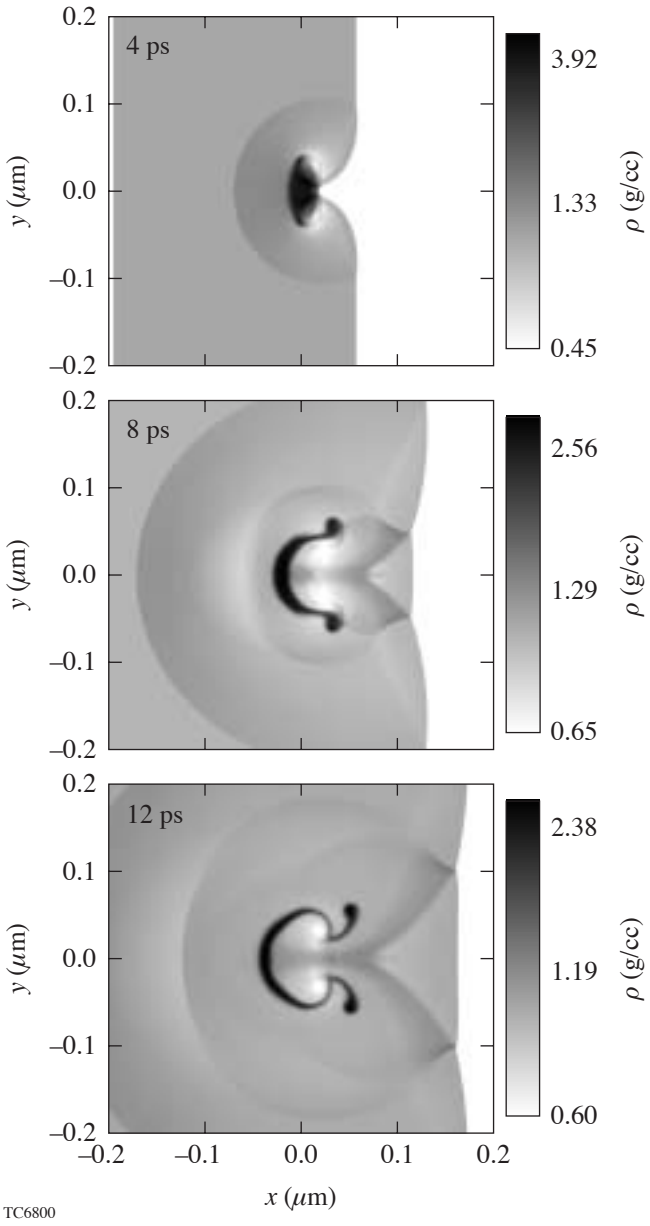


Figure 100.1
Density profiles at 4, 8, and 12 ps for a Mach-24 shock interacting with a CH fiber. The density ratio is 4:1.

**The Interaction of a Shock with Many Fibers**

Consider now the case of a shock driven into a field of randomly placed fibers. Here the shocked fibers interact with one another, creating a "mix" region in which the post-shock vorticity mixes the CH and DT. The density $\rho(x, y)$ at 96 ps is shown in Fig. 100.3(a) for a $\text{CH(DT)}_4$ wetted foam struck by an 8-Mbar shock with impedance-matched inflow boundary

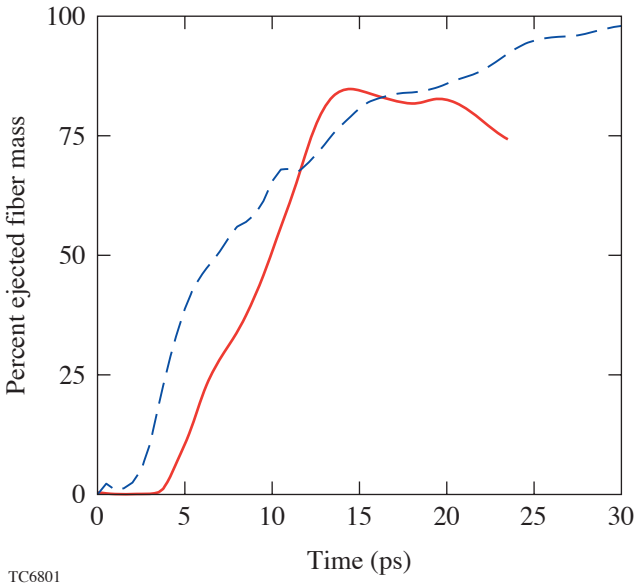


Figure 100.2
The fraction of fiber mass that lies outside the original fiber radius of the fiber's center of mass as a function of time. As the fiber material is mixed with the ambient material, it is flung outside of its original boundaries. The solid line is a single fiber with a 4:1 density ratio with the interfiber material (see Fig. 100.1). The dashed line is from a simulation of fiber destruction in the presence of other fibers. Taking the 75% mark as an arbitrary measure of fiber destruction, the fiber is destroyed after ~12.3 ps for a single fiber and ~13.5 ps in the presence of other fibers, although in this case the fiber destruction is much more thorough.

conditions. As was shown in Ref. 14, if the interfiber distance is sufficiently large, the fibers enter a noninteracting regime where the fibers are destroyed before they expand far enough to interact with one another. The parameters of interest here are in the interacting regime. The CH fiber density $\rho_{CH}$ alone is shown in Fig. 100.3(b). The dual-vortex motion and the resulting mushroom-shaped features due to shock passage can be seen in Fig. 100.3(b). From this figure we see that CH and DT, which are clearly distinct at the shock front (the dotted line at ~5.4 $\mu$m), are well mixed by the end of the mix region (at ~4 $\mu$m). We also note from this figure that there is a thin region between the shock front at ~5.4 $\mu$m and the shocked fibers (~5.3 $\mu$m at $y = 0.2$ $\mu$m). This gap between the shock and the entrained shocked CH is due to the finite time the post-shock flow takes to accelerate the fibers to the post-shock speed. In this region the average density, being primarily that of the shocked DT, is lower than in the rest of the mix region, contributing to an initial under-compression behind the shock.

Figure 100.2 shows that when a fiber is mixed in the presence of other fibers, the mixing proceeds more quickly initially and is more thorough (see also Ref. 14). For the simulation used here, the ejected fiber mass asymptotes near 100%. The degree of mixing may be demonstrated by designating one of the fibers as a third species identical physically to CH but maintained as a separate material numerically. Figure 100.4 shows contours of density for a particular fiber (solid lines), as well as the total density (grayscale). By 120 ps, the outermost contour, which represents 10% of the peak density, contains a volume of 0.063 $\mu$m$^2$. This is comparable to the specific volume 0.04 $\mu$m$^2$ of the fibers for this initial spacing.

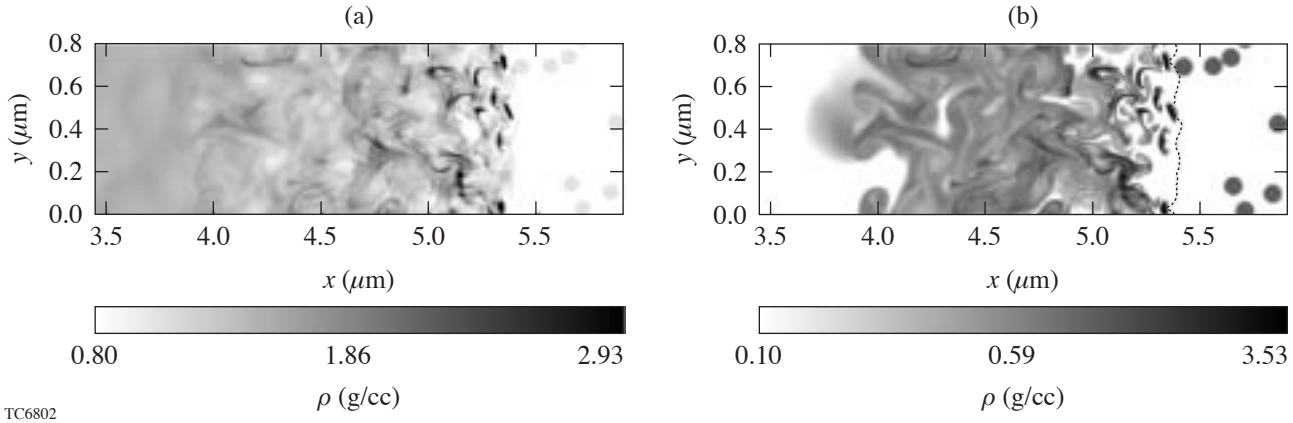


Figure 100.3
The total density (a) and CH density (b) at 96 ps for an 8-Mbar shock driven into wetted foam. The dotted line in (b) shows the location of the shock front.

The mix region is also the source of the bow shocks reflected when the main shock encounters the fibers. These shocks eventually propagate away from the main shock and out of the mix region. The fluctuations in density, pressure, and transverse velocity can be seen in their $y$ averages — $\overline{\rho}$, $\overline{p}$, and $\overline{u}_y$ — shown in Fig. 100.5 for the simulation of size 16 $\mu$m × 0.2 $\mu$m. (A horizontal bar is used to indicate an average over the $y$ coordinate.) The mixing flow, due to the reflected shocks and the post-shock vorticity, is generally both horizontal — parallel to the shock motion — and vertical. The vertically moving shocks are unsupported since the flow supporting the shock is entirely horizontal. The vertical shocks, then, decay as the shocked fibers sink into the mix region. In addition, since on average the upward-moving shocks will have the same strength as the downward-moving shocks, one might expect the net vertical speed once these have passed to be approximately zero. Because of the random fiber placement, though, some vertical motion remains behind the shock [Fig. 100.5(c)]. In the 0.2-$\mu$m-wide simulation, the periodic upper- and lower-boundary conditions, combined with the small vertical simulation size, mean that vertical motion as large as 10 $\mu$m/ns remains, even several microns behind the shock. In the 8-$\mu$m × 0.8-$\mu$m simulation, $\overline{u}_y$ in the mix region is smaller. This is because in the wider simulation there are fibers for a transverse shock to encounter other than the fiber that created it.

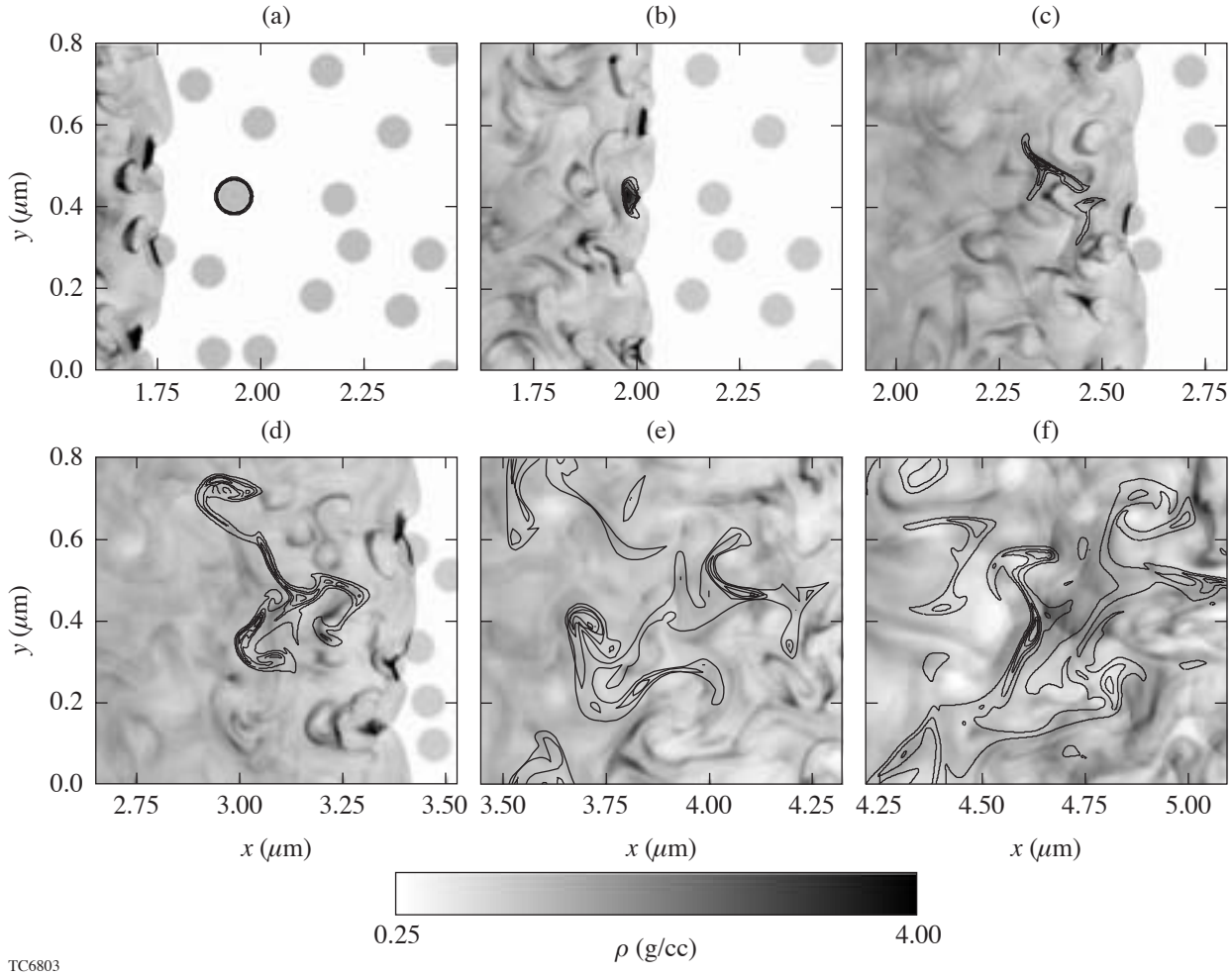


Figure 100.4
The total mass density (grayscale) and the mass density (lines) of material from a "tagged" fiber initially at $x$ = 1.93 $\mu$m and $y$ = 0.42 $\mu$m. The contour levels for the tagged fiber correspond to 10%, 32.5%, 55%, and 77.5% of the peak tagged-fiber density. The frames are from (a) 30 ps, (b) 35 ps, (c) 45 ps, (d) 60 ps, (e) 80 ps, and (f) 100 ps.

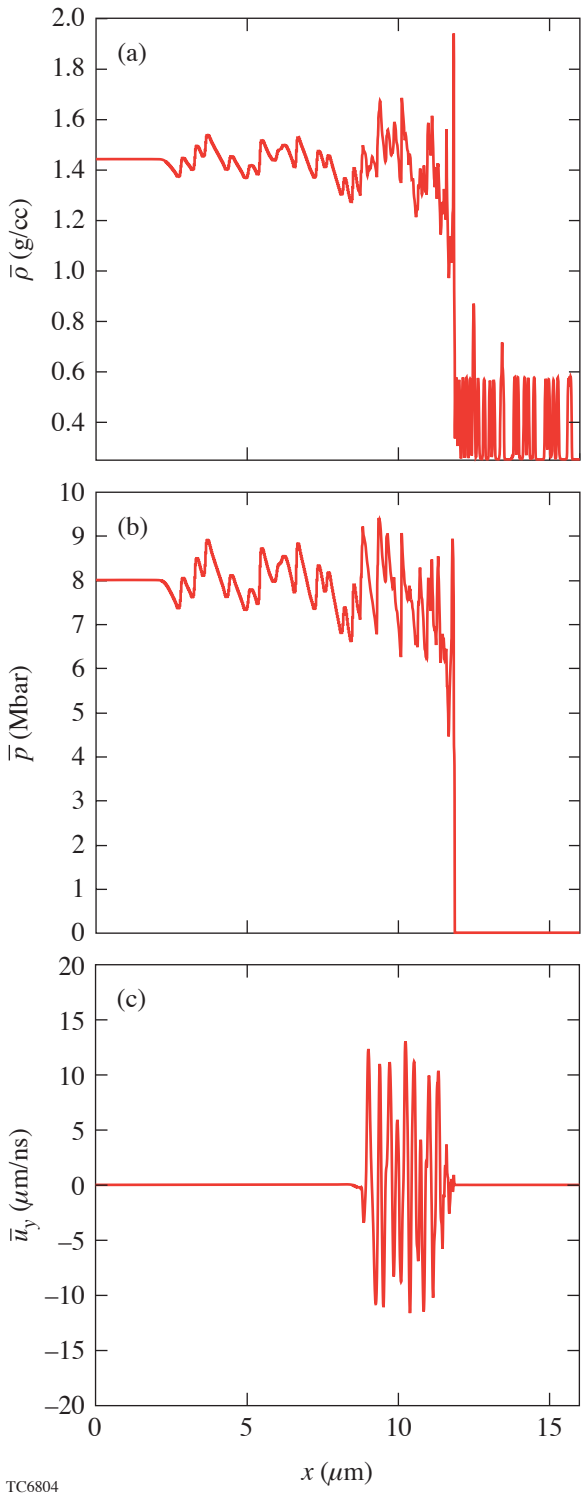


Figure 100.5
The $y$-averaged density (a), pressure (b), and $y$ velocity (c) at 300 ps for a 16-$\mu$m × 0.2-$\mu$m simulation.

To quantify this we have calculated average quantities related to the flow behind the shock. The mix region is given approximately by the region bounded on the right by the shock $x_s(y;t)$ (assuming the shock is a single-valued function of $y$) and on the left by the interface between the pusher (or inflowing material) and the shocked wetted foam, $x_i(y;t)$, as is shown in Fig. 100.6. If the wetted-foam layer is preceded by a CH layer, for instance, then there will be a contact discontinuity at the pusher/foam interface, where the density jumps but the pressure is constant. The location of the fiber material in the mix region is shown in Fig. 100.3(b), demonstrating that the vorticity quickly mixes the CH and the DT behind the shock front. For small fiber-to-DT density ratios the fluctuations in the shock-front position as a function of $y$ are small enough to allow us to define an average shock position $\bar{x}_s(t)$. The average pusher location $\bar{x}_s(t)$ is given, for a strong shock with $\gamma = 5/3$, approximately by $\bar{x}_i \approx \bar{x}_s(t=0) + 3\bar{D}t/4$, where $\bar{D}$ is the average shock speed. The interface position may be inverted to give the time $\bar{t}_i(x)$ when the interface is a distance $x$ behind the shock. The time average of a flow variable $q$, from when it is

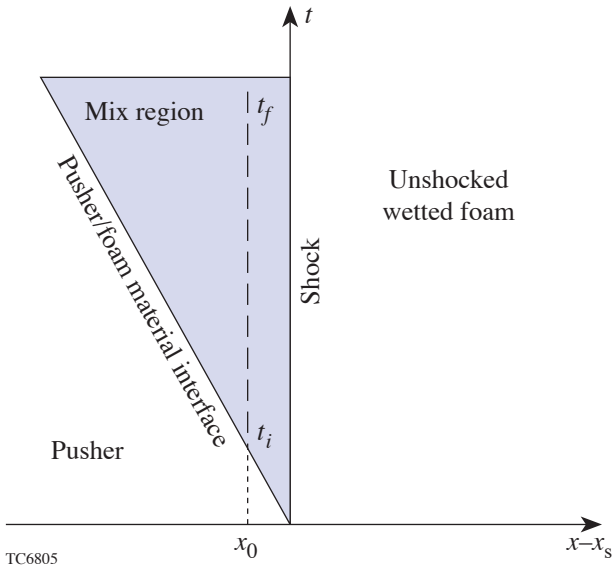


Figure 100.6
The mix region (shaded), pusher, and unshocked material are shown as a function of time, in the frame of the main shock. The time averages are computed of the flow variables in the mix region between the shock and the pusher as functions of the distance behind the shock. For instance, the time average at a distance $x_0$ behind the shock is found by averaging from time $t_i$ to time $t_f$.

first shocked to some final time $t_f$, as a function of the distance $x$ behind the shock, is then

$$\langle \bar{q} \rangle (x) = \left[ t_f - t_i(x) \right]^{-1} \int_{t_i(x)}^{t_f} \bar{q}(x,t)\, dt,$$

where $\bar{q}$ is the average of $q(x,y)$ over $y$ and brackets are used to indicate this *mixing-depth average*. The distance $x$ behind the main shock front may be thought of as a depth within the mix region. The mixing-depth average can also be taken of any quantity independent of $y$, such as $q_n$, the $n$th Fourier-mode amplitude of some variable $q$, in the $y$ direction, or $q_{\text{rms}}$, the root-mean-square (rms) deviation of $q$ as a function of $y$. This double average $\langle \bar{q} \rangle$ is meaningful when the flow reaches a steady state in which the average behavior of the fluctuations as a function of distance behind the shock is roughly constant in time. We have found this to be the case after the initial stages of our simulations. Note that the averaging time is inversely proportional to the distance from the shock front, so the statistical fluctuations tend to be larger for greater distances from the main shock front. The mix-depth averages of the root-mean-square variations in the $y$ direction are shown for the pressure, the density, and the ratio of kinetic energy (in the pre-shock frame) to total energy $E_{\text{kinetic}}/E_{\text{total}}$, and $u_y$ in Fig. 100.7, for the 8-$\mu$m × 0.8-$\mu$m and 16-$\mu$m × 0.2-$\mu$m simulations discussed above. The decay scale length

$$L_q = dx / d \ln \langle q_{\text{rms}} \rangle \qquad (1)$$

just behind the shock in the mixing region for these variables is comparable to 1 $\mu$m for this foam density. The relative Fourier-mode amplitudes of modes 1 to 6 of the pressure (not shown) remain roughly constant with mix-region depth, suggesting that the power is not moving to shorter or longer wavelengths, but decaying uniformly at a rate independent of mode number.

The rms amplitudes for a simulation of the same size but 50%-higher resolution are approximately equal to those in Fig. 100.7, indicating resolution convergence. Since the rate of decay of fluctuations is independent of resolution, the decay is not due to numerical losses, but to the mechanisms described above. When viscosity is negligible, the circulation in a given region is conserved according to Kelvin's circulation theorem (see, for instance, Ref. 29); in effect, vortices are "frozen" into the fluid and are advected with the flow. For the case of cylindrical fibers, as mentioned above, the vortices are created in opposing pairs with no net average vorticity generation. As

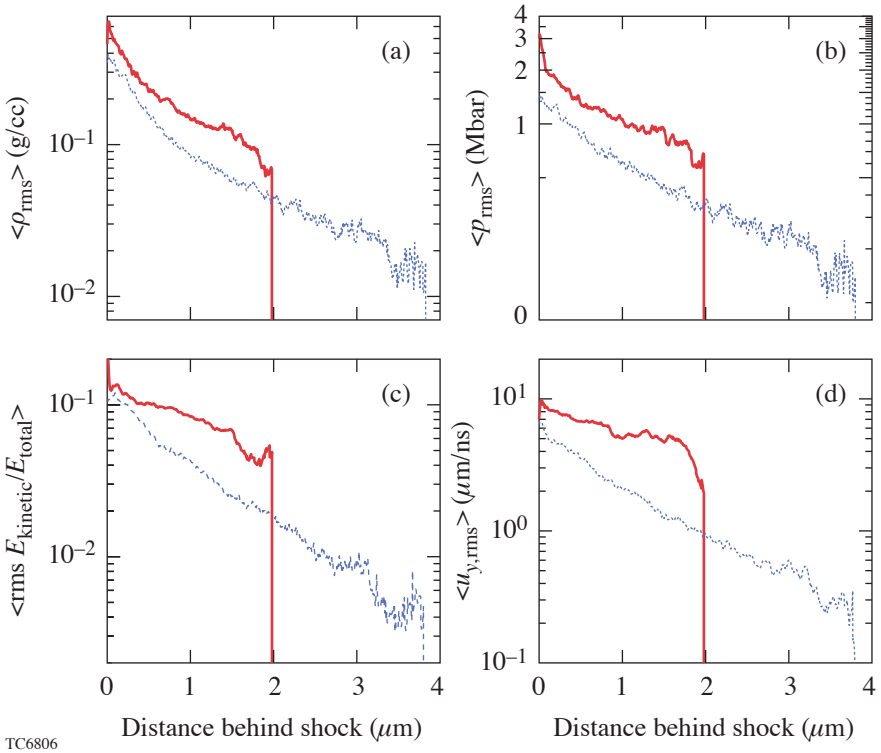


Figure 100.7
The rms variations of the time-averaged density (a), pressure (b), fraction of kinetic energy (in the pre-shock frame) (c), and vertical velocity (d) as functions of the distance behind the shock. These show a decay length comparable to 1 $\mu$m for this foam density.

the vortices interact behind the shock, they are free in time to mix, but not decay, because of the absence of physical viscosity and the small size of the numerical viscosity. The level of mixing can again be gauged qualitatively by Fig. 100.4. In the 16-$\mu$m simulation the mixing is sufficient to reduce the time average of the rms variations to 1.2% for $\rho$, 1.8% for $p$, and 0.9% for $E_{\text{kinetic}}/E_{\text{total}}$, of the average values.

The pressure decay length [Eq. (1)] behind the shock as a function of foam density is shown in Fig. 100.8. These values are taken from simulations that have a simulation region of $8 \times 0.2$ $\mu$m and an equivalent grid size of $6400 \times 160$. The error bars in this plot are given by the linear regression used to calculate the mixing length. Poludnenko *et al.* found,[14] for simulations with a larger ratio of fiber to interfiber density, that the mixing was more efficient when the average minimum interfiber distance was less than a critical distance. We find the same result: for dry-foam densities less than ~75 mg/cc, for which the interfiber distance is ~6.6 times the fiber radius, the mixing length is about 1.2 $\mu$m, as opposed to about 0.8 $\mu$m for higher densities. The difference between the interacting and noninteracting regimes is illustrated by considering the vorticity generated by the shock. This is shown in Fig. 100.9 for three foam densities—25, 75, and 150 mg/cc—for about the same shock position. For these three densities, as mentioned above, the average distance from fiber center to fiber center is the same, but the fibers are of different sizes. The fiber radius is given by $a = R\left[\rho_{\text{dry}}/\left(\pi\rho_{\text{CH}}\right)\right]^{1/2}$, so these densities correspond to fiber radii of 0.0175 $\mu$m, 0.0302 $\mu$m, and 0.0428 $\mu$m. For 25-mg/cc density, the vortex dipoles associated with each fiber remain paired and intact for much longer before interacting with other neighboring vortex dipoles. In contrast, for 150 mg/cc, the dipole length increases much more quickly, resulting in greater mixing.

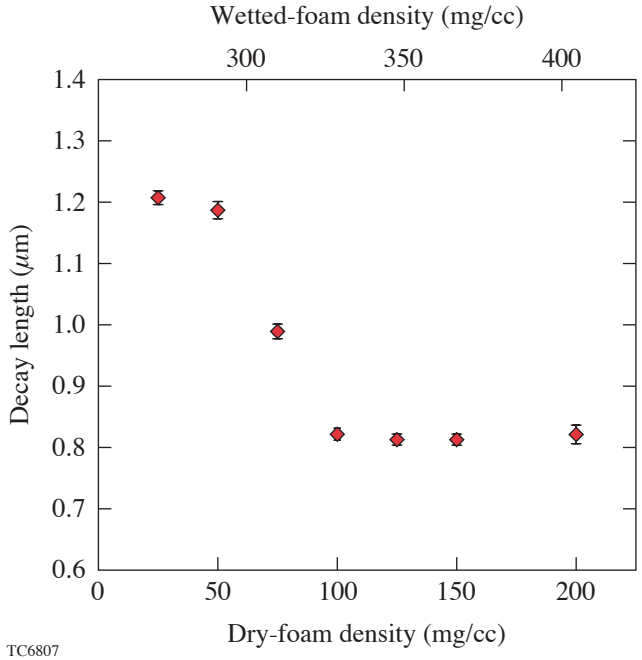


Figure 100.8
The decay length behind the shock as a function of foam density. The decay length is approximated by the scale length of the time-averaged decay of pressure variations just behind the shock. The error bars are given by the uncertainty in the exponential fit.

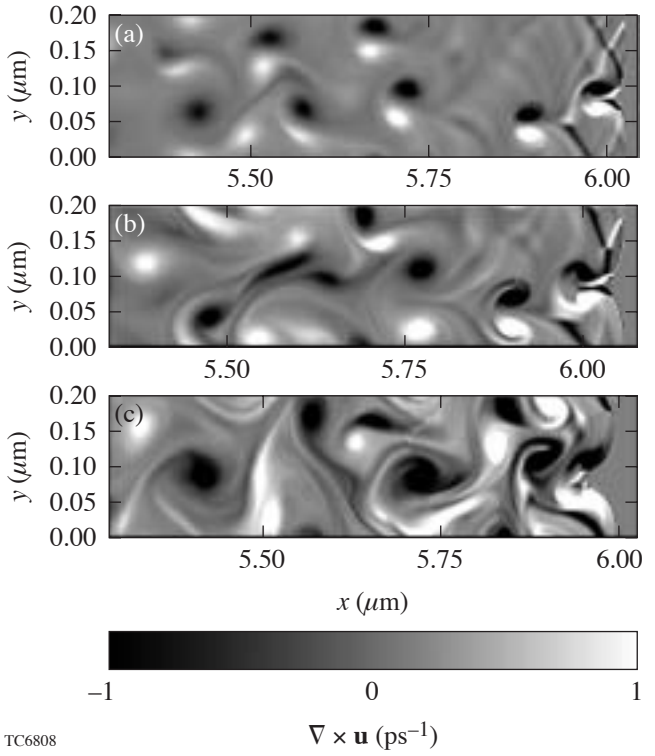


Figure 100.9
The vorticity is shown as the shock reaches ~6 $\mu$m for three dry-foam densities: (a) 25, (b) 75, and (c) 125 mg/cc. The average interfiber distance is the same in all three cases, while the fiber radius is larger for higher foam densities.

The Rankine–Hugoniot conditions represent conservation of energy, momentum, and mass for a steady flow of polytropic gas in the absence of transverse motion. The RH jump conditions will be met over a region only to the degree that (1) the shock is steady; (2) the flow in and out of the region is steady; (3) the fluctuations at the left and right boundaries are uncorrelated (e.g., $\langle\overline{\rho u}_x\rangle = \langle\overline{\rho}\rangle\langle\overline{u}_x\rangle$; see Ref. 10); and (4) the turbulence and transverse motion have decayed at the down-

stream boundary. The shock steadiness is given by the error of the linear regression used to determine the shock speed; for the 16-$\mu$m simulation, the speed is 54.32 $\mu$m/ns±0.033 $\mu$m/ns—an uncertainty of 0.12%. As mentioned above, the post-shock flow is approximately steady. The pre-shock flow is approximately steady when averaged over time scales much longer than the characteristic time scale for the inflowing density fluctuations, which is given by the time it takes the shock to move from one fiber to the next, ~$d/D$. For an 8-Mbar shock and a dry-foam density of 150 mg/cc, the shock speed is ~50 $\mu$m/ns, and the averaging time must be longer than ~4 ps. The duration of the 16-$\mu$m simulation is, for instance, ~300 ps. The fluctuations in the mix region are correlated by up to ~10% just behind the shock, but these correlations decrease to a fraction of a percent beyond 1 $\mu$m from the shock. The transverse velocity is ~1 $\mu$m/ns for most of the mix region, and the rms variations decay to ~0.4 $\mu$m/ns by a mix-region depth of 4 $\mu$m (see Fig. 100.7). Post-shock turbulence leads to an average excess of kinetic energy in the mix region (as in Ref. 9) of 2%. Figure 100.10 shows the double averages of the density, pressure, the ratio of kinetic energy to total energy (in the pre-shock frame), and $u_y$ for the 16-$\mu$m simulation. Each of these quantities approaches the value predicted by the Rankine–Hugoniot (RH) jump conditions and by the end of the mix region is within a few percent of those values. The pressure in the majority of the mix region is 7.86±0.05 Mbar, 2.5% lower than that of a homogeneous simulation with the same boundary conditions. The density over the same region is 1.47±0.01 g/cc, 1.7% higher than the RH value. Not surprisingly, the small deviation from the RH values results in a shock speed of 56.17±1.7 $\mu$m/ns, which is near the RH shock speed (here it is within 0.1%). The post-shock adiabat $\alpha \sim p\rho^{-5/3}$ deviates from the RH value by a comparably small amount:

$$\delta \ln \alpha = \delta \ln p - \frac{5}{3}\delta \ln \rho \sim -4\%.$$

This deviation from the RH jump conditions is well within the tolerance of high-gain, direct-drive foam designs for the NIF. The main effect of variation in the speed of the first shock is mistiming of the shocks. If the shock is too slow, for instance, then the first two shocks will meet in the inner-fuel regions of the shell, preheating the fuel and compromising target performance. This effect can be simulated in 1-D by deliberately mistiming the first shock, by varying the length of the foot pulse. This is shown for a particular high-gain, wetted-foam NIF target design (see Fig. 100.11).[4] Here a 10% change in shock speed corresponds to a shock mistiming of 300 ps, and

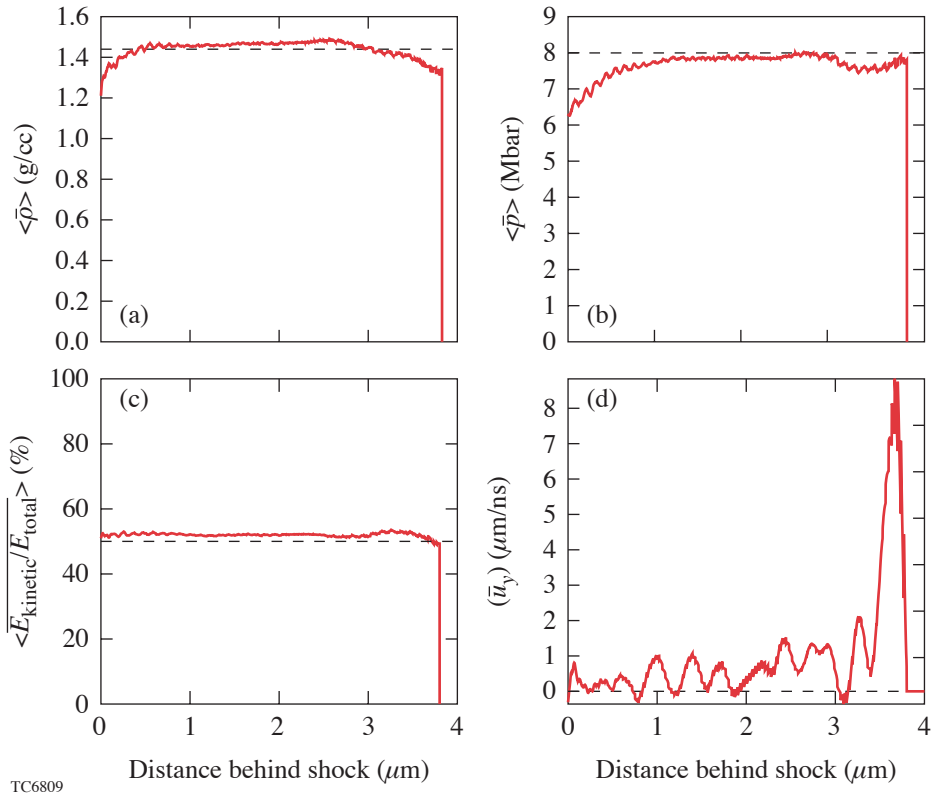


Figure 100.10
The time- and space-averaged density (a), pressure (b), ratio of kinetic to total energy (in the pre-shock frame) (c), and vertical velocity (d) as functions of the distance behind the shock front. The values given by the Rankine–Hugoniot jump conditions for a homogeneous mixture of the same density are also shown (dashed lines).

the target shows little change in gain for a mistiming of >400 ps. For this design, at least, this suggests that any change in shock speed due to foam microstructure will have little effect on target performance. While the shock speeds for relevant pressures in DT-wetted plastic foams have yet to be measured experimentally, dry-foam shock speeds have been shown to agree to within experimental error with Rankine–Hugoniot values over a wide range of densities.[30]

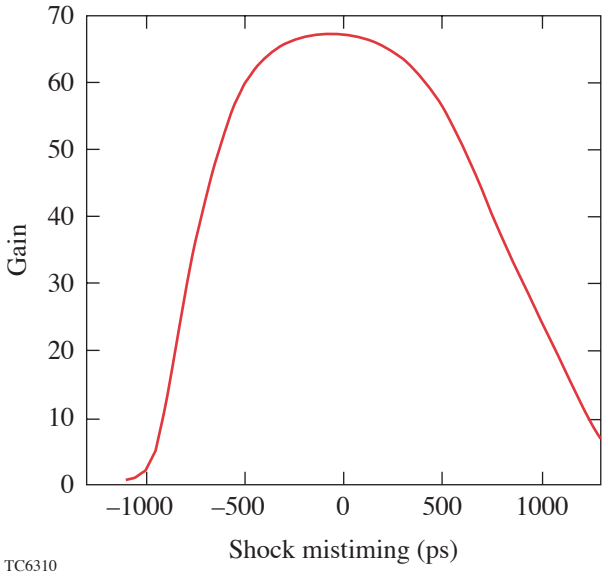


Figure 100.11
The target gain as a function of first-shock mistiming for a high-gain, wetted-foam, direct-drive NIF target design.

As the shock propagates through the wetted-foam layer, the shock front acquires perturbations due to the different shock speeds in the DT and CH [see Fig. 100.3(a)]. Shock-front perturbations are potentially able to seed velocity and surface perturbations on the inner surface of the target shell—a process called *feedthrough*. When the shock reaches the inner shell surface, a rarefaction wave is launched toward the outer surface of the shell. These inner-surface perturbations are carried to the outer surface of the shell by this rarefaction wave—so-called *feedout* (see, e.g., Ref. 31 for a further description of these phenomena). During the acceleration phase as the laser ablation drives the implosion of the shell, the outer surface is subject to the Rayleigh–Taylor instability, which may magnify position and velocity perturbations at the outer shell surface. During the deceleration phase of an implosion, the inner surface is also subject to the Rayleigh-Taylor instability, causing fed-through perturbations to grow, potentially reducing the core temperature and shell areal density and compromising target performance.

The rms variation in the amplitude of shock-front perturbations is shown in Fig. 100.12 for a simulation where the shock has propagated through 5 $\mu$m of wetted foam, into 5 $\mu$m of homogeneous DT (with a transverse simulation size of 0.2 $\mu$m). In the wetted foam, the shock-front perturbations are comparable to a few nanometers. Shock fronts are stable[32] because a concave perturbation leads to a locally converging shock, higher pressure, and higher local shock speed, while a convex perturbation has the opposite effect (see Ref. 33 for further discussion of shock stability). The shock-front stability causes the shock-front perturbations to decay quickly after entering the DT layer, to a level of ~0.1 nm. These levels of nonuniformity are well below the level of the inner-surface shell ice roughness required for direct drive on the NIF.[34]

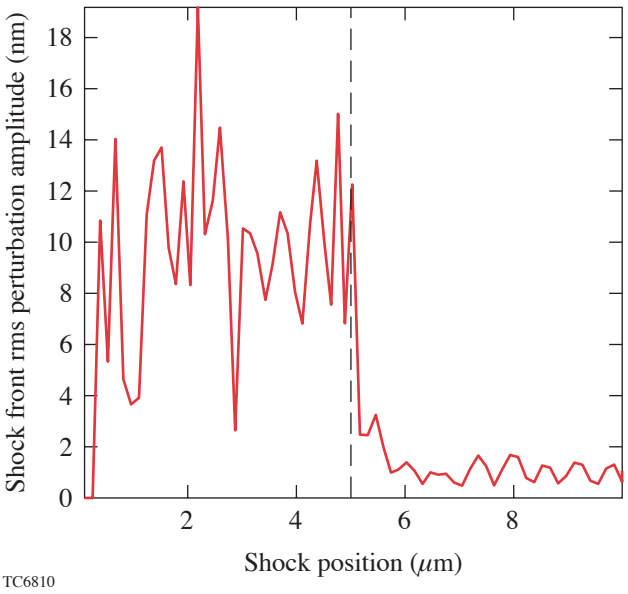


Figure 100.12
The rms shock-front perturbation amplitude as a function of shock position for a simulation consisting of 5 $\mu$m of wetted foam and 5 $\mu$m of DT. The transverse simulation size is 0.2 $\mu$m.

### Results for Different Pushers

We will now consider two different inflow boundary conditions, which correspond to different ablator materials, or "pushers." If these boundary conditions are not the same as the average post-shock conditions in the wetted foam as in the "impedance-matched" conditions used above, then secondary shocks or rarefaction waves will reflect off the wetted foam. To illustrate the role of these reflected waves, we will first con-

sider simulations in which the pusher is post-shock DT. This simulates a wetted-foam shell for which the DT ice overfills the foam shell. This will be followed by a description of simulations of a CH pusher.

The fibers and the DT are in pressure equilibrium before the shock with a pre-shock pressure $p_1$. As the shock, of Mach number $M$ and strength $z$, moves through the DT pusher, it raises the pressure to $p_2 = p_1\ (1 + z)$ and, since $z >> 1$ and $\gamma = 5/3$, the density to $\sim 4\rho_{DT}$. When the shock reaches the wetted foam, it encounters a jump in the average density. The strong shock is transmitted into the wetted foam, while a weak shock is reflected back into the DT pusher. The reflected shock further increases the DT pressure to $p_2 + \delta p_2$, where $\delta p_2$ depends on the density ratio and here $\delta p_2 < p_2$. In simulations where the fibers are resolved, this weak reflected shock is made up of the shocks reflected off the individual CH fibers. These reverse shocks are shown in Fig. 100.13, which shows the density averaged over $y$ (transverse to the shock propagation) at a particular time. In this case $p_2 = 3$ Mbar, and $\delta p_2 \sim 0.5$ Mbar. Since the post-shock DT and wetted foam are in pressure equilibrium, this is also the pressure in the post-shock wetted foam. Thus the post-shock pressure in the wetted foam is also higher than $p_2$, the post-shock pressure in the DT pusher. The resulting shock speed is given by $D_i = D_{DT}\left(1 + \delta p_2 / p_2\right)^{1/2}$, where $D_{DT} = \left[4 p_2 / \left(3\rho_{DT}\right)\right]^{1/2}$ is the shock speed in the DT.

For comparison, if a shock of the same Mach number (i.e., driven by the same pressure used to drive the DT above) is launched into a homogeneous wetted-foam mixture of CH and DT (rather than a DT pusher followed by a layer where the individual fibers are resolved), it will have a shock speed of $D_h = D_{DT}\left(\rho_{DT} / \rho_{ave}\right)^{1/2}$, where $\rho_{ave}$ is the average density of the wetted foam. For $\rho_{DT} < \rho_{ave}$, $\delta p_2 > 0$ and so $D_i > D_h$—i.e., when the shock is driven by a pusher of the same pressure $p_2$ the shock speed in an inhomogeneous mixture exceeds that in a homogeneous mixture. This is seen in Fig. 100.13, which shows $\bar{p}(x)$ and $\bar{\rho}(x)$ for a particular time for homogeneous and inhomogeneous mixtures driven by shocks of the same pressure $p_2$ and the same starting point. The degree by which it exceeds the homogeneous shock speed depends on the average fiber density and, while essentially a 1-D effect, can also be related to the fiber radius.[35]

For a laser-driven shock, this is not the steady-state solution. In this case, the reverse shock, when it reaches the ablation surface, is no longer supported at that pressure, and a rarefaction wave is launched into the target, lowering the

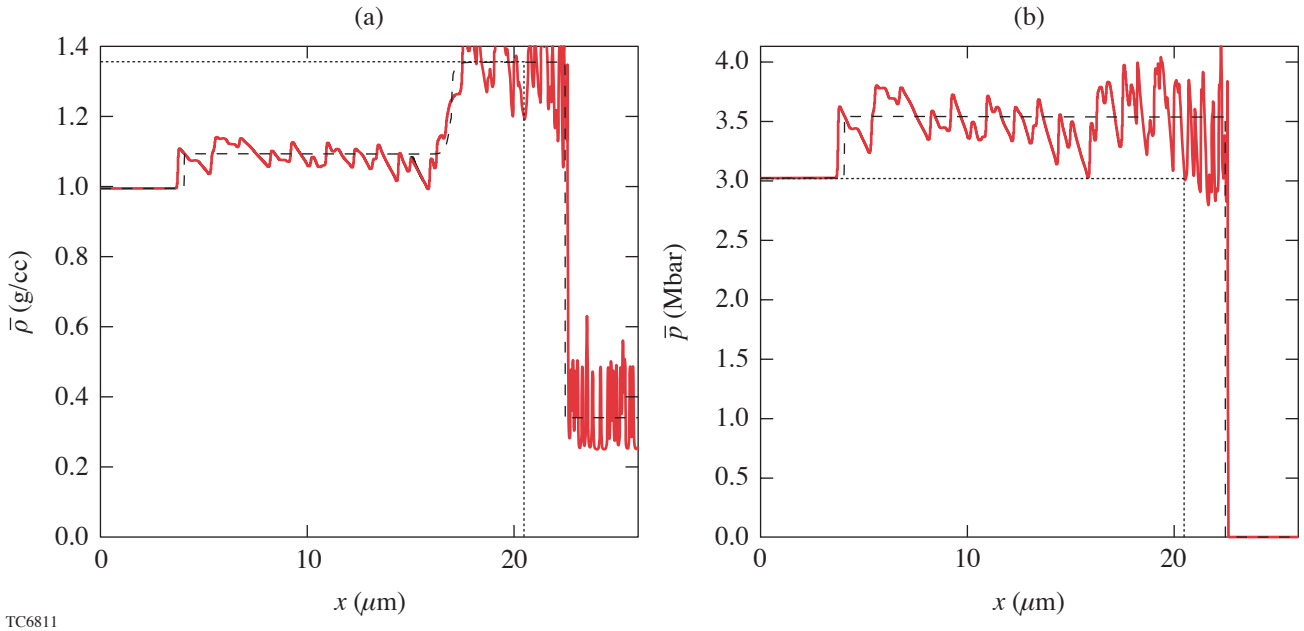


Figure 100.13
The density (a) and pressure (b) as functions of distance for a particular instance in time, for a simulation of a shock driven through wetted foam by a DT pusher. An equivalent homogeneous simulation is shown (dashed) as well as a simulation (dotted) in which pusher and foam are replaced by a homogeneous mixture with the same average density as the wetted foam.

pressure from $p_2 + \delta p_2$ to the ablation pressure, taken here to be $p_2$. The trajectories of the main and reflected shocks are shown in Fig 100.14, in which the inverse of the pressure scale length is plotted for a 1-D simulation of a high-gain, NIF wetted-foam target design with a DT ablator. For this design, this transient shock state persists for 70 ps. The RH jump conditions, which must be obeyed in the case of a homogeneous mixture, are also approximately obeyed for the fiber-resolved simulation (see Fig. 100.13, where the density of the inhomogeneous case is compared to that of a homogeneous case driven with a post-shock pressure $p_2 + \delta p_2$).

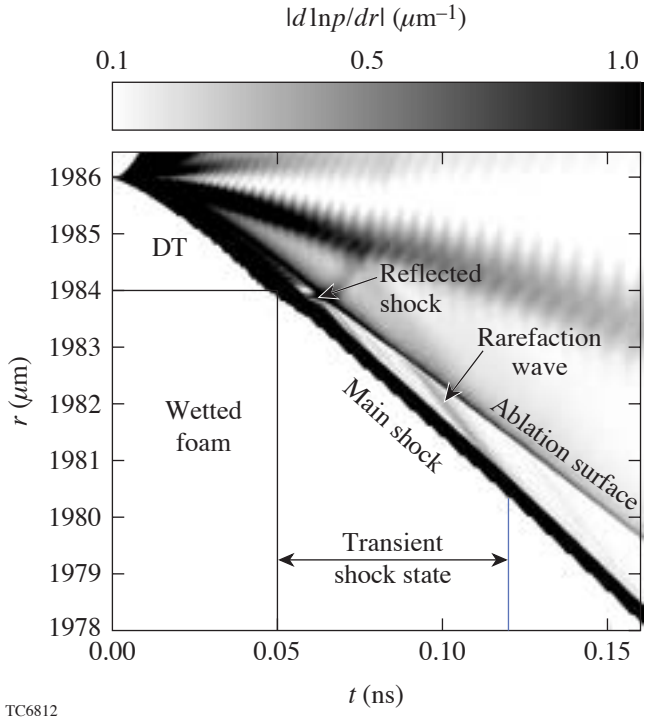


Figure 100.14
The magnitude of the inverse of the pressure scale length for a wetted-foam ignition target design in which the wetted-foam layer is overfilled, forming an external 2-$\mu$m layer of DT. Shocks and rarefaction waves are labeled.

For target fabrication reasons, wetted-foam targets are likely to be constructed with a thin outer layer of CH, the second inflow boundary condition discussed in this section. In this case, the ablator is of higher density than the wetted foam. As a result, when the main shock moves from the CH to the wetted foam, it increases in speed. Because of this, a rarefaction wave is reflected off the interface, rather than a shock. When the RW reaches the ablation surface, where the ablation pressure is determined by the laser energy deposition rate, a weak shock or compression wave is launched back into the target. These waves are shown in Fig. 100.15, which shows the inverse of the pressure scale length for a high-gain, NIF wetted-foam target with a ~2-$\mu$m-CH ablator. In contrast to the case above of the DT pusher, the shock is undersupported until the compression wave reaches it. This transient state lasts for 100 ps in this design. Figure 100.16 shows the $y$-averaged pressure and density compared with a homogeneous simulation also using a CH pusher. This shows again that the RH jump conditions are obeyed, and the average shock speed is approximately the same in both cases.

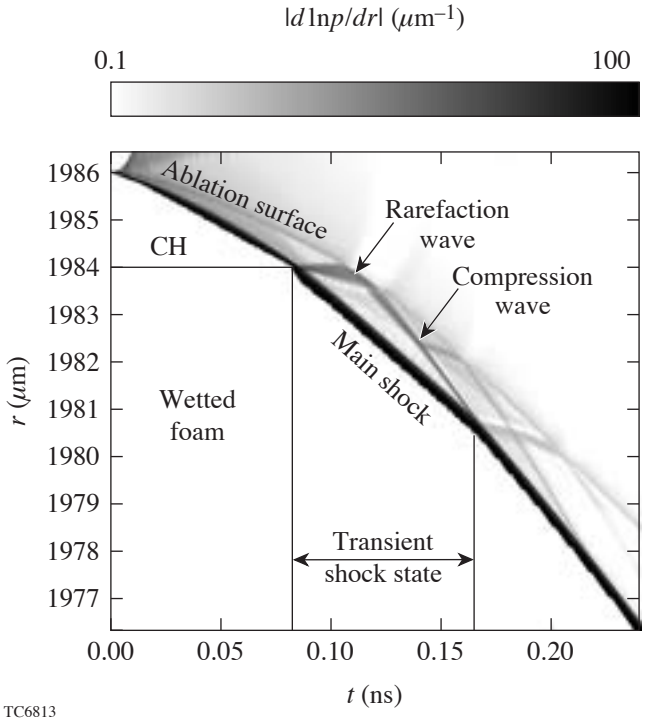


Figure 100.15
The magnitude of the inverse of the pressure scale length for a wetted-foam ignition target design with an external 2-$\mu$m layer of CH.

## Conclusions

High-gain, direct-drive, wetted-foam ICF targets have been designed previously for use on the NIF and in IFE. Due to the prohibitively large range of length scales from the foam microstructure to the pellet size, simulations of these designs generally assume a homogeneous mixture for the wetted foam. We have simulated shock propagation in wetted-foam mixtures. We have found that the size of the decay length behind the shock is of the order of a micron for relevant foam densities. In the mix region, the transverse and turbulent motion decay sufficiently that the Rankine–Hugoniot jump conditions are obeyed to within a few percent. As a result, the average shock

speeds are also within a few percent of their homogeneous values. This implies that designs, which are less sensitive than this to shock timing, may be simulated using the approximation of homogeneous mixtures.

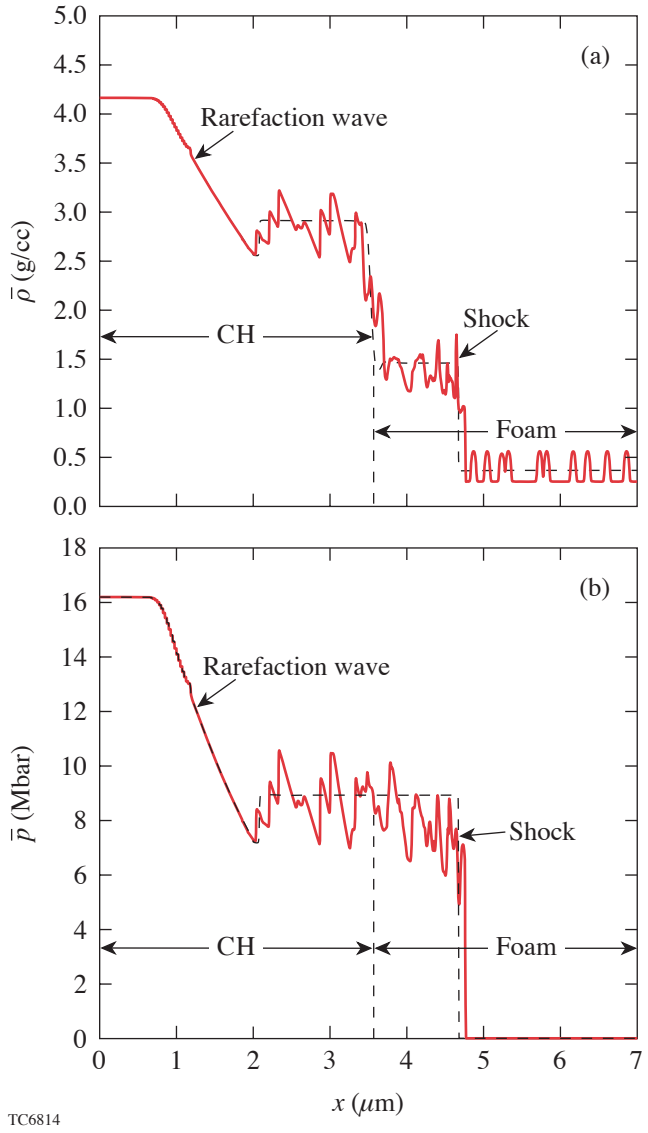


Figure 100.16
The density (a) and pressure (b) as functions of distance are shown for a particular time, along with the values from a simulation of a corresponding homogeneous medium with the same average pre-shock density (dashed). The inflow boundary conditions correspond to a CH pusher.

We have also considered the "lifetime" of shock-front perturbations. As expected, because shock fronts are stable, perturbations seeded by the wetted-foam layer decay quickly after the shock enters the homogeneous DT-ice layer. Therefore we expect the wetted-foam microstructure to have a negligible effect on feedthrough and feedout.

Finally, we have examined the effects of using other "pushers"—DT and CH—to simulate the transient states that occur early in a target overfilled with DT ice and a target with an outer CH overcoat. The RH conditions are also met to within a few percent for these inflow conditions.

## ACKNOWLEDGMENT

The author would like to thank I. Igumenshchev, P. B. Radha, and V. Goncharov for many useful discussions. This work was supported by the U.S. Department of Energy Office of Inertial Confinement Fusion under Cooperative Agreement No. DE-FC52-92SF19460, the University of Rochester, and the New York State Energy Research and Development Authority. The support of DOE does not constitute an endorsement by DOE of the views expressed in this article.

## REFERENCES

1. J. Nuckolls *et al.*, Nature **239**, 139 (1972).
2. L. M. Hair *et al.*, J. Vac. Sci. Technol. A **6**, 2559 (1988).
3. D. G. Colombant *et al.*, Phys. Plasmas **7**, 2046 (2000).
4. S. Skupsky, R. Betti, T. J. B. Collins, V. N. Goncharov, D. R. Harding, R. L. McCrory, P. W. McKenty, D. D. Meyerhofer, and R. P. J. Town, in *Inertial Fusion Sciences and Applications 2001*, edited by K. Tanaka, D. D. Meyerhofer, and J. Meyer-ter-Vehn (Elsevier, Paris, 2002), pp. 240–245.
5. J. D. Sethian *et al.*, Nucl. Fusion **43**, 1693 (2003).
6. M. Desselberger *et al.*, Phys. Rev. Lett. **74**, 2961 (1995).
7. J. D. Lindl, Phys. Plasmas **2**, 3933 (1995).
8. E. M. Campbell and W. J. Hogan, Plasma Phys. Control. Fusion **41**, B39 (1999).
9. L. Phillips, in *Shock Compression of Condensed Matter—1995*, edited by S. C. Schmidt and W. C. Tao (AIP Press, Woodbury, NY, 1996), pp. 459–462.
10. G. Hazak *et al.*, Phys. Plasmas **5**, 4357 (1998).
11. A. D. Kotelnikov and D. C. Montgomery, Phys. Fluids **10**, 2037 (1998).
12. F. Philippe *et al.*, Laser Part. Beams **22**, 171 (2004).

13. B.-I. Jun, T. W. Jones, and M. L. Norman, Astrophys. J. **468**, L59 (1996).

14. A. Y. Poludnenko, A. Frank, and E. G. Blackman, Astrophys. J. **576**, 832 (2002).

15. A. Poludnenko *et al.*, "AstroBEAR: AMR for Astrophysical Applications—I: Methods," to be published in *Adaptive Mesh Refinement—Theory and Applications*.

16. M. J. Berger and R. J. LeVeque, SIAM J. Numer. Anal. **35**, 2298 (1998).

17. R. J. LeVeque, J. Comput. Phys. **131**, 327 (1997).

18. M. Rudman, Int. J. Numer. Methods Fluids **24**, 671 (1998).

19. H. F. Robey, Phys. Plasmas **11**, 4123 (2004).

20. J. G. Clérouin, M. H. Cherfi, and G. Zérah, Europhys. Lett. **42**, 37 (1998).

21. M. C. Richardson, P. W. McKenty, F. J. Marshall, C. P. Verdon, J. M. Soures, R. L. McCrory, O. Barnouin, R. S. Craxton, J. Delettrez, R. L. Hutchison, P. A. Jaanimagi, R. Keck, T. Kessler, H. Kim, S. A. Letzring, D. M. Roback, W. Seka, S. Skupsky, B. Yaakobi, S. M. Lane, and S. Prussin, in *Laser Interaction and Related Plasma Phenomena*, edited by H. Hora and G. H. Miley (Plenum Publishing, New York, 1986), Vol. 7, pp. 421–448.

22. J.-Ch. Robinet *et al.*, J. Fluid Mech. **417**, 237 (2000).

23. A. Y. Poludnenko, K. K. Dannenberg, R. P. Drake, A. Frank, J. Knauer, D. D. Meyerhofer, M. Furnish, J. R. Asay, and S. Mitran, Astrophys. J. **604**, 213 (2004).

24. R. I. Klein, C. F. McKee, and P. Colella, Astrophys. J. **420**, 213 (1994).

25. J. M. Picone and J. P. Boris, J. Fluid Mech. **189**, 23 (1998).

26. N. Cowperthwaite, Physica D **37**, 264 (1989).

27. A. J. Lim and A. C. Raga, Mon. Not. R. Astron. Soc. **303**, 546 (1999).

28. M. M. Maclow *et al.*, Astrophys. J. **433**, 757 (1994).

29. L. D. Landau and E. M. Lifshitz, *Fluid Mechanics* (Pergamon Press, London, 1959).

30. M. Koenig *et al.*, Phys. Plasmas **6**, 3296 (1999).

31. R. Betti, V. Lobatchev, and R. L. McCrory, Phys. Rev. Lett. **81**, 5560 (1998).

32. A. E. Roberts, Los Alamos National Laboratory, Los Alamos, NM, Report LA-299 (1945).

33. G. B. Whitham, *Linear and Nonlinear Waves*, Pure and Applied Mathematics (Wiley, New York, 1974).

34. P. W. McKenty, V. N. Goncharov, R. P. J. Town, S. Skupsky, R. Betti, and R. L. McCrory, Phys. Plasmas **8**, 2315 (2001).

35. T. J. B. Collins, S. Skupsky, V. N. Goncharov, R. Betti, P. W. McKenty, P. B. Radha, R. Epstein, A. Poludnenko, A. Frank, and S. Mitran, in *Inertial Fusion Sciences and Applications 2003*, edited by B. A. Hammel, D. D. Meyerhofer, J. Meyer-ter-Vehn, and H. Azechi (American Nuclear Society, La Grange Park, IL, 2004), pp. 92–95.

# Demonstration of Real-Time, Phase-Locked Alignment of Tiled Gratings for Chirped-Pulse–Amplified Lasers

## Introduction

The OMEGA EP (extended performance) petawatt, multikilojoule, solid-state laser, presently under construction at LLE, includes compressors with four tiled-grating assemblies (TGA's), where each assembly contains three subaperture diffraction gratings, to compress the pulse before it is focused onto target.[1,2] The tiled-grating compressor (TGC) was chosen to stay within the damage-threshold limitations of the largest currently available multilayer dielectric (MLD) gratings, together with the anticipated intensity modulation of the laser output beam. The four-grating compressor is shown schematically in Fig. 100.17. The holographically generated grating tiles[3,4] have a line frequency of 1740 grooves/mm and a clear aperture of 400 × 470 mm. The individual BK-7 grating substrates have a thickness of nominally 100 mm and are approximately 50 kg in weight. For the TGC to deliver the compressed pulse with a near-diffraction–limited energy distribution on target, the individual tiles have to be aligned to each other with an optical-path difference (OPD) of less than 50 nm. An active control approach, similar to a three-actuator deformable mirror, has been chosen to maintain the correct alignment between grating tiles.

Between any two gratings there are six degrees of freedom that affect the optical performance of a tiled-grating system, as shown in Fig. 100.18. A three-control-variables approach has been chosen to bring the gratings into the condition of coherent energy addition.[5] This reduction in degrees of freedom is realized by grouping six variables into three pairs that mutually compensate. Differential tilt, caused by small differences in the average groove spacing, is removed by adjusting the individual grating tilt. Also, error in lateral placement of the gratings is compensated for by a small adjustment of piston. In addition, error in groove parallelism between gratings is compensated by a *y*-tip adjustment. Although each differential error must be kept small, compensation between pairs allows all six degrees of freedom to be nonzero while coherent addition is maintained. Using this pairing concept, a systematic alignment sequence provides convergence toward accurate coherent addition.

Several new alignment techniques have been demonstrated to achieve coherent addition of tiled gratings. The relative grating positions and all alignment measurements are made in real-time with an interferometer whose field of observation straddles the gap between the gratings. Any drift of the grating tiles from their optimal position is measured and compensated by a servo loop. The gratings are pre-aligned to have a differential piston of less than 10 $\mu$m, which is the capture range of the servo system. With the servo loop engaged, an alignment

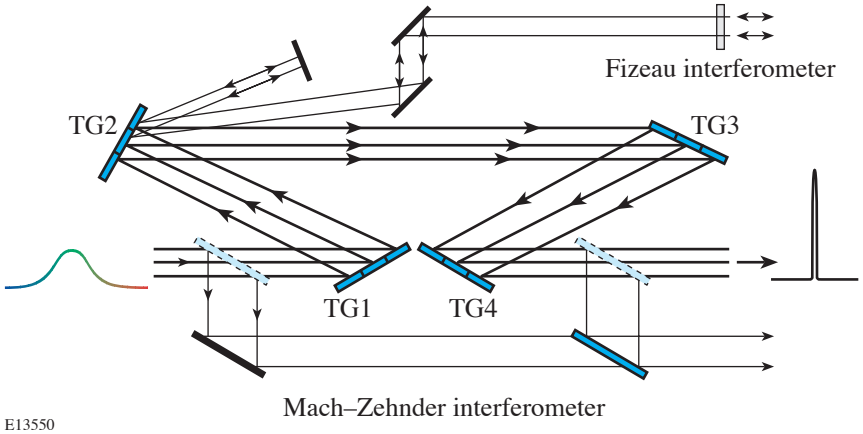


Figure 100.17
Each OMEGA EP compressor contains four tiled-grating assemblies (TGA's) per beamline, where each assembly contains three subaperture diffraction gratings. Each TGA interface requires three actuators to maintain the grating positioning needed for coherent addition of the three diffracting beams. The tiled-grating compressor (TGC) provides an aperture large enough to meet the energy requirements while operating below the laser-damage threshold of the final grating. Interferometers are deployed to maintain accurate alignment of the gratings within each TGA.

precision of ±25 nm, or λ/20 p–v, is reproducibly achieved. In addition, as schematically illustrated in Fig. 100.17, a robust alignment system, intended for use on the OMEGA EP laser system, contains two interferometers. Individual TGA's are aligned with a Fizeau interferometer, while alignment of the entire TGC is verified with a Mach–Zehnder interferometer and a focal-spot diagnostic.

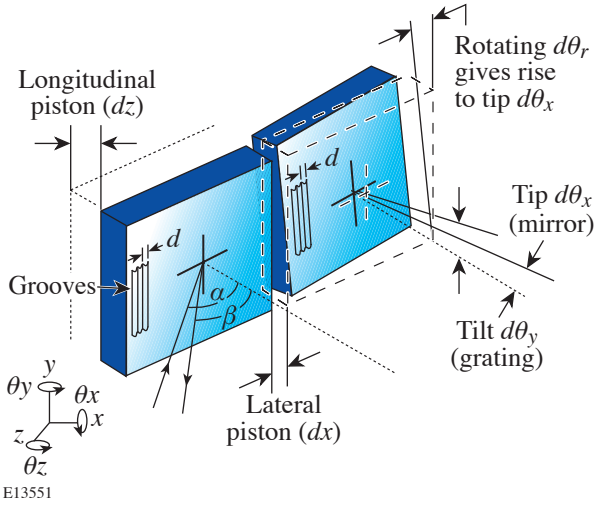


Figure 100.18
Between any two gratings there are six degrees of freedom that affect the optical performance of a tiled-grating system. These can be grouped into three compensating pairs of differential errors: longitudinal piston and lateral piston; in-plane rotation and angular tip; and average groove spacing and angular tilt. Although each differential error must be kept small, compensation between pairs removes the constraint that any particular error must be zero.

## Modeling

A measure of the accuracy with which two gratings operate in the coherently additive mode is the Strehl ratio, which is defined as the ratio of the peak irradiance of an aberrated focal spot to that of an aberration-free focal spot.[6] Computer simulations of one TGA interface show the effect of the differential grating misalignments as measured in the near field. Tip, tilt, or piston misalignment between the gratings affects the Strehl ratio to different degrees for the same magnitude of alignment error. This sensitivity is shown for piston, *x* tilt, *y* tip, and in-plane rotation in Fig. 100.19, which plots the Strehl ratio as a function of a misalignment error. Although the TGC in the OMEGA EP laser system will operate at a wavelength of 1054 nm, both modeling and prototype development were carried out at a wavelength of 633 nm because of the availability of an interferometer operating at this wavelength. To achieve accurate tiling at either wavelength, the misalignment errors, taken individually or as compensation pairs, must be kept below λ/20 to maintain close to a diffraction-limited focal spot.

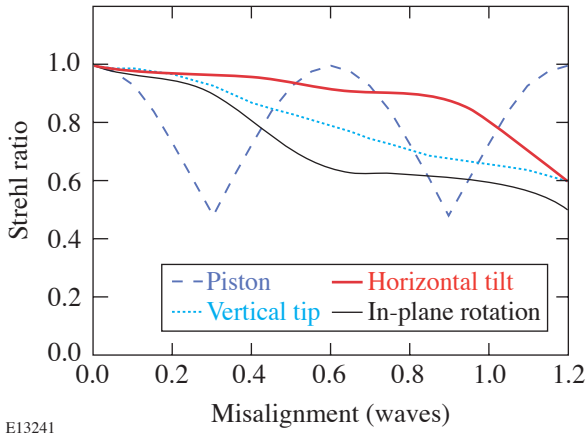


Figure 100.19
Computer simulations of one TGA interface show the effect of the differential grating misalignments as measured in the near field. The Strehl ratio is plotted as a function of individual misalignments for a wavelength of 633 nm and an incident angle of 33.4°. The misalignment errors, taken individually or as compensation pairs, must be kept below λ/20 to maintain close to a diffraction-limited focal spot.

These computer simulations show that piston is the most-sensitive drift parameter for two gratings and that the effects of piston error are cyclical with an OPD period of λ/2. Since the absolute piston error has to be less than one wavelength, any error must be corrected before it reaches λ/2; otherwise the absolute piston position can be lost due to a periodic π ambiguity. If the fringe system jumps by an error greater than λ/2, the piston must be reset independently and the tracking/correcting system restarted.

Three equations mathematically describe the paired relationship for the various degrees of freedom. Defining displacements as $\Delta z$ (longitudinal piston shift), $\Delta x$ (lateral piston shift), $\theta x$ [rotation about *x* axis (tip)], $\theta y$ [rotation about *y* axis (tilt)], $\theta z$ [rotation about *z* axis (in-plane rotation)], and $\Delta d$ (error in grating ruling spacing), the following three equations represent the resulting phase errors. Equation (1) represents the piston phase error while Eqs. (2) and (3) represent the phase gradients of tip and tilt, respectively, where $d\Phi/dy$ and $d\Phi/dx$ are the transverse phase gradients in the beam, $\alpha$ is the incident angle, and $\beta$ is the diffraction angle. The objective for accurate tiling involves setting each equation to zero for the majority of spectral components of the laser pulse.

$$\Delta\Phi_z = 2\pi/\lambda\left[(\sin\alpha + \sin\beta)\Delta x - (\cos\alpha + \cos\beta)\Delta z\right]. \quad (1)$$

$$d\Phi/dy = -2\pi/\lambda\left[(\cos\alpha + \cos\beta)\theta_x + (\sin\alpha + \sin\beta)\theta_z\right]. \quad (2)$$

$$d\phi/dx = 2\pi/\lambda\left[(\cos\alpha + \cos\beta)\theta_y - (\sin\alpha + \sin\beta)\Delta d/d\right]\sec\beta. \quad (3)$$

Three independent actuators that produce displacements normal to the surface of the grating are used to control differential tilt, tip, and piston. The motion of a single actuator rotates the grating about an axis defined by the other two actuators. This rotation is resolved into tilt and tip components by projection of the axis onto the coordinate system axes. Piston displacement is simply the corresponding normal displacement of the grating surface at a reference point selected for piston measurement. It is convenient to combine the coefficients for tip, tilt, and piston motion due to actuator displacements into a 3 × 3 matrix $M$ and to calculate its inverse $M^{-1}$, which is also a 3 × 3 matrix. Then the actuator motions required to produce a specified tilt, tip, and piston correction are described by $Z = M^{-1}C$, where $Z$ is the row vector of required actuator displacements and $C$ is the column vector of tilt, tip, and piston corrections.

**Experimental Setup**

Several different prototype assemblies were built to study error compensation, TGA-to-TGA compensation schemes, and various alignment techniques. The tiled-grating mounts are identical three-point, flexure suspensions that separate weight-bearing and adjustment functions, as shown in Fig. 100.20. The front view of a prototype TGA shows two gold-coated, 16 × 22-cm gratings, manufactured by Jobin-Yvon, while the back view shows both the manual and motorized actuators. The entire TGA is mounted on a precision rotating stage to achieve rapid and repeatable angular adjustment when positioning to a normal, Littrow, or near-Littrow angle of incidence. The design emphasizes pre-loaded, easy motion in the direction of control while being very stiff in two orthogonal directions, thus minimizing parasitic motions.

The experimental test bed used to demonstrate closed-loop control of TGA's is configured on an optical table containing a Fizeau interferometer (Fig. 100.21), with an ADE Phase Shift Mini Fiz 100 front end, operating at 632.8 nm. The out-

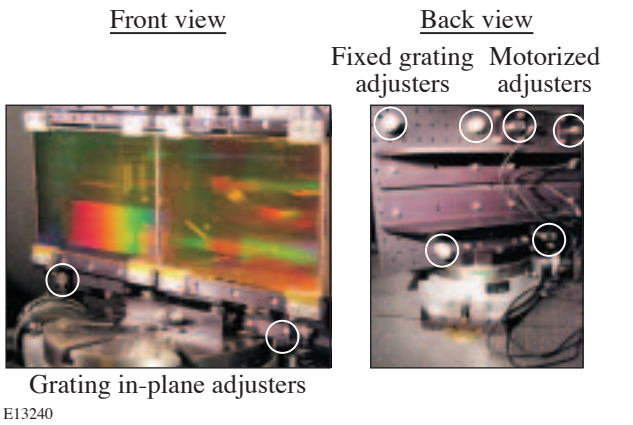


Figure 100.20
The front view of a prototype TGA shows two gold-coated, 16 × 22-cm gratings, while the back view shows both the manual and motorized actuators. The TGA is mounted on a precision rotating stage to achieve rapid and repeatable angular adjustment when positioning to a normal, Littrow, or near-Littrow angle of incidence. Several different prototype assemblies were built to study error compensation, TGA-to-TGA compensation schemes, and various alignment techniques.

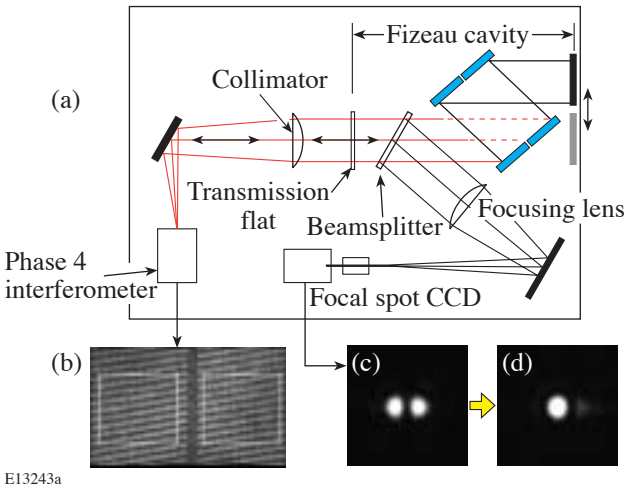


Figure 100.21
The experimental test bed used to demonstrate closed-loop control of tiled-grating assemblies (TGA's) is configured on an optical table containing a 10-in. Fizeau interferometer (a). The TGA's are positioned within the interferometer cavity for testing single- and double-pass alignment, using one TGA, or triple- and quadruple-pass alignment, using two TGA's. The fringe pattern (b) is a sample of a recorded interferogram, while (c) and (d) are examples of a piston phase error of $\lambda/2$ and a diffraction-limited focal spot, respectively.

put beam was expanded to 250 mm, using a 1.8-m-focal-length lens for collimation, as shown in Fig. 100.21. A 12-in.-diam transmission flat, manufactured by Zygo, was inserted into the Fizeau cavity to send a portion of the return beam for far-field analysis, as described previously.[7] The TGA's were positioned within the interferometer cavity for testing single- and double-pass alignment, using one TGA, or triple- and quadruple-pass alignment, using two TGA's. The fringe pattern [Fig. 100.21(b)] is a sample of a recorded interferogram, while Figs. 100.21(c) and 100.21(d) are examples of a piston phase error of $\lambda/2$ and a diffraction-limited focal spot, respectively.

One grating in the TGA was adjustable through remotely controlled piezo-type actuators (New Focus PicoMotors, model 8301)[8], while the second grating was held steady after manual adjustment with Aerotech Differential micrometers. The suspension mounts for both gratings were mounted on a common backplate. The backplate assembly was mounted on a 250-mm-diam rotary table with a resolution of 4 arc sec (manufactured by Phase II). Parallelism of the gratings' grooves was obtained by pivoting one of the gratings about the grating normal, while the TGA was alternately positioned at normal incidence and Littrow position within the Fizeau interferometer. After several iterations, grating parallelism was adjusted to within 0.1 wave. The functional systems diagram is shown in Fig. 100.22. The prototype control system monitors grating alignment in both the near field and far field (focal spot). The cw laser light probes the gratings and is transmitted to electronic cameras to record both the fringe pattern and the corresponding focal spot. Analysis of the fringe pattern yields differential tip, tilt, and piston. From these measurements, the system computer generates signals to drive three actuators, for each grating-to-grating interface, in a closed-loop cycle that minimizes the set of differential errors. The focal-spot diagnostic is used to verify successful convergence toward diffraction-limited performance.

### Phase Measurement and Error-Signal Computation

Any drift between the two gratings is determined from a single interferogram according to a Fourier-transform (FT) method known as spatially synchronous phase detection (SSPD).[9] Figure 100.23 shows the methodology by which this technique is used to analyze the high-frequency fringe patterns situated on either side of the TGA interface. The interferometer is adjusted with deliberate tilt between the reference and test wavefronts to produce an interferogram [Fig. 100.23(a)] that contains the surface information encoded onto a high-order spatial carrier frequency. A window function is applied to remove edge-ringing [Fig. 100.23(b)]. The FT of the interferogram [Fig. 100.23(c)] produces a dc component and two sidebands symmetrically displaced corresponding to the carrier frequency of the fringe pattern. Higher-order sidebands are present with nonsinusoidal fringe profiles. Each of the sidebands contains all of the desired phase information. The carrier frequency is chosen to place the side lobe to a position outside the noise spectrum of the interferometer system. One sideband is isolated by applying an appropriate filter in the Fourier plane and shifted to zero frequency before carrying out the inverse Fourier transform. Two-dimensional phase reconstruction of each side of the TGA interface is obtained with an inverse FT, followed by calculation of the phase from the real and imaginary components of the image. The complex phase of the inverse transform is unwrapped and represents the phase data of the surfaces [Fig. 100.23(d)]. Any remaining tip, tilt, or

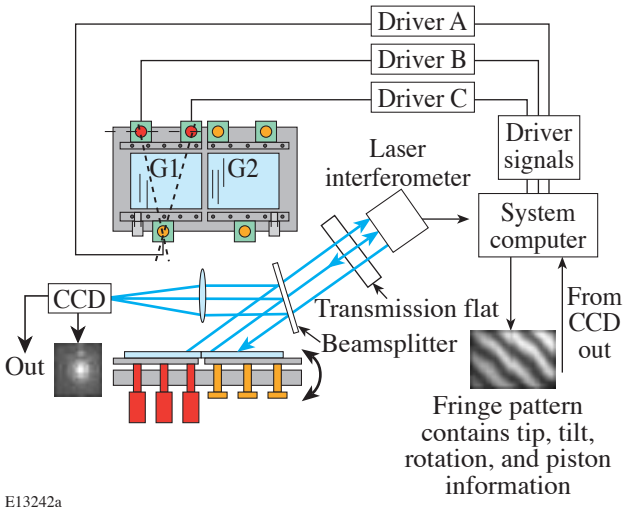


Figure 100.22
The control system monitors grating alignment in both the near field and far field (focal spot). The cw laser light probes the gratings and is transmitted to electronic cameras to record both the fringe pattern and the corresponding focal spot. Analysis of the fringe pattern yields differential tip, tilt, and piston. From these measurements, the system computer generates signals to drive three actuators in a closed-loop cycle that minimizes the set of differential errors. The focal-spot diagnostic is used to verify successful convergence toward diffraction-limited performance.

piston phase errors can be removed in the final stages of closed-loop operation. This technique is especially useful when operating in optically "noisy" environments since the single video frame measurement is fast compared to scanning interferometers and permits a high level of noise rejection, through averaging of multiple video frames in phase space.

The differential slope of the two elements represents the $x$ tilt and $y$ tip of the two tiles. The $x$ tilt and $y$ tip are determined unambiguously in the $x$–$y$ coordinate system. "Piston" is the out-of-plane offset in the $z$ direction. A linking of the left and right portions of the interferogram has to be applied across the gap to maintain phase continuity for the piston computation.

As previously described in this article, the three phase-error terms are the result of the joint effect of a pair of separate, independent grating misalignments. The piston term is the composite effect of both an actual $z$-direction tile offset and a lateral shift perpendicular to the grating rulings. The tip term comprises the joint effect of actual differential tip and in-plane rotation of one of the gratings with respect to the other. The tilt term is due to differential tilt between the gratings, which can, in part, be caused by a difference in groove spacing. An error in one of the components of a two-component term may be perfectly compensated by adjusting the other component; therefore, it is necessary to provide only three adjustments per tile, provided that the grating array is designed to minimize errors in the nonadjustable offsets.

After an initial system alignment where most of the tip and tilt have been removed and the relative piston has been set within $2\pi N$, the value of $N$ is checked by translating a high-resolution mechanical indicator across the gap on the grating surface outside of the clear aperture. The indicator is mounted on a slide that is parallel to the surface of the first grating and that places the indicator within a few millimeters, laterally, of the gap. Translating the indicator while in contact with gratings produces a step if there is an absolute piston error. The three

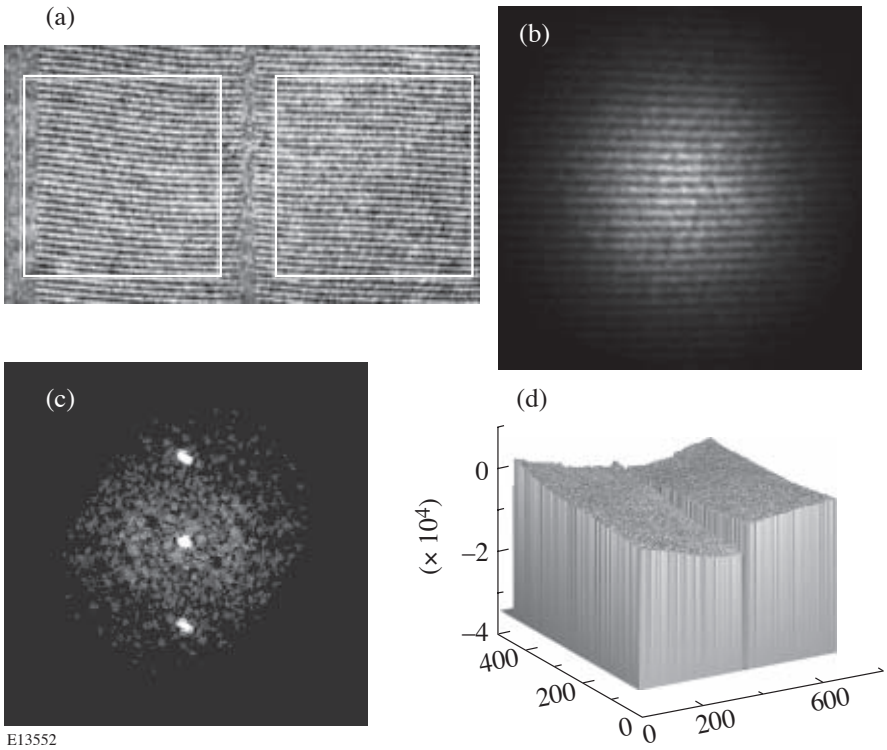


Figure 100.23
A Fourier-transform (FT)–based algorithm, referred to as spatial synchronous phase detection (SSPD), is used to analyze high-frequency fringe patterns (a) situated on either side of the TGA interface. A window function is applied to each fringe pattern (b) to reduce edge effects in the FT calculations. The carrier frequency is chosen to place the side lobe to a position outside the noise spectrum of the interferometer system (c). An inverse FT, followed by phase calculations, results in two-dimensional phase reconstruction of each side of the TGA interface. Any remaining tip, tilt, or piston phase errors (d) can be removed in the final stages of closed-loop operation.

actuators of the motorized gratings are now moved in concert by an appropriate amount to reduce the absolute piston to less than one wavelength.

### Computer System and Software

The software integrates the image acquisition, image analysis, parameter derivation, and actuator control, as well as all data logging, in the same computer. The speed of the control loop is of the order of 1 s, even though the actual alignment may be corrected much less frequently. For the purpose of thorough testing, the measurement system was designed to be sensitive to both low- and high-frequency disturbances. For example, a change in room temperature induces thermal drifts typically requiring corrections of the order of minutes to hours. High-frequency disturbances that can be induced by acoustics or air turbulence are removed by averaging many individual measurements. Close to 100 measurements were typically averaged to achieve the required level of noise reduction.

A Windows-based desktop computer, with five extension slots, running at 2.5 GHz, was used to acquire interferometric data. The fringes were acquired with a monochrome CCD camera, internal to the ADE MiniFiz interferometer with RS-170 interface, and digitized with a four-channel, 8-bit data acquisition card from National Instruments, model 1409.[10] Processing artificial fringe patterns showed the numerical resolution of the software to be better than $\lambda/1000$. One channel of that card was used to digitize the image of the fringe pattern, while another channel was used to acquire a far-field view used for the diagnostic of the alignment.

The control loop was completed with three Picomotor controllers (New Focus 8753) (Ref. 8) that were driven by a hardware and software package. The Picomotors are digital stepping devices that move in nominal increments of 20 nm. The data acquisition and control software was developed with a rapid prototyping environment called BlackBox Component Builder,[11] which is available free of charge, and compiled with a Component Pascal compiler. The Blackbox environment is very robust and stable and well suited to developing mission-critical software, which requires a low occurrence of failures. An engineering and scientific software library[12] was used to perform matrix calculations and also for data logging and display. The library, written by Robert Campbell for the Blackbox environment, is distributed in source code.

The start-up sequence involves manual grating adjustments in two different positions. The grating assembly is rotated to be perpendicular to the interferometer axis, and both gratings, acting as mirrors, are co-aligned with respect to the Fizeau transmission flat to better than 1 $\mu$rad. This technique is referred to as "fringe-nulling." The grating assembly is then rotated to the Littrow position, where any measured differential vertical tilt is due to in-plane grating rotation. The fringe pattern is "nulled" with separate adjustments for both gratings to ensure that the grating grooves are parallel to one another. It may be necessary to reiterate these last two steps to make certain that the adjustments have settled and the adjusters are locked.

The reference transmission flat is now tilted to produce approximately 15 to 20 fringes across the field to enable the SSPD techniques to work with sufficient precision. Care must be taken to maintain wedge orientation within the interferometer and to maintain the same sign convention throughout the processing software. Once the manual setup steps are complete, the system is ready to perform open-loop stability measurements with the motors disabled. Alternatively, the control loop may be closed for precise grating control.

### Experimental Results

The interferometric system was evaluated by measuring the differential phase between two regions of the same grating over an extended period of time. Each data point was acquired by averaging 16 sequential video frames. As shown in Fig. 100.24, an alignment variation of $\lambda/50$ rms was observed

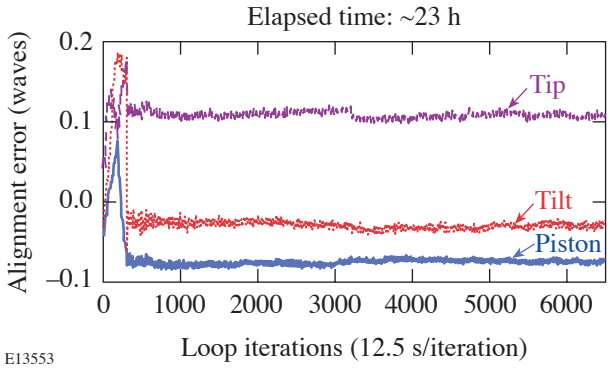


Figure 100.24
The stability of the phase sensor is evaluated by measuring the differential phase between two regions of a stable, monolithic grating. Long-term measurement of tip, tilt, and piston phase errors establishes the noise level of the system to be approximately $\lambda/50$. Statistical analysis, applied over time intervals of several minutes, reduces the measurement error to below $\lambda/100$. Extraneous fluctuations prior to sample 300 are reduced by applying temporal averaging in the SSPD routine.

over this period. Statistical analysis, applied over time intervals of several minutes, reduces the measurement error to below $\lambda/100$. Extraneous fluctuations prior to sample 300 were reduced by applying temporal averaging in the SSPD routine. After replacing the single grating with two gratings, phase measurements were made in open-loop mode over a 24-h period. As shown in Fig. 100.25, long-term monitoring of a TGA, with disabled actuators, indicates tip and tilt stability while the differential piston drifts by more than the wavelength of light. The system stability was found to vary by approximately five wavelengths of light per degree centigrade. The apparent phase jumps at $\pm\lambda/2$ are due to the $-\pi$ to $\pi$ range of the arctangent calculation performed in phase reconstruction.

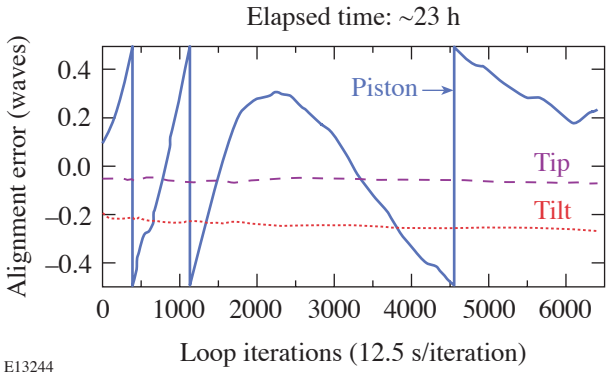


Figure 100.25
Long-term monitoring of a TGA, with disabled actuators, indicates tip and tilt stability while the differential piston drifts by more than the wavelength of light. The apparent phase jumps at $\pm\lambda/2$ are due to the $-\pi$ to $\pi$ range of the arctangent calculation performed in phase reconstruction. The overall cyclical behavior of the piston term is caused by the difference in the coefficient of thermal expansion between the Pyrex™ substrate and aluminum mount in the presence of small temperature changes in the environment.

As a result of the phase-pair compensation strategy, any drift in either "*y* tip" or "in-plane grating rotation" is contained in the vertical "tilt signal," and their sum can be corrected with the servo system. Similarly, any drift in longitudinal shift (piston) or lateral shift is contained in the "piston signal," and their sum can be corrected by the servo system. A temperature recording, and subsequent analysis, showed that the cyclical behavior of the piston term is caused by the difference in the coefficient of thermal expansion between the Pyrex™ substrate and the aluminum mount in the presence of small temperature changes in the environment. The largest dimensions of the assembly are the widths of the gratings and the support structure. Since changes of these dimensions, due to temperature variation, are different for dissimilar materials, a phase shift occurs between the sets of grooves from their respective grating.

Closed-loop control of a TGA is achieved by driving the actuators with signals derived from the phase sensor. Phase fluctuations (Fig. 100.26) were largely reduced when the actuators were activated at sample number 9, and $\lambda/10$ alignment was rapidly achieved at sample number 25. As marked by sudden shifts in the plots, differential piston occurred at sample numbers 52 and 142. Tip and tilt phase correction was not required over the same time period. At the end of closed-loop operation, piston corrections in one-step increments, or 20 nm, are observed. This is comparable to the operation with a single grating where the far-field signal approximates a steady Airy pattern, with a Strehl ratio of about 0.99. During operation of an OMEGA EP laser beam, closed-loop control of up to eight interfaces will be required.

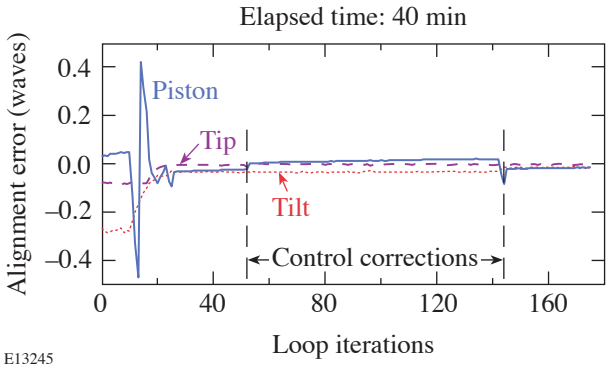


Figure 100.26
Closed-loop control of a TGA is achieved by enabling the actuators with signals derived from the phase sensor. Phase fluctuations were largely reduced when the actuators were enabled at sample number 9, and $\lambda/10$ alignment was achieved at sample number 25. As marked by sudden shifts in the plots, differential piston occurred at sample numbers 52 and 142. Tip and tilt phase correction was not required over the same time period.

An important demonstration of closed-loop control of the TGA involved obtaining convergence of all of the measured differential phase errors to zero following random offsets to the actuators [Fig. 100.27(a)]. Both the focal-spot irradiance and computed Strehl ratio tracked very well with the recorded differential piston. A focal spot splits into two lobes for a piston error of $(2N+1)\pi$ [Fig. 100.27(b)], while an Airy pattern [Fig. 100.27(c)] is recovered as the piston misalignment returns to near zero: For this experimental demonstration, the irradiance doubled after successful closed-loop alignment

[Figs. 100.27(d) and 100.27(e)]. A closed-loop run, requiring correction of initial tip, tilt, and piston errors, is completed in approximately 5 min. The settling time depends on the severity of the initial misalignments.

Operational ease can be achieved for closed-loop control of a tiled-grating compressor (TGC) through simultaneous alignment of all TGA's in a series configuration. Series alignment was demonstrated by positioning two TGA's in double-pass configuration using an auxiliary retroreflecting mirror. While one TGA was intentionally misaligned with a piston error of $\pi$ radians [Fig. 100.28(a)], the second TGA was adjusted to remove all piston error from the series configuration [Fig. 100.28(b)]. Closed-loop alignment was successful despite an increase in diffraction losses due to the cumulative phase errors of the eight diffraction gratings. For comparison, a single TGA, in Littrow configuration, was alternately adjusted to form either a split focal spot [Fig. 100.28(c)] or a diffraction-limited focal spot [Fig. 100.28(d)].

Monochromatic laser light, operating at the center wavelength of a typical high-intensity laser, was used to simulate in-series alignment of the TGA units for the outer spectral components of broadband laser light. Figure 100.29(a) shows an experimentally generated phase map with the left and right regions of the beam accurately tiled, even though the individual TGA's are not properly tiled. Due to a spatial chirp that forms in part of the compressor, the extreme spectral components of the laser pulse cannot be fully compensated. The central, narrow region of the beam is not compensated and contained a differential tip of about three waves. The focal spot [Fig. 100.29(b)] shows a corresponding increase in diffraction

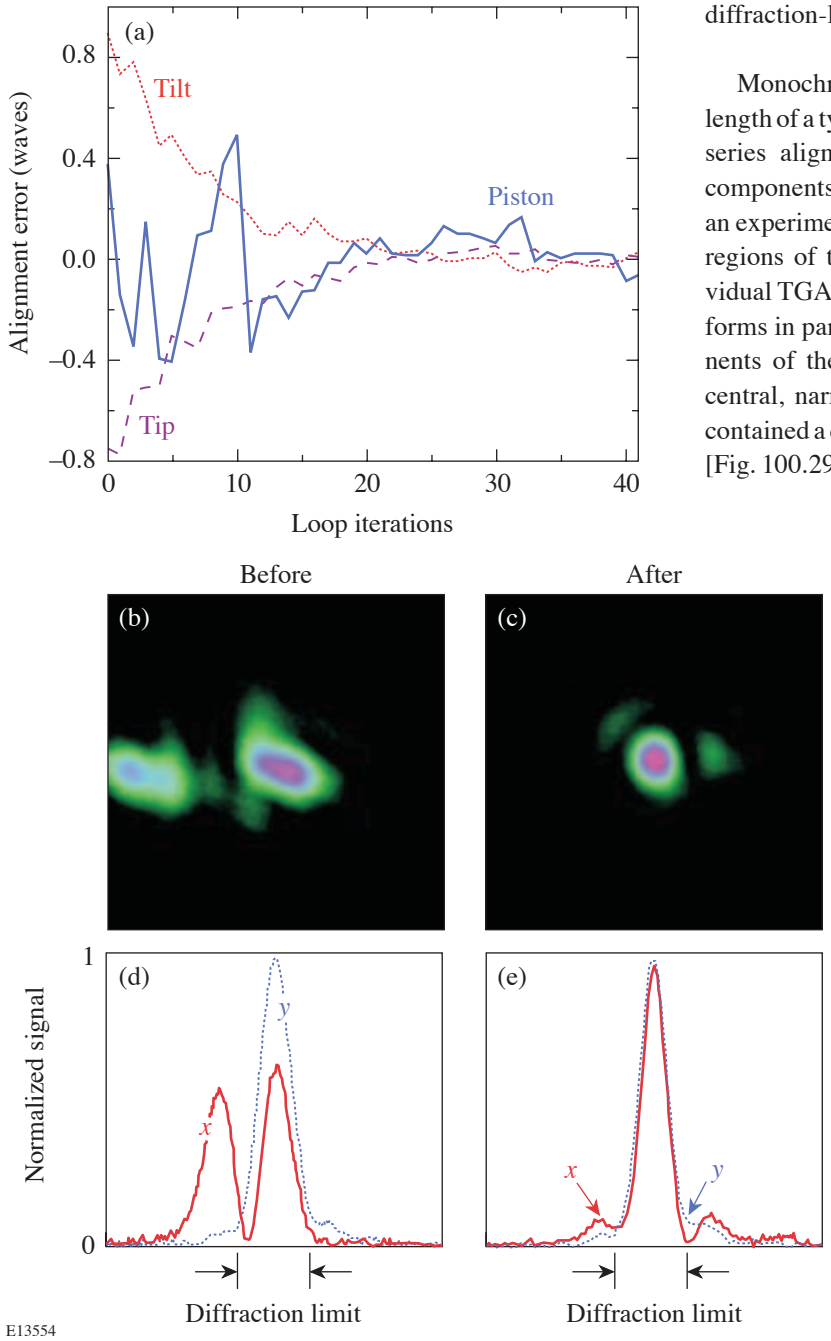


Figure 100.27
Closed-loop control of the TGA is achieved when all of the measured differential phase errors converge to zero following random offsets of the actuators (a). Corroboration between phase convergence and Strehl ratio indicates successful closed-loop control. A symmetrically split far-field pattern is observed for piston values of $(2N+1)\pi$ (b), while a single focal spot is observed for piston values of 0 and $2\pi n$ (c). The irradiance is doubled after successful alignment [(d) and (e)].

spreading in the horizontal plane due to the misregistration of the gaps. Diffraction spreading in the vertical plane is due to the differential tip of the central strip of light.

Theoretical calculations predict that integration over all spectral components of the laser pulse, carried through a TGC that is aligned with compensating TGA errors, yields negligible effects for pulses longer [Figs. 100.30(a) and 100.30(b)] than the Fourier-transform–limited ($\Delta\tau$) pulse [Fig. 100.30(c)]. Two-dimensional, space-time images clearly show that the effects from residual compensation error are pronounced only when maximum pulse compression is attempted. Further spatial integration of these images yields temporal pulses shapes [Fig. 100.30(d)] that show the small effect from a compensated $\pi$ piston error in a pair of TGA units. Further modeling will be carried out to explore the combined effects of differential tip, tilt, and piston differential errors when in-series alignment is deployed.

## Conclusion

Accurate closed-loop control of a tiled-grating assembly has been achieved over extended periods of time. Together with previous demonstrations involving coherent addition and pulse compression, this result further supports the feasibility of the tiled-grating compressor as the means to obtain multikilojoule-energy capability for petawatt-class lasers. In addition, in-series TGA alignment was successfully demonstrated in a compressor configuration.

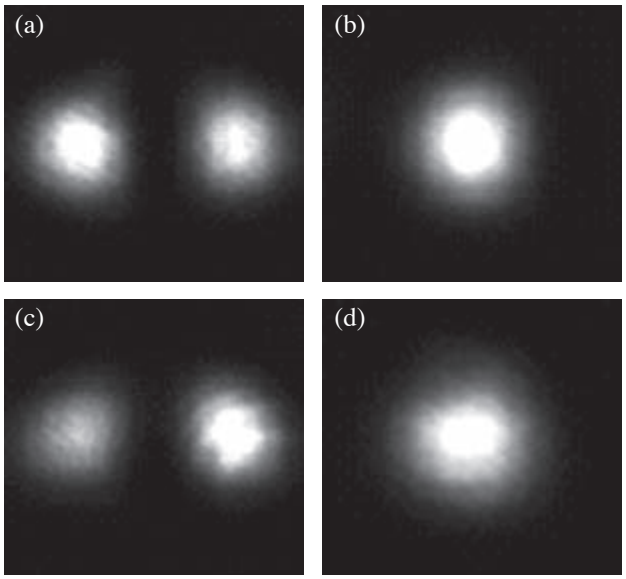


Figure 100.28
Operational ease can be achieved for closed-loop control of a tiled-grating compressor (TGC) through simultaneous alignment of all TGA's in series configuration. Series alignment was demonstrated by positioning two TGA's in double-pass configuration using an auxiliary retroreflecting mirror. While one TGA was intentionally misaligned with a piston error of $\pi$ radians (a), the second TGA was adjusted to remove all piston error from the series configuration (b). Closed-loop alignment was successful despite an increase in diffraction losses due to the cumulative phase errors of the eight diffraction gratings. For comparison, a single TGA, in Littrow configuration, was alternately adjusted to form either a split focal spot (c) or a diffraction-limited focal spot (d).

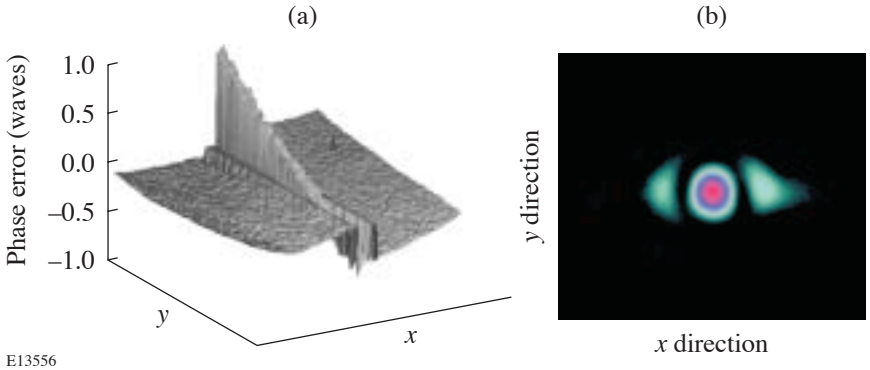


Figure 100.29
Monochromatic laser light was used to simulate in-series alignment of the TGA's for the outer-spectral components of broadband laser light. An experimentally generated phase map is shown in (a) with the left and right regions of the beam accurately tiled, even though the individual TGA's are not properly tiled. The central, narrow region of the beam is not compensated and contains a differential tilt of about three waves. The focal spot (b) shows a corresponding increase in diffraction spreading.

Further developments of the tiled-grating compressor are required to support the OMEGA EP project. A TMA with three tiled gratings is being constructed and tested to demonstrate full-aperture mounting, positioning, and closed-loop control. In addition, this prototype test apparatus will be outfitted with three full-aperture, MLD gratings to demonstrate phase-pair compensation and closed-loop control. Major emphasis will be placed on determining the minimum beam size required to accurately align a TGA containing three gratings using both near-field phase and far-field irradiance diagnostics.

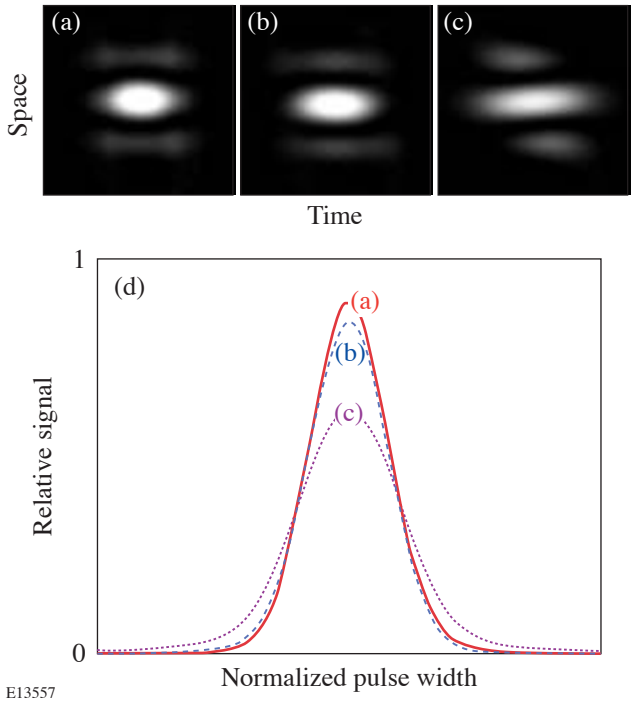


Figure 100.30
Theoretical calculations predict that integration over all spectral components of the laser pulse, carried through a TGC that is aligned with compensating TGA errors, yields negligible effects for pulses longer [(a) and (b)] than the Fourier-transform–limited ($\Delta\tau$) pulse (c). Two-dimensional, space-time images clearly show that the effects from residual compensation error are pronounced only when maximum pulse compression is attempted. Spatial integration of these images yields temporal pulse shapes (d) that show a relatively small effect.

## ACKNOWLEDGMENT

This work was supported by the U.S. Department of Energy Office of Inertial Confinement Fusion under Cooperative Agreement No. DE-FC52-92SF19460, the University of Rochester, and the New York State Energy Research and Development Authority. The support of DOE does not constitute an endorsement by DOE of the views expressed in this article.

## REFERENCES

1. T. J. Kessler, J. Bunkenburg, H. Huang, A. Kozlov, and D. D. Meyerhofer, Opt. Lett. **29**, 635 (2004).
2. Laboratory for Laser Energetics LLE Review **96**, 207, NTIS document No. DOE/SF/19460-509 (2003). Copies may be obtained from the National Technical Information Service, Springfield, VA 22161.
3. B. W. Shore *et al.*, J. Opt. Soc. Am. A **14**, 1124 (1997).
4. 2003 MLD Bulletin, Jobin Yvon, Inc., Gratings and OEM Division, Edison, NJ 08820-3012 (2003).
5. T. J. Kessler, J. Bunkenburg, and H. Huang, "Grating Array Systems for the Alignment and Control of the Spatial and Temporal Characteristics of Light," U.S. Patent Application (filed May 2003).
6. M. Born and E. Wolf, *Principles of Optics: Electromagnetic Theory of Propagation, Interference and Diffraction of Light*, 5th ed. (Pergamon Press, Oxford, 1975).
7. J. Bunkenburg, T. J. Kessler, H. Hu, C. Kellogg, and C. Kelly, presented at CLEO 2003, Baltimore, MD, 1–6 June 2003.
8. New Focus, Inc., a division of Brookham, http://www.newfocus.com (2004).
9. M. Takeda, H. Ina, and S. Kobayashi, J. Opt. Soc. Am. **72**, 156 (1982).
10. National Instruments, Austin, TX 78759-3504, http://www.ni.com (2004).
11. Oberon Microsystems, BlackBox Component Builder, available free of charge from http://www.oberon.ch./blackbox.html (2004).
12. R. Campbell, Engineering and Scientific Library for BlackBox Component Builder, available free of charge from http://www.zinnamturm.de/#Chill (2004).

# *In-Situ* Measurements of High-Intensity Laser Beams on OMEGA

## Introduction

Laser-driven, direct-drive inertial confinement fusion requires near-uniform illumination of the spherical fuel-bearing target;[1,2] therefore, the target must be illuminated symmetrically since uneven illumination will result in uneven acceleration disrupting the implosion. For a laser-driven system with uniformly distributed beams, this dictates that all beams must have equal energies, must have the proper profile, and must be positioned accurately.

Currently, the primary method for determining the energies of beams on the OMEGA laser is based on a calorimeter system [harmonic energy diagnostic (HED)]. The beams must then be transported to the target chamber: they first pass through distributed polarization rotators (DPR's)[3] and are then reflected off two mirrors and transmitted by a distributed phase plate (DPP),[4] a focusing lens, and a vacuum window interface. Losses due to this transport are inferred from measurements made with a cw laser, but variations due to nonlinear effects at high power and variations of the beam shape are not otherwise measured. Likewise, the beam position is determined by a co-propagated cw laser, but with unknown positioning error (centroid determination of the reflected cw beam is accurate to 20 $\mu$m). With the method described here, relative beam fluence, shapes, and positions of the beams are determined from x-ray images of the emission from a 4-mm-diam, Au-coated spherical target illuminated by the beams of OMEGA.[5] The UV light is converted to x rays in the Au coating with high efficiency,[6] and the resultant x-ray flux is imaged with x-ray pinhole cameras (XPHC's) and recorded by charge-injection devices (CID's).[7]

This analysis takes into account projection effects, conversion from UV to x rays, and detection efficiency. This process is sufficiently automated to allow for analysis to be completed within the OMEGA minimum shot cycle (45 min). Mispositioned beams can be repointed to an accuracy of 9 $\mu$m (rms over 60 beams) again within a shot cycle. This method has also been used to determine and minimize beam-to-beam peak fluence variations, thereby further improving on-target uniformity (enhanced fluence balance).[8]

## On-Target Beam Measurements

The data present in XPHC images of pointing shots must be extracted and quantified. Ideally, the beams incident on the target are circularly symmetric and have a radial profile given by a "super-Gaussian" of the form

$$I_{\mathrm{UV}}(r) = I_{\mathrm{UV}}(0) \times e^{-(r/r_0)^{\eta}}, \tag{1}$$

where $I_{\mathrm{UV}}(r)$ is the intensity of the beam as a function of radius, $I_{\mathrm{UV}}(0)$ is the peak intensity, $r$ is the distance from the beam center, $r_0$ is the beam-spot radius, and $\eta$ is the power of the super-Gaussian.

The gold target converts the incident UV energy into x rays with a high efficiency.[6] The result follows the proportionality[8]

$$I_x \propto I_{\mathrm{UV}}^{\gamma}, \tag{2}$$

where $I_x$ is the intensity of x rays produced by the target and $\gamma$ is a constant. For the detectors used in this work,[7] and a total filtration of 152 $\mu$m of Be, $\gamma$ was estimated to be 3.7. X rays from the target are then imaged by XPHC's and recorded by CID cameras.

In general, the beams are not perfectly circular; therefore, they are fitted to an elliptical super-Gaussian. Combining Eqs. (1) and (2) and introducing an elliptical beam shape yields

$$I_x(r) = I_{\mathrm{UV}}^{\gamma}(0) \times e^{-\gamma\left[(x'/a)^2+(y'/b)^2\right]^{\eta/2}}, \tag{3}$$

where $a$ and $b$ are the lengths of the major and minor axes of the ellipse, respectively. The values $x'$ and $y'$ are the coordinates

lying along the major and minor axes of the ellipse, given by

$$x' = (x - x_c)\cos(\alpha) + (y - y_c)\sin(\alpha),$$
$$y' = -(x - x_c)\sin(\alpha) + (y - y_c)\cos(\alpha), \quad (4)$$

where $x$ and $y$ are the coordinates in the camera image, $\alpha$ is the phase angle of the ellipse, and $x_c$ and $y_c$ are the locations of the center of the beam in image coordinates.

The x-ray fluence measured by the CID cameras is then fit to Eq. (3), yielding values for the beam's peak UV intensity, center position, super-Gaussian power, major and minor axes, and phase angle of the ellipse. Figure 100.31 shows a comparison of this fit to an actual XPHC image recorded by a CID camera. The lineouts in Fig. 100.31(c) show an example comparison between measured and fit beam profiles.

1. Correction for Limb Brightening

As shown schematically in Fig. 100.32, x-ray emission from the Au plasma resulting from absorption of the UV beams is, in general, seen at an angle $\theta$. If the emission comes from an optically thin medium, the increased path through the plasma will increase the observed x-ray fluence. It has been shown[8] that when the plasma is uniform on the surface of the sphere, the intensity seen at an angle $\theta$ to the normal is given by

$$I_x(\theta) = I_x(0)\left(r_{\text{emis}}/\Delta r\right) \times \left[\sqrt{1 + \left(\Delta r/r_{\text{emis}}\right)^2 - \sin^2\theta} - \cos\theta\right], \quad (5)$$

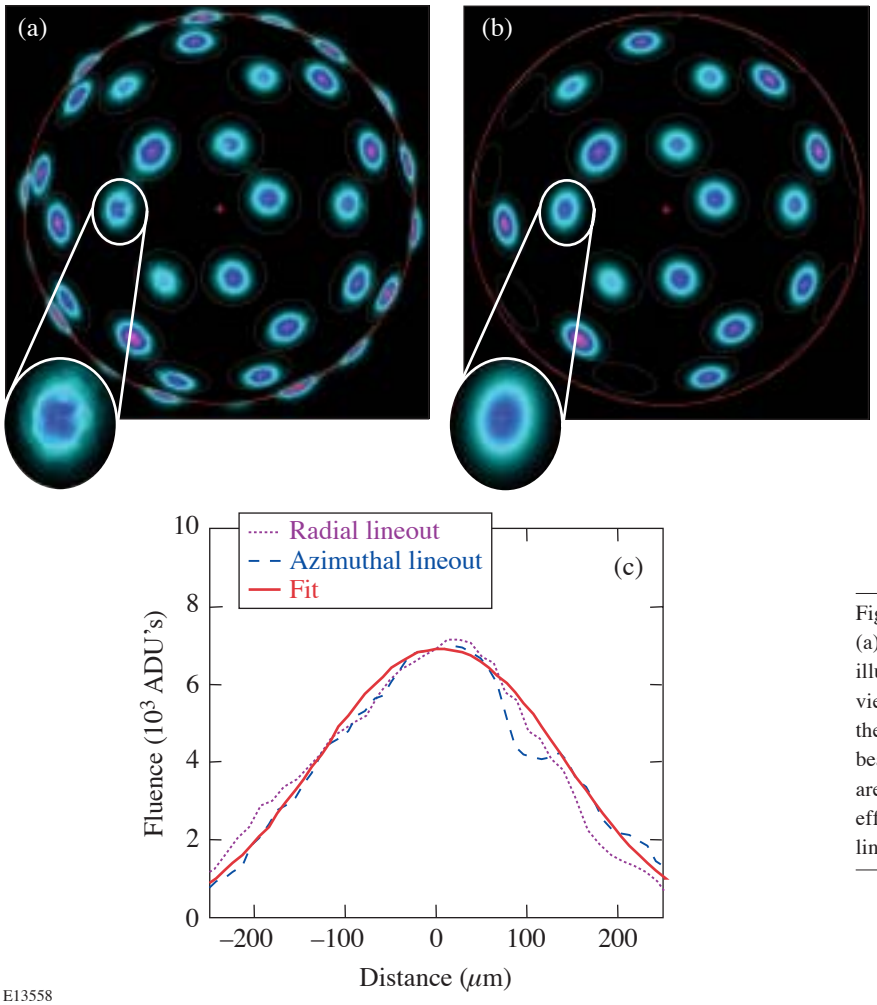


Figure 100.31
(a) CID image of a 4-mm-diam, Au-coated pointing sphere illuminated by all 60 OMEGA beams with an enlarged view of beams 6 to 8. (b) The fit to this image created by the method described herein with an enlarged view of beams 6 to 8. Beams greater than 64° from the view center are not fit since they are greatly distorted by view-angle effects. (c) Radial and azimuthal lineouts compared to a lineout of the fit for beams 6 to 8.

where $r_{emis}$ is the radius of the target and $\Delta r$ is the thickness of the plasma. A typical value of $\Delta r = 113$ $\mu$m was found on a uniformly irradiated, 1-mm-diam, Au-coated sphere with all other conditions the same as on a beam pointing shot (e.g., 1-ns square pulse at ~$10^{14}$ W/cm$^2$). Correction for limb brightening on the pointing target is then accomplished by solving Eq. (5) for the value of $I_x(0)$, the intensity as seen from the normal to the target, using the values $\Delta r = 113$ $\mu$m and $r_0 = 2$ mm. Since this correction is performed continuously for the entire x-ray image, the result is to approximately remove the effect of the curved surface on the measurements of beam fluence and beam position.

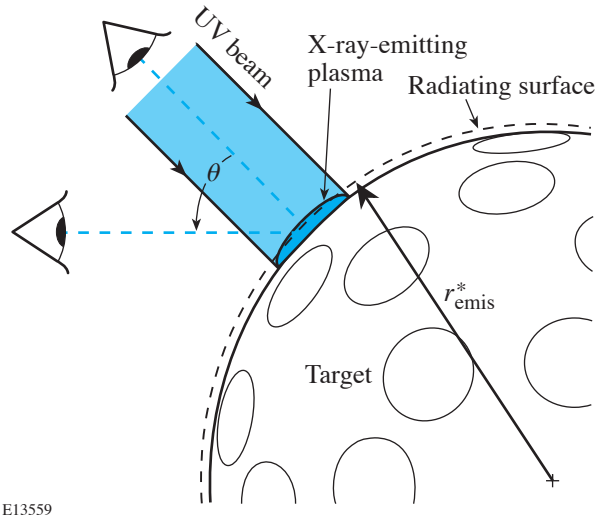


Figure 100.32
An OMEGA beam incident on a 4-mm-diam, Au-coated pointing target. The target will re-emit in the x-ray band with intensity and shape modified by conversion to x rays. However, since the beam is viewed by a camera off axis from the path of the beam, it appears to be distorted and to have a higher peak intensity than if it were viewed on axis, due to the limb-brightening effect. This also causes the apparent position of the beam on the radiating surface to be shifted from its actual position.

## 2. Determination of Beam Parameters

First, the images are fitted to a template of ideal beam positions (orthographic projections of beam-arrival directions), assuming the emission comes from the surface of a sphere [effective emission radius $r^*_{emis}$; see Fig. (100.32)]. The best fit of this template to the observed beam positions then determines $r^*_{emis}$ the target position and the orientation of the image with respect to target chamber coordinates (rotation angle).

After initial determination of the target position, radius, and image rotation angle, corrections for view angle are applied, contributions from surrounding beams are removed, and the beam shape and position are recomputed. Typically this procedure is applied to images from a set of eight XPHC's located at the positions shown in Fig. 100.33. For each image, beams within 64° of the center position are analyzed. Therefore, all beams are viewed by two or more cameras, and error on beam position may be calculated by comparing determinations from multiple views. Application of the procedure described above gives improved results, as evidenced by a reduction of this error.

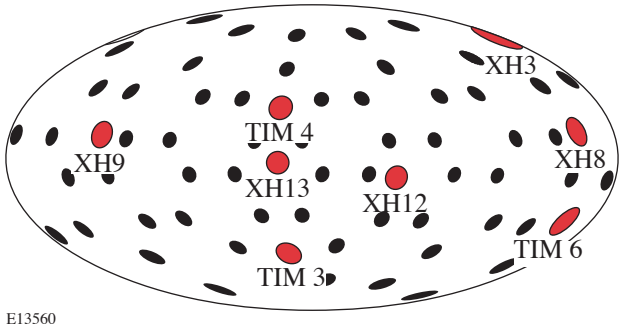


Figure 100.33
Aitoff projection plot of XPHC positions. The black circles represent beam positions. The red circles show the center position of each XPHC view, labeled with the viewport name.

After correction for projection effects, beam parameters may be measured with a high degree of accuracy. For any single SG3 beam on OMEGA, the radius may be determined to within 4%, ellipticity to within 4%, super-Gaussian power to within 4%, and peak fluence to within 4%. For a single SG4 beam, the radius may be determined to within 3%, ellipticity to within 2%, super-Gaussian power to within 6%, and peak fluence to within 4%. Differences between measurement accuracies for SG3 and SG4 beams are due to departures from the ideal beam shape.

This method has been used to determine the beam size, peak fluence variations, and pointing accuracy for the full 60 OMEGA beams when the beams are smoothed by 1-THz smoothing by spectral dispersion (SSD) with polarization smoothing (PS),[9] both with the original DPP's (SG3) and with an expanded, flatter beam shape resulting from a new set of DPP's (SG4).[10] The average beam shapes found from this analysis are $\eta = 2.27\pm0.02$ and $r_0 = 308\pm1$ $\mu$m with ellipticity of $1.072\pm0.005$ for the SG3 beams, and $\eta = 3.66\pm0.03$ and $r_0 = 380\pm1$ $\mu$m with ellipticity of $1.066\pm0.003$ for the SG4 beams. These

correspond to beam diameters of approximately 930 $\mu$m and 865 $\mu$m (diameter containing 95% of the energy) for the SG3 and SG4 DPP's, respectively.

3. Beam Repointing

Beam-position deviations from the desired template are determined from the final fits. The measured beam offsets are used to compute movements of the final turning mirrors, thereby correcting the pointing. Figure 100.34 shows the results of beam offset determinations before and after repointing (second pointing shot). The root-mean-square position error has been reduced from 23 $\mu$m to 11 $\mu$m. This beam-repointing method has been applied many times, and the minimum rms position error achieved is 9 $\mu$m.

## Conclusions

A method has been developed to accurately measure beam position, shape, and relative intensity from CID-recorded x-ray images of 4-mm-diam, Au-coated pointing targets irradiated with focused beams from the OMEGA laser. By taking into account projection effects, conversion from UV to x rays, and detection efficiency, this method is able to determine beam position to within 7 $\mu$m, beam radius to within 3%, ellipticity to within 2%, and relative intensity to within 4%.

Accurate characterization of beams is necessary to optimize the uniformity of target illumination since displacements from ideal beam positions and variations in beam shape and intensity cannot be minimized unless they are first measured. This analysis is currently being used on OMEGA to improve the uniformity of target illumination by improving beam pointing.

## ACKNOWLEDGMENT

This work was supported by the U.S. Department of Energy Office of Inertial Confinement Fusion under Cooperative Agreement No. DE-FC52-92SF19460, the University of Rochester, and the New York State Energy Research and Development Authority. The support of DOE does not constitute an endorsement by DOE of the views expressed in this article.

## REFERENCES

1. J. Nuckolls *et al.*, Nature **239**, 139 (1972).
2. J. J. Duderstadt and G. A. Moses, *Inertial Confinement Fusion* (Wiley, New York, 1982), Chap. 1, pp. 7–8.

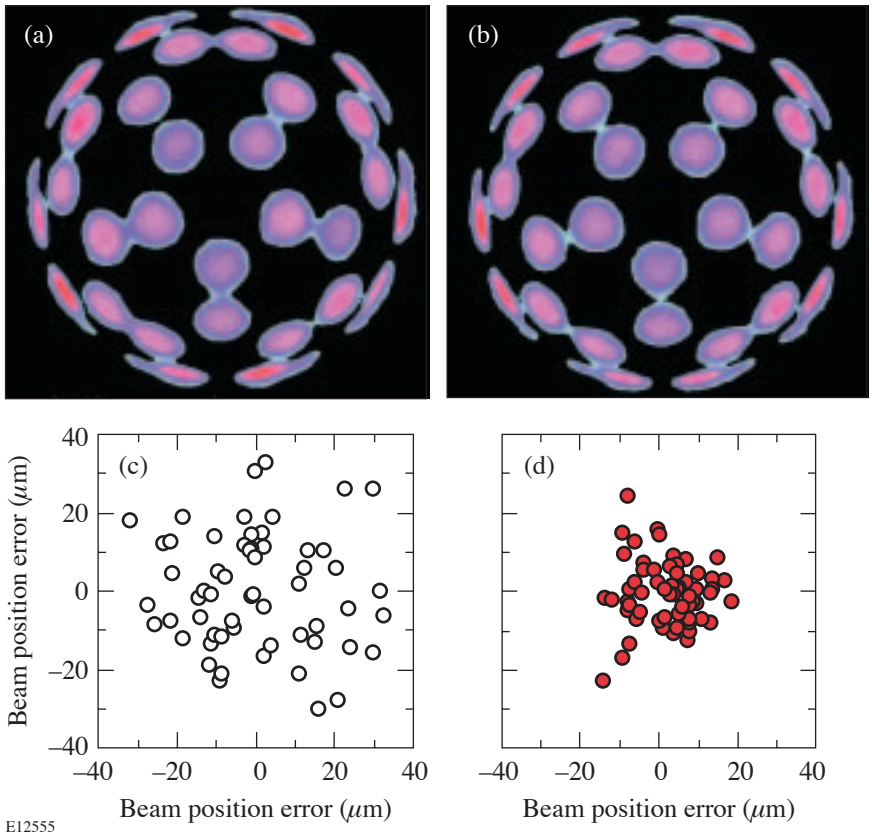


Figure 100.34
Result of repointing the OMEGA beams using the method described in this article. (a) XPHC image from the TIM 6 view showing beams before repointing. (b) XPHC image from the same view showing beams after repointing. Beam positions are visibly improved. (c) A plot of beam offsets from their ideal position before repointing. The root-mean-square offset is 23 $\mu$m. (d) A plot of beam offsets after repointing. The root-mean-square offset is reduced to 11 $\mu$m.

3. Laboratory for Laser Energetics LLE Review **45**, 1, NTIS document No. DOE/DP40200-149 (1990). Copies may be obtained from the National Technical Information Service, Springfield, VA 22161.

4. T. J. Kessler, Y. Lin, L. S. Iwan, W. P. Castle, C. Kellogg, J. Barone, E. Kowaluk, A. W. Schmid, K. L. Marshall, D. J. Smith, A. L. Rigatti, J. Warner, and A. R. Staley, in *Second Annual International Conference on Solid State Lasers for Application to Inertial Confinement Fusion*, edited by M. L. André (SPIE, Bellingham, WA, 1997), Vol. 3047, pp. 272–281.

5. J. M. Soures, R. L. McCrory, C. P. Verdon, A. Babushkin, R. E. Bahr, T. R. Boehly, R. Boni, D. K. Bradley, D. L. Brown, R. S. Craxton, J. A. Delettrez, W. R. Donaldson, R. Epstein, P. A. Jaanimagi, S. D. Jacobs, K. Kearney, R. L. Keck, J. H. Kelly, T. J. Kessler, R. L. Kremens, J. P. Knauer, S. A. Kumpan, S. A. Letzring, D. J. Lonobile, S. J. Loucks, L. D. Lund, F. J. Marshall, P. W. McKenty, D. D. Meyerhofer, S. F. B. Morse, A. Okishev, S. Papernov, G. Pien, W. Seka, R. Short, M. J. Shoup III, M. Skeldon, S. Skupsky, A. W. Schmid, D. J. Smith, S. Swales, M. Wittman, and B. Yaakobi, Phys. Plasmas **3**, 2108 (1996).

6. P. D. Goldstone, J. A. Cobble, A. Hauer, G. Stradling, W. C. Mead, S. R. Goldman, S. Coggeshall, M. C. Richardson, P. A. Jaanimagi, O. Barnouin, R. Marjoribanks, B. Yaakobi, F. J. Marshall, P. Audebert, and J. Knauer, in *X Rays from Laser Plasmas*, edited by M. C. Richardson (SPIE, Bellingham, WA, 1987), Vol. 831, pp. 54–61.

7. F. J. Marshall, T. Ohki, D. McInnis, Z. Ninkov, and J. Carbone, Rev. Sci. Instrum. **72**, 713 (2001).

8. F. J. Marshall, J. A. Delettrez, R. Epstein, R. Forties, R. L. Keck, J. H. Kelly, P. W. McKenty, S. P. Regan, and L. J. Waxer, Phys. Plasmas **11**, 251 (2004).

9. D. D. Meyerhofer, J. A. Delettrez, R. Epstein, V. Yu. Glebov, V. N. Goncharov, R. L. Keck, R. L. McCrory, P. W. McKenty, F. J. Marshall, P. B. Radha, S. P. Regan, S. Roberts, W. Seka, S. Skupsky, V. A. Smalyuk, C. Sorce, C. Stoeckl, J. M. Soures, R. P. J. Town, B. Yaakobi, J. D. Zuegel, J. Frenje, C. K. Li, R. D. Petrasso, D. G. Hicks, F. H. Séguin, K. Fletcher, S. Padalino, M. R. Freeman, N. Izumi, R. Lerche, T. W. Phillips, and T. C. Sangster, Phys. Plasmas **8**, 2251 (2001).

10. F. J. Marshall, J. A. Delettrez, R. Epstein, R. Forties, V. Yu. Glebov, J. H. Kelly, T. J. Kessler, J. P. Knauer, P. W. McKenty, S. P. Regan, V. A. Smalyuk, C. Stoeckl, J. A. Frenje, C. K. Li, R. D. Petrasso, and F. H. Séguin, Bull. Am. Phys. Soc. **48**, 56 (2003).

# Chemical Durability of Phosphate Laser Glasses Polished with Pitch, Pads, or MRF

## Introduction

Large, high-power laser systems are currently under construction; such systems include the National Ignition Facility (NIF) at Lawrence Livermore National Laboratory (LLNL),[1] the LMJ laser at CEA in France, and the OMEGA EP at LLE.[2] These new lasers will require large amounts of neodymium phosphate laser glass, which is known to be sensitive to water.[3] When improperly handled or exposed to too much humidity, phosphate glass surfaces may cloud—a result of increased surface roughness due to chemical reactions. Smooth surfaces are required for such lasers (for example, a 2- to 10-Å-rms roughness level is specified for the NIF[1]); rougher surfaces cause scatter, which can result in intensity modulation in the laser beam, leading to damage to downstream optics and "(increased) fluence on the spatial-filter pinholes."[1] Transmission loss also causes output energy loss, significantly reducing performance. Thus the chemical durability of the laser glass used is of great importance to its fabrication, storage, cleaning, and handling.

Cast Hoya LHG8 phosphate glass, which is made in small individual batches, has been handled and used for over 25 years at LLE in the OMEGA laser system. It was found that a 50/50 glycol and water mixture was required to cool the fine-ground barrels of laser rods without erosion of the LHG8 composition,[3,4] but no other chemical durability problems with the polished faces of cast LHG8 rods and disks were encountered. The new lasers will use phosphate glass manufactured by a continuous melting process[5] developed by LLNL for the NIF laser. In addition to the LHG8 composition used in OMEGA, a new phosphate glass composition, Schott LG770, will be used in the NIF. Changes in manufacturing technique and composition may affect chemical durability.

Previous work at LLNL[6] has shown the continuously melted LG770 to be less resistant to attack by water than the continuously melted LHG8. The quality of the surface finish (between grinding, inspection polishing, and optical finishing) was found to affect dramatically the rate at which the glasses weathered. Both compositions were shown to be sensitive to residual abrasives when they were allowed to dry on the surface after polishing,[6] which is a known effect on surfaces of low-durability glass.[7] The limited use of scrubbing with aqueous detergent solutions was specified for removing protective coating residues from phosphate glass surfaces after storage.[8]

After finishing, three practical issues for preserving the surface quality of phosphate glass are handling, storage, and sensitivity to cleaning. This work focused on determining how resistant each composition was to various levels of humidity; whether or not the manufacturing method (casting versus continuous melting) affected humidity resistance; what effect the surface-finishing process had on resistance to humidity or response to cleaning; the effect of periodic, gentle wiping during storage; and the effect of aggressive aqueous cleaning (of the sort typically used before installing optics into laser systems) on both "good" surfaces and degraded ones.

## Experimental Design

The following subsections summarize our general experimental design. Samples of each glass type were processed using three different finishing techniques: pitch polishing, pad polishing, or magnetorheological finishing (MRF). Samples were stored in chambers at four different controlled humidities at 22°C for 14 weeks. Half of the samples underwent a gentle weekly wiping during storage. A total of 48 samples with 80 prepared surfaces were monitored. The distribution of the samples is given in Fig. 100.35, where sample ID's are listed in bold and sides prepared with different polishing protocols are labeled as S1 and S2. For example, sample 13C denotes a continuously melted LG770 part intended for storage at 38% RH (relative humidity) that has undergone the gentle weekly wiping. Surface S1 of the part had been pitch polished, while surface S2 had been pad polished. Samples used to illustrate trends discussed extensively in this article are highlighted in Fig. 100.35 in gray. Surface microroughness analyses and power spectral density analyses were performed, and the visual appearance of each sample was monitored. After 14 weeks, samples stored in high humidity underwent a thorough visual and microscopic inspection before undergoing two aqueous

cleanings by technicians in the optics manufacturing facility at LLE. Some of these high-humidity samples were cleaned with water alone, and some with water and detergent. After each cleaning, these samples were measured and inspected again.

1. Sample Preparation

Testing was performed on identically processed, handled, and stored samples of cast LHG8 (designated C-LHG8), continuously melted LHG8 (designated CM-LHG8), and continuously melted LG770 (designated CM-LG770). Samples were nominally 25 mm × 25 mm × 5 mm. The samples of C-LHG8 came from in-house stock, and the samples of CM-LHG8 and CM-LG770 came from LLNL. Samples of C-LHG8 and CM-LHG8 underwent pitch polishing, rotational magneto-rheological finishing (MRF), and raster MRF. MRF is a finishing method that involves polishing a surface by moving it through a ribbon of a magnetic fluid that contains abrasives.[9] Samples of CM-LG770 underwent pitch polishing, pad polishing, rotational MRF, and raster MRF. Pitch polishing was done in-house on a 36-in. continuous polishing (CP) machine, with Gugolz #82 pitch, using an aqueous slurry containing Cerox 1663 cerium oxide. Samples were cleaned with acetone after pitch polishing. Pad polishing (on CM-LG770 only) was done by an outside vendor in a double-sided process using cerium oxide and pads. These parts were used "as-received." MRF using both rotational and raster modes of processing was done in-house on a QED Technologies Q22-Y machine using an experimental $ZrO_2$-based MR fluid.[10] For rotational MRF, samples were polished by rotating the surfaces of the spindle-mounted parts as they were moved through the magnetic ribbon. For raster MRF, the parts were translated without rotation through the ribbon in a raster fashion. MRF was performed on previously pitch- or pad-polished surfaces, with at least 0.2 $\mu$m of material uniformly removed. After MRF, samples were wiped with water, followed by acetone.

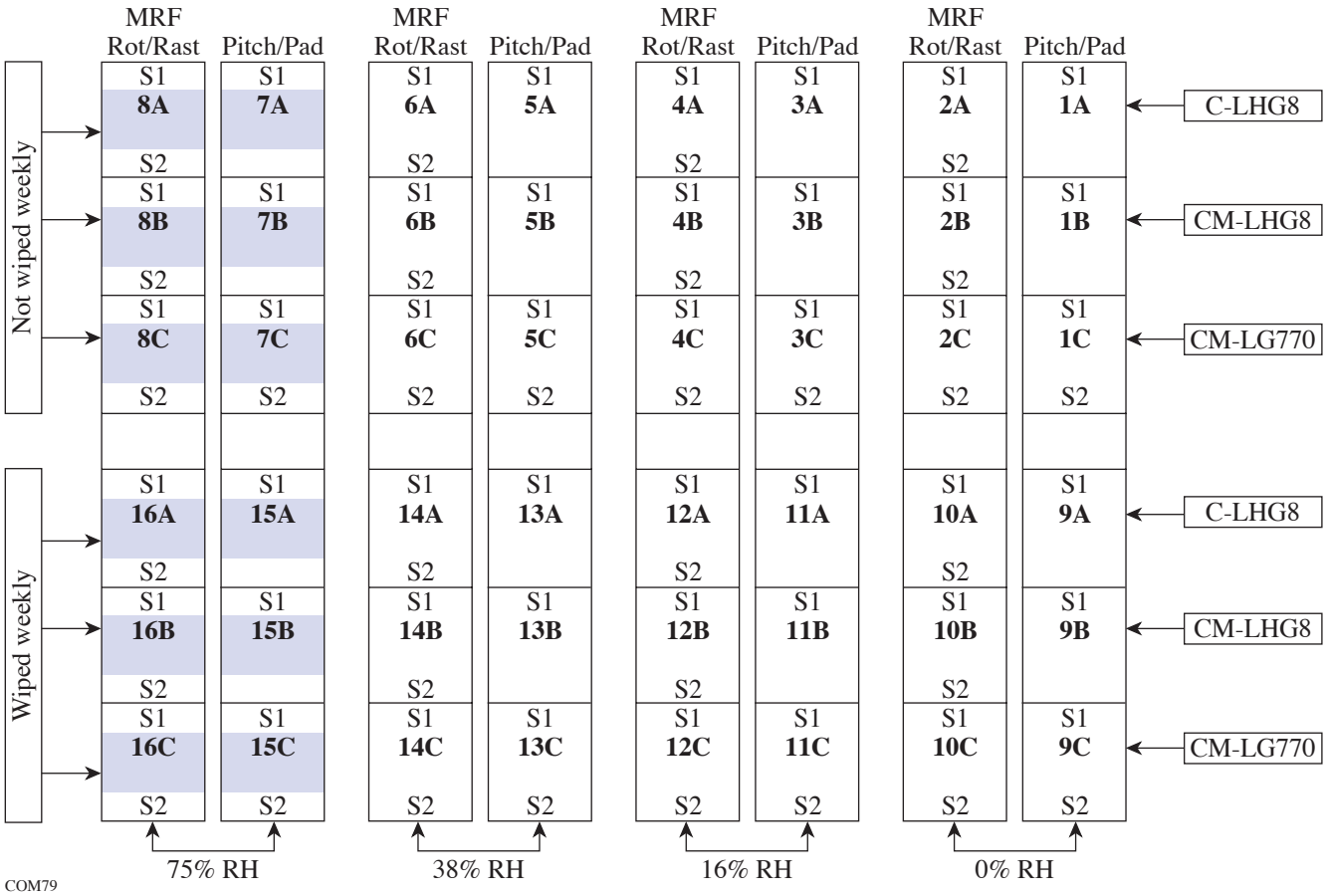


Figure 100.35
Distribution of 48 phosphate glass samples for chemical durability tests (see text).

2. Sample Handling and Storage

Four chambers were set up for the humidity testing. Each chamber maintained a static noncirculating air environment and was kept sealed except during removal and replacement of samples. Temperature in the chambers remained between 21°C and 22°C. Humidities of 0%, 16%, 38%, and 75% (±1%) RH were maintained in the chambers using desiccant (0% RH) and saturated aqueous solutions of LiCl, NaI, and NaCl, respectively. Temperature and humidity were monitored daily using hygrometer/thermometer pens,[11] which remained in the sealed chambers.

Samples were mounted upright in these humidity chambers in foam holders with the prepared surfaces exposed. They remained in the chambers for 14 weeks and were removed only for cleaning, measurement, and inspection. Samples were transported to and from the metrology lab in closed plastic boxes and were handled with nitrile gloves. During cleaning, measurement, and inspection, samples were exposed briefly to lab humidity conditions of between 20% and 60% RH, with an average of 32% RH, and temperatures between 21°C and 22°C.

3. Sample Cleaning

A gentle drag–wipe method with HPLC-grade methanol and lens tissue (Lens SX90 tissue from Berkshire) was chosen as an initial "cleaning" protocol for all surfaces. Although not a rigorous "cleaning" process, wiping was selected as being most likely to preserve the quality of initial surfaces for the ensuing humidity tests. Sample wiping consisted of a pair of orthogonally oriented drag wipes per side. Half of the samples underwent this procedure only once before being placed in the humidity chambers; these samples were designated "not weekly wiped" (NWW). The other half of the samples were wiped in this way prior to being placed in the humidity chambers and then wiped again every week for 13 weeks; these samples were designated "weekly wiped" (WW).

A true aqueous cleaning method involving gentle hand scrubbing was chosen as a more aggressive protocol, which was performed at the conclusion of testing, but only on the samples that had been stored in 75% RH. This protocol was chosen after reviewing existing procedures for cleaning laser glass surfaces.[8] After 14 weeks of storage, half of the samples from the 75%-RH chamber were cleaned with 18-Mohm deionized (DI) water alone, and half were cleaned with DI water and detergent (Micro-90 Microsoap). Each sample was held under running DI water while being scrubbed with synthetic nylon wipes (Miracle Wipes). Detergent was added to the surfaces of some of the samples during this process. After scrubbing, samples were rinsed in a DI water spray for 2 min and then set upright in a laminar flow hood[12] to dry. After evaluation, the samples were stored in 0% RH. After 5 additional weeks, the aqueous cleaning procedure was repeated. These cleaning methods are typical of what would be used on optics going into laser systems.

4. Surface-Evaluation Protocols

Although scatter is the main concern for laser systems, no simple, direct way to measure it on these samples was found in this facility. Four easily performed methods for surface evaluation were chosen: measurement of areal microroughness with and without electronic filtering, power spectral density (PSD) analysis, visual inspection, and microscopic inspection.

Areal microroughness measurements were made using a Zygo NewView 100 white-light interferometer, with a 5× Michelson objective.[13] Areal peak-to-valley (p–v) and root-mean-square (rms) values were obtained over areas of 1.41 mm × 1.05 mm. Measurements were made weekly on samples in the 38%- and 75%-RH chambers, and bi-weekly on samples in the 16%- and 0%-RH chambers for the first 10 weeks. Additional measurements were made on samples in the 75%-RH chamber at 13 weeks and after each aqueous cleaning with and without detergent. An average of measurements from five random sites in characteristic areas of the samples was recorded. Uncharacteristic areas, the center, and the edges of the substrates were avoided. Filtering was used on selected data to observe features in specific spatial-frequency ranges suggested by PSD analysis.

PSD analysis provided more-detailed information about what kinds of structures were contributing to the surface roughness. PSD data were gathered for selected surfaces from the New View 100[13] and plotted using in-house MATLAB codes[14] as power density ($nm^3$) as a function of spatial frequency (1/nm). With the 5× Michelson objective, information was obtained for structures contributing to roughness at spatial frequencies between ~$1 \times 10^{-4}$ 1/nm and ~$4 \times 10^{-7}$ 1/nm (corresponding to periodicities between ~10 $\mu$m and ~2.5 mm). Plotted data were compared to a typical specification for NIF laser disks.[15] Various types of visual inspection were employed. General observations were routinely made with the naked eye in fluorescent room light. Inspections with a fiber-optic light source in a dark room were made after 4 and 11 weeks of storage. At 14 weeks, surfaces were inspected, mapped, and described in writing before and after the first aqueous cleaning with and without detergent. Digital photos of the samples were taken in a darkened room with a flash before

and after the first (14 weeks) and second (19 weeks) aqueous cleanings. Microscopic inspection was carried out using a Nikon research-grade, white-light optical microscope before and after the first aqueous cleaning. Surfaces were observed in reflection using both bright-field and dark-field modes with 5×, 10×, 20×, and 50× objectives.

**Results of Humidity Study**

Very little change was seen on the majority of the surfaces monitored. After 10 weeks of storage, *no degradation* was seen on any of the samples stored at 38% RH, 16% RH, or 0% RH. The experiment was ended for these samples. Within the 75%-RH chamber, *no degradation was seen on any of the samples that underwent the gentle weekly wiping protocol, and no degradation was seen on any of the samples of CM-LHG8 with or without wiping* throughout the 14 weeks they were stored at elevated humidity. The samples of NWW C-LHG8 in the 75%-RH chamber (samples 7A and 8A; refer to Fig. 100.35) showed minor visible degradation, accompanied by increased rms microroughness and elevated levels of PSD, which was worse on the pitch-polished surface (surface S1 of 7A) than on the MRF-polished ones (surfaces S1 of 8A and S2 of 8A). Both of the samples of NWW CM-LG770 (samples 7C and 8C) in the 75%-RH chamber showed severe degradation, confirming the high degree of humidity sensitivity for this composition.

Degradation on samples of NWW CM-LG770 (samples 7C and 8C) first appeared in the form of large structures at low spatial frequencies, increased rms microroughness, and elevated PSD levels. By 13 weeks of storage, structures had developed at higher spatial frequencies, resulting in increased rms and p–v microroughness and elevated PSD levels at high spatial frequencies. The surfaces had also developed a grainy, highly scattering appearance. Although the quality of the initial surface finish did not affect the rate of degradation in samples of NWW CM-LG770 at 75% RH, the various surface-finishing processes appeared to influence how the degradation formed, with different types of structures appearing on surfaces that had been polished differently.

The following four subsections concentrate exclusively on the results observed for selected samples of all glass compositions *stored at 75% RH* and *not wiped weekly*.

1. Changes in Areal Microroughness

The *initial* rms surface areal microroughness of the phosphate glass samples varied from 0.6 nm to 2.2 nm as a result of the different surface-finishing protocols. In general, for all samples, the pad-polished surfaces were roughest, the pitch-polished surfaces were smoothest, and the MRF-processed surfaces fell somewhere in between. This did not depend on glass type. Variations in microroughness were not indicative of polishing process efficiency but were simply the result of polishing conditions available at the time. An example showing *good* environmental stability is given in Fig. 100.36 [(a) rms, (b) p–v] for NWW CM-LHG8 (samples 7B and 8B) stored at 75% RH. All initial surface microroughness values were below 1-nm rms, though differences in rms surface microroughness were seen between surfaces polished with either pitch (surface S1 of 7B) or MRF (surfaces S1 of 8B and S2 of 8B), with the pitch-polished surfaces being the smoothest. Peak-to-valley values generally overlapped and fell in a range between 10 nm and 30 nm. Microroughness levels remained unchanged after 13 weeks of storage.

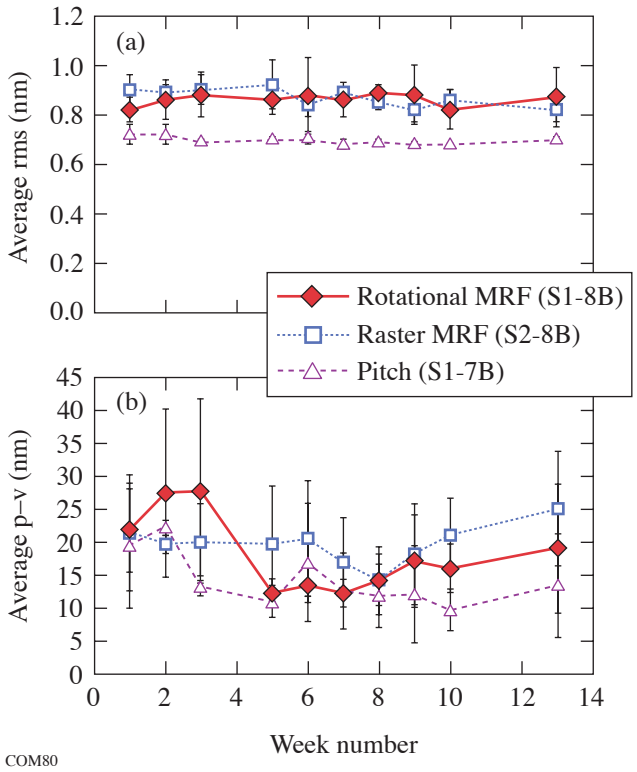


Figure 100.36
Areal microroughness of NWW CM-LHG8 (samples 7B and 8B) surfaces over 13 weeks of storage in 75% RH (lines to guide the eye). (a) Areal rms; (b) areal p–v.

An example showing *moderate* environmental stability is given in Fig. 100.37. No significant changes in either rms or p–v roughness were observed on samples of NWW C-LHG8 (samples 7A and 8A) throughout the first 8 weeks of storage at

75% RH. These samples showed increasing rms and p–v microroughness beginning at week 9 and week 10, respectively. Increases in microroughness continued through 13 weeks of storage [see Figs. 100.37(a) and 100.37(b)]. The increases were much more dramatic for the pitch-polished surface of sample 7A (rms: 3.9 nm±2.5 nm; p–v: 450 nm± 370 nm) than for the two MRF-polished surfaces of sample 8A.

An example of *significant* environmental *instability* is given in Fig. 100.38. Both the rms and p–v roughness values of the two samples of NWW CM-LG770 (samples 7C and 8C) remained stable throughout the first 4 weeks of storage. Measurable increases in rms microroughness on all four surfaces of these samples were detected after 5 to 7 weeks of storage [see Fig. 100.38(a)]. The rms roughness continued to increase on all four surfaces of both samples of NWW CM-LG770 through 10 weeks. These increases in rms roughness were *not* accompanied by increases in p–v roughness [see Fig. 100.38(b)]. By week 13, however, both rms and p–v roughness values had increased dramatically (rms: 8 nm to 24 nm; p–v: 480 nm to 1090 nm). The standard deviations on the week-13 measurements were very large (rms: ± >4.3 nm; p–v: ± >200 nm). There was no direct correlation between the initial surface rms roughness level and rate of degradation. In fact, the pad-polished surface (surface 7C of S2), which was initially the roughest, showed the *smallest* increase in rms roughness values after 13 weeks. The raster MRF-processed surface (surface 8C of S2) showed the greatest increase in rms roughness. The magnitudes of all of the changes on the NWW CM-LG770 surfaces were much greater than those detected on surfaces of any of the LHG8 samples.

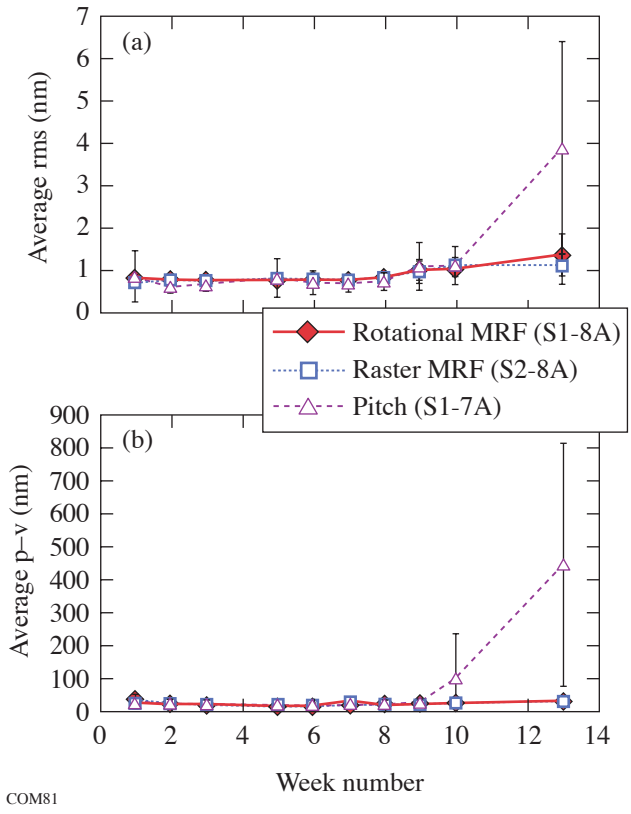


Figure 100.37
Areal microroughness of NWW C-LHG8 (samples 7A and 8A) surfaces over 13 weeks of storage in 75% RH (lines to guide the eye). (a) Areal rms; (b) areal p–v.

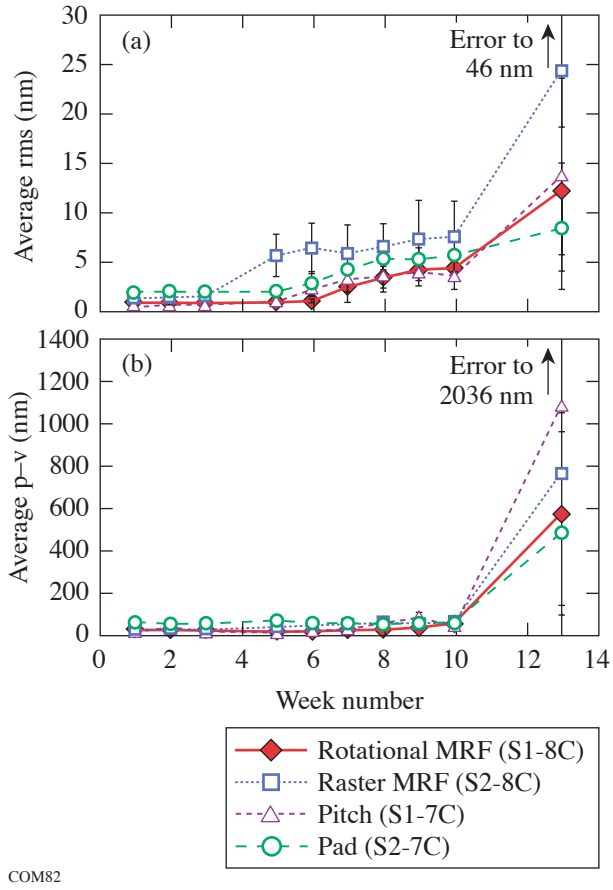


Figure 100.38
Areal microroughness of NWW CM-LG770 surfaces (samples 7C and 8C) over 13 weeks of storage in 75% RH. (a) Areal rms; (b) areal p–v.

2. Analyses of Power Spectral Density

As expected, since the area under a power spectral density (PSD) curve is proportional to the square of the rms,[16] *initial* surface-rms-roughness differences were also reflected in PSD data. Figure 100.39 gives PSD plots for initial surfaces of NWW CM-LHG8 and NWW CM-LG770 (surfaces S1 of 7B, S2 of 7C, S1 of 8B, and S2 of 8B). The pad-polished surface of 7C had the highest power-density levels (pad-polished surfaces were the only surfaces with power-density levels above the NIF specification for laser disks[15]), while the pitch-polished surface of 7B had the lowest. The power-density levels of the two MRF-polished surfaces of 8B were comparable to the pitch-polished surface at high spatial frequencies and rose to levels between the pitch-polished and pad-polished surfaces at low spatial frequencies.

Figure 100.40 shows selected PSD plots for the pitch-polished surface S1 of sample 7A of NWW C-LHG8 stored in the 75%-RH chamber, which was initially well polished and below the NIF reference level. The plot shows that power density increased by two orders of magnitude over all spatial frequencies after 13 weeks of storage. The other two surfaces of NWW C-LHG8 (the rotationally MRF-processed surface S1 of 8A and the raster MRF–processed surface S2 of 8A) showed small increases in power density over 13 weeks. Figure 100.41 shows results for the rotationally MRF-processed surface only. Increases by less than 10× were observed at spatial frequencies between $10^{-4}$ 1/nm and $10^{-5}$ 1/nm (periodicities between 10 $\mu$m and 100 $\mu$m), with no changes observed at lower spatial frequencies (longer periods). (Note: PSD data in Figs. 100.40–100.42 after aggressive aqueous cleaning are discussed in the **Aqueous Cleaning Results…** section, p. 265.)

All four surfaces of the two samples of NWW CM-LG770 (7C and 8C) showed significant increases in levels of power density between 5 weeks and 7 weeks. Figure 100.42 shows selected PSD plots for the rotationally MRF-processed surface S1 of 8C. At week 10 (not shown), power density at low spatial

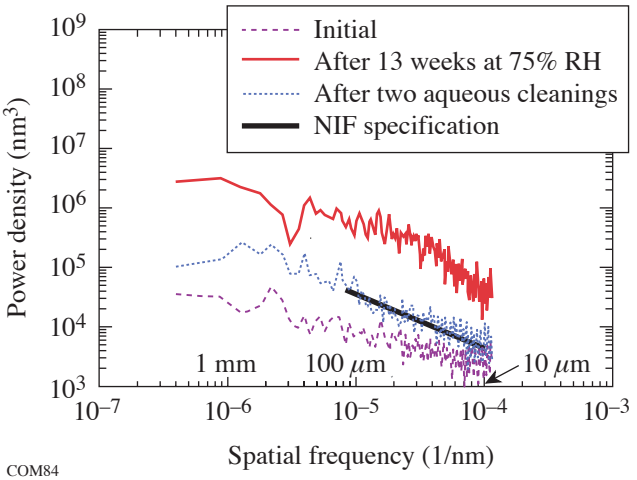


Figure 100.40
Selected PSD data for a pitch-polished surface of NWW C-LHG8 (S1 of 7A) stored in 75% RH for 13 weeks.

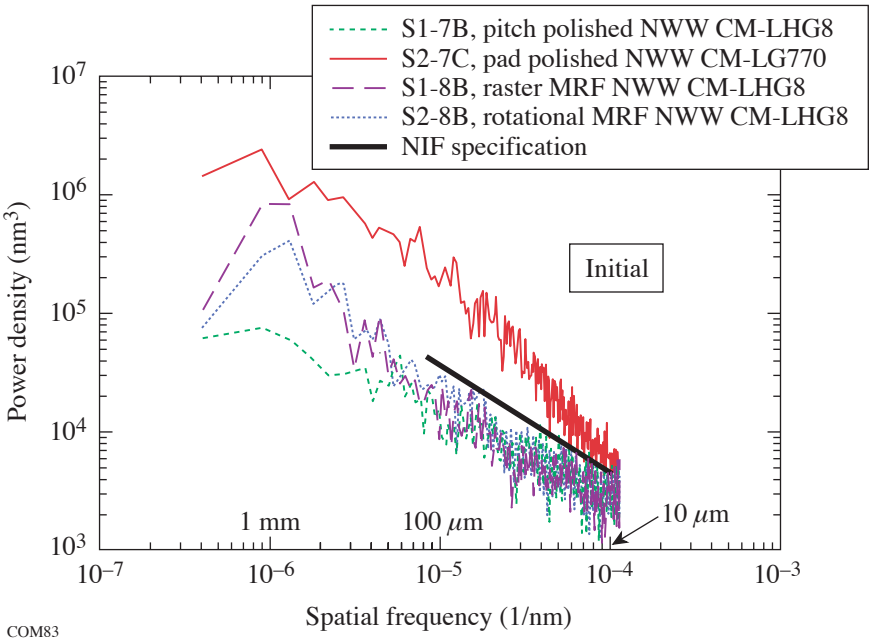


Figure 100.39
PSD plot of different initial surface finishes of NWW CM-LHG8 and NWW CM-LG770 before storage in 75% RH.

frequencies ($2 \times 10^{-6}$ 1/nm to $4 \times 10^{-7}$ 1/nm) had increased by ~15×, while at higher spatial frequencies the departure from the initial condition was less. By week 13, power-density levels at middle-to-high spatial frequencies had also increased significantly, with a "bump" in the data around a spatial frequency of $5 \times 10^{-5}$ 1/nm (corresponding to a periodicity of 20 $\mu$m; see Fig. 100.42).

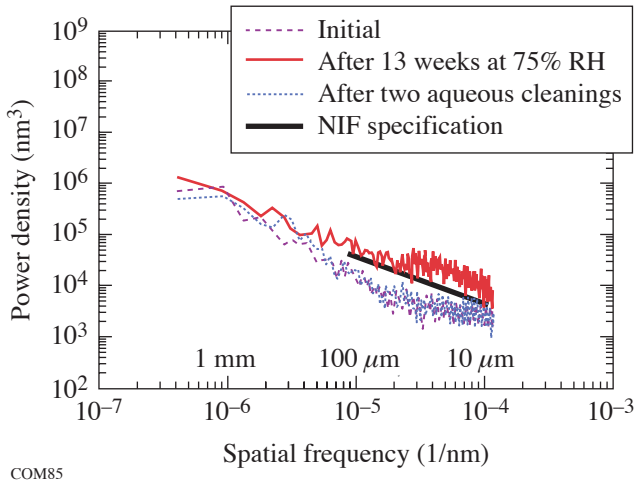


Figure 100.41
Selected PSD data for a rotationally MRF-processed surface of NWW C-LHG8 (S1 of 8A) stored in 75% RH for 13 weeks.

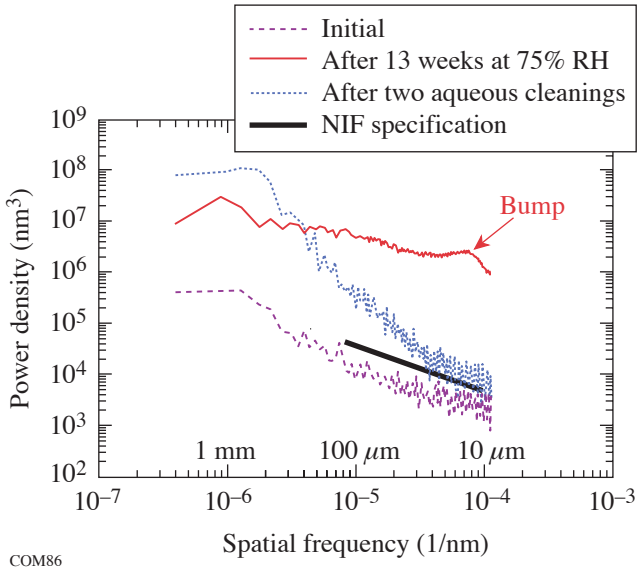


Figure 100.42
Selected PSD data for a rotationally MRF-processed surface of NWW CM-LG770 (S1 of 8C) stored in 75% RH for 13 weeks.

Rising PSD levels on S1 of 8C (see Fig. 100.42) corresponded to surface features observed with white-light interferometry. Increased power density at lower spatial frequencies correlated with large surface features that are best described as "mottling." Figure 100.43 shows this mottling as viewed with the NewView 100 using a low-pass filter (333 $\mu$m). By week 13, small structures varying in size from 4 $\mu$m to 50 $\mu$m in diameter, as measured by optical microscopy, had also developed on the surface. The size of the larger of these structures (>10 $\mu$m) corresponds to the "bump" in the PSD plot for week 13. Structures with sizes in the middle spatial frequencies ($1 \times 10^{-5}$ 1/nm to $4 \times 10^{-6}$ 1/nm) also appeared by week 13. Figure 100.44 shows these structures viewed on the white-light interferometer using a bandpass

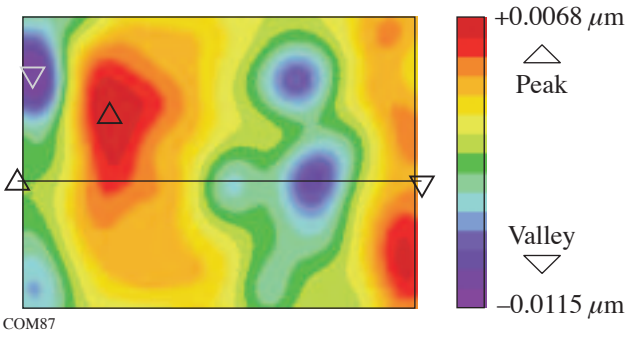


Figure 100.43
NewView 100 grayscale image of structures at low spatial frequencies on rotationally MRF-processed NWW CM-LG770 (S1 of 8C), stored in 75% RH for 13 weeks, viewed with a 333-$\mu$m, low-pass filter. 1.41-mm × 1.05-mm areal view. p–v: 18.4 nm; rms: 3.44 nm.

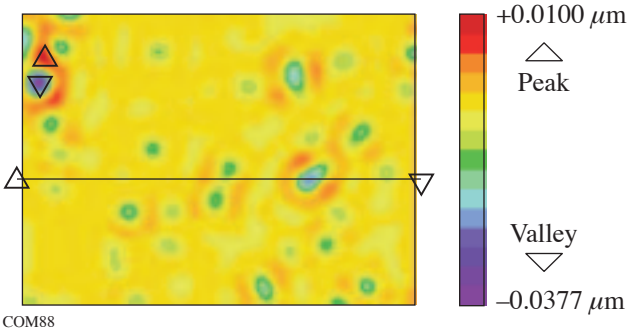


Figure 100.44
NewView 100 grayscale image of structures at middle-range spatial frequencies on rotationally MRF-processed NWW CM-LG770 (S1 of 8C), stored in 75% RH for 13 weeks, viewed with a 100- to 250-$\mu$m bandpass filter. 1.41-mm × 1.05-mm areal view. p–v: 55.6 nm; rms: 3.51 nm.

filter (100 μm to 250 μm). The increased power-density levels at middle-range spatial frequencies for week 13 (see Fig. 100.42) show that they make a significant contribution to increased rms roughness.

3. Visual Inspection

Visual inspection at 11 weeks and beyond agreed in general with more quantitative optical measurements. The presence of films, haziness, and graininess could be correlated to samples that had shown increases in microroughness and PSD levels. In some cases, visual inspection revealed differences among parts that were not measurable with metrology instrumentation, presumably because the human eye is more sensitive to scatter than the metrology instruments we used. Surfaces of some of the MRF-processed parts looked better than those of the pitch-polished and pad-polished ones, and surfaces on the samples of CM-LHG8 looked better than surfaces on the samples of C-LHG8. At the conclusion of 14 weeks of exposure, there was considerable particulate contamination and a "busy" appearance on many surfaces.

4. Microscopic Inspection

Microscopic inspection after 14 weeks of storage was useful for evaluating significantly degraded surfaces prior to aggressive cleaning and for observing structures with high spatial frequencies that developed on the surfaces. These structures varied in both size (4 μm to 50 μm in diameter) and appearance from surface to surface. We attribute these variations to the different initial finishing processes used and any residual contaminants unique to each finishing process that may have been left on each surface. The pitch-polished surface of NWW C-LHG8 (S1 of 7A) was covered in ran-domly distributed, nominally round features that were 8 μm to 12 μm in diameter, as seen in bright field mode using a 20× objective. These features are shown in Fig. 100.45(a). The pitch-polished surface of NWW CM-LG770 (S1 of 7C) was also covered in nominally round features that were smaller (about 4 μm in diameter) than those on the NWW C-LHG8 surface. The pad-polished surface of NWW CM-LG770 (S2 of 7C) showed oblong and elevated features that were ~4 μm wide and 8 μm to 16 μm long. The MRF-processed surfaces of NWW CM-LG770 (S1 of 8C and S2 of 8C) had asymmetrical, elevated features between 10 μm and 40 μm in diameter that resembled snowflakes. On the rotationally MRF-processed surface (S1 of 8C), these features were isolated from other defects, as shown in Fig. 100.46. On the raster-polished surface (S2 of 8C), the snowflake-like features appeared to surround some of the numerous dark, round artifacts that covered the surface (see Fig. 100.47). This finding suggests that the dark, round artifacts are defects (possibly residual contaminant from the polishing process) that act as initiation sites for degradation, as reported in previous work.[1]

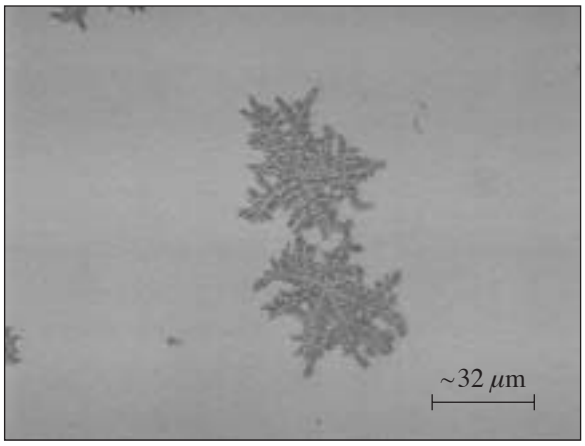


COM90

Figure 100.46
Optical microscope image of rotationally MRF-processed NWW CM-LG770 (S1 of 8C) after 14 weeks of storage at 75% RH, before cleaning, viewed in bright field at 50×.

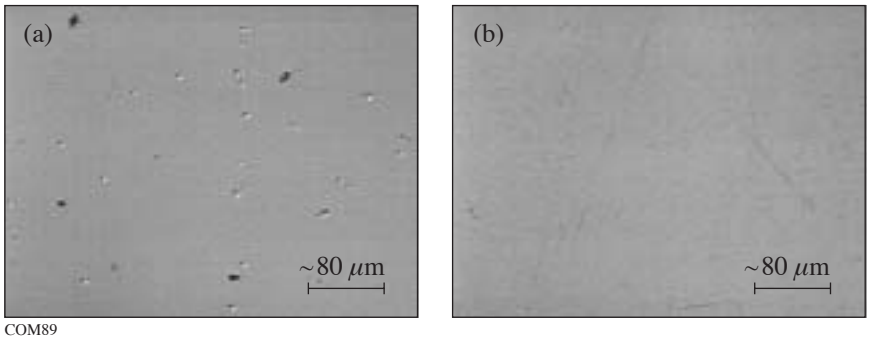


COM89

Figure 100.45
Optical microscope images of pitch-polished NWW C-LHG8 (S1 of 7A) at 14 weeks, before (a) and after (b) aqueous cleaning, viewed in bright field at 20×.

**Aqueous Cleaning Results for All Samples Stored at 75% RH**

More-aggressive cleaning protocols were employed at the conclusion of the 14-week humidity test to determine how readily degraded surfaces could be restored, to evaluate the permanence of degradation observed, and to evaluate the effects of aqueous cleaning on "good" surfaces. Because no differences were observed between the results for samples cleaned with DI water alone and those cleaned with DI water and detergent, in the following discussion we do not differentiate between the two aqueous cleaning protocols.

Initial aqueous cleaning visibly improved the appearance of all WW and NWW surfaces by removing films and particulates. All of the 4-$\mu$m to 50-$\mu$m structures observed microscopically [see Figs. 100.45(a), 100.46, and 100.47) were removed by a single cleaning. For NWW surfaces that exhibited degradation, this single cleaning removed surface structures that developed at high spatial frequencies, and it reduced the number density of surface structures that developed at middle-range spatial frequencies. It did not remove any of the low-spatial-frequency structures that developed on some surfaces.

A second aqueous cleaning did not further improve, and in some cases damaged, the surfaces. Both first and second cleanings generated hazing (that was visible to the naked eye) due to scratching (that was visible microscopically) on pitch-polished and pad-polished surfaces of NWW and WW samples of all glass types [as shown for surface S1 of 7A in Fig. 100.45(b)]. The microscopic scratches are believed to be caused by subsurface damage from finishing and not by cleaning. During cleaning, these scratches become enlarged (along with other defects) by water-induced corrosion of the glass surface.[7,17] Considerably less hazing and scratching were observed on the MRF-processed surfaces. We attribute this improved quality to the ability of MRF to both polish without creating subsurface damage and to remove subsurface damage from previous processing.[18] These obvious visible changes were only modestly supported by measured changes in areal rms roughness and power-density levels, as discussed below.

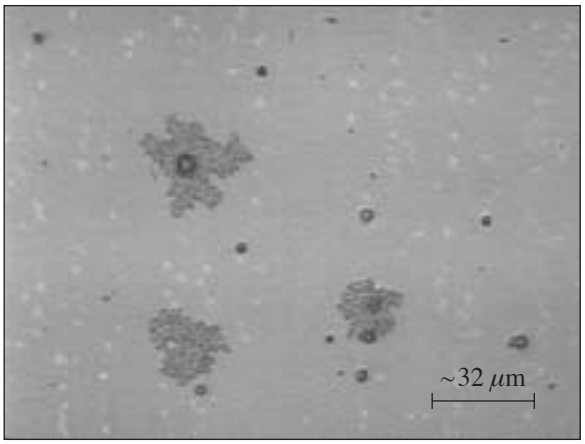


COM91

Figure 100.47
Optical microscope image of raster MRF-processed NWW-LG770 (S2 of 8C) after 14 weeks of storage at 75% RH, before cleaning, viewed in bright field at 50×.

Areal *p–v microroughness* was reduced to below initial levels on *WW surfaces of all glass types* after one aqueous cleaning. This finding indicates that the drag–wiping protocols performed on the samples before the experiment began were insufficient to rid the surfaces of debris remaining from the various finishing processes. One application of the more-aggressive aqueous cleaning process was sufficient to remove most of this debris. After a second aqueous cleaning, areal p–v values remained unchanged. *NWW surfaces of C-LHG8 and CM-LHG8* behaved similarly, exhibiting areal p–v levels reduced to below initial values after one aqueous cleaning, and these remained unchanged after a second aqueous cleaning. Cleaning was not as effective *on NWW surfaces of CM-LG770*. After one aqueous cleaning, these surfaces exhibited p–v values below those at 13 weeks, but still higher than initial. After a second aqueous cleaning, areal p–v generally increased on these surfaces.

Changes in *rms microroughness* for all *NWW* parts stored at 75% RH are given in Table 100.I. After the first aqueous cleaning, surfaces of CM-LHG8 were unchanged from what they were at the beginning of the experiment. Most surfaces of C-LHG8 and CM-LG770 samples showed significant improvement from their degraded (week 13) states. Areal roughness was reduced by 18% to 74%. All CM-LG770 surfaces were still much rougher than they had been at the beginning of the experiment. A second cleaning did not further reduce roughness. For seven out of ten surfaces, rms-roughness levels increased.

Changes in the rms-microroughness values on NWW samples after aqueous cleaning were reflected in the PSD data. On the pitch-polished sample of NWW C-LHG8 (S1 of 7A), two aqueous cleanings uniformly lowered power density over all spatial frequencies; however, they did not return the surface to its initial condition, as can be seen in Fig. 100.40. After two aqueous cleanings, areal rms roughness and PSD levels were

returned to their initial conditions for the MRF-processed surfaces of NWW C-LHG8 (S1 of 8A and S2 of 8A) (shown in Fig. 100.41).

On samples of NWW CM-LG770, different spatial-frequency regions were affected differently by aqueous cleaning. PSD data for the rotationally MRF-processed surfaces of NWW CM-LG770 (S1 of 8C) are shown in Fig. 100.42. Structures at high- and middle-range spatial frequencies were significantly reduced. Aqueous cleaning did not reduce structures at low spatial frequencies. Power density actually *increased* at spatial frequencies between $3 \times 10^{-6}$ 1/nm and $4 \times 10^{-7}$ 1/nm, which explains why rms-microroughness values remained high.

Changes in *rms microroughness* for all *WW* parts stored at 75% RH are given in Table 100.II. After the first aqueous cleaning, 6 of 10 surfaces were brought to a level equal to or better than that measured at the beginning of the experiment. *All* six of these surfaces had been processed with MRF. Most of the MRF-processed surfaces continued to improve after a second cleaning. Results were mixed for the surfaces that had been pitch polished or pad polished.

**Summary/Conclusions**

No samples of LHG8 (cast/continuously melted) or LG770 (continuously melted) exhibited any change after 10 weeks of exposure at 21°C to humidity at 38% RH or less. Changes *were* seen on *some* of the samples stored in 75% RH at 21°C, and several conclusions can be made regarding the sensitivity to humidity and cleaning of well-polished (with rms microroughness below 2 nm) LHG8 and LG770 surfaces exposed to these conditions.

Among glass types:

1. Continuously melted LHG8 is more resistant to humidity-induced degradation than cast LHG8. Continuously melted LHG8 surfaces exhibit no degradation after 14 weeks of exposure, while cast LHG8 surfaces exhibit little to moderate degradation.
2. Continuously melted LG770 surfaces exhibit severe degradation after 14 weeks of exposure, indicating that continuously melted LG770 is much more sensitive to humidity than either type of LHG8.

Table 100.I: Areal rms microroughness of NWW samples after aqueous cleaning. Percent changes in roughness after each cleaning are noted.

| NWW rms (nm) | | Initial (week 0) | Final (week 13) | After First Cleaning (week 14) | After Second Cleaning (week 19) |
|---|---|---|---|---|---|
| C-LHG8 | S1 of 7A (pitch) | 0.63±0.15 | 3.89±2.50 | 1.02±0.12 (–74%) | 1.75±0.94 (+72%) |
| | S1 of 8A (rot MRF) | 0.79±0.07 | 1.38±0.50 | 1.10±0.19 (–20%) | 0.89±0.07 (–19%) |
| | S2 of 8A (rast MRF) | 0.78±0.05 | 1.13±0.41 | 0.93±0.10 (–18%) | 0.98±0.16 (+5%) |
| CM-LHG8 | S1 of 7B (pitch) | 0.72±0.04 | 0.70±0.01 | 0.70±0.01 (+0%) | 0.78±0.01 (+11%) |
| | S1 of 8B (rot MRF) | 0.86±0.08 | 0.87±0.12 | 0.84±0.16 (–3%) | 0.80±0.08 (–5%) |
| | S2 of 8B (rast MRF) | 0.89±0.03 | 0.82±0.05 | 0.80±0.02 (–2%) | 0.92±0.14 (+15%) |
| CM-LG770 | S1 of 7C (pitch) | 0.70±0.01 | 13.84±9.72 | 5.93±1.16 (–58%) | 7.59±3.08 (+28%) |
| | S2 of 7C (pad) | 2.05±0.34 | 8.41±4.31 | 9.61±3.06 (+14%) | 12.51±5.97 (+30%) |
| | S1 of 8C (rot MRF) | 0.91±0.08 | 12.21±6.43 | 9.87±3.24 (–19%) | 16.68±13.21 (+69%) |
| | S2 of 8C (rast MRF) | 1.46±0.11 | 24.26±21.95 | 13.51±5.00 (–44%) | 10.01±2.30 (–26%) |

Table 100.II: Areal rms microroughness of WW samples after aqueous cleaning. Percent changes in roughness after each cleaning are noted.

| WW rms (nm) | | Initial (week 0) | Final (week 13) | After First Cleaning (week 14) | After Second Cleaning (week 19) |
|---|---|---|---|---|---|
| C-LHG8 | S1 of 15A (pitch) | 0.71±0.07 | 0.74±0.10 | 0.76±0.06 (+3%) | 0.74±0.03 (–3%) |
| | S1 of 16A (rot MRF) | 0.84±0.15 | 0.90±0.25 | 0.73±0.04 (–19%) | 0.72±0.05 (–1%) |
| | S2 of 16A (rast MRF) | 0.84±0.07 | 1.02±0.32 | 0.82±0.08 (–20%) | 0.76±0.07 (–7%) |
| CM-LHG8 | S1 of 15B (pitch) | 0.72±0.03 | 0.77±0.06 | 0.86±0.02 (+12%) | 0.93±0.02 (+8%) |
| | S1 of 16B (rot MRF) | 0.89±0.05 | 1.05±0.12 | 0.81±0.04 (–23%) | 0.79±0.09 (–2%) |
| | S2 of 16B (rast MRF) | 0.98±0.07 | 0.88±0.06 | 0.86±0.06 (–2%) | 0.86±0.02 (+0%) |
| CM-LG770 | S1 of 15C (pitch) | 0.72±0.03 | 0.76±0.07 | 0.98±0.08 (+29%) | 1.18±0.18 (+22%) |
| | S2 of 15C (pad) | 1.56±0.11 | 1.34±0.09 | 1.72±0.20 (+28%) | 1.66±0.05 (–3%) |
| | S1 of 16C (rot MRF) | 0.94±0.07 | 1.74±1.93 | 0.91±0.07 (–48%) | 0.89±0.11 (–2%) |
| | S2 of 16C (rast MRF) | 1.38±0.19 | 1.38±0.08 | 1.38±0.15 (+0%) | 1.38±0.19 (+0%) |

3. Aqueous cleaning can improve surfaces of cast LHG8 and continuously melted LG770 after *severe degradation* by humidity, but it cannot return them to their original conditions. (Aqueous cleaning of degraded continuously melted LG770 surfaces can significantly reduce structures at high- and middle-range spatial frequencies, but it is not effective at removing large structures at low spatial frequencies.)

For all glass types:

4. There is no clear correlation between initial finished surface quality (among surfaces with better-than-2-nm-rms microroughness) and quantifiable magnitude of degradation due to humidity; however, different surface structures develop on surfaces finished with different processes.
5. Gentle weekly drag wiping with methanol prevents humidity-induced degradation.
6. A single aqueous cleaning is sufficient to remove debris from polishing remaining on glass surfaces after gentle drag wiping and storage for 14 weeks.
7. One or two aqueous cleanings can cause increased haze from microscopic scratches on surfaces finished with pitch or pads.
8. MRF processing ensures that at least two aqueous cleanings can be performed to remove debris, without risk of increasing surface haze from microscopic scratches. We attribute this result to the low levels of subsurface damage remaining on surfaces after MRF processing.

## ACKNOWLEDGMENT

The authors thank H. Romanofsky of the Center for Optics Manufacturing at the University of Rochester for MRF processing of the samples. We thank A. Maltsev of LLE for pitch polishing and G. Kowski and G. Mitchell of LLE for sample cleaning, inspection, and microscopy. The idea for this work was prompted by an internal poster paper prepared by P. Ehrmann and J. Campbell of LLNL and made available to J. Kelly of LLE in January 2004. The authors acknowledge the Laboratory for Laser Energetics at the University of Rochester for continuing support. One of the authors (JD) is an LLE Horton Fellow. This research was also supported by the U.S. Department of Energy (DOE) Office of Inertial Confinement Fusion under cooperative agreement DE-FC52-92SF19460, the University of Rochester, and the New York State Energy Research and Development Authority. The support of the DOE does not constitute an endorsement by the DOE of the views expressed in this article.

## REFERENCES


1. T. I. Suratwala *et al.*, in *Optical Engineering at the Lawrence Livermore National Laboratory II: The National Ignition Facility*, edited by M. A. Lane and C. R. Wuest (SPIE, Bellingham, WA, 2004), Vol. 5341, pp. 102–113.

2. Laboratory for Laser Energetics LLE Review **96**, 207, NTIS document No. DOE/SF/19460-509 (2003). Copies may be obtained from the National Technical Information Service, Springfield, VA 22161.

3. D. C. Brown, S. D. Jacobs, J. A. Abate, O. Lewis, and J. Rinefierd, in *Laser Induced Damage in Optical Materials: 1977*, edited by A. J. Glass and A. H. Guenther, Natl. Bur. Stand. (U.S.), Spec. Publ. 509 (U.S. Government Printing Office, Washington, DC, 1977), pp. 416–422.

4. W. Seka, J. Soures, O. Lewis, J. Bunkenburg, S. Jacobs, G. Mourou, J. Zimmermann, and D. Brown, Appl. Opt. **19**, 409 (1980).

5. J. H. Campbell *et al.*, J. Non-Cryst. Solids **263–264**, 342 (2000).

6. T. I. Suratwala *et al.*, "Polishing Slurry Induced Haze on Phosphate Laser Glasses," to be submitted to the Journal of Non-Crystalline Solids.

7. "Staining and Dimming in Polishing Process," Technical Report No. HGW-0-6904E, Hoya Glass Works, Ltd. (1970).

8. "Receive, Clean, Inspect, and Package Laser Amplifier Slabs," NIF Operations Procedure No. NIF50100570A, Lawrence Livermore National Laboratory, Livermore, CA (2002).

9. D. Golini, S. Jacobs, W. Kordonski, and P. Dumas, in *Advanced Materials for Optics and Precision Structures*, edited by M. A. Ealey, R. A. Paquin, and T. B. Parsonage, Critical Reviews of Optical Science and Technology (SPIE, Bellingham, WA, 1997), Vol. CR67, pp. 251–274.

10. J. E. DeGroote, H. J. Romanofsky, I. A. Kozhinova, J. M. Schoen, and S. D. Jacobs, in *Manufacturing and Testing V*, edited by H. P. Stahl (SPIE, Bellingham, WA, 2004), Vol. 5180, pp. 123–134.

11. VWR Humidity/Temperature Pen with Memory, VWR Catalog No. 35519-049, VWR Scientific, St. Paul, MN 55121.

12. Horizontal laminar flow hood, surpasses Class 100 conditions, Dexon Manufacturing, Inc., Rush City, MN 55069.

13. Zygo NewView™ 100 Settings—Filter: Off; Remove: Cylinder; Remove Spikes: Off; Min Mod: 5%; Scan Length: 20-$\mu$m bipolar; FDA Res: High; Min Area Size: 7.

14. J. E. DeGroote, S. N. Shafrir, J. C. Lambropoulos, and S. D. Jacobs, presented at The 88th OSA Annual Meeting, Rochester, NY, 10–14 October 2004.

15. Specification taken from LLNL/NIF Drawing No. AAA96-105113, Lawrence Livermore National Laboratory, Livermore, CA.

16. E. L. Church, in *Precision Surface Metrology*, edited by J. C. Wyant (SPIE, Bellingham, WA, 1983), Vol. 429, pp. 105–112.

17. T. Izumitani *et al.*, in *The Science of Ceramic Machining and Surface Finishing II*, edited by B. J. Hockey and R. W. Rice, Natl. Bur. Stand. (U.S.), Spec. Publ. 562 (U.S. Government Printing Office, Washington, DC, 1979), pp. 417–425.

18. J. A. Menapace *et al.*, in *Laser-Induced Damage in Optical Materials: 2001*, edited by G. J. Exarhos *et al.* (SPIE, Bellingham, WA, 2002), Vol. 4679, pp. 56–68.

# Nanoscale Vibrational Analysis of Single-Walled Carbon Nanotubes

## Introduction

Since their discovery in the early 1990s by Iijima,[1] carbon nanotubes have become the focus of intense interest by a vast number of scientists and engineers. The main reason behind such wide-ranging attention lies in their unique electrical,[2] mechanical,[3] thermal,[3] and optical properties.[4] Furthermore, from their size and structure, carbon nanotubes provide a unique system for investigating one-dimensional quantum behavior.[5]

Although many detailed studies have focused on the electronic and mechanical properties of bundles and individual single-walled carbon nanotubes (SWNT's), there has been, to date, no extensive spectral analysis of the properties of SWNT's via their vibrational spectrum on the single-tube level with a spatial resolution of the order of 15 nm. Spectral analysis of individual SWNT's has been carried out in the past,[6] but the techniques used were limited by the inability of conventional confocal microscopy to image and localize nanoscale features with subwavelength resolution.[7–9] Consequently, localized features such as defects or dopants have not been resolved so far. In the work reported here, high-resolution microscopy was performed on individual SWNT's to avoid averaging of the Raman signal. Our unique ability to surpass this limit (i.e., sub-diffraction-limited imaging) lies at the heart of our near-field Raman technique.[10]

Raman spectroscopy is a powerful tool for studying the chemical composition of matter since the energy range of electronic transitions lies within the visible spectrum of electromagnetic radiation. This study focuses on the four main first-order features of SWNT Raman scattering: the radial breathing mode (RBM) (~100 to 300 $cm^{-1}$), the Raman active *D* band (~1300 $cm^{-1}$), *G* band (~1594 $cm^{-1}$), and *G′* band (~2600 $cm^{-1}$).[11–14]

The Raman spectrum can be thought of as a unique chemical fingerprint from which to extract a wealth of information on the electronic structure of SWNT's. For example, the nanotube diameter, chirality, and structure (*n,m*) [(*n,m*) defines the atomic coordinates for the one-dimensional (1-D) unit cell of the nanotube] are associated with the frequency of the RBM; metallic and semiconducting nanotubes can be distinguished based on the shape of the *G* band (and RBM frequency); and the *D*-band intensity indicates the presence of defects and other disorder-induced effects.

By introducing a sharp gold tip (tip-enhanced Raman spectroscopy[10,15–17]) in the focus of a tightly focused laser beam, the Raman excitation area can be localized to ~15 × 15 $nm^2$. The high spatial frequencies associated with this electromagnetic field confinement allow us to record (near-field) Raman images of SWNT's with a spatial resolution of the order of 10 to 20 nm. Precise spectroscopic information can be extracted as the tip is positioned along a SWNT of interest. In this way unique vibrational maps can be built that show the spatial variation of several Raman active modes along many different SWNT's. We believe that the ability to map spectral changes along SWNT's, with nanoscale precision, will lead to a greater understanding of the fundamental properties of such materials on the single-tube level.

## Experimental Section

Our near-field Raman setup[10] is based on an inverted optical microscope with the addition of an *x,y* stage for raster-scanning samples. Light from a He-Ne laser (633 nm, 50 to 200 $\mu$W) is reflected by means of a dichroic beam splitter and then focused onto the surface of the sample using a high-numerical-aperture objective (N.A. = 1.4).

Having obtained a tight focal spot at the sample surface, a sharp, gold tip is then positioned into the focal region. Care is taken to align the tip with one of the two longitudinal field components in the focal plane.[18] The gold tip is held at a constant height of 1 nm by means of a shear-force detection feedback mechanism[19] with an rms noise of ~0.5 Å in the *z* direction. Using the *x,y* stage to raster scan the sample, Raman-scattered light is collected with the same objective and is recorded using either a single-photon–counting avalanche photodiode (APD) or a spectrograph with a charge-coupled device (CCD) cooled to –124°C.

SWNT's were grown by the arc-discharge method[3] and purchased commercially. They were then dispersed in a solution of dichloroethane, sonicated in an ultrasonic bath, and spin cast at 3000 rpm onto a glass cover slip. Our metal tips were produced by electrochemically etching thin, gold wire in a solution of hydrochloric acid (HCl) for ~30 s.

**Results**

The primary motivation of this study is to probe, with nanoscale resolution, the main vibrational modes of spatially isolated, individual SWNT's; to relate spectral variations to the tube structure (RBM); and to localize defects (*D* band) along the tube axis.

Figure 100.48(a) shows a diffraction-limited, confocal Raman image recorded by raster scanning a sample with a single SWNT through the focused laser. The contrast in the image results from integrating the Raman spectrum for each image pixel over a narrow spectral range centered at $\nu$ = 2600 cm$^{-1}$ ($G'$ band). Figure 100.48(b) shows the corresponding near-field Raman image taken over the exact same sample area. This image results from placing a sharp metal tip (25-nm diameter) into the laser focus. The spatial resolution is ~14 nm [full width at half maximum (FWHM)] as shown by the inset of Fig. 100.48(b).

Figure 100.48(c) shows the corresponding Raman-scattering spectrum for a certain nanotube position with and without the tip present. The increase in Raman-scattering strength demonstrates clearly the effect of surface-enhanced Raman scattering (SERS). The SERS enhancement factor depends on the ratio of the near-field and confocal interaction volumes. Typical enhancement factors are in the range of $10^2$ to $10^4$ (Ref. 10).

In the next step, a sample area was located with single nanotubes that show detectable signals for all four Raman active bands. Figures 100.49(a)–100.49(d) show a series of near-field spectral images of two individual SWNT's corresponding to the *G*, *G*′, *D*, and RBM Raman bands.

From these images one can clearly observe the spatial variation in Raman-scattered light for all four Raman bands. Both the *G* and *G*′ bands [Figs. 100.49(a) and 100.49(b)] show a near-uniform-intensity profile along the nanotube in the center of the image, as one might expect for a defect-free SWNT. This observation is further strengthened by the weak intensity of the disorder-induced *D* band [Fig. 100.49(c)]. The most striking spectral feature is the localized scattering associated with the RBM. Figure 100.49(d) illustrates that only one nanotube, namely the SWNT in the center of the image, is

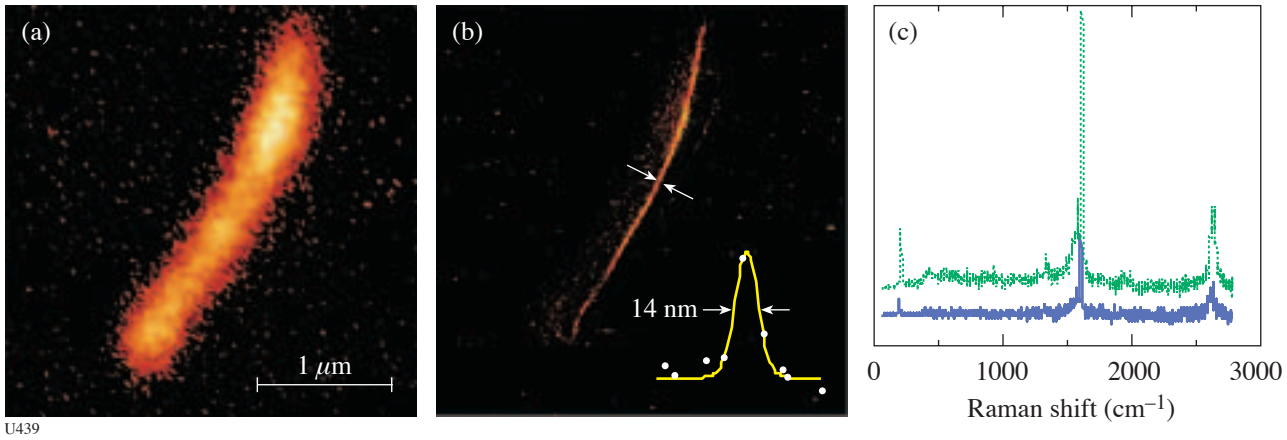


Figure 100.48
[(a) and (b)] Raman-scattering images of a single SWNT deposited on a glass coverslip. The contrast in the images reflects the local intensity of the Raman $G'$ band: 2600 cm$^{-1}$. (a) A confocal Raman image and (b) the corresponding near-field Raman image. The integration time was 10 ms per image pixel. The inset in (b) shows a Gaussian fit to the line section shown (FWHM of 14 nm). The FWHM taken from (a) was ~275 nm. (c) Raman-scattering spectrum for a single SWNT with (upper) and without (lower) a metal tip present. The graphs are offset for clarity.

resonantly excited with our light source. The detected RBM frequency was measured to be ~205 $cm^{-1}$, indicating that we observe a (14,1) nanotube. Using the relation $\nu_{RBM} = A/d_t + B$, (where $A$ = 223.5 nm/cm and $B$ = 12.5 $cm^{-1}$),[14] we calculate the tube diameter to be 1.16±0.2 nm. Atomic force microscopy (AFM) measurements confirm that it is indeed a single nanotube, its diameter being measured topographically to be ~1.3 nm±0.3 nm.

To understand the origin of these local variations, we first discuss the resonance conditions associated with the different Raman bands. The RBM resonance window is different compared to the resonance windows for the *G*, *G*′, and *D* Raman modes.[7] The RBM is more likely to change in the presence of nanotube defects, such as localized changes in the structure of the nanotube lattice [changes in (*n*,*m*)], kinks, and intertube junctions in addition to interactions with the glass substrate on which the SWNT's are dispersed. Any of these variations will affect the van Hove transition energy $E_{ii}$ and detune the RBM out of resonance. For the *G*, *G*′, and *D* Raman active bands respectively, any small change in $E_{ii}$ is unlikely to manifest itself in similarly dramatic spectral variations.

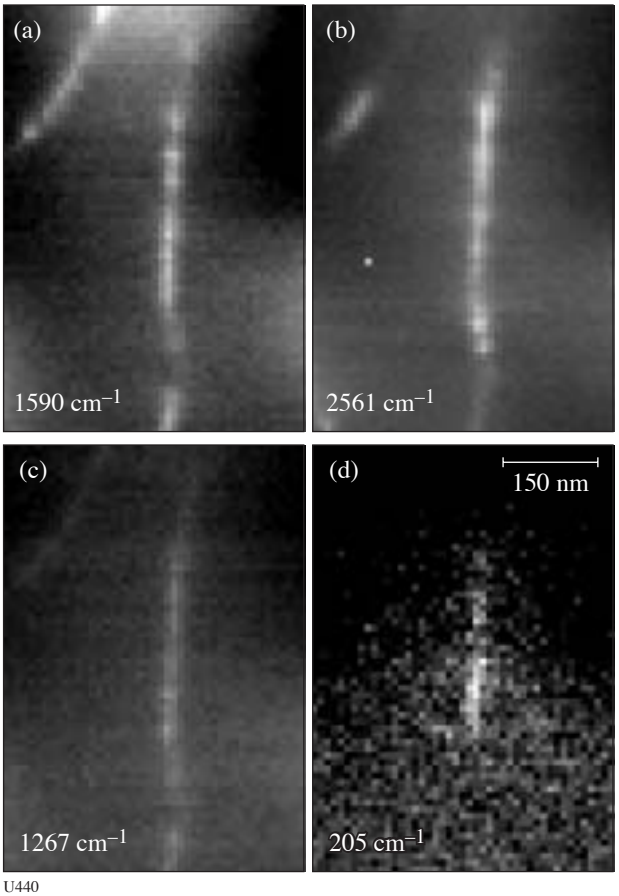


Figure 100.49
Near-field spectral images, upon laser excitation at 633 nm, for the Raman active (a) *G* band, (b) *G*′ band, (c) *D* band, and (d) RBM. The images were produced from the Raman-scattered light detected with a cooled CCD. (Integration time: 210 ms per image pixel.) The most-striking feature is the localization of the RBM associated with the vertically aligned SWNT.

The dispersive *G*, *G*′, and *D* bands are discussed in terms of a double resonance effect that relaxes the resonance condition.[12] On the other hand, the RBM originates from a single resonance process, resulting in a slightly narrower resonance window.[13] Since the resonance windows for the Raman active *G* and *G*′ bands are broader in nature, dramatic spectral changes are not as expected, as can be seen in Figs. 100.49(a) and 100.49(b). However, as will be reported in a later publication, we have observed significant spectral variations, on the single-tube level, in the *G* and *G*′ Raman bands for SWNT's that have been doped with elemental boron.[20]

Figure 100.49(c) reveals the presence of a small amount of scattered light associated with the Raman *D* band centered at 1267 $cm^{-1}$. In light of the weak signal associated with this band, we relate such scattering to disorder-induced effects within the tube lattice itself or the coupling to the supporting substrate. In a related study on boron-doped tubes, we have observed significant increases of *D*-band scattering, localized with 20-nm resolution, along several different SWNT's.[20]

In light of our work, it should be noted that recent experiments on SWNT's suspended from Si pillars have shown Raman signals that are more intense when compared to SWNT's in contact with a silicon surface;[21] however, no localized spectral analysis has been reported so far for suspended SWNT's. The ability to perform such localized analysis of suspended SWNT's should provide a better understanding of the effects of nanotube–surface interactions on the variations of the vibrational modes of SWNT's.

Our observation and explanation of the RBM localization are consistent with the results that we acquired for many different tube structures (assigned from RBM frequency). Figures 100.50(a)–100.50(e) show further evidence for localized Raman scattering associated with the following Raman active modes: namely, (a) the *G* band, (b) *D* band, (c) RBM, (d) intermediate-frequency modes (IFM),[13] and (e) *M* band.[22] Figure 100.50(f) shows a three-dimensional AFM profile of the nanotube studied.

Once again localized spectral variations of the RBM are observed. The RBM signal decreases dramatically in the presence of ~3-nm-high catalyst particles located at the tube's end. This observation is consistent with the idea that changes in the tube structure can lead to a loss of resonance Raman-scattering properties of SWNT's. From Fig. 100.50(b) considerable *D*-band scattering is also observed at the beginning of the tube, where a small kink is present, and near the end with the small catalyst particles. The vibrational modes shown in Figs. 100.50(d) and 100.50(e) are recorded along a single nanotube for the first time. The two bands are designated as an intermediate frequency mode (IFM) and *M* band, respectively, and are known from the literature.[13,22] The *M* band is the sum of the RBM and the *G* band, although it should be noted that the *M* band also appears in the Raman spectrum of graphite. Our calculations show that subtracting the frequency of the *G* band from the *M* band gives 142 cm$^{-1}$. This is consistent with the measured value of the RBM frequency: 143 cm$^{-1}$. From this measured RBM frequency we assign a nanotube structure of (23,1); i.e., (*n*,*m*) = (23,1). To the best of our knowledge, no previous attempt has been made to understand why both the IFM and *M* modes are localized similar to the observed spatial variations of the RBM. We conclude that both the IFM and *M* band are dependent on the tube structure (*n*,*m*) in the same manner as the RBM. This claim is strengthened by the fact that these bands are not always detectable for either SWNT bundles or individual SWNT's. Future work should provide more-detailed insight into the spatial variation of these two bands and any possible dependence on the tube diameter, i.e., (*n*,*m*).

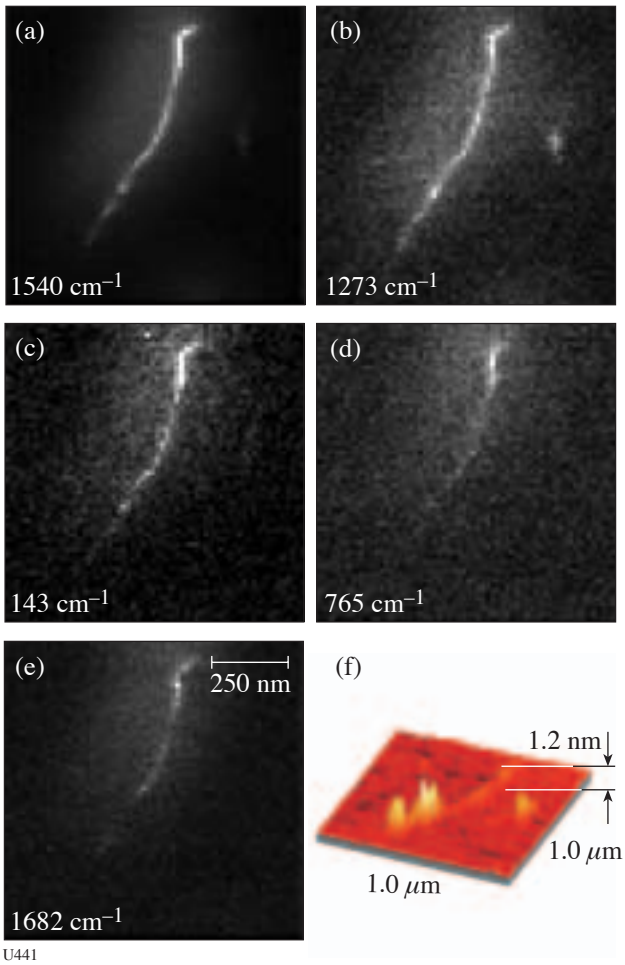


Figure 100.50
[(a)–(e)] Near-field spectral images for different Raman bands. (f) A 3-D topographical profile of the nanotube studied. Two bands previously unseen in our SWNT studies are (d) an intermediate-frequency mode (IFM)[13,23] and (e) the Raman active *M* mode.[22] Again the presence of a spatially varying RBM along the nanotube length is observed. The RBM, as well as the IFM and *M* bands, decrease in strength near the attached ~3-nm particle(s), which is presumably a residual Ni/Y catalyst particle left over from the growth process.

For all near-field Raman images, a topographic image (not shown in Figs. 100.48 and 100.49), acquired simultaneously, provides a valuable crosscheck for the (*n*,*m*) assignments based on the RBM frequency. All SWNT's studied had their diameters calculated from the spectral position of their (diameter-dependent) RBM frequencies. The calculated value was then compared with the corresponding AFM measurements to confirm that they were, indeed, individual SWNT's and not small bundles. In addition, the same gold tip was used to acquire all of the images shown.

**Conclusion**

In conclusion, using near-field Raman imaging and spectroscopy, several vibrational modes have been mapped along spatially isolated, individual SWNT's resting on a glass substrate with 20-nm resolution. Our results demonstrate that high-resolution microscopy is necessary to avoid averaging of the Raman spectrum along individual SWNT's. As such, our results reveal the highly localized nature of the light scattering associated with the RBM frequency from several different SWNT's. Such spectral features are ascribed to the sensitive nature of the RBM resonance condition. Variations in the RBM scattering are attributed to the surrounding environment (nanotube–substrate interactions) and its effect on the nanotube structure (*n*,*m*) and hence transition energy $E_{ii}$. Furthermore, little variation in intensity has been observed for both the *G* and *G*′ Raman bands. Such small variations result from the different resonance conditions for these bands in comparison with the resonance window of the RBM for SWNT's. Finally,

detectable Raman scattering associated with disorder-induced effects has been observed; however, for many perfectly aligned SWNT's, little or no *D*-band intensity has been detected.

## ACKNOWLEDGMENT

The authors wish to thank Dr. A. Bouhelier and Dr. A. Jorio for stimulating discussions and T. Osedac for tip fabrication. This research has been supported financially by the Air Force Office for Scientific Research (AFOSR) through the Multidisciplinary University Research Initiative (MURI) under Grant No. F-49620-03-1-0379.

## REFERENCES

1. S. Iijima, Nature **354**, 56 (1991).
2. M. T. Woodside and P. L. McEuen, Science **296**, 1098 (2002).
3. M. S. Dresselhaus, G. Dresselhaus, and P. Avouris, *Carbon Nanotubes: Synthesis, Structure, Properties, and Applications*, Topics in Applied Physics, Vol. 80 (Springer, Berlin, 2001).
4. A. Hartschuh *et al.*, Science **301**, 1354 (2003).
5. L. C. Venema *et al.*, Science **283**, 52 (1999).
6. A. Mews *et al.*, Adv. Mater. **12**, 1210 (2000).
7. M. Souza *et al.*, Phys. Rev. B **69**, 241403(R) (2004).
8. K. McGuire *et al.*, "Synthesis and Raman Characterization of Boron-Doped Single-Walled Carbon Nanotubes," submitted to Physical Review B.
9. S. B. Cronin *et al.*, Phys. Rev. Lett. **93**, 167401 (2004).
10. A. Hartschuh *et al.*, Phys. Rev. Lett. **90**, 095503 (2003).
11. A. Jorio *et al.*, Phys. Rev. Lett. **86**, 1118 (2001).
12. S. Reich, C. Thomsen, and J. Maultzsch, *Carbon Nanotubes: Basic Concepts and Physical Properties* (Wiley-VCH, Cambridge, England, 2004).
13. A. M. Rao *et al.*, Science **275**, 187 (1997).
14. S. W. Bacilo *et al.*, Science **298**, 2361 (2002).
15. J. Wessel, J. Opt. Soc. Am. B **2**, 1538 (1985).
16. N. Hayazawa *et al.*, Chem. Phys. Lett. **335**, 369 (2001).
17. R. M. Stöckle *et al.*, Chem. Phys. Lett. **318**, 131 (2000).
18. L. Novotny, E. J. Sánchez, and X. S. Xie, Ultramicroscopy **71**, 21 (1998).
19. K. Karrai and R. D. Grober, Appl. Phys. Lett. **66**, 18424 (1995).
20. N. Anderson *et al.*, in preparation.
21. Y. Kobayashi *et al.*, Chem. Phys. Lett. **386**, 153 (2004).
22. V. W. Brar *et al.*, Phys. Rev. B **66**, 155418 (2002).
23. In a recent article C. Fantini *et al.* discuss the origin of IFM's for many different laser wavelengths. See Phys. Rev. Lett. **93**, 087401 (2004) for further details.

# Polymer Cholesteric Liquid Crystal Flake Reorientation in an Alternating-Current Electric Field

## Introduction

The motion and orientation of nonspherical particles suspended in a host fluid and subjected to an alternating-current (ac) electric field have been well studied theoretically. Because the dielectric properties of the two phases of the suspension differ, charge will start to accumulate at the particle–fluid interface due to Maxwell–Wagner polarization. This charge accumulation induces a dipole moment, which is acted on by the electric field, causing the particle to reorient. Basic electromagnetic theory predicts that a particle in an electric field will orient in the direction corresponding to the lowest energy so as to minimize the potential energy of the system. Typically this requires a dielectric nonspherical particle to align its longest axis parallel to the external field.[1] Because the minimum energy orientation of the particle depends on the shape, the dielectric properties of the host fluid and particle, and the frequency of the ac field, it is possible that a particle will have varying stable orientations at different frequencies. Schwartz *et al*.[2] described the orientation of particles in an ac electric field and considered the conditions for particles with anisotropic dielectric properties or with additional membranes or layers, which is of particular use in the biological sciences. Okagawa *et al*.[3] derived similar equations for a uniform dielectric particle but included the effect of shear flow on the particle motion. Jones did further work in the field of particle electromechanics, including phenomena such as electrophoresis and dielectrophoresis,[4] and a comprehensive review of electromechanical behavior of particles was written by Gimsa.[5] In addition to conducting experiments with biological particles,[6] Miller and Jones investigated highly dielectric particles, such as titanium dioxide.[7] Bostwick and Labes also performed similar experiments using platelets of crystalline nafoxidine hydrochloride.[8] In this article we report on the orientation of highly dielectric polymer cholesteric liquid crystal (PCLC) particles (flakes), suspended in a low-viscosity host fluid. Though much of the theory on particle electromechanics is well supported by experimental work in the biological sciences, relatively little work has been done to study the behavior of highly dielectric particles like PCLC flakes, which have no inherent charge, a low dielectric constant, and a negligible dielectric anisotropy.

## PCLC Flakes

PCLC flakes were developed in the 1990s as an alternative to both low-molar-mass cholesteric liquid crystals (LMMLC's) and PCLC thin films. Typical LMMLC molecules can be switched with an electric field, which provides control over their optical properties, but LMMLC's tend to be temperature sensitive and require confining substrates to retain liquid crystalline order. Due to a relatively high glass transition point, PCLC films are not temperature sensitive and can stand alone without substrates. Despite this environmental stability and the usefulness for passive applications, freestanding polymer LC films cannot be manipulated in electric fields. PCLC flakes have the potential to combine two important properties of PCLC films and LMMLC's: environmental stability and electro-optic switching.[9]

PCLC flakes are formed by fracturing thin PCLC films into randomly shaped particles of the order of tens to hundreds of microns.[10] More recently, techniques for processing uniformly shaped flakes with replication methods such as soft lithography have been developed.[11]

An important and unique characteristic of PCLC flakes is that they display selective reflection, a Bragg-like effect resulting from the "helical" molecular structure of PCLC's aligned in the Grandjean texture. Selective reflection causes light of a specific wavelength and (circular) polarization to be reflected from the flake surface. Thus, a large visual effect is created if flakes are viewed off-axis or if they are tipped with respect to normally incident light, whereby the wavelength of selective reflection shifts toward shorter wavelengths and is also diminished. This optical effect provided the motivation for controlling the position, and thus the color and reflectivity, of a PCLC flake using an electric field.[12]

**Theory**

The response time for flake motion is determined by solving the equation of motion for an ellipsoid, which includes the electrostatic torque exerted on a polarized ellipsoid whose rotation is opposed by a hydrodynamic (viscous) torque from the surrounding host fluid. The mass moment of inertia is neglected because viscosity, and not the flake's inertia, dominates the system. The inertial contribution is several orders of magnitude smaller than contributions from the electrostatic and hydrodynamic torques, i.e., the system is critically damped.

The electrostatic torque $\vec{\Gamma}_E$ is defined as the cross product of the induced dipole moment $\vec{p}$ and the applied electric field $\vec{E}_o$:

$$\vec{\Gamma}_E = \vec{p} \times \vec{E}_o. \tag{1}$$

Here we assume that the particle material has no permanent dipole moment and that the applied electric field is uniform over the flake dimensions. The electric field inside the particle $E^+$, to which the particle responds, varies with the rotation of the ellipsoid and induces an effective polarization along each ellipsoidal axis $i$:

$$P_i = \left(\varepsilon_p - \varepsilon_h\right) E_i^+, \tag{2}$$

where

$$E_i^+ = \frac{\varepsilon_h E_{oi}}{\varepsilon_h + A_i\left(\varepsilon_{ii} - \varepsilon_h\right)}, \tag{3}$$

$\varepsilon_p$ and $\varepsilon_h$ are the dielectric permittivity of the particle and host fluid, respectively, and $E_{oi}$ is the applied electric field component along the particle axis $i$. Calculations for an electrically isotropic particle can be performed by considering $\varepsilon_{11} = \varepsilon_{22} = \varepsilon_{33} = \varepsilon_p$. The ellipsoid is described by axes lengths $a_i$, $a_j$, and $a_k$, and a depolarization factor $A_i$ must be defined along each axis (where $i$, $j$, and $k$ are indices ordered according to the right-handed coordinate system):

$$A_i = \frac{a_i a_j a_k}{2} \int_0^\infty \frac{ds}{\left(s + a_i^2\right)\sqrt{\left(s + a_i^2\right)\left(s + a_j^2\right)\left(s + a_k^2\right)}}. \tag{4}$$

The effective induced dipole moment along each particle axis $p_i$ is

$$p_i = \frac{4\pi}{3} a_i a_j a_k P_i = \frac{4\pi}{3} a_i a_j a_k \varepsilon_h K_i E_{oi}, \tag{5}$$

where we have defined the Clausius–Mosotti factor $K_i$ along each ellipsoidal axis as

$$K_i = \frac{\left(\varepsilon_p - \varepsilon_h\right)}{\left[\varepsilon_h + A_i\left(\varepsilon_p - \varepsilon_h\right)\right]}. \tag{6}$$

Since the dielectric particle and the surrounding medium are not ideal dielectrics, energy dissipation mechanisms such as conduction and dielectric relaxation require that a frequency-dependent complex dielectric constant $\varepsilon^*$ be considered:

$$\varepsilon^*(\omega) = \varepsilon - i\frac{\sigma}{\omega}, \tag{7}$$

where $\omega$ is the electric field frequency and $\sigma$ is the electric conductivity. The definitions for $K_i^*$ and $p_i^*$ remain unchanged except that $\varepsilon_p$ and $\varepsilon_h$ become complex and frequency dependent. Using Eqs. (1) and (5), we find the electrostatic torque $\Gamma_{Ei}$ along the particle axis $i$ to be

$$\Gamma_{Ei} = \frac{4\pi}{3} a_i a_j a_k \varepsilon_h K_j^* K_k^* \left(A_k - A_j\right) E_{oj} E_{ok}. \tag{8}$$

It is important to note that the $\varepsilon_h$ arising from the effective induced dipole moment [Eq. (5)] is not complex because it is not derived from Gauss's law.† The hydrodynamic torque $\Gamma_{Hi}$ about particle axis $i$ is defined as

$$\Gamma_{Hi} = -\frac{16\pi}{3} a_i a_j a_k \eta_o \frac{\left(a_j^2 + a_k^2\right)}{\left(a_j^2 A_j + a_k^2 A_k\right)} \Omega_i, \tag{9}$$

†See Jones[4] (Appendix G) for a derivation of the induced effective moment of a dielectric ellipsoid, which includes the electrostatic potential external to the ellipsoid.

where $\eta_o$ is the absolute viscosity of the host fluid and $\Omega_i$ is the angular velocity about axis $i$. The hydrodynamic and electrostatic torques about a specific axis are equated to give the equation of motion for a rotating flake. The angular velocity $\Omega_i$ relative to its corresponding axis $i$ is found to be

$$\Omega_i = \frac{\varepsilon_h \varepsilon_o K_j^* K_k^* \left(A_k - A_j\right) E_{oj} E_{ok}}{4\eta_o} \frac{\left(a_j^2 A_j + a_k^2 A_k\right)}{\left(a_j^2 + a_k^2\right)}. \quad (10)$$

We first examine the two-dimensional implication of this result. The two-dimensional coordinate system and reference frame for the flake are defined in Fig.100.51, where $\theta$ is the instantaneous angle between the flake's surface normal and the applied electric field.

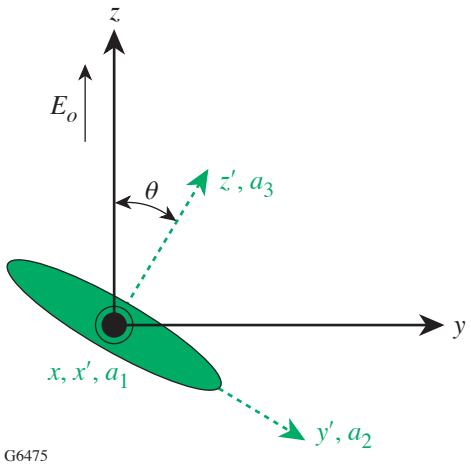


Figure 100.51
The flake reference frame (primed axes) rotates with respect to the laboratory (cell) reference frame (unprimed axes).

If we consider the case where the electric field $E_o$ is applied along the $z$ axis and the flake rotates about axis $a_1$ ($x'$), the angular velocity about the flake axis is found to be

$$\frac{d\theta}{dt} = \Omega_1$$

$$= \frac{\varepsilon_h \operatorname{Re}\left\{K_3^* K_2^*\right\}\left(A_3 - A_2\right) E_o^2}{4\eta_o} \frac{\left(a_2^2 A_2 + a_3^2 A_3\right)}{\left(a_2^2 + a_3^2\right)} \sin\theta\cos\theta. \quad (11)$$

We retain the real component of the equation because only the time-averaged term is significant in a heavily damped system where the particle moves slowly compared to the applied electric field. This equation is easily simplified and solved in the form

$$\frac{d\theta}{dt} = \frac{C}{2}\sin 2\theta, \text{ where}$$

$$C = \frac{\varepsilon_h \operatorname{Re}\left\{K_3^* K_2^*\right\}\left(A_3 - A_2\right) E_o^2}{4\eta_o} \frac{\left(a_2^2 A_2 + a_3^2 A_3\right)}{\left(a_2^2 + a_3^2\right)}. \quad (12)$$

Equation (12) can be integrated to obtain an equation for the angle $\theta$ at any given time:

$$\tan\theta = \tan\theta_o e^{t/\tau_c}, \quad (13)$$

where $\theta_o$ is the initial angle (position) of the flake and $\tau_c = 1/C$ is the time constant for flake relaxation. We can see that for all $\tau_c > 0$, as $t \to \infty$ the angle $\theta \to \pi/2$ is a stable configuration. It is now possible to determine the response time of the flake, or the time needed for $\theta$ to approach any final orientation, including $\theta \approx 90°$. The reorientation time from the initial angle $\theta_o$ to the current angle $\theta$ is given by

$$t = \tau_c \ln\left(\frac{\tan\theta}{\tan\theta_o}\right)$$

$$= \frac{4\eta_o}{\varepsilon_h \operatorname{Re}\left\{K_e^* K_2^*\right\}\left(A_3 - A_2\right) E_o^2} \frac{\left(a_2^2 + a_3^2\right)}{\left(a_2^2 A_2 + a_3^2 A_3\right)} \ln\left(\frac{\tan\theta}{\tan\theta_o}\right). \quad (14)$$

Equation (14) clearly shows that the flake reorientation time should have an inverse quadratic dependence on the applied electric field and a linear dependence on the fluid viscosity. There must be a slight perturbation in the flake position ($\theta_o > 0°$) in order for flake motion to commence.

A three-dimensional model that accounts for the coupling between the components of angular velocity about each axis was developed by Okagawa[3] (see Fig. 100.52). Based on Okagawa's work, the time rate of change of each angle can be found in terms of the components of angular velocity of the

flake defined by Eq. (10), where

$$\frac{d\theta}{dt} = \Omega_1 \cos\psi + \Omega_2 \sin\psi,$$

$$\frac{d\varphi}{dt} = \left(\Omega_2 \cos\psi - \Omega_1 \sin\psi\right)\cos\theta, \tag{15}$$

$$\frac{d\psi}{dt} = \Omega_3 - \left(\Omega_2 \cos\psi - \Omega_1 \sin\psi\right)\cot\theta.$$

Allowing $\psi = 0$ eliminates the angle describing the spin of the flake and simplifies the equations. We solved these equations numerically, and the results validated the two-dimensional analytic solution.

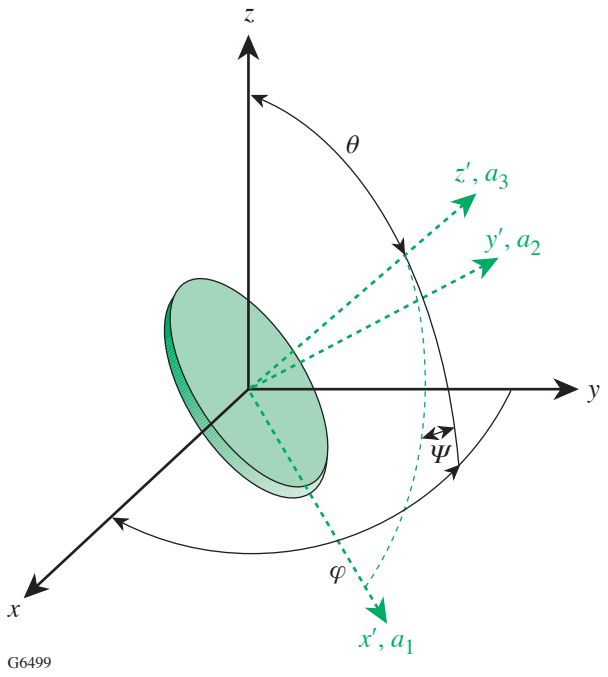


Figure 100.52
Coordinate systems of the (unprimed) laboratory reference frame and the (primed) ellipsoid reference frame. The $z'$ identifies the direction normal to the surface of an oblate particle.

## Experimental Procedure

Commercial polycyclosiloxane flakes,[13] typically 6 $\mu$m thick, with an arbitrary shape and a selective reflection peak at $\lambda_o$ = 520 nm (green), were sieved and dried to obtain batches with sizes between 20 and 40 $\mu$m [Fig. 100.53(a)]. The PCLC flakes were suspended in two host fluids: a silicone oil (Gelest, DMS-T05) and propylene carbonate (PC) (Aldrich, 99.7% HPLC grade). Though both fluids are transparent, chemically compatible with the PCLC material, and of a comparable density, their dielectric properties varied greatly. The silicone oil had a low dielectric permittivity and was highly insulating ($\varepsilon_h \sim 3\ \varepsilon_o$, $\sigma_h \sim 10^{-11}$ S/m), while the PC had a high dielectric permittivity and was significantly more conductive ($\varepsilon_h \sim 69\ \varepsilon_o$, $\sigma_h \sim 10^{-6}$ S/m). Test cells were constructed using pairs of indium tin oxide (ITO)–coated glass substrates. A mixture of soda lime glass spheres dispersed in a UV-curing epoxy was applied in four corners of one substrate to set the cell gap. Assembled cells were then filled with the flake/host fluid suspension by capillary action and sealed with additional epoxy.

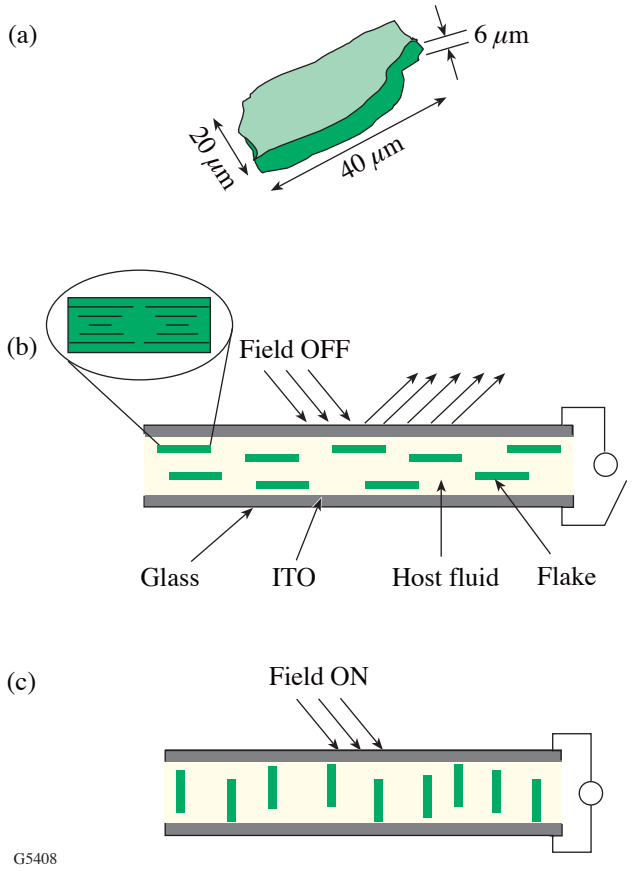


Figure 100.53
Dimensions of a typical irregularly shaped PCLC flake are depicted in (a). Flakes lie approximately parallel to cell substrates when no electric field is applied (b) and appear green due to selective reflection caused by the helical molecular structure of cholesteric liquid crystals, as depicted by the enlarged cross-sectional view of a flake. Flakes reorient with one long axis parallel to the applied field (c). They appear dark since light is no longer reflected off their flat surfaces.

Basic observations were made using a Leitz Orthoplan polarizing microscope. A Panasonic Digital 5100 camera with a timer was used to record flake motion with a time resolution of 100 ms. Data on subsecond flake motion were obtained by detecting the light reflected from the rotating flake surface using a Hamamatsu R905 photomultiplier tube (PMT) coupled to the microscope ocular by means of a fiber optic mounted in a precision fiber coupler. The PMT signal was displayed on one channel of an HP 54520A oscilloscope and directly compared with the field applied to the cell displayed on the second channel. Flake motion was easily detected under near-normal illumination through a 10× objective (N.A. = 0.2). Brightly reflecting flakes lying in the plane defined by the substrates [Fig. 100.53(b)] darkened substantially with only a few degrees of rotation [Fig. 100.53(c)] as they continue reorienting to align parallel with the electric field.

**Experimental Results and Discussion**

The motion of PCLC flakes in a sinusoidal ac electric field was investigated mainly in the propylene carbonate host system because no motion was observed in the silicone oil host system.* Reorienting PCLC flakes exhibited several characteristics: Flakes consistently rotated about the longest axis, so that the shorter major axis aligned parallel to the applied field direction. Furthermore, flakes with larger aspect ratios (length to width) reoriented more quickly than flakes of a comparable size, but with a smaller aspect ratio. Once the driving field was turned off, flakes returned to their initial position in the plane of the cell. This approximate 90° relaxation required anywhere from several seconds to several minutes to be completed. There was also a gradual and approximately linear increase in response time over the lifetime of the PCLC flake test device during test periods of 2 days.

Both the electric-field frequency and magnitude affected flake reorientation times. Flake motion was seen within a specific frequency bandwidth (~10 Hz to 1 kHz), above and below which flake reorientation did not occur (Fig. 100.54). Motion for a typical flake was detected in fields as low as 5 $mV_{rms}/\mu m$, but fields above 30 $mV_{rms}/\mu m$ were required for flake reorientation to occur on a subsecond time scale. The inverse quadratic dependence on the electric field was observed clearly as the flake reorientation time was tested as a function of applied voltage (Fig. 100.55).

From Eq. (14), it is clear that the measured inverse quadratic dependence of the response time on the applied field supports the theoretical model predictions of the previous section. The dependence on the flake shape is more complicated, but a study of seven specific PCLC flakes suspended in PC and observed in a 10.4-$mV_{rms}/\mu m$ field at 50 Hz showed clearly that the reorientation time decreases as the aspect ratio increases. This shape-dependent behavior was also as predicted by the theoretical model (Fig. 100.56).

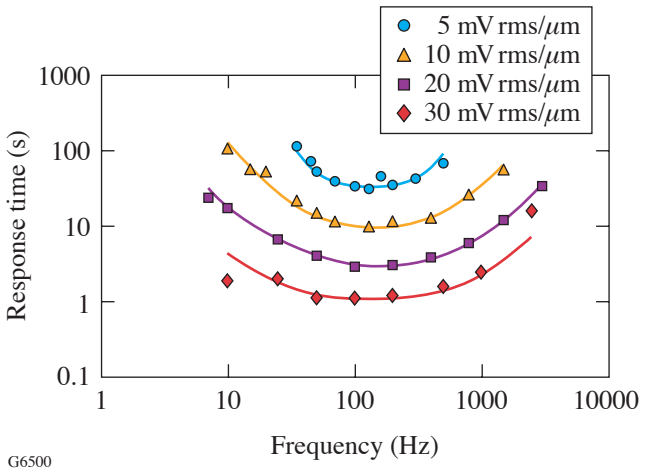


Figure 100.54
The characteristic time response of a representative PCLC flake as a function of frequency at specific electric-field values. Lines are drawn to guide the eye. Similar behavior was observed for dozens of individual flakes.

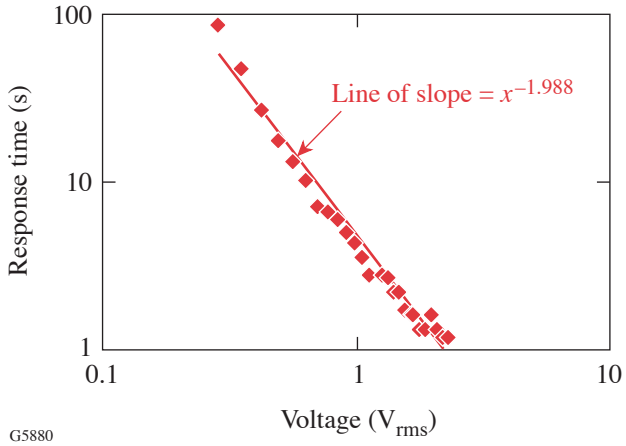


Figure 100.55
The average response time of several flakes exhibited an inverse quadratic dependence on the applied voltage. The standard deviation of 10% is of the order of the size of the data points. Data was collected at 50 Hz.

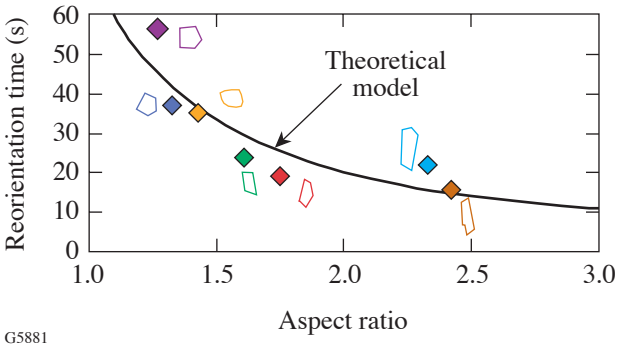


Figure 100.56
A correlation between response time and flake size and shape was observed. Flakes with the largest aspect (length to width) ratio reorient the fastest.

Though many of the observations above were supported by theory, two results were not supported by previous theoretical work. For flakes with axes $a_1 > a_2 > a_3$, we expected that the flakes would align with their longest axis $a_1$, parallel to the electric field. Instead, we observed that the flakes consistently aligned with the shorter major axis $a_2$, parallel to the applied electric field. Schwarz[2] used the Clausius–Mosotti factor $K_i$, which measures the energy of the ellipsoid when it is oriented with its $i$ axis parallel to the field, to predict the stable orientation of the particle. He suggested that the axis with the smallest $K_i$ would align parallel to the applied field. Using the following typical parameters we found that, for all frequencies, $K_1$ had the smallest value: $\varepsilon_h \sim 69\ \varepsilon_o$; $\sigma_h \sim 10^{-6}$ S/m; $\varepsilon_p \sim 2.89\ \varepsilon_o$; $\sigma_p < 10^{-11}$ S/m; $a_1 = 35\ \mu$m; $a_2 = 15\ \mu$m; and $a_3 = 5\ \mu$m. This result indicated that the longest axis $a_1$ should align with the electric field, which is contrary to our observations.

Jones produced a chart for determining the preferred axis alignment based on a combination of signs of the torque terms for each axis. In practice, only the sign of the real component of the Clausius–Mosotti term $\left(K_j^* K_k^*\right)$ was considered because it is proportional to the torque [Eq. (8)]. Considering only the Clausius–Mosotti terms excludes the difference in depolarization factors ($A_k$–$A_j$). This difference term can flip the sign of the torque if $A_k$ is less than $A_j$. We used the Jones chart, initially considering just $\mathrm{Re}\left\{K_j^* K_k^*\right\}$ and then including $\left(A_k - A_j\right)\mathrm{Re}\left\{K_j^* K_k^*\right\}$, to predict which flake axis would align with the electric field. Neither method produced results that correspond with our observations.

To predict which particle axis would align parallel to the electric field, we found it necessary to consider not only the electric torque but also contributions of the viscous drag (hydrodynamic torque), which become more important as the lengths of the two major axes become more similar. One way to include the effects of the viscous drag was to compare the magnitude of the angular velocity components about each axis. Assuming that the particle reorients about the axis with the largest angular velocity component, and for the material parameters given above, we found that a flake lying nearly parallel to the substrate will reorient about the longest axis $a_1$, so that the shorter of the two major axes, $a_2$, aligns parallel to the electric field, just as we had observed. This result will be true unless the flake's initial condition is already tilted largely about the shorter axis $a_2$.

The second result not supported by theoretical work arose when we compared our model of flake reorientation times with electric-field frequency. Initially we used the real part of the Clausius–Mosotti factor in the electric torque term, and the resultant theoretical model showed a weak frequency dependence. The characteristic $S$ shape of the theoretical curve (Fig. 100.57, insert) shifted toward higher (lower) frequencies when host fluids with a higher (lower) conductivity were modeled. However, the model predictions using the $S$-shaped curve agreed poorly with the experimental data. The data showed a minimum reorientation time at a specific frequency above and below which the reorientation times increased. The model based on the real component of the Clausius–Mosotti factor corresponded well only with the general order of magnitude of the flake reorientation time (Fig. 100.57).

Because the frequency dependence of the reorientation time data resembled the typical dispersion spectrum for the imaginary part of the dielectric constant, we also explored using the imaginary part of the Clausius–Mosotti factor in our model. Use of the imaginary component produced a theoretical curve with a $U$ shape that agreed well with the shape of the experimental data. However, the predicted response times were more than an order of magnitude higher than those observed.

The imaginary component of the Clausius–Mosotti term is typically used only in equations describing electro-rotation, which is the continuous rotation of a particle in the presence of a rotating electric field.[4] When there is a rotating electric field, it is necessary to consider the phase angle of $K_i^*$, which represents a (constant) phase lag between the applied electric field and the induced moment. Physically, the induced dipole lags behind the applied field by an angle related to the time necessary for the dipole moment to form as charge builds up at the particle–fluid interface. The angular velocity of the particle will vary from the angular velocity of the rotating electric field, and the particle will typically be rotating more slowly (due to

the viscous drag) than the surface charge on the particle that produced the induced dipole.

Since the conditions for PCLC flake reorientation include a linear electric field with which the induced dipole moment eventually aligns, we cannot assume a constant phase between these two vectors. However, the imaginary component also helps quantify the time required to induce the dipole moment, which might explain why using this term models the frequency-dependent behavior of the flake reorientation time so well.

The discrepancy between the predicted and observed reorientation times implies that either the viscosity of the host fluid is much lower or the *effective* electric field (to which the flake responds) is significantly larger than the applied electric field. The viscosity of propylene carbonate is well known, so it is possible that the effective electric field is larger. This possibility would imply that perhaps another electric-field–dependent term has not been considered in the expression for the electric torque.

## Summary

We have observed that flakes suspended in a moderately conductive host fluid, such as propylene carbonate, reorient about their longest axis to align the shorter major axis parallel to the applied electric field. This observation was contrary to most theories on particle reorientation, which predict that the longest axis will align with the applied electric field. We compared the components of the angular velocity about each axis, which include important parameters such as particle shape and host fluid viscosity, hypothesizing that the flake will rotate about the axis with the largest angular-momentum component. This approach was found to support our observations. Other standard characteristics of PCLC flake motion, such as the inverse quadratic dependence on the electric field and the tendency for longer, asymmetric flakes to reorient faster, were theoretically predicted and agreed with our experimental observations.

The frequency dependence of the flake reorientation time was difficult to model because it is unclear whether the real or the imaginary component of the Clausius–Mosotti term should

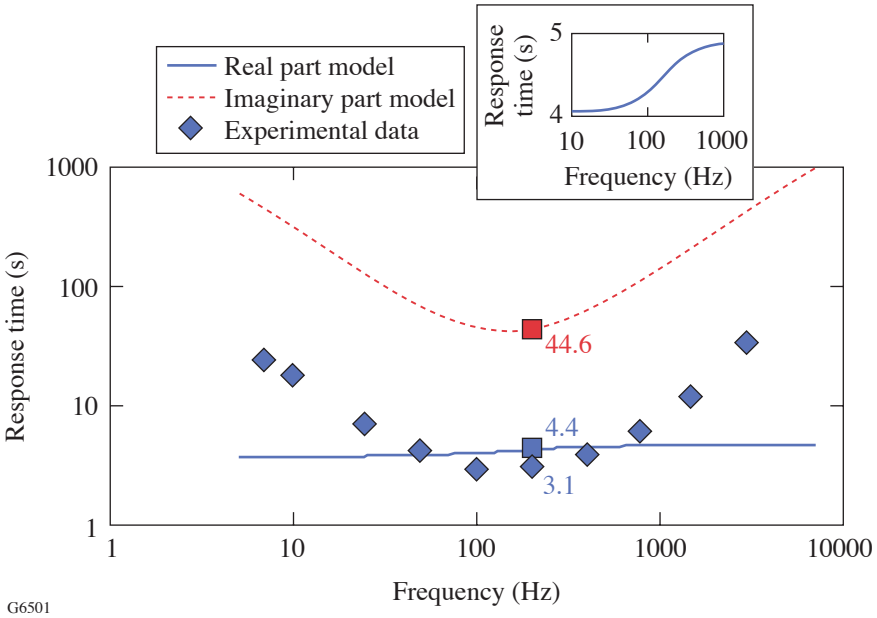


Figure 100.57
A comparison of experimental data and a theoretical model based on experimental parameters ($E_o$ = 20 mV/$\mu$m; $\eta_o$ = 2.9 cP; $\varepsilon_h \sim 69\ \varepsilon_o$; $\varepsilon_p \sim 2.89\ \varepsilon_o$; $\sigma_p < 10^{-12}$ S/cm) and estimated values ($\sigma_h \sim 10^{-6}$ S/m; $a_1$ = 35 $\mu$m; $a_2$ = 15 $\mu$m; $a_3$ = 5 $\mu$m). The open squares designate the theoretical values for comparison with the experimental data at 200 Hz. The insert shows the frequency dependence of the model that utilized the real component of the Clasius–Mosotti term on an expanded semi-log scale.

be used. Using the real component, which is a widely accepted approach, the model predicts reorientation times on the same order of magnitude as the observed reorientation times; however, the frequency dependence does not match the experimental data. This discrepancy is partially resolved by using the imaginary component in the model. The theoretical curve based on the imaginary component shows a minimum reorientation time at a specific electric-field frequency, which corresponds well with experimental data. This alternate method also predicts, however, reorientation times approximately an order of magnitude higher than what we observed. Future research will require investigating effects of electro-osmosis, double layers, and rotating electric fields. Similar frequency-dependent particle behavior has been observed when a rotating electric field causes a particle to rotate. The particle rotation results from a phase difference between the electric-field–induced polarization and the rotating field, thereby requiring theory to consider the imaginary component of the Clausius–Mosotti term.[14]

The ability to reorient, or switch, PCLC flakes provides a way to control their unique optical and polarizing properties with an electric field. Electro-optic devices based on switching PCLC flakes are useful in a broad class of applications in information displays, optics, and photonics. A PCLC flake device is of particular interest in the display industry (large-area signs, automobile dashboards, heads-up displays, and "electronic paper") because it easily provides both color and polarization without the use of filters and polarizers, which reduce brightness and add to the production cost. Possible applications in optics and photonics include switchable and tunable optical retardation or modulation elements for polarized light at any desired wavelength or bandwidth. It is also possible to produce conformal PCLC flake coatings for use in either decorative applications or military applications such as camouflage, document security, anti-counterfeiting, and object tagging and identification. Thus reorienting PCLC flakes has an unlimited number of potential applications, many of which have yet to be conceived.

## ACKNOWLEDGMENT

The authors would like to acknowledge the Laboratory for Laser Energetics at the University of Rochester for continuing support. This work was also supported by the U.S. Department of Energy Office of Inertial Confinement Fusion under Cooperative Agreement No. DE-FC52-92SF19460, the University of Rochester, and the New York State Energy Research and Development Authority. The support of DOE does not constitute an endorsement by DOE of the views expressed in this article.

## REFERENCES

*Flake motion in the silicone oil was observed only when dc fields were applied, whereby typical flake motion was random and uncontrolled. The system relaxation time was very long due to the low conductivity of the silicone oil host, which prevented a stable dipole moment from being induced.

1. J. A. Stratton, *Electromagnetic Theory*, 1st ed., International Series in Physics (McGraw-Hill, New York, 1941).

2. G. Schwarz, M. Saito, and H. P. Schwan, J. Chem. Phys. **43**, 3562 (1965).

3. A. Okagawa, R. G. Cox, and S. G. Mason, J. Colloid Interface Sci. **47**, 536 (1974).

4. T. B. Jones, *Electromechanics of Particles* (Cambridge University Press, New York, 1995).

5. J. Gimsa, Bioelectrochemistry **54**, 23 (2001).

6. R. D. Miller and T. B. Jones, Biophys. J. **64**, 1588 (1993).

7. R. D. Miller, "Frequency-Dependent Orientation of Lossy Dielectric Ellipsoids in AC Electric Fields," Ph.D. thesis, University of Rochester, 1989.

8. B. D. Bostwick and M. M. Labes, Appl. Phys. Lett. **45**, 358 (1984).

9. K. L. Marshall, T. Z. Kosc, S. D. Jacobs, S. M. Faris, and L. Li, U.S. Patent No. 6,665,042 B1 (16 December 2003).

10. E. M. Korenic, S. D. Jacobs, S. M. Faris, and L. Li, Mol. Cryst. Liq. Cryst. **317**, 197 (1998); S. M. Faris, U.S. Patent No. 5,364,557 (15 November 1994).

11. A. Trajkovska-Petkoska, R. Varshneya, T. Z. Kosc, K. L. Marshall, and S. D. Jacobs, "Enhanced Electro-Optic Behavior for Shaped Polymer Cholesteric Liquid Crystal (PCLC) Flakes Made by Soft Lithography," to be published in Advanced Functional Materials.

12. T. Z. Kosc, K. L. Marshall, S. D. Jacobs, J. C. Lambropoulos, and S. M. Faris, Appl. Opt. **41**, 5362 (2002).

13. Wacker-Chemie, Consortium für Electrochemische Industrie GmbH, Zielstattstrasse 20, D-81379, München, Germany.

14. W. M. Arnold and U. Zimmermann, J. Electrost. **21**, 151 (1988).

# LLE's Summer High School Research Program

During the summer of 2004, 16 students from Rochester-area high schools participated in the Laboratory for Laser Energetics' Summer High School Research Program. The goal of this program is to excite a group of high school students about careers in the areas of science and technology by exposing them to research in a state-of-the-art environment. Too often, students are exposed to "research" only through classroom laboratories, which have prescribed procedures and predictable results. In LLE's summer program, the students experience many of the trials, tribulations, and rewards of scientific research. By participating in research in a real environment, the students often become more excited about careers in science and technology. In addition, LLE gains from the contributions of the many highly talented students who are attracted to the program.

The students spent most of their time working on their individual research projects with members of LLE's technical staff. The projects were related to current research activities at LLE and covered a broad range of areas of interest including laser optics modeling, analysis of OMEGA implosion experiments, hydrodynamics modeling, cryogenic target characterization, liquid crystal physics and chemistry, materials science, the development and control of laser fusion diagnostics, and OMEGA EP laser system design and engineering (see Table 100.III).

The students attended weekly seminars on technical topics associated with LLE's research. Topics this year included laser physics, fusion, holographic optics, fiber optics, femtosecond lasers and their applications, computer-controlled optics manufacturing, and global warming. The students also received safety training, learned how to give scientific presentations, and were introduced to LLE's resources, especially the computational facilities.

The program culminated on 25 August with the "High School Student Summer Research Symposium," at which the students presented the results of their research to an audience including parents, teachers, and LLE staff. The students' written reports will be bound into a permanent record of their work that can be cited in scientific publications. These reports are available by contacting LLE.

One hundred and seventy-six high school students have now participated in the program since it began in 1989. This year's students were selected from approximately 50 applicants.

At the symposium, LLE presented its eighth William D. Ryan Inspirational Teacher Award to Mr. Claude Meyers, a former physics teacher at Greece Arcadia High School. This award is made to a teacher who motivated one of the participants in LLE's Summer High School Research Program to study in the areas of science, mathematics, or technology and includes a $1000 cash prize. Teachers are nominated by alumni of the summer program. Mr. Meyers was nominated by David Bowen, a participant in the 2001 Summer Program. "Claude Meyers impressed me as someone who was easily capable of being a college professor, or even a serious, doctorate-carrying researcher," David writes in his nomination letter. According to David, Mr. Meyers was an outstanding physics teacher with a deep love and understanding of physics, who was able to impart his students with excitement and respect for the principles of physics.

Table 100.III: High School Students and Projects—Summer 2004.

| Name | High School | Supervisor | Project Title |
|---|---|---|---|
| Daniel Balonek | Byron-Bergen HS | D. Jacobs-Perkins | Mechanical Characterization of Cryogenic Targets |
| Gregory Balonek | Byron-Bergen HS | S. Craxton | How Good Is the Bright-Ring Characterization of Cryogenic Target Uniformity? |
| Robert Balonek | Byron-Bergen HS | D. Lonobile | Design and Fabrication of a Handheld, Fiber Optic–Coupled, Coolant Water Flow Detector Test Fixture |
| Bruce Brewington | Fairport HS | S. Craxton | 3-D Characterization of Deuterium-Ice-Layer Imperfections |
| Daniel Butler | Brighton HS | R. Boni | Automated Focusing of the ROSS Streak Tube Electron Optics |
| Jeremy Chang | Penfield HS | M. Guardalben | Grating Compressor Modeling |
| Joseph Dudek | Honeoye-Falls-Lima HS | C. Stoeckl | Hexapods and Multiple Coordinate Systems |
| Laurie Graham | Bloomfield HS | S. Regan | Experimental Investigation of Far Fields on OMEGA |
| Jivan Kurinec | Rush-Henrietta HS | M. Bonino/ D. Harding | Material Properties of Spider Silk at Cryogenic Temperatures |
| Jonathan Kyle | Gates-Chili HS | J. DePatie | Two-State Motor Controller |
| Ted Lambropoulos | Pittsford-Mendon HS | J. Marozas | Optimal Pinhole Loading via Beam Apodization for OMEGA EP |
| Yekaterina Merkulova | Penfield HS | J. Delettrez | Spatial Distribution of the Reflected Laser Light at the Experimental Chamber Wall |
| Arun Thakar | Pittsford-Mendon HS | R. Epstein | Numerically Calculated Spherical Rayleigh–Taylor Growth Rates |
| Glen Wagner | Fairport HS | T. Kosc/ K. Marshall | Computer Modeling of Polymer Cholesteric Liquid Crystal Flake Reorientation |
| Tina Wang | Webster-Schroeder HS | V. Smalyuk | Modeling of X-Ray Emission in Spherical Implosions on OMEGA |
| Ariel White | East Irondequoit-Eastridge | K. Marshall | Photopatterning of Liquid Crystal Alignment Cells |

# FY04 Laser Facility Report

The OMEGA Facility conducted a record number 1558 target shots in FY04—a 13% increase over FY03—by operating extended shifts during select weeks to accommodate user demand (see Table 100.IV). Improvements to the Spherical Cryogenic Target Handling System increased system reliability and target positioning stability. More-complex planar cryogenic target assemblies were fielded including planar cryogenic $D_2$ cells for radiographic measurements of shock timing and cryogenic hohlraums for energy coupling and symmetry studies. Highlights of these changes and other FY04 achievements include the following:

- A total of 35 spherical and 35 planar cryogenic shots were performed. Eight spherical cryogenic target shots were conducted within one week in FY04, demonstrating increased system reliability. The rigidity of the lower pylon structure was improved, and electrically energized docking clamps were installed to increase the stability of cryogenic target alignment. This resulted in an approximately 2× improvement in the target offset at shot time for a series of 20 spherical cryogenic target implosions during Q2 and Q3.

- An improved multichannel IR streak camera (IR3) was installed and integrated into the OMEGA front end, enhancing pulse-shape measurement and prediction capability. This camera measures the temporal input to each of the three OMEGA driver lines, and its data are used in a system performance model that predicts the OMEGA output temporal pulse shape. The combination of the new streak camera's improved CCD camera, much shorter fiber signal delivery system, and the improved channel distribution on its photocathode resulted in a lower noise floor, higher bandwidth, and reduced channel crosstalk. An entirely recoded software user interface made it easy for the operators to use the streak camera. This new camera's enhanced performance was in large measure responsible for successfully fielding 80-ps, picket, low-adiabat pulse shapes used for both the imprint growth measurements on foam targets[1] and the cryogenic target implosion campaigns.

- Improved amplifier-gain-measurement hardware and gain-equalization procedures were implemented on OMEGA. Precision gain matching of all the amplifiers within a stage is crucial to obtaining on-target power balance objectives. OMEGA's harmonic energy diagnostic (HED) system was extended to measure the output of the driver lines, enabling simultaneous on-shot measurement of an amplifier stage's input and output energies. This provided absolute stage-gain-measurement capability and allowed the stage gains to be set to a predetermined value rather than just minimizing gain variance. This improved long-term stage-gain stability (see Fig. 100.58) and dramatically reduced the number of amplifiers that were being flagged for unnecessary maintenance. The more-efficient use of maintenance resources has resulted in their concentration on the worst-performing amplifiers.

- New target designs were also fielded to begin validation of the polar-direct-drive ignition concept proposed for the NIF. These included 40-beam, directly driven "Saturn" ring targets and 40-beam, directly driven CH cells. These were the first LLE experiments to combine symmetric illumination with radiographic diagnostics (backlighting).

- A new UV spectrometer was installed to measure the spectrum of all 60 beams with 0.02 to 0.07 Å of spectral resolution. The spectral data obtained from this instrument provided insight into *B*-integral effects on OMEGA's beamlines. Online spectral-based FCC tuning capability is planned for FY05.

- OMEGA conducted the first cryogenic gas hohlraum experiments for LLNL.

REFERENCES

1. "August 2004 Progress Report on the Laboratory for Laser Energetics, Inertial Confinement Fusion Program Activities," University of Rochester, Rochester, NY (2004).

Table 100.IV: The OMEGA target shot summary for FY04.

| Laboratory | Planned Number of Target Shots | Actual Number of Target Shots |
|---|---|---|
| LLE | 741 | 756 |
| LLNL | 405* | 431 |
| LANL | 150* | 168 |
| SNL | 20 | 31 |
| NLUF | 135 | 127 |
| CEA | 25 | 32 |
| NRL | 10 | 13 |
| Total | 1486 | 1558 |
| | | |
| LLE ISE | | 304 |
| LLE SSP | | 127 |
| LLE RTI | | 86 |
| LLE DD | | 69 |
| LLE LPI | | 60 |
| LLE CRYO | | 35 |
| LLE ASTRO | | 30 |
| LLE DDI | | 24 |
| LLE PB | | 21 |
| LLE Total | | 756 |
| * 20 shots in collaboration. | | |

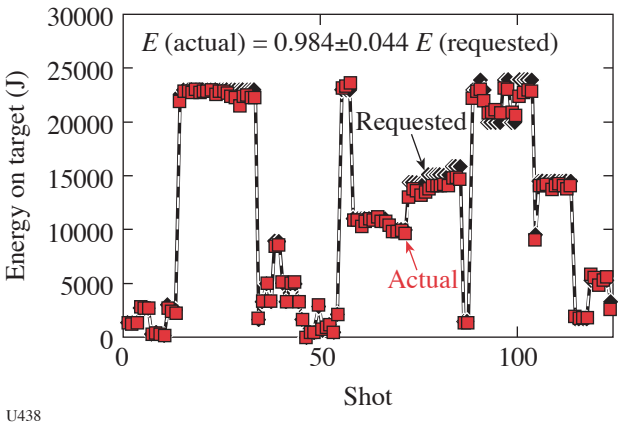


Figure 100.58
Record of requested and actual on-target energy for OMEGA shots in October 2004.

# National Laser Users' Facility and External Users' Programs

During FY04, 802 target shots were taken on OMEGA for external users' experiments, accounting for 51.5% of the total OMEGA shots produced this year. External users in FY04 included eight collaborative teams under the National Laser Users' Facility (NLUF) program as well as collaborations led by scientists from the Lawrence Livermore National Laboratory (LLNL), Los Alamos National Laboratory (LANL), Sandia National Laboratory (SNL), Naval Research Laboratory (NRL), and the Commissariat à l'Énergie Atomique (CEA) of France.

**NLUF Program**

FY04 was the second of a two-year period of performance for the nine NLUF projects approved for FY03–FY04 funding and OMEGA shot time. Eight of the nine NLUF campaigns received a total of 127 shots on OMEGA in FY04.

The Department of Energy (DOE) issued solicitations in FY04 for NLUF proposals for work to be carried out in FY05–FY06. DOE raised the available NLUF funding to $1,000,000 for FY04 proposals to accommodate the high level of interest in using OMEGA to carry out experiments of relevance to the National Nuclear Security Agency (NNSA) Stockpile Stewardship Program (SSP). NLUF participants use these funds to carry out experiments on OMEGA (including graduate student stipends, travel, supplies, etc.). The participants do not pay any portion of the OMEGA operating costs since these costs are funded directly by the DOE–LLE Cooperative Agreement.

A total of 16 NLUF proposals were submitted to DOE for consideration for FY05–FY06 support and OMEGA shot allocation. An independent DOE Technical Evaluation Panel comprised of Dr. Tina Back (LLNL), Dr. Robert Turner (LLNL), Dr. Steven Batha (LANL), Dr. Ramon Leeper (SNL), and Prof. Ani Aprahamian (University of Notre Dame) reviewed the proposals on 15 June 2004 and recommended that up to 8 of the 16 proposals receive DOE funding and 7 of the 8 teams be approved for shot time on OMEGA in FY05–FY06. Table 100.V lists the successful proposals.

**FY04 NLUF Experiments**

Programs carried out in FY04 by eight groups of NLUF participants included the following OMEGA experiments:

***Optical Mixing Controlled Simulated Scattering Instabilities (OMC SSI): Generating Electron Plasma Waves and Ion-Acoustic Waves to Suppress Backscattering Instabilities***
Principal Investigator: B. B. Afeyan (Polymath Research, Inc.)

The goal of this experiment is to examine the suppression of backscattering instabilities by the externally controlled generation of ion-acoustic-wave (IAW) or electron-plasma-wave (EPW) turbulence. The experiments consist of using optical mixing techniques to generate resonant waves in flowing plasmas created by the explosion of target foils by the OMEGA laser.

During FY04, experiments were conducted in which two blue beams as well as a blue beam and a green beam were crossed. Nineteen target shots were taken for this experiment in September 2004 using three new high-intensity-interaction-beam phase plates [known as continuous phase plates (CPP's)] designed by Sham Dixit of LLNL. They provided a near-$10^{15}$ W/cm$^2$ interaction-beam intensity for 1 ns with 500 J of blue-beam energy. The same design was used for a green-beam CPP. In addition, a polarization rotator was fielded on the probe beams of the pump–probe experiments so as to discriminate against processes that do not involve the ponderomotive force generated by the beating of the pump and probe beams directly. The results of these experiments will be described in future publications. The principal conclusion of this six-year-long effort with crossing blue–blue and blue–green beams on OMEGA is that OMC SSI via IAW's is a significant potential tool for the suppression of stimulated Raman backscattering SRBS in high-intensity laser–plasma interaction.

***Studies of Ion-Acoustic Waves (IAW's) Under Direct-Drive NIF Conditions***

Principal Investigator: H. Baldis (University of California, Davis)

Stimulated Brillouin scattering (SBS) is of concern to laser fusion using the indirect-drive or direct-drive approach. Generally, it is believed that SBS is only a minor effect for direct-drive inertial confinement implosion experiments, particularly those currently conducted on OMEGA. However, scattered-light spectra collected in these implosion experiments show changes from the incident spectra that can arise only from nonlinear effects such as SBS. To extrapolate the present results to future larger direct-drive laser fusion experiments, it is necessary to understand the details of the present observations.

To gain better insight into the underlying processes, a series of OMEGA shots was dedicated to measuring SBS in planar geometry with 11 low-intensity beams producing a plasma and one or two interaction beams at oblique incidence. One of the interaction beams was beam 30 for which there is a full-aperture backscattering station on OMEGA (FABS30). Beam 30 was incident at ~42° to the target normal. The target normal was pointed between the two interaction beams (beams 15 and 30). Thus the specular reflection from beam 15 was also collected by FABS30. In addition, one expects SBS side-scattering to be enhanced in the specular direction due to possible self-seeding of SBS by the specular reflection at the turning point of beam 15. There could be an additional contribution to the light collected by FABS30 from a synergistic interaction between beams 30 and 15 if they are present simultaneously.

All of these conditions are also encountered in spherical implosion experiments. In spherical implosion experiments, however, many different angles of incidence are present simultaneously and may contribute differently depending on the time during the laser pulse. This makes it difficult to unravel the subtleties of the interaction processes, hence the choice of the planar geometry for this series of experiments.

Table 100.V: FY05–FY06 Proposals.

| Principal Investigator | Affiliation | Proposal Title |
|---|---|---|
| J. Asay | Washington State University | Isentropic Compression Experiments for Measuring EOS on OMEGA |
| H. Baldis | University of California, Davis | Laser–Plasma Interactions in High-Energy-Density Plasmas |
| R.P. Drake | University of Michigan | Experimental Astrophysics on the OMEGA Laser |
| R. Falcone | University of California, Berkeley | NLUF Proposal: Plasmon Density of States in Dense Matter |
| R. Jeanloz | University of California, Berkeley | Recreating Planetary Core Conditions on OMEGA |
| P. Hartigan | Rice University | Astrophysical Jets and HED Laboratory Astrophysics |
| R. Mancini | University of Nevada, Reno | Three-Dimensional Study of the Spatial Structure of Direct-Drive Implosion Cores on OMEGA |
| R. Petrasso and C. K. Li | Massachusetts Institute of Technology | Implosion Dynamics and Symmetry from Proton Imaging, Spectrometry, and Temporal Measurements |

A typical purely sidescattered signal is shown in Fig. 100.59 for a 1-ns square pulse interaction beam at ~$2 \times 10^{14}$ W/cm$^2$ in beam 15 (beam 30 was not fired). Also shown in Fig. 100.59 for comparison is the input laser spectrum. We note that the basic features of this time-resolved spectrum are the same as for spherical implosions. The initial rapid blue shift reflects the increasing plasma column traversed by the interaction beam as the plasma is formed. This is followed by a return toward zero overall spectral shift as the plasma column becomes stationary. The important difference between the incident and reflected spectra is in the shape of the spectrum late in time, which is narrower with a peak on the red part of the spectrum, compared to the incident spectrum shown as reference on the right side of Fig. 100.59.

### *Experimental Astrophysics on the OMEGA Laser*

Principal Investigator: R. P. Drake (University of Michigan)

This NLUF project is led by the University of Michigan and involves collaborators from Lawrence Livermore National Laboratory; the Laboratory for Laser Energetics; the Universities of Arizona, Chicago, Princeton, and Stony Brook; as well as École Polytechnique and CEA from France. It uses OMEGA to study processes that are relevant to astrophysics, with a specific focus on the unstable nonlinear hydrodynamics that occurs when stars explode and on radiative shocks that occur during stellar explosions and in many other contexts. The experiments to study nonlinear hydrodynamics involved continuing examination of the role of initial conditions on the long-term nonlinear structure that develops after a blast wave encounters an interface. Data were obtained with a controlled variation of initial conditions and also to assess preheat levels. The experiments to study radiative shocks involved measurements of the change in shock velocity and structure with drive conditions and work to apply an improved diagnostic (a backlit pinhole) to obtain higher-resolution data.

Figure 100.60 shows a radiographic image from the radiative shock experiments, obtained using an area backlighter at 13.5 ns after the drive beams are fired. The grid and a fiducial feature establishing an absolute location are evident in the lower part of Fig. 100.60. The wall of the tube can be seen near the upper edge. The shock front is curved, and there are indi-

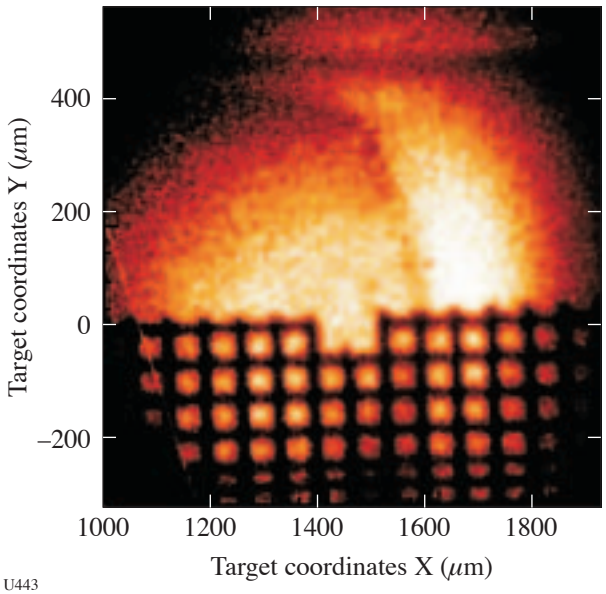


Figure 100.60
A radiographic image of collapsed radiative shock. This image is from an experiment with a polyimide drive disk attached to a polyimide tube of 912-$\mu$m inner diameter, irradiated (with SSD) at $9.3 \times 10^{14}$ W/cm$^2$ onto a 720-$\mu$m laser spot. The illumination was by x rays from Ti produced by overlapping six laser beams.

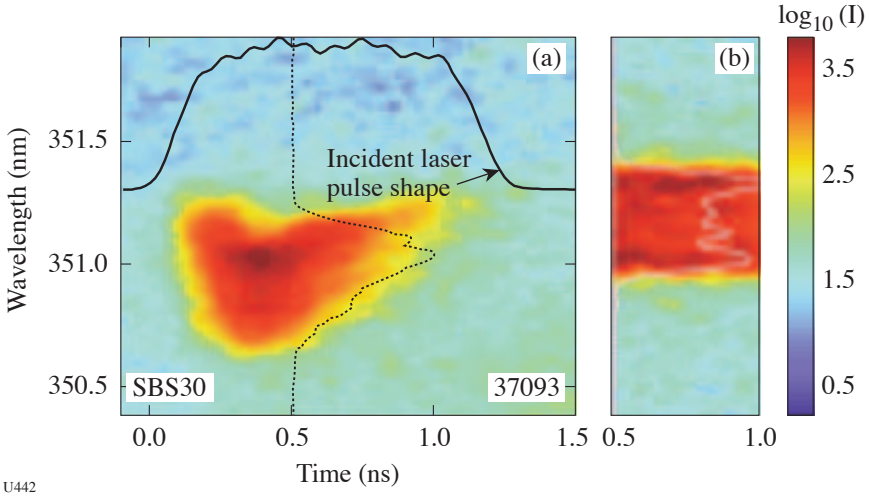


Figure 100.59
Stimulated Brillouin side scattering (a) from a planar plasma for an interaction beam at oblique (~42°) incidence at ~$2 \times 10^{14}$ W/cm$^2$. The plasma was simultaneously formed by 11 low-intensity laser beams. The incident laser pulse shape is shown as the dark line above the spectrum. A short but representative time slice of the incident laser spectrum is shown in (b). The vertical lineout through the spectra is also shown for both incident and reflected spectra.

cations of a trailing layer of dense xenon along the wall of the tube. The velocity and position of the center of the shock are within 10% of the values obtained from relevant 1-D simulations. The region of highest opacity is narrow, being 45 $\mu$m thick in this case. The layer of xenon produced by a nonradiative shock would be 140 to 220 $\mu$m thick at this location (depending on the exact equation of state). Thus, it appears that the density has increased another factor of 3 to 4 in consequence of radiative losses, reaching a total of 34 times the initial xenon density.

***Recreating Planetary Core Conditions on OMEGA***

Principal Investigator: R. Jeanloz (University of California, Berkeley)

During the past 18 months this team collected data on high-pressure $H_2$ and He fluids, combining diamond-anvil cells and laser-produced shocks (Fig. 100.61) to measure the first off-Hugoniot equation-of-state (EOS) data for both hydrogen (Figs. 100.62–100.64) and helium (Fig. 100.65) and to measure the highest-pressure EOS data ever for fluid helium. The

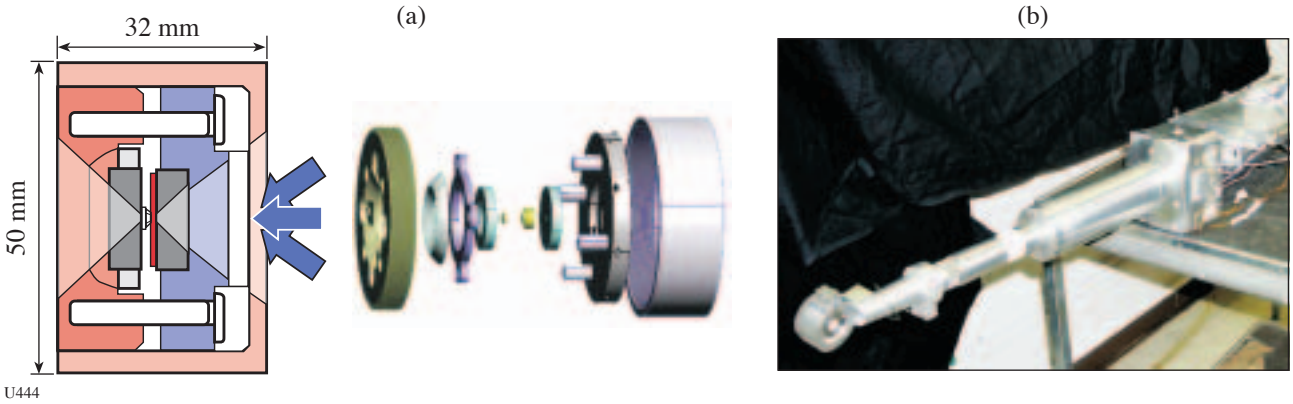


Figure 100.61
(a) Diamond-cell schematic and (b) photograph of target holder with diamond cell.

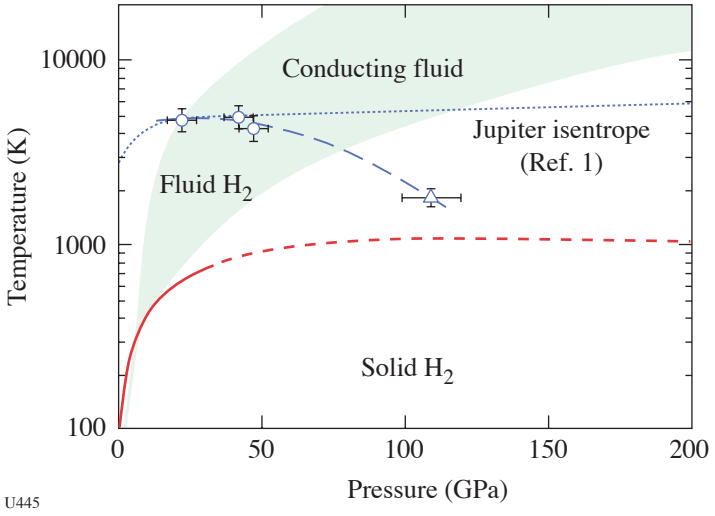


Figure 100.62
Phase diagram of fluid hydrogen, with results from laser-shock measurements on precompressed samples (circles with error bars) and reverberating-shock experiments (triangle with error bar) constraining the onset of conducting behavior with increasing pressure and temperature (dashed curve). The solid line (dashed where extrapolated beyond the pressure range of experiments) represents the determination of the melting curve of hydrogen, and the green area is the envelope of Hugoniot curves spanning the range from cryogenic hydrogen to hydrogen initially at 5 GPa

transformation of high-pressure helium from an insulator to an electronic conductor was observed [as documented by optical properties (Fig. 100.66)], and it was discovered that there is a correlation between the transition from insulating to conducting fluid phases of hydrogen and the proposed maximum in the melt curve.

A summary of how the new equation-of-state, reflectance, and temperature data impact our fundamental understanding of hydrogen is shown in Fig. 100.62. The open symbols show where, in T-P space, hydrogen is becoming electrically conducting, ~$10^{19}$e$^-$/cc; the conductivity saturates at slightly high pressure–temperature conditions, suggesting carrier concen-

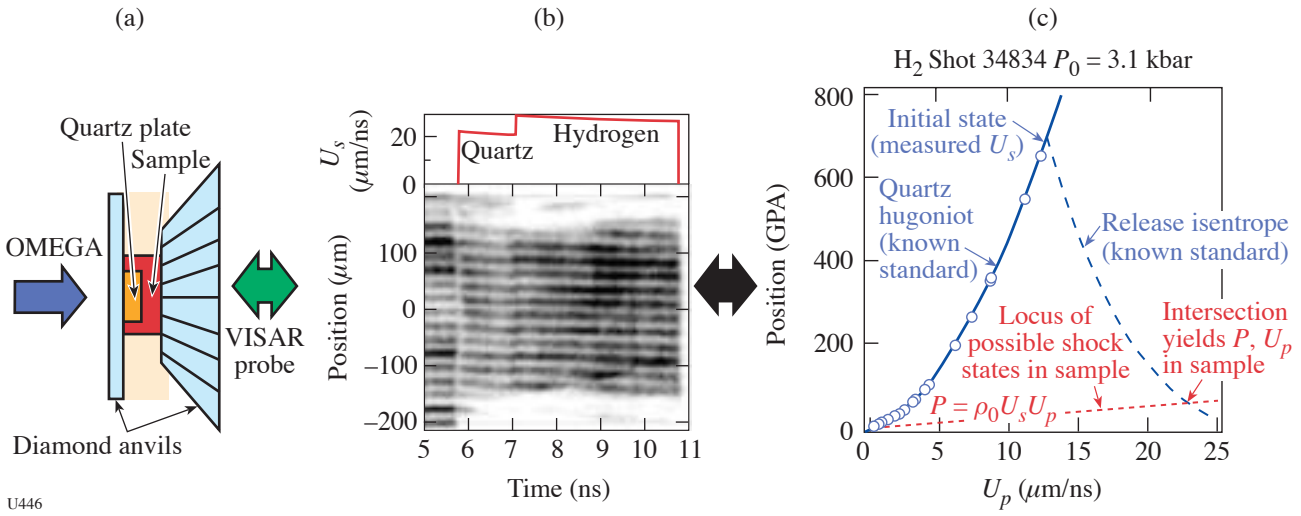


Figure 100.63
(a) Sketch of precompressed target, (b) sample VISAR record from precompressed $H_2$, and (c) example calculation for extracting pressure–density data. The beauty of this technique is that we observe the shock velocity in the quartz and the He or $H_2$ almost instantaneously, thus reducing much systematic and random uncertainties.

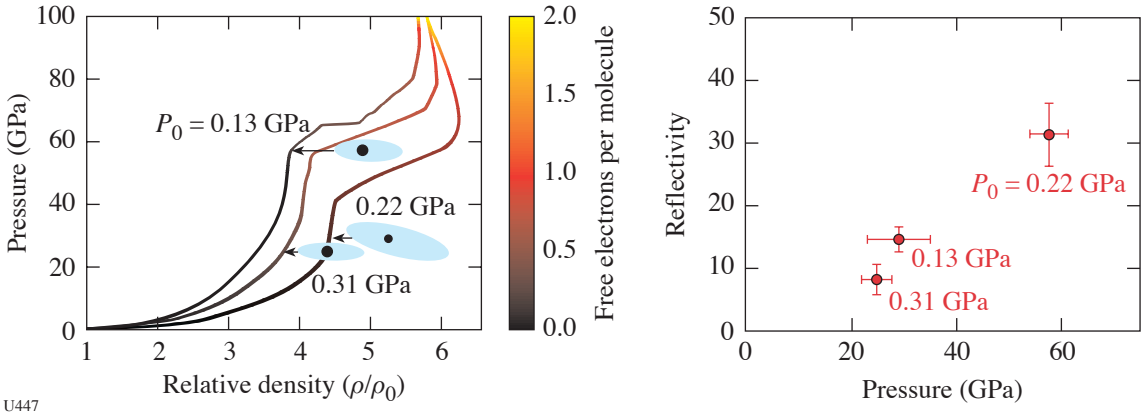


Figure 100.64
Measurements of shock density and optical reflectivity (532 nm) versus pressure for precompressed $H_2$.

trations near $10^{23}e^{-}$/cc. The line connecting the open symbols is very close to the theoretically predicted plasma phase transition, which is interesting, since in materials (such as carbon) that have a first-order liquid–liquid transition there is a maximum in the melt curve, as appears to be the case for hydrogen. Finally, note that this line also points to the single solid-state static experiment where conductivity is thought to be turning, or as evidenced by optical absorption above 310 GPa at 300 K. Each of these observations by itself is a notable result; all three represent a significant discovery.

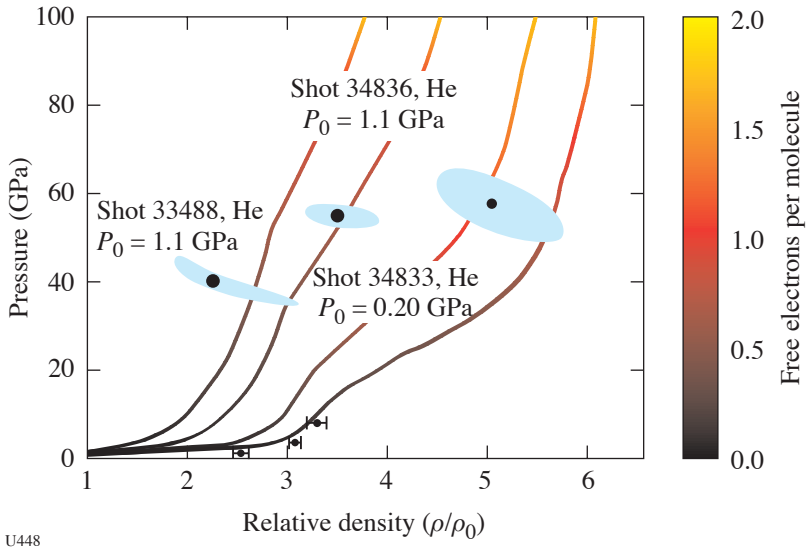


Figure 100.65
Pressure versus density shock-wave data for precompressed helium.

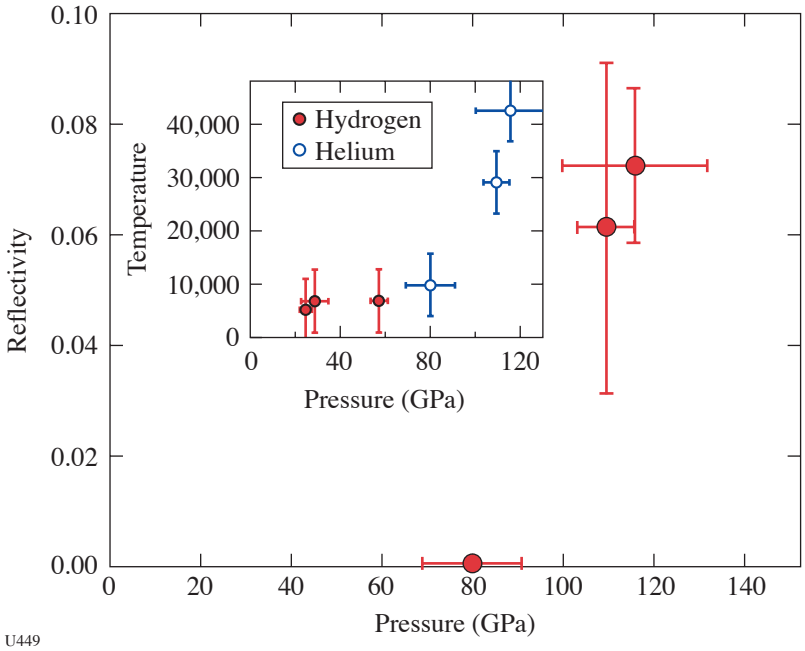


Figure 100.66
Shock reflectance at 532 nm as a function of shock pressure for He, with the inset showing the measured temperatures versus shock pressure for both He and $H_2$ data summarized in Figs. 100.64 and 100.65.

***Experimental and Modeling Studies of 2-D Core Gradients in OMEGA Implosions***

Principal Investigator: R. C. Mancini (University of Nevada, Reno)

During FY04, time-resolved (gated, $\Delta t$ = 50 ps) x-ray images of argon-doped implosion cores were recorded in OMEGA indirect-drive shots, based on line emission from $He_\beta$, $Ly_\alpha$, and $Ly_\beta$ line transitions in He- and H-like argon ions, respectively. Images were obtained simultaneously along two quasi-orthogonal directions [TIM2 and TIM3 line of sight (LOS)] with two Multi-Monochromatic Imager (MMI-3) instruments that record on framing cameras. Analysis of these image data permits the extraction of time-resolved information on the spatial distribution of temperature, density, and mixing in the implosion core. In turn, these results can be compared with a previous analysis done using time-integrated image data.

Figure 100.67 shows simultaneous $He_\beta$- and $Ly_\beta$-based x-ray-gated images of the implosion core recorded in OMEGA indirect-drive shot 36980 along the TIM2 LOS. These images are integrated over a time interval of 50 ps, close to the peak of x-ray emission. By implementing a generalized Abel inversion procedure, spatial distributions of line emissivity can be extracted from the data on several core slices perpendicular to the hohlraum axis and characterized by a coordinate along this axis. Analysis of these emissivity maps can be performed via a multi-objective search and reconstruction method driven by a genetic algorithm, and by an independent analytic method where temperature is extracted from emissivity ratio maps and density is subsequently determined from analysis of $He_\beta$ and $Ly_\beta$ emissivity maps. Figure 100.67 displays results for electron temperature and density radial distributions in a core slice through the hohlraum midplane. Additional information on spatial mixing profiles can also be obtained by looking at differences between relative intensity distributions in the data and those predicted by spectral modeling. These differences can be related to the amount of plastic mixed into the deuterium fuel and play an important role in the determination of the density profile. The temperature profile is relatively insensitive to this effect. Figure 100.67 displays this information in terms of $\gamma$, which is defined as the local ratio of plastic to fuel densities.

Work is in progress to include quantitative data from $Ly_\alpha$ images and to compare analysis results obtained along quasi-orthogonal LOS.

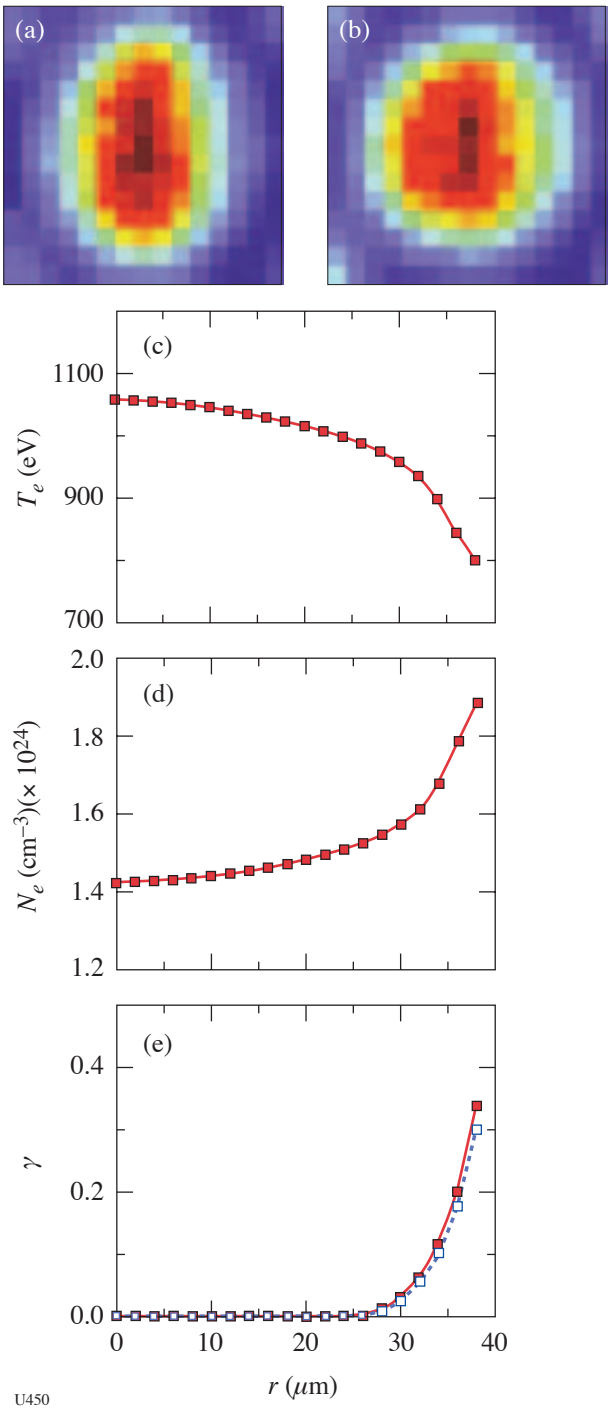


Figure 100.67
Simultaneous, time-resolved (gated, $\Delta t$ = 50 ps) x-ray images based on argon $He_\beta$ (a) and $Ly_\beta$ (b) line emission from OMEGA indirect-drive shot 36980. The hohlraum axis is along the horizontal direction. Radial spatial distribution in the core's midplane (perpendicular to the hohlraum axis) of electron temperature (c) and density (d), and mixing of plastic into the fuel (e). Analysis assumes an isobaric core.

***OMEGA Laser Studies of the Interaction of Supernova Blast Waves with Interstellar Clouds***

Principal Investigator: C. F. McKee (University of California, Berkeley)

In the NLUF Astro experiment a planar shock is driven by the OMEGA laser inside a cylindrical shock tube. The shock passes by a sphere that is more dense than the surrounding material (by about a factor of 9). The sphere material is "crushed" and set in motion; it rolls up in a classical Kelvin–Helmholz instability, then transitions to a fully 3-D flow through a Widnall instability. This experiment has been a pioneer in using backlit pinhole technology, and considerable efforts were made to make this technique work reliably (e.g., using tilted pinhole substrates, "destroyer beams," and target alignment using small corner reticles). By November 2003 the images could be obtained both reliably and with good signal-to-noise quality. Shots on 20 November were aimed at studying the shocked sphere material at late times (>60 ns after the start of the experiment), something that had never been done before. Experimental images (Fig. 100.68) showed sphere material being extensively shredded at these times, and by 80 ns the sphere material had reached the detectability limits for the very sensitive backlit pinhole technique, suggesting that the material is in a turbulent state by this time.

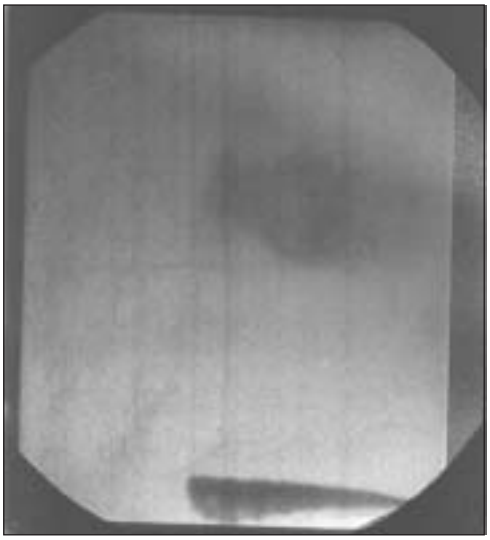

U451

Figure 100.68

Shocked sphere material 60 ns after the start of the experiment. Most of the sphere material makes up the bell-shaped object in the upper half of the image and has a volume more than 10 times larger than the original sphere (original sphere diameter 120 $\mu$m). Even with the high signal-to-noise ratio of the backlit pinhole technique, the sphere material is by this time quite diffuse; by 80 ns, it is no longer detectable. (The object in the lower half is a gold grid used as a spatial fiducial; one side of the image is approximately 1150 $\mu$m.)

The NLUF Astro experiment was awarded 15 shots (one and a half shot-days) on OMEGA during FY2004. One half-day of shots was carried out successfully on 20 November, but a full day of shots planned for 15 April could not be taken since other targets were given higher priority at LLNL's target fabrication facility.

***Time Evolution of Capsule ρR and Proton Emission Imaging of Core Structure***

Principal Investigators: R. D. Petrasso and C. K. Li (Plasma Science and Fusion Center, MIT)

During FY04 penumbral proton imaging was used to study the spatial distributions of D-D and D-$^3$He reactions in imploded D$^3$He-filled capsules on OMEGA. The imaging was performed with multiple cameras in which the recorder consists of stacked sheets of CR-39 nuclear track detector separated by ranging filters that result in the efficient detection of 14.7-MeV D$^3$He protons on one sheet and 3-MeV DD protons on another. The raw images were processed in two ways.

One approach was to assume that the emission distribution is spherical and to reconstruct a radial burn profile to study how the size of the burn region varies with capsule type and laser-illumination parameters. Figure 100.69 shows some data com-

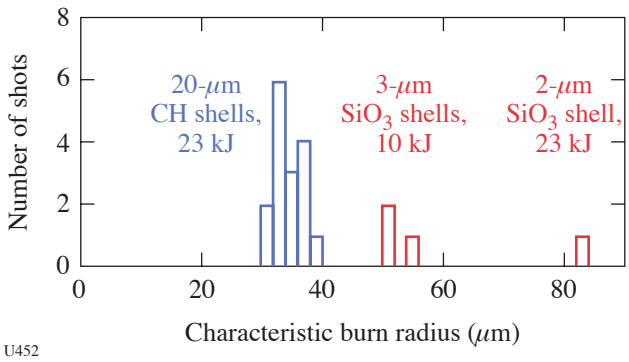


U452

Figure 100.69

The sizes of the D$^3$He burn regions in different types of implosions of D$^3$He-filled capsules (all capsules have 18-atm gas fills, and all laser pulses utilized SG3 phase plates). The burn profiles are nearly Gaussian, and the size is characterized by the radius at which the emissivity is down from the central value by 1/*e*. The thicker-CH-shell capsules implode with a higher convergence ratio than the thinner-$SiO_2$-shell capsules, resulting in smaller burn radii. The data point at 82 $\mu$m was obtained from an implosion with 23 kJ of incident laser energy, while the other $SiO_2$ data points had approximately 10 kJ of incident laser energy.

paring capsules with thin glass shells to capsules with thick CH shells. The thin-glass capsules clearly have a larger burn region and indicate less radial convergence at burn time.

The other approach was to reconstruct two-dimensional (2-D) images of the surface brightness of the capsule. There are now three cameras on OMEGA that can be used to image capsules from three orthogonal directions simultaneously for symmetry studies. Data from each are then used to reconstruct a 2-D map of surface brightness, and the three separate images provide information about three-dimensional (3-D) burn asymmetries. To study the relationship between illumination asymmetry and burn asymmetry, an experiment was performed recently with laser drive containing intentional P2 asymmetry. Laser intensity was reduced at the two poles of a symmetry axis, with the result that the capsule imploded with a prolate ("sausage"-shaped) asymmetry. Figure 100.70 shows the resultant burn asymmetry, measured with three orthogonally oriented proton-emission imaging cameras; one camera viewed the end of the sausage while the other two viewed the sides. A substantial elongation of the emission region is seen, with a ratio of about 3:1 between the long and short axes. The direction of the elongation is coincident with the axis of the illumination asymmetry. In addition, the data suggest that the emission is peaked at the two ends of the region, resulting in a "dumbbell"-like shape.

**FY04 LLNL OMEGA Experimental Program**

Lawrence Livermore National Laboratory (LLNL) conducted 431 target shots on OMEGA in FY04. Approximately half of the shots were for the High-Energy-Density Science (HEDS) Program, and the other half were for inertial confinement fusion (ICF) experiments. The ICF experiments are summarized as follows:

A campaign was initiated to examine the effect on a capsule of direct hydrodynamic pressure from the laser-heated fill gas in gas-filled hohlraums. Initial results (Fig. 100.71) showed that the backlit foamball surrogate gave good results at fill pressures above and below those ultimately desired. (This series will continue in FY05.) The interaction of a hohlraum gas fill during the hydrodynamically unstable deceleration phase was also measured; no substantial instability growth was observed, even from deliberately pre-roughened hohlraum surfaces (Fig. 100.72).

In the area of x-ray drive, experiments were continued with hohlraums constructed of a mixture of materials ("cocktails"), in an effort to optimize x-ray conversion efficiency, albedo, and also laser–plasma coupling. Currently, it is believed that the consistently lower-than-expected improvement in radiation temperature for cocktail hohlraums is due to low-$Z$ contaminants. Additional experiments were carried out to assess

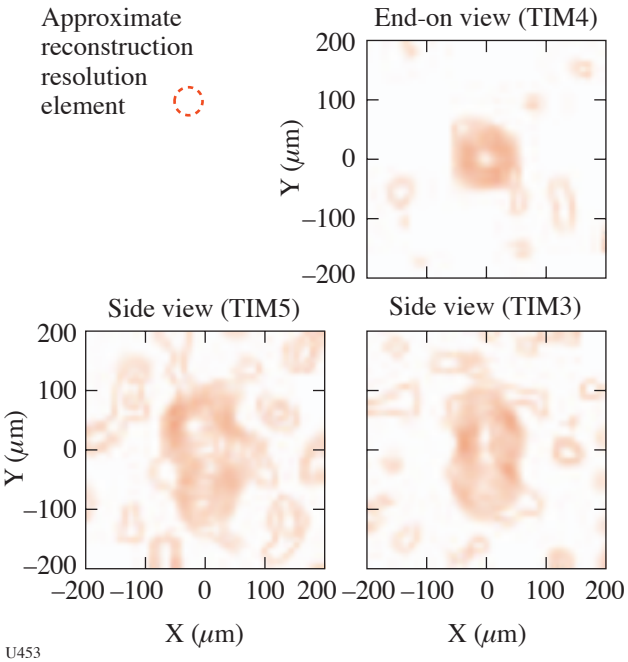


Figure 100.70
The first images of $D^3He$ nuclear burn in an asymmetric implosion. These three contour plots show nearly orthogonal views of the fusion burn region in OMEGA implosions 35172 and 35173, recorded by three proton-emission cameras operating simultaneously (data from the two implosions are summed). The burn asymmetry had a prolate, or "sausage," shape, resulting from intentional asymmetry in the laser drive. The target capsules consisted of 20 atm of $D^3He$ in 17-$\mu$m-thick CH shells, and the laser pulse delivered 17.5 kJ of on-target energy in a 1-ns square pulse. The laser intensity was lower than average in two directions 180° apart (on the TIM6–TIM4 axis), and the fusion burn is elongated in those directions. In the image reconstruction, bandwidth limitation for reducing noise resulted in an effective point-response function that is a Gaussian with ~20-$\mu$m radius; the dashed circle thus indicates the approximate reconstruction resolution.

the performance of lined or foam-filled hohlraums as alternates to the gas-filled National Ignition Facility (NIF) hohlraum point design. The early results are promising, showing radiation temperatures constant to within 5% between types of hohlraums and low levels of backscatter with smoothed beams at $5 \times 10^{14}$ W/cm$^2$.

Laser–plasma–interaction studies were done on large-scale-length plasmas created by preheating large gas-filled targets with the main laser (Fig. 100.73). Various experiments, some using a $2\omega$ or $4\omega$ probe beam, were conducted to obtain data on stimulated Raman scattering (SRS), stimulated Brillouin scattering (SBS), and beam propagation (Fig. 100.74) as functions of beam-smoothing level. The results show reduced beam spray and backscatter by using increased smoothing on a $2\omega$ probe beam. More crossing-beam power transfer experiments (a form of Brillouin scattering of special interest to the NIF) were performed as a function of polarization state (Fig. 100.75). Thomson scattering was used frequently to measure the electron temperature of these plasmas, while backscattered light (FABS) diagnostics monitored the amount of SBS or SRS. Still other experiments demonstrated the ability to measure the time-resolved spectrum of H- and He-like Ti (5-keV) x rays scattered by free electrons in a hot plasma; careful fits to the data yield temperature and density data (Fig. 100.76). Finally, a hohlraum experiment was conducted to quantify the amount of laser light that, at early times, is refracted from the hohlraum wall directly onto the implosion capsule.

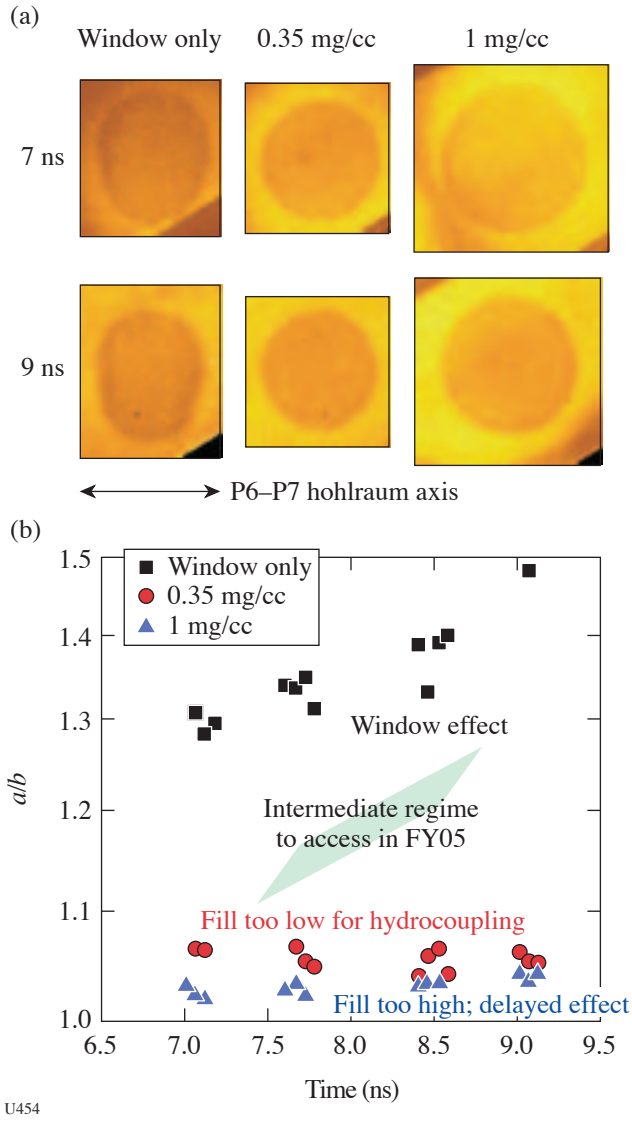


Figure 100.71
Backlit foam balls in CH (low-radiation)-gas–filled hohlraums are used to measure the gas-capsule hydrodynamic coupling. (a) Time-gated x-ray-backlit images of foam balls; (b) plot of foam-ball distortion versus time.

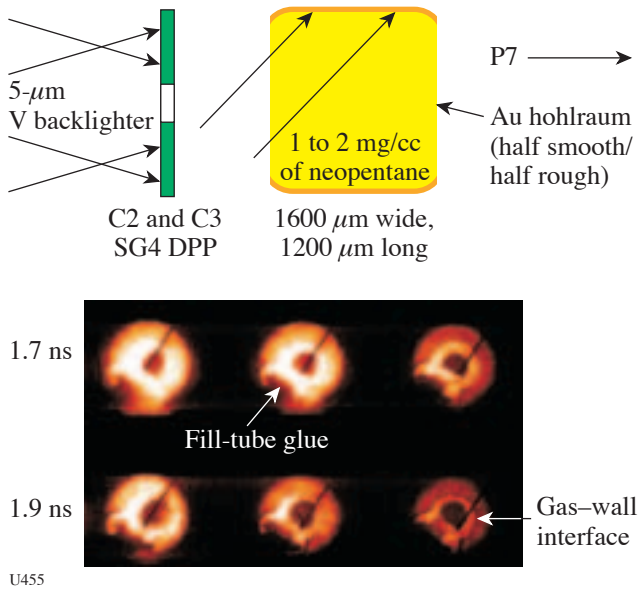


Figure 100.72
End-on view of an x-ray-backlit, gas-filled hohlraum shows wall motion and stagnation, with no signs of increased mix due to surface roughness.

Continued systematic improvements were made in using target-mounted pinholes to image implosion cores at moderately high (>7-keV) energies. Asymmetric core images were obtained at 87× magnification, demonstrating a method for measuring higher-order (up to 6, possibly 8) mode structure in the hohlraum drive (Fig. 100.77).

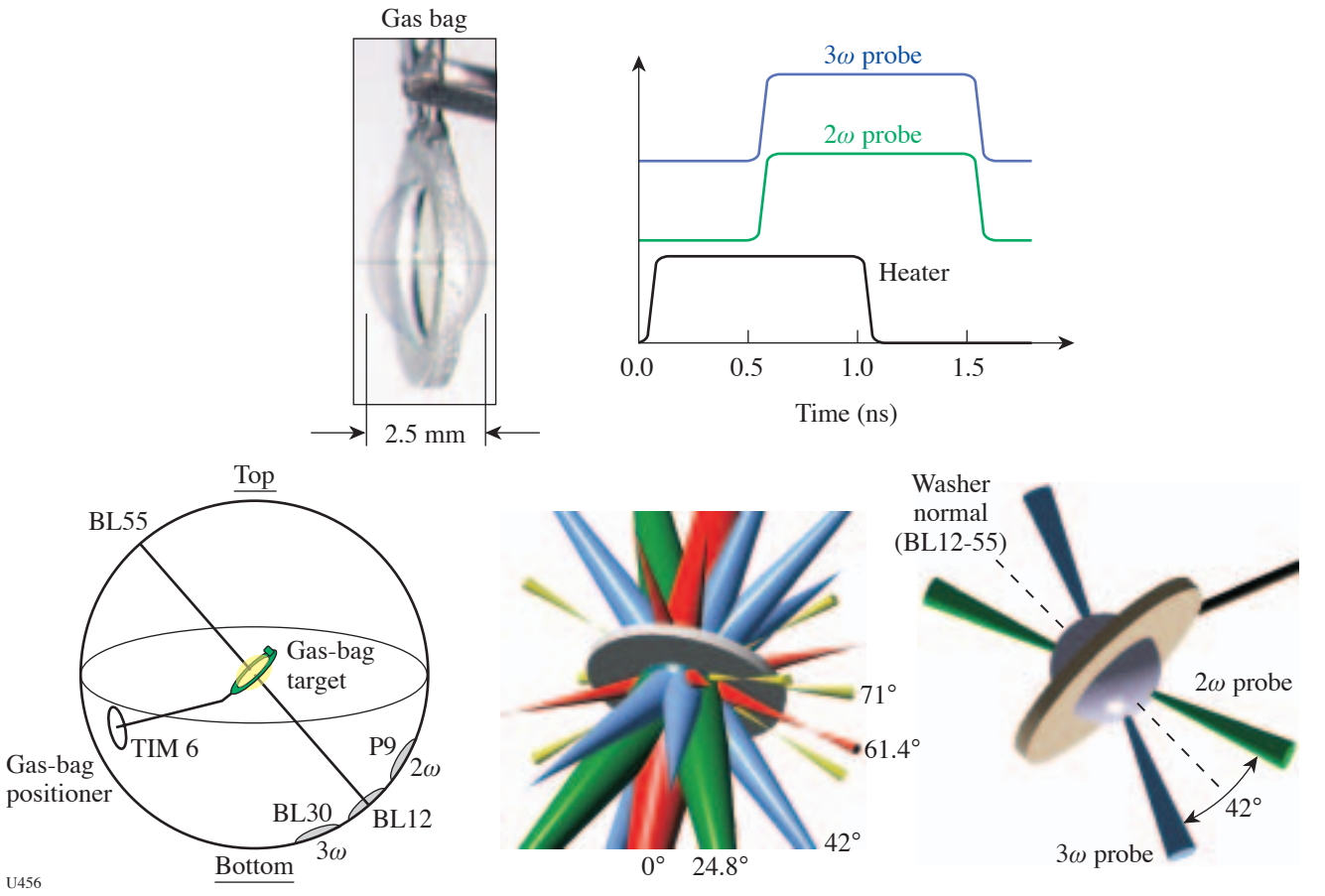


Figure 100.73
The LLNL laser–plasma interaction studies in FY04 used gas-bag targets to form large, well-characterized plasmas. The diagrams illustrate the target configuration used in these experiments.

New data were obtained on integrated hohlraum implosions with deliberately roughened capsules (Fig. 100.77). These experiments were performed with convergence ratios (CR's) of 15 and provide a stringent test for modeling hydrodynamic instabilities. These same experiments demonstrated a small difference in drive asymmetry—which resulted in a degradation in neutron yield—if the presence or absence of polarization rotators was not accounted for in the laser pointing.

Ablator material studies, focusing on the Rayleigh–Taylor growth factors, continued in FY04 on polyimide and brominated plastic (Fig. 100.78). The results confirmed greater-than-expected RM growth for the thinner samples, but as-predicted RT growth rates (Fig. 100.79). A new more-NIF-like, pulse-shaped, 2-D, symmetric, gas-filled halfraum experimental platform was designed for August 2004 shots. A first experiment was conducted to look at the effect of DT-fill tubes on an imploded capsule, using a deposited bump on the capsule as a surrogate for the fill tube.

Building on the work on hot hohlraums (see HEDS below), several implosion experiments were conducted using smaller-than-standard (3/4-size) hohlraums (Fig. 100.80). These represented the highest radiation-driven temperature implosions shot on laser facilities, reaching 275 to 285 eV, and producing symmetric cores. In some experiments $DHe^3$ supplied by LLE was used as the fuel; $DHe^3$ fusion proton yields and spectra were recorded and analyzed by MIT.

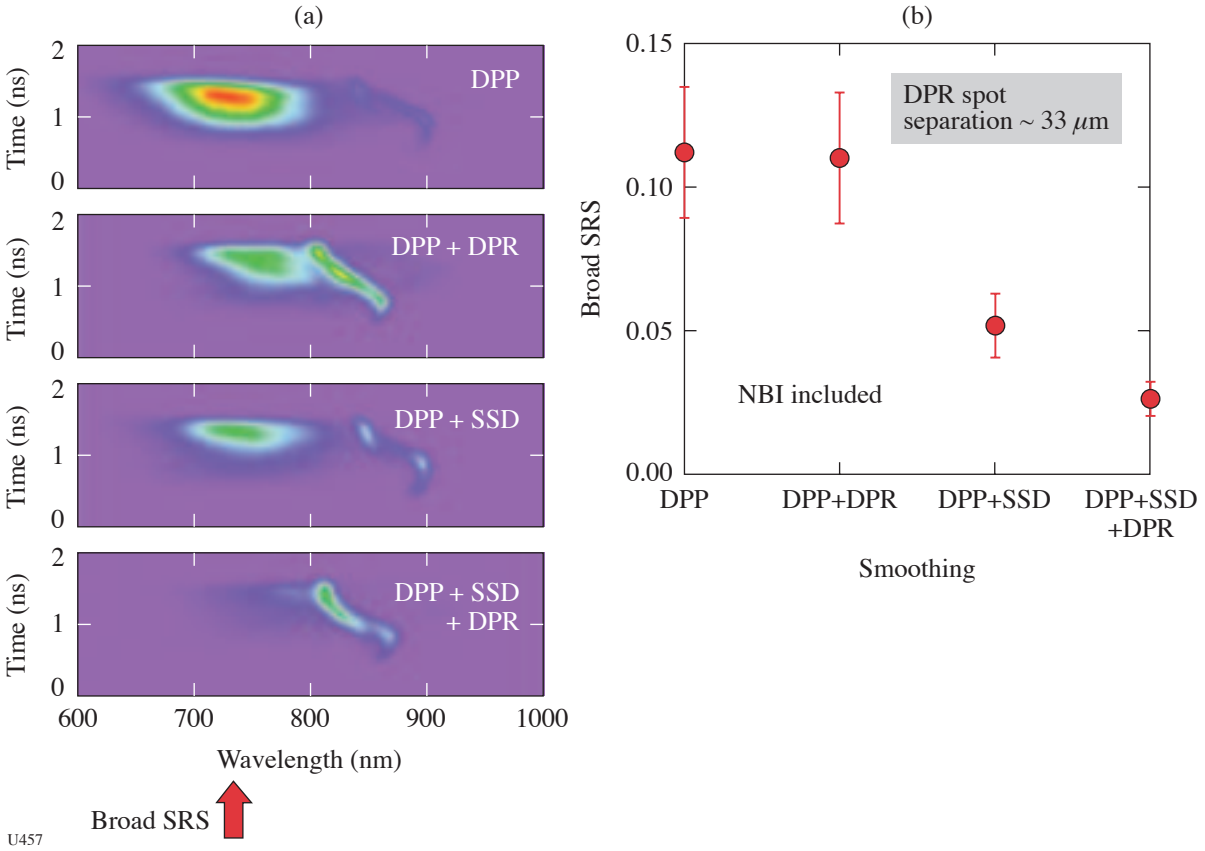


Figure 100.74
Laser-beam smoothing effectively reduces SRS in the low-density-plasma region. (a) Streaked SRS spectrum for four different laser irradiation beam-smoothing configurations. (b) Measured $2\omega$ SRS scattered traction for the four different beam-smoothing configurations.

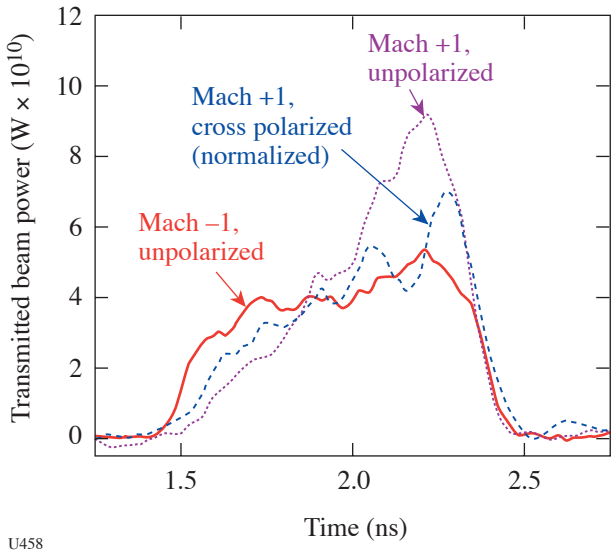


Figure 100.75
Crossed-beam experiments show energy transfer under the proper plasma flow conditions.

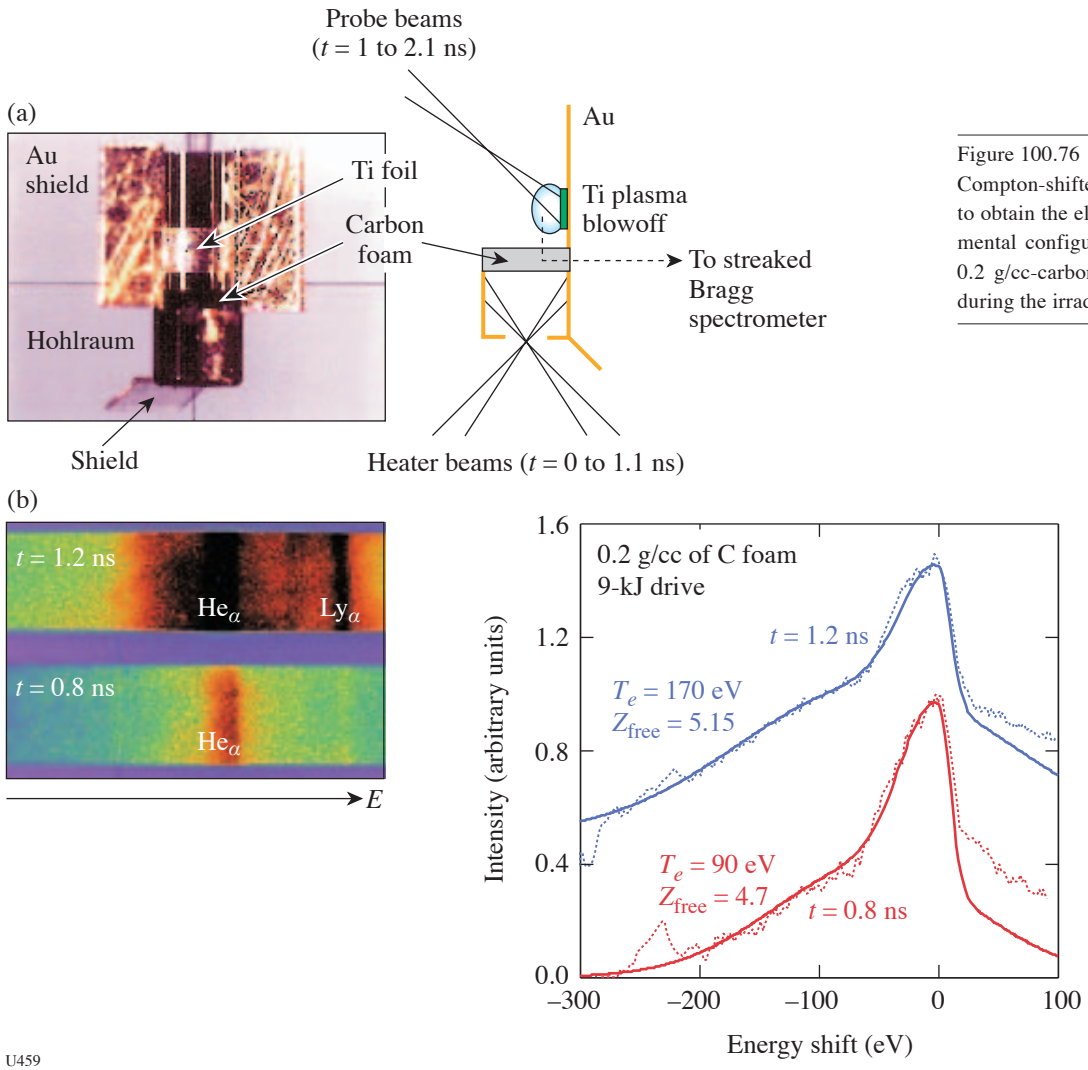


Figure 100.76
Compton-shifted scattered x rays are analyzed to obtain the electron temperature. (a) experimental configuration; (b) x-ray spectra from 0.2 g/cc-carbon foam at two different times during the irradiation.

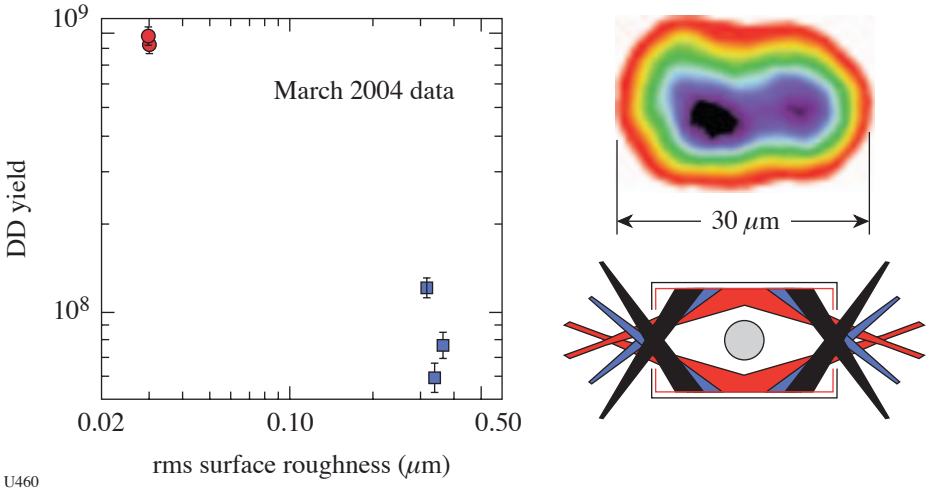


Figure 100.77
Neutron-yield degradation for implosions with a convergence ratio (CR) of 15 as a function of measured capsule-surface roughness. Also shown is a high-magnification x-ray image of an asymmetric imploded core, obtained at 8 keV.

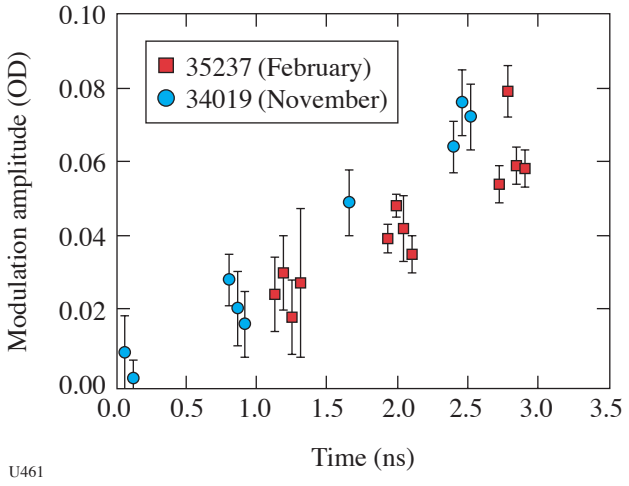


Figure 100.78
FY04 OMEGA polyimide Rayleigh–Taylor experiments measured the growth rate of hydrodynamic instabilities.

In collaboration with the University of Nevada, Reno (NLUF), multiple pinhole-imaged and spectrally dispersed data were obtained from indirectly driven, Ar-doped fuel implosions (Fig. 100.81).

Finally, several days of experiments were done in collaboration with LANL and LLE, using direct-drive, DT-filled targets, for the purpose of developing neutron diagnostics. These relatively high-yield shots have indicated that significant background will be present for any diagnostics or electronics that are neutron sensitive.

The other half of the LLNL shots were devoted to high-energy-density-science (HEDS)–relevant experiments. These are summarized as follows:

- Hot hohlraum experiments used hohlraums that were as small as possible to create as-high-as-possible radiation environments. Measurements were made on effective radiation temperature, high-energy ("suprathermal") x rays, and laser–target coupling.

- Equation-of-state (EOS) experiments continued on OMEGA in FY04. These involved VISAR measurements of shock propagation times in various materials. Other experiments focused on creating and using an adiabatic (shockless) drive (Fig. 100.82) to smoothly ramp up the pressure for EOS measurements of solid (not melted) materials (Fig. 100.83). Finally, experiments done in collaboration with an NLUF investigator used gases that were precompressed in a diamond anvil cell to explore equations of state relevant to the giant planets.

- OMEGA shots were also used to explore various options for obtaining x-ray point backlighters. It is expected this knowledge will be used on future OMEGA and NIF shots.

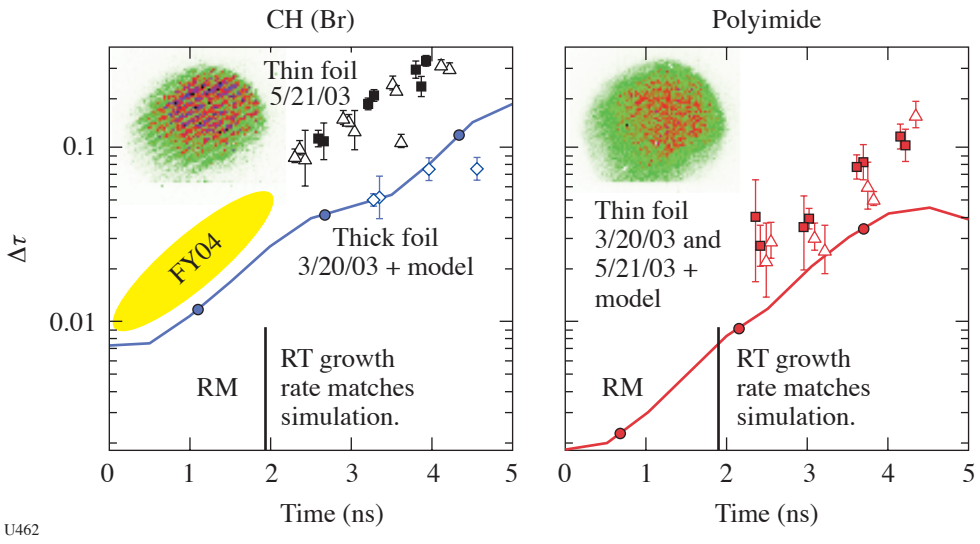


Figure 100.79
Plots of opacity versus time. The late-time data (~2 ns) show growth rates (slopes) consistent with the models, but a higher-than-expected growth during the early-time RM growth.

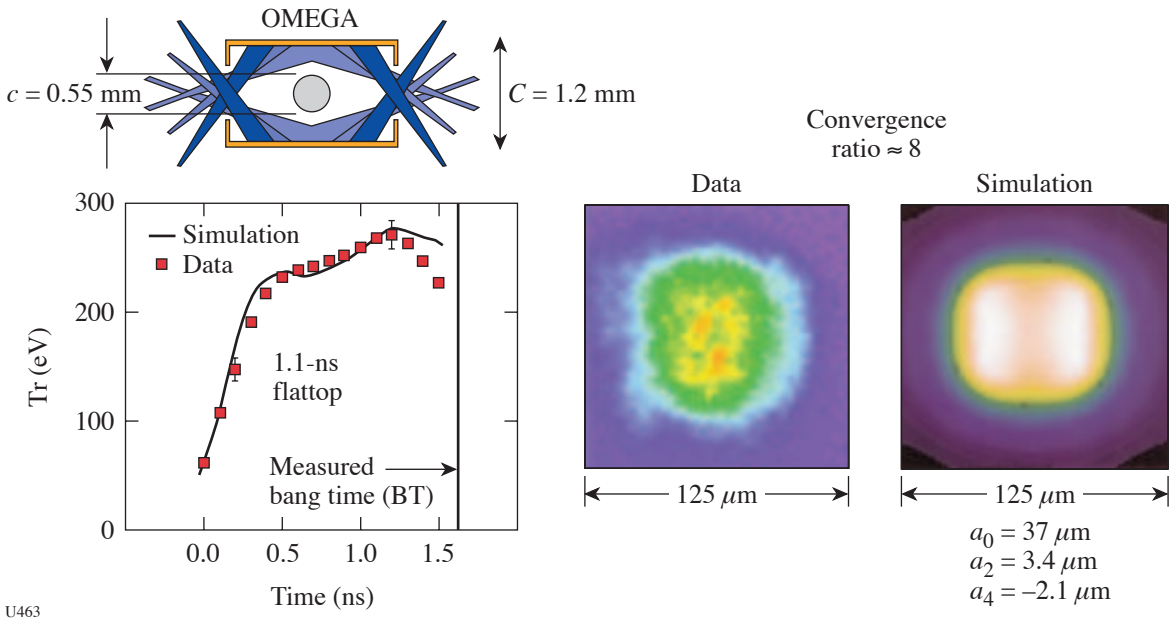


Figure 100.80
Low-convergence-ratio implosions in small, high-temperature hohlraums were used to confirm basic drive symmetry.

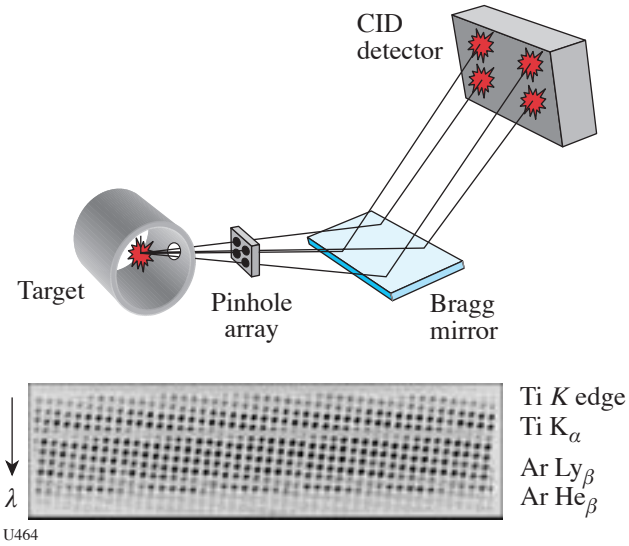


Figure 100.81
Geometry of spectrally dispersed imager used in NLUF experiments.

- A number of shots were devoted to studying alternative approaches to the standard indirect-drive concept of a simple hohlraum with a single-shell capsule. These included "dynamic hohlraums," where a high-$Z$ gas is directly driven and compressed and its resulting x rays are used to drive a second, concentric implosion capsule; and "double shells," where the first driven shell collides with an inner shell, resulting in implosion velocity multiplication.

- The radiation flow campaign continued in FY04, focusing on x-ray propagation through low-density foams.

- A series of experiments were conducted to develop appropriate backlighter sources and detectors to measure the opacity of warm materials. The results of this campaign are expected to be used on experiments in FY05.

- LLNL continued a collaboration with LANL and AWE (United Kingdom) on the "Jets" experiments, looking at large-scale hydrodynamic features.

- Finally, shots onto gas-bag targets were conducted with various mid- to high-$Z$ gases, in connection with developing x-ray sources (Fig. 100.84).

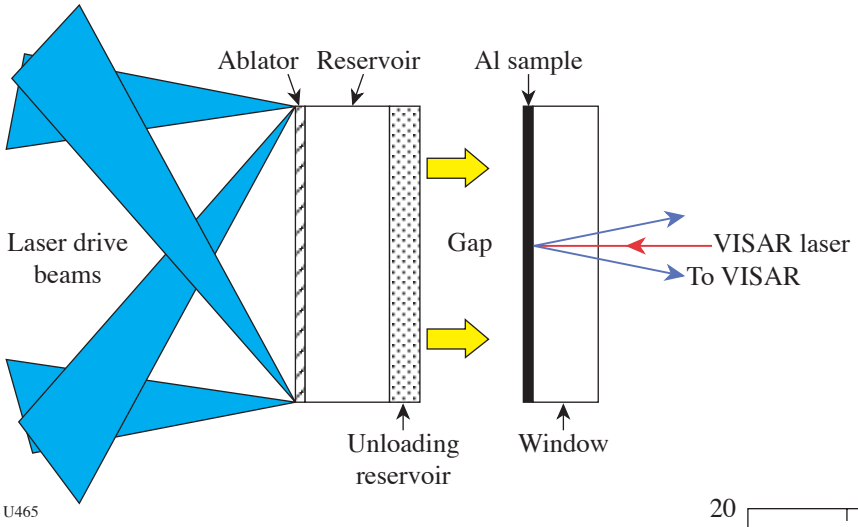


Figure 100.82
Experimental target setup used to produce smoothly increasing pressure drive for solid target physics.

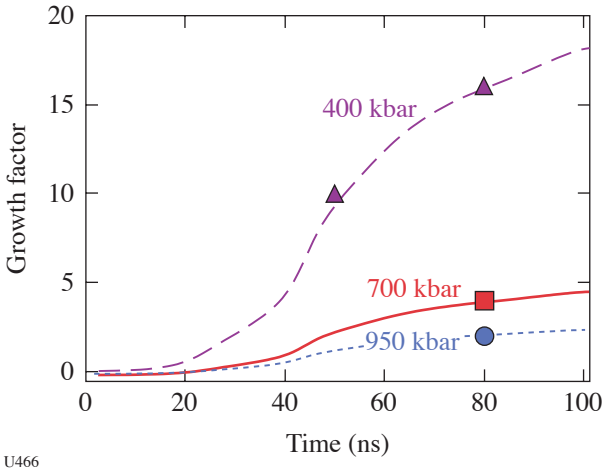


Figure 100.83
RT results for solid vanadium at three different pressures.

Targets:

Gas bag
Ar (0.1%) + $CH_4$ (99.9%)
$p$ = 0.5 atm
Bag o.d.: 2.8 mm
Washer o.d.: 4.5 mm
Transmission: >30%

Stopper
CH foil
Thickness = 100 $\mu$m
Diameter = 11.5 mm
Distance to gas-bag center = 2 mm

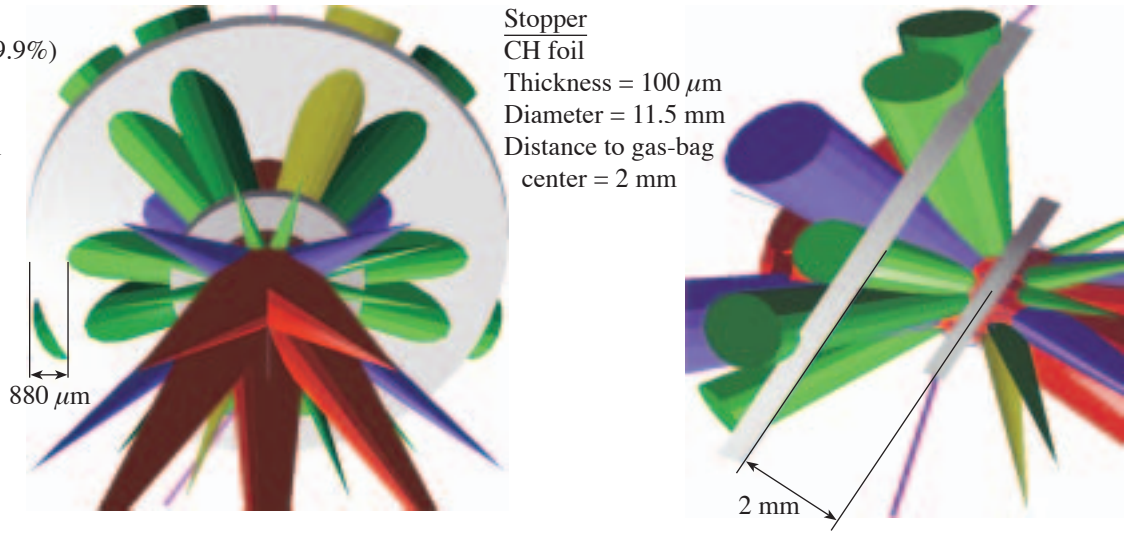


Figure 100.84
Ar-doped gas-bag targets used to measure conversion efficiency to x rays.

**FY04 LANL OMEGA Experimental Programs**

Los Alamos National Laboratory (LANL) fielded a wide range of direct-drive-implosion experiments in both spherical and cylindrical geometries during FY04. The primary emphasis of these experiments was to measure mixing in convergent geometries to understand basic hydrodynamic behavior that will help validate our inertial confinement fusion (ICF) codes. Direct measurements of the stability of grainy Be were performed as part of the national effort to characterize ignition-capsule ablator materials. Collaborations with LLNL, LLE, and AWE are an important part of LANL's program on the OMEGA laser at LLE. The Astrophysical Jets experiment and the development of the Burn-History diagnostic were continued with these collaborating institutions. LANL also fielded its first experiments designed specifically as staging experiments for future execution on the NIF. LANL conducted a total of 168 target shots on OMEGA in FY04.

*Time-Dependent Mix:* The time-dependent evolution of mix was measured by imploding $D_2$-filled, plastic ICF capsules. These capsules include a 0.1-$\mu$m-thick layer of titanium-doped plastic on the inside surface as a spectroscopic probe of the mix. Specifically, mixing of titanium into the $D_2$ fuel greatly enhances the intensity of the hydrogen-like Ti $\alpha$ line relative to the helium-like Ti $\alpha$ line because high temperatures consistent with the imploded fuel core (>2.5 keV) are required to populate the upper state of the hydrogen-like Ti $\alpha$ line. Therefore, the time evolution of the intensity ratio of the hydrogen-like Ti $\alpha$ line to the helium-like Ti $\alpha$ line is a strong indicator of the amount and timing of shell material mixing into the hot-core region of the fuel. The experimentally measured intensity ratio was up to 50% larger than that predicted by the simulations. This intensity ratio suggests that more mix is occurring in the center of the fuel region than that predicted by the mix model used in the simulation. We cannot, however, be certain of this because the simulations also predict lower temperatures than those measured by neutron time-of-flight data. The cause of the temperature discrepancy is still an open question that is being investigated.

In addition to spectral line information from the titanium, time-resolved spectroscopic measurements, data from x-ray time-gated-imaging diagnostics and neutron-yield diagnostics were also used as indicators of the level and timing of mix occurring within the imploding capsules. The gated x-ray images showed that even at the earliest time possible, near when the reflected shock first reaches the ablator and about 150 ps before peak burn, the images are not limb-brightened, but instead have a flat profile that later becomes centrally peaked. This profile indicates substantial mix at a time when other experiments have suggested little and backs up the observations in the intensity ratio of the $\alpha$ lines. Unfortunately, only a few images were obtained at times of interest near the burn with the x-ray framing cameras. The images showed indications useful for unique timing in future experiments (such as the outward expansion of the shock after peak burn, faint interference by gamma rays at peak burn, and the sudden brightening when the reflected shock first reaches the pusher layer).

Time-gated images (Fig. 100.85) show the full time history of the implosion with an interstrip time of 700 ps. The first strip shows the initial capsule size, the second strip shows the capsule imploding, the third strip shows the effect of the neutron emission at the implosion time, and the fourth strip shows an outgoing shock after the implosion.

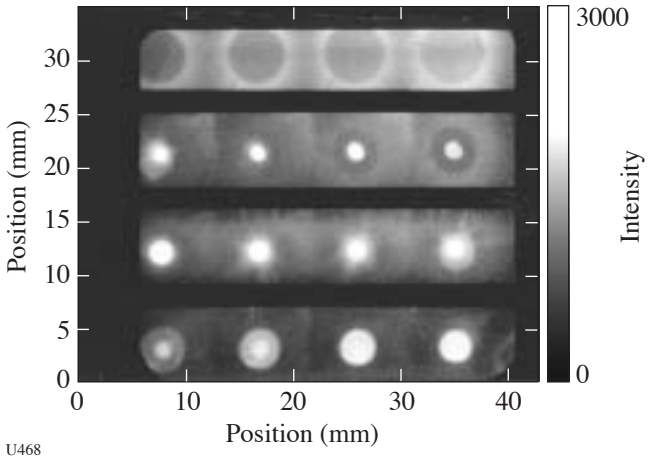


Figure 100.85
Time-gated x-ray images of a single capsule experiment showing both the implosion and explosion phases. Time runs from right to left and top to bottom.

*Double-Shell Implosions:* Imploding double-shell targets may provide an alternative, noncryogenic path to ignition on the NIF. Experiments are being pursued on OMEGA to understand the hydrodynamics of these implosions and the possibility of scaling to NIF designs. One line of inquiry this year measured the effect of foam structure on neutron yield. Carbon resorcinol foam [$C_6H_6O_2$], with cell sizes of a few nanometers, was used instead of the normal plastic foam with micron-size cells. Sixty beams with direct-drive symmetry imploded the capsules. As predicted, the smaller pores gave a measurably higher yield.

In other experiments, the zero-order hydrodynamic motion of the two shells was measured using a unique implosion scheme. Forty OMEGA beams were pointed at calculated offset distances from the center—not at the center of the capsule. The other 20 beams created two 6.7-keV backlighter sources to radiograph the shell locations. The use of a sulfur-doped CH marker layer allowed measurement of the implosion with good contrast. Four goals were attained: First, the implosion hydrodynamics were measured by backlit imaging. Radiography from two simultaneous directions was used to image and measure the hydrodynamics of capsules that were optically thin to the x rays from the backlighters at 6.7 keV. Second, neutron yield and x-ray emission were used to measure the output from the thicker capsules with two different foam compositions to assess the effect of foam cell sizes on the implosion. The carbon resorcinol foam was found to increase the yield, as in the 60-beam shots, but the early results indicate little observable effect on the hydrodynamic behavior. Third, investigations were carried out to find out whether a thin layer of plastic overcoat would help separate the effect of absorption at the seam of the outer capsule from the seam hydrodynamics. However, the target quality was not good enough to allow the observation of a measurable difference. Fourth, the radius versus time of the sulfur marker layer was measured for the implosion of Au-coated and uncoated targets to determine the difference in the implosion due to the gold *M*-band x rays that exist in some of the NIF-design ICF capsules. The results were in good agreement with one-dimensional simulations (Fig. 100.86) although little difference was observed between the coated and uncoated targets.

*Burn-History Diagnostic Development:* In collaboration with LLNL, LANL continued to develop diagnostics that record the temporal behavior of the fusion burn. Gamma rays are a by-product of the deuterium–tritium (D-T) reaction. Using our two Gas Cerenkov Detectors (GCD's) (Fig. 100.87), these gamma rays are converted to relativistic electrons that emit Cerenkov radiation, which is then recorded. The prototype instrument, GCD1, records the emission using a photomultiplier tube and fast oscilloscope. The newer instrument, GCD2, records the information with higher time resolution using a streak camera.

During high-neutron-yield DT and deuterium–deuterium (DD) experiments conducted by LLE, both the GCD's and the LLE Neutron Temporal Detector were successfully operated simultaneously for the first time. Much cleaner and stronger signals were obtained with the streaked GCD2 (Fig. 100.88). These higher-quality signals allowed a GCD2 sweep rate of 10× for the gamma-burn signal. Quality GCD1 results were also obtained for most implosions.

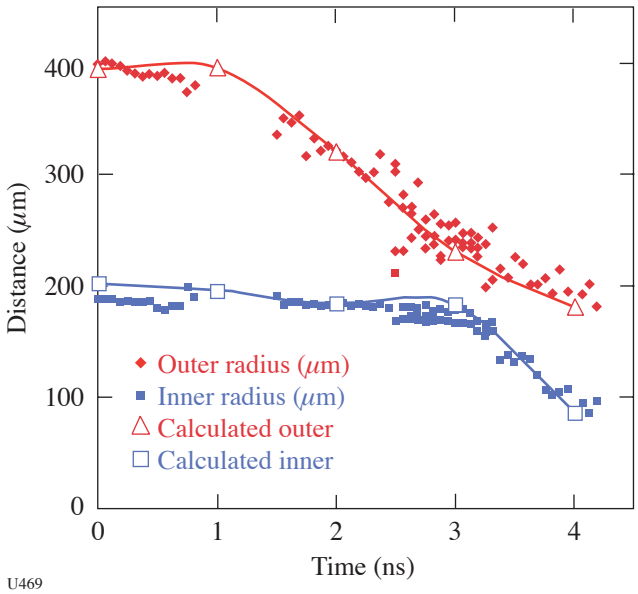


Figure 100.86
The temporal behavior of the outer and inner shells shows the momentum transfer between the two shells at about 3 ns. One-dimensional simulations are in good agreement with the measurements.


Figure 100.87
The GCD pressure cell and light-collecting optics are shown without the streak camera recording system.

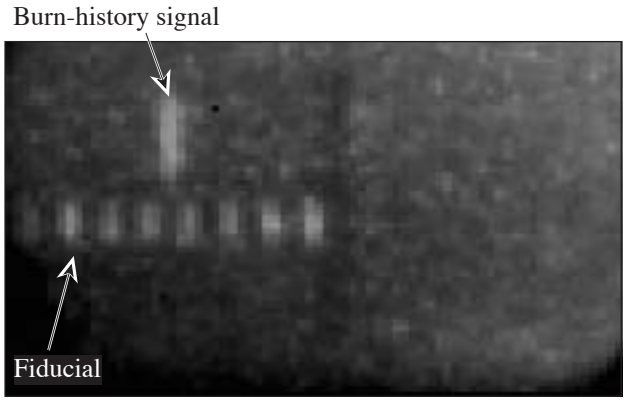


Figure 100.88
The time-resolved burn-history signal from a high-yield implosion demonstrated a 280-ps time resolution.

The feasibility of simultaneously recording a fusion gamma ray and fusion neutron signals using both the GCD1 *and* GCD2 was also successfully demonstrated; this simultaneous recording is an essential step in establishing the feasibility of a dual-mode capability in a single diagnostic. This recording was accomplished by placing either fused-silica glass or lead glass behind the normal converter foil and producing a *gas* Cerenkov signal and a *glass* Cerenkov signal on any given implosion. The neutron-burn signal was strong enough to allow a GCD2 sweep rate of 3×.

*Beryllium Ablator Microstructure Stability (BAMS):* An LANL goal is to deliver a specification for the microstructure of ignition-capsule ablators to the National ICF Program. The current focus is on beryllium–copper ablators, but other materials may be investigated as well.

LANL experiments make VISAR observations of ~1-Mbar shock waves in beryllium–copper samples, DANTE measurements of hohlraum temperature (verifying 6-ns-long composite pulses from OMEGA), x radiography of perturbations in samples, and characterization of the spectra from aluminum backlighters. In addition, LANL scientists also successfully recorded backlit ("side-lit") x radiographs of beryllium–copper samples viewed from the side, allowing a determination of the trajectory of the samples' motions. This permits one to make inferences about the radiation drive accelerating the samples, independent of the DANTE and VISAR data.

Another experimental series returned time-dependent data of the emission spectra of aluminum backlighters typical of those used in radiography of beryllium–copper samples. The relative contribution of line and continuum radiation was measured as a function of incident laser intensity to improve the contrast in our radiographs of intentionally perturbed samples and eventually in future radiographs of microstructure-perturbed samples.

*Cylinder Implosion:* Significant progress was made toward understanding the effect of convergence on shock-driven instability growth [Richtmyer–Meshkov (RM) instability] and initiated experiments that address variable acceleration (Rayleigh–Taylor) instability growth. Both types of instability can adversely affect ICF capsule implosions. High-quality data were also acquired on re-shock of already developing mix layers and defect–shell interactions. The primary effect of convergence on the single-mode RM instability is to postpone or suppress the growth of secondary instabilities resulting in an extended period of linear growth, well beyond that expected and observed in planar geometry.[2] The linear growth for several sinusoidal initial perturbations is shown in Fig. 100.89. Approximate linear growth is observed for amplitude-over-wavelength ratios as large as 4. The mechanism(s) responsible for the observed behavior has not been identified; however,

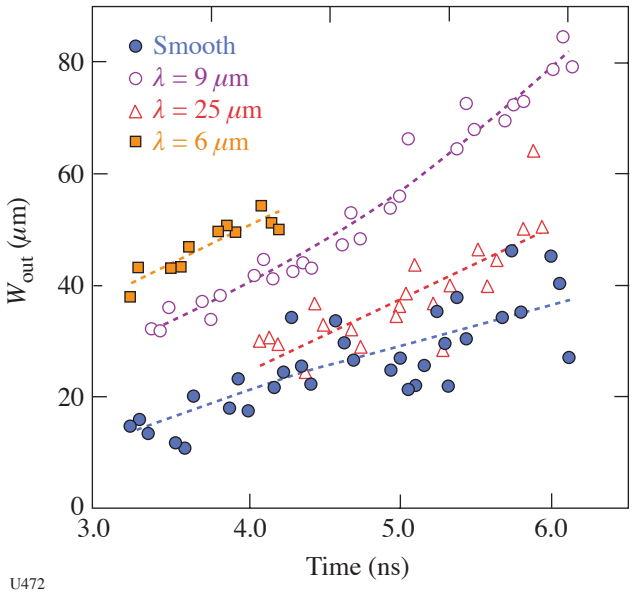


Figure 100.89
The growth of the mix layer width $W_{out}$ for sinusoidal perturbations with an initial amplitude of 2 $\mu$m varies with the wavelength of the perturbations.

the apparent postponement of saturation is a dramatic example of the effect of convergence. To date, comparisons with computational (*RAGE*)[3] results have yielded qualitative agreement, but quantitative differences are still being addressed. The transition to turbulent mixing for short-wavelength ($\lambda \leq 2.5$-$\mu$m), multimode perturbations was also identified. Again, the apparent effect of convergence is to prolong linear growth for extended periods rather than the power-law-growth behavior observed in planar geometry. The short-wavelength results are being used to verify and validate the BHR model[4] in *RAGE* and to provide guidance in implementing crenulative (convergence) effects in the BHR turbulence model.

*Off-Hugoniot Stability:* The initial proof-of-principal experiments for the Off-Hugoniot Stability project were conducted this year. The goals of the integrated experiments were to evaluate whether radiography provides sufficient resolution of interface locations and to demonstrate that sufficient heating can be applied to generate hydrodynamic motion. The wedge experiments were designed to characterize the tin preheat source. Two experimental packages were employed: an integrated target [Figs. 100.90(a) and 100.90(b)] and a wedge target [Fig. 100.90(c)].

Both target types returned data that surpassed expectations. Five shots using integrated targets successfully captured the temporal expansion of the heated epoxy into the foam. Measurements were made at 2, 3, 4, 6, and 8 ns after the heating drive beams turned off. Figure 100.91(a) shows the epoxy layer at 3 ns with a final resolution between 15 and 20 $\mu$m, confirming that the experimental design provides sufficient measurement accuracy to meet the physics objectives of the campaign.

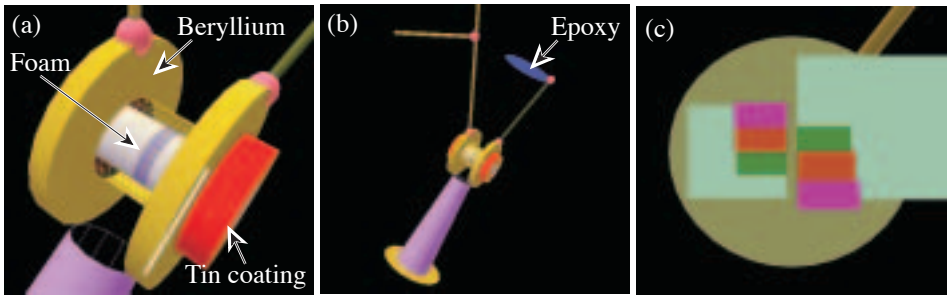


Figure 100.90
(a) The integrated target consists of a beryllium assembly, stuffed with epoxy and foam layers. A thin coating of tin is directly driven by 33 beams to produce *L*-shell emission that heats the package. (b) The integrated target showing backlighter foil and view shield. (c) The wedge target measures the transmission of tin *L*-shell emission through wedges of epoxy and beryllium and facilitates an accurate measure of the *L*-shell–emitted flux.

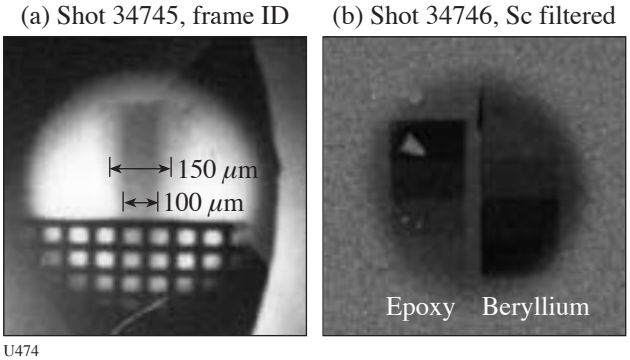


Figure 100.91
(a) Radiograph of the epoxy layer 3 ns after the start of tin *L*-shell preheat. At this time, only 60% of the epoxy is still near full density. (b) The flat-field transmission of tin *L*-shell emission through the epoxy (left) and beryllium (right) wedges.

In addition to the success of the integrated experiments, the wedge targets along with extensive spectroscopic measurements were very effective at characterizing both the spectral nature and conversion efficiency of the tin *L*-shell emission. Figure 100.91(b) shows the tin *L*-shell transmission through characterized epoxy and beryllium wedges. These data suggest that about 2% to 5% of ultraviolet laser energy on target is converted to the tin *L* shell.

*Astrophysical Jets:* The jet project is a collaboration between LANL, AWE, and LLNL designed to verify and validate turbulence models for astrophysical simulations in our radiation-hydrodynamic codes. The jet target consists of a titanium foil mounted to a washer. A low-density, 0.12-g/cm$^3$, resorcinol-formaldehyde (RF) foam is mounted to the rear side of the titanium washer. The laser beams strike the titanium foil and drive a titanium jet into the foam. The primary diagnostic is x radiography of the titanium jet in the foam.

High-quality radiographs using new noise-mitigation techniques were obtained. These measurements included placing a 4-$\mu$m-thick CH coating on the drive side of the titanium foil. In addition, a large gold shield was mounted to the front of the target that prevented x rays from the coronal plasma created by irradiating the titanium foil from reaching the x-ray detector. The background problems of the past were reduced with a new "spot-backlighter" design of a small square (200 $\mu$m) of vanadium, surrounded by CH. The low-atomic-number (low-*Z*) plasma that is created by the backlighter laser beams helps contain the vanadium blowoff and reduces the spatial extent of the high-energy background. The backlighter images the target orthogonally to the direction of jet propagation.

The temporal evolution of the jet was captured at three different times. The result from one of these times, 400 ns after the laser drive, is shown in Fig. 100.92(a). There is a great level of detail in the image. For example, refractive effects are observed at the bow shock edge [Fig. 100.92(b)] and also mixing between the titanium and the RF foam is apparent in Fig. 100.92(c).

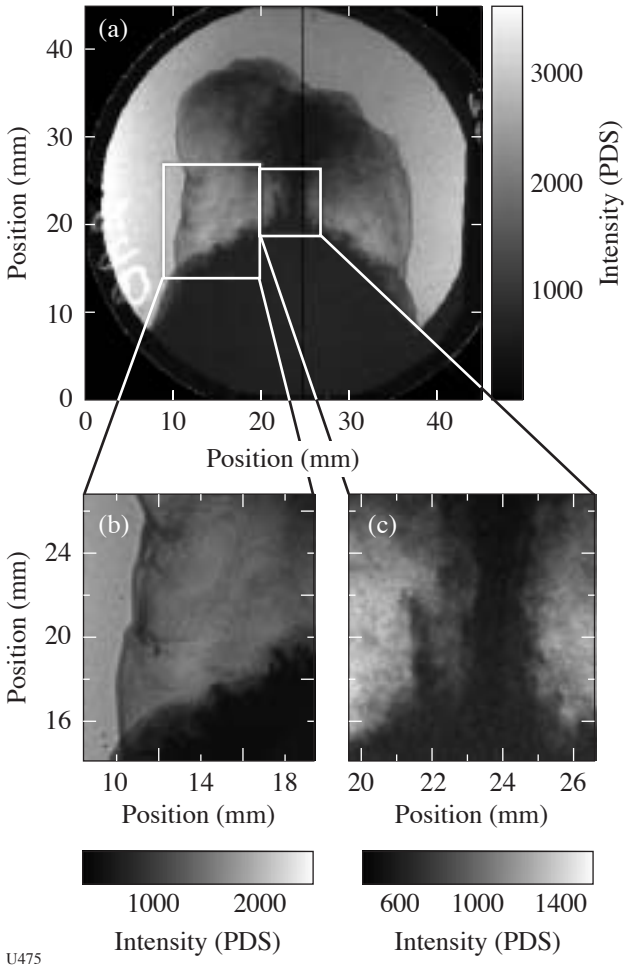


Figure 100.92
(a) Radiograph of the jet at 400 ns, magnified by a factor of 12. The jet stem is well collimated. The base (or pedestal) of the jet shows signs of hydrodynamic-instability growth. (b) Detail of the image showing the edge of the bow shock. Refractive enhancement of the bow shock is seen. (c) Detail of the jet stem showing the mixing between the titanium and the RF foam due to the Kelvin–Helmoltz instability.

*Hohlraum Filling:* Experiments on the NIF will use much more energy to heat a hohlraum of approximately the same size as an OMEGA hohlraum. An important constraint on the NIF experiments is how long the material will have to evolve before the hohlraum fills with gold from the wall of the hohlraum itself. A short series of experiments determined the amount of wall material influx in a hohlraum experiment and the effect of mitigation techniques on the radiation temperature achieved.[5]

It was found that coating the inner surface of the hohlraum with a 0.5-$\mu$m-thick layer of parylene would inhibit the amount of gold reaching the center of the hohlraum while decreasing the radiation temperature by only about 10 eV. Further experiments, however, showed that the number of hot electrons produced via laser–plasma interactions increased tremendously as measured by the level of hard x rays measured.

*Backlighter Yield Measurements:* The conversion efficiency of laser light into x-ray energy from titanium- and zinc-flat-disk targets was measured. These experiments were accomplished in half-day increments due to the simplicity of their configuration. Six drive beams illuminated the flat disks from one side using 1-ns square pulses. The number of beams and the focal-spot diameter were varied to produce orders-of-magnitude changes in the laser-irradiance conditions. Measurements were taken with framing cameras, streak cameras, and static pinhole cameras; however, the primary diagnostic was the Henway spectrometer [a time-integrated, x-ray-film–based survey spectrometer (Fig. 100.93)]. Every shot produced high-quality data that are currently being analyzed to determine the scaling of x-ray conversion efficiency as a function of laser irradiance. These results will be used to develop and refine area and point-backlighter configurations for OMEGA and future NIF experiments.

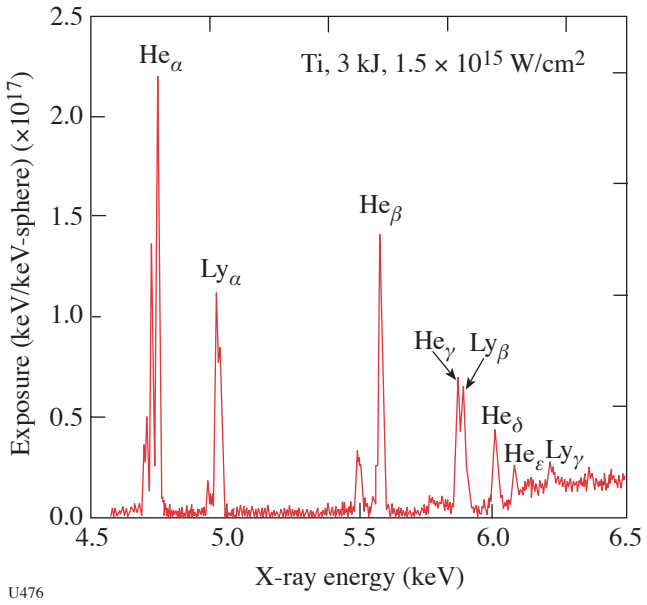


Figure 100.93
Example of data taken with the Henway spectrometer of the emission from a flat titanium target. Signals will be integrated over the helium-$\alpha$ emission line to determine conversion efficiency into bright line emission for future backlighter configurations.

## FY04 SNL OMEGA PROGRAMS

SNL carried out 31 target shots on the OMEGA laser in FY04 and also participated in several of the campaigns led by other laboratories. The SNL-led campaigns included the following:

*Modification of a Laser Hohlraum Spectrum via a Mid-Z Wall Liner:* A typical laser hohlraum has a radiation spectrum that includes a significant component of non-Planckian, high-energy photons (such as Au *M*-band x rays) that originate in and near the hot, low-density coronal plasma in which the laser light is absorbed and converted into x rays. These hard x rays can have undesirable effects for an ICF application, such as causing preheat ahead of the shock front in the ablator of an indirect-drive capsule.[6] One concept for tailoring the spectrum in a hohlraum is to employ a thin, mid-*Z* liner to supply plasma for the x-ray conversion, with an underlying high-*Z* wall for x-ray containment. In a recent series of laser hohlraum experiments performed on OMEGA, this concept was demonstrated by employing a thin (0.5-$\mu$m) Cu liner on the interior of an Au-walled hohlraum to significantly soften the radiation spectrum and yet retain the peak hohlraum temperature of a standard Au hohlraum. As shown in Fig. 100.94(c) and 100.94(d), this successful result was evident in the data from the DANTE array of *K*- and *L*-edge filtered x-ray photocathodes.[7] A 280-nm Streaked Optical Pyrometer[8] was used to confirm that the preheat ahead of the shock front in a CH ablator was significantly reduced when using the Cu-lined hohlraum, as compared to an ordinary hohlraum [Fig. 100.94(b)].

*The Effectiveness of Mid-Z Dopants in Reducing Preheat in Indirect-Drive ICF Ablator Materials:* In previous work,[6,9] we experimentally verified that mid-*Z* dopants can be used to significantly reduce preheat and shock temperature in low-*Z*, indirect-drive ICF ablator materials. The previous experiments with Ge-doped CH ablators were done with dopant concentrations of 2% (atomic) Ge. As shown in Fig. 100.95, FY04 experiments have demonstrated that a significantly lower dopant concentration (0.5% atomic Ge in CH) can also be effective for reducing shock temperatures and preheat levels in indirect-drive ablators.

*Long-Pulse Au Hohlraum Wall Albedo Measurements:* In previous work,[10] measurements of absolute hohlraum wall albedos for ignition foot drive temperatures were made for pulse lengths of up to 1.5 ns. In FY04, we began work to extend the albedo measurements to longer pulse lengths and achieved albedo measurements for pulse lengths of ~3 ns. Two experimental arrangements were used in the long-pulse albedo experiments: a secondary hohlraum driven by x rays from a single primary hohlraum [Fig. 100.96(a)], and a secondary hohlraum driven by x rays from two primary hohlraums [Fig. 100.96(b)]. The secondary hohraum temperature history is shown in Fig. 100.97(a), and the new extension of the Au

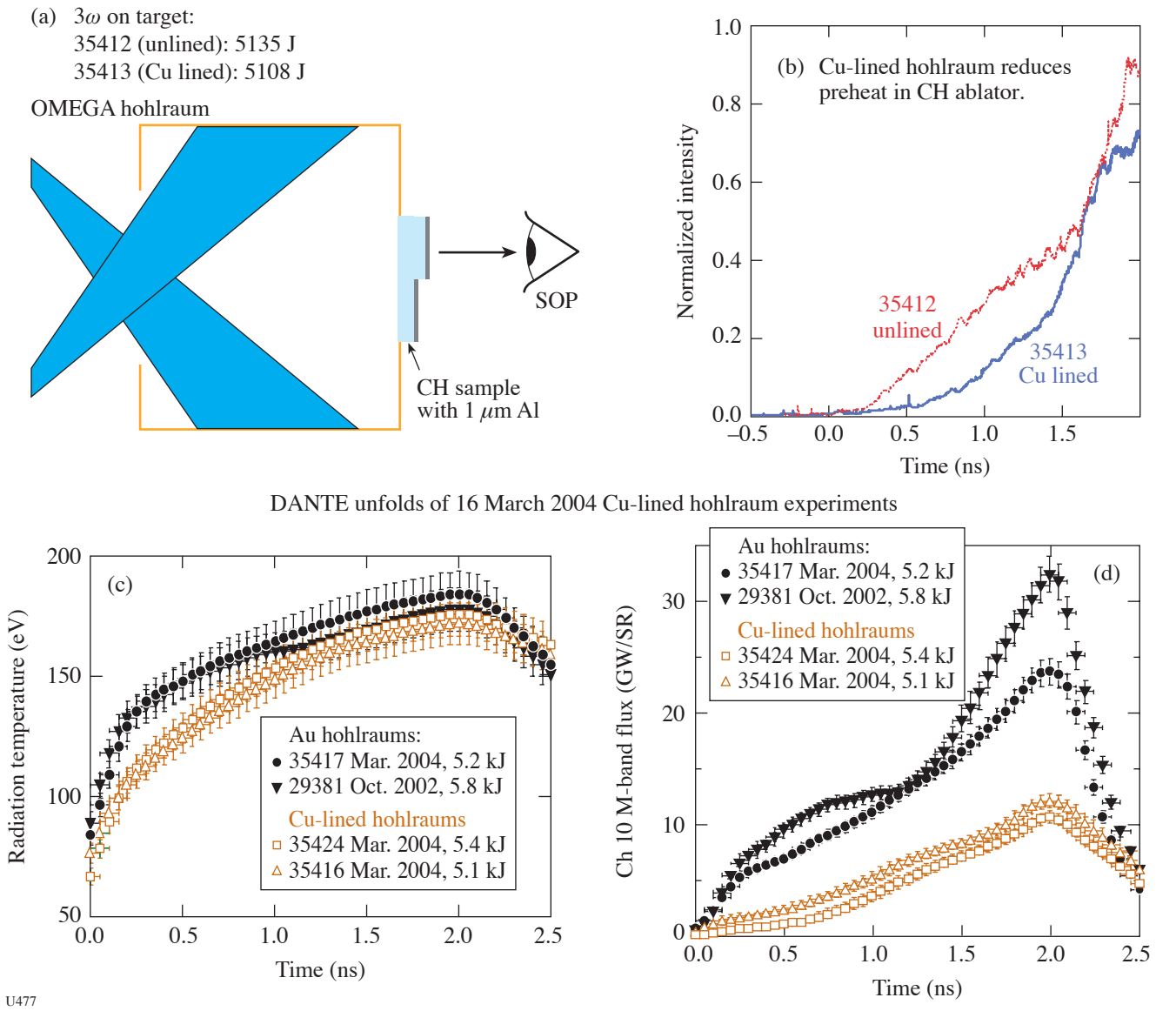


Figure 100.94
Results from experiments to demonstrate the modification of a laser hohlraum spectrum by using a mid-Z wall liner (Cu).

hohlraum wall albedo measurement is shown in Fig. 100.97(b).

*Tests of a VISAR Time-Resolved Hohlraum Temperature Measurement Technique:* In FY04, we began tests on a new technique for time-resolved hohlraum temperature measurement. The basic idea is to use VISAR[11] to track the velocity of a radiatively driven shock front in a quartz sample attached to the wall of a hohlraum. The experimental arrangement for the initial tests at OMEGA is depicted in Fig. 100.98. These initial tests utilized both DANTE and an aluminum step witness plate to confirm the drive temperature and were performed for hohlraum temperatures in the range of 110 to 190 eV. As shown in Fig. 100.99, the VISAR-measured shock velocity can be used to track the hohlraum temperature history. For the hohlraum radiation temperature range of these experiments, the empirical conversion $T_r = 21.7\, v_s^{0.57}$ has been used, where $T_r$ is hohlraum temperature in eV and $v_s$ is shock velocity in $\mu$m/ns. An important finding is that x-ray preheat presents a

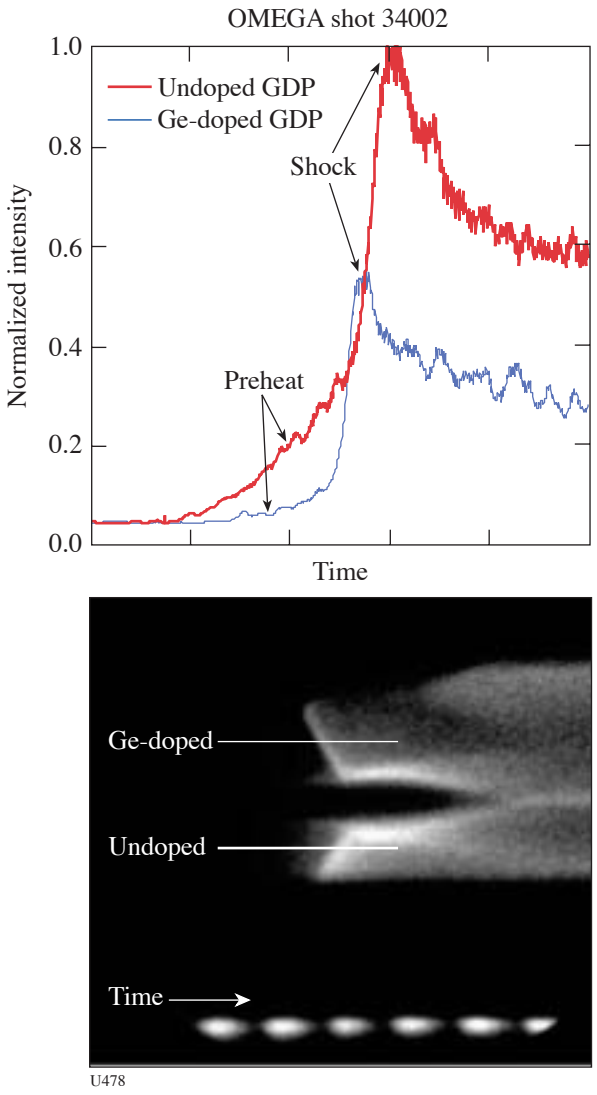


Figure 100.95
Results from experiments to demonstrate the effectiveness of mid-Z dopants to reduce preheat.

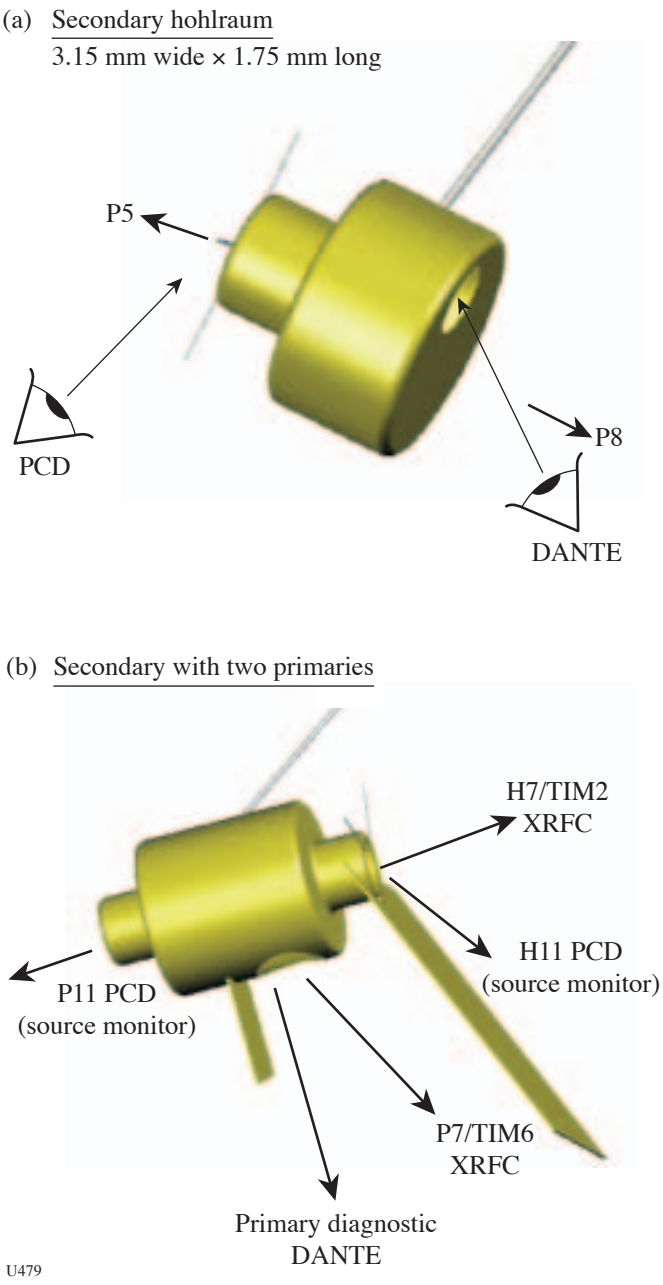


Figure 100.96
Schematic of long-pulse albedo experiments. (a) Secondary hohlraum driven with one primary hohlraum and (b) secondary hohlraum driven with two primary hohlraums.

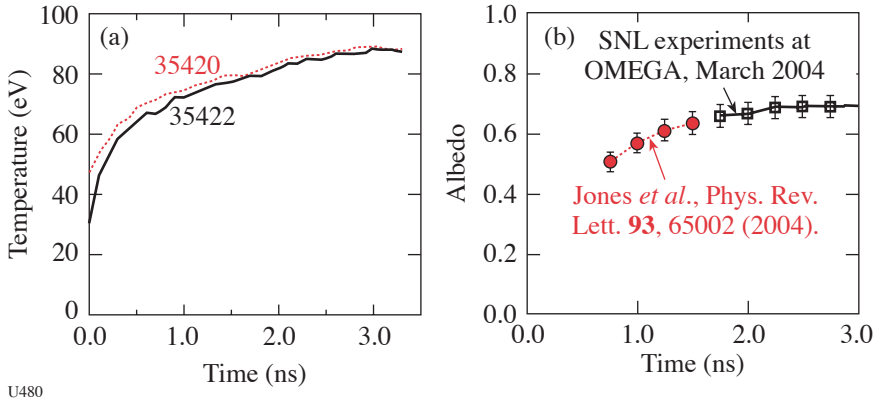


Figure 100.97
Temperature history of (a) secondary-hohlraum temperature and (b) albedo measurement.

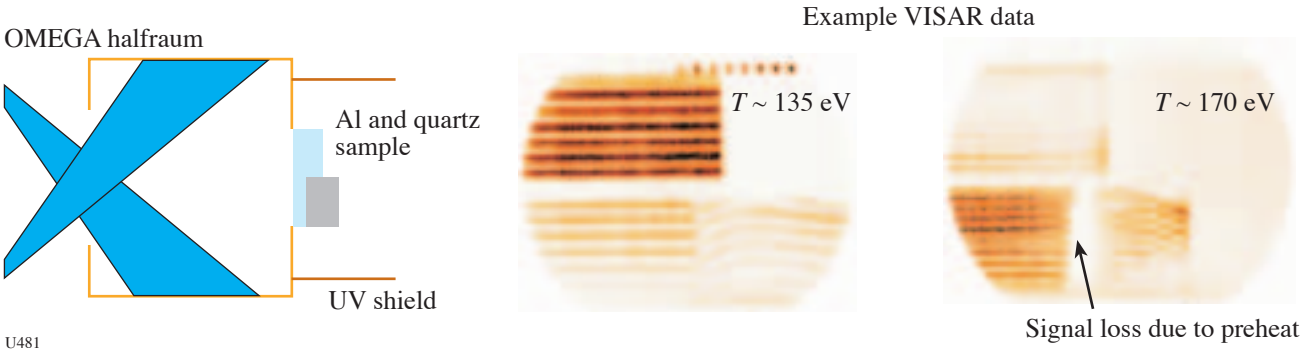


Figure 100.98
Experimental arrangement for SNL VISAR time-resolved hohlraum temperature measurement experiments.

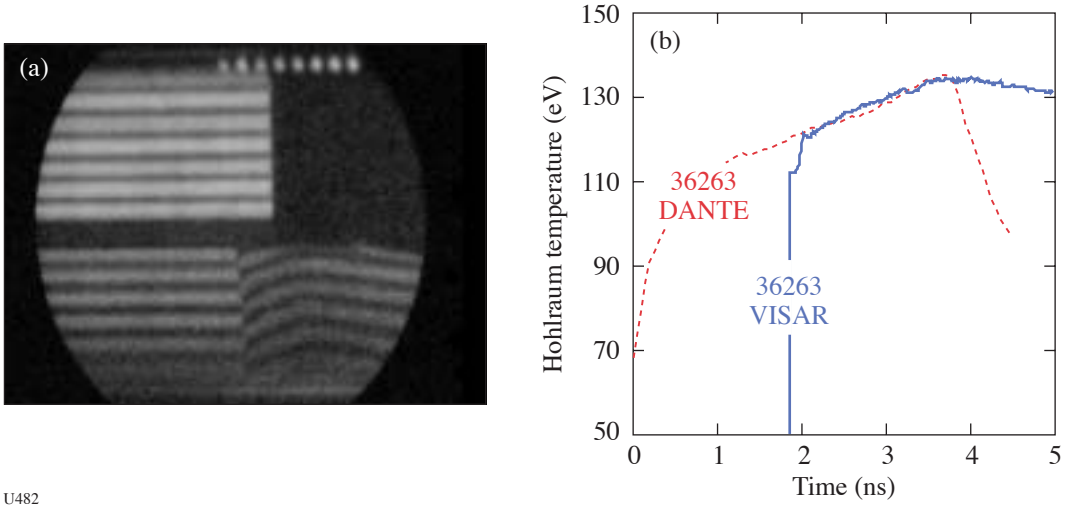


Figure 100.99
(a) VISAR velocity record and (b) resulting hohlraum temperature history from SNL experiment on OMEGA.

significant limitation to this technique for hohlraum temperatures above ~170 eV (as indicated in Fig. 100.98).

### *FY04 NRL Program Control of Laser Imprinting with High-Z Thin-Layer Targets*

Principal Investigator: A. Mostovych

As part of a collaborative effort with NRL, a series of 13 OMEGA target shots were taken to investigate the control of laser imprinting.

The objectives of this experiment were to evaluate the impact of laser imprint under conditions similar to ICF-like reactor implosions and to test the effectiveness of controlling imprint from a high-power glass laser with the use of thin, high-*Z*-layer targets. In earlier work,[12] on the Nike KrF laser facility, it was demonstrated that thin, high-*Z*-layer targets are, in fact, very effective in mitigating imprint. It was not clear, however, if the differences between glass and KrF laser drivers, such as ASE, wavelength, or imprint details, are important and if the observed imprint mitigation had general validity irrespective of the laser driver.

In this work, the OMEGA laser was configured to drive a planar 30-$\mu$m CH target with multiple, full SSD beams. As is needed for high-gain target implosions, the target was accelerated on a low adiabat by compressing it with a single, low-intensity ($10^{12}$ W/cm$^2$), early beam foot (~2 ns) and subsequently accelerating it with three to five full-intensity beams (~$5 \times 10^{13}$ W/cm$^2$). The residual laser nonuniformities that imprint the target in the compression phase are amplified by RT growth in the acceleration phase and are measured in the experiment by x-ray radiography. An example of the measured RT amplified imprint is shown in Fig. 100.100. If the same target is now coated with a thin layer of high-*Z* material (250 Å of gold in this work), the foot pulse quickly ablates this layer and creates a region of strong laser absorption that moves with the ablating gold away from the target surface. At the point of absorption, the gold becomes a strong soft-x-ray radiator and drives target ablation farther from a standoff distance of several hundred microns. The separation of the absorption and ablation regions leads to a strong reduction in pressure nonuniformities on the target surface, thus mitigating the role of laser imprint. An example of this reduction is displayed in Fig. 100.101. Initial measurements of the Rayleigh–Taylor instability amplified imprint are displayed for targets with and without the thin gold layer. A clear reduction for the layered targets is observed. These results are in agreement with the initial Nike measurements but do not show as large of an effect. This is expected because thinner gold layers had to be used to compensate for the shorter foot and thinner targets that could be deployed on the OMEGA facility. The initial results indicate that the control of imprint with high-*Z*-layer targets is a robust effect, not sensitive to the type of laser driver. It is expected that

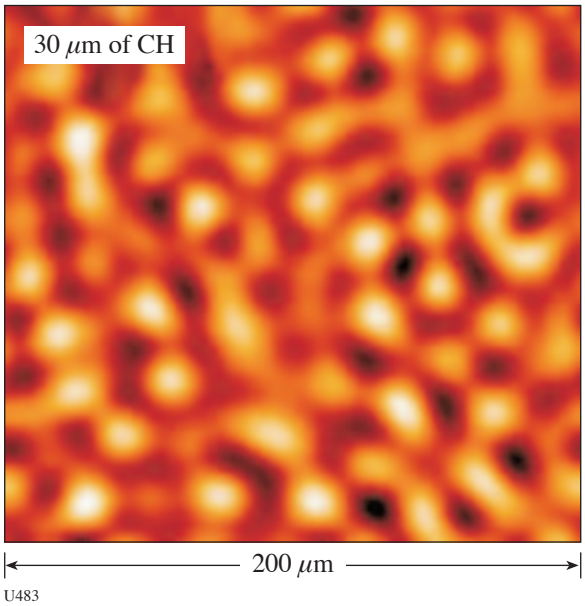


Figure 100.100
Typical mass nonuniformity of Rayleigh–Taylor amplified laser imprint at 3 ns into the main acceleration phase of a planar CH target.

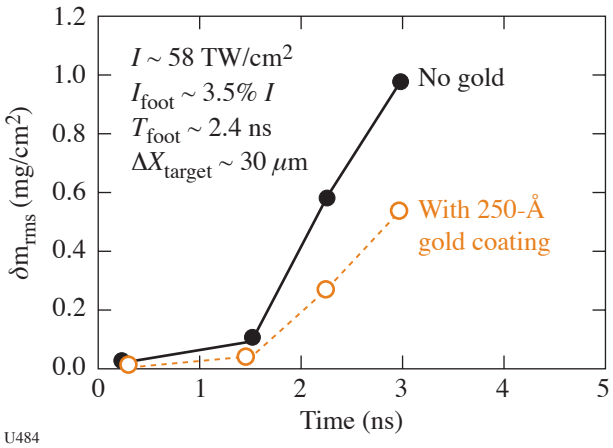


Figure 100.101
Comparison of amplified imprint with and without a thin gold coating on the ablation surface of the target. The thin, high-*Z* layer has a pronounced effect in reducing the level of imprint by almost 50%.

future near-term experiments will investigate the role of such high-*Z* layers in spherical implosions.

### FY04 CEA Program

A total of 32 target shots led by CEA (Commissariat à l'Énergie Atomique, France) were carried out on OMEGA in FY04. The corresponding four experimental campaigns studied (a) laser–plasma interaction (LPI) in long-scale-length plasmas relevant to NIF/LMJ indirect-drive conditions; (b) irradiation symmetry and x-ray conversion efficiency in empty gold hohlraums; (c) production and optimization of multi-keV x-ray sources (performed on LLNL-owned shots); and (d) hydrodynamic instabilities in planar geometry. A summary of the LPI campaign is given in this section. The CEA diagnostics team also pursues a strong activity in the area of neutron detectors and neutron-induced effects on MJ-class laser detectors in collaboration with LLE teams. LLE direct-drive implosions provide a valuable neutron source for testing new concepts in this field.

The Thomson-scattering configuration for probing electron-plasma waves stimulated by the Raman backscattering instability (SRS) tested on OMEGA in FY03 was used in FY04 to study the SRS growth and saturation in gas-bag plasmas. As a first step, space-resolved measurements of SRS activity were performed along the interaction-beam propagation axis ($z$). This is achieved by pointing the probe beam at different locations along the $z$ axis (see Fig. 100.102). With a series of five shots, we have been able to assess the SRS growth along the $z$ axis (see Fig. 100.103). These space-resolved measurements evidence a completely different spatial SRS growth depending on the time during the interaction pulse. At early time, when the heaters are on, the SRS activity is saturated with a constant level observed over more than 1 mm. Toward the end of the interaction pulse, the SRS activity peaks sharply near the input side of the interaction beam as expected from linear convective amplification theory.

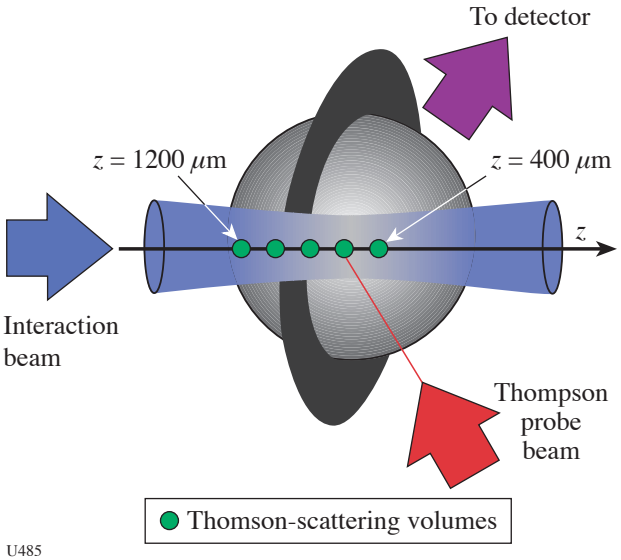


Figure 100.102
Schematic showing experimental configuration and the different probe-pointing locations of gas-bag targets.

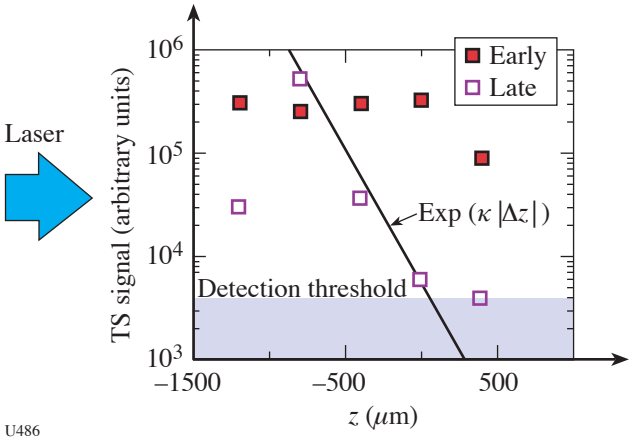


Figure 100.103
Thomson-scattering signals as a function of $z$ in the early ($t$ = 0.6 to 1.1 ns, when the heaters are on) and late ($t$ = 1.2 to 1.7 ns) time periods. The exponential fit of the late time measurements gives a spatial growth rate of $\kappa = 6 \times 10^{-3}$ $\mu m^{-1}$.

## REFERENCES

1. P. Loubeyre *et al.*, High Press. Res. **24**, 25 (2004).
2. J. R. Fincke *et al.*, Phys. Rev. Lett. **93**, 115003 (2004).
3. R. M. Baltrusaitis *et al.*, Phys. Fluids **8**, 2471 (1996).
4. D. Besnard, F. H. Harlow, and R. Rauenzahn, Los Alamos National Laboratory, Los Alamos, NM, Report LA-10911-MS (1987).
5. S. H. Batha and J. R. Fincke, "Quantified Reduction of Wall Material Influx During Hohlraum Experiments," to be published in the Review of Scientific Instruments.

6. R. E. Olson *et al.*, Phys. Rev. Lett. **91**, 235002 (2003).

7. H. N. Kornblum, R. L. Kauffman, and J. A. Smith, Rev. Sci. Instrum. **57**, 2179 (1986).

8. J. A. Oertel *et al.*, Rev. Sci. Instrum. **70**, 803 (1999).

9. R. E. Olson, R. J. Leeper, A. Nobile, J. A. Oertel, G. A. Chandler, K. Cochrane, S. C. Dropinski, S. Evans, S. W. Haan, J. L. Kaae, J. P. Knauer, K. Lash, L. P. Mix, A. Nikroo, G. A. Rochau, G. Rivera, C. Russell, D. Schroen, R. J. Sebring, D. L. Tanner, R. E. Turner, and R. J. Wallace, Phys. Plasmas **11**, 2778 (2003).

10. O. S. Jones *et al.*, Phys. Rev. Lett. **93**, 065002 (2004).

11. L. M. Barker and R. E. Hollenbach, J. Appl. Phys. **43**, 4669 (1972).

12. S. P. Obenschain *et al.*, Phys. Plasmas **9**, 2234 (2002).

# Publications and Conference Presentations

## Publications


A. Agarwal, S. Banerjee, D. F. Grosz, A. P. Küng, D. N. Maywar, and T. H. Wood, "Ultralong-Haul Transmission of 40-Gb/s RZ-DPSK in a 10/40 G Hybrid System Over 2500 km of NZ-DSF," IEEE Photonics Technol. Lett. **15**, 1779 (2003).

E. L. Alfonso, R. Q. Gram, and D. R. Harding, "Modeling Temperature and Pressure Gradients During Cooling of Thin-Walled Cryogenic Targets," Fusion Sci. Technol. **45**, 218 (2004).

K. Anderson and R. Betti, "Laser-Induced Adiabat Shaping by Relaxation in Inertial Fusion Implosions," Phys. Plasmas **11**, 5 (2004).

K. Anderson and R. Betti, "Theory of Laser-Induced Adiabat Shaping in Inertial Fusion Implosions: The Decaying Shock," Phys. Plasmas **10**, 4448 (2003).

V. Bagnoud, I. A. Begishev, M. J. Guardalben, J. Keegan, J. Puth, L. J. Waxer, and J. D. Zuegel, "Optical Parametric Chirped-Pulse Amplifier as the Front End for the OMEGA EP Laser Chain," in *Inertial Fusion Sciences and Applications 2003*, edited by B. A. Hammel, D. D. Meyerhofer, J. Meyer-ter-Vehn, and H. Azechi (American Nuclear Society, La Grange Park, IL, 2004), pp. 670–673.

V. Bagnoud and J. D. Zuegel, "Independent Phase and Amplitude Control of a Laser Beam by Use of a Single-Phase-Only Spatial Light Modulator," Opt. Lett. **29**, 295 (2004).

I. A. Begishev, V. Bagnoud, M. J. Guardalben, J. Puth, L. J. Waxer, and J. D. Zuegel, "Parasitic Second-Harmonic Generation in Optical Parametric Chirped-Pulse Amplification," in *OSA Trends in Optics and Photonics (TOPS) Vol. 94, Advanced Solid-State Photonics*, edited by G. J. Quarles (Optical Society of America, Washington, DC, 2004), pp. 32–34.

T. R. Boehly, D. G. Hicks, P. M. Celliers, T. J. B. Collins, R. Earley, J. H. Eggert, D. Jacobs-Perkins, S. J. Moon, E. Vianello, D. D. Meyerhofer, and G. W. Collins, "Properties of Fluid Deuterium Under Double-Shock Compression to Several Mbar," Phys. Plasmas **11**, L49 (2004).

B. Buerke and D. D. Meyerhofer, "Measurement of Hydrogenic Tunneling Rates in a High-Intensity Laser Focus," Phys. Rev. A **69**, 051402 (2004).

A. C. A. Chen, S. W. Culligan, Y. Geng, S. H. Chen, K. P. Klubek, K. M. Vaeth, and C. W. Tang, "Organic Polarized Light-Emitting Diodes via Förster Energy Transfer Using Monodisperse Conjugated Oligomers," Adv. Mater. **16**, 783 (2004).

C. R. Christensen, D. C. Wilson, C. W. Barnes, G. P. Grim, G. L. Morgan, M. D. Wilke, F. J. Marshall, V. Yu. Glebov, and C. Stoeckl, "The Influence of Asymmetry on Mix in Direct-Drive Inertial Confinement Fusion Experiments," Phys. Plasmas **11**, 2771 (2004).

T. J. B. Collins, J. P. Knauer, R. Betti, T. R. Boehly, J. A. Delettrez, V. N. Goncharov, D. D. Meyerhofer, P. W. McKenty, S. Skupsky, and R. P. J. Town, "Reduction of the Ablative Rayleigh–Taylor Growth Rate with Gaussian Picket Pulses," Phys. Plasmas **11**, 1569 (2004).

T. J. B. Collins, S. Skupsky, V. N. Goncharov, R. Betti, P. W. McKenty, P. B. Radha, R. Epstein, A. Poludnenko, A. Frank, and S. Mitran, "High-Gain, Direct-Drive Foam Target Designs for the National Ignition Facility," in *Inertial Fusion Sciences and Applications 2003*, edited by B. A. Hammel, D. D. Meyerhofer, J. Meyer-ter-Vehn, and H. Azechi (American Nuclear Society, La Grange Park, IL, 2004), pp. 92–95.

J. E. DeGroote, H. J. Romanofsky, I. A. Kozhinova, J. M. Schoen, and S. D. Jacobs, "Polishing PMMA and Other Optical Polymers with Magnetorheological Finishing," in *Optical Manufacturing and Testing V*, edited by H. P. Stahl (SPIE, Bellingham, WA, 2003), Vol. 5180, pp. 123–134.

L. Disdier, R. A. Lerche, J. L. Bourgade, and V. Yu. Glebov, "Capillary Detector with Deuterated Scintillator for Inertial Confinement Fusion Neutron Images," Rev. Sci. Instrum. **75**, 2134 (2004).

C. Dorrer and D. N. Maywar, "RF Spectrum Analysis of Optical Signals Using Nonlinear Optics," J. Lightwave Technol. **22**, 266 (2004).

J. A. Frenje, C. K. Li, F. H. Séguin, J. Deciantis, S. Kurebayashi, J. R. Rygg, R. D. Petrasso, J. A. Delettrez, V. Yu. Glebov, C. Stoeckl, F. J. Marshall, D. D. Meyerhofer, T. C. Sangster, V. A. Smalyuk, and J. M. Soures, "Measuring Shock-Bang Timing and $\rho R$ Evolution of $D^3He$ Implosions at OMEGA," Phys. Plasmas **11**, 2798 (2004) (invited).

Y. Geng, A. C. A. Chen, J. J. Ou, S. H. Chen, K. Klubek, K. M. Vaeth, and C. W. Tang, "Monodisperse Glassy-Nematic Conjugated Oligomers with Chemically Tunable Polarized Light Emission," Chem. Mater. **15**, 4352 (2003).

Y. Geng, A. Trajkovska, S. W. Culligan, J. J. Ou, H. M. P. Chen, D. Katsis, and S. H. Chen, "Origin of Strong Chiroptical Activities in Films of Nonafluorenes with a Varying Extent of Pendant Chirality," J. Am. Chem. Soc. **125**, 14,032 (2003).

O. V. Gotchev, L. J. Hayes, P. A. Jaanimagi, J. P. Knauer, F. J. Marshall, and D. D. Meyerhofer, "Large-Grazing-Angle, Multi-Image Kirkpatrick–Baez Microscope as the Front End to a High-Resolution Streak Camera for OMEGA," Rev. Sci. Instrum. **74**, 5065 (2003).

L. L. Gregg, A. E. Marino, J. C. Hayes, and S. D. Jacobs, "Grain Decoration in Aluminum Oxynitride (ALON) from Polishing on Bound Abrasive Laps," in *Optical Manufacturing and Testing V*, edited by H. P. Stahl (SPIE, Bellingham, WA, 2003), Vol. 5180, pp. 47–54.

D. F. Grosz, A. Agarwal, S. Banerjee, D. N. Maywar, and A. P. Küng, "All-Raman Ultralong-Haul Single-Wideband DWDM Transmission Systems with OADM Capability," J. Lightwave Technol. **22**, 423 (2004).

D. F. Grosz, A. Agarwal, A. P. Küng, S. Banerjee, D. N. Maywar, and T. H. Wood, "Performance of a ULH Single Wide-Band All-Raman DWDM Transmission System Over Dispersion-Managed Spans," IEEE Photonics Technol. Lett. **16**, 1197 (2004).

D. F. Grosz, D. N. Maywar, A. P. Küng, A. Agarwal, and S. Banerjee, "Performance of Non-Fibre Based Dispersion Compensation for Long-Haul 10.7 Gbit/s DWDM Transmission," Electron. Lett. **40**, 825 (2004).

M. J. Guardalben, J. Keegan, L. J. Waxer, V. Bagnoud, I. A. Begishev, J. Puth, and J. D. Zuegel, "Design of a Highly Stable, High-Conversion-Efficiency, Optical Parametric Chirped-Pulse Amplification System with Good Beam Quality," Opt. Express **11**, 2511 (2003).

L. Guazzotto, R. Betti, J. Manickam, and S. Kaye, "Numerical Study of Tokamak Equilibria with Arbitrary Flow," Phys. Plasmas **11**, 604 (2004).

Q. Guo, X. Teng, and H. Yang, "Fabrication of Magnetic FePt Patterns from Langmuir–Blodgett Films of Platinum–Iron Oxide Core-Shell Nanoparticles," Adv. Mater. **16**, 1337 (2004).

Q. Guo, X. Teng, and H. Yang, "Overpressure Contact Printing," Nano Lett. **4**, 1657 (2004).

B. Hou, J. A. Nees, W. Theobald, G. A. Mourou, L. M. Chen, J.-C. Kieffer, A. Krol, and C. C. Chamberlain, "Dependence of Hard X-Ray Yield on Laser Pulse Parameters in the Wavelength-Cubed Regime," Appl. Phys. Lett. **84**, 2259 (2004).

B. Hu and R. Betti, "Resistive Wall Mode in Collisionless Quasistationary Plasmas," Phys. Rev. Lett. **93**, 105002 (2004).

S. D. Jacobs, "Innovations in Polishing of Precision Optics," in *International Progress on Advanced Optics and Sensors,* Frontiers Science Series, Vol. 40, edited by H. Ohmori and H. M. Shimizu (Universal Academy Press, Tokyo, Japan, 2003), pp. 3–14 (invited).

T. J. Kessler, J. Bunkenburg, H. Huang, A. Kozlov, C. Kelly, and D. D. Meyerhofer, "The Coherent Addition of Gratings for Pulse Compression in High-Energy Laser Systems," in *Inertial Fusion Sciences and Applications 2003*, edited by B. A. Hammel, D. D. Meyerhofer, J. Meyer-ter-Vehn, and H. Azechi (American Nuclear Society, La Grange Park, IL, 2004), pp. 621–625.

T. J. Kessler, J. Bunkenburg, H. Huang, A. Kozlov, and D. D. Meyerhofer, "Demonstration of Coherent Addition of Multiple Gratings for High-Energy Chirped-Pulse-Amplified Lasers," Opt. Lett. **29**, 635 (2004).

A. K. Knight, F.-Y. Tsai, M. J. Bonino, and D. R. Harding, "Suitability of Different Polyimide Capsule Materials for Use as ICF Targets," Fusion Sci. Technol. **45**, 187 (2004).

J. A. Koch, T. W. Barbee, Jr., S. Dalhed, S. Haan, N. Izumi, R. W. Lee, L. A. Welser, R. C. Mancini, F. J. Marshall, T. C. Sangster, V. A. Smalyuk, J. M. Soures, and L. Klein, "Core Temperature and Density Profiles from Multispectral Imaging of ICF Plasmas," in *Inertial Fusion Sciences and Applications 2003*, edited by B. A. Hammel, D. D. Meyerhofer, J. Meyer-ter-Vehn, and H. Azechi (American Nuclear Society, La Grange Park, IL, 2004), pp. 857–861.

A. Korneev, P. Kouminov, V. Matvienko, G. Chulkova, K. Smirnov, B. Voronov, G. N. Gol'tsman, M. Currie, W. Lo, K. Wilsher, J. Zhang, W. Slysz, A. Pearlman, A. Verevkin, and R. Sobolewski, "Sensitivity and Gigahertz Counting Performance of NbN Superconducting Single-Photon Detectors," Appl. Phys. Lett. **84**, 5338 (2004).

T. Z. Kosc, K. L. Marshall, and S. D. Jacobs, "Polymer Cholesteric Liquid Crystal Flake Particle Displays Utilizing Maxwell-Wagner Polarization Effects for Switching," in the *Conference Record of the 23rd International Display Research Conference* (Society for Information Display, San Jose, CA, 2003), pp. 237–239.

T. Kosteski, N. P. Kherani, P. Stradins, F. Gaspari, W. T. Shmayda, L. S. Sidhu, and S. Zukotynski, "Tritiated Amorphous Silicon Betavoltaic Devices," IEE Proc.-Circuits Devices Syst. **150**, 274 (2003).

T. I. Lakoba, C. Dorrer, and D. N. Maywar, "Polarization-Mode Dispersion of a Circulating Loop," J. Opt. Soc. Am. B **21**, 243 (2004).

J. Leuthold, R. Ryf, D. N. Maywar, S. Cabot, J. Jaques, and S. S. Patel, "Nonblocking All-Optical Cross Connect Based on Regenerative All-Optical Wavelength Converter in a Transparent Demonstration Over 42 Nodes and 16800 km," J. Lightwave Technol. **21**, 2863 (2003).

C. K. Li, F. H. Séguin, J. A. Frenje, R. D. Petrasso, J. A. Delettrez, P. W. McKenty, T. C. Sangster, R. L. Keck, J. M. Soures, F. J. Marshall, D. D. Meyerhofer, V. N. Goncharov, J. P. Knauer, P. B. Radha, S. P. Regan, and W. Seka, "Effects of Nonuniform Illumination on Implosion Asymmetry in Direct-Drive Inertial Confinement Fusion," Phys. Rev. Lett. **92**, 205001 (2004).

J. Li, W. R. Donaldson, and T. Y. Hsiang, "Simulation of Submicrometer Metal–Semiconductor–Metal Ultraviolet Photodiodes on Gallium Nitride," Solid-State Electron. **48**, 2329 (2004).

J. Li, Y. Xu, T. Y. Hsiang, and W. R. Donaldson, "Picosecond Response of Gallium-Nitride Metal–Semiconductor–Metal Photodetectors," Appl. Phys. Lett. **84**, 2091 (2004).

X. Z. Lin, X. Teng, and H. Yang, "Direct Synthesis of Narrowly Dispersed Silver Nanoparticles Using a Single-Source Precursor," Langmuir **19**, 10,081 (2003).

J. D. Lindl, B. A. Hammel, B. G. Logan, D. D. Meyerhofer, S. A. Payne, and J. D. Sethian, "The US Inertial Confinement Fusion (ICF) Ignition Programme and the Inertial Fusion Energy (IFE) Programme," Plasma Phys. Control. Fusion **45**, A217 (2003).

S. G. Lukishova, A. W. Schmid, A. J. McNamara, R. W. Boyd, and C. R. Stroud, Jr., "Room-Temperature Single-Photon Source: Single-Dye Molecule Fluorescence in Liquid Crystal Host," IEEE J. Sel. Top. Quantum Electron. **9**, 1512 (2003).

S. G. Lukishova, A. W. Schmid, C. M. Supranowitz, N. Lippa, A. J. McNamara, R. W. Boyd, and C. R. Stroud, Jr., "Dye-Doped Cholesteric-Liquid-Crystal Room-Temperature Single-Photon Source," J. Mod. Opt. **51**, 1535 (2004).

J. R. Marciante and D. H. Raguin, "High-Efficiency, High-Dispersion Diffraction Gratings Based on Total Internal Reflection," Opt. Lett. **29**, 542 (2004).

F. J. Marshall, J. A. Delettrez, R. Epstein, R. Forties, R. L. Keck, J. H. Kelly, P. W. McKenty, S. P. Regan, and L. J. Waxer, "Direct-Drive-Implosion Experiments with Enhanced Fluence Balance on OMEGA," Phys. Plasmas **11**, 251 (2004).

K. L. Marshall, B. Klehn, B. Watson, and D. W. Griffin, "Recent Advances in the Development of Phase-Shifting Liquid Crystal Interferometers for Visible and Near-IR Applications," in *Advanced Characterization Techniques for Optics, Semiconductors, and Nanotechnologies*, edited by A. Duparré and B. Singh (SPIE, Bellingham, WA, 2003), Vol. 5188, pp. 48–60.

K. L. Marshall, B. Schudel, and I. A. Lippa, "Transition Metal Dithiolene Complexes as Near-IR Dyes for Liquid Crystal Device Applications," in *Liquid Crystals VII*, edited by I.-C. Khoo (SPIE, Bellingham, WA, 2003), Vol. 5213, pp. 201–212.

A. V. Maximov, J. Myatt, W. Seka, R. W. Short, and R. S. Craxton, "Modeling of Stimulated Brillouin Scattering Near the Critical-Density Surface in the Plasmas of Direct-Drive Targets," Phys. Plasmas **11**, 2994 (2004).

R. L. McCrory (keynote speaker), "Progress in Inertial Confinement Fusion in the United States," in *Inertial Fusion Sciences and Applications 2003*, edited by B. A. Hammel, D. D. Meyerhofer, J. Meyer-ter-Vehn, and H. Azechi (American Nuclear Society, La Grange Park, IL, 2004), pp. 3–8.

P. W. McKenty, T. C. Sangster, M. Alexander, R. Betti, R. S. Craxton, J. A. Delettrez, L. Elasky, R. Epstein, A. Frank, V. Yu. Glebov, V. N. Goncharov, D. R. Harding, S. Jin, J. P. Knauer, R. L. Keck, S. J. Loucks, L. D. Lund, R. L. McCrory, F. J. Marshall, D. D. Meyerhofer, S. P. Regan, P. B. Radha, S. Roberts, W. Seka, S. Skupsky, V. A. Smalyuk, J. M. Soures, K. A. Thorp, M. Wozniak, J. A. Frenje, C. K. Li, R. D. Petrasso, F. H. Séguin, K. A. Fletcher, S. Padalino, C. Freeman, N. Izumi, J. A. Koch, R. A. Lerche, M. J. Moran, T. W. Phillips, G. J. Schmid, and C. Sorce, "Direct-Drive Cryogenic Target Implosion Performance on OMEGA," Phys. Plasmas **11**, 2790 (2004) (invited).

J. Myatt, A. V. Maximov, W. Seka, R. S. Craxton, and R. W. Short, "Modeling Stimulated Brillouin Scattering in the Underdense Corona of a Direct Drive Inertial Confinement Fusion Target," Phys. Plasmas **11**, 3394 (2004).

R. Narayan, I. V. Igumenshchev, and M. A. Abramowicz, "Magnetically Arrested Disk: An Energetically Efficient Accretion Flow," Publ. Astron. Soc. Jpn. **55**, L69 (2003).

J.-R. Park, W. R. Donaldson, R. Boni, and R. Sobolewski, "Characterization of Single and Double Fiber-Coupled Diffusing Spheres," Appl. Opt. **43**, 3967 (2004).

S. P. Regan, J. A. Delettrez, V. N. Goncharov, F. J. Marshall, J. M. Soures, V. A. Smalyuk, P. B. Radha, B. Yaakobi, R. Epstein, V. Yu. Glebov, P. A. Jaanimagi, D. D. Meyerhofer, T. C. Sangster, W. Seka, S. Skupsky, C. Stoeckl, D. A. Haynes, Jr., J. A. Frenje, C. K. Li, R. D. Petrasso, and F. H. Séguin, "Dependence of Shell Mix on Feedthrough in Direct-Drive Inertial Confinement Fusion," Phys. Rev. Lett. **92**, 185002 (2004).

B. A. Remington, G. Bazan, J. Belak, E. Bringa, M. Caturla, J. D. Colvin, M. J. Edwards, S. G. Glendinning, D. S. Ivanov, B. Kad, D. H. Kalantar, M. Kumar, B. F. Lasinski, K. T. Lorenz, J. M. McNaney, D. D. Meyerhofer, M. A. Meyers, S. M. Pollaine, D. Rowley, M. Schneider, J. S. Stölken, J. S. Wark, S. V. Weber, W. G. Wolfer, B. Yaakobi, and L. V. Zhigilei, "Materials Science Under Extreme Conditions of Pressure and Strain Rate," Metall. Trans. A, Phys. Metall. Mater. Sci. **35A**, 2587 (2004).

S. Skupsky, R. Betti, T. J. B. Collins, V. N. Goncharov, J. A. Marozas, P. W. McKenty, P. B. Radha, T. R. Boehly, J. P. Knauer, F. J. Marshall, D. R. Harding, J. D. Kilkenny, D. D. Meyerhofer, T. C. Sangster, and R. L. McCrory, "Advanced Direct-Drive Target Designs for the NIF," in *Inertial Fusion Sciences and Applications 2003*, edited by B. A. Hammel, D. D. Meyerhofer, J. Meyer-ter-Vehn, and H. Azechi (American Nuclear Society, La Grange Park, IL, 2004), pp. 61–64.

S. Skupsky, J. A. Marozas, R. S. Craxton, R. Betti, T. J. B. Collins, J. A. Delettrez, V. N. Goncharov, P. W. McKenty, P. B. Radha, T. R. Boehly, J. P. Knauer, F. J. Marshall, D. R. Harding, J. D. Kilkenny, D. D. Meyerhofer, T. C. Sangster, and R. L. McCrory, "Polar Direct Drive on the National Ignition Facility," Phys. Plasmas **11**, 2763 (2004) (invited).

X. Teng and H. Yang, "Effects of Surfactants and Synthetic Conditions on the Sizes and Self-Assembly of Monodisperse Iron Oxide Nanoparticles," J. Mater. Chem. **14**, 774 (2004).

X. Teng and H. Yang, "Synthesis of Face-Centered Tetragonal FePt Nanoparticles and Granular Films from $Pt@Fe_2O_3$ Core–Shell Nanoparticles," J. Am. Chem. Soc. **125**, 14,559 (2003).

L. Veisz, W. Theobald, T. Feurer, H. Schwoerer, I. Uschmann, O. Renner, and R. Sauerbrey, "Three-Halves Harmonic Emission from Femtosecond Laser Produced Plasmas with Steep Density Gradients," Phys. Plasmas **11**, 3311 (2004).

A. Verevkin, A. Pearlman, W. Slysz, J. Zhang, M. Currie, A. Korneev, G. Chulkova, O. Okunev, P. Kouminov, K. Smirnov, B. Voronov, G. N. Gol'tsman, and R. Sobolewski, "Ultrafast Superconducting Single-Photon Detectors for Near-Infrared-Wavelength Quantum Communications," J. Mod. Opt. **51**, 1447 (2004).

Y. Wang, J. F. Wong, X. Teng, X. Z. Lin, and H. Yang, " 'Pulling' Nanoparticles into Water: Phase Transfer of Oleic Acid Stabilized Monodisperse Nanoparticles into Aqueous Solutions of $\alpha$-Cyclodextrin," Nano Lett. **3**, 1555 (2003).

D. C. Wilson, C. W. Cranfill, C. Christensen, R. A. Forster, R. R. Peterson, N. M. Hoffman, G. D. Pollak, C. K. Li, F. H. Séguin, J. A. Frenje, R. D. Petrasso, P. W. McKenty, F. J. Marshall, V. Yu. Glebov, C. Stoeckl, G. J. Schmid, N. Izumi, and P. Amendt, "Multifluid Interpenetration Mixing in Directly Driven Inertial Confinement Fusion Capsule Implosions," Phys. Plasmas **11**, 2723 (2004).

Y. Xu, M. Khafizov, L. Satrapinsky, P. Kúš, A. Plecenik, and R. Sobolewski, "Time-Resolved Photoexcitation of the Superconducting Two-Gap State in $MgB_2$ Thin Films," Phys. Rev. Lett. **91**, 197004 (2003).

B. Yaakobi, D. D. Meyerhofer, T. R. Boehly, J. J. Rehr, B. A. Remington, P. G. Allen, S. M. Pollaine, and R. C. Albers, "Extended X-Ray Absorption Fine Structure Measurements of Laser-Shocked V and Ti and Crystal Phase Transformation in Ti," Phys. Rev. Lett. **92**, 095504 (2004).

B. Yaakobi, D. D. Meyerhofer, T. R. Boehly, J. J. Rehr, B. A. Remington, P. G. Allen, S. M. Pollaine, and R. C. Albers, "Extended X-Ray Absorption Fine Structure Measurements of Laser Shocks in Ti and V and Phase Transformation in Ti," Phys. Plasmas **11**, 2688 (2004) (invited).

J. Zhang, N. Boiadjieva, G. Chulkova, H. Deslandes, G. N. Gol'tsman, A. Korneev, P. Kouminov, M. Leibowitz, W. Lo, R. Malinsky, O. Okunev, A. Pearlman, W. Slysz, K. Smirnov, C. Tsao, A. Verevkin, V. Voronov, K. Wilsher, and R. Sobolewski, "Noninvasive CMOS Circuit Testing with NbN Superconducting Single-Photon Detectors," Electron. Lett. **39**, 1086 (2003).

J. D. Zuegel and D. W. Jacobs-Perkins, "Efficient, High-Frequency Bulk Phase Modulator," Appl. Opt. **43**, 1946 (2004).

## OMEGA External Users' Publications

B. Afeyan, M. Mardirian, K. Won, D. S. Montgomery, J. Hammer, R. K. Kirkwood, and A. J. Schmitt, "Optical Mixing Controlled Stimulated Scattering Instabilities: Suppression of SRS by the Controlled Introduction of Ion Acoustic and Electron Plasma Wave Turbulence," in *Inertial Fusion Sciences and Applications 2003*, edited by B. A. Hammel, D. D. Meyerhofer, J. Meyer-ter-Vehn, and H. Azechi (American Nuclear Society, La Grange Park, IL, 2004), pp. 264–267

P. Amendt, H. F. Robey, H.-S. Park, R. E. Turner, R. E. Tipton, J. L. Milovich, J. D. Colvin, M. J. Edwards, R. Hibbard, H. Louis, R. Wallace, D. P. Rowley, W. S. Varnum, R. G. Watt, D. C. Wilson, W. Garbett, and A. M. Dunne, "Hohlraum-Driven Ignition-Like Double-Shell Implosion Experiments on OMEGA: Analysis and Interpretation," in *Inertial Fusion Sciences and Applications 2003*, edited by B. A. Hammel, D. D. Meyerhofer, J. Meyer-ter-Vehn, and H. Azechi (American Nuclear Society, La Grange Park, IL, 2004), pp. 80–84.

P. M. Celliers, G. W. Collins, D. G. Hicks, M. Koenig, E. Henry, A. Benuzzi-Mounaix, D. Batani, D. K. Bradley, L. B. Da Silva, R. J. Wallace, S. J. Moon, J. H. Eggert, K. K. M. Lee, L. R. Benedetti, R. Jeanloz, I. Masclet, N. Dague, B. Marchet, M. Rabec le Gloahec, Ch. Reverdin, J. Pasley, O. Willi, D. Neely, and C. Danson, "Electronic Conduction in Shock-Compressed Water," Phys. Plasmas **11**, L41 (2004).

C. R. Christensen, D. C. Wilson, C. W. Barnes, G. P. Grim, G. L. Morgan, M. D. Wilke, and F. J. Marshall, "Asymmetry and Mix in Direct-Drive ICF Experiments," in *Inertial Fusion Sciences and Applications 2003*, edited by B. A. Hammel, D. D. Meyerhofer, J. Meyer-ter-Vehn, and H. Azechi (American Nuclear Society, La Grange Park, IL, 2004), pp. 158–161.

D. H. Cohen, J. J. MacFarlane, P. Jaanimagi, O. L. Landen, D. A. Haynes, D. S. Conners, K. L. Penrose, and N. C. Shupe, "Tracer Spectroscopy Diagnostics of Doped Ablators in Inertial Confinement Fusion Experiments on OMEGA," Phys. Plasmas **11**, 2702 (2004).

N. Delameter, G. Kyrala, D. Wilson, R. Watt, J. Guzik, W. M. Wood, W. Varnum, and D. Haynes, "Progress with Double Shell Target Implosions on OMEGA," in *Inertial Fusion Sciences and Applications 2003*, edited by B. A. Hammel, D. D. Meyerhofer, J. Meyer-ter-Vehn, and H. Azechi (American Nuclear Society, La Grange Park, IL, 2004), pp. 190–192.

E. L. DeWald, S. W. Pollaine, O. L. Landen, P. A. Amendt, R. E. Turner, R. J. Wallace, K. M. Campbell, and S. H. Glenzer, "Hydro-Coupling Effects on Compression Symmetry in Gas-Filled Hohlraum Experiments at the OMEGA Laser," in *Inertial Fusion Sciences and Applications 2003*, edited by B. A. Hammel, D. D. Meyerhofer, J. Meyer-ter-Vehn, and H. Azechi (American Nuclear Society, La Grange Park, IL, 2004), pp. 490–493.

L. Disdier, R. A. Lerche, J. L. Bourgade, and V. Yu. Glebov, "Capillary Detector with Deuterated Scintillator for Inertial Confinement Fusion Neutron Images," Rev. Sci. Instrum. **75**, 2134 (2004).

R. P. Drake, D. R. Leibrandt, E. C. Harding, C. C. Kuranz, M. A. Blackburn, H. F. Robey, B. A. Remington, M. J. Edwards, A. R. Miles, T. S. Perry, R. J. Wallace, H. Louis, J. P. Knauer, and D. Arnett, "Nonlinear Mixing Behavior of the Three-Dimensional Rayleigh–Taylor Instability at a Decelerating Interface," Phys. Plasmas **11**, 2829 (2004).

J. Edwards, K. T. Lorenz, B. A. Remington, S. Pollaine, J. Colvin, D. Braun, B. F. Lasinski, D. Reisman, J. M. McNaney, J. A. Greenough, R. Wallace, H. Louis, and D. Kalantar, "Laser-Driven Plasma Loader for Shockless Compression and Acceleration of Samples in the Solid State," Phys. Rev. Lett. **92**, 075002 (2004).

W. Garbett, P. Graham, and A. M. Dunne, "An Assessment of Mix in OMEGA Double Shell Capsule Implosions," in *Inertial Fusion Sciences and Applications 2003*, edited by B. A. Hammel, D. D. Meyerhofer, J. Meyer-ter-Vehn, and H. Azechi (American Nuclear Society, La Grange Park, IL, 2004), pp. 126–130.

S. H. Glenzer, P. Arnold, G. Bardsley, R. L. Berger, G. Bonnano, T. Borger, D. E. Bower, M. Bowers, R. Bryant, S. Buckman, S. C. Burkhart, K. Campbell, M. P. Chrisp, B. I. Cohen, C. Constantin, F. Cooper, J. Cox, E. DeWald, L. Divol, S. Dixit, J. Duncan, D. Eder, J. Edwards, G. Erbert, B. Felker, J. Fornes, G. Frieders, D. H. Froula, S. D. Gardner, C. Gates, M. Gonzalez, S. Grace, G. Gregori, A. Greenwood, R. Griffith, T. Hall, B. A. Hammel, C. Haynam, G. Heestand, M. Henesian, G. Hermes, D. Hinkel, J. Holder, F. Holdner, G. Holtmeier, W. Hsing, S. Huber, T. James, S. Johnson, O. S. Jones, D. Kalantar, J. H. Kampschroer, R. Kauffman, T. Kelleher, J. Knight, R. K. Kirkwood, W. L. Kruer, W. Labiak, O. L. Landen, A. B. Langdon, S. Langer, D. Latray, A. Lee, F. D. Lee, D. Lund, B. MacGowan, S. Marshall, J. McBride, T. McCarville, L. McGrew, A. J. Mackinnon, S. Mahavandi, K. Manes, C. Marshall, J. Menapace, E. Metens, N. Meezan, G. Miller, S. Montelongo, J. D. Moody, E. Moses, D. Munro, J. Murray, J. Neumann, M. Newton, E. Ng, C. Niemann, A. Nikitin, P. Opsahl, E. Padilla, T. Parham, G. Parrish, C. Petty, M. Polk, C. Powell, I. Reinbachs, V. Rekow, R. Rinnert, B. Riordan, M. Rhodes, V. Roberts, H. Robey, G. Ross, S. Sailors, R. Saunders, M. Schmitt, M. B. Schneider, S. Shiromizu, M. Spaeth, A. Stephens, B. Still, L. J. Suter, G. Tietbohl, M. Tobin, J. Tuck, B. M. Van Wonterghem, R. Vidal, D. Voloshin, R. Wallace, P. Wegner, P. Whitman, E. A. Williams, K. Williams, K. Winward, K. Work, B. Young, P. E. Young, P. Zapata, R. E. Bahr, W. Seka, J. Fernandez, D. Montgomery, and H. Rose, "Progress in Long Scale Length Laser–Plasma Interactions," in *Inertial Fusion Sciences and Applications 2003*, edited by B. A. Hammel, D. D. Meyerhofer, J. Meyer-ter-Vehn, and H. Azechi (American Nuclear Society, La Grange Park, IL, 2004), pp. 207–212.

I. E. Golovkin, J. J. MacFarlane, P. R. Woodruff, L. A. Welser, D. L. McCrorey, R. C. Mancini, and J. A. Koch, "Modeling of Indirect-Drive ICF Implosions Using 1-D Hydrodynamics Code with Inline Collisional-Radiative Atomic Kinetics," in *Inertial Fusion Sciences and Applications 2003*, edited by B. A. Hammel, D. D. Meyerhofer, J. Meyer-ter-Vehn, and H. Azechi (American Nuclear Society, La Grange Park, IL, 2004), pp. 166–169.

G. Gregori, S. H. Glenzer, F. J. Rogers, O. L. Landen, C. Blancard, G. Faussurier, P. Renaudin, S. Kuhlbrodt, and R. Redmer, "Electronic Structure Measurement of Solid Density Plasmas Using X-Ray Scattering," in *Inertial Fusion Sciences and Applications 2003*, edited by B. A. Hammel, D. D. Meyerhofer, J. Meyer-ter-Vehn, and H. Azechi (American Nuclear Society, La Grange Park, IL, 2004), pp. 902–906.

G. Gregori, S. H. Glenzer, F. J. Rogers, S. M. Pollaine, O. L. Landen, C. Blancard, G. Faussier, P. Renaudin, S. Kuhlbrodt, and R. Redmer, "Electronic Structure Measurements of Dense Plasmas," Phys. Plasmas **11**, 2754 (2004).

M. A. Gunderson, D. A. Haynes, Jr., N. D. Delameter, and S. P. Regan, "Experimental Results on the Effects of Line Merging in Spectral Line Data Analysis," in *Inertial Fusion Sciences and Applications 2003*, edited by B. A. Hammel, D. D. Meyerhofer, J. Meyer-ter-Vehn, and H. Azechi (American Nuclear Society, La Grange Park, IL, 2004), pp. 884–887.

J. F. Hansen, M. J. Edwards, H. F. Robey, A. Miles, D. Froula, G. Gregori, A. Edens, and T. Ditmire, "Laboratory Simulations of Supernova Shockwave Propagation and ISM Reaction," in *Inertial Fusion Sciences and Applications 2003*, edited by B. A. Hammel, D. D. Meyerhofer, J. Meyer-ter-Vehn, and H. Azechi (American Nuclear Society, La Grange Park, IL, 2004), pp. 962–965.

R. F. Heeter, M. E. Foord, K. B. Fournier, K. B. Froula, A. J. MacKinnon, M. J. May, M. B. Schneider, and B. K. F. Young, "Characterization of Non-LTE Gold Plasmas in controlled Conditions with Finite $T_r$," in *Inertial Fusion Sciences and Applications 2003*, edited by B. A. Hammel, D. D. Meyerhofer, J. Meyer-ter-Vehn, and H. Azechi (American Nuclear Society, La Grange Park, IL, 2004), pp. 1018–1021.

D. E. Hinkel, M. B. Schneider, E. A. Williams, A. B. Langdon, L. J. Suter, and P. T. Springer, "Filamentation, Deflection, Scatter, and Crossed Beam Energy Transfer in High Temperature Hohlraums," in *Inertial Fusion Sciences and Applications 2003*, edited by B. A. Hammel, D. D. Meyerhofer, J. Meyer-ter-Vehn, and H. Azechi (American Nuclear Society, La Grange Park, IL, 2004), pp. 242–246.

P. A. Holstein, D. Babonneau, C. Bowen, F. Chaland, C. Cherfils, E. Dattolo, S. Depierreux, D. Galmiche, P. Gauthier, J. Giorla, J. P. Jadaud, L. Masse, M. C. Monteil, F. Poggi, G. Riazuelo, P. Seytor, and F. Wagon, "Progress in Target Physics for LMJ at CEA," in *Inertial Fusion Sciences and Applications 2003*, edited by B. A. Hammel, D. D. Meyerhofer, J. Meyer-ter-Vehn, and H. Azechi (American Nuclear Society, La Grange Park, IL, 2004), pp. 65–69.

H. Ji, M. Brown, S. C. Hsu, H. Li, and R. P. Drake, "Mini-Conference and Related Sessions on Laboratory Plasma Astrophysics," Phys. Plasmas **11**, 2976 (2004).

J. A. King, R. R. Freeman, M. H. Key, K. Akli, M. Borghesi, R. Clarke, T. Cowan, H. Habara, H. Heathcote, S. Karsch, R. Kodama, K. Lancaster, A. MacKinnon, C. Murphy, P. Norreys, P. Patel, L. Romagnani, R. Snavely, R. Stephens, C. Stoeckl, Y. Toyama, M. Zepf, and B. Zhang, "Ti *K*-alpha Radiography of Imploding Cu Doped Cd Shells and Coned Shells," in *Inertial Fusion Sciences and Applications 2003*, edited by B. A. Hammel, D. D. Meyerhofer, J. Meyer-ter-Vehn, and H. Azechi (American Nuclear Society, La Grange Park, IL, 2004), pp. 449–452.

J. A. Koch, T. W. Barbee, Jr., S. Dalhed, S. Haan, N. Izumi, R. W. Lee, L. A. Welser, R. C. Mancini, F. J. Marshall, T. C. Sangster, V. A. Smalyuk, J. M. Soures, and L. Klein, "Core Temperature and Density Profiles from Multispectral Imaging of ICF Plasmas," in *Inertial Fusion Sciences and Applications 2003*, edited by B. A. Hammel, D. D. Meyerhofer, J. Meyer-ter-Vehn, and H. Azechi (American Nuclear Society, La Grange Park, IL, 2004), pp. 857–861.

M. Koenig, E. Henry, A. Benuzzi-Mounaix, G. Huser, B. Faral, E. Martinolli, S. Lepape, P. Audebert, T. Vinci, D. Batani, M. Tomasini, B. Telaro, B. Marchet, I. Masclet, M. Rabec, Ch. Reverdin, P. Loubeyre, T. Hall, P. Celliers, G. Collins, L. DaSilva, R. Cauble, D. Hicks, D. Bradley, A. MacKinnon, P. Patel, J. Eggert, J. Pasley, O. Willi, D. Neely, M. Notley, C. Danson, M. Borghesi, L. Romagnani, T. Boehly, and K. Lee, "Recent Developments in High Pressure Physics Using Laser Driven Shocks," in *Inertial Fusion Sciences and Applications 2003*, edited by B. A. Hammel, D. D. Meyerhofer, J. Meyer-ter-Vehn, and H. Azechi (American Nuclear Society, La Grange Park, IL, 2004), pp. 897–901.

B. J. Kozioziemski, R. A. London, R. L. McEachern, and D. N. Bittner, "Demonstration of Symmetry Control of Infrared Heated Deuterium Lasers in Hohlraums," in *Inertial Fusion Sciences and Applications 2003*, edited by B. A. Hammel, D. D. Meyerhofer, J. Meyer-ter-Vehn, and H. Azechi (American Nuclear Society, La Grange Park, IL, 2004), pp. 762–765.

W. Kruer, J. Moody, L. Suter, S. Glenzer, A. MacKinnon, D. Froula, G. Gregori, L. Divol, M. Miller, R. Bahr, W. Seka, K. Oades, and R. M. Stevenson, "Blue and Green Light? Wavelength Scaling for NIF," in *Inertial Fusion Sciences and Applications 2003*, edited by B. A. Hammel, D. D. Meyerhofer, J. Meyer-ter-Vehn, and H. Azechi (American Nuclear Society, La Grange Park, IL, 2004), pp. 223–227.

N. E. Lanier, M. M. Balkey, C. W. Barnes, S. H. Batha, R. D. Day, N. D. Delameter, J. R. Fincke, G. R. Magelssen, R. M. Hueckstaedt, J. M. Scott, W. P. Steckle, Jr., A. M. Dunne, C. Horsfield, K. W. Parker, and S. D. Rothman, "Richtmyer–Meshkov Mixing in Directly Driven Cylindrically Convergent Systems," in *Inertial Fusion Sciences and Applications 2003*,

edited by B. A. Hammel, D. D. Meyerhofer, J. Meyer-ter-Vehn, and H. Azechi (American Nuclear Society, La Grange Park, IL, 2004), pp. 140–144.

C. K. Li, F. H. Séguin, J. A. Frenje, R. D. Petrasso, J. A. Delettrez, P. W. McKenty, T. C. Sangster, R. L. Keck, J. M. Soures, F. J. Marshall, D. D. Meyerhofer, V. N. Goncharov, J. P. Knauer, P. B. Radha, S. P. Regan, and W. Seka, "Effects of Nonuniform Illumination on Implosion Asymmetry in Direct-Drive Inertial Confinement Fusion," Phys. Rev. Lett. **92**, 205001 (2004).

S. B. Libby, M. Tabak, R. D. Hoffman, M. A. Stoyer, S. W. Haan, S. P. Hatchett, D. P. McNabb, W. E. Ormand, J. Escher, P. Navratil, D. Gogny, M. S. Weiss, M. Mustafa, J. Becker, W. Younes, E. Hartouni, and R. A. Ward, "Prospects for Investigating Unusual Nuclear Reaction Environments Using the National Ignition Facility," in *Inertial Fusion Sciences and Applications 2003*, edited by B. A. Hammel, D. D. Meyerhofer, J. Meyer-ter-Vehn, and H. Azechi (American Nuclear Society, La Grange Park, IL, 2004), pp. 935–939.

J. D. Lindl, P. Amendt, R. L. Berger, S. G. Glendinning, S. H. Glenzer, S. W. Haan, R. L. Kauffman, O. L. Landen, and L. J. Suter, "The Physics Basis for Ignition Using Indirect-Drive Targets on the National Ignition Facility," Phys. Plasmas **11**, 339 (2004).

A. R. Miles, D. G. Braun, M. J. Edwards, H. F. Robey, R. P. Drake, and D. R. Leibrandt, "Numerical Simulation of Supernova-Relevant Laser-Driven Hydro Experiments on OMEGA," Phys. Plasmas **11**, 3631 (2004).

A. R. Miles, M. J. Edwards, and H. F. Robey, "The Effect of a Short Wavelength Mode on the Nonlinear Evolution of a Long Wavelength Perturbation Driven by a Strong Blast Wave," in *Inertial Fusion Sciences and Applications 2003*, edited by B. A. Hammel, D. D. Meyerhofer, J. Meyer-ter-Vehn, and H. Azechi (American Nuclear Society, La Grange Park, IL, 2004), pp. 145–149.

G. H. Miller, "The National Ignition Facility: Experimental Capability," in *Inertial Fusion Sciences and Applications 2003*, edited by B. A. Hammel, D. D. Meyerhofer, J. Meyer-ter-Vehn, and H. Azechi (American Nuclear Society, La Grange Park, IL, 2004), pp. 529–534.

J. L. Milovich, P. Amendt, M. Marinak, and H. Robey, "Multimode Short-Wavelength Perturbation Growth Studies for the National Ignition Facility Double-Shell Ignition Target Designs," Phys. Plasmas **11**, 1552 (2004).

J. D. Moody, L. Divol, S. H. Glenzer, A. J. MacKinnon, D. H. Froula, G. Gregori, W. L. Kruer, L. J. Suter, E. A. Williams, R. Bahr, and W. Seka, "Experimental Studies of Simultaneous 351 nm and 527 nm Laser Beam Interactions in a Long Scale Length Plasma," in *Inertial Fusion Sciences and Applications 2003*, edited by B. A. Hammel, D. D. Meyerhofer, J. Meyer-ter-Vehn, and H. Azechi (American Nuclear Society, La Grange Park, IL, 2004), pp. 218–222.

R. E. Olson, R. J. Leeper, A. Nobile, and J. A. Oertel, "Preheat Effects on Shock Propagation in Indirect-Drive Inertial Confinement Fusion Ablator Materials," Phys. Rev. Lett. **91**, 235002 (2003).

R. E. Olson, R. J. Leeper, A. Nobile, J. A. Oertel, G. A. Chandler, K. Cochrane, S. C. Dropinski, S. Evans, S. W. Haan, J. L. Kaae, J. P. Knauer, K. Lash, L. P. Mix, A. Nikroo, G. A. Rochau, G. Rivera, C. Russell, D. Schroen, R. J. Sebring, D. L. Tanner, R. E. Turner, and R. J. Wallace, "Shock Propagation, Preheat, and X-Ray Burnthrough in Indirect-Drive Inertial Confinement Fusion Ablator Materials," Phys. Plasmas **11**, 2778 (2004).

H.-S. Park, J. A. Koch, O. L. Landen, T. W. Phillips, T. J. Goldsack, E. Clark, R. Eagleton, and R. D. Edwards, "High Energy X-ray Source Generation by Short Pulse High Intensity Lasers," in *Laser-Generated and Other Laboratory X-Ray and EUV Sources, Optics, and Applications*, edited by G. A. Kyrala, J.-C. J. Gauthier, C. A. MacDonald, and A. M. Khounsary (SPIE, Bellingham, WA, 2004), Vol. 5196, pp. 213–219.

K. Parker, C. J. Horsfield, S. D. Rothman, S. H. Batha, M. M. Balkey, N. D. Delameter, J. R. Fincke, R. M. Hueckstaedt, N. E. Lanier, and G. R. Magelssen, "Observation and Simulation of Plasma Mix After Reshock in a Convergent Geometry," Phys. Plasmas **11**, 2696 (2004).

A. B. Reighard, R. P. Drake, K. Dannenberg, T. S. Perry, H. F. Robey, B. A. Remington, R. J. Wallace, D. D. Ryutov, J. Greenough, J. Knauer, T. Boehly, S. Bouquet, A. Calder, R. Rosner, B. Fryxell, D. Arnett, M. Koenig, and J. Stone, "Collapsing Radiative Shocks in Argon Gas on the OMEGA Laser," in *Inertial Fusion Sciences and Applications 2003*,

edited by B. A. Hammel, D. D. Meyerhofer, J. Meyer-ter-Vehn, and H. Azechi (American Nuclear Society, La Grange Park, IL, 2004), pp. 950–953.

B. A. Remington, G. Bazan, J. Belak, E. Bringa, M. Caturla, J. D. Colvin, M. J. Edwards, S. G. Glendinning, D. Ivanov, B. Kad, D. H. Kalantar, M. Kumar, B. F. Lasinski, K. T. Lorenz, J. M. McNaney, D. D. Meyerhofer, M. A. Meyers, S. M. Pollaine, D. Rowley, M. Schneider, J. S. Stolken, J. S. Wark, S. V. Weber, W. G. Wolfer, and B. Yaakobi, "Materials Science Under Extreme Conditions of Pressure and Strain Rate," Metall. Mater. Trans. A **35A**, 2587 (2004).

B. A. Remington, R. M. Cavallo, M. J. Edwards, B. F. Lasinski, K. T. Lorenz, H. E. Lorenzana, J. McNaney, S. M. Pollaine, D. P. Rowley, and B. Yaakobi, "Materials Science at the Extremes of Pressure and Strain Rate," in *Inertial Fusion Sciences and Applications 2003*, edited by B. A. Hammel, D. D. Meyerhofer, J. Meyer-ter-Vehn, and H. Azechi (American Nuclear Society, La Grange Park, IL, 2004), pp. 917–921.

H. F. Robey, P. A. Amendt, H.-S. Park, O. L. Landen, R. G. Watt, and W. S. Varnum, "Experimental Investigation of the Effect of *M*-Band Preheating in Indirectly-Driven Double-Shell Implosions," in *Inertial Fusion Sciences and Applications 2003*, edited by B. A. Hammel, D. D. Meyerhofer, J. Meyer-ter-Vehn, and H. Azechi (American Nuclear Society, La Grange Park, IL, 2004), pp. 162–165.

H. F. Robey, A. R. Miles, J. F. Hansen, B. E. Blue, and R. P. Drake, "Laser-Driven Hydrodynamic Experiments in the Turbulent Plasma Regime: From OMEGA to NIF," in *Inertial Fusion Sciences and Applications 2003*, edited by B. A. Hammel, D. D. Meyerhofer, J. Meyer-ter-Vehn, and H. Azechi (American Nuclear Society, La Grange Park, IL, 2004), pp. 135–139.

G. J. Schmid, J. A. Koch, M. J. Moran, R. A. Lerche, N. Izumi, T. Phillips, V. Glebov, T. C. Sangster, and C. Stoeckl, "CVD Diamond Detector Stability Issues for Operation at the National Ignition Facility," in *Inertial Fusion Sciences and Applications 2003*, edited by B. A. Hammel, D. D. Meyerhofer, J. Meyer-ter-Vehn, and H. Azechi (American Nuclear Society, La Grange Park, IL, 2004), pp. 881–883.

H. Shiraga, S. Fujioka, R. Kodama, K. A. Tanaka, R. B. Stephens, P. Jaanimagi, C. Stoeckl, T. C. Sangster, D. D. Meyerhofer, and S. P. Hatchett, "10-ps X-Ray Imaging of Cone-Shell Target Implosions at OMEGA Laser," in *Inertial Fusion Sciences and Applications 2003*, edited by B. A. Hammel, D. D. Meyerhofer, J. Meyer-ter-Vehn, and H. Azechi (American Nuclear Society, La Grange Park, IL, 2004), pp. 438–440.

W. P. Steckle, Jr., K. V. Wilson, R. J. Sebring, and A. Nobile, "Evaluation of Low Density Materials for Use in Inertial Fusion Targets," in *Inertial Fusion Sciences and Applications 2003*, edited by B. A. Hammel, D. D. Meyerhofer, J. Meyer-ter-Vehn, and H. Azechi (American Nuclear Society, La Grange Park, IL, 2004), pp. 783–786.

R. B. Stephens, A. Nikroo, D. Hill, J. N. Smith, Jr., S. P. Hatchett, C. Stoeckl, M. J. Bonino, T. C. Sangster, H. Shiraga, S. Fujioka, and K. A. Tanaka, "Hydrodynamics of Direct Drive Reentrant Cone Targets for Fast Ignition," in *Inertial Fusion Sciences and Applications 2003*, edited by B. A. Hammel, D. D. Meyerhofer, J. Meyer-ter-Vehn, and H. Azechi (American Nuclear Society, La Grange Park, IL, 2004), pp. 383–386.

L. J. Suter, S. Glenzer, S. Haan, B. Hammel, K. Manes, N. Meezan, J. Moody, M. Spaeth, L. Divol, K. Oades, and M. Stevenson, "Prospects for High-Gain, High Yield National Ignition Facility Targets Driven by $2\omega$ (Green) Light," Phys. Plasmas **11**, 2738 (2004).

L. J. Suter, S. Glenzer, S. Haan, B. Hammel, K. Manes, N. Meezan, J. Moody, M. Spaeth, L. Divol, K. Oades, and M. Stevenson, "Prospects for High-Gain, High Yield NIF Targets Driven by $2\omega$ (Green) Light," in *Inertial Fusion Sciences and Applications 2003*, edited by B. A. Hammel, D. D. Meyerhofer, J. Meyer-ter-Vehn, and H. Azechi (American Nuclear Society, La Grange Park, IL, 2004), pp. 23–34.

J. Tassart, "Inertial Fusion Science in Europe," in *Inertial Fusion Sciences and Applications 2003*, edited by B. A. Hammel, D. D. Meyerhofer, J. Meyer-ter-Vehn, and H. Azechi (American Nuclear Society, La Grange Park, IL, 2004), pp. 15–20.

M. Taylor, J. Foster, P. Rosen, R. Williams, B. H. Wilde, T. S. Perry, P. Keiter, R. Coker, R. P. Drake, and A. M. Khokhlov, "Transition to Turbulence in Plasma Jet Experiments," in *Inertial Fusion Sciences and Applications 2003*, edited by B. A. Hammel, D. D. Meyerhofer, J. Meyer-ter-Vehn, and H. Azechi (American Nuclear Society, La Grange Park, IL, 2004), pp. 485–489.

E. A. Williams, B. I. Cohen, L. Divol, M. R. Dorr, J. A. Hittinger, D. E. Hinkel, A. B. Langdon, R. K. Kirkwood, D. H. Froula, and S. H. Glenzer, "Effects of Ion Trapping on Crossed-Laser-Beam Stimulated Brillouin Scattering," Phys. Plasmas **11**, 231 (2004)

D. C. Wilson, C. W. Cranfill, C. Christensen, R. A. Forster, R. R. Peterson, N. M. Hoffman, G. D. Pollak, C. K. Li, F. H. Séguin, J. A. Frenje, R. D. Petrasso, P. W. McKenty, F. J. Marshall, V. Yu. Glebov, C. Stoeckl, G. J. Schmid, N. Izumi, and P. Amendt, "Multifluid Interpretation Mixing in Directly Driven Inertial Confinement Fusion Capsule Implosions," Phys. Plasmas **11**, 2723 (2004).

D. C. Wilson, N. D. Delameter, G. D. Pollak, R. G. Watt, C. W. Cranfill, W. S. Varnum, and P. Amendt, "Mixing in Double Shell Capsules," in *Inertial Fusion Sciences and Applications 2003*, edited by B. A. Hammel, D. D. Meyerhofer, J. Meyer-ter-Vehn, and H. Azechi (American Nuclear Society, La Grange Park, IL, 2004), pp. 121–125.

## Conference Presentations

The following presentations were made at the 87th OSA Annual Meeting, Tucson, AZ, 5–9 October 2003:

S. G. Lukishova, A. W. Schmid, A. J. McNamara, R. W. Boyd, and C. R. Stroud, "Efficient Room Temperature Single-Photon Source: Single Dye Molecule Fluorescence in Photonic-Band-Gap Cholesteric Liquid Crystal Host."

J. R. Marciante, N. O. Farmiga, J. P. Kondis, and J. R. Frederick, "Phase Effects of Secondary Reflections on the Performance of Reflective Liquid-Crystal Cells."

J. R. Marciante, N. O. Farmiga, H. T. Ta, J. I. Hirsh, and M. S. Evans, "Optical Measurement of Depth and Duty Cycle for Binary Diffraction Gratings with Sub-$\lambda$ Features."

J. R. Marciante and D. H. Raguin, "A New Class of High-Efficiency, High-Dispersion Diffraction Gratings Based on Total Internal Reflection."

J. R. Marciante, D. H. Raguin, J. I. Hirsh, and E. T. Prince, "Polarization-Insensitive High-Dispersion TIR Diffraction Gratings."

---

The following presentations were made at Education and Training in Optics and Photonics, Tucson, AZ, 6–8 October 2003:

S. D. Jacobs and L. L. Gregg, "OSA Rochester Section Optics Suitcase: A Forty-Minute Middle School Outreach Program for the Cost of a Postage Stamp."

S. D. Jacobs, L. L. Gregg, E. M. Fess, and J. M. Schoen, "Optics Manufacturing Research Projects by Undergraduates Who Happen to be Women."

---

W. R. Donaldson, J. A. Marozas, R. S. Craxton, D. Jacobs-Perkins, and M. Millecchia, "Spectroscopy of Broadband Harmonic Generation," LEOS 2003, Tucson, AZ, 26–30 October 2003.

---

The following presentations were made at the 45th Annual Meeting of the APS Division of Plasma Physics, Albuquerque, NM, 27–31 October 2003:

K. Anderson, R. Betti, and J. P. Knauer, "Adiabat Shaping by Relaxation in Plastic and Cryogenic Shells for Experiments on the OMEGA Laser."

R. Betti and K. Anderson, "Laser-Induced Adiabat Shaping by Relaxation."

T. R. Boehly, D. G. Hicks, T. J. B. Collins, G. W. Collins, P. M. Celliers, E. Vianello, D. D. Meyerhofer, R. C. Cauble, W. Unites, D. Jacobs-Perkins, R. Earley, M. J. Bonino, W. J. Armstrong, S. G. Noyes, D. Turner, D. Guy, S. Scarantino, T. Lewis, F. A. Rister, and L. D. Lund, "Quartz Equation-of-State (EOS) Measurements at the OMEGA Laser Facility."

M. Canavan, J. R. Rygg, J. A. Frenje, C. K. Li, F. H. Séguin, R. D. Petrasso, S. W. Haan, S. P. Hatchett, J. A. Koch, O. L. Landen, V. Yu. Glebov, D. D. Meyerhofer, and T. C. Sangster, "The Utility of Knock-On D, T, and P for Diagnosing NIF Implosions."

T. J. B. Collins and S. Skupsky, "High-Gain Direct-Drive Foam Target Designs for the National Ignition Facility."

R. S. Craxton, "Hydrodynamic Simulations of Polar Direct Drive on the NIF and LMJ Based on Three-Dimensional Ray Tracing."

J. DeCiantis, B. E. Schwartz, J. A. Frenje, F. H. Séguin, S. Kurebayashi, C. K. Li, R. D. Petrasso, J. A. Delettrez, J. M. Soures, V. Yu. Glebov, D. D. Meyerhofer, S. Roberts, T. C. Sangster, and S. P. Hatchett, "Studying the Burn Region in ICF Implosions with Proton-Emission Imaging."

J. A. Delettrez, P. B. Radha, C. Stoeckl, S. Skupsky, and D. D. Meyerhofer, "Simulation of Enhanced Neutron Production in OMEGA EP Cryogenic Implosions."

R. Epstein, F. J. Marshall, J. A. Delettrez, P. W. McKenty, P. B. Radha, and V. A. Smalyuk, "Effects of Low-Order Irradiation Nonuniformity on X-Ray Images of ICF Implosions Experiments on OMEGA."

J. A. Frenje, C. K. Li, F. H. Séguin, J. DeCiantis, J. R. Rygg, S. Kurebayashi, B. E. Schwartz, R. D. Petrasso, J. A. Delettrez, V. Yu. Glebov, D. D. Meyerhofer, T. C. Sangster, J. M. Soures, and C. Stoeckl, "Measuring Shock-Coalescence Timing and $\rho R$ Evolution of $D^3He$ Implosions at OMEGA" (invited).

J. A. Frenje, R. D. Petrasso, C. K. Li, F. H. Séguin, J. DeCiantis, S. Kurebayashi, J. R. Rygg, B. E. Schwartz, J. A. Delettrez, V. Yu. Glebov, D. D. Meyerhofer, T. C. Sangster, J. M. Soures, S. P. Hatchett, S. W. Haan, G. J. Schmid, O. L. Landen, N. Izumi, and D. Stelter, "A Magnetic Recoil Spectrometer (MRS) for $\rho R_{\text{fuel}}$ and Ti Measurements of Warm, Fizzle, and Ignited Implosions on OMEGA and NIF."

V. Yu. Glebov, C. Stoeckl, T. C. Sangster, P. B. Radha, S. Roberts, S. Mott, S. Padalino, L. Baumgart, K. Voltz, H. M. Jiang, S. P. Hatchett, M. J. Moran, S. Kurebayashi, F. H. Séguin, and R. D. Petrasso, "Secondary Neutron Energy Spectra Measurements with the 1020 Array on OMEGA."

V. Yu. Glebov, C. Stoeckl, S. Roberts, T. C. Sangster, J. A. Frenje, R. D. Petrasso, R. A. Lerche, and R. L. Griffith, "Proton Temporal Diagnostic for ICF Experiments on OMEGA."

V. N. Goncharov, T. R. Boehly, J. P. Knauer, V. A. Smalyuk, S. P. Regan, O. V. Gotchev, P. W. McKenty, S. Skupsky, P. B. Radha, and D. D. Meyerhofer, "Designing Shock-Timing and Imprint Experiments for the Direct-Drive Inertial Confinement Fusion Implosions."

O. V. Gotchev, V. N. Goncharov, P. A. Jaanimagi, J. P. Knauer, and D. D. Meyerhofer, "Streaked Imaging of Ablative Richtmyer–Meshkov Growth in ICF Targets on OMEGA."

L. Guazzotto and R. Betti, "High-$\beta$ Tokamak Equilibria with Poloidal Flows Exceeding the Poloidal Alfvén Velocity."

J. P. Knauer, V. N. Goncharov, K. Anderson, R. Betti, V. Yu. Glebov, F. J. Marshall, P. W. McKenty, P. B. Radha, S. P. Regan, T. C. Sangster, C. Stoeckl, J. A. Frenje, C. K. Li, R. D. Petrasso, and F. H. Séguin, "Direct-Drive ICF Implosions with Picket-Fence Pulse Shapes."

J. P. Knauer, S. Sublett, T. J. B. Collins, A. Frank, I. V. Igumenshchev, D. D. Meyerhofer, A. Poludnenko, J. M. Foster, P. A. Rosen, P. Keiter, B. H. Wilde, B. Blue, T. S. Perry, H. F. Robey, A. M. Khokhlov, and R. P. Drake, "Development of a Test Bed for Astrophysical Jet Hydrodynamics."

S. Kurebayashi, F. H. Séguin, J. A. Frenje, C. K. Li, R. D. Petrasso, J. R. Rygg, B. E. Schwartz, J. DeCiantis, V. Yu. Glebov, J. A. Delettrez, T. C. Sangster, J. M. Soures, and S. P. Hatchett, "Investigation of the Use of Secondary Protons and Neutrons for Studying Fuel Areal Density in Imploded, $D_2$-Filled Capsules."

J. A. Marozas, P. B. Radha, T. J. B. Collins, P. W. McKenty, and S. Skupsky, "Optimization of Low-Order Uniformity for Polar Direct Drive on the National Ignition Facility (NIF)."

F. J. Marshall, J. A. Delettrez, R. Epstein, R. Forties, V. Yu. Glebov, J. H. Kelly, T. J. Kessler, J. P. Knauer, P. W. McKenty, S. P. Regan, V. A. Smalyuk, C. Stoeckl, J. A. Frenje, C. K. Li, R. D. Petrasso, and F. H. Séguin, "Direct-Drive Implosions on OMEGA with Optimized Illumination Uniformity."

A. V. Maximov, J. Myatt, R. W. Short, W. Seka, and C. Stoeckl, "Modeling of the Two-Plasmon-Decay Instability Driven by Incoherent Laser Beams."

P. W. McKenty, T. C. Sangster, J. A. Delettrez, R. Epstein, V. Yu. Glebov, D. R. Harding, J. P. Knauer, R. L. Keck, S. J. Loucks, L. D. Lund, R. L. McCrory, F. J. Marshall, D. D. Meyerhofer, S. F. B. Morse, S. P. Regan, P. B. Radha, S. Roberts, W. Seka, S. Skupsky, V. A. Smalyuk, C. Sorce, J. M. Soures, J. A. Frenje, C. K. Li, R. D. Petrasso, F. H. Séguin, K. A. Fletcher, S. Padalino, C. Freeman, N. Izumi, J. A. Koch, R. A. Lerche, M. J. Moran, T. W. Phillips, and G. J. Schmid, "Direct-Drive Cryogenic Target Performance Issues on OMEGA" (invited).

D. D. Meyerhofer, W. Seka, M. Alexander, R. S. Craxton, M. D. Wittman, M. Pandina, L. S. Iwan, L. M. Elasky, D. R. Harding, T. J. Kessler, R. L. Keck, L. D. Lund, D. Weiner, A. Warrick, T. G. Brown, and C. Cotton, "Cryogenic Target Characterization at LLE."

J. Myatt, A. V. Maximov, R. W. Short, J. A. Delettrez, and C. Stoeckl, "Intense Electron-Beam Transport in Dense Cryogenic DT Fast-Ignition Fusion Targets."

R. D. Petrasso, J. R. Rygg, C. K. Li, F. H. Séguin, S. P. Hatchett, V. Yu. Glebov, D. D. Meyerhofer, T. C. Sangster, and J. M. Soures, "Experimental Studies of Time-Dependent Mix in OMEGA Direct-Drive Implosions."

S. P. Regan, H. Sawada, V. A. Smalyuk, V. N. Goncharov, J. A. Delettrez, P. B. Radha, R. Epstein, F. J. Marshall, B. Yaakobi, D. D. Meyerhofer, T. C. Sangster, and D. A. Haynes, Jr., "Diagnosing Shell Mix in Direct-Drive with Time-Resolved X-Ray Spectroscopy."

J. R. Rygg, F. H. Séguin, C. K. Li, J. A. Frenje, R. D. Petrasso, S. P. Hatchett, J. A. Delettrez, V. Yu. Glebov, V. N. Goncharov, R. L. Keck, J. P. Knauer, F. J. Marshall, D. D. Meyerhofer, T. C. Sangster, and V. A. Smalyuk, "The Effects of Implosion Asymmetry on Shock Dynamics in OMEGA Direct-Drive Experiments."

T. C. Sangster, J. A. Delettrez, R. Epstein, V. Yu. Glebov, V. N. Goncharov, D. R. Harding, D. Jacobs-Perkins, R. L. Keck, J. D. Kilkenny, J. P. Knauer, S. J. Loucks, L. D. Lund, R. L. McCrory, P. W. McKenty, J. A. Marozas, F. J. Marshall, D. D. Meyerhofer, S. F. B. Morse, S. P. Regan, P. B. Radha, W. Seka, S. Skupsky, V. A. Smalyuk, J. M. Soures, C. Stoeckl, K. A. Thorp, J. A. Frenje, C. K. Li, R. D. Petrasso, F. H. Séguin, K. A. Fletcher, S. Padalino, and C. Freeman, "Experimental Results from Cryogenic $D_2$ Implosions on the OMEGA Laser."

H. Sawada, S. P. Regan, V. N. Goncharov, J. P. Knauer, R. Epstein, R. S. Craxton, J. A. Delettrez, F. J. Marshall, B. Yaakobi, D. D. Meyerhofer, P. B. Radha, T. C. Sangster, and W. Seka, "Experimental Investigation of Coronal Plasma Conditions in Direct-Drive ICF Using Time-Resolved X-Ray Spectroscopy."

F. H. Séguin, J. R. Rygg, J. A. Frenje, C. K. Li, R. D. Petrasso, V. Yu. Glebov, V. N. Goncharov, J. P. Knauer, J. P. Marshall, D. D. Meyerhofer, T. C. Sangster, V. A. Smalyuk, J. M. Soures, and S. P. Hatchett, "Measuring Time Evolution of Areal-Density Asymmetries in OMEGA Direct-Drive Implosions."

W. Seka, C. Stoeckl, A. V. Maximov, R. S. Craxton, R. W. Short, S. P. Regan, H. Baldis, S. Depierreux, J. Myatt, and R. E. Bahr, "Experimental Investigation of the Two-Plasmon-Decay Instability at Oblique Incidence."

R. W. Short, "On the Role of Electron-Acoustic Waves in Two-Plasmon Decay and Stimulated Raman Scattering."

A. Simon and R. W. Short, "Convective Growth of the Three-Wave Parametric Instability in a Nonuniform Plasma."

S. Skupsky, J. A. Marozas, R. S. Craxton, R. Betti, T. J. B. Collins, J. A. Delettrez, V. N. Goncharov, P. W. McKenty, P. B. Radha, T. R. Boehly, J. P. Knauer, F. J. Marshall, D. R. Harding, J. D. Kilkenny, D. D. Meyerhofer, T. C. Sangster, and R. L. McCrory, "Polar Direct Drive on the National Ignition Facility" (invited).

J. M. Soures, S. J. Loucks, R. L. McCrory, D. D. Meyerhofer, S. F. B. Morse, T. C. Sangster, and C. Stoeckl, "Inertial Confinement Fusion and High-Energy-Density Physics Research Opportunities at the National Laser Users' Facility (NLUF)."

C. Stoeckl, J. A. Delettrez, T. C. Sangster, R. B. Stephens, S. P. Hatchett, J. A. Frenje, S. Fujioka, H. Shiraga, and K. A. Tanaka, "Fuel Assembly Experiments with Fast-Ignitor Cone Targets on OMEGA."

S. Sublett, J. P. Knauer, H. F. Robey, and B. Blue, "Development of a Point Projection Backlighter for Laboratory Astrophysics Experiments on OMEGA."

W. Theobald, L. Veisz, and R. Sauerbrey, "Three-Halves-Harmonic Generation in Femtosecond-Laser-Produced, Solid-Density Plasmas."

E. Vianello, T. R. Boehly, R. S. Craxton, V. N. Goncharov, J. P. Knauer, D. D. Meyerhofer, J. E. Miller, T. C. Sangster, D. G. Hicks, and P. M. Celliers, "Timing of Multiple Shocks in Planar Direct-Drive Laser-Driven Targets."

B. Yaakobi, D. D. Meyerhofer, T. R. Boehly, J. J. Rehr, B. A. Remington, P. G. Allen, S. M. Pollaine, and R. C. Albers, "Extended X-Ray Absorption Fine Structure Measurements of Laser Shocks in Ti and V and Phase Transformation in Ti" (invited).

---

I. V. Igumenshchev, "Radiatively Inefficient Accretion Flows," Stellar-Mass, Intermediate-Mass, and Supermassive Black Holes, Kyoto, Japan, 28–31 October 2003.

---

D. R. Harding, F.-Y. Tsai, E. L. Alfonso, S. H. Chen, A. K. Knight, and T. N. Blanton, "Properties of Vapor-Deposited Polyimide Films," Third International Symposium on Polyimides and Other High Temperature Polymers, Orlando, FL, 17–19 December 2003 (invited).

---

J.-R. Park, W. R. Donaldson, and R. Sobolewski, "Time-Resolved Imaging of a Spatially Modulated Laser Pulse," LASE 2004, San Jose, CA, 24–29 January 2004.

---

The following presentations were made at the 2004 Advanced Solid-State Photonics, Santa Fe, NM, 1–4 February 2004:

V. Bagnoud, J. Puth, and J. D. Zuegel, "High-Energy, 5-Hz-Repetition-Rate Laser Amplifier Using Wavefront-Corrected Nd:YLF Laser Rods."

I. A. Begishev, V. Bagnoud, M. J. Guardalben, J. Puth, L. J. Waxer, and J. D. Zuegel, "Parasitic Second-Harmonic Generation in Optical Parametric Chirped-Pulse Amplification."

J. D. Zuegel, J. R. Marciante, A. Galvanauskas, and C.-H. Liu, "High-Energy Fiber Power Amplifier for Broadband Beam Smoothing with FM-Modulated Laser Pulses on OMEGA."

---

The following presentations were made at the 5th International Conference on High Energy Density Laboratory Astrophysics, Tucson, AZ, 10–13 March 2004:

T. R. Boehly, E. Vianello, J. E. Miller, R. S. Craxton, V. N. Goncharov, D. D. Meyerhofer, T. C. Sangster, D. G. Hicks, and P. M. Celliers, "Laser-Driven, Multishock Experiments in Planar Targets."

S. P. Regan, T. C. Sangster, D. D. Meyerhofer, K. Anderson, R. Betti, T. R. Boehly, T. J. B. Collins, R. S. Craxton, J. A. Delettrez, R. Epstein, O. V. Gotchev, V. Yu. Glebov, V. N. Goncharov, P. A. Jaanimagi, J. P. Knauer, J. A. Marozas, F. J. Marshall, P. W. McKenty, P. B. Radha, W. Seka, S. Skupsky, H. Sawada, V. A. Smalyuk, J. M. Soures, C. Stoeckl, B. Yaakobi, J. A. Frenje, C. K. Li, R. D. Petrasso, and F. H. Séguin, "Direct-Drive Inertial Confinement Fusion Implosions on OMEGA."

---

A. Trajkovska-Petkoska, R. Varshneya, T. Z. Kosc, K. L. Marshall, and S. D. Jacobs, "Manufacture of Shaped Polymer Cholesteric Liquid Crystal Flakes Using Soft Lithography," 12th Annual University of Rochester Symposium on Materials Research (SOMR), Rochester, NY, 3 April 2004.

---

A. Marino, K. Spencer, J. DeGroote, and S. D. Jacobs, "Chemical Durability of Phosphate Glasses," Industrial Associates, Rochester, NY, 5 April 2004.

---

J. D. Zuegel, "Wavefront Correction of Laser Rods Using Magnetorheological Finishing (MRF)," QED Executive Symposium, Rochester, NY, 7 April 2004.

---

The following presentations were made at the 15th Topical Conference on High Temperature Plasma Diagnostics, San Diego, CA, 19–22 April 2004:

S. Ghosh, R. Boni, and P. A. Jaanimagi, "Optical and X-Ray Streak Camera Gain Measurements."

V. Yu. Glebov, C. Stoeckl, T. C. Sangster, S. Roberts, G. J. Schmid, R. A. Lerche, and M. Moran, "NIF Neutron Time-of-Flight Detector Prototypes Test on OMEGA."

O. V. Gotchev, P. A. Jaanimagi, J. P. Knauer, F. J. Marshall, and D. D. Meyerhofer, "KB-PJX — A Streaked Imager Based on a Versatile X-Ray Microscope Coupled to a High-Current Streak Tube" (invited).

J. P. Knauer and C. Gindele, "Temporal and Spectral Deconvolution of Data from Diamond, Photoconductive Devices."

F. J. Marshall, J. A. Oertel, and P. J. Walsh, "A Framed, 16-Image Kirkpatrick–Baez Microscope for Laser–Plasma X-Ray Emission."

V. A. Smalyuk, V. N. Goncharov, T. R. Boehly, J. P. Knauer, D. D. Meyerhofer, and T. C. Sangster, "Self-Consistent Determination of Rayleigh–Taylor Growth Rates and Ablation-Front Density in Planar Targets Accelerated by Laser Light."

C. Stoeckl, W. Theobald, T. C. Sangster, M. H. Key, P. Patel, B. B. Zhang, R. Clarke, S. Karsch, and P. Norreys, "Operation of a Single-Photon–Counting X-Ray CCD Camera Spectrometer in a Petawatt Environment."

---

The following presentations were made at the International Workshop on Fast Ignition and High Field Physics, Kyoto, Japan, 25–29 April 2004:

D. D. Meyerhofer, "Fast Ignition Research at LLE: Progress and Plans."

D. D. Meyerhofer, "Two High-Energy Beamlines at LLE: OMEGA EP."

W. Theobald, C. Stoeckl, J. A. Delettrez, V. Yu. Glebov, D. D. Meyerhofer, P. B. Radha, T. C. Sangster, V. A. Smalyuk, R. B. Stephens, S. P. Hatchett, J. A. Frenje, C. K. Li, R. D. Petrasso, F. H. Séguin, S. Fujioka, H. Shiraga, and K. A. Tanaka, "Fast-Ignitor Cone Target Fuel Assembly Experiments."

---

The following presentations were made at the 34th Anomalous Absorption Conference, Gleneden Beach, OR, 2–7 May 2004:

K. Anderson, R. Betti, J. P. Knauer, and V. N. Goncharov, "Simulations and Experiments on Adiabat Shaping by Relaxation."

R. S. Craxton, F. J. Marshall, S. Skupsky, J. A. Delettrez, R. Epstein, J. P. Knauer, P. W. McKenty, and W. Seka, "Polar-Direct-Drive Experiments on OMEGA."

J. DeCiantis, F. H. Séguin, J. R. Rygg, J. A. Frenje, S. Kurebayashi, C. K. Li, C. Chen, V. Berube, R. D. Petrasso, J. A. Delettrez, V. Yu. Glebov, D. D. Meyerhofer, S. Roberts, T. C. Sangster, and J. M. Soures, "Studying the Burn Region in ICF Implosions with Proton Emission Imaging."

J. A. Delettrez, J. Myatt, P. B. Radha, C. Stoeckl, and S. Skupsky, "Simulation of Enhanced Neutron Production in OMEGA EP Cryogenic Implosions."

R. Epstein and W. Fong, "Non-LTE Speed of Sound, Irreversibility, and Thermodynamic Consistency."

J. A. Frenje, C. K. Li, F. H. Séguin, J. DeCiantis, S. Kurebayashi, J. R. Rygg, R. D. Petrasso, J. A. Delettrez, V. Yu. Glebov, D. D. Meyerhofer, T. C. Sangster, J. M. Soures, S. P. Hatchett, S. W. Haan, M. Moran, G. J. Schmid, O. L. Landen, N. Izumi, and R. Stelter, "A High-Resolution Neutron Spectrometer for $\rho R_{\text{fuel}}$ and Ti Measurements at OMEGA and the NIF."

C. K. Li and R. D. Petrasso, "Stopping and Scattering of Directed Energetic Electrons in High-Temperature Hydrogenic Plasmas."

C. K. Li, F. H. Séguin, J. A. Frenje, R. D. Petrasso, J. A. Delettrez, P. W. McKenty, T. C. Sangster, R. L. Keck, J. M. Soures, F. J. Marshall, D. D. Meyerhofer, V. N. Goncharov, J. P. Knauer, P. B. Radha, S. P. Regan, and W. Seka, "Effects of Nonuniform Illumination on Implosion Asymmetry in Direct-Drive Inertial Confinement Fusion."

A. V. Maximov, J. Myatt, R. W. Short, W. Seka, and C. Stoeckl, "Modeling of Two-Plasmon-Decay Instability in Direct-Drive ICF Experiments."

J. Myatt, A. V. Maximov, R. W. Short, J. A. Delettrez, and C. Stoeckl, "Hybrid Particle-in-Cell Simulations of MeV Electron Transport in Fast-Ignition Targets."

J. R. Rygg, J. A. Frenje, C. K. Li, F. H. Séguin, R. D. Petrasso, J. A. Delettrez, V. Yu. Glebov, V. N. Goncharov, D. D. Meyerhofer, T. C. Sangster, J. M. Soures, and C. Stoeckl, "An Empirical, Dynamic Mix Model for ICF Implosions."

W. Seka, C. Stoeckl, R. Jiang, R. E. Bahr, T. C. Sangster, R. S. Craxton, J. A. Delettrez, A. V. Maximov, J. Myatt, and R. W. Short, "Scattered Light Measurements from Spherical Implosions on OMEGA."

R. W. Short, "On the Convective Two-Plasmon-Decay Instability in Inhomogeneous Plasmas."

---

The following presentations were made at CLEO 2004, San Francisco, CA, 16–21 May 2004:

V. Bagnoud, I. A. Begishev, M. J. Guardalben, J. Puth, and J. D. Zuegel, "Multiterawatt Laser as a Front End for the OMEGA EP (Extended Performance) Laser Chain."

J. Li, T. Y. Hsiang, and W. R. Donaldson, "Study of Metal–Semiconductor–Metal Ultraviolet Photodiodes in Picosecond Regime."

A. V. Okishev, J. R. Marciante, and J. D. Zuegel, "A Novel Discrete-Arbitrary-Picket-Pulse–Shaping System for the OMEGA Laser Fusion Facility."

J.-R. Park, W. R. Donaldson, K. Kearney, and R. Sobolewski, "Arbitrary Wave Profile Generation of a Laser Using a Digital Micromirror Device."

J. D. Zuegel, V. Bagnoud, T. Mooney, and P. Dumas, "Wavefront Correction of Laser Rods Using Magnetorheological Finishing (MRF)."

---

S. G. Lukishova, A. W. Schmid, C. M. Supranowitz, N. Lippa, A. J. McNamara, R. W. Boyd, and C. R. Stroud, Jr., "Deterministically Polarized, Room-Temperature Single-Photon Source: Single-Dye Molecule Fluorescence in Liquid Crystal Host," IQEC, San Francisco, CA, 16–21 May 2004.

---

A. Trajkovska-Petkoska, R. Varshneya, T. Z. Kosc, K. L. Marshall, and S. D. Jacobs, "Electro-Optical Response of Shaped Polymer Cholesteric Liquid Crystal Flakes in an AC Field," Great Lakes Photonics Symposium, Cleveland OH, 7–11 June 2004.

---

L. B. Glebov, L. N. Glebova, V. I. Smirnov, M. Dubinskii, L. D. Merkle, S. Papernov, and A. W. Schmid, "Laser Damage Resistance of Photo-Thermo-Refractive Glass Bragg Gratings," Solid State and Diode Laser Technology Review, Albuquerque, NM, 8–10 June 2004.

---

J. B. Oliver and D. Talbot, "Optimization of Electron-Beam Deposition for Large-Aperture NIF Substrates in a Planetary Rotation System," Optical Interference Coatings, Ninth Topical Meeting, Tucson, AZ, 27 June–2 July 2004.

---

V. Yu. Glebov, C. Stoeckl, T. C. Sangster, S. Roberts, and G. J. Schmid, "NIF Neutron Bang-Time Detector Prototype Test on OMEGA," ICOPS 2004 31st IEEE International Conference on Plasma Science, Baltimore, MD, 28 June–1 July 2004.

---

T. C. Sangster, "Progress Toward Validation of the Direct-Drive Ignition Concept at OMEGA," 31st European Physical Society Conference on Plasmas Physics, London, United Kingdom, 28 June–2 July 2004.

---

The following presentations were made at SPIE's 49th Annual Meeting, Denver, CO, 2–6 August 2004:

S. D. Jacobs, "International Innovations in Optical Finishing."

K. L. Marshall, E. Kimball, S. McNamara, T. Z. Kosc, A. Trajkovska-Petkoska, and S. D. Jacobs, "Electro-Optical Behavior of Polymer Cholesteric Liquid Crystal Flake/Fluid Suspensions in a Microencapsulation Matrix."

---

The following presentations were made at the 7th International Conference on Tritium Science and Technology, Baden-Baden, Germany, 12–17 September 2004:

S. Costea, S. Pisana, N. P. Kherani, F. Gaspari, T. Kosteski, W. T. Shmayda, and S. Zukotynski, "The Use of Tritium in the Study of Defects in Amorphous Silicon."

T. Kosteski, N. P. Kherani, W. T. Shmayda, S. Costea, and S. Zukotynski, "Nuclear Batteries Using Tritium and Thin-Film Hydrogenated Amorphous Silicon."

W. T. Shmayda, "Metal Decontamination Using Low-Temperature Plasmas."

W. T. Shmayda and R. D. Gallagher, "Recovering Tritium from a Variety of Tritiated Waste Streams."

W. T. Shmayda, D. R. Harding, L. D. Lund, R. Janezic, and T. W. Duffy, "Handling Cryogenic DT Targets at the Laboratory for Laser Energetics."

W. T. Shmayda and N. P. Kherani, "Measuring Tritium Activity in Process Loops with Nude Baynard–Alpert Gauges."

---

P. A. Jaanimagi, R. Boni, D. Butler, S. Ghosh, W. R. Donaldson, and R. L. Keck, "The Streak Camera Development at LLE," 26th International Congress on High-Speed Photography and Photonics, Alexandria, VA, 20–24 September 2004.

---

The following presentations were made at the Boulder Damage Symposium XXXVI, Boulder, CO, 20–22 September 2004:

S. Papernov and A. W. Schmid, "High-Spatial Resolution Studies of UV-Laser Damage Morphology in $SiO_2$ Thin Films with Artificial Defects."

A. L. Rigatti, "Cleaning Process Versus Laser Damage Threshold of Coated Optical Components."

UNIVERSITY OF
ROCHESTER